frontiers | Research Topics

Characterization and application of magneto-sensitive soft materials

Edited by
Zhili Zhang, Decai Li, Miao Yu, Xiaodong Niu and Weihua Li

Published in
Frontiers in Materials

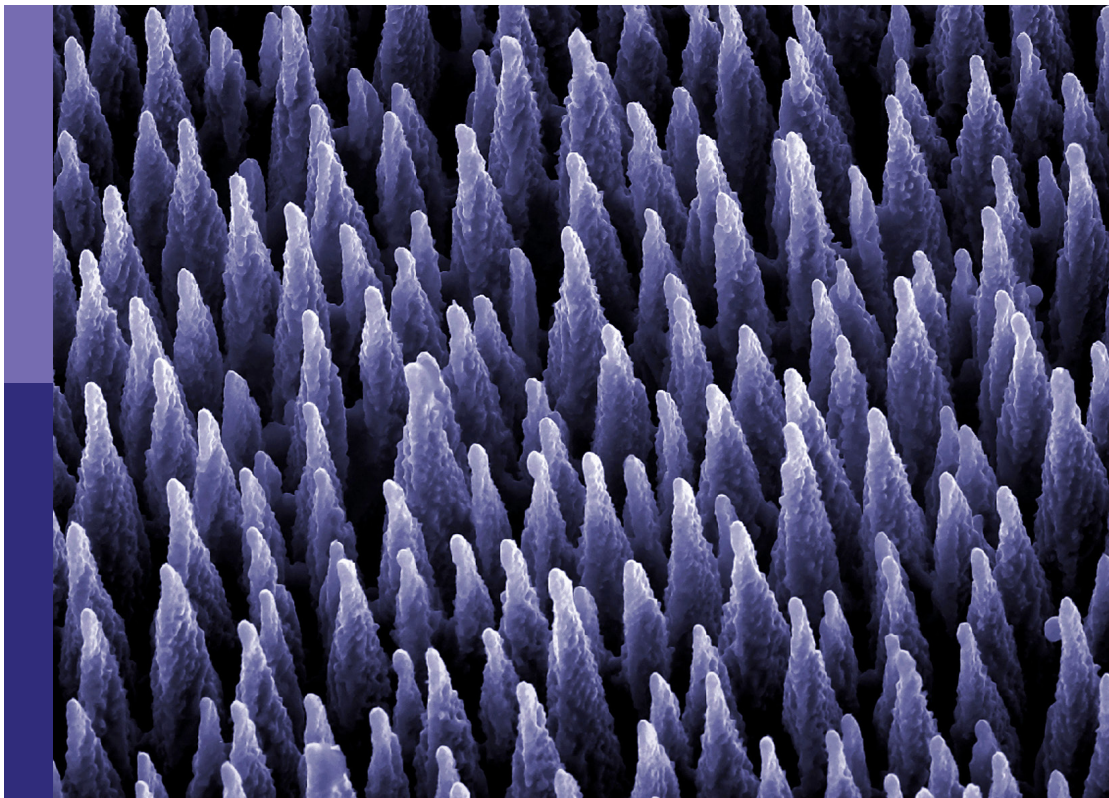

ISSN 1664-8714
ISBN 978-2-8325-2562-3
DOI 10.3389/978-2-8325-2562-3

About Frontiers

Frontiers is more than just an open access publisher of scholarly articles: it is a pioneering approach to the world of academia, radically improving the way scholarly research is managed. The grand vision of Frontiers is a world where all people have an equal opportunity to seek, share and generate knowledge. Frontiers provides immediate and permanent online open access to all its publications, but this alone is not enough to realize our grand goals.

Frontiers journal series

The Frontiers journal series is a multi-tier and interdisciplinary set of open-access, online journals, promising a paradigm shift from the current review, selection and dissemination processes in academic publishing. All Frontiers journals are driven by researchers for researchers; therefore, they constitute a service to the scholarly community. At the same time, the *Frontiers journal series* operates on a revolutionary invention, the tiered publishing system, initially addressing specific communities of scholars, and gradually climbing up to broader public understanding, thus serving the interests of the lay society, too.

Dedication to quality

Each Frontiers article is a landmark of the highest quality, thanks to genuinely collaborative interactions between authors and review editors, who include some of the world's best academicians. Research must be certified by peers before entering a stream of knowledge that may eventually reach the public - and shape society; therefore, Frontiers only applies the most rigorous and unbiased reviews. Frontiers revolutionizes research publishing by freely delivering the most outstanding research, evaluated with no bias from both the academic and social point of view. By applying the most advanced information technologies, Frontiers is catapulting scholarly publishing into a new generation.

What are Frontiers Research Topics?

Frontiers Research Topics are very popular trademarks of the *Frontiers journals series*: they are collections of at least ten articles, all centered on a particular subject. With their unique mix of varied contributions from Original Research to Review Articles, Frontiers Research Topics unify the most influential researchers, the latest key findings and historical advances in a hot research area.

Find out more on how to host your own Frontiers Research Topic or contribute to one as an author by contacting the Frontiers editorial office: frontiersin.org/about/contact

Characterization and application of magneto-sensitive soft materials

Topic editors

Zhili Zhang — Beijing Jiaotong University, China
Decai Li — Tsinghua University, China
Miao Yu — Chongqing University, China
Xiaodong Niu — Shantou University, China
Weihua Li — University of Wollongong, Australia

Citation

Zhang, Z., Li, D., Yu, M., Niu, X., Li, W., eds. (2023). *Characterization and application of magneto-sensitive soft materials*. Lausanne: Frontiers Media SA. doi: 10.3389/978-2-8325-2562-3

Table of contents

frontiers | Frontiers in Materials

TYPE Editorial
PUBLISHED 15 May 2023
DOI 10.3389/fmats.2023.1210416

OPEN ACCESS

EDITED AND REVIEWED BY
Yancheng Li,
Nanjing Tech University, China

*CORRESPONDENCE
Zhili Zhang,
zlzhang@bjtu.edu.cn

RECEIVED 22 April 2023
ACCEPTED 08 May 2023
PUBLISHED 15 May 2023

CITATION
Zhang Z, Li D, Yu M, Niu X and Li W (2023), Editorial: Characterization and application of magneto-sensitive soft materials.
Front. Mater. 10:1210416.
doi: 10.3389/fmats.2023.1210416

Editorial: Characterization and application of magneto-sensitive soft materials

Zhili Zhang[1]*, Decai Li[2], Miao Yu[3], Xiaodong Niu[4] and Weihua Li[5]

[1]Institute of Magnetic Fluids, School of Mechanical, Electronic and Control Engineering, Beijing Jiaotong University, Beijing, China, [2]State Key Laboratory of Tribology, Tsinghua University, Beijing, China, [3]Key Laboratory for Optoelectronic Technology and Systems, Ministry of Education, College of Optoelectronic Engineering, Chongqing University, Chongqing, China, [4]Department of Mechanical Engineering, College of Engineering, Shantou University, Shantou, China, [5]School of Mechanical, Materials Mechatronic and Biomedical Engineering, University of Wollongong, Wollongong, NSW, Australia

KEYWORDS

magnetic fluids (MF), magnetorheological fluids (MRF), magneto-sensitive soft materials, non-contact sealing, torsional vibration damper, intelligent material, energy absorber

Editorial on the Research Topic
Characterization and application of magneto-sensitive soft materials

Background

Magneto-sensitive soft materials are new synthetic functional materials that is normally composed of ferromagnetic or ferrimagnetic particles (size in a range from several nanometers to hundreds of micrometers), carriers (including water, organic solvent, liquids, gels, polymer and foams), surfactants and necessary additives. Being different from "hard" solid materials, "soft" means magneto-sensitive materials exist in the form of colloidal liquids, gels, and elastomers, such as magnetic fluids (MF), also called ferrofluids or magnetic liquids, magnetorheological fluids (MRF), magnetorheological gels (MRG), magnetorheological elastomers (MRE) and magnetorheological foams (MRFoam), so as to possess fluidity and magnetism simultaneously and can be easily deformed by applying external magnetic field force. Differences in the size of the magnetic particles and different carriers bring to magneto-sensitive soft materials distinct characteristics and behavior and provide many new perspectives and ideas for engineering application. This Research Topic covers innovations and applications in the field of different magneto-sensitive soft materials. We are proud to present 10 peer-reviewed contributions offering the latest insights on magnetic fluids and magnetorheological fluids.

Major highlights of the contributions

Magnetic fluids are nanocolloids made up of nanometer-sized ferromagnetic particles dispersing in a carrier liquid (typically comprises three parts: base carrier liquid, surfactant, and ferromagnetic particles). Since the particles are easier to agglomerate, ferromagnetic particles are typically coated with surfactants to prevent

agglomeration. Magnetic nanoparticles are uniformly disseminated in the carrier liquid with the assistance of surfactants, which play a crucial role in the magnetic fluid composition. Li et al. systematically studied the coating state and colloidal stability of oleic acid (OA) and 3-(N,N-Dimethylmyristylammonio) propanesulfonate (DP) coated magnetite nanoparticles in the polar and apolar carrier liquid. The total Gibbs interfacial energy was analyzed based on Van Oss-Chaudhry-Good and DLVO theory to describe the behaviors of coated particles in solvents. Zang et al. studied the effect of different fatty acids as surfactants on the rheological properties of magnetic fluids. The results showed that the mixed fatty acids showed greater viscosity growth and a greater slope of the viscosity growth curve than the magnetic fluids dispersed with a single acid. This indicates that the mixed fatty acids have more stable rheological properties. The viscousity-temperature performance of kerosene-base magnetic fluids at low temperatures can be improved by adjusting the ratio of mixed fatty acids. The most typical application of magnetic liquids is sealing, which has the outstanding advantages of zero leakage, long life and low resistance. Magnetic fluid seals as a class of non-contact sealing technology have been a research focus. In order to solve the problem of the pole shoes in the ferrofluid seal being easily damaged under the situation of the large radial beating of the main shaft, Liu et al. proposed a new structure of the ferrofluid seal that use a radial-charged ring magnet as the magnetic source. Considering that the ring magnets have problems of uneven magnetization and installation difficulties, use split magnets to take the place of ring magnets. Experiments and simulations were conducted on the above new structures, and all structures have a certain sealing pressure, which presents a reference example for the innovative design of magnetic fluid sealing structures. For the requirement of high vacuum and leakage rate of some small diameter low speed devices, Liu et al. designed a dual magnetic multi-stage magnetic fluid seal device by analyzing the advantages and disadvantages of four different vacuum magnetic fluid seal devices. The magnetic field strength and distribution of this seal device were analyzed using Ansys simulation software, and the proposed device was optimized by the calculation results. Compared with the traditional seal form, the multi-magnetic multi-stage magnetic fluid seal device has low processing difficulty, high reliability, and good pressure resistance performance. Although magnetic liquid sealing is widely used, but once magnetic liquid is injected into the structure of seal, it is difficult to estimate the working status of the magnetic fluid in the gap and then predict the failure. This hinders the further application of magnetic fluid seals in some important application, such as nuclear reaction. Therefore, it is imperative to find a non-destructive testing method to estimate the sealing status of the magnetic fluid seal. Chen et al. found that the state of the seal could be estimated by analyzing the acoustic emission (AE) signals generated during different magnetic fluid seals. By conducting the pressure test, analyzing the characteristic value of the acoustic emission signal, this is the first experiment of verifying the acoustic emission technique of magnetic fluid sealing. Dai et al. further proposed to perform higher-order cumulative image processing on sound signals and train convolutional neural network models for autonomous learning of image features, and experiments showed that the accuracy of the trained models for image recognition was much higher than other methods.

In addition to magnetic fluids, magnetorheological fluids (MRF) is another magneto-sensitive soft materials which been studied extensively. MRF are promising in controllable damping based on regulated apparent viscosity under magnetic field control and have been employed in various damping devices. He et al. designed a new type of variable damping MR torsional damper (MRTD) and proposed a semi-active control method to effectively control the torsional vibration of the crankshaft under multiple harmonic resonances, and a joint control simulation analysis was performed using Amesim and Matlab software. The simulation results indicated that the skyhook damping control significantly reduced the torsional vibration amplitude under both acceleration and uniform speed conditions, verifying the effectiveness of the skyhook-based control strategy for MRTD. Zou et al. signed and fabricated a magnetorheological energy absorber (MREA) with disc springs as recoiling parts, modeled the MR fluid flow based on the Bingham constitutive model, and then carried out unsteady extension based on the quasi-steady model. The experimental tests of the MREA show that the unsteady extension of the quasi-steady model can designate the behaviors of the MREA in different impact speeds better than the original; thus, the controllability of the MREA is verified. MR foam is a newly developed porous intelligent material, which can change its characteristics continuously, actively and reversibly under controllable external magnetic action, but its stiffness and storage modulus of foam are still very low and insufficient, thus limiting its application potential. Thus, Khaidir et al. improved the structure and storage modulus of MR foam by adding silica nanoparticles as an additive. By examining its rheological properties, it is known that the storage modulus of MR foam was increased by 260% with the addition of silica nanoparticles, especially at 4 wt%, due to the highest stiffness between 45 and 162 kPa. The results show that silica nanoparticles have good dispersion in the foam matrix, improve and strengthen the microstructure of MR foam, thus increasing the stiffness and storage modulus of MR foam. To reveal the transient temperature distribution pattern inside the MR grease torsional vibration damper and explore the relationship between the current and internal temperature of the device. Xiao et al. performed transient temperature simulation for MR grease devices, the results of the analysis reveal the internal temperature distribution and temperature rise characteristics of the torsional vibration damper, which provide a theoretical basis for the structural optimization and control strategy design of the MRG torsional vibration damper considering temperature as a factor.

Summary

These Research Topic contributions provide information about the latest developments in magneto-sensitive soft

materials in relation to various aspects, such as material development and characterization, modelling, new structural design of the equipment, numerical calculation, simulation. The editors hope that you find these articles useful and are inspired by them.

Author contributions

ZZ prepared the draft. DL, MY, XN, and WL edited the draft. All authors listed have made a substantial, direct, and intellectual contribution to the work and approved it for publication. All authors contributed to the article and approved the submitted version.

Conflict of interest

The authors declare that the research was conducted in the absence of any commercial or financial relationships that could be construed as a potential conflict of interest.

Publisher's note

frontiers | Frontiers in Materials

ORIGINAL RESEARCH
published: 13 June 2022
doi: 10.3389/fmats.2022.879699

Experimental Study and Simulation on the Seal Pressure of a Ferrofluid Seal Using Radial-Charged Magnets

Jiawei Liu[1]*, *Decai Li*[1,2] *and Zhili Zhang*[1]

[1]School of Mechanical and Electronic Control Engineering, Beijing Jiaotong University, Beijing, China, [2]State Key Laboratory of Tribology Tsinghua University, Beijing, China

As one of the most mature applications of ferrofluid, the pole shoes of a ferrofluid seal are easily damaged under the situation of the large radial beating of the main shaft. Meanwhile, due to the small size, the pole teeth commonly used in pole shoes harbor problems such as poor processability and low seal pressure under a large gap. In order to solve the aforementioned problems, we proposed a new structure of the ferrofluid seal that uses a radial-charged ring magnet as the magnetic source. Then, considering that the ring magnets have problems of uneven magnetization and installation difficulties, we used split magnets to take the place of ring magnets and proposed the second new structure. According to the study on the distribution of magnetic field in seal gap axially and circumferentially, we obtained the simulation results of the two new structures' seal pressure. The results revealed that the new structure of the ferrofluid seal with rectangular magnets can solve the aforementioned problems and exhibited a certain amount of sealing pressure.

Keywords: ferrofluid seal, experimental study, finite element analysis, without pole shoes, split magnet

OPEN ACCESS

Edited by:
Marcelo J. Dapino,
The Ohio State University,
United States

Reviewed by:
Xingzhe Wang,
Lanzhou University, China
Xufeng Dong,
Dalian University of Technology, China

***Correspondence:**
Jiawei Liu
lidecai@tsinghua.mail.edu.cn

Specialty section:
This article was submitted to Smart Materials, a section of the journal Frontiers in Materials

Received: *20 February 2022*
Accepted: *28 April 2022*
Published: *13 June 2022*

Citation:
Liu J, Li D and Zhang Z (2022) Experimental Study and Simulation on the Seal Pressure of a Ferrofluid Seal Using Radial-Charged Magnets. Front. Mater. 9:879699. doi: 10.3389/fmats.2022.879699

INTRODUCTION

Ferrofluid (FF) is a new class of nano-functional materials, which has fluidity and magnetic performance (Li, 2010). Magnetic performance enables it to respond to the effects of external magnetic fields, and fluidity allows it to form any shape to meet various needs. FF has been widely used in aerospace, military industry, and petrochemical fields (Rosensweig, 1985; Raj and Boulton, 1987; Li et al., 2012; Yang et al., 2012; Wang et al., 2019). The most mature application of the magnetic liquid is a magnetic liquid seal. The FF seal has a very wide range of applications, which can be applied in the static seal, dynamic seal, rotary seal, and reciprocating seal. The FF seal has the following advantages: zero leakage, long service life, high reliability, non-pollution, high-speed resistance, optimal torque transfer, and low viscosity friction. In some ways, due to the aforementioned advantages of the FF seal, it cannot be replaced by a traditional seal. Therefore, the FF seal has been widely used in many fields. (Du and Lin, 2006; Li, 2010). Though the FF seal has many irreplaceable advantages, we still need to make structural innovations to adapt to complex working conditions. So due to their small size, pole shoes and pole teeth have poor processability and quality. When the main shaft has unavoidable radial runout, the seal gap changes, and the pole teeth get hurt easily and have problems of poor sealing performance. To solve the aforementioned problems, we used a radial-charged ring magnet as the magnetic source of the new FF seal, also called the FF radial-charged seal. Then, considering the uneven magnetization problem and the installation difficulty of the ring magnet, referring to the traditional replacement solution, we used split magnets

to replace the ring magnet. We compared the seal pressure of the new structure with the classic FF seal, analyzed their characteristics and applicable conditions, and provided reference examples for the innovative design of the FF seal structure.

PRINCIPLE AND STRUCTURE

Principle of the FF Seal

The FF seal uses the magnetic response properties of the FF to the magnetic field to seal. After injecting into the gap between the magnetic circuit formed by the magnetic pole pieces and the shaft, FF will become several "O"-shaped seals. The number of seal rings is also written as the seal stages. When the FF is affected by the external pressure, it moves in the heterogeneous magnetic field, but the uneven magnetic field will create a magnetic gradient to provide the magnetic force to fight against the external pressure, and reach a new balance in the end (Li, 2010; Yang and Li, 2016a).

Structure of FF Seal

Earlier, to get the maximum seal pressure of FF seals, WALOWIT, J A et al. (Szczech and Horak, 2017) had found the best structure of rectangular pole teeth, which can make the seal pressure equal at both sides of the pole teeth. Without being collided or scraped by the shaft, we can guarantee the seal performance of this structure easily. The sealing gap between the relatively rotating shaft and the pole shoes is the main working area of the FF seal. We often use a small seal gap such as 0.05–0.2 mm to improve the seal pressure of FF seals. However, the structure will be easily collided or scraped by the shaft, which could cause a decrease in the seal pressure or leakage. In particular, for the shaft with the big radial runout, the aforementioned structure is commonly unreliable. Most of the solutions to solve this problem are increasing the sealing gap between the relatively rotating shaft and pole shoes, but the seal pressure of the FF seal will decrease significantly. In Yang and Li (2016a), in order to solve this problem, X. Yang had studied a converging stepped FF seal for a large seal gap, which improves the seal pressure of the FF seal under the large gap. However, the complexity of the device and high requirements for installation reduce the reliability of the seal and add the difficulties of adding FF. In van der Wal et al. (2020), in order to solve the aforementioned problems, Karoen van der Wal proposed a FF seal whose magnetic source is an axial-charged ring magnet setting on the shaft. As shown in **Figure 1A**, the seal contains a nonmagnetic ring, an axial-charged ring magnet, and a nonmagnetic ring successively set on the shaft. Then, the FF will be injected into the seal gap to offer seal pressure. Inspired by this, we proposed a new structure of the FF seal using radial-charged magnetized magnetic rings as a magnetic source, as shown in **Figure 1B**. In terms of optimization of permanent magnets, many types of optimization are designed to avoid problems such as installation difficulties and uneven magnetization of the ring magnet. In He et al. (2014), to solve the aforementioned problems, D. Li had studied a magnet structure composed of many small cylindrical magnets and verified the seal pressure by experiments. It also certificated the feasibility of replacement with split magnets first. In publication (Wang) Szczech, M designed and analyzed the seal pressure of the FF seal by experiments, whose magnetic source is made up of a cylindrical magnet but did not propose the optimal design and application conditions of the magnetic source. In He et al. (2019) J. Liu made an optimized design and the simulation analysis of the various structures of the permanent magnets through the simulation analysis and provided a selection scheme for the magnetic source structure of large-diameter FF seals. However, the optimization design of the aforementioned scholars is only limited to the classic structure of the FF seal. There are still poor seal reliability and high scrap possibility caused by the shaft runout and installation difficulties. When the ring magnets have difficulties in processability, installation, and uneven magnetization, we can replace them with split magnets named FF split magnet seal, as shown in **Figure 1C**, which not only solve the problems but also provide enough magnetic field for seal.

THEORETICAL RESEARCH

From the Bernoulli equation of FF and the corresponding assumption, the total seal pressure of the FF seal can be approximately expressed as (Li et al., 2004; Li, 2010; Yuichi et al., 2015; Yang and Li, 2016b; Li and Hao, 2018; Zhang et al., 2018)

$$p=\sum_{i=1}^{n} p_i = \sum_{i=1}^{n} \int_{H_{i_{\min}}}^{H_{i_{\max}}} \mu_0 M_s dH, \tag{1}$$

where n is the number of seal stages, and p_i is the seal pressure of stage i in the FF seal. The seal pressure provided by each seal stage could be approximately considered identical; H_{imin} and H_{imax} are the minimum and maximum magnetic field strength under stage i of the seal gap, respectively; μ_0 is the permeability of vacuum; M_s is the saturation magnetization of the magnetic fluid. We can use coal-based FF here. According to its magnetization curve that is shown in **Figure 2**, when the magnetic field strength is greater than 200 kA/m, its saturation magnetization M_s is taken as 20 kA/m.

FEA OF FF SEALS

Relevant Parameter and Experiment

As shown in **Figure 3A**, it is a classic rectangular pole teeth structure of FF seal whose seal gap (distance between pole teeth and shaft) is 0.1 mm. With this gap confirmed, we set the pole teeth width L_t, pole teeth distance L_s, and pole teeth height L_h as 0.2 mm,、0.8 mm,、and 0.7 mm, respectively. The design theory has been successfully applied to many FF seals (Chi, 1993; Zhao et al., 2006; Yang et al., 2013), which are well sealed and highly reliable under many situations. Due to

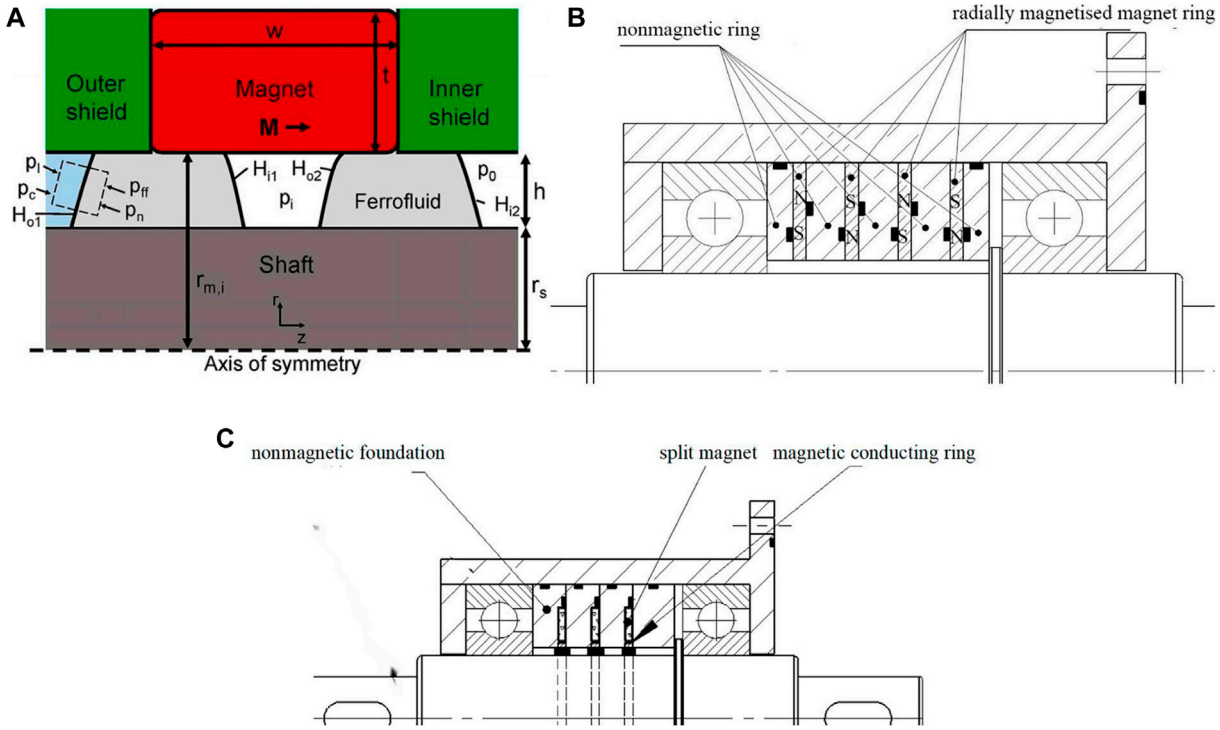

FIGURE 1 | Structure of the FF seal. **(A)** FF seal proposed by Karoen van der Wal etc (van der Wal et al., 2020); **(B)** FF radial-charged seal; **(C)** FF split magnet seal.

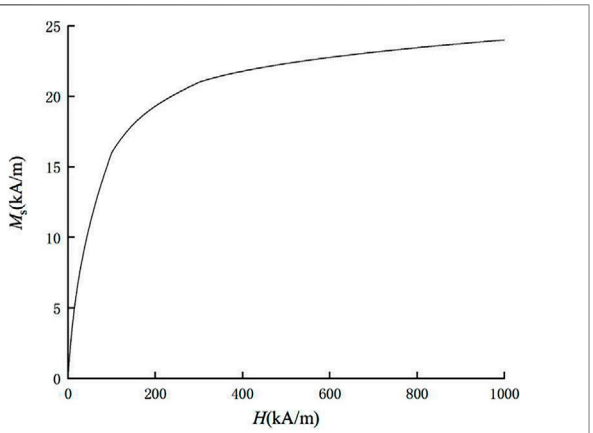

FIGURE 2 | Magnetization curve of the coal-based FF.

their small size, pole teeth have poor processability and quality. The main shaft has unavoidable radial runout; therefore, when the seal gap is changing, the pole teeth get hurt easily and have poor sealing performance. So we let the newly structured FF radial-charged seal remove the pole teeth, as shown in **Figure 3B**. To solve the ring magnets' problems of processability, installation, and uneven magnetization, we replaced ring magnets with split magnets. To install split magnets stably, we adjusted the structure of the nonmagnetic ring to a nonmagnetic foundation, as shown in **Figures 3C,D**, which can not only raise the magnetic field but also meet the positioning needs of split magnets.

At first, we found out the better structural parameter of the FF seal by FEA, as shown in **Figure 4** and **Table 1**. **Table 1** shows the structural size of the classic FF seal, the FF radial-charged seal, and the FF split magnet seal. We set the shaft of the seal as 30 mm to make the calculation more accurate and reduce the calculation time. Then, we used FEA to compare the seal pressure of these structures and analyze the best choice of split magnets, in order to get the optimal structural design of the FF split magnet seal. Here, we mainly discussed the diameter or thickness L_{h1} of the split magnet, the space L_{h2} between split magnets, and the length L_{h3} of the split magnet. In order to reduce demagnetization, the magnet cross section of the working site should be designed as a square. We simulated the FF cuboid magnet seal with $L_{h1} = L_{h3} = 3$ mm and $L_{h2} = 3$ mm under the sealing gap of 0.1 mm that has 0.1 MPa seal capacity. We considered such a structure as an example and used the control variable method to discuss the effects of L_{h1} and L_{h2} on seal capacity. The results are shown in **Figure 4**. Considering the restrictive condition of process accuracy, the strength of the wall between magnets, and magnet size restriction, we take $L_{h1} = 4$ mm and $L_{h2} = 2$ mm. Twenty small magnets can be installed on one nonmagnetic foundation.

Then, according to the parameter, we processed the FF split magnet seal device to test its seal capacity. During the test, the

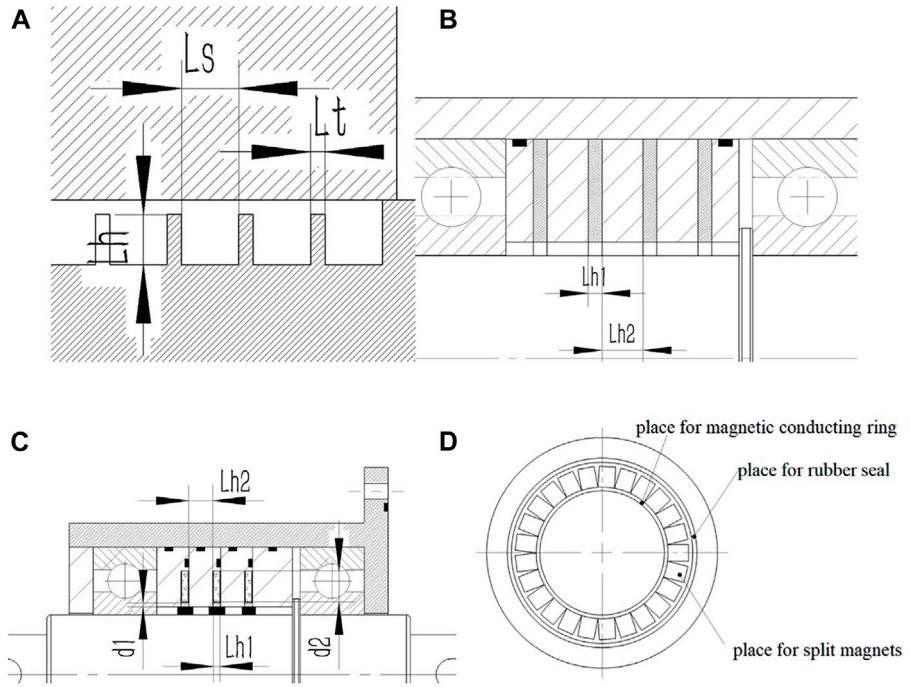

FIGURE 3 | Structural size of the FF seal. **(A)** Classic FF seal; **(B)** FF radial-charged seal; **(C)** FF split magnet seal; **(D)** nonmagnetic foundation.

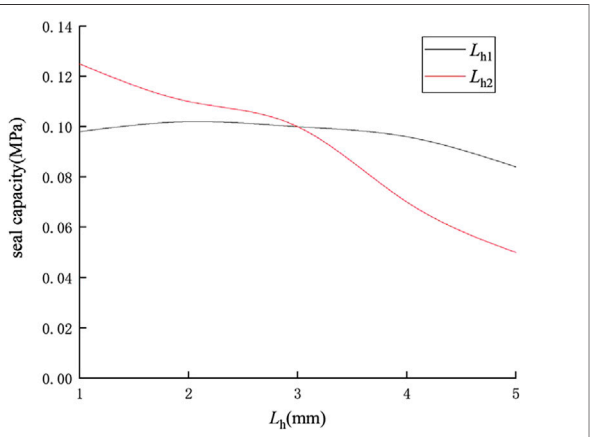

FIGURE 4 | Relationship between seal capacity and Lh.

air pressure is delivered from a pressure cylinder and adjusted by a pressure-reducing valve. The pressure in the sealed chamber is measured with a pressure gauge to range from 0 to 2 MPa. The rotational speed of the motor is controlled and displayed by using a controller. (Li et al., 2021). To examine cuboid magnet and cylindrical magnet seal capacity, the experimental study on the FF split magnet seal is divided into two parts: a static pressure test and a dynamic pressure test. In the experiment table, the two kinds of magnets installed on a nonmagnetic foundation and their relevant sizes are shown in **Figure 5** and **Table 1**, respectively. The device consists of a nonmagnetic shell, a shaft, bearings, nonmagnetic foundations, split magnets, and ferrofluids. About the choice of materials, magnetic parts, such as the shaft and the pole shoes, are made of magnetic materials, 2Cr13 here. Nonmagnetic sections, such as the nonmagnetic ring and the shell, are made of NdFeB with a

TABLE 1 | Relevant size (mm).

Name	Classic FF seal	FF Radial-Charged seal	FF split magnet seal	FF radial-charged seal with larger gap
Seal gap	0.1	0.1	0.1	0.5
Diameter of the shaft	30	30	30	30
Magnet size	Φ36 × 48 × 2	Φ30.6 × 56 × 2	Φ4×5 or 4 × 4×5	Φ31 × 56 × 2
Pole piece type	pole teeth	nonmagnetic ring	nonmagnetic foundation	nonmagnetic ring
Length of each seal stage	3	2	6	2

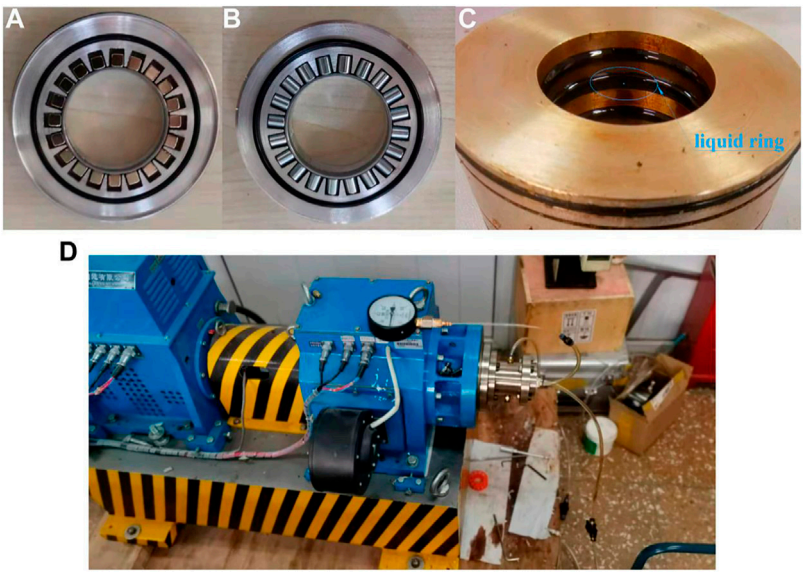

FIGURE 5 | Experimental device.**(A)** Cuboid magnets installed on nonmagnetic foundation; **(B)** cylindrical magnets installed on nonmagnetic foundation; **(C)** seal ring injected with FFs; **(D)** rotary seal experiment table.

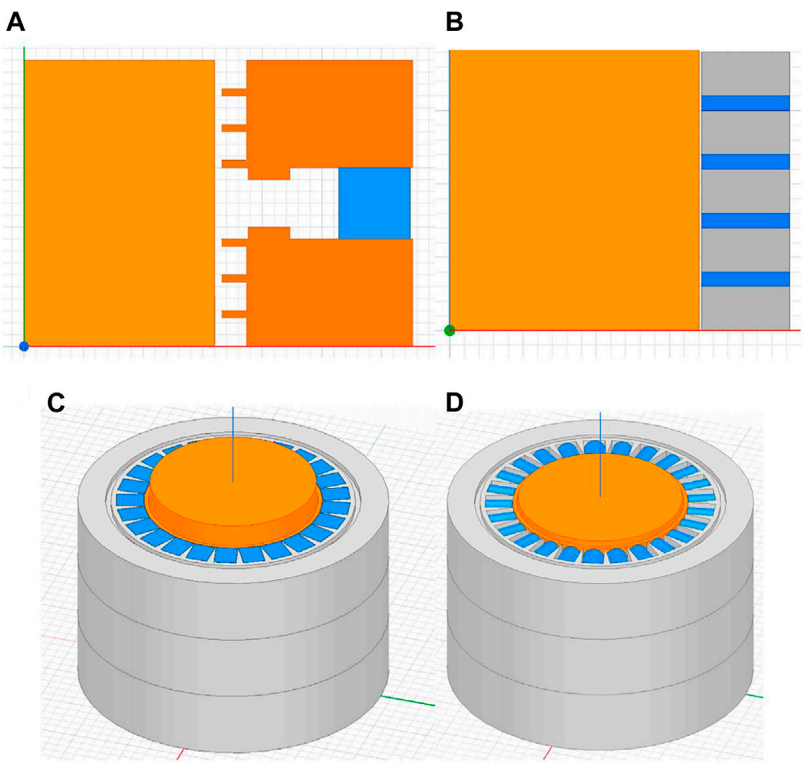

FIGURE 6 | Figure of the seal model. **(A)** Classic FF seal; **(B)** FF radial-charged seal; **(C)** FF cuboid magnet seal; **(D)** FF cylindrical magnet seal.

relative permeability of 1.05 and a coercive force of 8.9 e^5. The magnetization of the radial-charged ring magnet is shown in **Figure 5**.

Modeling and Simulation

For the classic FF seal and FF radial-charged seal, we used SolidWorks to draw the core of the sealing device of the

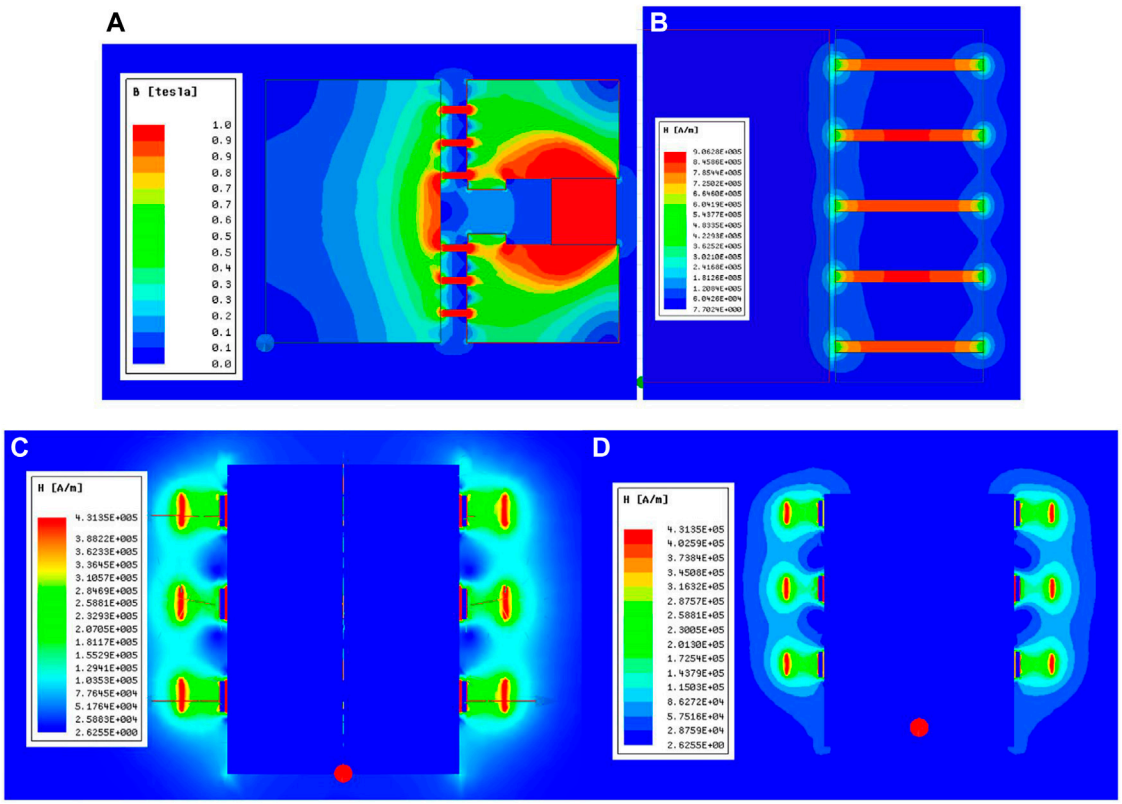

FIGURE 7 | Contour plot. **(A)** Classic FF seal; **(B)** FF radial-charged seal; **(C)** FF cuboid magnet seal; **(D)** FF cylindrical magnet seal.

aforementioned structure scheme. Then, we imported it to the Maxwell 2D module and set the geometry module as cylindrical about Z. The magnetization direction of radial-charged ring magnets is r in the cylindrical coordinate system. According to the Maxwell FEA, we can optimize the seal structure. It is not rigorous to analyze the FF split magnet seal by the Maxwell 2D module. So we decided to use the Maxwell 3D module to analyze, which can not only analyze the stability of FF "O"-shaped seals but also find the difference between the cuboid and cylindrical magnet, which are the most commonly used split magnets. The seal model, contour plot, and magnetic lines distribution are respectively shown in **Figures 6**–**8**. The classic FF seal, FF radial-charged seal, FF cuboid magnet seal, and FF cylindrical magnet seal are respectively shown in Figures (A), (B), (C), (D). In **Figure 6**, the blue part represents the magnet parts, the orange part represents the magnetic parts, and the gray represents the non-magnetic parts. Compared to **Figures 7C,D**, we can find the magnetic line distribution of a cuboid magnet is more centralized than a cylindrical magnet. So we can guess the magnetic fluid of the FF cuboid magnet seal is stronger and more uniform.

Date Processability

According to simulation and calculation, we get the magnetic field strength curve of all kinds of FF seals, which is shown in **Figure 8**. According to the aforementioned formula and the relevant knowledge of the magnetic fluid seal, in order to meet the saturation of the magnetic fluid, we observed that the magnetic field strength in the working gap, where magnetic fluid exists, should be greater than the 200 kA/m. In this condition, the difference in the axial magnetic field strength determines the maximum seal pressure. Then, we treated the simulation results by **formula (2)**. The results are shown in **Figure 8** and **Table 2**. From **Figure 9**, it is obvious to find out that the magnetic field strength curves in the seal gap of these new structures of FF seals are both similar to those of the classic FF seal, which has a significant magnetic field strength gradient. Therefore, we can preliminarily consider that these seals need to be analyzed. The seal pressure is calculated and analyzed in the following. In order to analyze the influence of the magnetic rings on the magnetic field distribution and choose the better split magnets between the cylindrical magnet and the cuboid magnet, we set two arcs at the mid and the edge of magnets in the seal gap to analyze the degree of magnetic field uniformity, which is shown in **Figure 10**. The results are shown in **Figures 11**,**12**, whose abscissa indicates the arc angle rotating around the shaft.

In terms of the experiment, the static pressure resistance experiment of the FF cuboid magnet seal and the FF cylindrical magnet seal were first carried out. Then, the experimental results and the simulation results are shown in **Figure 13**. The structure of the conductive ring is very important. If the conductive ring is removed, the small magnet will attach to

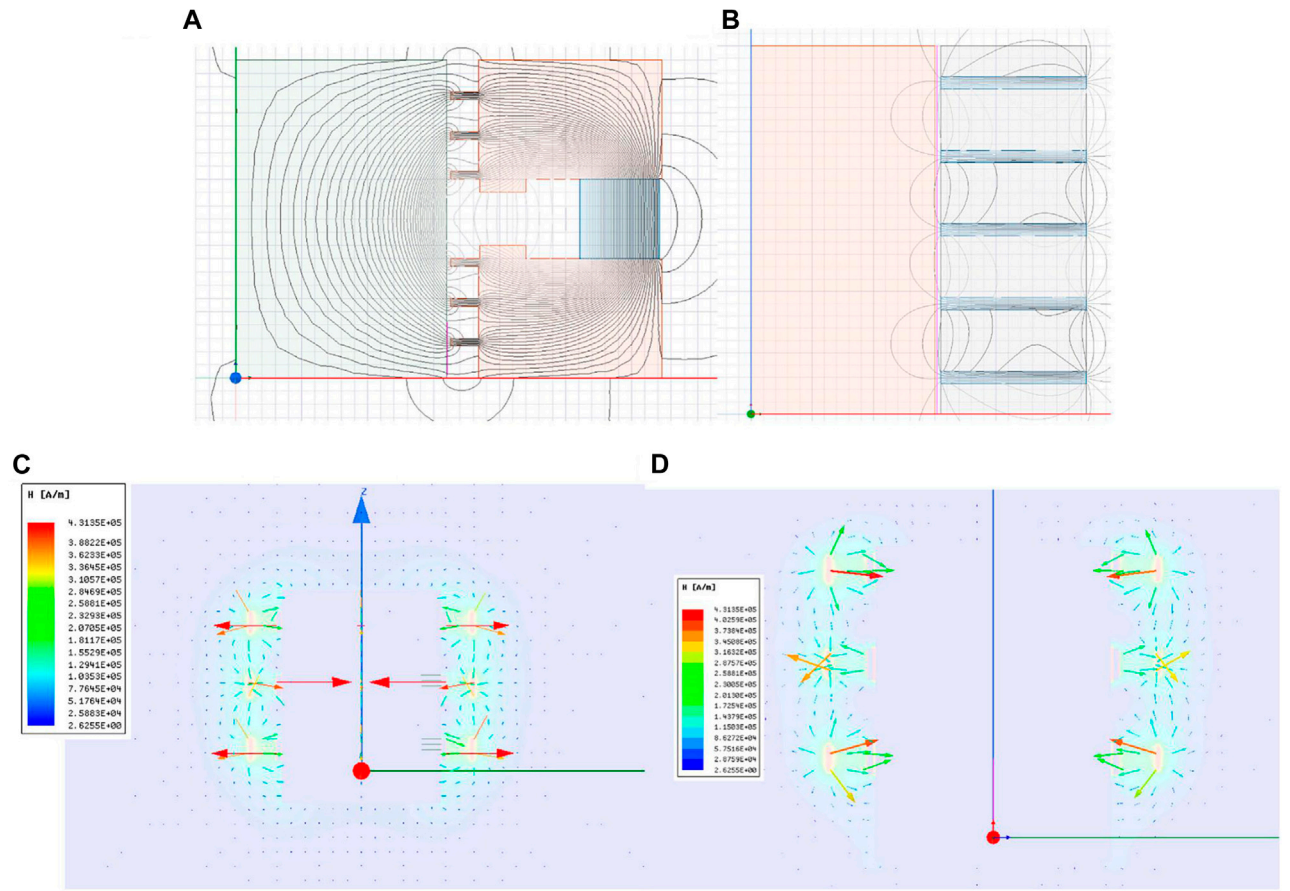

FIGURE 8 | Distribution map of magnetic lines. **(A)** Classic FF seal; **(B)** FF radial-charged seal; **(C)** FF cuboid magnet seal; **(D)** FF cylindrical magnet seal.

TABLE 2 | Simulation result.

Name	FF cuboid magnet seal	FF cylindrical magnet seal	classic FF seal	FF radial-charged seal	FF radial-charged seal with larger gap
Seal pressure of each stage (MPa)	0.025	0.018	0.029	0.033	0.26
H_{max} on the edge of magnets (A/m)	463	396		uniform distribution	
H_{min} on the edge of magnets (A/m)	371	251			
H_{max} on the middle of magnets (A/m)	648	558			
H_{min} on the middle of magnets (A/m)	462	372			

the shaft and cannot form a uniform magnetic fluid o-ring in the sealing gap. So the pressure capacity of the seal group without a conductive ring is 0. In order to prevent the leakage from the gap between the magnets and conductive rings or magnets and nonmagnetic foundations, we used silicone sealant to fill these gaps. A rotational pressure resistance experiment for the FF cuboid magnet seal was performed subsequently. But no matter how we adjust the sealing device, it seems to have a little gap between the shaft and the ring, and the starting torque was much larger than we imagined. We cannot find any rational result in the rotational experiment.

Result and Discussion

In this study, we analyzed the magnetic field of the classic FF seal, FF radial-charged seal, FF cuboid magnet seal, and FF cylindrical magnet seal in the seal gap. 1) From the magnetic field strength curve of the seal gap in **Figure 9**, we can find that the new structures of FF radial-charged seal and the FF split magnet seal can form a magnetic field with an axial gradient in the seal gap. From **formula (2)**, the magnetic field strength gradient can fix FF in the seal gap, which offers the seal pressure. According to the static experiment result in **Figure 13**, the seal capacity of the FF cuboid magnet seal

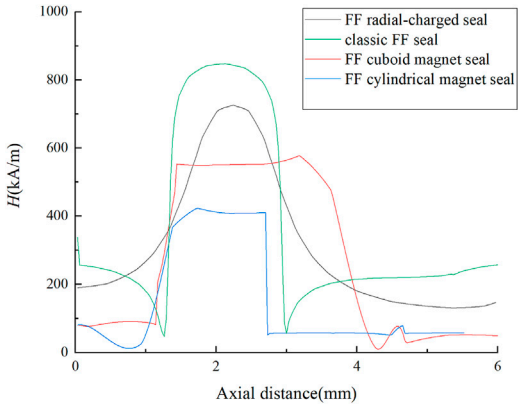

FIGURE 9 | Magnetic field strength curve of the seal gap of different structures of the magnetic fluid seal.

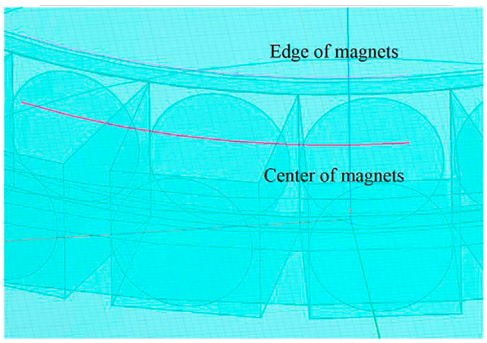

FIGURE 10 | Arcs in the seal gap.

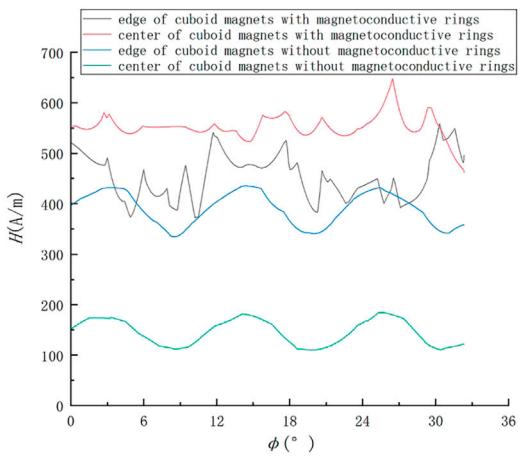

FIGURE 11 | Magnetic field in the seal gap with magnetic rings or not.

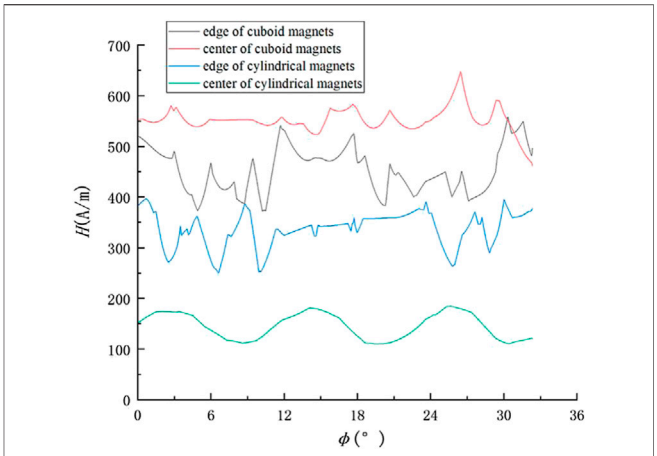

FIGURE 12 | Magnetic field in the seal gap with a different type of split magnets.

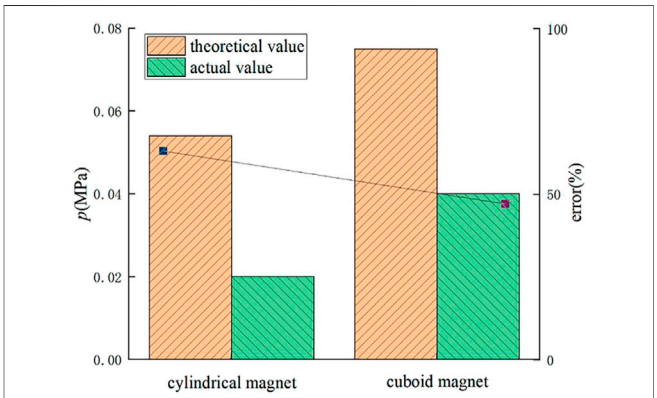

FIGURE 13 | Results of the static seal capacity experiment.

and the FF cylindrical magnet seal can be proved. 2) From **Table 2**, in terms of seal pressure, the FF radial-charged seal is larger than the other two FF split magnet seals. In **Figure 11**, the magnetic field intensity along the split magnets in the seal gap has regular fluctuation. The reason for this phenomenon is the presence of small gaps between the split magnets, which is greatly different from ring magnets. If we do not use the magnetic ring, the small magnets will stick to the shaft and lead to the leakage of the seal. So we set a magnetic ring between FF and magnets to address these problems. The design allows the seal to form a uniform and dense FF "O"-shaped sealing rings in the seal gap. 3) According to the seal size in **Table 2**, compared with the FF cuboid magnet seal and the FF cylindrical magnet seal, the FF radial-charged seal has more seal stages in the same space, larger seal pressure, and stability. It seems that the FF radial-charged seal is the best choice to solve the problems of the radial beating of the main shaft and low seal pressure under the large gap. However, the ring magnet is facing the problems of processability, installation, and uneven magnetization, so the seal pressure will drop or even fail. For seal, the seal pressure is not an absolute criterion, but how to meet the actual needs is more

important. 4) In **Figure 13**, we can find the FF cuboid magnet seal has a larger seal capacity than the FF cylindrical magnet seal. Meanwhile, the error of the latter is much larger than the former. The reason for the difference in error is probably that the FF liquid ring quality of the FF cylindrical magnet seal is poor. It can also be proved by **Table 2** and **Figure 12**. So we can consider that the FF cuboid magnet seal is the better choice than the FF cylindrical magnet seal.

CONCLUSION

1) According to FEA, we find that the three new structures have a certain seal pressure.
2) According to the experiments, the FF cuboid magnet seal has a larger seal capacity than the FF cylindrical magnet seal. It has solved the installation difficulties, vulnerability of pole teeth, and poor seal performance of classic FF seals in engineering. It has solved the problems of processability, installation, and uneven magnetization from ring magnets. Meanwhile, its seal pressure can meet the needs of many situations.
3) Although the nonmagnetic foundation of the FF cuboid magnet seal and the FF cylindrical magnet seal is complex, it can bring split magnets and magnetic rings before installation, which can reduce installation difficulties. However, due to the disadvantage of its large size, the FF split magnet seal has been better applied to the shaft with a large sealing space. So it is essential to analyze how to raise the utilization of seal space.

For future research directions: in **Figure 13**, the error in comparison between the actual value and theoretical value is larger than 40%, which is too high to convince us that the seal in the experiment is the best one. Along with the situation in the rotational experiment, we can find the problems with the structure. Due to the uneven distribution of the silicone sealant, there is a fixed problem with the magnetic ring. In future research, we will improve the structure of multiple small magnetic rings into the integrated magnetic ring and finish the rotational seal experiment.

DATA AVAILABILITY STATEMENT

The original contributions presented in the study are included in the article/Supplementary Material; further inquiries can be directed to the corresponding author.

AUTHOR CONTRIBUTIONS

Under the guidance of LD and ZZ, the author finished the manuscript.

REFERENCES

Chi, C. (1993). *Magnetic Fluid Hydrodynamics [M]*. Beijing: Beihang University Press.

Li, D. C., Zhang., H. N., and Zhang, Z. L.. Study on Magnetic Fluid Static Seal of Large Gap, *Kem*, 512-515. 2012. 1448-1454. doi:10.4028/www.scientific.net/kem.512-515.1448

Du, C., and Lin, H. (2006). Effect of the Magnetoconductive Pole Piece Structure on the Magnetic Fluid Seal Capacity[J]. *Chem. Equip. Technol.* (02), 71–73. doi:10.3969/j.issn.10077251.2006.02.021

He, X., Li, D., and Wang, H. (2014). Effects of Gravity on the Sealing Properties of Magnetic Fluids[J]. *Chin. J. Vac. Sci. Technol.* 34 (11), 1160–1163. doi:10.13922/j.cnki.cjovst.2014.11.05

He, X., Miao, Y., Wang, L., and Li, Z. (2019). Latest Development in Sealing of Liquid Medium with Magnetic Fluid[J]. *Chin. J. Vac. Sci. Technol.* 39 (05), 361–366. doi:10.13922/j.cnki.cjovst.2019.05.01

Li, D., and Hao, D. (2018). Major Problems and Solutions in Applications of Magnetic Fluid Rotation Seal[J]. *Chin. J. Vac. Sci. Technol.* 38 (07), 564–574. doi:10.13922/j.cnki.cjovst.2018.07.04

Li, D. (2010). *Theory and Application of Magnetic Fluid Seal[M]*. Beijing: Science Press.

Li, D., Xu, H., He, X., and Lan, H. (2004). Study on the Magnetic Fluid Sealing for Dry Roots Pump[J]. *J. Magnetism Magnetic Mater.* 289, 419–422. doi:10.1016/j.jmmm.2004.11.118

Li, D., and Yang, W. (2010). Experimental Study on Static Sealing of Magnetic Liquid with Large Diameter and Large Gap [J]. *Acta Armamentarii* 31 (03), 355–359.

Li, Z., Li, S., Wang, X., and Li, D. (2021). Numerical Simulation and Experimental Study on Magnetorheological Fluid Seals with Flexible Pole Pieces[J]. *IEEE Trans. MAGNETICS* 57 (10). doi:10.1109/tmag.2021.3094868

Liu, J., Li, D., and Zhang, Z. (2021). Magnet Design and Anti-pressure Analysis of New Magnetic Fluid Seal[J]. *J. Beijing Jiaot. Univ.* 42 (3), 1–7. (in Chinese). doi:10.11860/j.issn.1673-0291.20210035

Luo, E. (1993). The Cutting Point Effect and its Mathematical Expressions [J]. *Coll. Phys.* (06), 20–25.

Raj, K., and Boulton, R. J. (1987). Ferrofluids a Properties and Applications[J]. *Mater. Des.* 8 (4). doi:10.1016/0261-3069(87)90139-7

Rosensweig, R. E. (1985). *Ferrohydrodynamics[M]*. Cambridge: Cambridge University Press.

Szczech, M., and Horak, W. (2017). Numerical Simulation and Experimental Validation of the Critical Pressure Value in Ferromagnetic Fluid Seals[J]. *IEEE Trans. Magnetics* 53 (7), 4600601–4600605. doi:10.1109/tmag.2017.2672922

van der Wal, K., van Ostayen, R. A. J., and Lampaert, S. G. E. (2020). Ferrofluid Rotary Seal with Replenishment System for Sealing Liquids. *Tribol. Int.* 150, 106372. doi:10.1016/j.triboint.2020.106372

Wang, Z. *A Theoretical and Experimental Study on Mechanical-Magnetic Fluid Combined Sealing[D]*. Beijing: Beijing Jiaotong University.

Wang, Z., Li, D., Zhang, Y., Gao, Y., and Neumann, H. R. (2019). The Pressure Loading Process Among Stages of Magnetic Fluid Seal in Aqueous Environment[J]. *Tribol. Trans.* 62 (4). doi:10.1080/10402004.2019.1597241

Yang, X., and Li, D. C. (2016). Experimental Investigation of Diverging Stepped Magnetic Fluid Seals with Large Sealing Gap[J]. *Int. J. Appl. Electromagn. Mech.* 50 (3), 407–415. doi:10.3233/JAE-150117

Yang, X., and Li, D. C. (2016). Design and Experimental Study on Large Gap Polymerization Stair Type Magnetic Fluid Seal[J]. *Chin. J. Vac. Sci. Technol.* 36 (03), 258–262. doi:10.13922/j.cnki.cjovst.2016.03.02

Yang, X., Li, D., and Yang, W. (2012). Fluid Sealed Magnetic Road Design and Magnetic Field Analysis [J]. *J. Vac. Sci. Technol.* 32 (10), 919–922.

Yang, X., Li, Z., and Li, D. (2013). Numerical and Experimental Study of Magnetic Fluid Seal with Large Sealing Gap and Multiple Magnetic Sources[J]. *Sci. China Technol. Sci.* 56 (11). doi:10.1007/s11431-013-5365-4

Yuichi, M., Hiroshi, S., Hayato, Y., and Hidenori, S. (2015). Magnetic Fluid Seal for Linear Motion System with Gravity Compensator[J]. *Procedia CIRP* 33, 581–586. doi:10.1016/j.procir.2015.06.088

Zhang, Y., Li, D., Chen, Y., and Li, Z. (2018). A Comparative Study of Ferrofluid Seal and Magnetorheological Fluid Seal[J].

IEEE Trans. MAGNETICS 54 (12). doi:10.1109/tmag.2018.2868298

Zhao, M., Zou, J., and Hu, J. (2006). An Analysis on the Magnetic Fluid Seal Capacity[J]. *J. Magnetism Magnetic Mater.* 303 (2). doi:10.1016/j.jmmm.2006.01.060

Conflict of Interest: The authors declare that the research was conducted in the absence of any commercial or financial relationships that could be construed as a potential conflict of interest.

Publisher's Note: All claims expressed in this article are solely those of the authors and do not necessarily represent those of their affiliated organizations, or those of the publisher, the editors, and the reviewers. Any product that may be evaluated in this article, or claim that may be made by its manufacturer, is not guaranteed or endorsed by the publisher.

frontiers | Frontiers in Materials

ORIGINAL RESEARCH
published: 27 June 2022
doi: 10.3389/fmats.2022.893072

Colloidal Stability of Magnetite Nanoparticles Coated by Oleic Acid and 3-(N,N-Dimethylmyristylammonio) propanesulfonate in Solvents

Liu Li[1], *Decai Li*[1,2]* *and Zhili Zhang*[1]

[1]School of Mechanical, Electronic and Control Engineering, Beijing Jiaotong University, Beijing, China, [2]State Key Laboratory of Tribology, Tsinghua University, Beijing, China

In order to understand the factors affecting the colloidal stability in the carrier liquids of different ferrofluids, magnetite nanoparticles coated by surfactants 3-(N,N-dimethylmyristylammonio)propanesulfonate (DP) and oleic acid (OA) were fabricated as dispersions in diverse colloidal systems. The OA-coated magnetite could only be dispersed in the apolar carrier liquid ($\varepsilon_r < 5$), while DP-coated magnetite particles could establish a stable colloidal system in the polar base liquid ($\varepsilon_r > 5$) such as water and ethanol. The colloidal stability of OA-coated particles in the apolar solvents was mainly attributed to the steric repulsion of its outer thick liquid shell (~3 nm). Due to the absence of steric repulsion on the solid thin shell (~1 nm) on DP-coated magnetite, DP-coated particles could not be dispersed in the apolar liquid. In the polar liquid-based ferrofluids, DP-coated magnetite could form an electric double layer (EDL). The total Gibbs interfacial energy was analyzed based on Van Oss-Chaudhry-Good and DLVO theory to describe the behaviors of coated particles in solvents. In the case of neutral (pH = 7) water-based colloidal, DP-coated magnetite could establish an energy barrier of ~2.2 k_BT to prevent the particles from precipitation. Bare magnetite particles could form a relatively fragile colloid in a water system with an energy repulsion of ~1.2 k_BT. In contrast, OA-coated magnetite exhibited a severe phase separation in a water-based colloidal system due to its net attraction ~ −1.3 k_BT.

Keywords: ferrofluids, nanoparticls, surfactants, electrical double layer, DLVO theories

OPEN ACCESS

Edited by:
Wenbo Wang,
Inner Mongolia University, China

Reviewed by:
Andrew Jackson,
Lund University, Sweden
R. P. Pant,
National Physical Laboratory (CSIR), India

***Correspondence:**
Decai Li
lidecai@tsinghua.edu.cn

Specialty section:
This article was submitted to Polymeric and Composite Materials, a section of the journal Frontiers in Materials

Received: *09 March 2022*
Accepted: *05 May 2022*
Published: *27 June 2022*

Citation:
Li L, Li D and Zhang Z (2022) Colloidal Stability of Magnetite Nanoparticles Coated by Oleic Acid and 3-(N,N-Dimethylmyristylammonio) propanesulfonate in Solvents. Front. Mater. 9:893072. doi: 10.3389/fmats.2022.893072

INTRODUCTION

Ferrofluids are stable colloidal suspensions composed of carrier liquids and nanosized magnetic iron oxide particles (Rodríguez-Arco et al., 2011a; Jain et al., 2011; Medeiros et al., 2012; Pathak et al., 2019; Kumar et al., 2020). Due to the standard nanodiameter of iron oxide particles, magnetic colloidal suspension maintains its stability under gravitational and magnetic field gradients. As a combination of magnet and liquid, ferrofluids can be controlled by the magnetic field, which makes it become a promising candidate for many specific applications (Dailey et al., 1999; Hartshorne et al., 2004; Torres-Díaz and Rinaldi, 2014). The magnetic particles in ordinary ferrofluids are generally coated by a variety of long-chain organic surfactants (Hong et al., 2008; Okabe et al., 2017; Shi et al., 2018; Kumar et al., 2021; Kumar et al., 2022). These surfactants have a polar hydrophilic head group and an apolar hydrophobic end (Sawisai et al., 2019). The surfaces of magnetic iron oxide are

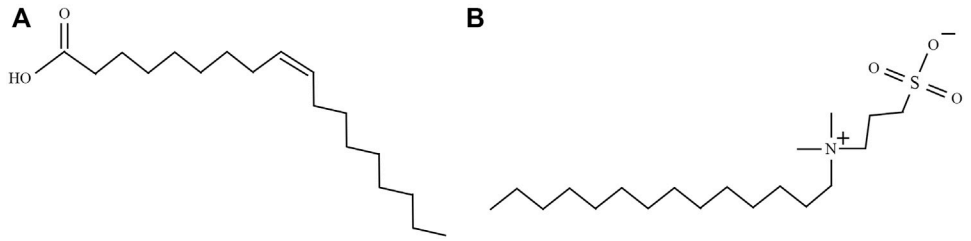

FIGURE 1 | Structural formulae of two kinds of surfactants: **(A)** oleic acid (OA) and **(B)** 3-(N,N-dimethylmyristylammonio)propanesulfonate (DP).

generally hydrophilic, which enables these surfaces to be combined with the polar head group of surfactants. The long chain of surfactants provides nanoparticles with a steric repulsion force which prevents the colloidal system from aggregation (Rodríguez-Arco et al., 2011b).

Oleic acid (OA), as one of the easily obtained classical surfactants, has been extensively studied in recent years (Lobaz et al., 2012; Etemadi and Plieger, 2020; Saputro et al., 2020). The oleic acid has a polar carboxyl group, allowing it to be attached to the surface of nanoparticles (López-López et al., 2005; Zhang et al., 2006; Rodríguez-Arco et al., 2011b; Gyergyek et al., 2011). The other side of oleic acid has a long C_{18} chain, making nanoparticles stable in colloidal solvents. The mechanisms of colloidal stability in ferrofluids with non-polar based liquid have been widely studied (López-López et al., 2005; Gyergyek et al., 2011). The association between stability and interfacial free energy in ferrofluids was proposed by Lopez-Lopez et al. (2005). The calculation of surface free energy of OA-coated magnetic particles is based on formal VOCG theory by calculating Lifshitz-van der Waals forces (LW forces) and acid-base interfacial interactions (AB interactions) (van Oss, 1993). Gyergyek et al. (2011) group take an additional steric repulsion into account, which is interpreted as the influence of the surfactants overlapping between neighbor particles (Gyergyek et al., 2011). However, oleic acid-coated nanoparticles can only be dispersed in the carrier liquid with a dielectric constant ($\varepsilon_r < 5$) (López-López et al., 2005). The explanation of the instability of polar colloidal could be the hydrophobic/hydrophilic bond between particles and carrier base liquid. Oleic acid-covered particles would have a phase separation when they were dispersed in water. For special applications in water or other polar liquid environments, a surfactant with a modified polarized functional group should be adopted. In our study, 3-(N,N-Dimethylmyristylammonio)propanesulfonate (DP) is adopted as surfactants to fabricate modified magnetic nanoparticles which can be dispersed in the polar carrier liquid to further fabricate ferrofluids. The structural formulae of oleic acid and DP are shown in **Figure 1**. The oleic acid-covered nanoparticles are settled as a control group to identify the factors which are responsible for the colloidal stability in polar or apolar base liquid. Oleic acid-covered particles (P1) can be dispersed into apolar carrier liquid. In contrast, DP-coated magnetite nanopowders (P2) can only be separated into polar liquids such as water and ethanol (ε_r larger than 5). The use of surfactant DP is intended to permit the synthesis of a polar solvent-based colloidal suspension of magnetic nanoparticles. In order to justify the properties of the cover layers on particles, several theoretical models combined with experiment results are raised. This study is meaningful for us to understand the fitting relationships between surfactants and nanoparticles. It can become a guideline in choosing the right surfactants for a specific base fluid.

EXPERIMENTAL

Materials

Materials include ferric chloride hexahydrate powders ($FeCl_3{\cdot}6H_2O$, 99%), ferrous chloride tetrahydrate powders ($FeCl_2{\cdot}4H_2O$, 99%), ammonium hydroxide ($NH_3{\cdot}H_2O$, 25%), oleic acid (OA, $C_{18}H_{34}O_2$, 95%), 3-(N,N-dimethylmyristylammonio)propanesulfonate (DP, 98%), ethanol (p.a.), hexamethylene (p.a.), and carbon tetrachloride (p.a.). Most of these chemicals used for the synthesis of magnetic particles were purchased from Alfa Aesar and Macklin Biochemical Company. The probe agents adopted for contact angle measurement, that is, water (WT), formamide (FA), and ethanediol (ED), were purchased from Macklin Biochemical Company.

Nanoparticle Synthesis

The chemical co-precipitation approach was used to produce bare magnetic particles (Laurent et al., 2008; Rebodos and Vikesland, 2010; Cui et al., 2015; Rajput et al., 2016). To begin with, 23.64 g of ferric chloride hexahydrate powders ($FeCl_3{\cdot}6H_2O$) and 9.94 g of ferrous chloride tetrahydrate powders ($FeCl_2{\cdot}4H_2O$) were dissolved into 300 ml deionized water. In order to fit the final stoichiometric ratio of Fe^{3+}: Fe^{2+} = 2: 1, the molar ratio of Fe^{3+}: Fe^{2+} = 1.75: 1 was adopted in initial reactants to compensate for the oxidation of Fe^{2+}. After heating the solvent to 80°C, 80 ml ammonium aquation (25%) was added under high-speed stirring (350 rpm) to adjust pH value to be higher than 9.5. Subsequently, the mixture reacted for 45 min at 80°C to ensure that Fe^{3+} and Fe^{2+} were fully converted into Fe_3O_4. Then the magnetic nanoparticles were separated by a permanent magnet and washed with deionized water and ethanol several times until the pH value was 7. The obtained uncoated bare magnetic nanoparticle (BM) was used as the precursor to fabricate surfactant covered particles. The precursor BM was evenly divided into two parts. One part of the BM was added to

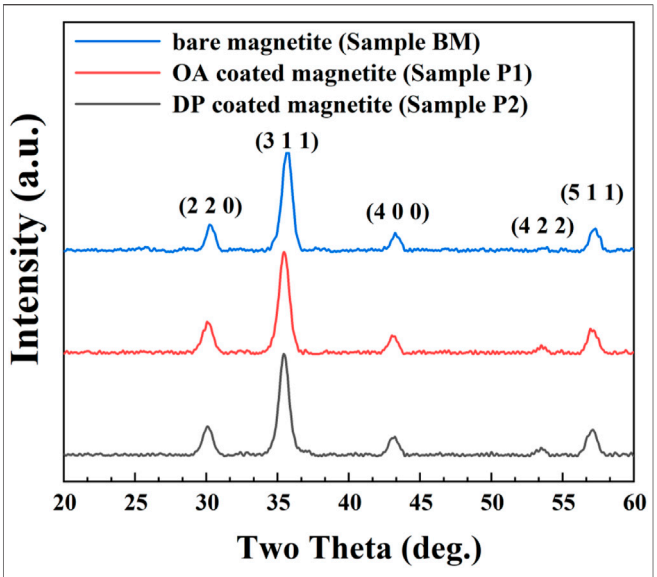

FIGURE 2 | XRD patterns of bare magnetite particles (BM), OA-coated particles (sample P1), and DP-coated magnetic nanoparticles (sample P2).

300 ml of deionized water. After the solvation process, 2 ml oleic acid was added to the solvation. In order to ensure that the particles were fully charged by H^+, pH was adjusted to six, lower than isoelectric point pH_{iep} = 6.5 (pH_{iep}: pH of zero zeta potential) (Galindo-González et al., 2005; López-López et al., 2005; Kosmulski, 2016). The mixture was heated to 80°C with vigorous stirring. The reacting process was kept for 30 min to get the BM completely covered by oleic acid. The oleic acid-covered magnetic particles (P1) were washed with deionized water to remove the unreacted oleic acid. The other part of BM was added to 300 ml of deionized water in a similar process. After that, 2.5 g of DP was dissolved into the mixture. The pH of the mixture was adjusted to 6. The reaction temperature was maintained at 80°C. After reacting for 30 min, the DP covered magnetic particles (P2) were washed by hexamethylene to ensure the coated surfaces not to be destroyed. Finally, two kinds of coated nanoparticles were dehydrated in a vacuum oven at 60°C for 4 h.

Methods

The crystalline structure of surfactants covered and uncovered nanoparticles was characterized by X-ray diffraction (Rigaku miniflex 600). Microstructures of nanoparticles were observed using transmission electron microscopy (TEM, JEM-100CXII). The functional groups of particles were examined by Fourier transform infrared spectroscopy (FT-IR, Thermo Scientific Nicolet iS 50). The zeta potential measurements were performed on the Malvern Zetasizer Nano ZS90. The magnetic properties of the magnetic nanoparticles were exanimated by a vibrating sample magnetometer (VSM, BKT-4500). The contact angle measurements were performed on a goniometer and its image-analysis software (HKCA-15). Smooth surfaces of magnetic nanoparticles were fabricated by depositing particles on a glass slide. Due to the dispersing ability differences of nanoparticles in polar of apolar carrier liquid, carbon tetrachloride and ethanol were used to disperse oleic acid covered particles (P1) and DP covered magnetite nanopowders (P2) respectively. A volume of 10 ml of these suspensions (10% volume fraction of particles) was enough to prepare a thick and smooth surface. The slides with colloidal suspension on them were dried under ambient conditions for 24 h. After that, the deposited surface on glass slides was placed in a vacuum oven heated to 60°C for 1 h.

RESULTS AND DISCUSSION

Physical Chemical Properties of Magnetic Particles

The X-ray diffraction patterns for particles from bare magnetite (BM), OA-coated magnetite (P1), and DP-coated magnetite (P2) are presented in **Figure 2**, respectively. As shown in **Figure 2**, the diffraction peaks could be ascribed to the inverse spinel phase. The positions of diffraction peaks were remained alike for different samples. The coating process of surfactant would not change the crystalline. However, magnetite (Fe_3O_4, JCPDS no. 19-0629) and maghemite (γ-Fe_2O_3, JCPDS no. 39-1346) patterns could be well adjusted to the experimental results (the analogous inverse cubic spinel structure may be responsible for their similarity in crystalline) (Rodríguez-Arco et al., 2011a; Gyergyek et al., 2011). According to the experimental conditions, starting materials and potassium dichromate titration, the nanoparticles could be deduced as magnetite nanoparticles.

From the X-ray diffraction results, the average particle size could be estimated by the Scherrer formula (Rodríguez-Arco et al., 2011a; Manikandan et al., 2015):

$$d_a = \frac{\delta\lambda}{\beta \cos\theta}, \quad (1)$$

where d_a is the average nanoparticle size, δ is the shape factor (0.9 for spherical magnetite nanograins), λ is the x-ray wavelength of Cu-K_α = 0.154 nm, θ is the Bragg diffraction angle of a certain diffraction peak, and β is full width at half maximum of the diffraction peak (FWHM). According to the calculation result, the average diameters for samples BM, P1, and P2 were obtained as 10.27 ± 0.10 nm, 10.58 ± 0.10 nm, and 10.09 ± 0.10 nm, respectively.

Transmission Electron Microscope (TEM) images of BM, P1, and P2 magnetic particles are shown in **Figure 3**. As presented in **Figure 3A**, spherical magnetite particles with a mean diameter of 9.97 ± 0.10 nm were well depicted. The mean diameter results in the TEM image well corresponded with the XRD results. The core-shell structures of surfactant-covered magnetite nanoparticles are well presented in **Figures 3B,C**. The thickness of cover layers of P1 and P2 were different. In sample P1, a coating layer with a thickness of ~2–3 nm was mainly formed by surfactant OA. According to the physical and chemical properties of oleic acid under ambient conditions, the coating layer of P1 was a layer of liquid organic phase mainly composed of oleic acid attached to the magnetite surface. In contrast, the surfactant shell formed by DP only had a thickness

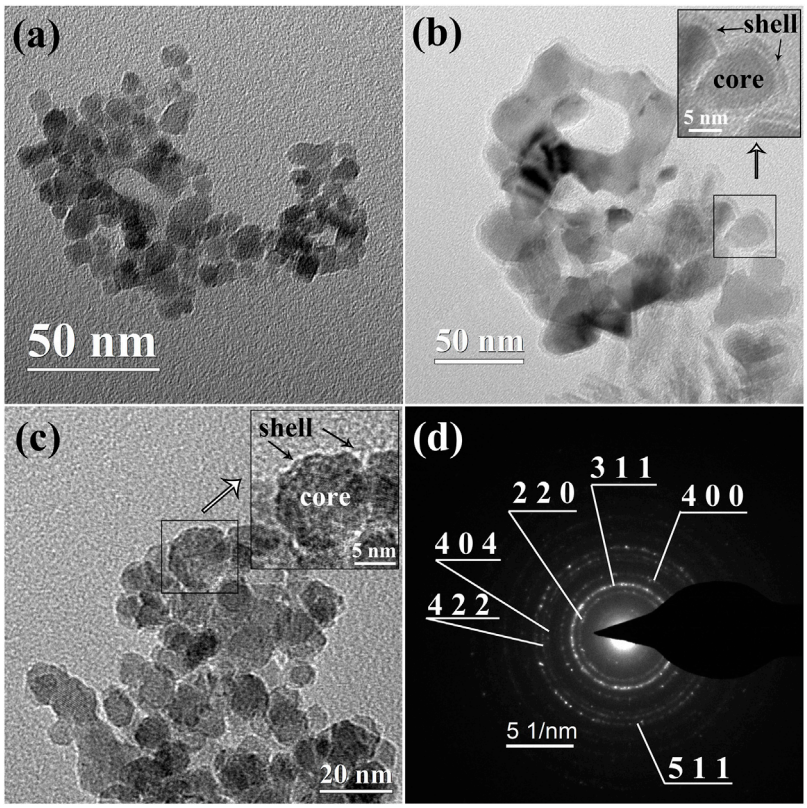

FIGURE 3 | TEM images of **(A)** BM magnetic nanoparticles, **(B)** P1 magnetic nanoparticles, and **(C)** magnetic nanoparticles P2. The inserts in **(B, C)** are the coating details in the selected area. **(D)**: selected area electron diffraction (SAED) of BM.

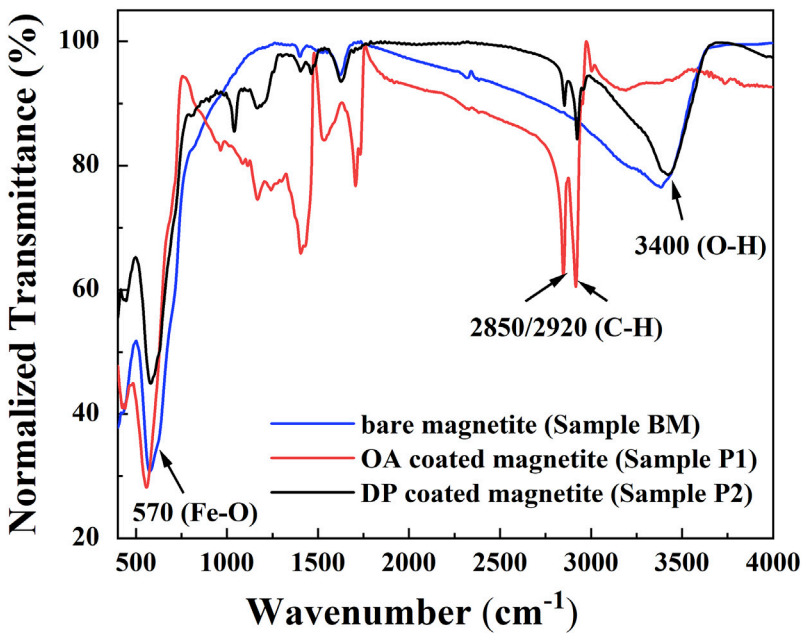

FIGURE 4 | FT-IR spectra of bare magnetite particles (BM), OA-coated particles (sample P1), and DP-coated magnetic nanoparticles (sample P2).

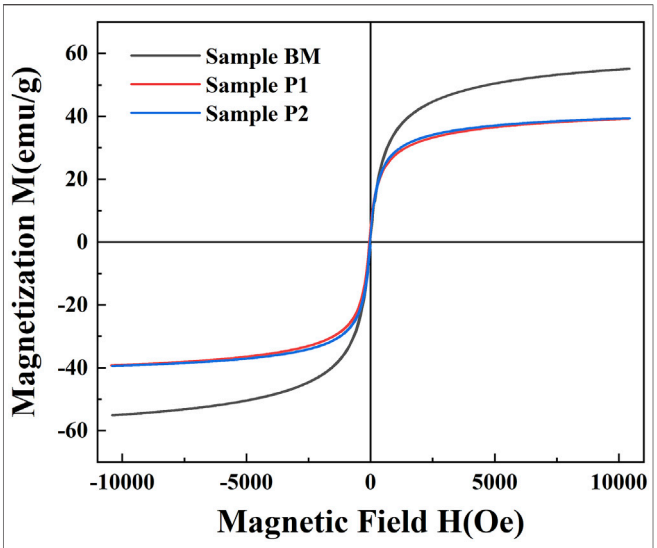

FIGURE 5 | Magnetization curves for bare magnetite particles (BM), OA-coated particles (sample P1), and DP-coated magnetic nanoparticles (sample P2).

of ~1 nm. Since the DP was solid under ambient conditions, the surfactant DP covering the magnetite was speculated to be the solid phase. The thin coating layer was unable to get the nanoparticles fully coated, which was attributed to the absence of surface tension in the solid-state coating layer. In **Figure 3D**, diffraction rings in electron diffraction are well fitted to the results of X-ray diffraction peaks, which is also an approvement of magnetite crystalline (Masui et al., 1997).

To further figure out the coating conditions of surfactant OA and DP, Fourier transform infrared measurements (FT-IR) were carried out. The FT-IR spectra results of BM, sample P1, and sample P2 are well depicted in **Figure 4**. As presented in **Figure 4**, sharp adsorption peaks at 570 cm^{-1} were obtained in all kinds of magnetic nanoparticles (Hong et al., 2006). The peaks at 570 cm^{-1} were attributed to the Fe-O bond. In samples P1 and P2, two sharp bonds at 2,850 cm^{-1} and 2,920 cm^{-1} were derived from the asymmetric CH_2 stretch and the symmetric CH_2 stretch, respectively (Zhang et al., 2006). This result was evidence of the presence of an organic coating layer on the magnetite particle surfaces. The strong peaks at 3,400 cm^{-1} were the demonstration of the exist of O-H on the particle surface (Cui et al., 2015). The functional group O-H on BM was the anchor point of surfactant. The disappearance of O-H in sample P1 was an indication that the functional group O-H was fully combined by OA. This result had the consistency of a thick coating layer of OA observed in the TEM image. The showing up of O-H in sample P2 was a piece of evidence that the particle surface was not fully coated by surfactant DP. This conclusion was also consistent with the TEM results.

The magnetization for bare magnetite particles (BM), OA-coated particles (sample P1), and DP-coated magnetic nanoparticles (sample P2) are shown in **Figure 5**. The hysteresis loops of nanoparticles had no remanence and coercivity. All the samples presented superparamagnetic properties. The saturated magnetization of BM, P1, and P2 were 55.1 emu/g, 39.3 emu/g, and 39.4 emu/g, respectively. The decreases in saturated magnetization in the coated magnetite samples were attributed to the non-magnetic surfactants.

In order to identify the colloidal stability of OA-coated particles and DP-coated particles in polar or apolar carrier liquid, water (polar, $\varepsilon_r > 5$) and carbon tetrachloride (apolar, $\varepsilon_r < 5$) were chosen as a base liquid to establish a colloidal system. As shown in **Figures 6B,C**, OA-coated particles could form a stable colloid system in an apolar carrier liquid. DP-coated nanoparticles underwent a severe phase separation in an apolar carrier liquid. As depicted in **Figures 6E,F**, DP-coated particles could form a stable colloidal system in polar carrier liquid while OA-coated particles could not. The particles coated by OA and DP had completely opposite stabilities in polar or apolar liquids. As shown in **Figures 6A,D**, uncoated magnetite particles could form a metastable colloidal system, which could be regarded as a standard to judge the stability of the colloidal system. Aiming to figure out the factors that contributed to the colloidal stability, theoretical analysis was performed in the colloidal systems of polar or apolar base liquid.

Theoretical Analysis of Colloidal Stability in Polar or Apolar Base Liquid

OA-coated magnetite nanoparticles (sample P1) could only be dispersed in the apolar organic base liquid ($\varepsilon_r < 5$) (López-López et al., 2005). In contrast, DP-coated magnetic particles (sample P2) could form stable colloidal solvation with a high particle concentration in the polar base fluid ($\varepsilon_r > 5$). The colloidal stability for magnetite particles dispersed in the apolar liquid could be explained by the Van Oss-Chaudhry-Good (VOCG) theory (Van Oss et al., 1988; van Oss, 1993) and surface free energy analysis. The total Gibbs free energy ΔG^{TOT} has multipart contributions of Lifshitz-van der Waals (LW) interaction, Lewis acid-base interaction, and steric repulsion potentials. The surface free energy could be obtained by measuring the surface tension (γ). Therefore, the surface tension of a material i can be expressed by Lifshitz-van der Waals part (γ_i^{LW}) and Lewis acid-base part (γ_i^{AB}) as:

$$\gamma_i = \gamma_i^{LW} + \gamma_i^{AB} = \gamma_i^{LW} + \sqrt{\gamma_i^+ \gamma_i^-}, \tag{2}$$

where γ_i^- and γ_i^+ are the electron-donor parameter and the electron-acceptor parameter. The Gibbs free energy of a certain solid surface (S) contacted by a certain liquid (L) could be calculated by the Young–Dupré equation and VOCG theory (van Oss, 1993):

$$\gamma_L (1 + \cos\theta) = 2\left(\sqrt{\gamma_S^{LW} \gamma_L^{LW}} + \sqrt{\gamma_S^+ \gamma_L^-} + \sqrt{\gamma_S^- \gamma_L^+} \right). \tag{3}$$

The surface tension components of a solid surface (γ_S^{LW}, γ_S^+ and γ_S^-) could be identified by three standard probe liquids. The probe liquids used in this study were water (WT), formamide (FA), and ethanediol (ED). The surface tension components of probe liquids are presented in **Table 1**.

In order to identify the solid surface free energy of oleic acid (OA) coated magnetic particles (sample P1) and 3-(N,N-Dimethylmyristylammonio)propanesulfonate (DP) coated

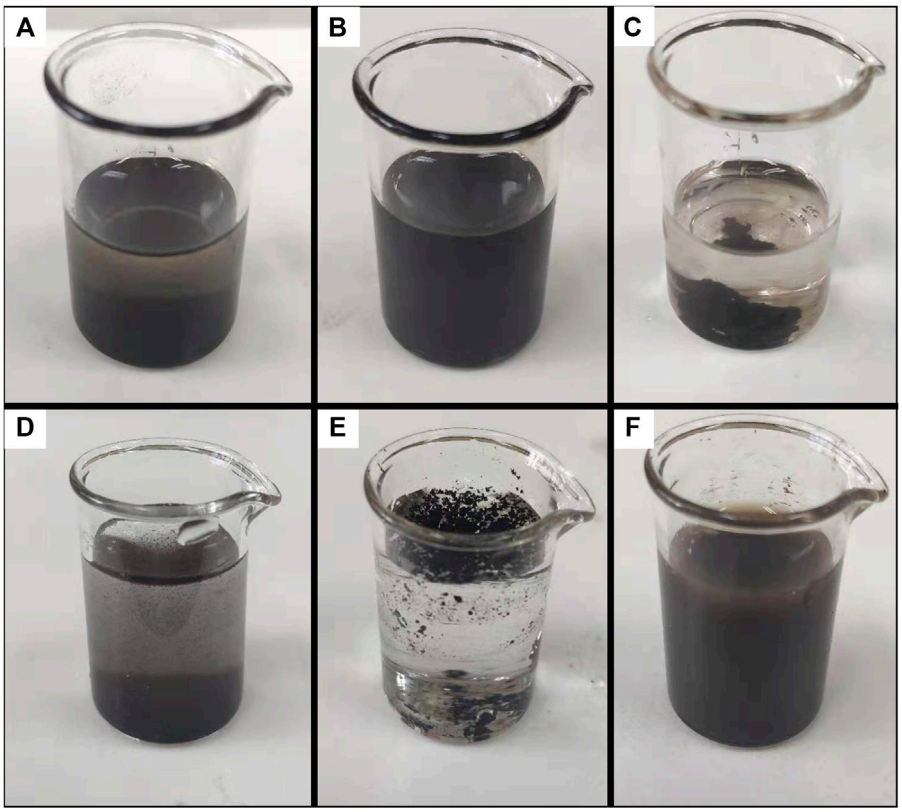

FIGURE 6 | Colloidal systems formed by magnetite particles coated by different surfactants in polar or apolar carrier liquid. **(A)** Uncoated particles in carbon tetrachloride. **(B)** OA-coated particles in carbon tetrachloride. **(C)** DP-coated particles in carbon tetrachloride. **(D)** Uncoated particles in water. **(E)** OA-coated particles in water. **(F)** DP-coated particles in water.

TABLE 1 | The electron-donor parameter γ_i^-, electron-acceptor parameter γ_i^+, Lifshitz-van der Waals part of surface tension (γ_i^{LW}), and total surface tension γ_L in probe liquids. All the units are in mJ/m^2. All the ambient temperatures of the surface tensions are at 20°C.

Liquid	γ_L	γ_i^{LW}	γ_i^+	γ_i^-
Water (WA)	72.8	21.8	25.5	25.5
Formamide (FA)	58.0	39.0	2.28	39.6
Ethanediol (ED)	48.0	29.0	1.92	47

The surface tension values of liquids are taken from Sawisai et al. (2019 and van Oss (1993).

TABLE 2 | The surface free energy components (mJ/m^2) of magnetite nanoparticles.

Samples	γ_i^{LW}	γ_i^+	γ_i^-
Bare magnetite[a]	49.3	0.17	55.4
OA-coated magnetite	24.4	0.00[c]	4.4
OA-coated magnetite[b]	25.3	0.15	5.2
DP-coated magnetite	92.3	0.00[c]	58.9

[a]*Taken from López-López et al. (2005) and Galindo-González et al. (2005).*
[b]*Taken from Shi et al. (2018) and López-López et al. (2005).*
[c]*The square root is negative. The error is larger than the value itself.*

nanoparticles (sample P2), the contact angle measurements were performed on smooth surfaces fabricated by magnetic particles. The results of contact angles measured on the surface of P1 were 95° ± 3° (water), 81° ± 5° (formamide), and 78° ± 5° (ethanediol). After that, contact angles are measured on the surface of P2 particles. The average results were 5° ± 1° (water), 8° ± 1° (formamide), and 15° ± 2° (ethanediol). The measured contact angles of OA-coated magnetite are consistent with the data in reference (López-López et al., 2005). Surface tension parameters could be obtained by solving **Eqs 2**, **3** using contact angles of probe liquids. The surface tension parameters are presented in **Table 2**. As shown in **Table 2**, the OA-coated magnetite surface shifted from a strong electron-donor property ($\gamma_i^+ \approx 0, \gamma_i^- = 55.4\, mJ/m^2$) on a bare magnetite surface to weak electron donor property ($\gamma_i^+ \approx 0$, $\gamma_i^- = 4.4\, mJ/m^2$). Meanwhile, the Lifshitz-van der Waals parameter was decreased on the OA-coated magnetite surface compared to the pure magnetite surface. The OA surfactant blocks the interaction between magnetite and carrier liquid. In contrast, DP-coated magnetite remained the same in electron-donor parameter and electron-acceptor parameter compared to the bare magnetite surface. The Lifshitz-van der Waals parameter (γ_i^{LW}), on DP covered magnetite surface was significantly increased from 49.3 mJ/m^2 to 92.3 mJ/m^2. The properties and working mechanisms of the

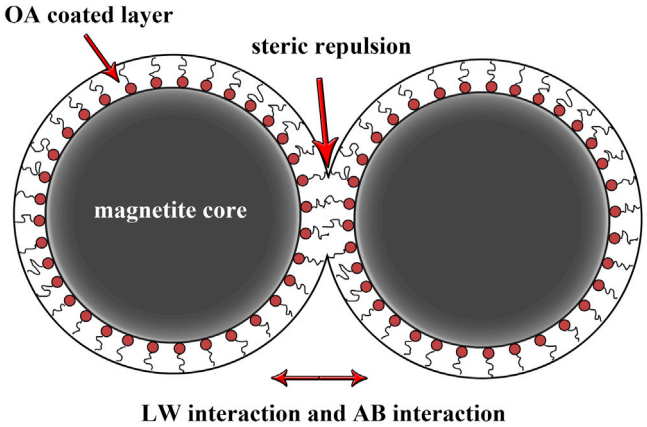

FIGURE 7 | Lifshitz-van der Waals (LW) interaction, acid-base (AB) interaction, and steric repulsion between OA-coated magnetite particles.

OA surfactant cover layer and DP surfactant cover layer were different.

In the apolar carrier liquid (phase 1), the colloidal stability of OA-coated magnetite particles (phase 2) could be explained by the surface free energy of Lifshitz-van der Waals (ΔG_{121}^{LW}), acid-base interaction (ΔG_{121}^{AB}), and steric repulsion (ΔG_{121}^{ST}). Steric interaction between particles in an apolar liquid phase is presented in **Figure 7**. Although DP-coated magnetite particles (phase 3) had a larger ΔG_{131}^{LW} due to their higher γ_i^{LW} compared to OA-coated particles, DP-coated particles almost had no steric repulsion between their solid phase thin cover layers. The steric repulsion ΔG_{121}^{ST} could be one of the main contributions to the colloidal stability in the apolar carrier liquid (Rodríguez-Arco et al., 2011b; Gyergyek et al., 2011). This may explain why OA-coated magnetic nanoparticles (P1 sample) could be dispersed in the polar organic liquid ($\varepsilon_r < 5$) to form a stable colloidal system, while DP-coated magnetite could not.

In the polar carrier liquid, the cohesion between carrier liquid molecular particles and hydrophilic magnetite particles was stronger due to their larger van der Waals force and hydrogen bond (van Oss, 2007). According to the DLVO theory, the colloidal nanoparticles could establish an electrical double layer (EDL). The potential of a shear plane in EDL is the zeta potential. As shown in **Figures 8A,B**, the zeta potential associated with electrical repulsion is one of the important contributions to the colloidal stability of ferrofluids. According to our experimental results, the zeta potentials of DP-coated magnetite under neutral conditions (pH = 7) in water and ethanol colloidal systems were 29.7 and 26.0 mV, respectively. According to the reference (Galindo-González et al., 2005), the zeta potential of uncoated magnetite particles was supposed to be −12 mV in the neutral water colloidal system. The DP surfactant coating layer on the magnetite surface was responsible for this zeta potential increase. This could be explained by the zeta potential presented in **Figure 8B**. As shown in **Figure 8B**, the surfactant DP, which could be seen as an electrical dipole, had its own electrical potential. The zeta potential (φ_{z2}) of DP-coated magnetite particles was calculated by adding the electrical

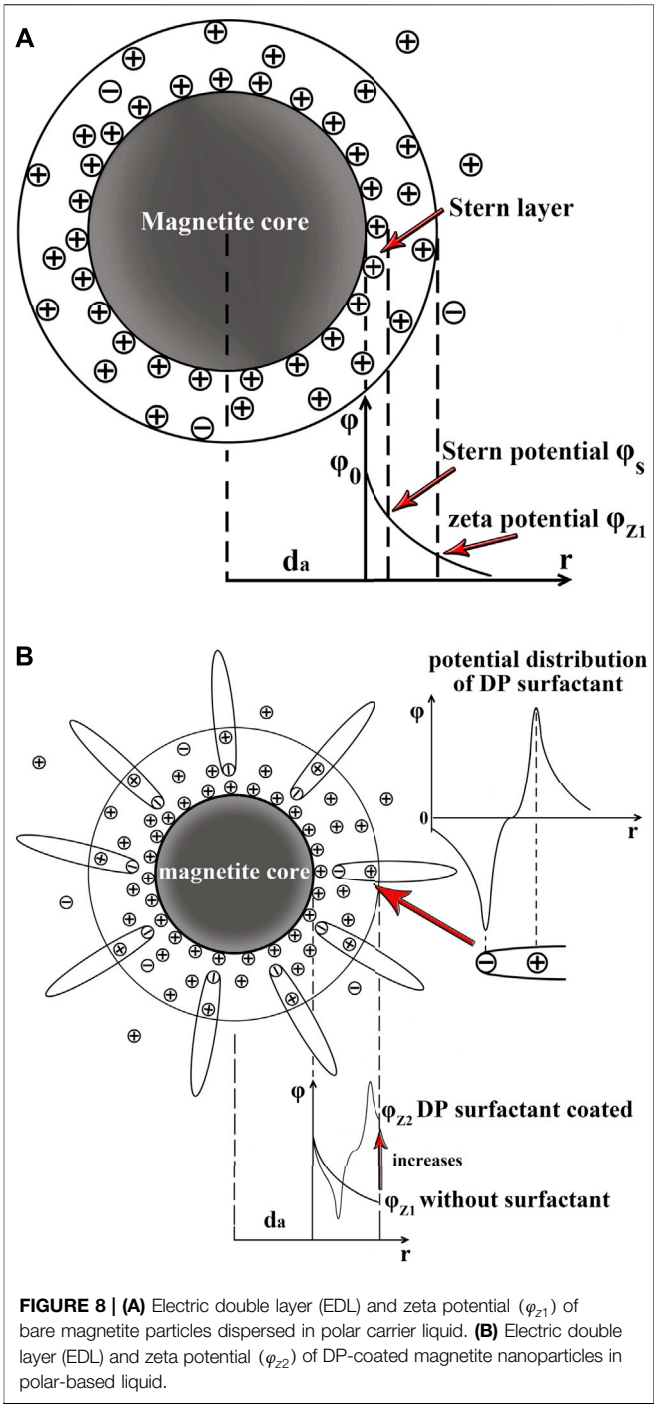

FIGURE 8 | (A) Electric double layer (EDL) and zeta potential (φ_{z1}) of bare magnetite particles dispersed in polar carrier liquid. **(B)** Electric double layer (EDL) and zeta potential (φ_{z2}) of DP-coated magnetite nanoparticles in polar-based liquid.

potential of the surfactant DP to the zeta potential φ_{z1} of bare magnetite particles.

Finally, the Lifshitz-van der Waals part (ΔG_{131}^{LW}), acid-base interaction part (ΔG_{131}^{AB}), and electrical repulsion part (ΔG_{131}^{EL}) of interfacial Gibbs free energy (1 = DP-coated magnetite, 3 = water) were calculated. ΔG_{131}^{LW} was obtained by **Eq. 4** (Gyergyek et al., 2011; Galindo-González et al., 2005; Gregory, 1981) and **(5)** (Gregory, 1981; Galindo-González et al., 2005; Gyergyek et al., 2011):

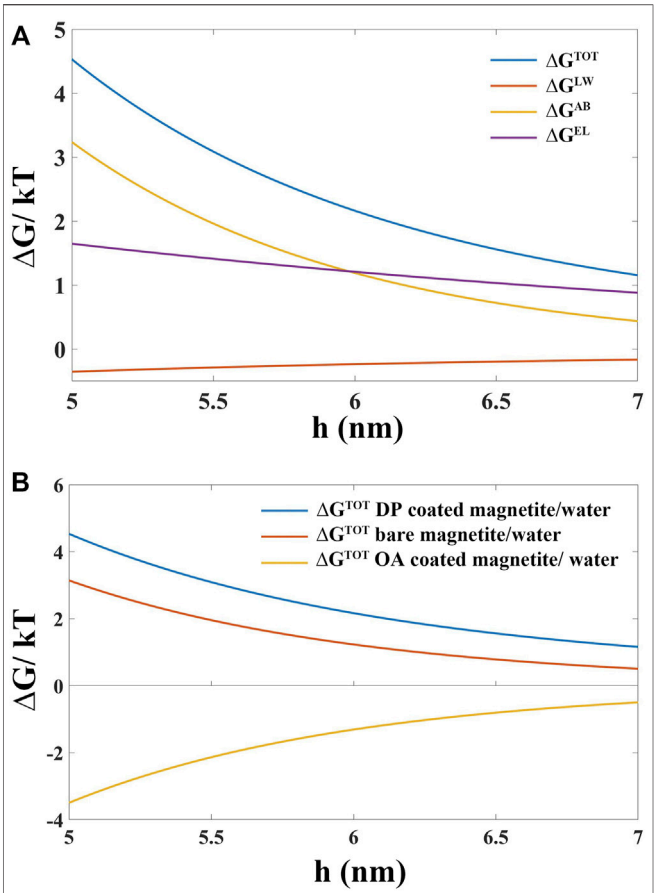

FIGURE 9 | (A) Interfacial distance (h) dependence of total surface interaction free energy (ΔG_{131}^{TOT}), Lifshitz-van der Waals part (ΔG_{131}^{LW}), acid-base interaction part (ΔG_{131}^{AB}) , and electrical part (ΔG_{131}^{EL}) of interfacial Gibbs free energy between magnetic particles coated by DP under water-based neutral condition (pH = 7). **(B)** Interfacial distance (h) dependence of total surface interaction free energy (ΔG_{sws}^{TOT}) of DP-coated magnetite, bare magnetite, and OA-coated magnetite in the neutral water-based colloidal system.

$$\Delta G_{131}^{LW}(h) = -\frac{A_{131}}{6}\left[\frac{2d_a^2}{h(4d_a+h)} - \frac{2d_a^2}{(2d_a+h)^2} + \ln\frac{h(4d_a+h)}{(2d_a+h)^2}\right], \tag{4}$$

$$A_{131} = 24\pi h_0^2\left(\sqrt{\gamma_1^{LW}} - \sqrt{\gamma_3^{LW}}\right)^2, \tag{5}$$

where d_a is the average diameter of nanoparticles. h_0 is the minimum equilibrium distance between interfaces, which is supposed to be $1.58 \pm 0.08\,\AA$ in a water-based colloidal system (Galindo-González et al., 2005; Gyergyek et al., 2011). h is the distance between neighbor interfaces of nanoparticles in the colloidal system. A_{131} is the Hamaker constant.

ΔG_{131}^{AB} was calculated by **Eq. 6** (van Oss, 1993; López-López et al., 2005; Gyergyek et al., 2011) and **(7)** (van Oss, 1993; Galindo-González et al., 2005):

$$\Delta G_{131}^{AB}(h_0) = -4\left(\sqrt{\gamma_1^+} - \sqrt{\gamma_3^+}\right)\left(\sqrt{\gamma_1^-} - \sqrt{\gamma_3^-}\right), \tag{6}$$

$$\Delta G_{131}^{AB}(h) = \Delta G_{131}^{AB}(h_0)\pi\lambda d_a\, exp\left(\frac{h_0 - h}{\lambda}\right), \tag{7}$$

where λ is the correlation length, or the decay length of the molecules of liquid medium (in water, $\lambda \approx 1\,nm$) (van Oss, 1993). d_a, h_0, and h have already been given in **Eqs 4**, **5**.

ΔG_{131}^{EL} was calculated by **Eq. 8** (Galindo-González et al., 2005) and **(9)** (Galindo-González et al., 2005; Ueno et al., 2008; Rodríguez-Arco et al., 2011a):

$$\Delta G_{131}^{EL}(h) = 2\pi\varepsilon_0\varepsilon_r d_a\zeta^2 \ln\left(1 + e^{-\kappa h}\right), \tag{8}$$

$$\kappa = \left(\frac{(2\times 10^3)N_A e^2 C_{eff}}{\varepsilon_0\varepsilon_r kT}\right)^{1/2}, \tag{9}$$

where ε_r is the dielectric constant of the carrier liquid, ε_0 is the permittivity of vacuum, ζ is the zeta potential of particles, d_a is the average diameter of magnetite particles, κ is the reciprocal Debye length. h is the average distance between neighbor interfaces of nanoparticles in the colloidal system, N_A is Avogadro's number, e is electronic charge, k (k_B) is Boltzmann constant, T is the absolute temperature (room temperature, 293.15 K), and C_{eff} is effective ionic charge concentration (the surfactant concentration is the main contribution to C_{eff}. Based on the amount of the surfactant, $C_{eff} \approx 0.01 mol\,L^{-1}$, the Debye length $\kappa^{-1} = 3\,nm$).

Total interaction surface free energy (ΔG_{131}^{TOT}) between DP-coated magnetic particles dispersed into water was the sum of the Lifshitz-van der Waals part (ΔG_{131}^{LW}), acid-base interaction part (ΔG_{131}^{AB}) , and electrical part (ΔG_{131}^{EL}) of interfacial Gibbs free energy:

$$\Delta G_{131}^{TOT}(h) = \Delta G_{131}^{LW}(h) + \Delta G_{131}^{AB}(h) + \Delta G_{131}^{EL}(h). \tag{10}$$

As shown in **Figure 9A**, the total interfacial free energy ΔG_{131}^{TOT} between magnetic particles coated by DP under neutral water-based conditions (a typical polar liquid-based colloidal system) is calculated. According to the Debye length ($\kappa^{-1} = 3\,nm$) result which was the thickness of EDL, the proper value of interfacial distance h between two particles was 6 nm (2 times of Debye length κ^{-1}). At this point, the main repulsion contributions of ΔG_{131}^{TOT} were electrical double layer repulsion energy ($\Delta G_{131}^{EL}(6nm) = 1.2\,k_BT$) and acid-base interaction surface interfacial energy ($\Delta G_{131}^{AB}(6nm) = 1.2\,k_BT$). The contribution of $\Delta G_{131}^{LW}(6\,nm)$ was - $0.2\,k_BT$, which indicated that the L-W force between magnetite particles was a mild attractive force. The total interfacial free energy ($\Delta G_{131}^{TOT}(6\,nm)$) of 2.2 k_BT (larger than the Brownian free energy of 1.5 k_BT) was large enough to resist the precipitation resulting from the gravitational field. If magnetite particles were not coated by DP, $\Delta G_{131}^{EL}(6\,nm)$ would significantly decrease from 1.2 k_BT to 0.1 k_BT (assuming the ionic concentration was maintained) due to the smaller zeta potential and ionic concentration. As shown in **Figure 9B**, the total interfacial free energy $\Delta G_{131}^{TOT}(6\,nm)$ of bare magnetite particles not coated by DP was reduced from 2.2 k_BT to 1.2 k_BT. The colloidal stability became fragile due to the absence of EDL repulsion. If the OA-coated magnetite particles were dispersed into water, ΔG_{121}^{TOT} would decrease to

-1.3 k_BT. This could be a plausible reason for a severe phase separation between OA-coated magnetite and water.

CONCLUSION

The coating state and colloidal stability of oleic acid (OA) and 3-(N,N-Dimethylmyristylammonio)propanesulfonate (DP) coated magnetite nanoparticles in the polar and apolar carrier liquid were systematically studied. Bare magnetite particles (with an average diameter of 10 nm), as precursors to fabricate surfactant-coated nanoparticles, were prepared by coprecipitation of Fe^{3+} and Fe^{2+} under aqueous conditions. The OA surfactant covering layer was a thick oil-state shell (~2–3 nm) which enabled the magnetite surface to be fully coated. The DP coating layer was a kind of solid-state thin shell (~1 nm), which did not allow the surface of magnetite to be fully coated. Different coating states enabled OA- and DP-coated magnetite particles to be dispersed in the base liquid with different dielectric constant ε_r. OA-coated magnetite particles could only be dispersed in the apolar carrier liquid ($\varepsilon_r < 5$) to form a stable colloidal system. In contrast, DP-coated magnetite particles could establish a stable dispersion in the polar base liquid ($\varepsilon_r > 5$). The stable colloidal system of OA covered magnetite in apolar base liquid was attributed to the steric repulsion of thick organic coating layers. Due to the solid-state thin coating layer, the DP-coated particles could not establish an organic barrier to keep adjacent nanoparticles from precipitation in the apolar carrier liquid system. From the calculating results of total Gibbs interfacial free energy ΔG_{131}^{TOT} in a neutral water-based colloidal system (a typical polar carrier liquid system), DP-coated magnetite particles had the highest $\Delta G_{131}^{TOT} = 2.2\,k_BT$. This high value of repulsive energy was the reason why DP-coated magnetite could form a stable dispersion in a water-based colloidal system. Bare magnetite particles could form a compared fragile colloidal system for its smaller $\Delta G_{131}^{TOT} = 1.2\,k_BT$ in neutral water base liquid. The shrinkage of interfacial free energy ΔG_{131}^{TOT} was attributed to the weak interparticle EDL electric repulsion (zeta potential reduced from 29.7 mV to -12 mV). The interparticle EDL electric repulsion was an important factor for the polar liquid-based colloidal system. The OA-coated particles had the lowest $\Delta G_{131}^{TOT} = -1.3\,k_BT$. The negative interfacial free energy indicated a strong attraction force between neighbor OA-coated nanoparticles in a water-based colloidal system. As a result, severe phase separation between OA-coated magnetite and water occurred.

DATA AVAILABILITY STATEMENT

The original contributions presented in the study are included in the article/Supplementary Material; further inquiries can be directed to the corresponding author.

AUTHOR CONTRIBUTIONS

LL: research, experiments, and manuscript. DL: teacher and adviser. ZZ: teacher and adviser.

FUNDING

This research is supported by the National Natural Science Foundation of China (No. 51735006, No. 51927810, and No. U1837206) and Beijing Municipal Natural Science Foundation (No. 3182013).

REFERENCES

Cui, H., Li, D., and Zhang, Z. (2015). Preparation and Characterization of Fe_3O_4 Magnetic Nanoparticles Modified by Perfluoropolyether Carboxylic Acid Surfactant. *Mater. Lett.* 143, 38–40. doi:10.1016/j.matlet.2014.12.037

Dailey, J. P., Phillips, J. P., Li, C., and Riffle, J. S. (1999). Synthesis of Silicone Magnetic Fluid for Use in Eye Surgery. *J. Magnetism Magnetic Mater.* 194, 140–148. doi:10.1016/s0304-8853(98)00562-9

Etemadi, H., and Plieger, P. G. (2020). Improvements in the Organic-Phase Hydrothermal Synthesis of Monodisperse MxFe3-xO4 (M = Fe, Mg, Zn) Spinel Nanoferrites for Magnetic Fluid Hyperthermia Application. *ACS omega* 5, 18091–18104. doi:10.1021/acsomega.0c01641

Galindo-González, C., de Vicente, J., Ramos-Tejada, M. M., López-López, M. T., González-Caballero, F., and Durán, J. D. G. (2005). Preparation and Sedimentation Behavior in Magnetic Fields of Magnetite-Covered Clay Particles. *Langmuir* 21, 4410–4419. doi:10.1021/la047393q

Gregory, J. (1981). Approximate expressions for retarded van der waals interaction. *J. Colloid Interface Sci.* 83, 138–145. doi:10.1016/0021-9797(81)90018-7

Gyergyek, S., Makovec, D., and Drofenik, M. (2011). Colloidal Stability of Oleic- and Ricinoleic-Acid-Coated Magnetic Nanoparticles in Organic Solvents. *J. Colloid Interface Sci.* 354, 498–505. doi:10.1016/j.jcis.2010.11.043

Hartshorne, H., Backhouse, C. J., and Lee, W. E. (2004). Ferrofluid-based Microchip Pump and Valve. *Sensors Actuators B Chem.* 99, 592–600. doi:10.1016/j.snb.2004.01.016

Hong, R. Y., Li, J. H., Li, H. Z., Ding, J., Zheng, Y., and Wei, D. G. (2008). Synthesis of Fe3O4 Nanoparticles without Inert Gas Protection Used as Precursors of Magnetic Fluids. *J. Magnetism Magnetic Mater.* 320, 1605–1614. doi:10.1016/j.jmmm.2008.01.015

Hong, R. Y., Pan, T. T., and Li, H. Z. (2006). Microwave Synthesis of Magnetic Fe_3O_4 Nanoparticles Used as a Precursor of Nanocomposites and Ferrofluids. *J. Magnetism Magnetic Mater.* 303, 60–68. doi:10.1016/j.jmmm.2005.10.230

Jain, N., Zhang, X., Hawkett, B. S., and Warr, G. G. (2011). Stable and Water-Tolerant Ionic Liquid Ferrofluids. *ACS Appl. Mat. Interfaces* 3, 662–667. doi:10.1021/am1012112

Kosmulski, M. (2016). Isoelectric Points and Points of Zero Charge of Metal (Hydr) oxides: 50years after Parks' Review. *Adv. colloid interface Sci.* 238, 1–61. doi:10.1016/j.cis.2016.10.005

Kumar, P., Khanduri, H., Pathak, S., Singh, A., Basheed, G. A., and Pant, R. P. (2020). Temperature Selectivity for Single Phase Hydrothermal Synthesis of PEG-400 Coated Magnetite Nanoparticles. *Dalton Trans.* 49, 8672–8683. doi:10.1039/d0dt01318h

Kumar, P., Pathak, S., Jain, K., Singh, A., KuldeepBasheed, G. A., et al. (2022). Low-temperature Large-Scale Hydrothermal Synthesis of Optically Active PEG-200 Capped Single Domain $MnFe_2O_4$ Nanoparticles. *J. Alloys Compd.* 904, 12. doi:10.1016/j.jallcom.2022.163992

Kumar, P., Pathak, S., Singh, A., Khanduri, H., KuldeepJain, K., et al. (2021). Enhanced Static and Dynamic Magnetic Properties of PEG-40 0 Coated $CoFe_2$-xErxO4 (0.7 X 0) Nanoferrites. *J. Alloys Compd.* 887, 24. doi:10.1016/j.jallcom.2021.161418

Laurent, S., Forge, D., Port, M., Roch, A., Robic, C., Vander Elst, L., et al. (2008). Magnetic Iron Oxide Nanoparticles: Synthesis, Stabilization, Vectorization, Physicochemical Characterizations, and Biological Applications. *Chem. Rev.* 108, 2064–2110. doi:10.1021/cr068445e

Lobaz, V., Klupp Taylor, R. N., and Peukert, W. (2012). Highly Magnetizable Superparamagnetic Colloidal Aggregates with Narrowed Size Distribution from Ferrofluid Emulsion. *J. Colloid Interface Sci.* 374, 102–110. doi:10.1016/j.jcis.2012.01.057

López-López, M. T., Durán, J. D. G., Delgado, A. V., and González-Caballero, F. (2005). Stability and Magnetic Characterization of Oleate-Covered Magnetite Ferrofluids in Different Nonpolar Carriers. *J. Colloid Interface Sci.* 291, 144–151. doi:10.1016/j.jcis.2005.04.099

Manikandan, A., Saravanan, A., Antony, S. A., and Bououdina, M. (2015). One-Pot Low Temperature Synthesis and Characterization Studies of Nanocrystalline α-Fe_2O_3 Based Dye Sensitized Solar Cells. *J. Nanosci. Nanotechnol.* 15, 4358–4366. doi:10.1166/jnn.2015.9804

Masui, T., Fujiwara, K., Machida, K.-i., Adachi, G.-y., Sakata, T., and Mori, H. (1997). Characterization of Cerium(IV) Oxide Ultrafine Particles Prepared Using Reversed Micelles. *Chem. Mat.* 9, 2197–2204. doi:10.1021/cm970359v

Medeiros, A. M. M. S., Parize, A. L., Oliveira, V. M., Neto, B. A. D., Bakuzis, A. F., Sousa, M. H., et al. (2012). Magnetic Ionic Liquids Produced by the Dispersion of Magnetic Nanoparticles in 1-N-Butyl-3-Methylimidazolium Bis(trifluoromethanesulfonyl)imide (BMI.NTf2). *ACS Appl. Mat. Interfaces* 4, 5458–5465. doi:10.1021/am301367d

Okabe, T., Moritaka, D., Miyatake, M., Kondo, Y., Sasaki, S., and Yoshimoto, S. (2017). Development and Performance of a Magnetic Ionic Liquid for Use in Vacuum-Compatible Non-contact Seals. *Precis. Eng.* 47, 97–103. doi:10.1016/j.precisioneng.2016.07.010

Pathak, S., Jain, K., Kumar, P., Wang, X., and Pant, R. P. (2019). Improved Thermal Performance of Annular Fin-Shell Tube Storage System Using Magnetic Fluid. *Appl. Energy* 239, 1524–1535. doi:10.1016/j.apenergy.2019.01.098

Rajput, S., Pittman, C. U., and Mohan, D. (2016). Magnetic Magnetite (Fe_3O_4) Nanoparticle Synthesis and Applications for Lead (Pb^{2+}) and Chromium (Cr^{6+}) Removal from Water. *J. Colloid Interface Sci.* 468, 334–346. doi:10.1016/j.jcis.2015.12.008

Rebodos, R. L., and Vikesland, P. J. (2010). Effects of Oxidation on the Magnetization of Nanoparticulate Magnetite. *Langmuir* 26, 16745–16753. doi:10.1021/la102461z

Rodríguez-Arco, L., López-López, M. T., Durán, J. D., Zubarev, A., and Chirikov, D. (2011). Stability and Magnetorheological Behaviour of Magnetic Fluids Based on Ionic Liquids. *J. Phys. Condens Matter* 23, 455101. doi:10.1088/0953-8984/23/45/455101

Rodríguez-Arco, L., López-López, M. T., González-Caballero, F., and Durán, J. D. G. (2011). Steric Repulsion as a Way to Achieve the Required Stability for the Preparation of Ionic Liquid-Based Ferrofluids. *J. Colloid Interface Sci.* 357, 252–254. doi:10.1016/j.jcis.2011.01.083

Saputro, R. E., Taufiq, A., SunaryonoHidayat, N., and Hidayat, A. (2020). Effects of DMSO Content on the Optical Properties, Liquid Stability, and Antimicrobial Activity of Fe3O4/OA/DMSO Ferrofluids. *Nano* 15, 10. doi:10.1142/s1793292020500678

Sawisai, R., Wanchanthuek, R., Radchatawedchakoon, W., and Sakee, U. (2019). Simple Continuous Flow Synthesis of Linoleic and Palmitic Acid-Coated Magnetite Nanoparticles. *Surfaces Interfaces* 17, 11. doi:10.1016/j.surfin.2019.100344

Shi, X., Huang, W., and Wang, X. (2018). Ionic Liquids-Based Magnetic Nanofluids as Lubricants. *Lubr. Sci.* 30, 73–82. doi:10.1002/ls.1405

Torres-Díaz, I., and Rinaldi, C. (2014). Recent Progress in Ferrofluids Research: Novel Applications of Magnetically Controllable and Tunable Fluids. *Soft Matter* 10, 8584–8602. doi:10.1039/c4sm01308e

Ueno, K., Inaba, A., Kondoh, M., and Watanabe, M. (2008). Colloidal Stability of Bare and Polymer-Grafted Silica Nanoparticles in Ionic Liquids. *Langmuir* 24, 5253–5259. doi:10.1021/la704066v

van Oss, C. J. (1993). Acid-base Interfacial Interactions in Aqueous Media. *Colloids Surfaces A Physicochem. Eng. Aspects* 78, 1–49. doi:10.1016/0927-7757(93)80308-2

van Oss, C. J. (2007). Development and Applications of the Interfacial Tension between Water and Organic or Biological Surfaces. *Colloids Surfaces B Biointerfaces* 54, 2–9. doi:10.1016/j.colsurfb.2006.05.024

Van Oss, C. J., Good, R. J., and Chaudhury, M. K. (1988). Additive and Nonadditive Surface Tension Components and the Interpretation of Contact Angles. *Langmuir* 4, 884–891. doi:10.1021/la00082a018

Zhang, L., He, R., and Gu, H.-C. (2006). Oleic Acid Coating on the Monodisperse Magnetite Nanoparticles. *Appl. Surf. Sci.* 253, 2611–2617. doi:10.1016/j.apsusc.2006.05.023

Conflict of Interest: The authors declare that the research was conducted in the absence of any commercial or financial relationships that could be construed as a potential conflict of interest.

Publisher's Note: All claims expressed in this article are solely those of the authors and do not necessarily represent those of their affiliated organizations, or those of the publisher, the editors, and the reviewers. Any product that may be evaluated in this article, or claim that may be made by its manufacturer, is not guaranteed or endorsed by the publisher.

frontiers | Frontiers in Materials

ORIGINAL RESEARCH
published: 05 July 2022
doi: 10.3389/fmats.2022.930633

Effects of Different Fatty Acids as Surfactants on the Rheological Properties of Kerosene-Based Magnetic Fluids

Guobao Zang[1], *Zhili Zhang*[1]*, *Wenjuan Yu*[1], *Deyi Wang*[1] *and Decai Li*[1,2]

[1]Country School of Mechanical Electronic and Control Engineering, Beijing Jiaotong University, Beijing, China, [2]State Key Laboratory of Tribology, Tsinghua University, Beijing, China

Three types of surfactants (oleic acid, linoleic acid, and a mixture of oleic acid and linoleic acid) were coated on ferromagnetic particles, which were dispersed in kerosene to prepare magnetic fluids, to study the effect of different fatty acids as surfactants on the rheological properties of magnetic fluids. The particles were analyzed by XRD, TEM, FT-IR, and VSM. Furthermore, a rheometer was used to examine the rheological properties of kerosene-based magnetic fluids dispersed with various surfactants. The yield stress at different magnetic fields was calculated by fitting the Herschel–Bulkley model. The fitted curve and the observed values of mixed fatty acids are identical. The graphs of viscosity increase with the shear rate for each magnetic fluid were measured at constant magnetic field strengths. At constant shear rates, the curves of viscosity increase with magnetic field intensity were measured. In the absence of a magnetic field, the relative change in viscosity from 40°C to 0°C was observed. The rheological measurements of the mixed fatty acid-dispersed ferrofluid with a rising magnetic field at a constant shear rate are smoother than the single-fatty-acid-dispersed ferrofluid, indicating that it is more stable. As the temperature is dropped, the viscosity–temperature curve evidence that mixed fatty acids as surfactants can lower the proportion of magnetic fluid viscosity rise.

Keywords: magnetic fluids, magnetite, surfactants, kerosene-based, rheological properties

OPEN ACCESS

Edited by:
Yang Yu,
Western Sydney University, Australia

Reviewed by:
U. Ubaidillah,
Sebelas Maret University, Indonesia
Qing Ouyang,
Jiaxing University, China

***Correspondence:**
Zhili Zhang
zlzhang@bjtu.edu.cn

Specialty section:
This article was submitted to Smart Materials, a section of the journal Frontiers in Materials

Received: *28 April 2022*
Accepted: *30 May 2022*
Published: *05 July 2022*

Citation:
Zang G, Zhang Z, Yu W, Wang D and Li D (2022) Effects of Different Fatty Acids as Surfactants on the Rheological Properties of Kerosene-Based Magnetic Fluids. Front. Mater. 9:930633. doi: 10.3389/fmats.2022.930633

1 INTRODUCTION

Magnetic fluids, also known as ferrofluids, are nanocolloids made up of nanometer-sized ferromagnetic particles dispersing in a carrier liquid (typically comprises three parts: base carrier liquid, surfactant, and ferromagnetic particles) (Wang et al., 2018; Dubreuil and Bobowski, 2019). Since the particles are easier to agglomerate, ferromagnetic particles are typically coated with surfactants to prevent agglomeration (Asahi et al., 2011). Magnetic fluids can exhibit both the fluidity of liquids and magnetic properties under an external magnetic field. Hence, magnetic fluids have always received extensive attention and become a research hotspot and have a wide variety of applications because of their fluidity and magnetism (Batter et al., 2013; Cui et al., 2015), including sealing (Li et al., 2017; Marcin, 2018; Szczech, 2020), lubrication (Shahrivar and de Vicente, 2014), sensors (Yao et al., 2015; Yu et al., 2018; Yu et al., 2019), biomedicine (Hensley et al., 2017; Metelkina et al., 2017), and so on. In particular, magnetic fluid sealing is one of the advanced applications of magnetic fluids. Compared with other seals, it has zero leakage, a long life, high rotational speed capability, low viscosity friction, and great reliability. Therefore, it offers significant engineering

application value in aerospace, military equipment, mechanical engineering, and other industries, and broad development potential (Wang and Decai, 2015; Yang et al., 2019).

Magnetic fluid sealing is very suitable for high-end sealing equipment in aerospace and military fields such as missile launchers, tank panoramic mirrors, radar waveguide components, etc. However, in these sealing applications, the start-up resistance torque of the sealing structure is usually strictly required and should be kept within a stable range in any case. Also, magnetic fluid rheological properties are the key factors affecting magnetic fluid sealing (Cheng et al., 2021). It has a significant impact on the starting torque and rotating torque of magnetic fluid rotary seals, and the failure of pressure resistance. In particular, magnetic fluid seals are used in tank panoramic mirrors and radar waveguide components, and the ambient temperature is sometimes very low.

Research on the rheological properties of magnetic liquids mainly focuses on the base carrier liquid and particles (Felicia and Philip, 2012; Paul et al., 2016; Yu et al., 2016; Yang et al., 2020; Cheng et al., 2021). Cheng et al. (2021) studied the effect of rheological properties on seals using magnetic fluids with relatively large viscosity differences between PFPE and diester based. Paul et al. (2016) prepared water-based magnetic liquids with different particle concentrations and studied the non-Newtonian rheological properties of magnetic fluids with different concentrations of viscosity increasing with shear rate, and the non-Newtonian behavior was enhanced by applying a magnetic field. Felicia and Philip (2012) synthesized oil-based ferrofluids and investigated their magnetorheological properties under different magnetic field strengths and volume fractions. They observed a distinct "plateau-like region" in the shear-thinning viscosity curve, under an external magnetic field at extremely small shear rates, and the structure is stable against fragmentation because of a particular alignment of the chains concerning the field direction. Yu et al. (2016) dispersed $Fe_{78}Si_9B_{13}$ amorphous particles into silicone oil to study their rheological properties, confirming that amorphous particles have an improved magnetorheological response compared with magnetic fluids with Fe_3O_4 nanoparticles under an applied magnetic field. Yang et al. (2020) synthesized an Fe_3O_4 hydrocarbon oil-based ferrofluid and its magnetorheological behavior was investigated. A clear hysteresis effect was observed from the viscosity-shear rate flow curve.

Magnetic nanoparticles are uniformly disseminated in the carrier liquid with the assistance of surfactants, which play a crucial role in the magnetic fluid composition (Asahi et al., 2011). Lebedev (2010) prepared mixed fatty acid-modified particles dispersed in isopropanol. Compared with a single oleic acid-modified magnetic liquid, the solidification temperature was reduced to −100°C, which greatly expanded the working range of the magnetic fluid. It is proven that the mixed fatty acid has an important effect on the viscosity of the magnetic fluid at low temperatures. However, surfactant effects on magnetorheological properties have received very little attention. The choice of a surfactant is closely related to the properties of the base carrier fluid, fatty acids are commonly used to stabilize hydrocarbons (Lebedev, 2010), and kerosene is a mixture of hydrocarbons and is commonly used to synthesize magnetic fluids. An oleic acid-stabilized kerosene-based magnetic fluid is the most stable application (Lebedev and Lysenko, 2010). Because of the volatility of kerosene, kerosene-based magnetic fluid seals are usually not used in high-temperature environments, and more choices are used in low-temperature environments. Hao et al. (2015) investigated the viscosity-temperature curves of magnetic fluids with various carrier fluids and demonstrated that the rise in the rotational resistance torque of the magnetic fluid seal was caused by the magnetic fluid's viscosity increasing as the temperature decreased. To make the kerosene-based magnetic fluid used in a lower environment, the surfactant should be chosen with a lower melting point to further minimize the rotating resistance torque of the ferrofluid at low temperatures. The optimum choice is linoleic acid, which has the same chain length as oleic acid and two double bonds. Furthermore, mixing two fatty acids to combine the advantages of two fatty acids is a new approach for better application.

Thence, to investigate the properties of magnetic particles and magnetic fluids, single oleic acid and linoleic acid, and two types of fatty acids combined with modified magnetic fluids, were prepared. Abbreviations for the different surfactants and the meaning of the letters in the figures are shown in **Table 1**. This article aims to further verify and explain the influence of different surfactants on the magnetic fluid by comparing three magnetic fluids with different surfactants modified.

2 MATERIALS AND METHODS

2.1 Materials

Ferric chloride hexahydrate ($FeCl_3{\cdot}6H_2O$), ferrous chloride tetrahydrate ($FeCl_2{\cdot}4H_2O$), and ethanol were procured from Sinopharm Chemical Reagent Beijing Co., Ltd. Ammonium hydroxide ($NH_3{\cdot}H_2O$, 25%), oleic acid ($C_{18}H_{34}O_2$, melting point, 14°C), linoleic acid (C_{18} $H_{32}O_2$, melting point, −5°C), kerosene, and tris(n-nonylphenyl) phosphite were purchased from Beijing Chemical Reagents Company. All compounds are analytical grade and are used without being purified further.

2.2 Experiments

Chemical co-precipitation is the most widely used method to prepare Fe_3O_4 nanoparticles, and the reaction is $Fe^{2+} + 2Fe^{3+} + 8OH^- \rightarrow Fe_3O_4 \downarrow + 8H_2O$. Considering that ferrous irons would be oxidized to ferric irons in the air, the molar ratio of Fe^{2+}: Fe^{3+} was 1:1.75. Taking 20.85 g $FeCl_3 \cdot 6H_2O$ and 8.85 g $FeCl_2 \cdot 4H_2O$ dissolved in 300 ml deionized water under mechanical stirring at 60°C–70°C, ammonium hydroxide was added to the mixed solution whose color changed from red-brown to black immediately and reacted for 30 min under mechanical stirring of 300 rad min^{-1}. Afterward, it heats up to 70°C, keep stirring, and OA as a surfactant was added to the mixture solution for 1 h. Then modified Fe_3O_4 NPs could be obtained by centrifugation or magnetic sedimentation through a

TABLE 1 | Labels for different samples and their meanings.

Labeling of different samples	Meanings
OA	Oleic acids
LA	Linoleic acids
MA	Mixed fatty acids of oleic and linoleic acids
MOA	Oleic acid-coated magnetic nanoparticles and their corresponding magnetic fluids
MLA	Linoleic acid-coated magnetic nanoparticles and their corresponding magnetic fluids
MMA	Mixed fatty acid-coated magnetic nanoparticles and their corresponding magnetic fluids

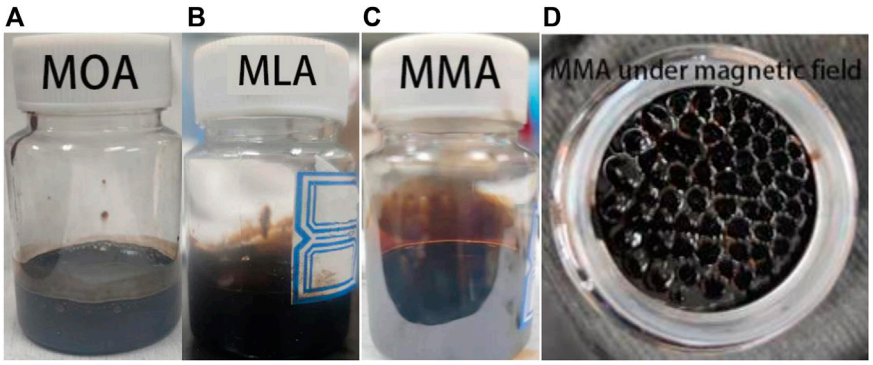

FIGURE 1 | Prepared images of **(A)** MOA, **(B)** MLA, **(C)** MMA, and **(D)** MMA under a magnetic field.

permanent. The modified Fe_3O_4 NPs were washed with ethanol or ultra-pure water several times until the pH was 7 and dried in a vacuum oven for 8 h at 60°C. LA and MA (which could be mixed with ethanol or ultra-pure water, the ratio of oleic and linoleic was 1:1) were used as surfactants to modify the magnetic nanoparticles by the same preparation process. Finally, the quantitative Fe_3O_4 NPs were dispersed in kerosene by ultrasonic for 2 h to obtain a stable magnetic fluid.

For kerosene-based magnetic fluids containing LA, antioxidants are finally added to prevent the oxidation of linoleic acid. The prepared MLA is added with a little tris(*n*-nonylphenyl) phosphite.

The magnetic fluids dispersed with different surfactants are shown in **Figures 1A–C**. **Figure 1D** shows the response of MMA under a magnetic field.

2.3 Characterization of Nanoparticles

The synthesized nanoparticles were characterized by X-ray diffraction (XRD), transmission electron microscopy (TEM), infrared spectroscopy (IR), and vibrating sample magnetometry (VSM) to identify the shape, size, surfactant coating type, and magnetic properties of the samples.

XRD using a D8 Advance Bruker AXS diffractometer with a scan speed of 0.1° per second in the range of 20°–80° was used to determine the identity, phase, and crystallite size of the produced powder sample.

The morphology and nanoparticle size was characterized with a JEM-F200 transmission electron microscope (TEM). The

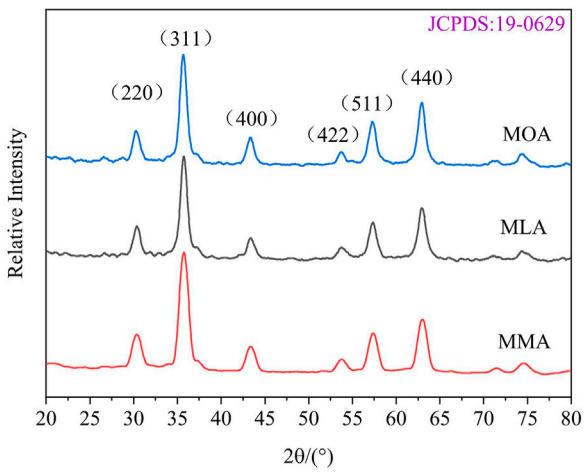

FIGURE 2 | XRD images of Fe_3O_4 particles in three magnetic fluids.

nanoparticles were diluted sufficiently with ethanol and a single drop of the liquid suspension was deposited on a duplex copper mesh. The sample is dried by allowing the ethanol to evaporate through the double copper mesh for a length of time.

The $Fe_3O_4@OA$, $Fe_3O_4@MFA$, and $Fe_3O_4@LA$ nanoparticles were first defined for the functional groups by using an FT-IR spectrometer (NETZSCH, X70). The scanning range of the infrared spectrum is 4,000 cm^{-1}–600 cm^{-1}.

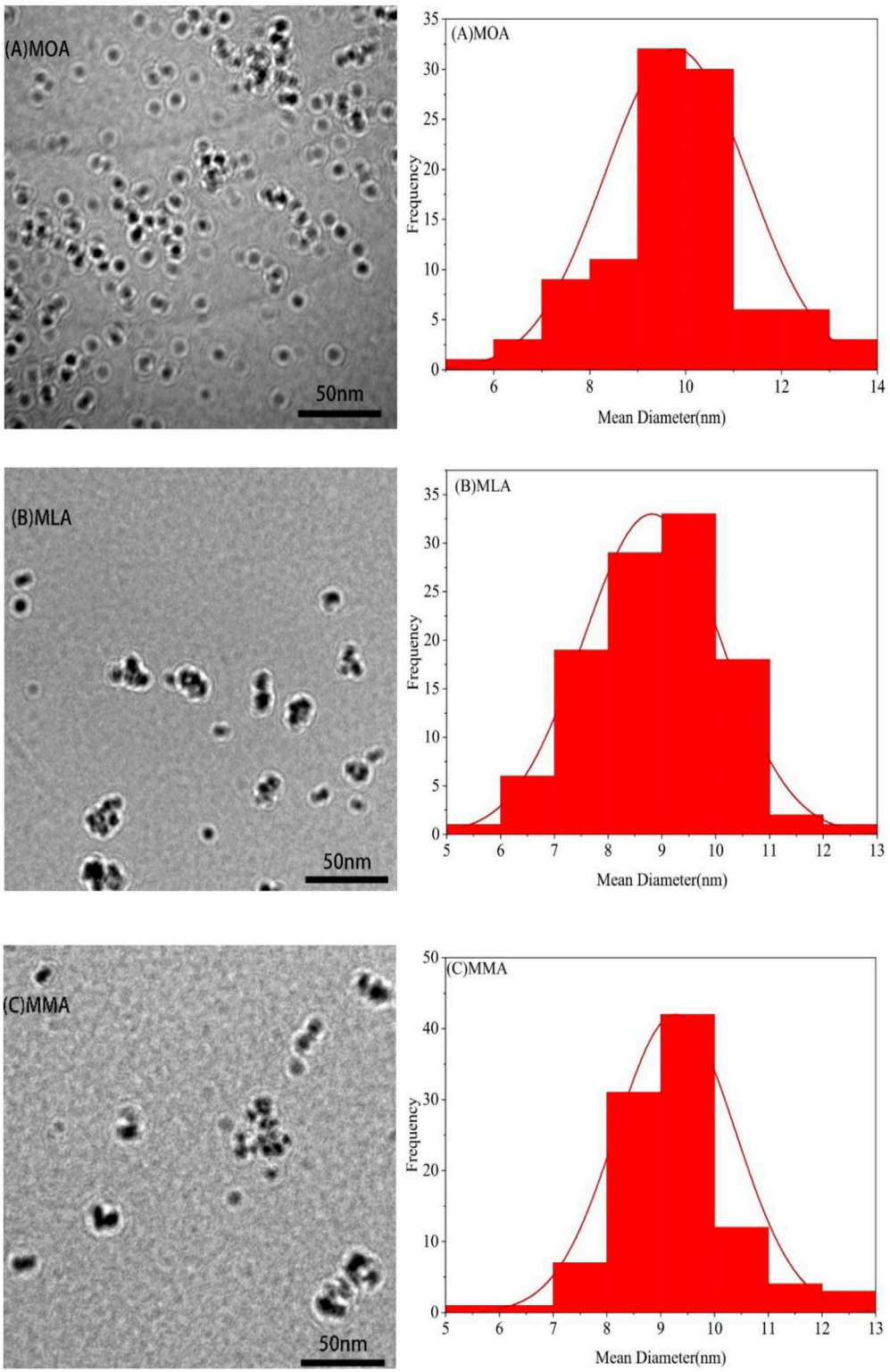

FIGURE 3 | TEM images of particles in three magnetic fluids (left) and the corresponding particle size distribution histograms (right).

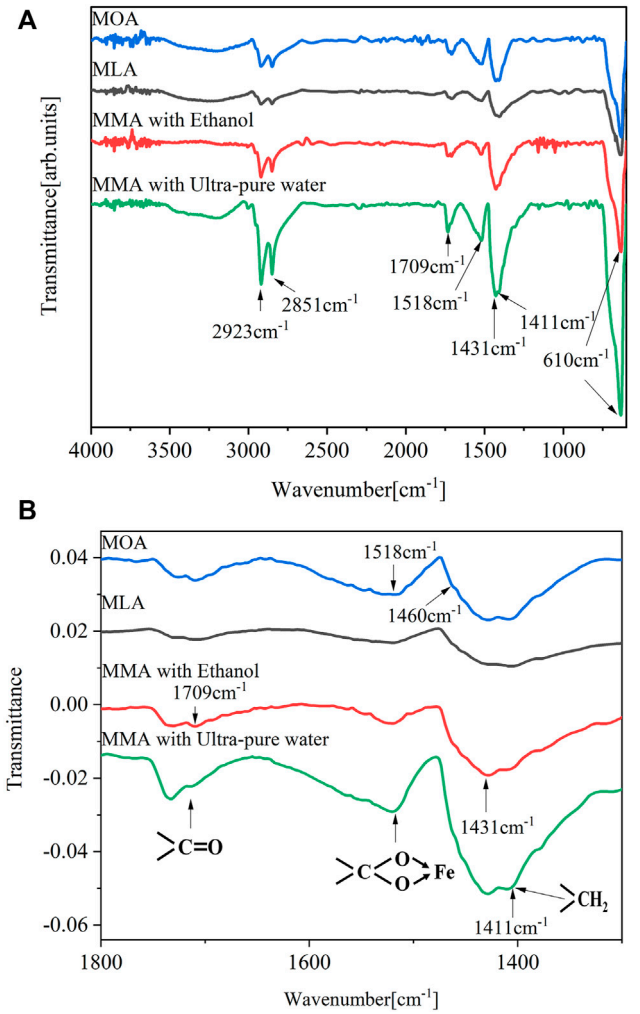

FIGURE 4 | (A) Infrared spectra images of particles in three magnetic fluids, **(B)** 1,300–1800 cm^{-1} zoomed spectra in the carboxylate region.

Magnetic measurements were performed at room temperature on a vibrating sample magnetometer (VSM, LakeShore, model 7307) in a ± 8 kOe external magnetic field.

The rheological properties of the samples were investigated using an MCR302 rheometer, M/s Anton Paar GmbH. A special plate–plate spindle, CP20-MRD, was used for all the measurements in a magnetic field. A coaxial magnetic field in the perpendicular direction to the sample was applied during the rheological measurement. A thermostatic bath (±0.1°C) was used to maintain a constant temperature of the samples during rheology tests. The gap between the plates was 0.084 mm unless otherwise mentioned.

3 RESULTS AND DISCUSSION

3.1 X-Ray Diffraction Analysis

The XRD pattern of the prepared nanoparticles with coating surfactants is shown in **Figure 2**. The crystal structures of Fe_3O_4 nanoparticles using OA, LA, and MA as surfactants are confirmed by an XRD analysis as shown in **Figure 2**. The peak at 30.3°, 35.6°, 43.2°, 53.8°, 57.2°, and 62.8° can be indexed to (2 2 0), (3 1 1), (4 0 0), (4 2 2), (5 1 1), and (4 4 0) lattice planes, respectively, characteristic of Fe_3O_4, which is confirmed by JCPDS card no: 19-0629. The pattern of the three nanoparticles is almost identical, which implies that the modification will not affect the Fe_3O_4 crystal phase of the inverse spinel structure. The average crystallite size of the samples is calculated from the width of the major peak corresponding to the (311) plane using the Scherrer equation.

$$D = \frac{0.9\lambda}{\beta \cos \theta}, \tag{1}$$

where D is the average crystallite size, λ is the wavelength of X-rays, β is full width at half maximum of the peak after correcting the instrumental contribution to the peak broadening, and θ is the angle of diffraction. The calculated particle sizes of the OA, LA, and MA-modified particles are 9.3, 8.7, and 9.5 nm, respectively.

3.2 Transmission Electron Microscope Analysis

The TEM images of the magnetite nanoparticles at high magnifications (left) and the corresponding particle size distribution histograms (right) are shown in **Figures 3A–C**, respectively. The magnetite nanoparticles are observed to be nearly spherical. The particle size distribution histogram, shown in **Figure 3** (right), has been constructed from the image analysis of a series of TEM images. The average particle size was calculated from the micrographs as 9.8, 8.8, and 9.3 nm with a standard deviation of 1.49, 1.28, and 1.1 for OA, LA, and MA-modified particles, respectively. The particle size distribution observed from TEM fairly matches that observed from XRD.

3.3 Infrared Spectroscopy Analysis

Figure 4A compares the infrared spectra of fatty acid-coated powder samples. The Fe-O stretching vibration of Fe_3O_4 corresponds to 610 cm^{-1} (Lenin and Joy, 2017). The symmetric and asymmetric stretching vibrations of methylene (-CH_2-) groups in the fatty acid molecule are represented by the two bands at 2,851 cm^{-1} and 2,923 cm^{-1}, respectively, in all spectra. The bands at 1,411 cm^{-1} and 1,431 cm^{-1} in the spectra of the free acid and the coated particles correspond to -CH_2- deformation. The intensities of OA and MA-coated part bands are higher than those of single LA-coated particles because of increasing unsaturation (-CH=CH-) in the carbon chain. The carbonyl (-C=O) stretching vibration of free fatty acids is represented by the weak band at 1,709 cm^{-1} in all samples. These free fatty acid molecules are most likely caused by the secondary layer present on the surface of the nanoparticles, which is attached to the chemically bound primary layer of fatty acid molecules *via* a weak hydrophobic interaction.

As shown in **Figure 4B**, the bands observed in the range of 1800 cm^{-1}–1,300 cm^{-1} correspond to metal carboxylates, which are

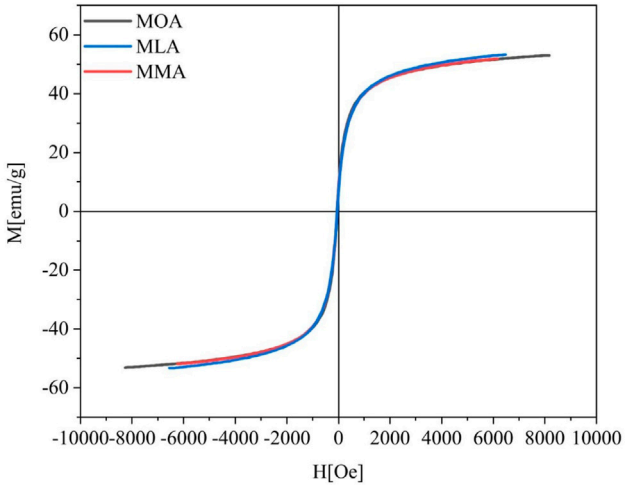

FIGURE 5 | Magnetization curve of particles in three magnetic fluids.

in the range of 1,650 cm^{-1}–1,510 cm^{-1} for the asymmetric carboxyl vibration and 1,431 cm^{-1} for the symmetric carboxyl vibration. The position and separation of carboxyl bands, Δ, deduced the carboxylate coordination mode. More than 200 cm^{-1} indicates monodentate, between 200 and 140 cm^{-1} indicates a bridged bidentate ligand, and less than 110 cm^{-1} indicates a chelating bidentate. For all samples, the difference between the two characteristic bands at 1,518 cm^{-1} and 1,431 cm^{-1} is 87 cm^{-1}, revealing bidentate coordination. The 1,431 cm^{-1} band's location is unknown since it may occur from the overlapping of the carboxylate (COO-) stretching and methylene (-CH_2-) scissoring bands. The shoulder on the peak at 1,431 cm^{-1} is around 1,411 cm^{-1}, making Δ = 104 while still meeting the bidentate coordination (Bronstein et al., 2007; Lenin and Joy, 2016). The intensity of the bands is affected by the washing method used. Moreover, different mixing methods have a huge impact on the intensity of the bands for MA-coated nanoparticles. Peak intensities are much higher when ultra-pure water-mixed fatty acids are used as surfactants than when other surfactants are used. When compared with the fatty acids, the strength of the carbon-based tape at 1709 cm^{-1} in **Figure 4B** decreased significantly after coating (Bronstein et al., 2007). All coated samples had only a weak band at 1709 cm^{-1}, indicating that only a small amount of free acid groups were present. However, the bands of ultra-pure water mixed-fatty acids have a stronger intensity than those of other surfactants, indicating that more free acid is excited.

The carboxylic acid group is bonded to the surface of the nanoparticles, according to the IR analyses. The variation in the conformation of the surfactant molecules, which directly impacts the number of molecules bound to the surface of the nanoparticles, might explain the decrease in the strength of the symmetric and asymmetric stretching of the carboxylate group.

3.4 Vibration Sample Magnetometer Analysis

Magnetic properties of different surfactant-modified nanoparticles are measured at 300 K, at ±8 kOe, as shown in **Figure 5** Magnetization is the most distinctive physical property for ferrofluids. The saturation magnetization of OA, LA, and MA-dispersed magnetic fluid is 53.4, 50.2, and 52.8 emu/g, respectively, and the observed tiny changes in magnetization are consistent with the observed particle size from the TEM histogram (**Figure 3**). The nanoparticles exhibit super-paramagnetism similar to bulk magnetic material, but they have no residual magnetism or remanence when the magnetic field is removed, and particles with different surfactant-modified nanoparticles exhibit excellent super-paramagnetism.

3.5 Rheological Property Analysis

3.5.1 Effect of Shear Rate on Shear Stress

To compare the properties of several magnetic fluids more clearly, **Table 2** gives the density of the magnetic fluid, and the particle size and saturation magnetization of the particles measured by TEM and VSM.

The shear rate of different surfactant-coated magnetic fluids' dependence on the effect of shear stress is shown in **Figures 6A–C**. At room temperature (20°C), rheological studies for various coated magnetic fluids were carried out by altering the shear rate in the range of 0–500 s^{-1}. The samples have been subjected to pre-shearing for about 200 s at a shear rate of 500 s^{-1} without recording any data.

In the absence of a magnetic field, the shear stress increases linearly with the shear rate. In the presence of a magnetic field, the shear stress increases nonlinearly with the increase of the shear rate at a constant magnetic field strength, and there is yield stress. Each solidus line in **Figures 6A–C** shows the fitted values of the flow curves by the power-law relation as predicted by the Herschel–Bulkley model given by

$$\tau = \tau_{H-B} + k \cdot \dot{\gamma}^n,$$

where τ_{H-B} is the yield stress under the magnetic field strength H and k, $\dot{\gamma}$, and n are the consistency parameter, shear rate, and power-law index, respectively. As shown in **Figures 6A–C**, the value of shear stress increases with increasing shear rate. At a constant magnetic field of 200 mT, the fitted curve of the single fatty acid-modified magnetic fluids deviates slightly from the experimental value at a high shear rate. However, the simulation value of the MMA is most consistent with the experimental value. The yield stress is related to the actuation torque in the magnetic fluid seal and a higher viscosity fluid has a higher starting torque of seals (Cheng et al., 2021). The magnetic fluids can flow freely only when the applied force is greater than the yield stress.

The numerical values of and k,$\dot{\gamma}$, and n for different applied constant magnetic fields for each of the three magnetic fluids are shown in **Table 3**. It can be seen that all the magnetic fluids have n < 1 under different magnetic fields, indicating that the fluid is shear thinning, and different surfactants dispersed in the magnetic fluids will not affect the shear-thinning phenomenon.

Under the action of the magnetic field, the force of the interparticle interaction hindering the movement of the fluid leads to the appearance of yield stress. **Figure 6D** shows the fitted yield stress of magnetic fluids with different magnetic fluids under different constant magnetic fields. The figure

TABLE 2 | Parameters of three magnetic fluids at 20°.

Symbol	Meaning	MOA	MLA	MMA
ρ	Magnetic fluid density	1.14 g/cm^3	1.25 g/cm^3	1.17 g/cm^3
d	Particle diameter from TEM	9.8 nm	8.8 nm	9.3 nm
M_S	Particle saturation magnetization	53.4 emu/g	50.2 emu/g	52.8 emu/g

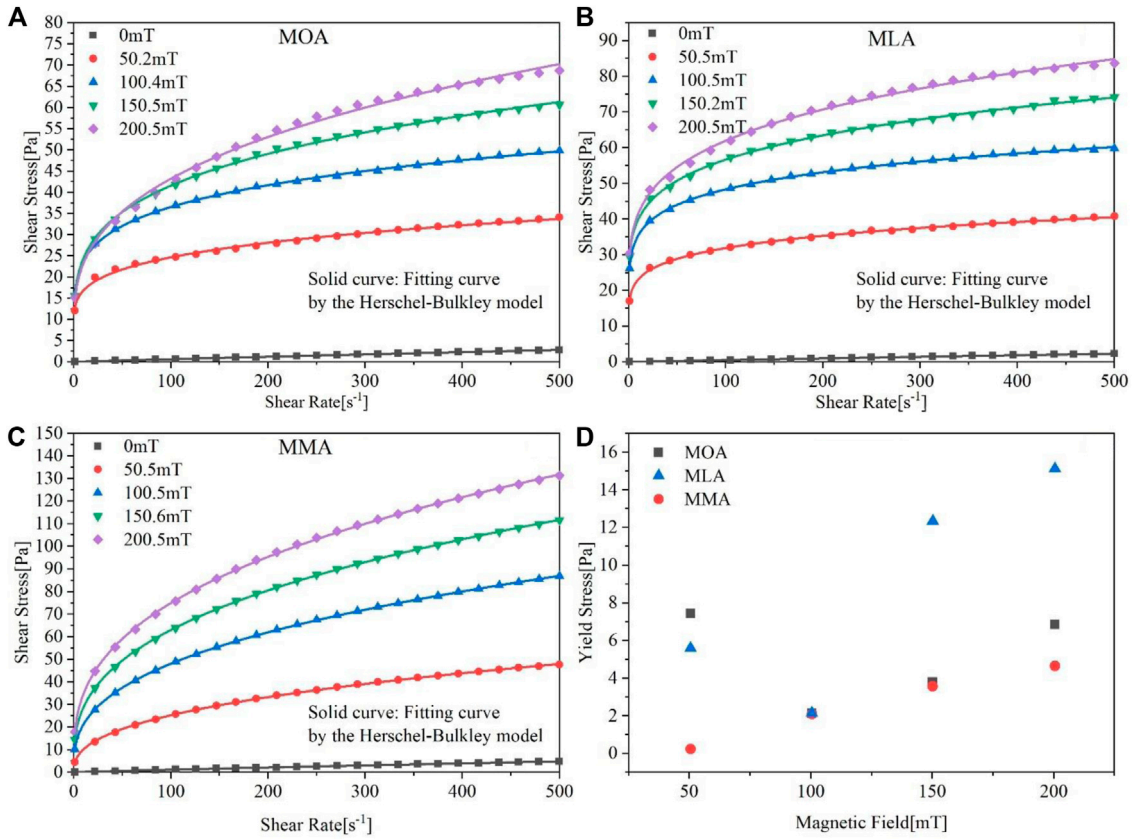

FIGURE 6 | Stress-strain images of **(A)** MOA, **(B)** MLA, and **(C)** MMA. **(D)** Fitted yield stress values of three magnetic fluids by the Herschel–Bulkley model under a constant magnetic field.

TABLE 3 | Rheometric parameters estimated by fitting the Herschel–Bulkley model to the shear stress variation with the shear rate.

Magnetic fluid type	Coefficient value	Applied magnetic field, H			
		50.5 mT	100.5 mT	150.2 mT	200.5 mT
MOA	Yield stress, τ_{H-B}	7.42693	2.13692	3.79829	6.84633
	Consistency parameter, *k*	5.15828	13.65195	11.36512	7.41169
	Power law index, *n*	0.26212	0.20077	0.26093	0.34545
MLA	Yield stress, τ_{H-B}	5.58165	2.14793	12.33298	15.11992
	Consistency parameter, *k*	11.67134	24.03183	17.20449	15.00951
	Power law index, *n*	0.17655	0.14195	0.20561	0.24716
MFA	Yield stress, τ_{H-B}	0.23542	2.10149	3.56683	4.64928
	Consistency parameter, *k*	3.9549	7.99188	10.72927	12.88907
	Power law index, *n*	0.40082	0.38015	0.37184	0.36834

shows that the yield stress of different magnetic fluids increases with increasing constant magnetic field strength, and the dynamic yield stress at a higher magnetic fields indicates that the formation of a large number of chain structures hinders the flow (Felicia and Philip, 2012). Yield stress of the MMA increases with the increase in the magnetic

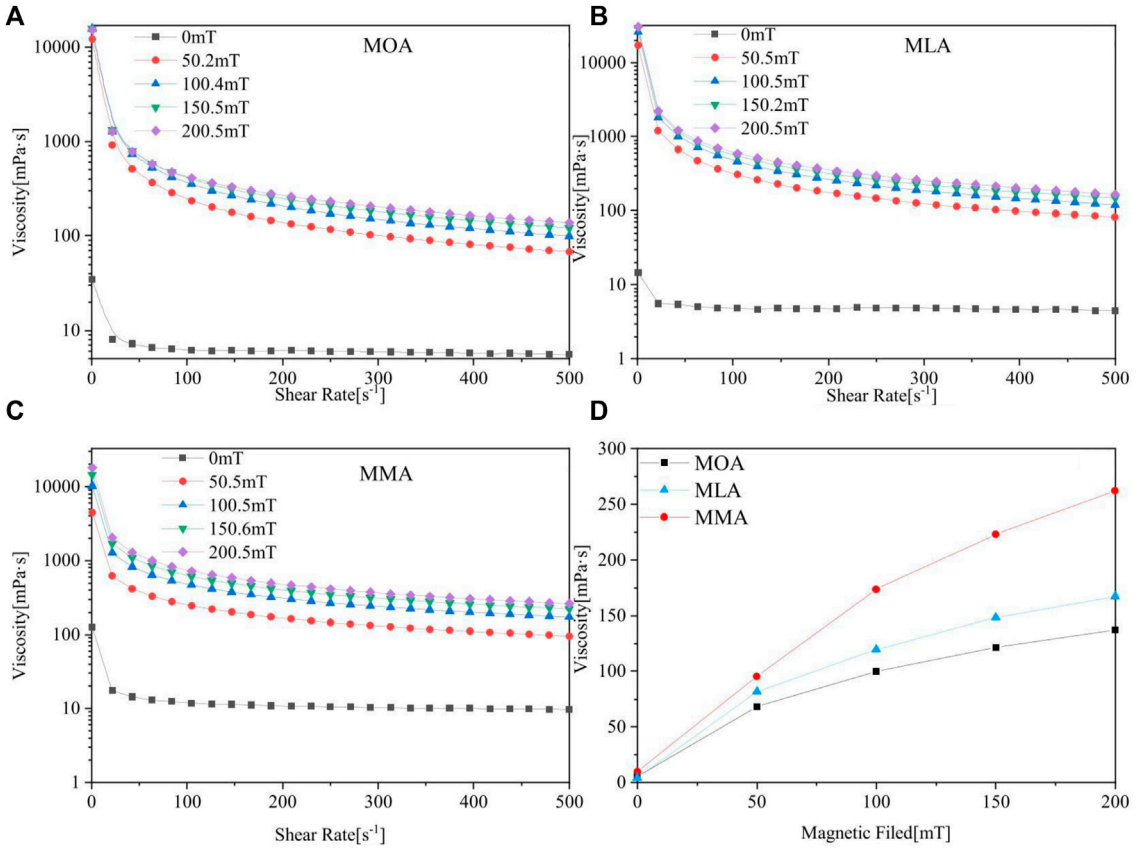

FIGURE 7 | Viscosity-strain images of **(A)** MOA, **(B)** MLA, and **(C)** MMA. **(D)** Maximum shear rate limiting viscosity-constant magnetic field comparison images of three magnetic fluids.

field. While the yield stress at 50 mT for MOA shows an unusual increase and MLA shows a decrease at 100 mT, depending on the choice of data points in the curve, the higher shear rate value affects to some extent. The determination of the fitting equation has an impact on the yield stress obtained from the fitting and an error occurs.

However, it will not affect the overall judgment. The reaction of MLA to the magnetic field is still better, wherefore it has larger yield stress, while the yield stress values of MOA and MMA vary in a similar range, and the performance of MMA is more stable.

3.5.2 Effect of Shear Rate on Viscosity

The dependence of viscosity on the shear rate has been studied under the shear rate-controlled measurements for high values of shear rate (0–500 s^{-1}), MOA, MLA, and MMA as shown in **Figures 7A–C**, respectively. The flow curves of magnetic nanofluids under the influence of a magnetic field exhibit shear-thinning non-Newtonian behavior. The non-linearity observed in the flow curves for the different coats of the magnetic nanofluids depicts the pseudo-plastic behavior of the system.

In the absence of a magnetic field, the viscosity (the viscosity value of each magnetic fluid is about 8 mpa s) of ferrofluids is slightly greater than that of kerosene (20°C, 2.5 mpa s). When a magnetic field is applied, the nanoparticles form chain-like structures, which induce fluid motion resistance and as a result, a rise in viscosity (Zubarev et al., 2002). When the magnetic field strength is 50 mT, many chain-like structures are formed, which increase the fluid resistance and the viscosity performance. With the increase in the magnitude of the applied field, the lengths of the chains also increase. It can be seen from **Figures 7A–C** that the viscosity value of magnetic fluids is closer at higher magnetic field strengths of 100, 150, and 200 mT. Each magnetic fluid has the same trend of change. With the increase in shear rate, the viscosity decreases rapidly, and up to a certain shear rate (about 200 s^{-1}) above which the rate of decrease slows down.

It is pertinent to mention that the increase in viscosity takes place only in the low shear rate region while shear thinning occurs for the remaining applied shear rates. Similar shear-thinning behavior with enhanced viscosity under the application of a magnetic field has been earlier reported (Hosseini et al., 2010; Nowak et al., 2014; Shahnazian et al., 2016). The applied magnetic field causes a strong interaction between the magnetic nanoparticles and leads to the formation of magnetic structures. But with the increase in shearing rate, structures in the form of agglomerates tend to break down and the nanoparticles arrange themselves along

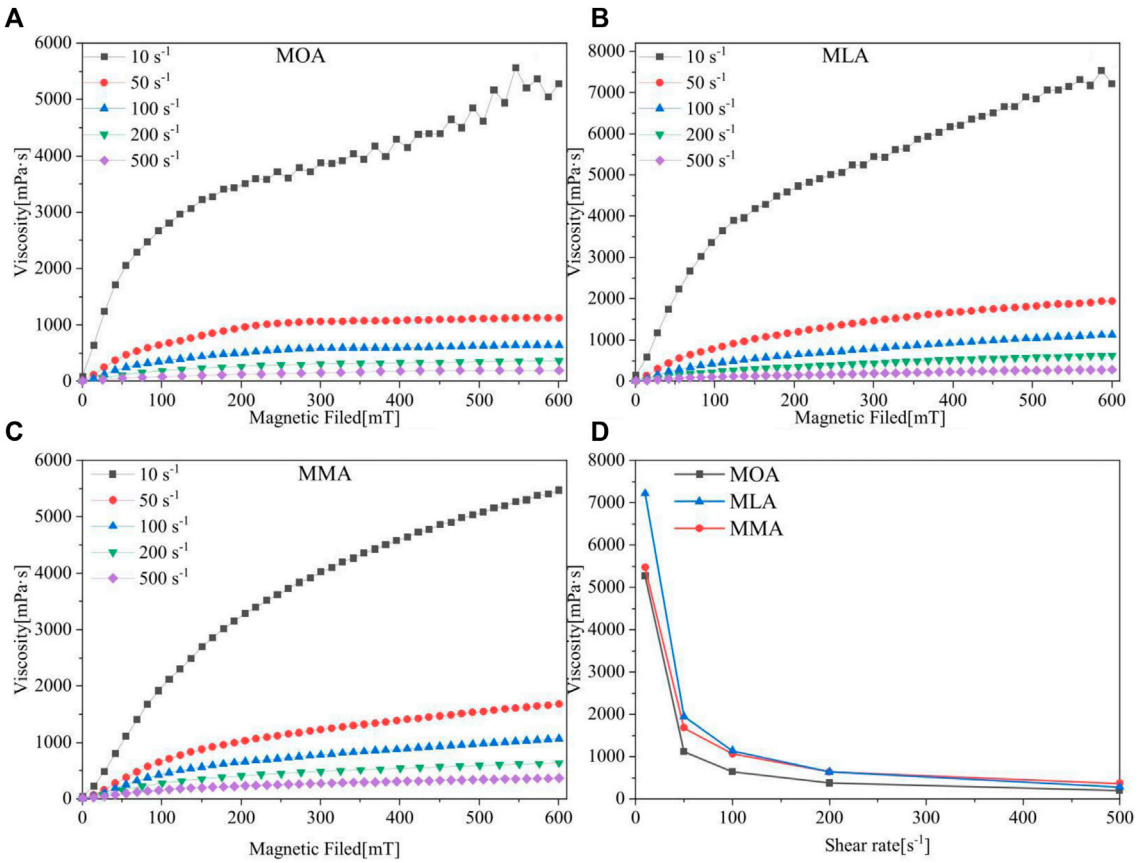

FIGURE 8 | Viscosity-magnetic field images of **(A)** MOA, **(B)** MLA, and **(C)** MMA. **(D)** Maximum magnetic field limit viscosity-constant shear rate comparison images of three magnetic fluids.

the shearing direction. This leads to a decrease in the fluid viscosity at high shear rates (Felicia and Philip, 2012).

The viscosity of the nanofluids at the highest shear rates is called the high shear limiting viscosity, as shown in **Figure 7D**. Thus, it may be noted that the structures that are formed by the application of a magnetic field, although broken down by the application of a high shear rate but are not completely destroyed, has a strong effect on the limiting viscosity of the magnetic fluids. **Figure 7D** shows that when the shear rate increases, the viscosity of the MMA becomes greater than that of the single acid-dispersed magnetic fluids, and a greater slope of viscosity increases the curve. The structure created by the particles of the MMA was influenced more by the action of shear and shows a gradual increase in viscosity. The shear rate has a minor influence, and the performance is more stable.

3.5.3 Effect of Magnetic Field on Viscosity

The magneto-viscous effect was investigated by increasing the magnetic field from 0– 600 mT at different shear rates, as shown in **Figures 8A–C**, respectively. Before each start, pre-shearing was performed for 90 s without a magnetic field and this part of the data was not recorded. During the experiment, the shear rate was kept constant. When a magnetic field is applied, magnetic nanoparticles are polarized and arrange their orientation along the direction of the magnetic field. The nanoparticles form a chain-like structure, causing motion resistance of the fluid and a continuous rise in viscosity.

As the strength of the magnetic field increases, the length of the chains also increases, the shear rate remains constant, and with further increases in the field, multiple chains attract each other, forming a columnar structure that further increases the viscosity of the fluid. After most of the nanoparticles present in the nanofluid dispersion participated in the formation of the column structure, a further increase in the applied field resulted in no further increase in viscosity and reached a saturation value. It is worth mentioning here that a higher dispersion concentration means a higher number and density of nanoparticles. Under an applied magnetic field, the chain-like structures that eventually formed the pillars contained more nanoparticles than the chain-like structures (Felicia and Philip, 2012).

The shear rate has a significant effect on the viscosity of the magnetic fluids with the magnetic field. The viscosity change value under the magnetic field from 0– 200 mT is expanded. Under the influence of the magnetic field, the particles

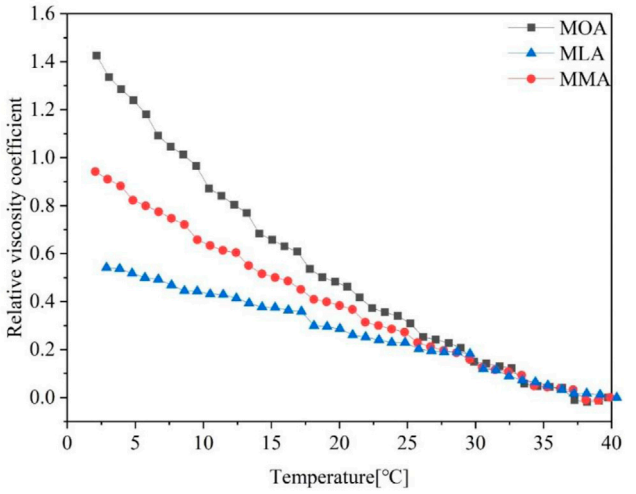

FIGURE 9 | Relative viscosity coefficient-temperature images of three magnetic fluids.

continuously form chain-like formations and are sheared. The shear rate is 10 s^{-1}, and the magnetic field strength of various modified magnetic fluids increased dramatically with the rising magnetic field strength at a low field strength, practically linearly increasing. The shear force was insufficient at the moment to disintegrate the particles' structure and increase the shear rate. The shear rate is 50 s^{-1}, and the massive shear force decomposes the particle-forming structure, resulting in a significant decrease in the degree of reactivity of different magnetic fluids to the magnetic field. Under a magnetic field, the shear force is substantially larger than the yield stress. The viscosity change is further minimized as the shear rate is increased.

The viscosity of all magnetic fluids increases as the magnetic field intensity increases, and the viscosity value progressively tends to be saturated at the highest magnetic field strength, as shown in **Figures 8A–C**. **Figure 8D** shows the change in the viscosity value with an increasing constant shear rate at a magnetic field strength of 600 mT.

When the magnetic field is 600 mT and the shear rate is 10 s^{-1}, the viscosity value of the MLA is 7,300 mpa s higher than that of the MOA and MMA 5,400 mpa s, showing a stronger magneto-viscosity effect. With the increasing shear rate, the viscosity value of the MMA is higher than that of the single fatty acid-modified magnetic fluids at 600 mT, which is consistent with the effect of viscosity on the shear rate. The shear rate is 10 s^{-1}, the single fatty acid-dispersed magnetic fluids both fluctuated at the highest magnetic field strength, and the cause of the oscillations could be the particles' instability as they reorganized. Even with a high magnetic field intensity and a moderate shear rate, the viscosity of the MMA gradually increases, and the performance becomes more stable.

3.5.4 Effect of Temperature on Viscosity

From 40°C to 0°C, the viscosity variations of several magnetic fluids were measured in the absence of a magnetic field. A pre-shear of 100 s^{-1} for 180 s was conducted before that. This portion of the data will not be saved, and it was kept at 100 s^{-1} throughout the experiment. The shear rate remains constant.

Because the viscosity values of different modified magnetic liquids differ at 40°C, the relative viscosity coefficient is used to express the relationship between viscosity and temperature.

$$R = \frac{\eta - \eta_0}{\eta_0}, \tag{2}$$

where R, η, and η_0 are the relative viscosity coefficient, viscosity values at different temperatures, and viscosity values at 40°C, respectively. The relative change in viscosity with temperature is shown in **Figure 9**. When the temperature is reduced to 0°C from 40°C, the viscosity of the MOA increases by 1.5 times. The viscosity of the MLA, on the other hand, increased by 0.6 times. When the temperature lowers to 0°C from 40°C, the viscosity of the MMA doubles, as seen in the figure. On the one hand, different magnetic fluids have different initial viscosity values at 40°C, and on the other hand, this could be due to the surfactant affecting the temperature-induced viscosity shift. Mixed surfactants can ameliorate the viscosity–temperature properties of magnetic fluids to some extent.

Therefore, when the ambient environment of kerosene-based or other hydrocarbon magnetic fluids is at a certain low temperature, it can be considered to use a single fatty acid with a lower melting point to disperse, or a fatty acid with a lower melting point can be mixed with oleic acid. The starting torque of the magnetic fluid seal is related to the amount of viscosity rise at low temperatures. To content the performance, for example, magnetic fluids with good viscosity–temperature performance are required for magnetic liquid sealing in tank panoramic mirrors and radar waveguide components, etc. At this time, surfactant-dispersed magnetic fluids with lower melting points can play an important role. This allows kerosene-based magnetic fluid seals to be used across a wider temperature range.

4 CONCLUSION

The dispersion of several fatty acid-modified particles into kerosene was examined in this work. The following conclusions can be drawn from particle characterization and rheological experiments on magnetic fluids.

1) The particle size will be impacted to some extent when the particles are adjusted by different surfactants, but the crystal phase structure of the particles will not be changed. Bidentate coordination patterns between fatty acids and particles are identified by infrared spectroscopy. MA (mixed fatty acids) have no effect on the coordination mode.

2) The Herschel and Bulkley model was used to fit the stress-strain curve, and the fitted curve for the MMA perfectly matched the experimental value. Under a given magnetic field and a shear rate of 500 s^{-1}, the viscosity of the MMA grows larger than that of single acid-dispersed magnetic fluids, with a greater slope of the viscosity growth curve. This indicates that the mixed fatty acids have more stable rheological properties.
3) When the temperature is changed from 40°C to 0°C, it demonstrates that using a mixed fatty acid as a surfactant can improve the viscosity–temperature performance of magnetic fluids by adjusting the increase ratio of viscosity as the temperature decreases. This work provides a new technique to optimize the viscosity–temperature performance of kerosene-based magnetic fluids when used in low-temperature situations and can lower the increase in the starting torque when magnetic fluids are sealed. Magnetic fluid seals based on kerosene or hydrocarbons can withstand lower ambient temperatures by using surfactants with lower melting points, allowing for a wider application range.

DATA AVAILABILITY STATEMENT

The original contributions presented in the study are included in the article/Supplementary Material; further inquiries can be directed to the corresponding author.

AUTHOR CONTRIBUTIONS

ZZ was in charge of the whole trial; GZ wrote the manuscript and performed laboratory analyses; WY participated in rheological experiments; and DW and DL contributed to the revision of the manuscript.

FUNDING

This work was supported by the National Natural Science Foundation of China major instrument development project (51927810).

REFERENCES

Asahi, T., Koshi, T., Hatsugai, S., Yamada, T., and Takemura, Y. (2011). Magnetic Characterization of Surface-Coated Magnetic Nanoparticles for Biomedical Application. *J. Magnetism Magnetic Mater.* 323, 1398–1403. doi:10.1016/j.jmmm.2010.11.054

Batter, B., Qu, Y., Meng, X., Tian, C., Du, S., Wang, R., et al. (2013). Preparation and Magnetic Performance of the Magnetic Fluid Stabilized by Bi-surfactant. *J. Magnetism Magnetic Mater.* 332, 151–156. doi:10.1016/j.jmmm.2012.12.009

Bronstein, L. M., Huang, X., Retrum, J., Schmucker, A., Pink, M., Stein, B. D., et al. (2007). Influence of Iron Oleate Complex Structure on Iron Oxide Nanoparticle Formation. *Chem. Mat.* 19 (15), 3624–3632. doi:10.1021/cm062948j

Cheng, Y., Li, D., and Li, Z. (2021). Influence of Rheological Properties on the Starting Torque of Magnetic Fluid Seal. *IEEE Trans. Magnetics* 57, 4600308. doi:10.1109/tmag.2019.2934716

Cui, H., Li, D., and Zhang, Z. (2015). Preparation and Characterization of Fe3O4 Magnetic Nanoparticles Modified by Perfluoropolyether Carboxylic Acid Surfactant. *Mater. Lett.* 143, 38–40. doi:10.1016/j.matlet.2014.12.037

Dubreuil, J., and Bobowski, J. S. (2019). Ferromagnetic Resonance in the Complex Permeability of an Fe_3O_4-Based Ferrofluid at Radio and Microwave Frequencies. *J. magnetism magnetic Mater.* 489, 1653871–1653876. doi:10.1016/j.jmmm.2019.165387

Felicia, L. J., and Philip, J. (2012). Probing of Field-Induced Structures and Tunable Rheological Properties of Surfactant Capped Magnetically Polarizable Nanofluids. *Langmuir* 29, 110–120. doi:10.1021/la304118b

Hao, D., Li, D., Chen, J., and Yu, J. (2015). Theoretical Analysis and Experimental Study of the Characteristics of Magnetic Fluid Seal with a Large Diameter at High/low Temperatures. *Int. J. Appl. Electromagn. Mech.*, 58:531–550. doi:10.3233/JAE-180065

Hensley, D., Zhi, W. T., and Dhavalikar, R. (2017). Combining Magnetic Particle Imaging and Magnetic Fluid Hyperthermia in a Theranostic Platform. *Phys. Med. Biol.* 62 (9), 3483–3500. doi:10.1088/1361-6560/aa5601

Hosseini, M., Fazlali, A., Ghasemi, E., and Moghaddam, H. (2010). Rheological Properties of a γ-Fe2O3 Paraffin-Based Ferrofluid. *J. Magnetism Magnetic Mater.* 22 (23), 3792–3796. doi:10.1016/j.jmmm.2010.08.003

Lebedev, A. V. (2010). Low-temperature Magnetic Fluid Stabilized with Mixed Fatty Acids. *Colloid J.* 72 (6), 815–819. doi:10.1134/s1061933x10060128

Lebedev, A. V., and Lysenko, S. N. (2010). Magnetic Fluids Stabilized by Polypropylene Glycol. *J. Magnetism Magnetic Mater.* 323 (10), 1198–1202. doi:10.1016/j.jmmm.2010.11.005

Lenin, R., and Joy, P, A. (2016). Role of Primary and Secondary Surfactant Layers on the Thermal Conductivity of Lauric Acid Coated Magnetite Nanofluids. *J. Phys. Chem. C. Nanomater. interfaces*, 120:11640–11651. doi:10.1021/acs.jpcc.5b12476

Lenin, R., and Joy, P. A. (2017). Studies on the Role of Unsaturation in the Fatty Acid Surfactant Molecule on the Thermal Conductivity of Magnetite Nanofluids. *J. Colloid Interface Sci.* 506, 162–168. doi:10.1016/j.jcis.2017.07.038

Li, Z., Li, D., Chen, Y., Yilong, Y., and Yao, J. (2017). Influence of Viscosity and Magnetoviscous Effect on the Performance of a Magnetic Fluid Seal in a Water Environment. *Tribol. Trans.*, 61:367–375. doi:10.1080/10402004.2017.1324071

Marcin, S. (2018). Experimental Study on the Pressure Distribution Mechanism Among Stages of the Magnetic Fluid Seal. *IEEE Trans. Magn.* 54, 1–7. doi:10.1109/tmag.2018.2816567

Metelkina, O. N., Lodge, R. W., Rudakovskaya, P. G., Gerasimov, V. M., Lucas, C. H., Grebennikov, I. S., et al. (2017). Nanoscale Engineering of Hybrid Magnetite-Carbon Nanofibre Materials for Magnetic Resonance Imaging Contrast Agents. *J. Mat. Chem. C* 5 (8), 2167–2174. doi:10.1039/c6tc04141h

Nowak, J., Wolf, D., and Odenbach, S. (2014). A Rheological and Microscopical Characterization of Biocompatible Ferrofluids. *J. Magnetism Magnetic Mater.* 354 (mar), 98–104. doi:10.1016/j.jmmm.2013.10.050

Paul, G., Kumar Das, P., and Manna, I. (2016). Synthesis, Characterization and Studies on Magneto-Viscous Properties of Magnetite Dispersed Water Based Nanofluids. *J. Magnetism Magnetic Mater.* 404, 29–39. doi:10.1016/j.jmmm.2015.11.085

Shahnazian, H., Graf, D., Borin, D. Y., and Odenbach, S. (2016). Rheology of a Ferrofluid Based on Nanodisc Cobalt Particles. *J. Phys. D-Applied Phys.* 49, 279501. doi:10.1088/0022-3727/42/20/205004

Shahrivar, K., and de Vicente, J. (2014). Ferrofluid Lubrication of Compliant Polymeric Contacts: Effect of Non-homogeneous Magnetic Fields. *Tribol. Lett.* 56 (2), 281–292. doi:10.1007/s11249-014-0408-y

Szczech, M. (2020). Experimental Studies of Magnetic Fluid Seals and Their Influence on Rolling Bearings. *J. Magnetics* 25 (1), 48–55. doi:10.4283/JMAG.2020.25.1.048

Wang, J., Fan, M., Bian, X., Yu, M., Wang, T., Liu, S., et al. (2018). Enhanced Magnetic Heating Efficiency and Thermal Conductivity of Magnetic Nanofluids with FeZrB Amorphous Nanoparticles. *J. magnetism magnetic Mater.* 465, 480–488. doi:10.1016/j.jmmm.2018.06.043

Wang, Z., and Decai, L. (2015). Theoretical Analysis and Experimental Study on Loading Process Among Stages of Magnetic Fluid Seal. *Int. J. Appl. Electromagn. Mech.* 48, 101–110. doi:10.3233/JAE-140126

Yang, C., Liu, Z., Yu, M., and Bian, X. (2020). The Influence of Thixotropy on the Magnetorheological Property of Oil-Based Ferrofluid. *J. Mol. Liq.* 320 (3), 114425. doi:10.1016/j.molliq.2020.114425

Yang, X., Sun, P., Chen, F., Hao, F., Li, D., and Thomas, P. J. (2019). *Numerical and Experimental Studies of a Novel Converging Stepped Ferrofluid Seal*. New Jersy(US): IEEE Transactions on Magnetics.

Yao, J., Huang, C., and Li, D. (2015). Research on A Novel Ferrofluid Inertial Sensor with Levitating Nonmagnetic Rod. *IEEE Sensors J.* 16 (5), 1. doi:10.1109/JSEN.2015.2490253

Yu, M., Yang, C., Bian, X., Zhao, S., Wang, T., Liu, S., et al. (2016). Application of Fe78Si9B13 Amorphous Particles in Magnetorheological Fluids. *RSC Adv.* 6, 22511–22518. doi:10.1039/C5RA24106E

Yu, J., He, X., Li, D., and Li, W. (2018). Effective and Practical Methods to Calculate the Second-Order Buoyancy in Magnetic Fluid Acceleration Sensor. *IEEE Sensors J.* 18, 2278–2284. doi:10.1109/jsen.2018.2793944

Yu, J., Chen, D., Cai, Z., Li, D., Cao, Q., and Qian, L. (2019). Research on the Magnetic Fluid Levitation Force Received by a Permanent Magnet Suspended in Magnetic Fluid: Consideration a Surface Instability. *J. Magnetism Magnetic Mater.* 492, 165678. doi:10.1016/j.jmmm.2019.165678

Zubarev, A. Y., Odenbach, S., and Fleischer, J. (2002). Rheological Properties of Dense Ferrofluids. Effect of Chain-like Aggregates. *J. Magnetism Magnetic Mater.* 252, 241–243. doi:10.1016/s0304-8853(02)00674-1

Conflict of Interest: The authors declare that the research was conducted in the absence of any commercial or financial relationships that could be construed as a potential conflict of interest.

Publisher's Note: All claims expressed in this article are solely those of the authors and do not necessarily represent those of their affiliated organizations, or those of the publisher, the editors, and the reviewers. Any product that may be evaluated in this article, or claim that may be made by its manufacturer, is not guaranteed or endorsed by the publisher.

frontiers | Frontiers in Materials

ORIGINAL RESEARCH
published: 06 July 2022
doi: 10.3389/fmats.2022.930825

Multi-Condition Temperature Field Simulation Analysis of Magnetorheological Grease Torsional Vibration Damper

Zida Xiao[1], Hongsheng Hu[2], Qing Ouyang[2], Liyang Shan[3] and Hongbo Su[3]*

[1]College of Mechanical Engineering, Zhejiang University of Technology, Hangzhou, China, [2]College of Information Science and Engineering, Jiaxing University, Jiaxing, China, [3]School of Mechanical Engineering, Anhui Polytechnic University, Wuhu, China

To reveal the transient temperature distribution pattern inside the magnetorheological grease (MRG) torsional vibration damper and explore the relationship between the current and internal temperature of the device, the transient temperature simulation analysis of the MRG device was conducted in this study. Firstly, a theoretical heat transfer model of MRG torsional vibration damper with dual heat source structural feature was established based on the Bingham constitutive model and the temperature-dependent viscosity characteristic of MRG. Then, the transient temperature field model of the MRG torsional vibration damper was developed by the finite element method, the temperature field distribution and temperature–time variation characteristics of the MRG torsional vibration damper at 0A, 1A, and 2A working conditions were analyzed, and the effects of viscosity and slip factors on the temperature rise of the device were investigated. The simulation results show that the temperature rise of MRG in the working domain is the fastest, but a gradual slowing of the temperature rise rate. The magnitude and rate of temperature rise are maximum when the 1A current is applied to the torsional vibration damper. Finally, the current–temperature curve is obtained by fitting the simulation results. The results of the analysis reveal the internal temperature distribution and temperature rise characteristics of the torsional vibration damper, which provide a theoretical basis for the structural optimization and control strategy design of the MRG torsional vibration damper considering temperature as a factor.

Keywords: MRG torsional vibration damper, multi-condition analysis, temperature field simulation, viscosity–temperature characteristics, Bingham model

OPEN ACCESS

Edited by:
Weihua Li,
University of Wollongong, Australia

Reviewed by:
Lei Deng,
University of Wollongong, Australia
Xuan Shouhu,
University of Science and Technology of China, China

****Correspondence:***
Hongsheng Hu
hhs999@mail.zjxu.edu.cn

Specialty section:
This article was submitted to Smart Materials, a section of the journal Frontiers in Materials

Received: *28 April 2022*
Accepted: *26 May 2022*
Published: *06 July 2022*

Citation:
Xiao Z, Hu H, Ouyang Q, Shan L and Su H (2022) Multi-Condition Temperature Field Simulation Analysis of Magnetorheological Grease Torsional Vibration Damper. Front. Mater. 9:930825. doi: 10.3389/fmats.2022.930825

1 INTRODUCTION

In engine systems, the power source for crankshaft rotation is the explosive force generated by the instantaneous combustion of combustible gases in the cylinder, and explosive force is transmitted to the crankshaft through the piston and other parts. This process leads to torsional–detorsional effects on the crankshaft, which further lead to torsional vibration of the crankshaft (Boysal and Rahnejat 1997). For multi-cylinder engines, the crankshaft system comes with a large number of pistons, connecting rods, flywheels, and other accessories (Periyasamy and Alwarsamy 2012). Large rotational inertia, high speed, high load (Karabulut 2012), and cylinder ignition unevenness (Zhang and Yu 2009) make the torsional vibration of the crankshaft more intense, especially in

the starting phase with high acceleration. To prevent the crankshaft from torsional deformation or failure, the crankshaft torsional vibration must take effective reduction measures (Fonte and de Freitas 2009). At present, the main reduction measure for crankshaft torsional vibration is to install a torsional vibration damper in the crankshaft system, which can well avoid crankshaft torsional vibration caused by resonance and reduce the amplitude of torsional vibration (Mendes et al., 2008).

So far, the torsional vibration damper that has been produced and put into use are silicone oil dampers (Pistek et al., 2017), rubber dampers (Silva et al., 2019), silicone oil–rubber composite torsional vibration dampers (Li et al., 2020) and dual-mass flywheel torsional vibration dampers (Long et al., 2021). However, these dampers only show a good damping effect at a specific resonance frequency due to which the damping is uncontrollable (Shu et al., 2015). Therefore, magnetorheological smart materials were introduced to develop the magnetorheological torsional vibration damper (Abouobaia et al., 2016, 2020; Brancati et al., 2019). The installation of the damper at the free end of the crankshaft can prevent the crankshaft from torsional failure, but then comes the problem of damper heat dissipation. Generally, damping materials such as silicone oil, MRG, and other viscous liquids need to be overhauled after a period of operation to ensure that the damping material does not fail due to high temperature (Homik 2010).

MRG is a variable damping smart material whose damping characteristics, magnetic field characteristics, and settlement characteristics have obvious temperature dependence (Sahin et al., 2009; Meyer et al., 2016; McKee et al., 2017; Liang et al., 2021). Rheological characteristics of MRG vary in different magnetic fields and temperatures (Kamble et al., 2021). If the temperature is not analyzed and suppressed, the MRG torsional vibration damper will not only fail to dampen the torsional vibration but also further aggravate the vibration of the crankshaft system due to its own heavy mass.

At present, there are many studies on the temperature analysis of viscous fluid torsional vibration dampers and magnetorheological rotary dampers. Homik et al. proposed a thermal fluid dynamics model for viscous torsional vibration dampers and investigated the effect of temperature and viscosity variations of the damping fluid inside the torsional vibration damper on the efficiency of the torsional vibration damper (Homik, 2012; Homik et al., 2021). Venczel et al. developed a two-dimensional thermal calculation program based on the finite difference method, analyzed the heat transfer process inside silicone oil dampers, and developed a temperature and shear rate–dependent viscosity model for the silicone fluid (Venczel and Veress. 2020; Venczel et al., 2021). Gordaninejad et al. conducted an experimental and theoretical study of heat generation and dissipation in magnetorheological dampers, developed a theoretical model for predicting the temperature rise of magnetorheological dampers, and developed a control equation in the dimensionless form (Gordaninejad and Breese, 1999). Batterbee et al. quantified the effect of temperature on the damper between 15°C and 75°C and studied the effect of elevated temperature on magnetorheological fluid viscosity and yield stress (Batterbee and Sims 2008). Kavlicoglu et al. (2007) conducted a theoretical and experimental study of heat generation in a high-torque magnetorheological differential clutch, mainly for the effect of temperature on the torque performance of the clutch, and analyzed the temperature rise distribution inside the clutch. Nguyen et al. proposed an optimization method based on finite element analysis for magnetorheological brakes considering temperature factors and used the Bingham model and Herschel–Bulkley model to analyze the braking torque of the brake (Nguyen and Choi 2010). Park et al. (2008) introduced a magnetorheological braking system, and the fluid flow and heat transfer system of the magnetorheological fluid were analyzed considering the critical issues of brake size, performance, and temperature. Patil et al. (2016) performed a thermal analysis of a magnetorheological brake to evaluate the temperature rise of the magnetic fluid due to brake manipulation and performed a finite element analysis of the temperature field of the brake. So far, there have been many studies on the temperature aspects of viscous fluid torsional vibration dampers and magnetorheological dampers. However, there is a lack of temperature analyses of MRG torsional vibration dampers under different working conditions. This study adopts the multi-field coupling method of flow field–temperature field for simulation analysis, which reveals the temperature gradient distribution inside the device in more detail. In this study, based on the temperature rise theory of torsional vibration dampers and the temperature analysis of magnetorheological dampers, the temperature analyses of MRG torsional vibration dampers under different working conditions have been developed.

In this article, a theoretical model of the temperature field of MRG was established based on the Bingham mechanics model and viscosity–temperature model, the heat transfer system of the MRG torsion damper was analyzed, and the heat source and heat generation rate of MRG torsion damper and the internal forced convection heat transfer coefficient were calculated. Secondly, the three-dimensional model of MRG torsional vibration damper was established, and its temperature rise principle was analyzed. The transient temperature field of the MRG torsional vibration damper was simulated and analyzed in the 0A, 1A, and 2A three working conditions. The influence of slip between the inner and outer rotors and the viscosity of MRG on temperature rise was investigated. The results show the distribution pattern of temperature and provide the simulation and theoretical basis for subsequent heat dissipation optimization and temperature compensation control.

The remainder of the article is organized as follows. In **Section 2**, the temperature characteristics and magnetic field characteristics of MRG were analyzed, the mathematical model of the temperature field of MRG torsional vibration damper was established, and the forced convection heat transfer coefficient was calculated. In **Section 3**, the three-dimensional transient temperature simulation model of the MRG torsional vibration damper was established, and the temperature rise principle inside the device was analyzed. In **Section 4**, the results of transient temperature field simulation were analyzed, and the relationship between the current and internal temperature characteristics of

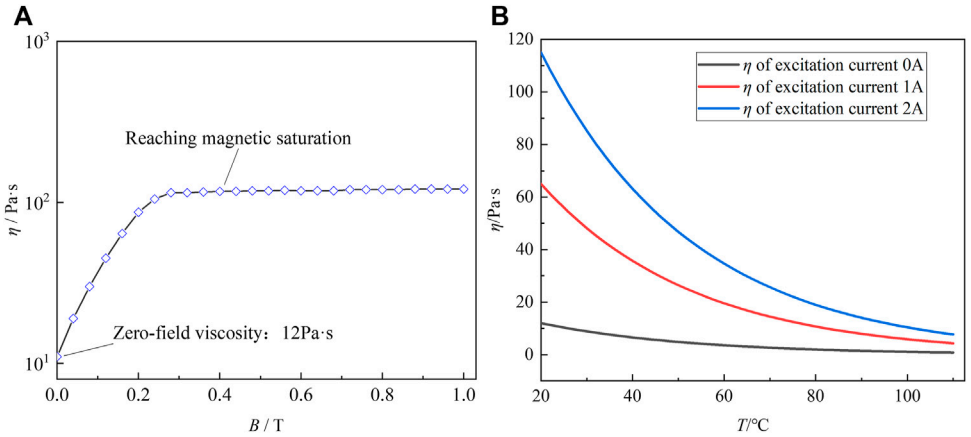

FIGURE 1 | (A) Curve of magnetic field characteristics of MRG. **(B)** Curve of temperature characteristics of MRG.

the device was explored. **Section 5** put forward the conclusion of the study.

2 MATHEMATICAL MODEL OF MAGNETORHEOLOGICAL GREASE TORSIONAL VIBRATION DAMPER

2.1 Magnetic Field Characteristics and Temperature Characteristics of Magnetorheological Grease

The rheological behavior of MRG is described based on the Bingham constitutive model, which is **Eq. 1**.

$$\begin{cases} \tau = \boldsymbol{\tau}_y \mathbf{sgn}(\dot{\boldsymbol{\gamma}}) + \boldsymbol{\eta}_0 \dot{\boldsymbol{\gamma}} & |\boldsymbol{\tau}| > |\boldsymbol{\tau}_y| \\ \dot{\boldsymbol{\gamma}} = \mathbf{0} & |\boldsymbol{\tau}| < |\boldsymbol{\tau}_y| \end{cases}, \tag{1}$$

where $\boldsymbol{\tau}$ is the shear stress, $\boldsymbol{\tau}_y$ is the shear yield stress caused by the applied magnetic field, $\dot{\boldsymbol{\gamma}}$ is the shear rate, and $\boldsymbol{\eta}_0$ is the zero-field viscosity of MRG. According to the magnetic field characteristics of MRG, its viscosity is closely related to *B*, and the relationship curve is shown in **Figure 1A** (Wang et al., 2019). When *B* is between 0 and 300 mT, the viscosity growth gradually becomes slower, and when *B* is greater than 300 mT, MRG reaches the magnetic saturation state.

The viscosity–temperature characteristics of MRG are considered, and the viscosity–temperature equation is **Eq. 2** (Zhai et al., 2019).

$$\boldsymbol{\eta}_T = \boldsymbol{\eta}_{T_0} \boldsymbol{e}^{-\boldsymbol{\beta}(T-T_0)}, \tag{2}$$

where $\boldsymbol{\eta}_{T_0}$ is the viscosity when the temperature is $\mathbf{T}_0$, $\boldsymbol{\eta}_T$ is the viscosity when the temperature is *T*, $\boldsymbol{\beta}$ is the viscosity–temperature coefficient, taken as 0.03 (1/°C). The viscosity–temperature curves in the three working conditions with 1A (working condition Ⅰ), 2A (working condition Ⅱ), and 0A (working condition Ⅲ) current applied to the internal coil of the MRG torsional vibration damper are shown in **Figure 1B**.

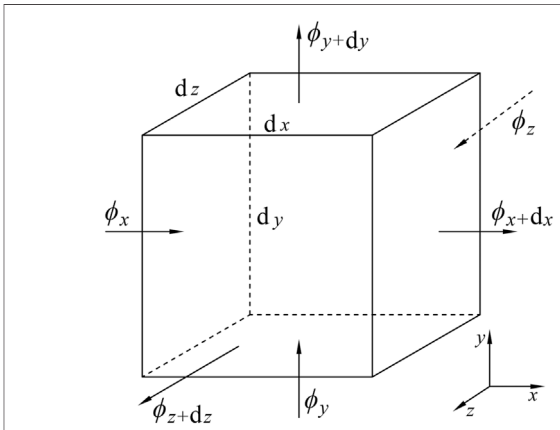

FIGURE 2 | Thermal equilibrium analysis of the microelement.

2.2 Temperature Field Mathematical Model of Magnetorheological Grease Torsional Vibration Damper

2.2.1 Heat Conduction Differential Equation

In the rectangular coordinate system, choose a volume element from the MRG torsional vibration damper with length d*x*, width d*y*, and height d*z*. From Fourier's law of heat conduction, the heat fluxes flow into the element and the heat fluxes flow out of the element are **Eq. 3** and **4**, respectively.

$$\begin{cases} \boldsymbol{\phi}_x = -\boldsymbol{\lambda}\dfrac{\partial \boldsymbol{t}}{\partial \boldsymbol{x}}\mathbf{d}\boldsymbol{y}\mathbf{d}\boldsymbol{z};\ \boldsymbol{\phi}_{x+\mathbf{d}x} = \boldsymbol{\phi}_x + \dfrac{\partial \boldsymbol{\phi}_x}{\partial \boldsymbol{x}}\mathbf{d}\boldsymbol{x} = \boldsymbol{\phi}_x + \dfrac{\partial}{\partial \boldsymbol{x}}\left(-\boldsymbol{\lambda}\dfrac{\partial \boldsymbol{t}}{\partial \boldsymbol{x}}\mathbf{d}\boldsymbol{y}\mathbf{d}\boldsymbol{z}\right)\mathbf{d}\boldsymbol{x} \\ \boldsymbol{\phi}_y = -\boldsymbol{\lambda}\dfrac{\partial \boldsymbol{t}}{\partial \boldsymbol{y}}\mathbf{d}\boldsymbol{x}\mathbf{d}\boldsymbol{z};\ \boldsymbol{\phi}_{y+\mathbf{d}y} = \boldsymbol{\phi}_y + \dfrac{\partial \boldsymbol{\phi}_y}{\partial \boldsymbol{y}}\mathbf{d}\boldsymbol{y} = \boldsymbol{\phi}_y + \dfrac{\partial}{\partial \boldsymbol{y}}\left(-\boldsymbol{\lambda}\dfrac{\partial \boldsymbol{t}}{\partial \boldsymbol{y}}\mathbf{d}\boldsymbol{x}\mathbf{d}\boldsymbol{z}\right)\mathbf{d}\boldsymbol{y} \\ \boldsymbol{\phi}_z = -\boldsymbol{\lambda}\dfrac{\partial \boldsymbol{t}}{\partial \boldsymbol{z}}\mathbf{d}\boldsymbol{x}\mathbf{d}\boldsymbol{y};\ \boldsymbol{\phi}_{z+\mathbf{d}z} = \boldsymbol{\phi}_z + \dfrac{\partial \boldsymbol{\phi}_z}{\partial \boldsymbol{z}}\mathbf{d}\boldsymbol{z} = \boldsymbol{\phi}_z + \dfrac{\partial}{\partial \boldsymbol{z}}\left(-\boldsymbol{\lambda}\dfrac{\partial \boldsymbol{t}}{\partial \boldsymbol{z}}\mathbf{d}\boldsymbol{x}\mathbf{d}\boldsymbol{y}\right)\mathbf{d}\boldsymbol{z} \end{cases}, \tag{3}$$

$$\begin{cases} \mathbf{d}\boldsymbol{\phi}_{in} = \boldsymbol{\phi}_x + \boldsymbol{\phi}_y + \boldsymbol{\phi}_z \\ \mathbf{d}\boldsymbol{\phi}_{out} = \boldsymbol{\phi}_{x+\mathbf{d}x} + \boldsymbol{\phi}_{y+\mathbf{d}y} + \boldsymbol{\phi}_{z+\mathbf{d}z} \end{cases}, \tag{4}$$

TABLE 1 | Parameters of heat transfer model.

Symbol	Parameter	Value
N_c	Number of turns of the coil	30
$\overline{d_c}$	Average diameter of the coil	19.8 mm
A_W	Cross-sectional area of the coil	10.26 mm^2
D	Diameter of MRG fluid domain	250 mm
L	Height of MRG fluid domain	40 mm

where $\boldsymbol{\Phi_x}$, $\boldsymbol{\Phi_y}$, and $\boldsymbol{\Phi_z}$ are the heat fluxes flow into the element in the directions of x, y, and z at the surfaces of $x = x$, $y = y$, and $z = z$. $\boldsymbol{\Phi_{x+dx}}$, $\boldsymbol{\Phi_{y+dy}}$, and $\boldsymbol{\Phi_{z+dz}}$ are the heat fluxes flow out of the element in the directions of x, y, and z at the surfaces of $x = x + dx$, $y = y + dy$, and $z = z + dz$. t is the temperature of the microelement, $\boldsymbol{\lambda}$ is the thermal conductivity, $d\boldsymbol{\phi_{in}}$ is the total heat flow rate of the imported microelement per unit time, and $d\boldsymbol{\phi_{out}}$ is the total heat flow rate of the exported microelement per unit time. The geometrical description is shown in **Figure 2**.

The differential equation for the thermal conductivity of the volume element is shown in **Eq. 5**.

$$\boldsymbol{\rho c_p}\frac{\partial \boldsymbol{t}}{\partial \boldsymbol{\tau}} = \frac{\partial}{\partial \boldsymbol{x}}\left(\boldsymbol{\lambda}\frac{\partial \boldsymbol{t}}{\partial \boldsymbol{x}}\right) + \frac{\partial}{\partial \boldsymbol{y}}\left(\boldsymbol{\lambda}\frac{\partial \boldsymbol{t}}{\partial \boldsymbol{y}}\right) + \frac{\partial}{\partial \boldsymbol{z}}\left(\boldsymbol{\lambda}\frac{\partial \boldsymbol{t}}{\partial \boldsymbol{z}}\right) + \dot{\boldsymbol{\phi}}, \tag{5}$$

where $\dot{\boldsymbol{\Phi}}$ is the intensity of the internal heat source, $\boldsymbol{\rho}$ is the density, and $\boldsymbol{c_p}$ is the isobaric specific heat capacity.

2.2.2 Coil Resistance Heat and Forced Convection Heat Transfer Coefficient

The control energy generated by the coil resistance heat (coil power consumption N) can be expressed by **Eq. 6**.

$$\boldsymbol{N} = \boldsymbol{I^2 R_W}, \tag{6}$$

where I is the current applied to the excitation coil, and $\boldsymbol{R_W}$ is the resistance of the coil wire. $\boldsymbol{R_W}$ can be approximated by **Eq. 7** (Nguyen et al., 2008).

$$\boldsymbol{R_W} = \boldsymbol{L_W r_W} = \boldsymbol{N_c \pi \overline{d_c}}\frac{\boldsymbol{r}}{\boldsymbol{A_W}}, \tag{7}$$

where r is the resistivity of copper wire (0.01726 [$\Omega \cdot$ m]), $\boldsymbol{L_W}$ is the length of the coil, $\boldsymbol{r_W}$ is the resistance of the coil per unit length, $\boldsymbol{N_c}$ is the number of turns of the coil, where four coils are arranged in the circumferential direction in this model, the radius of copper wire selected is 0.33 mm, $\boldsymbol{\overline{d_c}}$ is the average diameter of the coil, and $\boldsymbol{A_W}$ is the cross-sectional area of the coil. The parameters of the coil are shown in **Table 1**. According to **Eqs. 6**, **7**, the resistance heat generated by the coil can be calculated. In different working conditions, the resistance heat generated by the coil is different. During the operation of the MRG torsional vibration damper, resistance heat is generated by the coil and the surrounding MRG for forced convection heat transfer, calculation of convective heat transfer according to **Eq. 8** (Newton's law of cooling).

$$\boldsymbol{\phi} = \boldsymbol{hA}\frac{\boldsymbol{d_t}}{\boldsymbol{d_x}}, \tag{8}$$

where $\boldsymbol{\phi}$ is the heat flow rate, A is the contact area, $\boldsymbol{d_t/d_x}$ is the temperature gradient, and h is the convective heat transfer coefficient. The Reynolds number is calculated by **Eq. 9** to describe the flow behavior of MRG.

$$\boldsymbol{R_{ef}} = \frac{\boldsymbol{u \cdot D}}{\boldsymbol{v}}, \tag{9}$$

where $\boldsymbol{R_{ef}}$ is the Reynolds number for determining the fluid flow mode, D is the diameter of MRG fluid domain, u is the flow velocity, and $\boldsymbol{v}$ is the kinematic viscosity. The process of calculating the forced convection heat transfer coefficient h is as follows:

$$\begin{cases} \boldsymbol{N_{uf}} = 1.86\left(\boldsymbol{R_{ef}} \cdot \boldsymbol{P_{rf}} \cdot \dfrac{\boldsymbol{D}}{\boldsymbol{L}}\right)^{\frac{1}{3}} \\ \boldsymbol{P_{rf}} = \dfrac{\boldsymbol{c \cdot \rho \cdot v}}{\boldsymbol{\lambda}} \\ \boldsymbol{h} = \dfrac{\boldsymbol{N_{uf}} \cdot \boldsymbol{\lambda}}{\boldsymbol{D}} \end{cases}, \tag{10}$$

where L is the geometric characteristic of the heat transfer surface; in this model, it is the geometric height of the MRG domain. The geometric parameters of the MRG fluid domain are shown in **Table 1**. c is the specific heat ratio, and its value is 1 (set MRG as incompressible fluid). According to **Eq. 10** (Haque et al., 2021), the forced convection heat transfer coefficient h can be calculated. It can be known that the forced convection heat transfer coefficient h is related to the slip, and the h variation curve is shown in **Figure 3**. The forced convection heat transfer coefficient increases with the increase of slip and the trend is shown in **Figure 3A**. The heat transfer coefficient is different at each moment due to the different slips at each moment, as is shown in **Figure 3B**. Since no current is introduced in working condition III, the coil does not generate resistive heat, and the heat transfer coefficient of working condition III is not studied.

3 DESIGN AND MODELING OF MAGNETORHEOLOGICAL GREASE TORSIONAL VIBRATION DAMPER

3.1 Simulation Model

In order to meet the damping requirements of reducing the torsional vibration of the crankshaft under multiple resonance frequencies and ensure closure of the magnetic circuit inside the device, the structure of the internal inertia ring of the MRG torsional damper is designed based on the adjustable damping characteristics of MRG as shown in **Figure 4**. The MRG is filled between the inner surface of the magnetically conductive ring and the outer surface of the inertia ring and the inner surfaces of the two end caps. When the coil is not energized, the MRG behaves as a free-flowing Newtonian fluid. When the coil is energized, the magnetic field is generated in the working gap and the MRG transforms into a solid-like state, thus viscous damping forces are generated. The MRG torsional vibration damper cross-sectional view and exploded diagram model are shown in **Figure 4**.

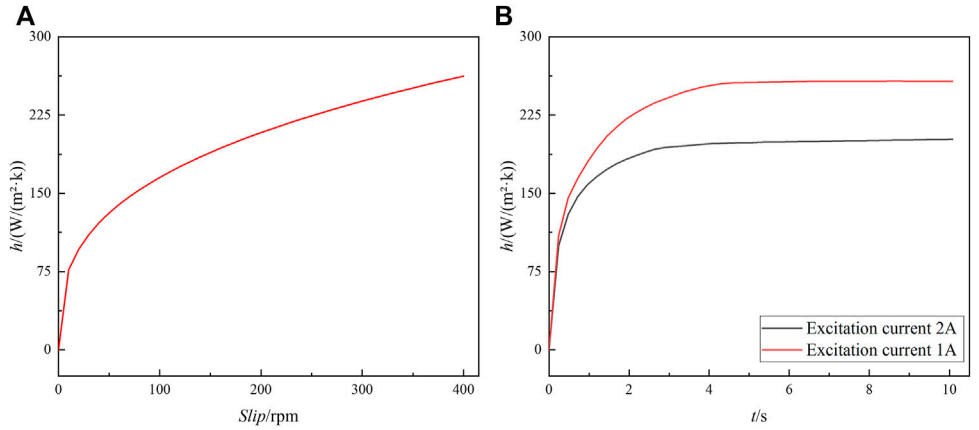

FIGURE 3 | *h* variation curve: **(A)** *h-slip* curve and **(B)** *h-t* curve of each working condition.

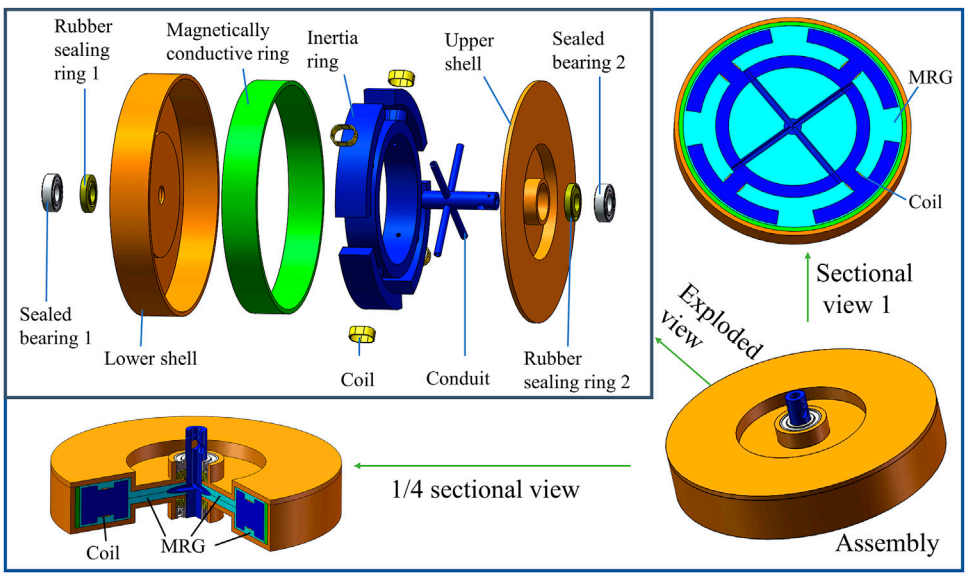

FIGURE 4 | MRG torsional vibration damper model.

The MRG torsional vibration damper consists of three key parts: shell, inertia ring, and MRG. The working clearance of MRG is 2 mm. After the crankshaft is fixedly connected to the MRG torsional vibration damper shell, the shell drives the internal inertia ring to rotate through the viscous damping force of the internal MRG.

3.2 Thermal Analysis of Magnetorheological Grease Torsional Vibration Damper

3.2.1 Temperature Rise Principle of Magnetorheological Grease Torsional Vibration Damper

The main reason for the torsional vibration of crankshaft systems is that the excitation frequency is similar to the natural frequency, resulting in resonance. To avoid resonance, the frequency shift principle is usually adopted, with a change to the natural frequency of the system by changing the stiffness and mass. The MRG torsional vibration damper can change the viscous damping of the internal MRG by adjusting the current, which can control the natural frequency of the whole crankshaft system. Therefore, MRG torsional vibration damper can play a better damping effect at any resonance frequency.

The MRG inside the MRG vibration damper can convert the energy of torsional vibration into internal energy, and the temperature gets warmer as time accumulates due to the engine crankshaft system being a continuous working system. Due to the large rotational inertia of the inertia ring, slip exists between the inner and outer rotors, and the high-viscosity MRG will generate a higher temperature in the gap between the shell

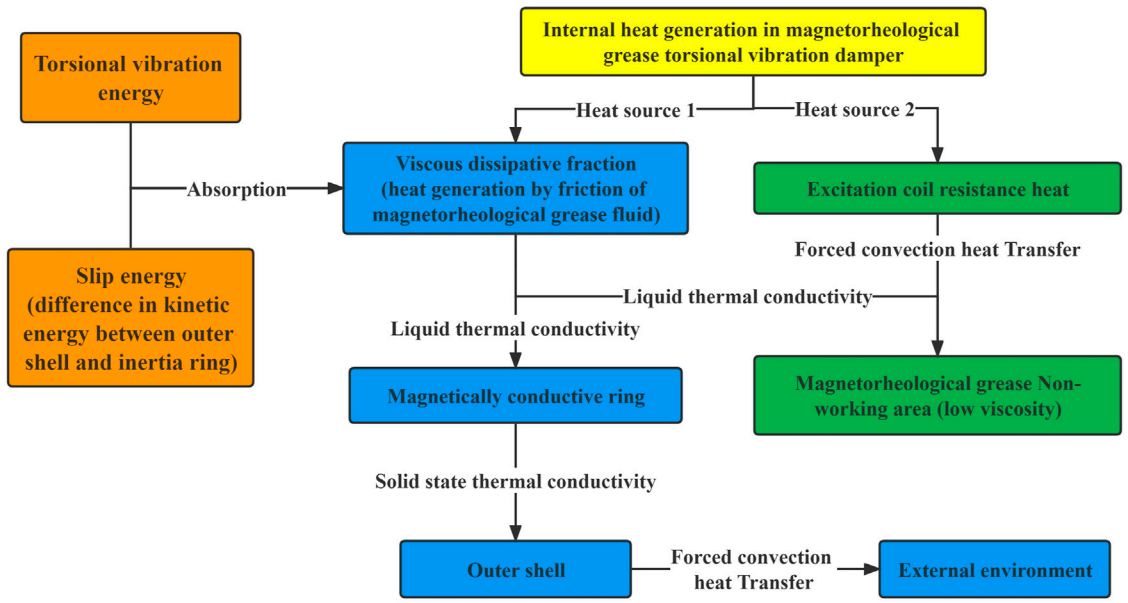

FIGURE 5 | Thermal conductivity system.

and inertia ring due to fluid friction. On the other hand, the coil inside the MRG torsional vibration damper will generate resistance heat, which will also affect the viscous damping effect of the MRG and further affect the damping performance of the MRG torsional vibration damper.

3.2.2 Analysis of Thermal Conductivity

There is a slip between the inner and outer rotors of the MRG torsional vibration damper, and heat will be generated inside the device due to fluid friction. In addition, the coil inside the MRG torsional vibration damper will also generate resistance heat. MRG torsional vibration damper internal heat conduction system is the "dual heat source structure," the specific heat transfer process is shown in **Figure 5**.

According to **Figure 5**, the MRG will transform the slip energy and torsional vibration energy into internal energy, and the heat will be further transferred to the outer shell through the magnetically conductive ring. The shell carries out forced convection heat transfer with the external air, and the heat will dissipate. The resistance heat generated by the coil first conducts forced convection heat transfer with the surrounding MRG, and the temperature of the working domain of the MRG is transferred to the non–working domain of the MRG by liquid heat transfer.

3.3 Analysis of Magnetic Field Simulation

In order to analyze the magnetic excitation line distribution of MRG torsional vibration damper more accurately, the magnetic field simulation of the "Sectional view1" model in **Figure 4** is carried out by COMSOL Multiphysics. **Figure 6A** shows the distribution of magnetic excitation lines inside the MRG torsional vibration damper. When the magnetic field is simulated for the MRG torsional vibration damper, the simulation model is simplified due to the conductor tubes, bearings, and seals that have little influence on the results of the magnetic field simulation. The outermost ring of the MRG fluid domain with higher magnetic excitation line density is defined as the "Working domain of MRG"; the MRG fluid domain with lower internal magnetic excitation line density is defined as the "Non-working domain of MRG." And the "Route" of the MRG working domain is chosen between the inertia ring and magnetically conductive ring, the magnetic field distribution pattern through this Route is shown in **Figure 6B**. The magnetic excitation line density decreases from the left end to the right end of the Route, and B decreases with the increase of the distance d between the measurement point and the left end point. The magnetic excitation lines on the left and right sides of the right end point of the Route are symmetrically distributed, and a small amount of coupling exists in the magnetic excitation line, which can be neglected.

3.4 Modeling of Transient Temperature Field

3.4.1 Parameters of Transient Temperature Field Simulation

The COMSOL Multiphysics fluid–solid coupling simulation of the MRG torsional vibration damper requires a Boolean operation to model the fluid domain and divide the overall internal MRG domain into the working domain of MRG and the non–working domain of MRG. The internal inertia ring affects the MRG motion, the rotating inner wall, outer wall, and dynamic mesh settings are needed for the MRG domain separately. During the simulation, the effects of bolts, bearings, seals, friction pads, conductor tubes, etc. are ignored to shorten the simulation time for the Multiphysics field coupling simulation. The reference pressure is 101.325 KPa (standard atmospheric pressure). The model of magnetorheological grease used in this article is MRG-50, the mass fraction of

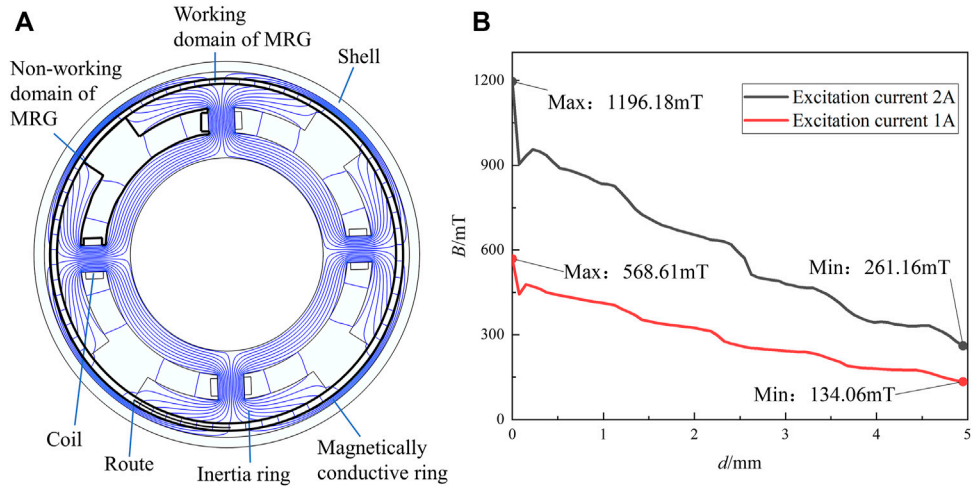

FIGURE 6 | Magnetic field simulation: **(A)** magnetic excitation line distribution and **(B)** *B-d* curve.

TABLE 2 | Fluid parameters of MRG.

Symbol	Parameter	Value
η_0	Initial viscosity	12 Pa s
ρ	Density	2.68 g/cm^3
λ	Thermal conductivity	1W/(m k)
c_p	Isobaric specific heat capacity	1000J/(kg k)

hydroxy iron powder and lubricating grease in this model is 50% each (the lubricating grease adopts No. 2 high-temperature lubricating grease of Shandong Kunlun Lubricating Oil Sales Co., Ltd.). The initial viscosity is 12 Pa s. According to the known density, isobaric specific heat capacity and mass fraction of hydroxyl iron powder and lubricating grease, the density and isobaric specific heat capacity of MRG-50 can be calculated, respectively (Wang et al., 2019). According to the thermal conductivity and mass fraction of hydroxyl iron powder and lubricating grease, the thermal conductivity of MRG-50 is calculated by Filipoov equation (Reid et al., 1987). The fluid properties of the MRG are shown in **Table 2**.

The MRG material is defined according to the Bingham model and the viscosity–temperature characteristic equation coupling. The corresponding boundary conditions are set for the fluid: the outer boundary of the fluid is all the inner surfaces of the shell and the rotational boundary inside the fluid is all the outer surfaces of the inertia ring. The whole model is set to "Form the assembly," and static and dynamic domains are used in "a consistent pair" to ensure the data transfer. The dynamic deformation domain is set by the method of dynamic mesh rotational domain, the rotational boundary speed inside the MRG domain is set and the parameter values are the slip value of the inner and outer rotors. The measured slip values of the tests for the three working conditions are shown in **Figure 7**.

According to **Figure 7**, the slip between the inner and outer rotors is different when three different currents are applied to the coil: 1A (working condition I), 2A (working condition II), and 0A (working condition III). In working condition II, due to the higher flux density of the working domain of MRG, the viscous damping force of the MRG is the largest and the slip of the inner and outer rotors is the smallest among the three working conditions, with a slow linear growth trend after the slip reaches 171.34 rpm at 4.08 s. The linear growth trend is shown after the slip reaches 373.66 and 618.60 rpm at 5.28 and 6.72 s for working condition I and working condition III, respectively.

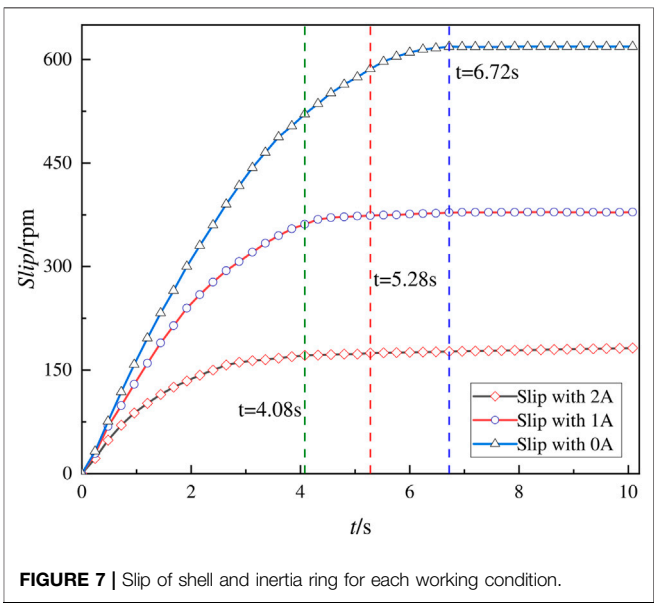

FIGURE 7 | Slip of shell and inertia ring for each working condition.

3.4.2 Grid Cell Setting and Temperature Measurement Point Selection

To ensure the quality of the grid cells, the hydrodynamic refinement grid is set according to the "non-isothermal laminar flow" Multiphysics field simulation. The corner refinement grid is processed for the internal rotating boundary chamfers and edges. The free tetrahedral grid is used for the

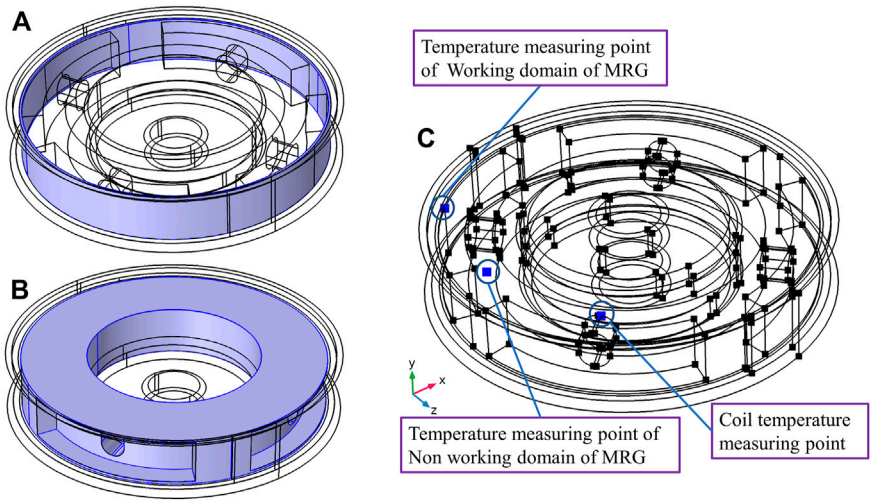

FIGURE 8 | Simulation model of transient temperature field: **(A)** working domain of the MRG, **(B)** non–working domain of the MRG, and **(C)** temperature probe picking point.

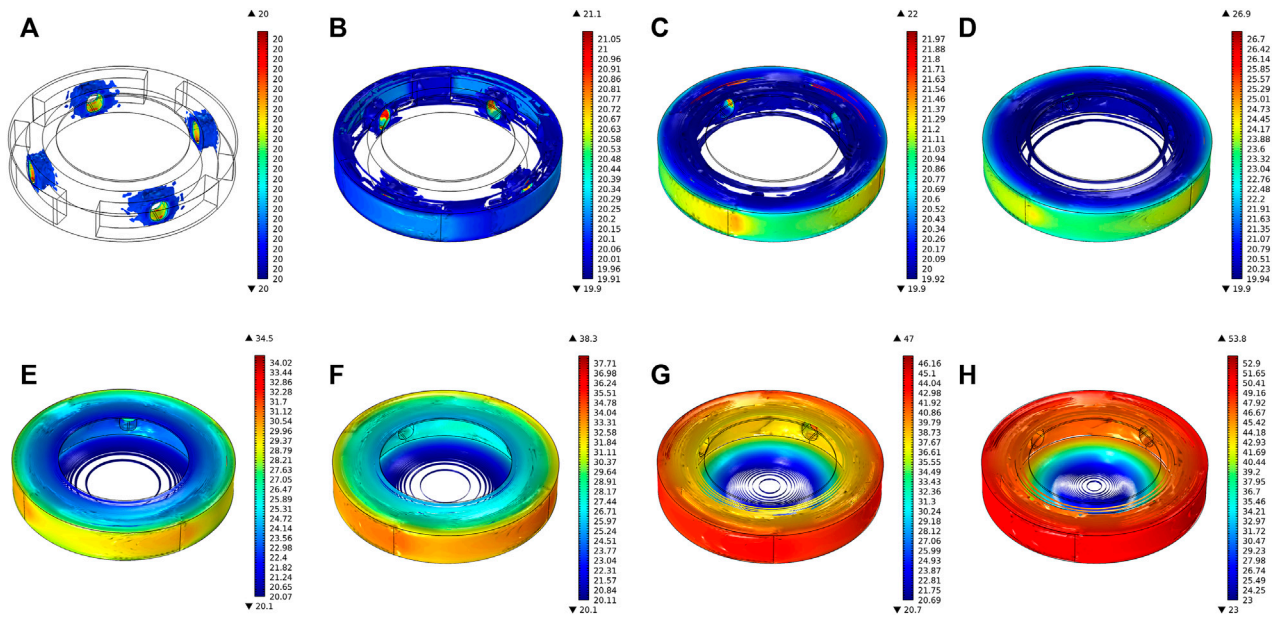

FIGURE 9 | Transient temperature distribution of MRG torsional vibration damper for each moment of working condition I: **(A)** t = 0 s, **(B)** t = 0.4 s, **(C)** t = 0.8 s, **(D)** t = 1.5 s, **(E)** t = 3 s, **(F)** t = 4 s, **(G)** t = 7 s, and **(H)** t = 10 s.

whole rotating domain and set as the dynamic grid–rotating domain. The grid refinement is conducted for the internal rotating boundary and external boundary of the MRG domain.

To distinguish and judge the temperature rise amplitude and rate of MRG in the different domains, as well as the temperature distribution within the MRG domain, the internal overall MRG domain is divided into the working domain (**Figure 8A**) and non–working domain (**Figure 8B**). The spatial coordinates of the temperature measurement points selected in the working domain of MRG, the non–working domain of MRG, and coil domain are as follows: $(-123/\sqrt{2}, 43, -123/\sqrt{2})$, (−85, 22.5, −40), and (−64.4, 38, 59.9), taking the center of the circle on the bottom surface of the model as the origin, as shown in **Figure 8C**.

4 RESULTS AND DISCUSSION

The temperature distribution and temperature rise inside the torsional vibration damper are carried out for working condition

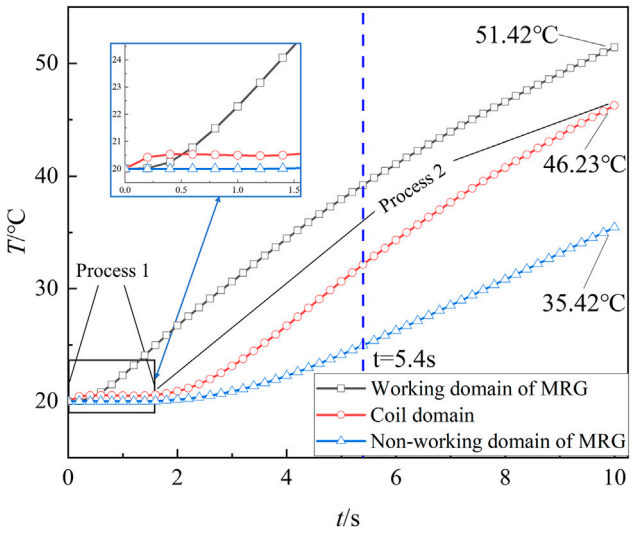

FIGURE 10 | Temperature rise curve of each domain in working condition I

I, working condition II, and working condition III. The simulation step is taken as 0.1 s, and the results are analyzed according to the simulated results of each 0.1 s.

4.1 Temperature Characteristics Analysis

4.1.1 In Working Condition I

Figure 9 shows the simulation results of the transient temperature field of the MRG torsional vibration damper for working condition I. When the 1A current is applied, the coil generates resistance heat at the initial stage, then it conducts forced convection heat transfer with the surrounding MRG. When the slip gradually becomes larger between the inner and outer rotors, the fluid friction gradually becomes more intense in the MRG working domain and the amplitude and rate of temperature rise increase faster. When running for 10 s, the highest temperature domain inside the damper is the MRG work domain, and the temperature of both sides of the end phase is in the range of 47–51°C. The specific temperature rise trend of each domain is shown in **Figure 10**.

According to **Figure 10**, when the 1A current is applied to the coil, the magnitude and rate of temperature rise in the working domain of MRG are the greatest due to higher viscosity, higher slip, and smaller working gap of this domain. The temperature rises rapidly from the initial 20°C–51.42°C. As the temperature increases, the degree of fluid friction is reduced due to the slowing of the increase in the slip and the viscosity–temperature properties of MRG, and the temperature rise rate slows down after 5.4 s. In the process1 stage of **Figure 10**, the coil is fed with a 1A current, generating resistance heat and forced convection heat transfer with the surrounding MRG. In the process 2 stage, after 1.6 s, the temperature starts to increase due to the heat transfer from the working domain of MRG to the vicinity of the coil through the MRG. The temperature of the MRG at the coil domain is indicated in the "Coil domain" of **Figure 10**. For the non–working domain of the MRG, the temperature rise amplitude and rate are the lowest due to MRG with low viscosity and a large working gap.

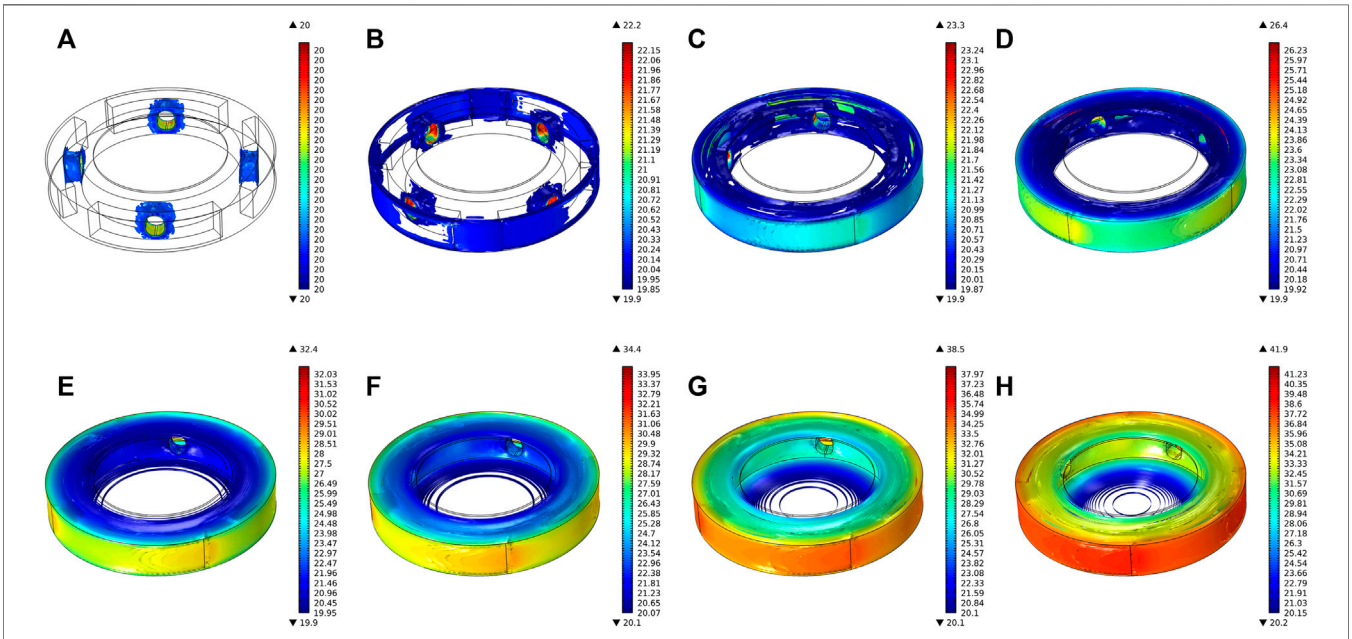

FIGURE 11 | Transient temperature distribution of MRG torsional vibration damper for each moment of working condition II: **(A)** t = 0 s, **(B)** t = 0.4 s, **(C)** t = 0.8 s, **(D)** t = 1.5 s, **(E)** t = 3 s, **(F)** t = 4 s, **(G)** t = 7 s, and **(H)** t = 10 s.

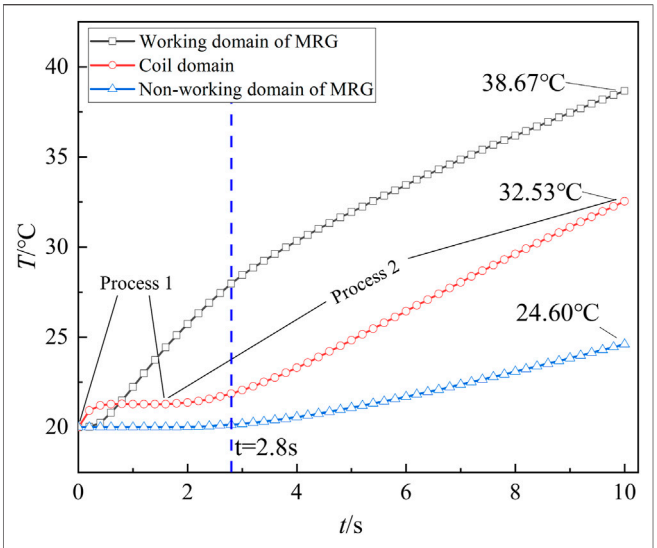

FIGURE 12 | Temperature rise curve of each domain in working condition II

4.1.2 In Working Condition II

Figure 11 shows the simulation results of the MRG torsional vibration damper working condition II. When the 2A current is applied, the coil will generate resistance heat at the initial stage, then it conducts forced convection heat transfer with the surrounding MRG. The degree of friction of the MRG at the outermost ring increases sharply due to the gradual increase of slip, and the magnitude and rate of temperature rise increase. The specific temperature rise trend of each domain in working condition II is shown in **Figure 12**.

According to **Figure 12**, when the 2A current is applied, MRG reaches the magnetic saturation state in the working domain of MRG, when MRG viscosity is maximum but the slip is minimum. Compared to working condition I, the degree of fluid friction is less, the temperature rises rapidly from the initial 20°C to 38.67°C. Due to the slowing of the increase in the slip, the temperature rise rate slows down after 2.8 s. In the process 1 stage of **Figure 12**, compared to working condition I, the resistance heat generated is higher due to increased input current. The resistance heat conducts forced convection heat transfer with the surrounding MRG. In the process 2 stage, after 2 s, the temperature starts to increase due to the heat transfer from the working domain of MRG to the vicinity of the coil through the MRG. The temperature of the MRG at the coil domain is indicated in the "Coil domain" of **Figure 12**. The temperature at the non–working domain of MRG has the lowest temperature rise amplitude and rate due to the small viscosity and large working gap.

4.1.3 In Working Condition III

Figure 13 shows the simulation results of the MRG torsional vibration damper under working condition III. When no current is applied to the coil, the viscosity and viscous damping force of MRG are minimum. The slip is the largest between the inner and outer rotors under working condition III. In the starting stage, the internal temperature is set at the initial ambient temperature of 20°C. The amplitude and rate of temperature rise at the working domain due to the slip gradually increase. According to the simulation results, the temperature at the outermost ring on both sides of the end face is nearly the same as the temperature at

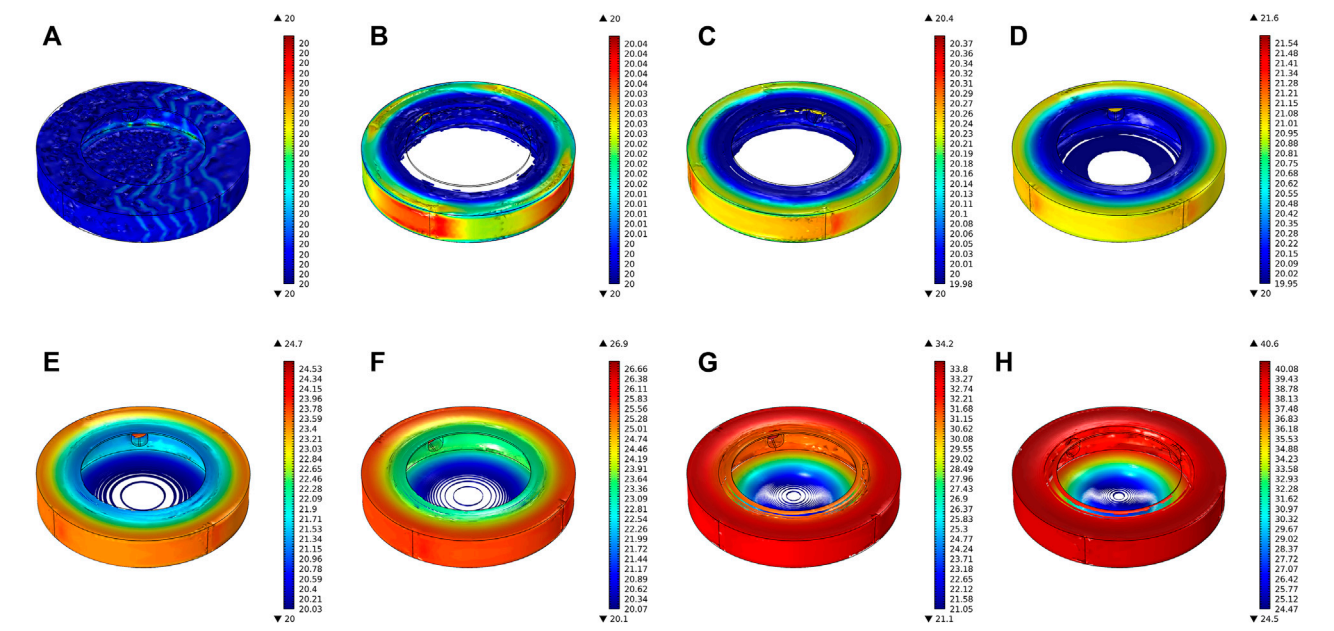

FIGURE 13 | Transient temperature distribution of MRG torsional vibration damper for each moment of working condition III: **(A)** t = 0 s, **(B)** t = 0.4 s, **(C)** t = 0.8 s, **(D)** t = 1.5 s, **(E)** t = 3 s, **(F)** t = 4 s, **(G)** t = 7 s, and **(H)** t = 10 s.

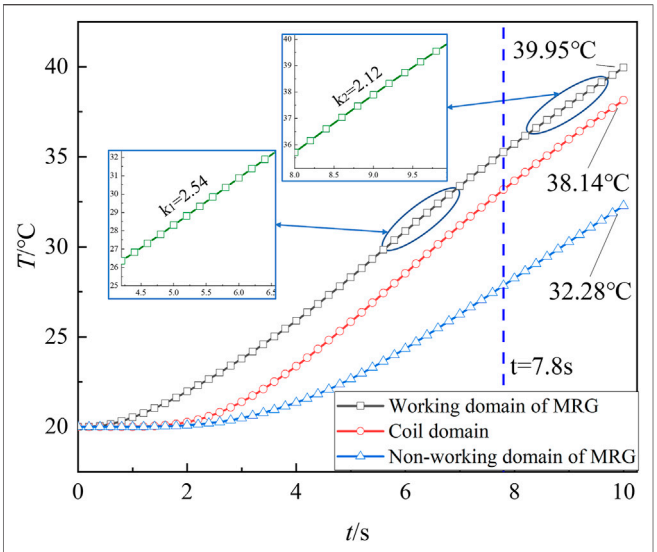

FIGURE 14 | Temperature rise curve of each domain in working condition III

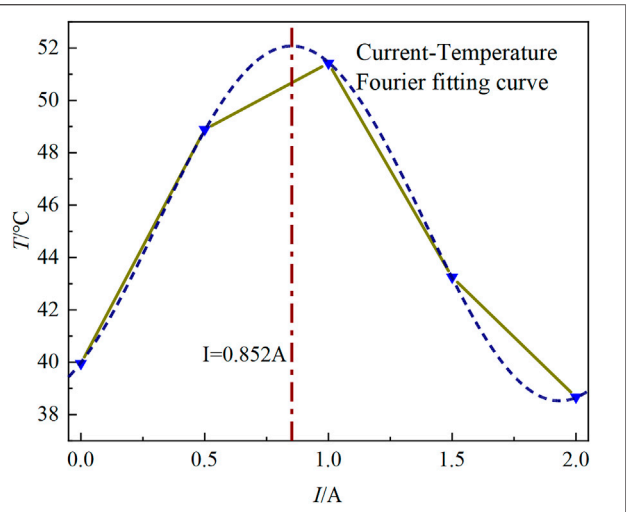

FIGURE 15 | Current–temperature curve.

the working domain in 0–10 s. Since the viscosity of the MRG inside the device is the same in working condition III, the highest temperature inside the torsional vibration damper is at the working domain of the MRG when running for 10s, and the temperature at the two end surfaces is in the range of 38–39°C, which is nearly the same as the temperature of the MRG in the working domain. The specific temperature rise trend in each domain of working condition III is shown in **Figure 14**.

According to **Figure 14**, the viscosity of MRG inside the device is consistent when no current is introduced inside the MRG torsional vibration damper. Due to the small working gap in the working domain, the temperature rise of MRG is the largest, and the temperature rises rapidly from the initial 20°C to 39.95°C within 10 s. After 7.8 s, the temperature rise rate slows down due to the slowing of the increase in the slip and the viscosity–temperature characteristics of MRG, and the temperature rise rate decreases from 2.54 to 2.12. The temperature at the coil domain still has a high-temperature rise amplitude and rate due to the heat transfer of MRG. The amplitude and rate of temperature rise at the non–working domain of MRG are the lowest due to the large working gap.

4.2 Analysis of Factors of Temperature Rise

When increasing the current applied to the coil, the viscosity of MRG increases while decreasing the slip between the inner and outer rotors. To explore the relationship between the input current and the internal temperature of the device more precisely, the same transient temperature field simulation analysis was performed for the incoming 0.5 and 1.5A currents, and the peak temperature at the 10-s moment was obtained as shown in **Figure 15**. When the applied current is 0–1A, the viscosity of the MRG increases rapidly from the initial viscosity to about 75 Pa s, and the slip between the inner and outer rotors decreases accordingly. The increase of viscosity intensifies the fluid friction in the working domain of MRG, which increases the temperature rise rate. When the applied current is 1–2A, the slip of the inner and outer rotors decreases due to the increase of MRG viscosity, and the fluid friction degree is weakened, which reduces the amplitude and rate of temperature rise. For the several common working conditions of the MRG torsional vibration damper studied in this article, the increase of MRG viscosity is the main factor affecting the temperature rise when the applied current is 0–1A. The amplitude and rate of temperature rise are maximum when the 0.852A current is applied by fitting the curve in **Figure 15**. When the applied current is 1–2A, fluid friction is weakened due to the reduced slip between the inner and outer rotors, thus the amplitude and rate of the temperature rise are lower.

5 DISCUSSION

In this study, a multi-field coupling approach is used to simulate and analyze the working conditions of the torsional vibration in the starting phase. The distribution results of the transient temperature field simulation reveal the temperature field distribution and change law inside the MRG torsional vibration damper, and the relationship curve between current and temperature is derived from the simulation results, which provides simulation and theoretical basis for the subsequent heat dissipation optimization and temperature compensation control. Due to the simulation time of the Multiphysics simulation software, this study only simulates several common working conditions, for the effect of current on temperature, the corresponding discrete results are obtained, and then the results are fitted. For the Multiphysics simulation, the corresponding device model is simplified, which has little effect on the simulation of the temperature field.

6 CONCLUSION

According to the simulation results of each working condition, the internal temperature distribution pattern of the device is the highest temperature domain for the working domain of MRG. The temperature of both end surfaces gradually increases from the center of the circle along the radial direction. In this study, the simulation method of fluid–solid coupling was used to reveal the internal transient temperature gradient in more detail. It provides guidance for further optimization of heat dissipation considering the temperature factor.

In this study, the maximum temperature of each working condition was collated and fitted to obtain the relationship between current and temperature. By analyzing the five working conditions, when the applied current is 0–1A, the increase in MRG viscosity leads to an increase in the rate and magnitude of temperature rise inside the device. When the applied current is 1–2A, the viscosity of MRG gradually reaches the peak, the slip of the inner and outer rotors decreases, and the magnitude and rate of temperature rise decrease. When 0.852A current is applied, the amplitude of the temperature rise reaches the peak. The results provide the simulation basis for further study of critical parameters.

DATA AVAILABILITY STATEMENT

The original contributions presented in the study are included in the article/Supplementary Material, and further inquiries can be directed to the corresponding author.

AUTHOR CONTRIBUTIONS

Reviewing, guidance and support: HH and QO; modeling, simulation, and original draft preparation: ZX; data analysis and simulation results analysis: ZX, LS, and HS.

FUNDING

This work was supported by the Zhejiang Provincial Natural Science Foundation of China (Grant Nos. LGG20E050022 and LGG19E050017) and in part by the National Natural Science Foundation of China (NSFC) grant funded by the Chinese Government (Grant No. 51805209) and the Jiaxing Municipal Science and Technology Project (Grant No. 2020AY10036).

REFERENCES

Abouobaia, E., Bhat, R., and Sedaghati, R. (2016). Development of a New Torsional Vibration Damper Incorporating Conventional Centrifugal Pendulum Absorber and Magnetorheological Damper. *J. Intelligent Material Syst. Struct.* 27 (7), 980–992. doi:10.1177/1045389x15590275

Abouobaia, E., Sedaghati, R., and Bhat, R. (2020). Design Optimization and Experimental Characterization of a Rotary Magneto-Rheological Fluid Damper to Control Torsional Vibration. *Smart Mater. Struct.* 29 (4), 045010. doi:10.1088/1361-665x/ab74ba

Batterbee, D., and Sims, N. D. (2008). Temperature Sensitive Controller Performance of MR Dampers. *J. Intelligent Material Syst. Struct.* 20 (3), 297–309. doi:10.1177/1045389x08093824

Boysal, A., and Rahnejat, H. (1997). Torsional Vibration Analysis of a Multi-Body Single Cylinder Internal Combustion Engine Model. *Appl. Math. Model.* 21 (8), 481–493. doi:10.1016/s0307-904x(97)00032-2

Brancati, R., Rocca, E., and Russo, R. (2019). Gear Rattle Reduction in an Automotive Driveline by the Adoption of a Flywheel with an Innovative Torsional Vibration Damper. *Proc. IMechE* 233 (4), 777–791. doi:10.1177/1464419319850664

Fonte, M., and de Freitas, M. (2009). Marine Main Engine Crankshaft Failure Analysis: A Case Study. *Eng. Fail. Anal.* 16 (6), 1940–1947. doi:10.1016/j.engfailanal.2008.10.013

Gordaninejad, F., and Breese, D. G. (1999). Heating of Magnetorheological Fluid Dampers. *J. Intelligent Material Syst. Struct.* 10 (8), 634–645. doi:10.1106/55d1-xaxp-yfh6-b2fb

Haque, M. E., Hossain, M. S., and Ali, H. M. (2021). Laminar Forced Convection Heat Transfer of Nanofluids inside Non-circular Ducts: A Review. *Powder Technol.* 378, 808–830. doi:10.1016/j.powtec.2020.10.042

Homik, W., Mazurkow, A., and Woś, P. (2021). Application of a Thermo-Hydrodynamic Model of a Viscous Torsional Vibration Damper to Determining its Operating Temperature in a Steady State. *Mater. (Basel)* 14 (18). doi:10.3390/ma14185234

Homik, W. (2010). Diagnostics, Maintenance and Regeneration of Torsional Vibration Dampers for Crankshafts of Ship Diesel Engines. *Pol. Marit. Res.* 17 (1), 62–68. doi:10.2478/v10012-010-0007-2

Homik, W. (2012). The Effect of Liquid Temperature and Viscosity on the Amplitude-Frequency Characteristics of a Viscotic Torsion Damper. *Pol. Marit. Res.* 19 (4), 71–77. doi:10.2478/v10012-012-0042-2

Kamble, V. G., Kolekar, S., Panda, H. S., Ammourah, S., and Jagadeesha, T. (2021). Magneto Rheological Fluid: Fabrication and Characterization of its Temperature-dependent Properties. *Mater. Today Proc.* 45, 4813–4818. doi:10.1016/j.matpr.2021.01.292

Karabulut, H. (2012). Dynamic Model of a Two-Cylinder Four-Stroke Internal Combustion Engine and Vibration Treatment. *Int. J. Engine Res.* 13 (6), 616–627. doi:10.1177/1468087412442618

Kavlicoglu, B. M., Gordaninejad, F., Evrensel, C. A., Yanming Liu, L., Kavlicoglu, N., and Fuchs, A. (2007). Heating of a High-Torque Magnetorheological Fluid Limited Slip Differential Clutch. *J. Intelligent Material Syst. Struct.* 19 (2), 235–241. doi:10.1177/1045389x06074762

Li, M., Zhang, J., Wu, C., Zhu, R., Chen, W., Duan, C., et al. (2020). Effects of Silicone Oil on Stiffness and Damping of Rubber-Silicone Oil Combined Damper for Reducing Shaft Vibration. *Ieee Access* 8, 218554–218564. doi:10.1109/access.2020.3041359

Liang, G., Zhao, T., Li, N., Wei, Y., and Savaresi, S. M. (2021). Magnetorheological Damper Temperature Characteristics and Control-Oriented Temperature-Revised Model. *Smart Mater. Struct.* 30 (12). doi:10.1088/1361-665x/ac2de4

Long, C., Shi, W., and Chen, Z. (2021). Research on Dynamic Behavior of Torsional Absorber in Powertrain System Considering Nonlinear Factors. *J. Vib. Control* 27 (13-14), 1656–1667. doi:10.1177/1077546320947338

McKee, M., Gordaninejad, F., and Wang, X. (2017). Effects of Temperature on Performance of Compressible Magnetorheological Fluid Suspension Systems. *J. Intelligent Material Syst. Struct.* 29 (1), 41–51. doi:10.1177/1045389x17705203

Mendes, A. S., Meirelles, P. S., and Zampieri, D. E. (2008). Analysis of Torsional Vibration in Internal Combustion Engines: Modelling and Experimental Validation. *Proc. Institution Mech. Eng. Part K J. Multi-body Dyn.* 222 (2), 155–178. doi:10.1243/14644193jmbd126

Meyer, J. P., Adio, S. A., Sharifpur, M., and Nwosu, P. N. (2016). The Viscosity of Nanofluids: A Review of the Theoretical, Empirical, and Numerical Models. *Heat. Transf. Eng.* 37 (5), 387–421. doi:10.1080/01457632.2015.1057447

Nguyen, Q.-H., Choi, S.-B., and Wereley, N. M. (2008). Optimal Design of Magnetorheological Valves via a Finite Element Method Considering

Control Energy and a Time Constant. *Smart Mater. Struct.* 17 (2), 025024. doi:10.1088/0964-1726/17/2/025024

Nguyen, Q. H., and Choi, S. B. (2010). Optimal Design of an Automotive Magnetorheological Brake Considering Geometric Dimensions and Zero-Field Friction Heat. *Smart Mater. Struct.* 19 (11), 115024. doi:10.1088/0964-1726/19/11/115024

Park, E. J., da Luz, L. F., and Suleman, A. (2008). Multidisciplinary Design Optimization of an Automotive Magnetorheological Brake Design. *Comput. Struct.* 86 (3-5), 207–216. doi:10.1016/j.compstruc.2007.01.035

Patil, S. R., Powar, K. P., and Sawant, S. M. (2016). Thermal Analysis of Magnetorheological Brake for Automotive Application. *Appl. Therm. Eng.* 98, 238–245. doi:10.1016/j.applthermaleng.2015.11.128

Periyasamy, S., and Alwarsamy, T. (2012). Combined Effects of Inertia and Pressure on Engine Vibration. *J. Vib. Control* 19 (16), 2469–2480. doi:10.1177/1077546312454321

Pistek, V., Klimes, L., Mauder, T., and Kucera, P. (2017). Optimal Design of Structure in Rheological Models: an Automotive Application to Dampers with High Viscosity Silicone Fluids. *J. Vibroeng* 19 (6), 4459–4470. 2615. doi:10.21595/jve.2017.18348

Reid, R. C., Prausnitz, J. M., and Poling, B. E. (1987). *The Properties of Gases and Liquids*. 4th edition. New York: McGraw-Hill.

Sahin, H., Wang, X., and Gordaninejad, F. (2009). Temperature Dependence of Magneto-Rheological Materials. *J. Intelligent Material Syst. Struct.* 20 (18), 2215–2222. doi:10.1177/1045389x09351608

Shu, G., Wang, B., and Liang, X. (2015). Torsional Vibration Reduction Analysis of Variable Damping Torsional Vibration Damper for Engine Crankshaft. *J. Tianjin Univ.* 48 (1), 19–24.

Silva, C. A. F., Manin, L., Rinaldi, R. G., Besnier, E., and Remond, D. (2019). Dynamics of Torsional Vibration Damper (TVD) Pulley, Implementation of a Rubber Elastomeric Behavior, Simulations and Experiments. *Mech. Mach. Theory* 142, 103583. doi:10.1016/j.mechmachtheory.2019.103583

Venczel, M., Bognár, G., and Veress, Á. (2021). Temperature-Dependent Viscosity Model for Silicone Oil and its Application in Viscous Dampers. *Processes* 9 (2), 331. doi:10.3390/pr9020331

Venczel, M., and Veress, Á. (2020). "Model Development with Verification for Thermal Analysis of Torsional Vibration Dampers," in Paper presented at the International Conference of Numerical Analysis and Applied Mathematics Icnaam 2019 (AIP Publishing). doi:10.1063/5.0026437

Wang, H., Zhang, G., Ouyang, Q., and Wang, J. (2019). Rheological Properties of Magnetorheological Grease under Shear Mode. *Shanghai Jiaot. Daxue Xuebao/ Journal Shanghai Jiaot. Univ.* 53 (3), 380–386.

Zhai, S., Song, L., and Lv, X. (2019). "Measurement and Analysis of Silicone Oil Characteristics and Viscosity-Temperature Index," in Paper presented at the 2019 International Conference on Advances in Civil Engineering, Energy Resources and Environment Engineering, Changchun, Jilin, China, June 28, 2019 - June 30, 2019 (IOP science). doi:10.1088/1755-1315/330/3/032049

Zhang, X., and Yu, S. D. (2009). Torsional Vibration of Crankshaft in an Engine–Propeller Nonlinear Dynamical System. *J. Sound Vib.* 319 (1-2), 491–514. doi:10.1016/j.jsv.2008.06.004

Conflict of Interest: The authors declare that the research was conducted in the absence of any commercial or financial relationships that could be construed as a potential conflict of interest.

Publisher's Note: All claims expressed in this article are solely those of the authors and do not necessarily represent those of their affiliated organizations, or those of the publisher, the editors, and the reviewers. Any product that may be evaluated in this article, or claim that may be made by its manufacturer, is not guaranteed or endorsed by the publisher.

frontiers | Frontiers in Materials

ORIGINAL RESEARCH
published: 12 July 2022
doi: 10.3389/fmats.2022.932964

Error Analysis in Numerical Simulation of the Static Pressure Capability of Magnetic Fluid Seals

*Zhenghao Li and Decai Li**

State Key Laboratory of Tribology, Tsinghua University, Beijing, China

Magnetic fluid is a typical type of functional fluid which can be magnetized and controlled by an external magnetic field. In magnetic fluid seals, magnetic fluid is attracted in sealing gaps by a magnetic field gradient to form non-contact sealing. Compared to traditional sealing methods, they possess unique advantages such as zero leakage, long lifetime, low friction torque, and high reliability. Although the design and performance estimation of magnetic fluid seals rely mostly on numerical simulation, a number of simplifications or even mistakes during the simulation process exist in previous studies. The error caused by simplifications and mistakes has not been studied, leading to a possible problem of simulation results in reliability and consistency with experimental data. Here, we examined the influence of common simplifications and mistakes in numerical simulation of the static pressure capability of magnetic fluid seals, including material properties, geometric modeling, and theoretical formulas. A novel method of structure optimization based on a derivative-free multiparameter algorithm is also presented. A test bench for magnetic fluid seals is established, and the difference between simulation and experimental results is discussed. This research provides a precise, efficient, and standard procedure for numerical simulation of magnetic fluid seals.

Keywords: magnetic fluid, seal, pressure capability, simulation, FEM, optimization

OPEN ACCESS

Edited by:
Miao Yu,
Chongqing University, China

Reviewed by:
Ying-Qing Guo,
Nanjing Forestry University, China
Qing Ouyang,
Jiaxing University, China

****Correspondence:***
Decai Li
lidecai@mail.tsinghua.edu.cn

Specialty section:
This article was submitted to Smart Materials, a section of the journal Frontiers in Materials

Received: *30 April 2022*
Accepted: *06 June 2022*
Published: *12 July 2022*

Citation:
Li Z and Li D (2022) Error Analysis in Numerical Simulation of the Static Pressure Capability of Magnetic Fluid Seals. Front. Mater. 9:932964. doi: 10.3389/fmats.2022.932964

1 INTRODUCTION

Magnetic fluid is a typical type of magneto-sensitive functional material, which contains magnetic nanoparticles, surfactants, and carrier fluid. To enhance stability, magnetic nanoparticles (usually 10–100 nm) are coated with proper surfactants before they are dispersed in a carrier fluid. Magnetic fluid can be magnetized and controlled by an external magnetic field. Its response and tunable characteristics including rheological, morphological, thermal, and optical properties have become a research focus recently (Zhao et al., 2014; Afifah et al., 2016; Chen et al., 2021). Due to its unique and controllable properties, magnetic fluid has been widely applied in fields such as cancer treatment (Kozissnik et al., 2013), high accuracy sensors (Alberto et al., 2018), dampers (Li and Gong, 2019), water purification (Yang et al., 2019), and so on (Huang et al., 2021).

Among them, magnetic fluid seals (MFSs) are one of the most mature applications. In an MFS, magnetic fluid is attracted in sealing gaps by a magnetic field gradient to resist a pressure difference. As a non-contact sealing technology, it possesses unique advantages including zero leakage, long lifetime, low friction torque, and high reliability (Li, 2010). Therefore, it is suitable for high-demand sealing conditions such as rotary blood pumps (Mitamura et al., 2008), robot joints (Yang et al.,

2018), and silicon crystal growing furnaces (Zahn, 2001), especially with a requirement of vacuum environment and a long maintenance cycle.

Numerical simulation is a necessary procedure during the design and performance estimation of MFSs. Generally, the finite element method (FEM) is used to obtain the magnetic field distribution. The static pressure capability of an MFS depends on the magnetization intensity of applied magnetic fluid and the gradient of magnetic field intensity in sealing gaps. However, it is practically impossible to measure the magnetic field intensity experimentally, because the sealing gaps are usually smaller than 0.2 mm, far narrower than the thickness of the smallest Hall sensor available (about 1 mm) (Szczech and Horak, 2017). Meanwhile, to realize the largest pressure capability with a limited axial length and sealing part volume, it is essential to optimize the geometric structure and predict the pressure capability during the design process. Kim et al. (2010) designed an MFS for underwater robotic vehicles by FEM, and conducted sealing experiments as a comparison. The difference in the static pressure capability between simulation and experiments is 9.3%, and the largest difference 33.5% occurs at a rotary speed of 400 rpm. Yang et al. (2013) proposed an MFS structure with multiple magnetic sources to improve pressure capability for sealing gaps larger than 0.25 mm. The simulation result was in good consistency with experiments when gaps were 0.4 mm, but the difference increased with the increase of sealing gaps. The difference was up to 36.0% when gaps were 0.7 mm. Szczęch (2020) studied the influence of pole tooth shapes and magnetic fluid volume on the difference, as well as the pressure transfer mechanism among stages. He found that the difference was mainly due to the simplification in determining the magnetic fluid–free surface, and errors accumulated from individual stages. Cong et al. (2012) designed a twin-shaft MFSs for wafer-handling robots, and optimized the geometric dimensions in numerical simulation by varying sealing gaps, tooth width, slot width, tooth height, and thickness of the shaft in turn. Parmar et al. (2021) realized the optimization of design parameters using mass data generated by FEM simulation and then multivariate regression analysis.

In summary, previous studies have provided a general numerical simulation of pressure capability during the design of various MFS structures, and extended MFSs to many engineering applications. However, the difference between simulation results and experimental data has always been a problem for researchers. The influence of simplifications and mistakes on the simulation error has not been thoroughly studied yet. A precise and standard procedure for numerical simulation of MFSs still needs to be proposed. Moreover, most researchers optimized the geometric structures of MFSs by varying different parameters in turn, which was inefficient and neglected the complex joint influence of those parameters.

In this research, the source of errors in numerical simulation of the static pressure capability of MFSs is examined. The influence of common simplifications and mistakes in existing studies is analyzed, including material properties, geometric modeling, and theoretical formulas. A standard procedure for FEM simulation of MFSs is proposed. Furthermore, a novel method of geometric parameter optimization based on a derivative-free multiparameter optimization algorithm is put forward. Finally, a test bench for MFSs is established and sealing experiments are conducted. Differences between improved numerical simulation and experimental results are discussed.

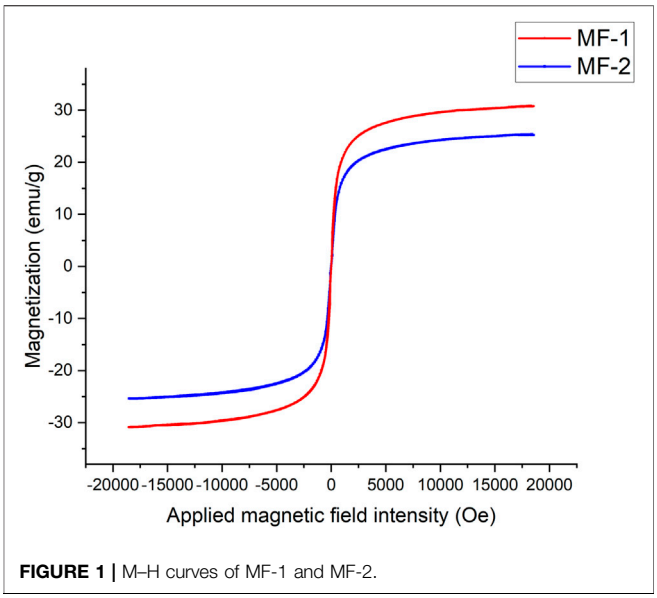

FIGURE 1 | M–H curves of MF-1 and MF-2.

2 MATERIAL AND STRUCTURE

Magnetic properties of magnetic fluid have a direct influence on the pressure capability of MFSs, and are key properties in the definition of materials in numerical simulation. Here, we take two types of magnetic fluid prepared in our laboratory as examples, MF-1 and MF-2. The relationship between the applied magnetic field and magnetization of magnetic fluid (*M-H* curves) shown in **Figure 1** was measured using a vibrating sample magnetometer (VSM, *LDJ Model 9600*) at 20 °C. Important physical and magnetic properties are listed in **Table 1**. The coercivity of these two types of magnetic fluid is low enough, so they can be regarded as superparamagnetic materials. Therefore, a single-valued relationship exists between magnetization M and magnetic field intensity H, and between magnetic induction B and magnetic field intensity H. MF-1 is taken as an example in the demonstration of the following simulation, while both types are used in sealing experiments.

Figure 2 shows the schematic diagram of a typical MFS structure. The components to form a closed magnetic circuit are colored in the figure. The red loop indicates that the magnetic flux travels from the north pole of the magnet, through the pole piece, magnet fluid, the shaft, and the other pole piece, and finally ends at the south pole. Sleeves made of magnetically non-conductive materials are placed between pole pieces and bearings, so that the magnet does not affect the performance of bearings. Pole teeth are placed annularly at the end of the pole pieces. A strong magnetic field gradient exists in the sealing gaps between pole teeth and the shaft. As a result, magnetic fluid is

TABLE 1 | Physical and magnetic properties of MF-1 and MF-2.

Magnetic fluid type	Carrier fluid	Density (g/cm^3)	Saturation magnetization (emu/g)	Coercivity (Oe)
MF-1	Kerosene	1.414	33.22	3.10
MF-2	Motor oil	1.275	26.18	14.52

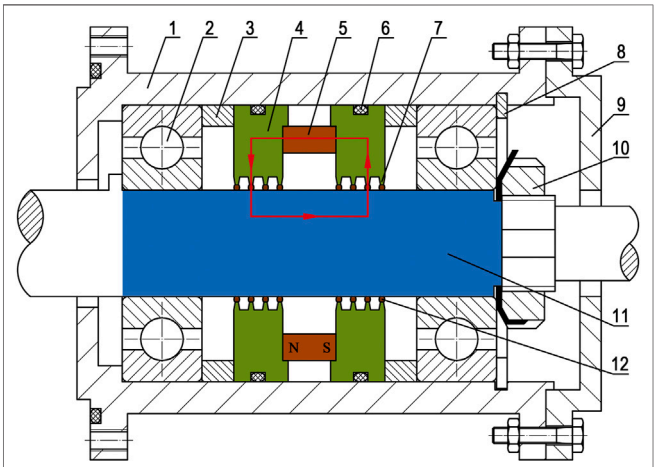

FIGURE 2 | Schematic representation of a typical MFS structure (1-shell, 2-bearing, 3-sleeve, 4-pole piece, 5-magnet, 6-rubber ring, 7-pole tooth, 8-elastic collar, 9-end cover, 10-round nut, 11-shaft, and 12-magnetic fluid).

attracted there by the magnetic force to resist a pressure difference, forming eight sealing stages. There are several commonly used shapes of pole teeth, such as triangular, rectangular, single-side trapezoidal, and isosceles trapezoidal (Parmar et al., 2018). Here, we focus on isosceles trapezoidal pole teeth.

3 THEORETICAL BASIS

The pressure capability of MFSs is derived based on the Bernoulli equation of magnetic fluid. This equation takes mechanical and magnetic energy into consideration, and is the foundation of industrial applications of magnetic fluid. For incompressible Newtonian steady-state liquid, for collinear and temperature-independent magnetization and in an irrotational flow field, the Bernoulli equation of magnetic fluid is (Rosensweig, 2013)

$$p + \frac{1}{2}\rho_f v^2 + \rho_f gh - \mu_0 \int_0^H MdH = C, \tag{1}$$

where p, ρ_f, and v are the pressure, density, and velocity of magnetic fluid, respectively. g is the gravitational acceleration, h is the height of magnetic fluid, μ_0 is vacuum permeability, M is the magnetization intensity, H is the magnetic field intensity, and C is a constant. For a static MFS, if the gravity of magnetic fluid is negligible compared to the magnetic force, and the boundary of fluid coincides with the contour line of the magnetic field intensity approximately, then

$$p_1 - \mu_0 \int_0^{H_1} MdH = p_2 - \mu_0 \int_0^{H_2} MdH, \tag{2}$$

$$\Delta p = p_1 - p_2 = \mu_0 \int_{H_1}^{H_2} MdH, \tag{3}$$

where p_1, p_2, H_1, and H_2 are the pressure and magnetic field intensity on two sides of magnetic fluid, respectively. The maximum pressure capability $\triangle p_{\max}$ occurs when

$$\Delta p_{\max} = \mu_0 \int_{H_{\min}}^{H_{\max}} MdH, \tag{4}$$

$$\Delta p_{\max} \approx \mu_0 M_s (H_{\max} - H_{\min}), \tag{5}$$

where M_s is the saturation magnetization of magnetic fluid, $H_{\max}$ and $H_{\min}$ are the maximum and minimum magnetic field intensity in the sealing gap, respectively. The approximation in **Eq. 5** is under the assumption that the magnetic field intensity is strong enough for magnetic fluid to reach saturation magnetization. The error will be discussed later. The total pressure capability of an MFS is calculated as the sum of each pole tooth.

4 METHODS

4.1 General Procedure of Numerical Simulation

Magnetic field simulation of MFSs is usually performed by the finite element method, which divides the entire system into discrete meshes, establishes algebraic equations of each domain, assembles them into a larger system of equations and solves it (Cendes et al., 1983). A general procedure of numerical simulation of MFSs includes the modeling of geometric structures, definition of material properties, definition of magnetization and boundary conditions, meshing, calculation, and post-processing.

During the simulation process, several assumptions are followed. First, the magnet is magnetized uniformly axially, and the magnetic properties of other parts are axisymmetric. Therefore, the 3D structure can be reduced to a 2D axisymmetric model. Second, those parts made of magnetically non-conductive materials, such as aluminum alloy and stainless steel, have permeability equal to vacuum. So only magnetically conductive parts are modeled. Third, the dimensional error by manufacturing and assembly is neglectable, and the width of sealing gaps is uniform and constant as designed. The materials are defined to match the actual experimental situation, where the magnet is NdFeB grade N35, and the shaft and pole pieces are made of low carbon steel 45#. The magnetization

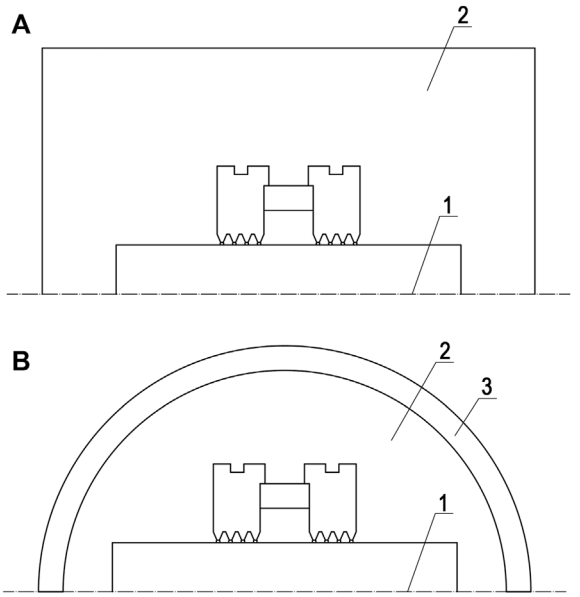

FIGURE 3 | Geometric modeling of an MFS structure with **(A)** rectangular air domain **(B)** circular air domain with infinite elements (1-axis of symmetry, 2-air domain, and 3-infinite domain).

characteristics are defined by their *B–H* curves. The axisymmetric condition is applied on the axis of symmetry, and the magnetic insulation condition is applied on the air boundaries. The initial magnetic scalar potential of the whole field is zero. The minimum meshing number in sealing gaps is 10.

4.2 Magnetic Property of Magnetic Fluid

The magnetic property of magnetic fluid is a key factor to determine the pressure capability. However, the influence of magnetic fluid on the magnetic field intensity is often ignored. Because the relative permeability of magnetic fluid is close to 1, the region of magnetic fluid is usually simplified as the air. This simplification brings apparent convenience to the modeling of the sealing structure, but when the magnetic field intensity is low, the permeability of magnetic fluid is significantly different from the air. As a result, for MFSs of a large sealing gap or weak magnetic sources, the error is magnified.

The error in the magnetic field intensity caused by the magnetic fluid can be solved by defining the *B–H* relationship of magnetic fluid during the simulation. The relationship can be derived from the experimental data of the VSM. However, because VSM measurements are an open-circuit process, the demagnetization effect must be taken into consideration. (Pugh et al., 2011). The magnetic induction B is calculated by

$$B = \mu_0 (H_{in} + M) = \mu_0 (H_a + H_d + M) = \mu_0 (H_a + (1 - N) \cdot M), \tag{6}$$

where H_{in}, H_a, and H_d are the internal, applied, and demagnetizing magnetic field intensity, respectively; N is the demagnetizing factor. The demagnetizing factor depends on the geometry and permeability of the sample. For cylindrical samples, former research (Chen et al., 1991) has provided a precise estimation of magnetometric demagnetizing factors of different ratios of length to diameter. Therefore, with the geometric dimensions of the cylindrical sample box used in VSM, the true relationship between B and H can be obtained by **Eq. 6**. To study the influence of magnetic fluid on the magnetic field intensity in sealing gaps, the areas occupied by the magnetic fluid under pole teeth are defined by the *B–H* relationship earlier.

4.3 Geometric Modeling

4.3.1 Air Domain

In former studies, a rectangular air domain is usually established to calculate the magnetic field in the surrounding region, as is shown in **Figure 3A**. But theoretically, magnetic energy is distributed in the whole field, and magnetic lines can extend to infinity. So a limited air domain will inevitably lead to an overestimated pressure capability of MFSs, due to the neglection of magnetic energy loss in the far field. On the other hand, the expansion of the air domain significantly increases the grid numbers and lowers the computational efficiency. Therefore, a proper dimension of the air domain needs to be defined, so that the exterior boundaries have little effect on the magnetic field intensity of the central working area, and the computing time is acceptable as well.

Furthermore, to realize better calculation accuracy and higher computing efficiency, infinite elements are employed in the geometric modeling of the air domain for the first time. In **Figure 3B**, region three is a layer of virtual domains which can be stretched out toward infinity. A semi-infinite coordinate stretching in the radial direction is applied to the infinite elements by a mapping function of a dimensionless coordinate, which changes from 0 to 1 in the infinite element layer (Jin, 2015). The function is usually rational, so that the infinite domain is extremely large compared to the geometry dimensions. By this means, the magnetic field solution of the central working area is not affected by the artificial boundaries.

4.3.2 Parallel Magnets

In engineering applications, especially when the diameter of the shaft is large, a single annular permanent magnet as the magnetic source is too difficult to manufacture or assemble. In these cases, several or even tens of cylindrical magnets are placed between adjacent pole pieces in parallel. The problem is that, a 3D model is more complex and computationally consuming than a 2D axisymmetric model of the same sealing structure. Therefore, this study aimed to find a reasonable simplification method of parallel magnets into a 2D model. The diameter-equivalent method indicates that the equivalent magnet in a 2D model has the same radial length as a 3D model, and the volume-equivalent method refers to the same volume as a 3D model. The errors of these two methods are then compared.

4.3.3 Magnetic Fluid Boundary

According to **Eq. 2**, if the surface tension of magnetic fluid is neglectable, then the boundaries of magnetic fluid are assumed to overlap the contour line of the magnetic field intensity. There are two possible sources of errors. First, because the boundaries of

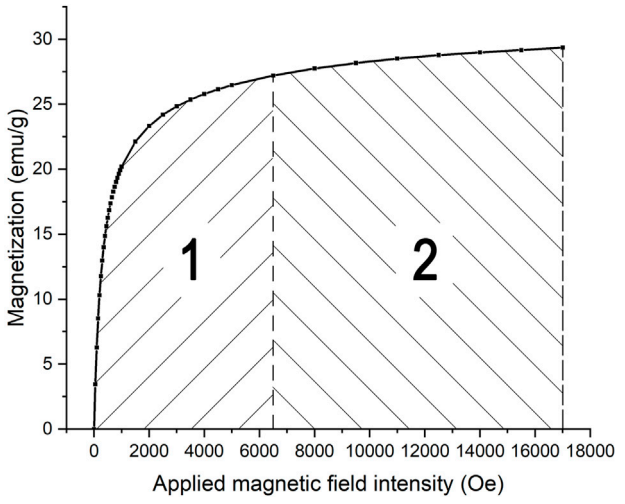

FIGURE 4 | M–H curve of the typical magnetic fluid (1-unsaturated zone, 2-saturated zone).

magnetic fluid at the critical position before a sealing failure occurs are complex to depict, former studies tend to simplify the boundaries as parts of a circle or ellipse, or even replace the magnetic fluid as the air. But the influence of dynamically changing boundaries of magnetic fluid on the magnetic field distribution, further on the pressure capability remains unfocused. Second, the minimum magnetic field intensity under each pole tooth is determined by the magnetic fluid boundary on the low-pressure side. As a result, the volume of magnetic fluid at each sealing stage is the main determinant of pressure capability. In this part, the precise boundaries of magnetic fluid overlapping the contour lines of the magnetic field intensity are calculated and depicted, and the magnetic field distribution is compared with simplified boundaries. The relationship between the volume of magnetic fluid and pressure capability is studied quantitatively.

4.4 Pressure Capability Formula

In previous studies (Zhang et al., 2019; Parmar et al., 2020) about MFSs, **Eq. 5** is mostly adopted to evaluate the pressure capability. The popularity of this formula lies in its simple form, which divides the magnetic property of magnetic fluid M_s and magnetic field intensity difference H_{max}–H_{min} as two separate objects. The basic assumption here is that, the magnetic field intensity in sealing gaps is large enough for magnetic fluid to reach magnetic saturation. However, as is shown in **Figure 4**, the *M*–*H* curve of typical magnetic fluid can be divided into two zones, the unsaturated zone and saturated zone. In the unsaturated zone, as the magnetic field intensity increases, more domains inside the magnetic fluid reorientate and stay parallel with the magnetic field. After most domains have been reorientated, further increase in the magnetic field intensity only results in a minor change of magnetization.

As a result, the commonly used formula has two problems. First, when the sealing gap is large, or the magnetic source is not strong enough, part of the magnetic fluid is far from saturation. The pressure capability is overestimated consequently. Second, the saturation magnetization is only an estimated value, because the magnetization keeps elevating slowly but incessantly. Some former researchers tried to divide the curve into segments and calculate the area separately (Li, 2010). In this research, a more accurate and straightforward method is proposed, which calculates the integral of interpolation function of the *M*–*H* curve based on **Eq. 4**.

4.5 Structure Optimization

During the design and evaluation of an MFS structure, the optimization of geometric parameters of pole teeth is crucial. It determines the difference of magnetic field intensity in sealing gaps, and further the pressure capability. Former researchers (Cong et al., 2012; Szczęch et al., 2017) adopted a "one-by-one" method to optimize different parameters of pole teeth, which varies one parameter at a time. Taking rectangular pole teeth as an example, the width of pole teeth is first varied to find the largest pressure capability, with the height of pole teeth and interval between adjacent pole teeth fixed. Then, the optimized width is fixed and the other parameters are varied one by one. This optimization method ignores the joint influence on the pressure capability by different parameters. In other words, an optimal pole tooth height at a certain width may not be the optimal value at another width. So this method cannot acquire a global optimal variable set. Moreover, the efficiency gets poorer if more variables are considered during the design process.

Here, the coordinate descent method as a derivative-free multiparameter optimization algorithm is applied to optimize the geometric parameters of pole teeth. This is a class of optimization algorithms, where the optimization process is not based on the derivative of the objective function (Larson et al., 2019). It is especially appropriate for pole tooth design, because the relationship between pressure capability and structural parameters can hardly be solved analytically. By the coordinate descent method, starting with the control variable set at the start of *k*th iteration $\boldsymbol{x}^{(k)}$, a finite number of points are searched along coordinate directions so that $f(\boldsymbol{x}) < f(\boldsymbol{x}^{(k)})$. If so, the new variable set is replaced as $\boldsymbol{x}^{(k+1)} = \boldsymbol{x}^{(k)}$. Otherwise, points are evaluated from the poll set $\boldsymbol{P}^{(k)}$.

$$\boldsymbol{P}^{(k)} = \left\{\boldsymbol{x}^{(k)} + \alpha_k \boldsymbol{d} \middle| \boldsymbol{d} \in D_k\right\}, \tag{7}$$

where α_k is the step size and D_k is a positive basis of the variable space. If a better point with a smaller objective value in the poll set is found so that $f(\boldsymbol{x}^{(k)} + \alpha_k \boldsymbol{d}^{(k)}) < f(\boldsymbol{x}^{(k)})$, then the variable set is updated. Otherwise, the variable set remains unchanged, and the step size is decreased. The optimization process ends when the step size is less than a prescribed limitation, or the maximum iteration number is reached. The optimization results obtained using the coordinate descent method and "one-by-one" method are compared and discussed.

4.6 Experimental Setup

To validate the improved numerical simulation method, a test bench for MFSs is established. Key components of the sealing prototype are shown in **Figure 5**, including a gas chamber, a

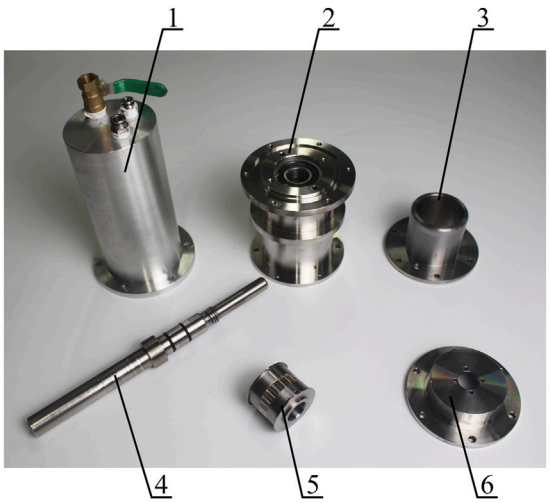

FIGURE 5 | Key components of the sealing prototype (1-gas chamber, 2-shell with bearings inside, 3-inner sleeve, 4-shell, 5-magnetic unit, and 6-end cover).

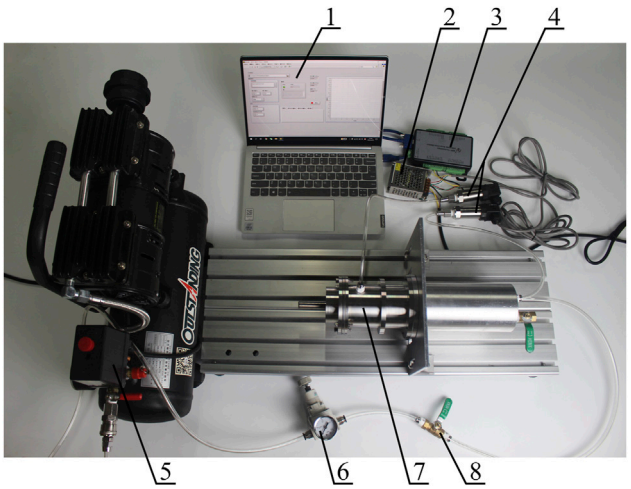

FIGURE 6 | Test bench for MFSs (1-computer, 2-power supply, 3-data acquisition card, 4-pressure sensor, 5-air compressor, 6-regulator valve, 7-sealing prototype, and 8-ball valve).

shell with two bearings inside, a magnetically conductive inner sleeve, a shaft, a magnetic unit consisting of parallel magnets and two pole pieces, and an end cover. The pole pieces are assembled on the shaft instead of the shell, so that pole teeth are exposed for the ease of magnetic fluid injection. Two pairs of pole pieces are manufactured and used. One pair has one rectangular pole tooth per pole piece, with the width of pole teeth 1 mm and the height 2 mm. The other pair has five rectangular pole teeth per pole piece, with the width 0.5 mm, the height 2 mm, and the interval 2.5 mm. The sealing gap is 0.3 mm.

Figure 6 indicates the set-up of MFS experiments. In each sealing experiment, a certain amount of magnetic fluid is injected into each pole tooth, as is shown in **Figure 7**. Then, the shaft is pushed into the shell and fixed. The end cover is installed and the gas and electric circuits are connected. At the beginning, all valves are closed except for the air compressor. The outflow air is adjusted to a modest stable pressure (100 kPa for example). After that, the ball valve is turned on slowly and the air in the gas chamber is compressed. The pressure in the first and second stages of the MFS is collected by pressure sensors and written on the computer. Finally, a sudden pressure drop occurs, indicating the bursting of magnetic fluid and a sealing failure. The critical pressure before the failure is recorded as the pressure capability. For each different sealing condition, the experiments are repeated three times and the average value and standard deviation are calculated.

5 RESULTS AND DISCUSSION

5.1 Effect of the Magnetic Property of Magnetic Fluid

The ratio of length to diameter of the sample box is measured as 0.422, and the demagnetization factor along the magnetic field direction is 0.242 by interpolation. In **Figure 8A**, the *M–H* curve of MF-1 by different demagnetizing factors is plotted. After demagnetization correction, the magnetization is higher than original values, and the largest deviation exists in the unsaturated zone, where the magnetic field intensity is rather low. For the sample box used in the experiment, the demagnetization effect is not obvious.

As is shown in **Figure 8B**, the magnetic induction of magnetic fluid is higher than vacuum (or air), but the curves with and without the demagnetization correction are almost overlapped. The maximum difference caused by the demagnetization effect is lower than 1%. The main reason is the relatively low magnetization intensity of magnetic fluid. The pressure capability of magnetic fluid with and without the demagnetization correction and of air is 229.48, 229.04, and 232.86 kPa, respectively. Consequently, an error of 1.5% exists if magnetic fluid is simplified as air, but the influence of the demagnetization effect is negligible.

5.2 Effect of Geometric Modeling

5.2.1 Air Domain

For the traditional rectangular air domain, the width of the air domain is varied from 35 to 200 mm and the pressure capability is calculated, as is shown in **Figure 9**. The length of the air domain is twice the width. The total degrees of freedom are also depicted reflecting the computing complexity. As the air domain expands, the pressure capability decreases rapidly at first, and then converges to about 229.6 kPa. Meanwhile, the total degrees of freedom rise, indicating a larger computing amount due to more grids generated in the air domain. For this traditional air domain method, a balance between magnetic energy loss in the far field and computing efficiency needs to be considered, and five times the size of the working area is recommended in practice. In comparison, the simulation result by infinite elements is

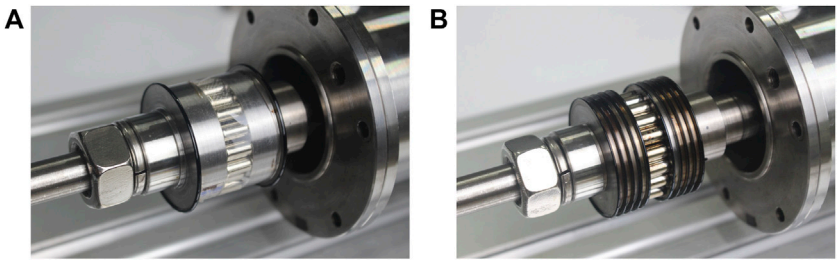

FIGURE 7 | Magnetic fluid injection on pole teeth. **(A)** One pole tooth and **(B)** five pole teeth per pole piece.

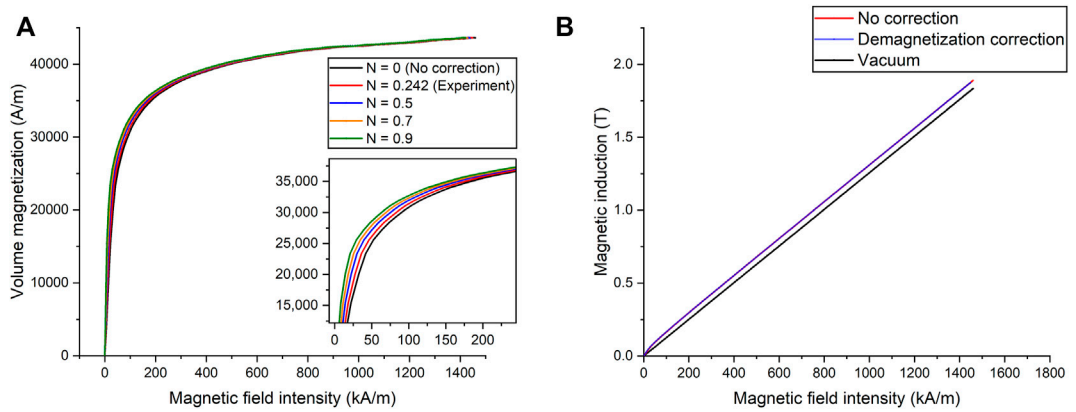

FIGURE 8 | (A) M–H curve and **(B)** B–H curve of MF-1 with and without demagnetization correction.

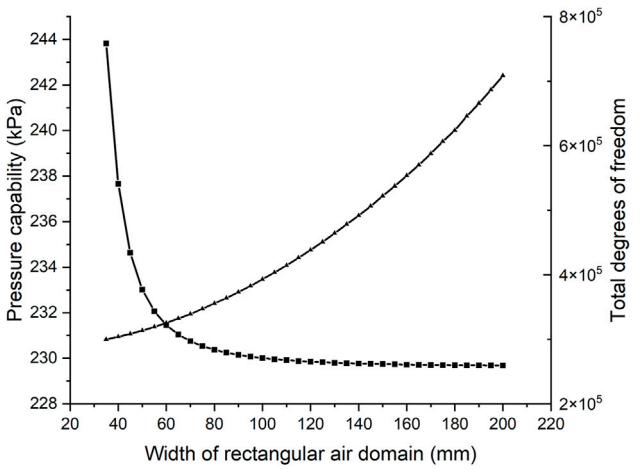

FIGURE 9 | Pressure capability (block) and total degrees of freedom (triangle) with different widths of the rectangular air domain.

229.63 kPa, and the total degree of freedom is 3.1×10^5. By an infinite element layer, the error of energy loss the in the far field is significantly decreased, while the computing efficiency remains satisfactory. Infinite elements prove to be a better method to model the air domain.

5.2.2 Parallel Magnets

For MFSs with parallel magnets, the number of magnets used in the device is determined by the requirement of pressure capability, the inner space, assembling difficulty, etc. In this case, different numbers of cylindrical magnets of 10 mm height and 5 mm diameter are simulated by 3D models. 3D simulation provides the most precise result evidently, but is not applicable practically due to the computing time as long as 100 times of 2D models. Therefore, 2D simulation with diameter-equivalent and volume-equivalent methods is conducted. The pressure capability of the former method is 229.48 kPa and the latter is shown in **Table 2**.

Numerical simulation indicates a significant influence on the pressure capability by the number or volume of magnets. The pressure capability increases linearly with the number of parallel magnets (linear correlation coefficient R = 0.99999), which has not been reported by previous studies. This indicates a relatively fixed magnetic energy provided by a certain volume of magnets. As a result, a large error exists between 3D simulation and 2D simulation with the diameter-equivalent method, and the error decreases with more magnets. The relative error from 3D simulation is 33.3% with 24 parallel magnets. It is mainly because the gaps between adjacent magnets cannot provide magnetic energy. Meanwhile, the volume-equivalent method shows a great consistency with the 3D model for different

TABLE 2 | Pressure capability of 3D and 2D volume-equivalent models with parallel magnets.

Number of parallel magnet	Pressure capability by the 3D model (kPa)	Pressure capability by the 2D volume-equivalent model (kPa)	Relative error (%)
19	132.63	132.83	0.2
20	140.57	140.83	0.2
21	148.53	148.77	0.2
22	156.50	156.75	0.2
23	164.46	164.75	0.2
24	172.18	172.73	0.3

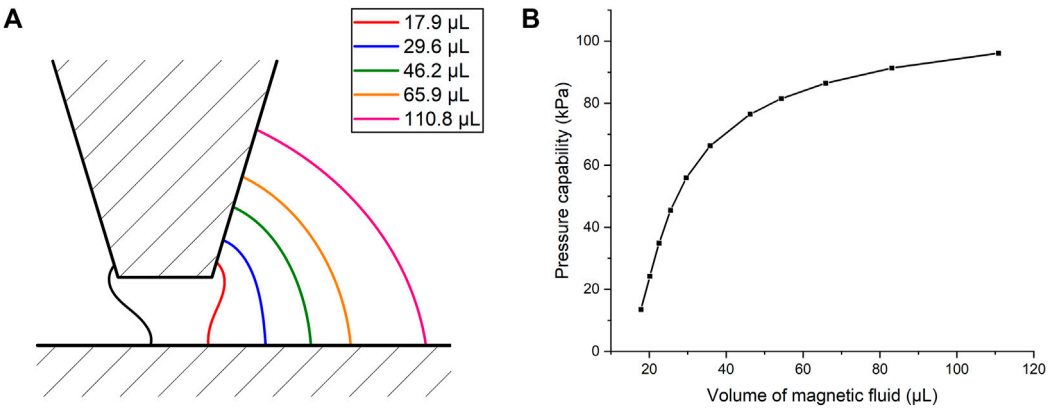

FIGURE 10 | (A) Magnetic fluid boundaries at critical positions with different volumes. **(B)** Pressure capability varying with the volume of the magnetic fluid.

numbers of parallel magnets, which is preferred to simplify a 3D model with parallel magnets into a 2D axisymmetric one.

5.2.3 Magnetic Fluid Boundary

Three common descriptions of the magnetic fluid boundary are studied, including the contour line of magnetic field intensity, ellipses, and simplification as air. The maximum magnetic field intensity under three conditions is similar, and the largest difference is about 1%. Consequently, the magnetization of the magnetic fluid itself has little effect on the magnetic field distribution. The major influence of the magnetic fluid boundary is on the determination of minimum magnetic field intensity in **Eq. 4**, which is related to the volume of magnetic fluid under the pole tooth. Due to an uncertainty pattern of magnetic fluid distribution among multiple stages, here we take a single pole tooth per pole piece as an example.

Figure 10A demonstrates the magnetic fluid boundaries (calculated as contour lines of magnetic field intensity) at critical positions with different volumes. The black line on the left represents the boundary on the high pressure side, and part of it is deformed by the concentration of the magnetic field at the corner of pole teeth. In **Figure 10B**, the pressure capability increases with more magnetic fluid injected under the pole tooth. However, the increase is significant at first but then slows down. Also, the variation of pressure capability by the volume can be quite large. In conclusion, the influence of magnetic fluid boundaries lies in the determination of the minimum magnetic field intensity, and further the pressure capability. Although the theoretical volume is small, an excessive volume of magnetic fluid is usually injected in experiments. The resulting experimental errors are discussed later.

5.3 Effect of the Pressure Capability Formula

For the MFS simulation model presented earlier, **Eq. 5** as the most adopted simplification of the pressure capability formula gives a result of 266.61 kPa, and the integral of interpolation function of the *M–H* curve based on **Eq. 4** obtains 229.53 kPa. The error of 16.2% comes from the overestimation of saturation magnetization of magnetic fluid by the simplified formula, because in this case where the sealing gap is 0.3 mm, the magnetic field intensity in the sealing gaps is relatively low, and a large amount of magnetic fluid is far from saturation. In conclusion, the integral formula based on **Eq. 4** is essential to decrease the simulation error, especially for large sealing gaps or a weak magnetic source.

5.4 Structure Optimization

For MFSs with isosceles trapezoidal pole teeth, four geometric parameters have a major influence on the magnetic field

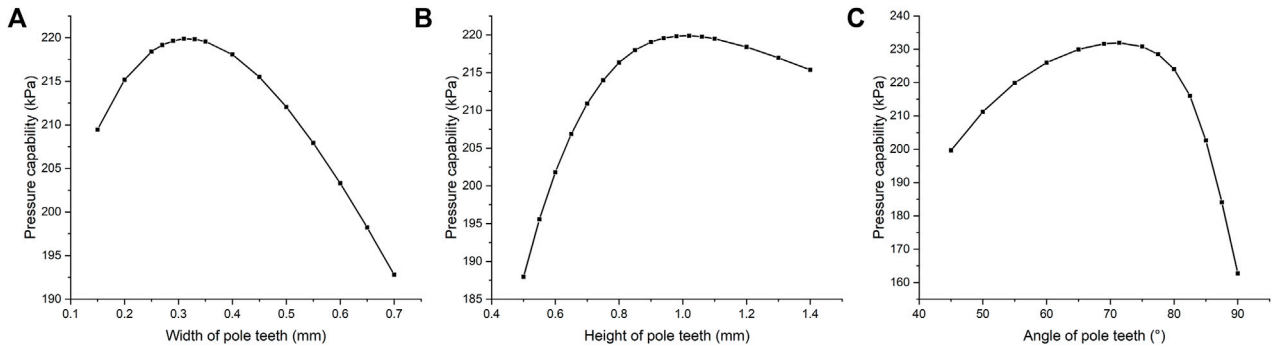

FIGURE 11 | Pressure capability varying with **(A)** width, **(B)** height, and **(C)** angle of pole teeth.

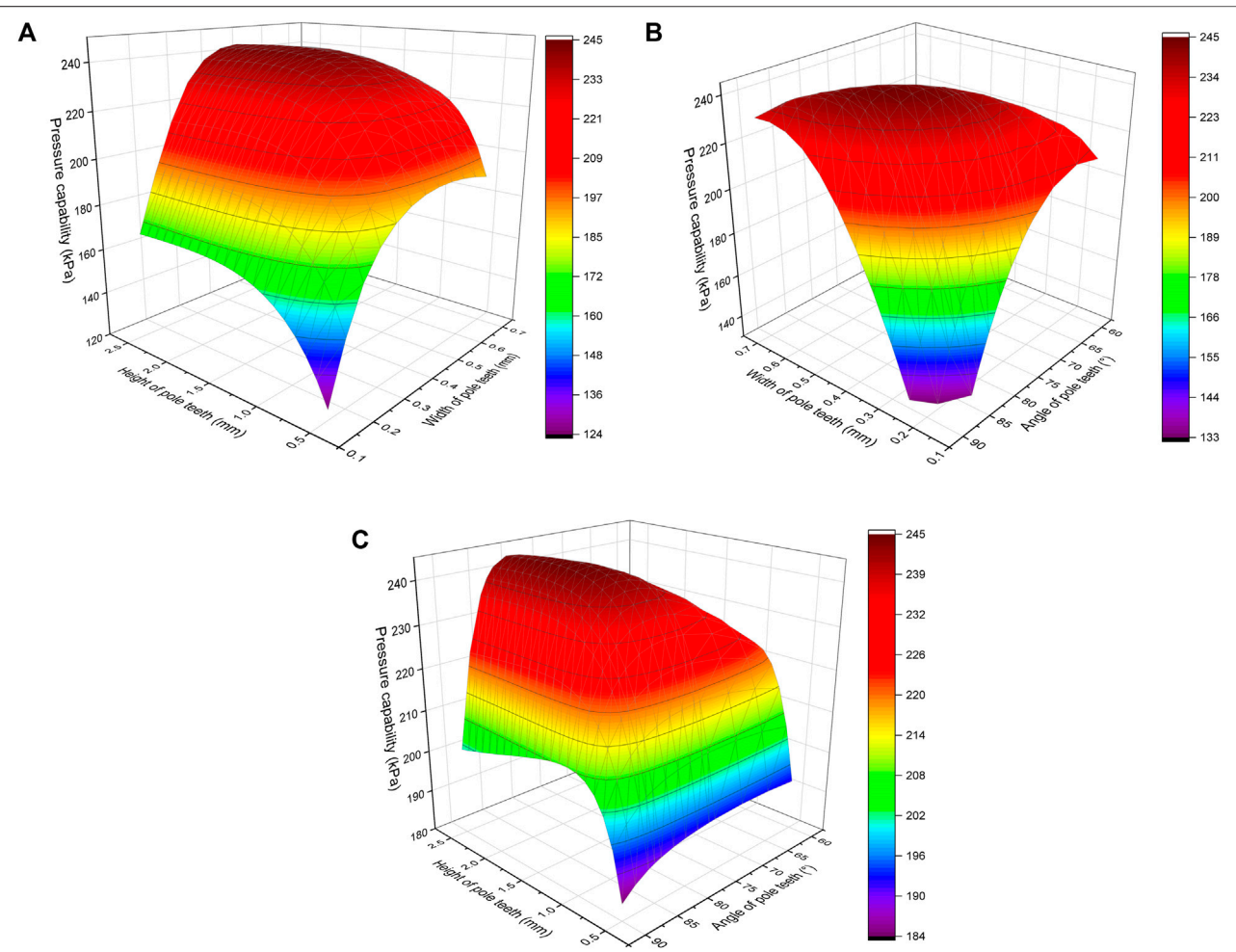

FIGURE 12 | Joint influence on pressure capability by **(A)** width and height, **(B)** width and angle, and **(C)** height and angle.

distribution, the width of pole teeth L_t, the height of pole teeth L_h, the angle of pole teeth α, and the interval between adjacent pole teeth L_m. Since the axial length of pole pieces is usually fixed, the first three parameters are independent control variables during the structure optimization, and the pressure capability is the objective function. The initial parameter set is selected as $L_t = 0.8$ mm, $L_h = 1$ mm and $\alpha = 55°$.

Figure 11 shows the optimization process of the "one-by-one" method. Pressure capability with different widths of pole teeth is calculated, and the optimal width value is used in the next step. The

TABLE 3 | Comparison between experimental and simulation results under different MFS conditions.

Number of pole teeth per pole piece	Magnetic fluid type	Experimental result (kPa)	Simulation result before improvement (kPa)	Relative error (%)	Simulation result after improvement (kPa)	Relative error (%)
1	MF-1	40.62 ± 1.39	61.85	34.3	48.28	15.9
1	MF-2	29.55 ± 1.51	43.95	32.8	35.62	17.0
5	MF-1	77.96 ± 3.46	142.21	45.2	99.83	21.9
5	MF-2	63.50 ± 3.17	101.05	37.2	73.82	14.0

optimization result of this method is 231.93 kPa, where the optimal variable set is $L_t = 0.31$ mm, $L_h = 1.01$ mm, and $\alpha = 71.0^{\circ}$. Meanwhile, the optimization result of the coordinate descent method is 244.64 kPa, with an iteration number of 183. The corresponding variable set is $L_t = 0.45$ mm, $L_h = 1.81$ mm, and $\alpha = 80.7^{\circ}$. Obviously, the multiparameter optimization obtains a 5.5% higher objective value than the traditional method. The main reason is the joint influence on pressure capability by different geometric parameters, as is demonstrated in **Figure 12**. This figure shows a stationary point in the variable set space, indicating the existence of a global optimal solution. However, the solution is not likely to be reached by variation of one control variable when the other variables remain fixed.

To test the robustness of these two methods, another two initial variable sets are adopted. The first set is $L_t = 0.5$ mm, $L_h = 2$ mm, and $\alpha = 70^{\circ}$. The second set is $L_t = 1$ mm, $L_h = 1.5$ mm, and $\alpha = 90^{\circ}$. The "one-by-one" method leads to 241.66 and 236.30 kPa as maximum pressure capability, respectively. In comparison, the coordinate descent method obtains nearly the same result about 244.6 kPa at nearly the same variable set for all three conditions. Apparently, the multiparameter optimization algorithm is insensitive to initial values, and has higher design efficiency and a better optimization result compared to the traditional method.

5.5 Experimental Studies

MFS experiments with two types of magnetic fluid and two pairs of pole pieces are conducted. For each different sealing condition, the average value of pressure capability as well as standard deviation is calculated. The comparison between experimental and simulation results before and after improvement is shown in **Table 3**. For the unimproved simulation, the area of sealing gaps is simplified as air. The air domain is rectangular with 80 mm width and 160 mm length. The calculation of pressure capability is according to **Eq. 5**. For the improved simulation, the area occupied by the magnetic fluid under pole teeth is defined by the B–H relationship of magnetic fluid after demagnetization correction in **Figure 8B**. The air domain is circular with a radius of 70 mm and an 8 mm thick layer defined as infinite domains. The calculation of pressure capability is carried out by the integral of interpolation function of the M–H curve of magnetic fluid. Parallel magnets are both simplified with the volume-equivalent method. The improved simulation method reduces the errors to a large extent. The main reason is the integral of interpolation function of the M–H curve as the pressure capability formula in **Section 4.4**. The advantage and importance of this formula stand out, especially when the magnetic fluid is far from magnetic saturation, just like the sealing prototype. In addition, the application of infinite domains and proper simplification of magnets also enhance the calculation precision and efficiency.

However, for both simulation methods, the errors of MFSs with five pole teeth per pole piece are generally higher than that of single pole tooth, which indicates a major problem of the current simulation. During the present simulation of multiple pole teeth, it is assumed that different sealing stages reach their maximum pressure capability at the same time, and they add up to the total pressure capability. But in fact, the mechanism of pressure transferring through stages is complex. The distribution of pressure among different pole teeth depends on the position of magnetic fluid, the compression process and even the sealing history, and remains unsolved theoretically. This leads to a general overestimation of pressure capability with multiple pole teeth compared to a single pole tooth.

In addition, the experimental setup and operation also account for part of the error. First, although a certain amount of magnetic fluid is injected into each pole tooth, redistribution and loss of magnetic fluid are likely to occur during the push-in process. Some magnetic fluid will be attracted near the magnets because of magnetic concentration. As a result, the actual volume remaining under pole teeth may be insufficient, and the pressure capability will decrease. Second, the sealing gap is not always uniform as 0.3 mm circularly, so the bursting of magnetic fluid tends to occur where the sealing gap is larger. The dimensional error by manufacturing and assembly also leads to deviation.

6 CONCLUSION

In this research, the source of errors in numerical simulation of the static pressure capability of MFSs is analyzed. The influence of common simplification and mistakes on the simulation result in former research works is studied, including magnetic properties, geometric modeling, and pressure capability formulas. Modeling of parallel magnets, the volume of magnetic fluid, and simplification of pressure capability formula prove to be main sources of the error. Novel techniques are raised to enhance the precision and efficiency of numerical simulation, such as demagnetization correction, infinite elements, and integral formula of pressure capability. In addition, the coordinate descent method as a derivative-free multiparameter optimization algorithm is first used to optimize geometric parameters of pole teeth. Finally, MFS experiments are conducted, and the improved simulation method shows a smaller deviation from experimental results than

the traditional one. This research provides a precise, efficient, and standard procedure for numerical simulation of magnetic fluid seals. For rotating seals, this procedure is still fundamental and applicable, but the influence of the centrifugal force and elevating temperature should be taken in consideration. Future research will focus on *in situ* observation of magnetic fluid and its distribution among multiple pole teeth.

DATA AVAILABILITY STATEMENT

The raw data supporting the conclusions of this article will be made available by the authors, without undue reservation.

AUTHOR CONTRIBUTIONS

ZL conducted the numerical simulation and sealing experiments of the magnetic fluid and completed the writing of this manuscript. DL prepared two types of magnetic fluid and designed the research approach.

FUNDING

This work was supported by the National Natural Science Foundation of China (grant numbers U1837206, 51735006, and 51927810).

REFERENCES

Afifah, A. N., Syahrullail, S., and Sidik, N. (2016). Magnetoviscous Effect and Thermomagnetic Convection of Magnetic Fluid: A Review. *Renew. Sustain. Energy Rev.* 55, 1030–1040. doi:10.1016/j.rser.2015.11.018

Alberto, N., Domingues, M., Marques, C., André, P., and Antunes, P. (2018). Optical Fiber Magnetic Field Sensors Based on Magnetic Fluid: A Review. *Sensors* 18 (12), 4325. doi:10.3390/s18124325

Cendes, Z., Shenton, D., and Shahnasser, H. (1983). Magnetic Field Computation Using Delaunay Triangulation and Complementary Finite Element Methods. *IEEE Trans. Magn.* 19 (6), 2551–2554. doi:10.1109/tmag.1983.1062841

Chen, D.-X., Brug, J. A., and Goldfarb, R. B. (1991). Demagnetizing Factors for Cylinders. *IEEE Trans. Magn.* 27 (4), 3601–3619. doi:10.1109/20.102932

Chen, F., Ilyas, N., Liu, X., Li, Z., Yan, S., and Fu, H. (2021). Size Effect of Fe3O4 Nanoparticles on Magnetism and Dispersion Stability of Magnetic Nanofluid. *Front. Energy Res.* 9, 780008. doi:10.3389/fenrg.2021.780008

Cong, M., Wen, H., Du, Y., and Dai, P. (2012). Coaxial Twin-Shaft Magnetic Fluid Seals Applied in Vacuum Wafer-Handling Robot. *Chin. J. Mech. Eng.* 25 (4), 706–714. doi:10.3901/CJME.2012.04.706

Huang, T., Song, F., Wang, R., and Huang, X. (2021). Numerical Simulation Study of Tracking the Displacement Fronts and Enhancing Oil Recovery Based on Ferrofluid Flooding. *Front. Earth Sci.* 9, 759862. doi:10.3389/feart.2021.759862

Jin, J. (2015). *The Finite Element Method in Electromagnetics*. Hoboken, NJ: John Wiley & Sons.

Kim, D.-Y., Bae, H.-S., Park, M.-K., Yu, S.-C., Yun, Y.-S., Cho, C. P., et al. (2010). A Study of Magnetic Fluid Seals for Underwater Robotic Vehicles. *Int. J. Appl. Electrom.* 33 (1-2), 857–863. doi:10.3233/JAE-2010-1195

Kozissnik, B., Bohorquez, A. C., Dobson, J., and Rinaldi, C. (2013). Magnetic Fluid Hyperthermia: Advances, Challenges, and Opportunity. *Int. J. Hyperth.* 29 (8), 706–714. doi:10.3109/02656736.2013.837200

Larson, J., Menickelly, M., and Wild, S. M. (2019). Derivative-Free Optimization Methods. *Acta Numer.* 28, 287–404. doi:10.1017/S0962492919000060

Li, D. (2010). *Theories and Applications of Magnetic Fluid Sealing*. Beijing, China: China Science Press.

Li, Z., and Gong, Y. (2019). Research on Ferromagnetic Hysteresis of a Magnetorheological Fluid Damper. *Front. Mat.* 6, 111. doi:10.3389/fmats.2019.00111

Mitamura, Y., Arioka, S., Sakota, D., Sekine, K., and Azegami, M. (2008). Application of a Magnetic Fluid Seal to Rotary Blood Pumps. *J. Phys. Condens. Matter* 20 (20), 204145. doi:10.1088/0953-8984/20/20/204145

Parmar, S., Ramani, V., Upadhyay, R. V., and Parekh, K. (2018). Design and Development of Large Radial Clearance Static and Dynamic Magnetic Fluid Seal. *Vacuum* 156, 325–333. doi:10.1016/j.vacuum.2018.07.055

Parmar, S., Ramani, V., Upadhyay, R. V., and Parekh, K. (2020). Two Stage Magnetic Fluid Vacuum Seal for Variable Radial Clearance. *Vacuum* 172, 109087. doi:10.1016/j.vacuum.2019.109087

Parmar, S., Upadhyay, R. V., and Parekh, K. (2021). Optimization of Design Parameters Affecting the Performance of a Magnetic Fluid Rotary Seal. *Arab. J. Sci. Eng.* 46 (3), 2343–2348. doi:10.1007/s13369-020-05094-1

Pugh, B. K., Kramer, D. P., and Chen, C. H. (2011). Demagnetizing Factors for Various Geometries Precisely Determined Using 3-D Electromagnetic Field Simulation. *IEEE Trans. Magn.* 47 (10), 4100–4103. doi:10.1109/TMAG.2011.2157994

Rosensweig, R. E. (2013). *Ferrohydrodynamics*. Mineola, NY: Courier Corporation.

Szczech, M., and Horak, W. (2017). Numerical Simulation and Experimental Validation of the Critical Pressure Value in Ferromagnetic Fluid Seals. *IEEE Trans. Magn.* 53 (7), 1–5. doi:10.1109/TMAG.2017.2672922

Szczęch, M., Horak, W., and Salwiński, J. (2017). The Influence of Selected Parameters on Magnetic Fluid Seal Tightness and Motion Resistance. *Tribologia* 4, 71–76. doi:10.5604/01.3001.0010.5997

Szczęch, M. (2020). Magnetic Fluid Seal Critical Pressure Calculation Based on Numerical Simulations. *Simulation* 96 (4), 403–413. doi:10.1177/0037549719885168

Yang, C., Yu, M., Cao, X., and Bian, X. (2019). Application of Amorphous Nanoparticle Fe-B Magnetic Fluid in Wastewater Treatment. *Nano* 14 (09), 1950119. doi:10.1142/S1793292019501194

Yang, X., Chen, F., Gao, S., and Chen, Y. (2018). Magnetic Field Finite Element Analysis of Concentric Biaxial Stepped Ferrofluid Seals. *Int. J. Appl. Electrom.* 58 (4), 471–481. doi:10.3233/JAE-180060

Yang, X., Zhang, Z., and Li, D. (2013). Numerical and Experimental Study of Magnetic Fluid Seal with Large Sealing Gap and Multiple Magnetic Sources. *Sci. China Technol. Sci.* 56 (11), 2865–2869. doi:10.1007/s11431-013-5365-4

Zahn, M. (2001). Magnetic Fluid and Nanoparticle Applications to Nanotechnology. *J. Nanopart Res.* 3 (1), 73–78. doi:10.1023/A:1011497813424

Zhang, Y., Chen, Y., Li, D., Yang, Z., and Yang, Y. (2019). Experimental Validation and Numerical Simulation of Static Pressure in Multi-Stage Ferrofluid Seals. *IEEE Trans. Magn.* 55 (3), 1–8. doi:10.1109/TMAG.2017.2744606

Zhao, Y., Wu, D., Lv, R.-Q., and Ying, Y. (2014). Tunable Characteristics and Mechanism Analysis of the Magnetic Fluid Refractive Index with Applied Magnetic Field. *IEEE Trans. Magn.* 50 (8), 1–5. doi:10.1109/TMAG.2014.2310710

Conflict of Interest: The authors declare that the research was conducted in the absence of any commercial or financial relationships that could be construed as a potential conflict of interest.

Publisher's Note: All claims expressed in this article are solely those of the authors and do not necessarily represent those of their affiliated organizations, or those of the publisher, the editors, and the reviewers. Any product that may be evaluated in this article, or claim that may be made by its manufacturer, is not guaranteed or endorsed by the publisher.

frontiers | Frontiers in Materials

TYPE Original Research
PUBLISHED 15 July 2022
DOI 10.3389/fmats.2022.942318

OPEN ACCESS

EDITED BY
Zhili Zhang,
Beijing Jiaotong University, China

REVIEWED BY
Domenico De Tommasi,
Politecnico di Bari, Italy
Xiaomin Dong,
Chongqing University, China
Manjesh Kumar,
Indian Institute of Technology Guwahati, India
Yancheng Li,
Nanjing Tech University, China
U Ubaidillah,
Sebelas Maret University, Indonesia
Jiong Wang,
Nanjing University of Science and Technology, China

*CORRESPONDENCE
Honghui Zhang,
hhzhang@cqu.edu.cn

SPECIALTY SECTION
This article was submitted to Smart Materials,
a section of the journal
Frontiers in Materials

RECEIVED 12 May 2022
ACCEPTED 27 June 2022
PUBLISHED 15 July 2022

CITATION
Zou Z, Zhang H, Liao C and Wang N (2022), Unsteady extension of quasi-steady physical modeling and experimental verification of a magnetorheological energy absorber. *Front. Mater.* 9:942318.
doi: 10.3389/fmats.2022.942318

Unsteady extension of quasi-steady physical modeling and experimental verification of a magnetorheological energy absorber

Zhiyuan Zou, Honghui Zhang*, Changrong Liao and Ning Wang

The Key Laboratory of Opto-electronics Technology and Systems, Ministry of Education, Chongqing University, Chongqing, China

Magnetorheological (MR) fluids are promising in controllable damping based on regulated apparent viscosity under magnetic field control, and they are employed in various damping devices such as automotive dampers and energy absorbers for artillery or landing gears by medium substitution with structural adaptations. In this study, we designed and fabricated a magnetorheological energy absorber (MREA) with disc springs as recoiling parts, modeled the MR fluid flow based on the Bingham constitutive model, and then carried out unsteady extension based on the quasi-steady model. The experimental tests of the MREA show that the unsteady extension of the quasi-steady model can designate the behaviors of the MREA in different impact speeds better than the original; thus, the controllability of the MREA is verified. An interesting phenomenon, where a rippled MREA peak force is observed at the saturated excitation when the impact speed is not so high and disappears when the impact speed is high enough, is accounted from the viewpoint of flow modeling and finally verified by more experimental results.

KEYWORDS

magnetorheological, energy absorber, quasi-steady modeling, unsteady modeling, experimental verification

Introduction

For several decades, we have witnessed the progressive prosperity of MR-based technologies from the 1990s with the invention of MR fluid by J. Rabinow (). However, nowadays, the lack of investigation of new theories or proposal of new applications and the dilemma of performance uncertainty partly resulting from MR fluid sedimentation have confined related research to the descending channel. MR fluid, however, is still advantageous for its effectiveness and efficiency when adopted for vibration suppression and shock absorption because of the quick and reversible change in the yielding stress under the applied magnetic field, and thus the apparent viscosity.

MR devices can be classified into rotary types such as MR clutch (Bucchi et al., 2014; Rizzo et al., 2015; Park et al., 2021) and MR brake (Poznic et al., 2017; Wang and Bi, 2020),

which are less troubled by the performance estimation because they are in pure shearing mode, and reciprocal types such as MR damper (Wang et al., 2018; Li and Yang, 2020; Sheng et al., 2022) and MR energy absorber (MREA), which are always employed for vibration and shock mitigation. The MR damper is mostly utilized in an automotive suspension, however, the MREA is mostly employed in a high-speed impact such as an anti-recoil system of artillery (Li and Wang, 2012), there are difficulties in the behavior prediction to an extent because of the working modes based on pressure differences resulting from piston movement.

A traditional buffer can reduce the impact of the moving mass by gradually decreasing the speed until zero at the end of their stroke. In the process, the buffer performance is controlled through a specified throttling which is varied with the stroke, such as the throttling bar in a gun recoil mechanism and the metering pin in a landing gear for airplanes. The stroke-controlled throttling is optimized with a specified working condition and it is impossible to adapt to varying requirements. For example, in a carrier-based aircraft landing gear design, the landing speed is crucial and full of contradictions. The aircraft parameters such as entry speed, ship engagement speed, and landing weight and the sea conditions including the instability of the ocean caused by the hull of the ship swaying, vertical shaking, and hanging have significant impacts on the aircraft carrier, and all of these demands a smart controlled buffer that can handle the landing process based on the real-time circumstances. MREA is a promising scheme in this regard. M. Wang (Wang et al., 2020) presented a minimum duration deceleration exposure (MDDE) control method for a drop-induced shock mitigation system using an MREA at high sink rates, and the key goal of MDDE control is that the payload should come to rest after fully using the available MREA stroke, that is, to accomplish a soft landing without exceeding the maximum allowable deceleration and simultaneously minimizing the duration of exposure to the maximum allowable deceleration.

For continuous operation, an MREA is generally equipped with parallel spring elements which provide the power for driving the piston back, and the MR fluid is activated by the magnetic structure situated in the piston to provide controllable damping in its operation stroke. The damping force can be adjusted by the excitation current until the magnetic path is saturated. N. Werely (Wereley and Pang, 1998) initiated the quasi-steady modeling for MR dampers based on parallel plate models, and Bai (Bai et al., 2012) proposed an MREA structure with dual concentric annular valves, which employed an inner-set permanent magnet to decrease the field-off damping force by decreasing the baseline damping force, while keeping an appropriate dynamic range for improving shock and vibration mitigation performance. To estimate the mechanical behavior of the MREA, M. Mao (Mao et al., 2013) focused on nonlinear MREA models that can predict MREA dynamic behavior more accurately for

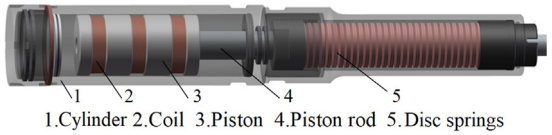

FIGURE 1
MREA structure.

nominal impact speeds up to 6 m/s. A hydromechanical model with nonlinear behavior was employed to estimate the impact progress, but the unsteady performance with time-variant flow development was not actually realized. B.E. Powers (Powers et al., 2016) presented the improvement of a Bingham-plastic damper model incorporated with refined minor losses by considering fluid friction models so as to predict the stroking load of a magnetorheological energy absorber (MREA) during high-speed impact.

In the MREA control application, Hu (Hu et al., 2012) et al. investigated the MREA systematically and paid attention to the delay from the powering circuit and magnetic hysteresis and thus the response time. Q. Ouyang (Ouyang et al., 2020) verified the feasibility and controllability of a designed multi-stage MREA in two kinds of recoil buffer system; the conducted impact tests under different current loadings showed that the different buffer control effects were realized by changing the input current, but the ideal “platform effect” could not be completely realized because the controllable damping force was not big enough.

Generally speaking, a well-designed MREA is promising for the controllable buffering control, but because of the complicated constitutive model of MR fluid, the performance of the designed MREA is difficult to predict, and so it is not easy to optimize the MREA design. Traditionally, MR flow modeling is based on a quasi-steady condition at a steady or slow-changing impact speed, which is not fully qualified for the force prediction of MREA. In this paper, we propose an unsteady extension of the quasi-steady modeling to better forecast the behavior of a fabricated MREA, and experimental tests are carried out to make the appraisal.

Design of MREA

We proposed a study on MREA in a previous paper (Shou et al., 2018) and carried out the modeling considering inertia effects. In this paper, we optimize the MREA design with a piston of a larger radius, which decreased the flow velocity in the gap with a relatively large pressure area. The number of disc springs was reduced but the size was increased to decrease the nonlinearity according to Ref. (Du et al., 2021), because the spring combination is treated linearly when the deformation is less than 15% relative to the free height.

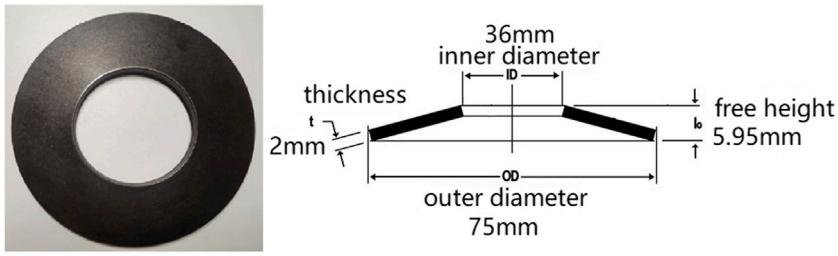

FIGURE 2
Outline and parameters of a piece of disc spring.

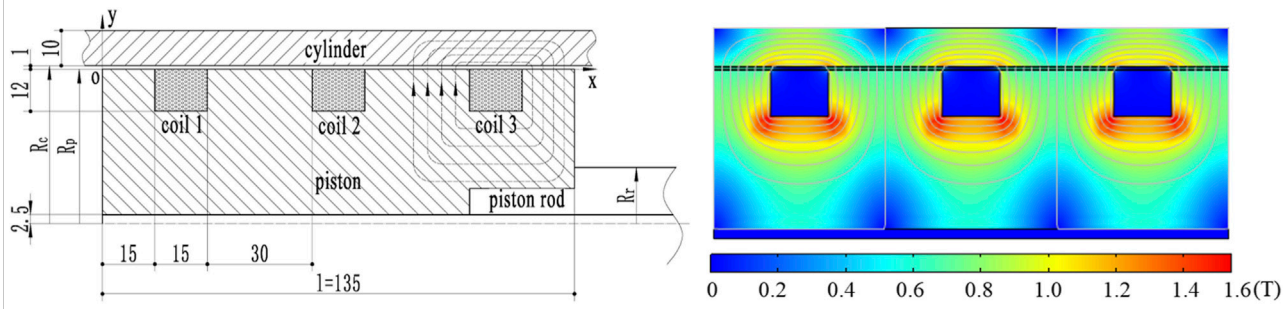

FIGURE 3
Schematic and magnetic distribution of the magnetorheological valve in MREA.

A general design of an MREA is shown in Figure 1. Passing through the neck of the cylinder with seals, a piston rod is connected with the electro-magnetic piston. A volume compensation is set at the other end of the cylinder to adapt the movement the piston rod with a floating piston.

A uniform disc spring (UDS) with a rectangular section is adopted as the restoring mechanism; the parameters are shown in Figure 2. In this work, we designed an MREA with 95 restoring disc springs to satisfy a maximum stroke of 60 mm with 20 mm pre-compression, where the single spring will deform as much as 0.84 mm under the impact if they are uniformly distributed.

An axisymmetric schematic of the magnetorheological valve is shown in Figure 3. It is separated with three coils each 180 turns. Four segments of magnetic yoke with a radius R_p of 44 mm made of pure iron take the role of piston, and the wiring is threaded out of the piston rod in a radius R_r of 16 mm with a center hole of 5 mm in diameter. The cylinder is made of mild steel with a radius R_c of 45 mm, and a flow gap of 1 mm is formed with the piston. When the piston is pulled out of the cylinder under the impact load, the MR fluid is forced flow through the gap under the induced pressure with the relative shear motion between the cylinder and piston, which forms the so-called mixed working mode.

The MR valving principle is somewhat difficult in consideration of MR fluid characteristics, magnetic field distribution, and the transmission from electromagnetic to magnetorheological, but undisputedly, it can be regarded as a valve with the capability of controlling the MR fluid flow between zero field and saturation (Hu et al., 2016). In this research, the piston and the cylinder thickness are sufficiently sized to make a strong enough magnetic induction in the MR gap, and then the maximum shear yielding stress of MR fluid will be applicable. As shown in Figure 3, the average magnetic flux in the gap approaches 0.65 Tesla, which is strong enough for MR fluid to reach its saturation condition. According to the MR effect, MR fluid behaves like a Newtonian fluid in zero field, which can be demonstrated with density ρ and viscosity η_0, and like a Bingham fluid (Li et al., 2021) when stimulated:

$$\begin{cases} \dot{\gamma} = 0, \ |\tau| < \tau_y \\ \tau = sgn\left(\dot{\gamma}\right)\tau_y + \eta\dot{\gamma}, \ |\tau| \geq \tau_y \end{cases} \tag{1}$$

This means that the stimulated MR fluid is capable of bearing static load until the shear yield flow happens, where τ is the dynamic stress, $\dot{\gamma}$ is the shear rate, and τ_y is the shear yielding stress of MR fluid. $\eta \approx \eta_0$ according to the rheological test.

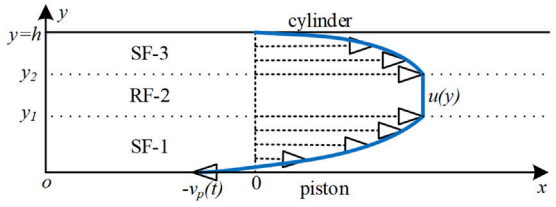

FIGURE 4
The flow profile modeling for MREA.

Physical modeling

The dynamic behaviors of an MREA are complicated because there are many contributing factors. Generally speaking, the total force comprises the damping force resulting from the MR fluid flow and the elastic force of the disc springs; the friction between moving parts and the interaction with volume compensation are always neglected to better understand the rheological mechanism because they are relatively small. Moreover, the averaged magnetic distribution and thus homogeneous MR fluid properties are assumed in the physical modeling.

Quasi-steady modeling of MREA

MR fluid flow in the gap is assumed to be uncompressible and continuous and the gravity effect neglectable; the N-S equations can be expressed as:

$$\rho\frac{\partial u(y,t)}{\partial t}+\frac{\partial p(x,t)}{\partial x}=\frac{\partial \tau(y,t)}{\partial y} \tag{2}$$

Based on the pressure transmission in the gap, the pressure gradient in the gap can be treated as constant, and then:

$$\rho\frac{\partial u(y,t)}{\partial t}-\frac{\partial \tau(y,t)}{\partial y}=\frac{\Delta p(t)}{l} \tag{3}$$

Where u is the unidirectional flow velocity distribution along the y-axis and $l = 135\ mm$ is the total length of the piston. When the flow is granted as a quasi-steady model, the momentum term will be zero, and then:

$$\frac{d\tau(y)}{dy}+\frac{\Delta p}{l}=0 \tag{4}$$

So,

$$\tau(\mathrm{y})=-\frac{\Delta p}{l}y+c \tag{5}$$

When the MR fluid is excited, as shown in Figure 4, the flow in the gap can be divided into three layers: the layers of shear yield flow close to the piston and cylinder, called SF-1 and SF-3, and the rigid flow layer RF-2 sandwiched between the shear yield layers. The origin of the coordinate is fixed at the point where the gap flow starts, neighboring the piston surface, but it does not move with the piston. The cylinder is kept static, but the piston is pulled out at the speed of $-v_p(t)$, $\mathrm{u}(y_1)=\mathrm{u}(y_2)$ because the RF-2 is in rigid flow and no-slip walls apply. The velocity profile u(y) of MR fluid flow is shown in Figure 4, and can be solved as follows.

$$u(\mathrm{y})=\begin{cases}-\dfrac{\Delta p}{2\eta l}\left(y^2-2y_1y\right)-v_p,\ 0<y<y_1\\ u(y_1)=u(y_2),\ y_1<y<y_2\\ -\dfrac{\Delta p}{2\eta l}\left[y^2-h^2+2y_2(h-y)\right],\ y_2<y<h\end{cases} \tag{6}$$

The MR fluid volume can be calculated as:

$$\mathrm{Q}=2\pi\left(R_p+R_c\right)\int_0^h u(y)dy=\pi v_p\left(R_p^2-R_r^2\right) \tag{7}$$

The force of the MR valve generated is:

$$\mathrm{F}_{quasi}=\pi\left(R_p^2-R_r^2\right)\cdot\Delta p \tag{8}$$

Unsteady extension of quasi-steady model

In the quasi-steady modeling of the MR valve, estimation error would result if all the momentum terms related to time and MR fluid density were omitted, which would deviate the experimental results in the preliminary design of a landing gear or anti-recoil system. The MR fluid flow of the three layers can be reanalyzed by considering the momentum terms as follows.

In the SF-1 layer, $\mathrm{u}(\mathrm{y})=u_1(y)$ and $|\tau|\geq\tau_y, \frac{du}{dy}>0, u(0,t)=-v_p(t), u(y,0)=0$. So,

$$u_1(y,t)=\int_0^t w_1(y,t;\sigma)d\sigma-v_p(t) \tag{9}$$

Where $\upsilon=\frac{\eta}{\rho}$ is the kinetic viscosity of MR fluid, and

$$\begin{cases}w_{1t}(y,t)-\upsilon w_{1yy}(y,t)=0\\ w_1(0,t)=0, w_{1y}(y_1,t)=0\\ w_1(y,\sigma)=v_p(0)+\dot{v}_p(\sigma)+\dfrac{\Delta p(\sigma)}{\rho l}\end{cases} \tag{10}$$

Equation 10 is partial differential equation with homogeneous boundary conditions; the variable separation method can be used to transform it into two ordinary differential equations and obtain the solution, where $w_1(y,t;\sigma)=Y(y)T(t)$, and then

10.3389/fmats.2022.942318

$$\begin{cases} Y', (y) + \lambda Y(y) = 0 \\ T^{'}(t) + \lambda v T(t) = 0 \end{cases} \tag{11}$$

So, the solution will be

$$\begin{cases} Y(y) = A\cos(\sqrt{\lambda}\, y) + B\sin(\sqrt{\lambda}\, y) \\ T(t) = Ce^{-\lambda v t} \end{cases} \tag{12}$$

A, B, and C are constants. The boundary conditions apply, and we can obtain:

$$\mathrm{A} = 0, \lambda_{1n} = \left(\frac{n\pi}{h}\right)^2 (n = 1, 2, 3, \ldots) \tag{12a}$$

The general solution of $w_1(y,t;\sigma)$ is

$$w_1(y,t;\sigma) = \sum_{n=1}^{\infty} C_n \sin\left(\sqrt{\lambda_{1n}}\, y\right) \exp(-\lambda_{1n} v t) \tag{13}$$

Substituting the initial condition of $w_1(y,\sigma) = v_p(0) + \dot{v}_p(\sigma) + \frac{\Delta p(\sigma)}{\rho l}$ into the above equation,

$$w_1(y,t;\sigma) = \sum_{n=1}^{\infty} \left\{ \frac{4\left[v_p(0) + \dot{v}_p(\sigma) + \dfrac{\Delta p(\sigma)}{\rho l}\right]}{(2n-1)\pi} \times \sin\left(\sqrt{\lambda_{1n}}\, y\right) \exp[-\lambda_{1n} v (t-\sigma)] \right\} \tag{14}$$

Then, the velocity profile in the SF-1 layer can be expressed as:

$$u_1(y,t) = \sum_{n=1}^{\infty} \frac{4}{(2n-1)\pi} \sin\left(\sqrt{\lambda_{1n}}\, y\right) \int_0^t \left\{ \left[v_p(0) + \dot{v}_p(\sigma) + \frac{\Delta p(\sigma)}{\rho l} \right] \times \exp[-\lambda_{1n} v (t-\sigma)] \right\} d\sigma - v_p(t) \tag{15}$$

In the SF-3 layer, $\mathrm{u}(\mathrm{y}) = u_3(y)$ and $|\tau| \geq \tau_y$, $\frac{du}{dy} < 0$, $u(h,t) = 0$, and $u(y,0) = 0$. Similarly, we can have the velocity profile as follows:

$$u_3(y,t) = \sum_{n=1}^{\infty} \left\{ \frac{4(-1)^{n-1}}{(2n-1)\pi} \cos\left[\sqrt{\lambda_{3n}}\,(y - y_2)\right] \times \int_0^t \frac{\Delta p(\sigma)}{\rho l} \exp[-\lambda_{3n} v (t-\sigma)] d\sigma \right\} \tag{16}$$

where

$$\lambda_{3n} = \left[\frac{2n-1}{2(h-y_2)}\right]^2 \tag{16a}$$

In the RF-2 layer, $\mathrm{u}(\mathrm{y}) = u_2(y)$, $|\tau| < \tau_y$, $\frac{du}{dy} < 0$, and $u_2(y,t) = u_1(y_1,t) = u_3(y_2,t)$, so,

$$u_2(y,t) = \sum_{n=1}^{\infty} \frac{4(-1)^{n-1}}{(2n-1)\pi} \int_0^t \left\{ \left[v_p(0) + \dot{v}_p(\sigma) + \frac{\Delta p(\sigma)}{\rho l} \right] \times \exp[-\lambda_{1n} v (t-\sigma)] \right\} d\sigma - v_p(t) = \sum_{n=1}^{\infty} \frac{4(-1)^{n-1}}{(2n-1)\pi} \int_0^t \frac{\Delta p(\sigma)}{\rho l} \exp[-\lambda_{3n} v (t-\sigma)] d\sigma \tag{17}$$

We can write the N-S equation again as follows:

$$\frac{\partial u(y,t)}{\partial t} - v \frac{\partial^2 u(y,t)}{\partial y^2} = \frac{\Delta p(t)}{\rho l} \tag{18}$$

We can substitute the velocity profile $u_2(y,t)$ into it to obtain

$$\tau = \left[\rho \frac{\partial u_2(y,t)}{\partial t} - \frac{\Delta p(t)}{l} \right] y + \mathrm{E} \tag{19}$$

Where $u_2(y,t)$ is a function of time and independent with y because the velocity keeps constant in layer RF-2, and the boundary condition of $\tau(y_1) = \tau_y$ and $\tau(y_2) = -\tau_y$ applies, then:

$$\begin{aligned} \tau_y &= \left[\rho \frac{\partial u_2(y,t)}{\partial t} - \frac{\Delta p(t)}{l} \right] \mathrm{y}_1 + \mathrm{E} \\ -\tau_y &= \left[\rho \frac{\partial u_2(y,t)}{\partial t} - \frac{\Delta p(t)}{l} \right] \mathrm{y}_2 + \mathrm{E} \end{aligned} \tag{19a}$$

So,

$$y_2 - y_1 = 2\tau_y \left[\frac{\Delta p(t)}{l} - \rho \frac{\partial u_2(y,t)}{\partial t} \right]^{-1} \tag{20}$$

Lastly, the MR fluid volume should satisfy that.

$$\mathrm{Q} = \pi v_p(t)\left(R_p^2 - R_r^2\right) = b\left(\int_0^{y_1} u_1(y) dy + \int_{y_1}^{y_2} u_2(y) dy \right) + \int_{y_2}^{h} u_3(y) dy \tag{21}$$

where

$$\mathrm{b} = 2\pi\left(R_p + R_c\right) \tag{21a}$$

So,

$$\mathrm{F}_{unsteady} = \pi\left(R_p^2 - R_r^2\right) \cdot \Delta p(t) \tag{22}$$

TABLE 1 Parameters of MR fluid.

Density	2.65 g/cm^3
Viscosity at 20°C	0.8 Pa.s
Maximum shear yielding stress	50 kPa at 0.6 Tesla

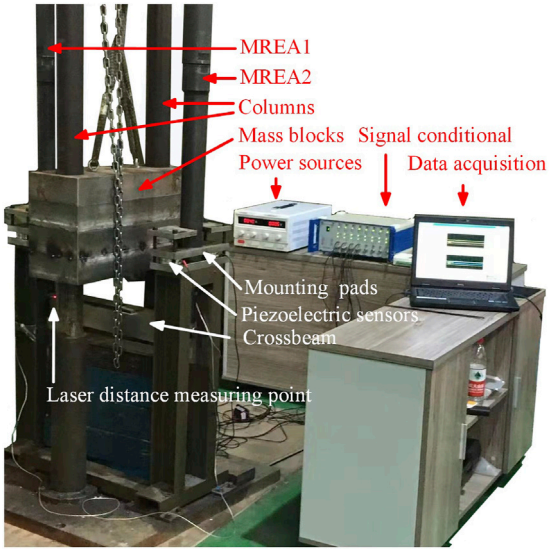

FIGURE 5
Experiments based on the drop test bench.

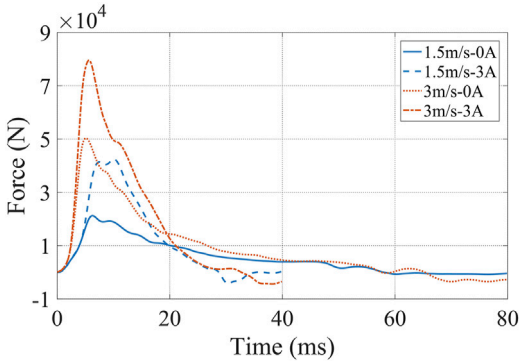

FIGURE 6
The experimental results for MREA at different impact speeds and excitations.

Experimental verification

Drop test of MREA

Two MREAs were manufactured and assembled with the parameters mentioned above. MR fluid was produced by the Chongqing Materials Research Institute; its main parameters are listed in Table 1. Only the maximum shear yielding stress is presented here because the utmost performance of the MREA is concerned.

The disc springs were fabricated by a company in Yangzhou, China, and 50CrVA spring steel was employed to prepare the disk spring samples without heat processing including hardening (Shou et al., 2018). A microcomputer-controlled spring tension and compression tester were utilized to measure the load–deflection relationship of the disk springs and a loading rate of 0.3 mm/s was applied in the testing. Lubricating oil was smeared to reduce the friction between the spring pieces. The deformation parameters were tested but the behavior under the impact was not investigated because of the device limit, so the springs were taken as a linear series combination. The elastic modulus of a single spring was 5.7 kN/mm and about 60 N/mm for the series combination to fulfil a preload of 1.2 kN.

The coils of the MR valve were wrapped manually and the enameled wire with diameter of 0.8 mm was used. The outside layer of the coils was sealed with epoxy resin for isolating and flow smoothing. To ensure the magnetic field between the coils, the three coils were wrapped as clockwise–counter clockwise–clockwise. The finite element analysis was carried out to guarantee that the magnetic flux is strong enough to approach the yielding stress saturation of MR fluid when the current is 3.0 A, which reduces the MREA appraisal into the range determination between saturation and zero field.

A drop test bench illustrated in Figure 5 was prepared for the MREA appraisal. Two MREAs were installed upside-down on the mounting pads at both sides with a connecting crossbeam to accept the impact from a mass block of 120 kg, guided by the column when dropped under gravity. A laser distance measuring instrument was used to record the movement, and two piezoelectric sensors were clamped between the load plates with each MREA. The total force of two MREAs generated in the impact is the sum of the four sensors, and includes the forces from the disc springs and damping force. However, when in zero field, the damping force is purely the viscous damping, but the Coulomb damping force arises when the MREA is powered.

The MREA works under the impact to avoid too long strokes by heightening the damping force under the control, and the initial impact speeds when the mass block hits the connecting crossbeam were set to 1.5 m/s and 3.0 m/s, fulfilled by adjusting the drop heights of the mass block. To compare the controllability of the MREA, the tests were carried out both at zero field and the saturated excitation at two impact velocities of 1.5 m/s and 3.0 m/s to obtain the total forces by summing four parallel force sensors, and the data are shown in Figure 6.

When the MREA is not excited, the total forces at both 1.5 m/s and 3.0 m/s experience a sudden growth and reach their peak at about 5–6 ms where the maximum impact speeds are reached, and then the buffering lasts with a smooth and slow total force decrement. There is a little recoil motion at the end of the buffering process, and the larger the impact speed is, the sooner the peak force reaches and the more apparent the recoil motion will be. When the MREA is excited, the peak force is tremendously heightened,

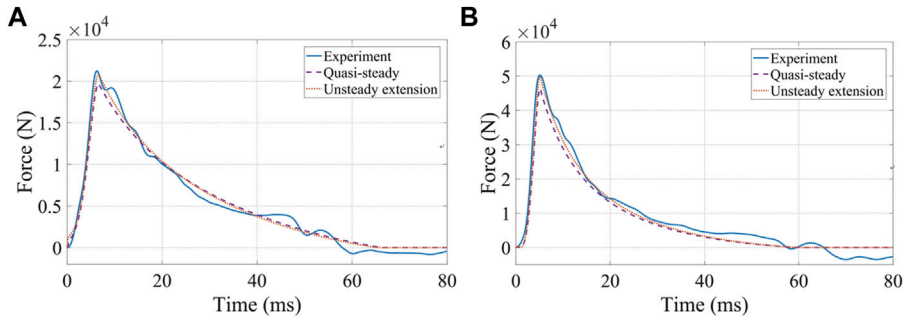

FIGURE 7
The force between the experiments and the models at zero field: **(A)** 1.5 m/s; **(B)** 3.0 m/s.

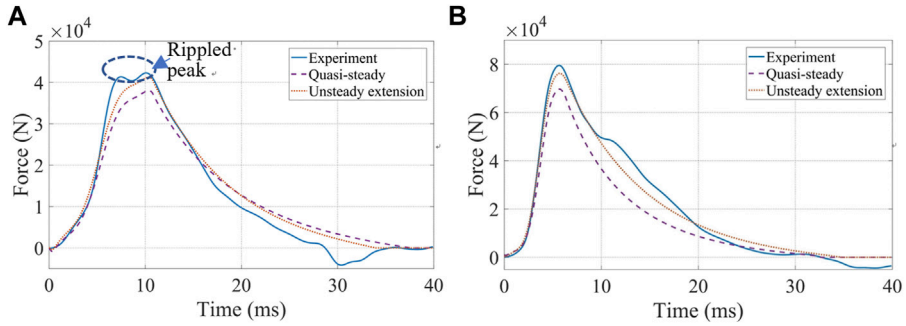

FIGURE 8
The force between the experiments and the models at 3.0 A: **(A)** 1.5 m/s; **(B)** 3.0 m/s.

which results quick energy absorption at the early stage of the buffering. In terms of the peak force of the MREA, there is over twofold growth when the impact speed is 1.5 m/s between the saturated current excitation and zero field, and almost 1.6-fold growth at 3.0 m/s impact speed. The growth ratio decreases with the impact speed because the viscous damping force increases while the Coulomb damping force remains constant.

Modeling comparison

To make a comparison with the experimental results, both the quasi-steady model and its unsteady extension were calculated with MATLAB platform. Figure 7 shows the comparison between the experimental results with the quasi-steady modeling and its unsteady extension at zero field, and the impact speeds are 1.5 m/s and 3.0 m/s, respectively. Because it is in zero field, the yielding stress of MR fluid is zero, and the quasi-steady model is degraded to

$$\mathrm{u}(\mathrm{y}) = \begin{cases} -\dfrac{\Delta p}{2\eta l}\left(y^2 - 2y_1 y\right) - v_p(t), & 0 < y < y_1 \\ y_1 = y_2 & \\ -\dfrac{\Delta p}{2\eta l}\left[y^2 - h^2 + 2y_2(h - y)\right], & y_2 < y < h \end{cases} \tag{23}$$

The velocity profile is an asymmetrical parabola in the narrow flow gap because of the shear motion between the walls. In the same way, Eqn. 17 will disappear because the condition of $|\tau| < \tau_y$ is no longer set since the yielding stress is zero. Thus, the boundary conditions of $y_1 = y_2$ and $u_1(y_1, t) = u_3(y_2, t)$ established for Eqs. 15, 16 give rise to a small difference between the quasi-steady model and its unsteady extension. As a conclusion, the analytical predictions of both models approximate the experimental results well, although the unsteady modeling behaves slightly better because there is a momentum effect as long as the flow is established.

The same comparison is carried out when the MREA is excited at the saturated condition of the 3.0 A current both in 1.5 m/s and

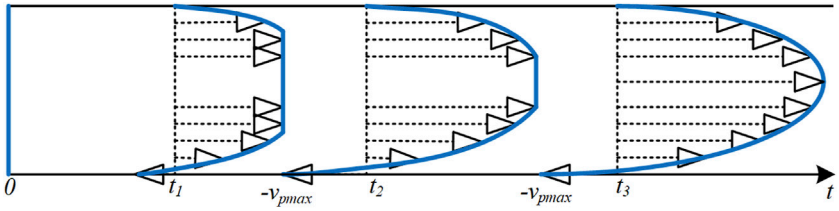

FIGURE 9
Dynamic development of the flow layer modeling for MREA.

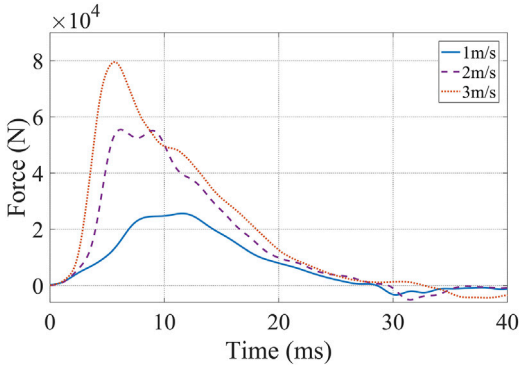

FIGURE 10
Experimental results of excited MREA at 3.0 A and more impact speeds.

3.0 m/s, and the results are shown in Figure 8. It is obvious that with impact progress, both the models successfully predict the buffering to zero in shorter time because of more energy absorption compared to zero field. Both models reflect the total force tendency as the experimental results have relatively large errors. The quasi-steady model experiences similar start processes with the experimental tests at the start period of the impact, and then diverges when total forces accumulate because the neglected inertial effect becomes notable. The unsteady extension behaves better to trace the experimental results than the original after taking the inertial effect into consideration, and generally gives out acceptable prediction.

However, it is interesting that a rippled peak, which is shown in Figure 8A, appears for the experimental total force of a fully excited MREA at 1.5 m/s impact speed, whereas a single peak remains at 3.0 m/s impact speed, and this can be explained by the dynamic development of the flow layer modeling. When the MREA buffering starts from the very beginning, the RF-2 layer will be gradually narrowed to allow more MR fluid to go through the magnetic controlled gap. The dynamic development of the flow layer modeling is shown in Figure 9 at the early stage of buffering under the current excitation, where $t = 0$, t_1, t_2, and t_3 are some typical moments. $t = 0$ is regarded as the start of the impact when the flow does not happen, and $t = t_1$ is in the development progress of the rigid flow forms. When the impact speed is 1.5 m/s, $t = t_2$ is regarded as the end of flow layer development when the piston reaches its maximum impact speed, where the rigid flow layer remains constant. With the piston speed decreasing and thus the peak flow velocity, the rigid flow layer RF-2 broadens again, and the total force increases again to produce the rippled peak. However, when the impact speed is as high as 3.0 m/s, the rigid flow layer cannot be maintained because the yielding stress of the MR fluid under the magnetic field cannot endure too high shear motion even when the magnetic field is saturated; $t = t_3$ is regarded as the end of flow layer development when the piston reaches its maximum impact speed and the rigid flow layer RF-2 disappears, so the MR fluid behaves more like Newtonian fluid with higher viscosity than in its original state.

To better testify the explanation of the flow layer development, more experimental tests were carried out for the MREA at the saturated current of 3.0 A at different impact speeds. As shown in Figure 10, it is obvious that the rippled peak of the total force appears at the lower impact speed, and with the increase in the impact speed, the rippled peak gradually evolves to a single peak.

Conclusion

Based on the Bingham constitutive model of magnetorheological fluid, we carried out quasi-steady flow modeling to designate the magnetorheological valving for an energy absorber; however, our behavior prediction somewhat deviated from the behavior of the actual device. To better estimate the performance of the magnetorheological energy absorber under impact load by taking the momentum terms into consideration in the flow modeling, the unsteady extension of the quasi-steady model was developed. A magnetorheological energy absorber was actually fabricated with disc springs as the recoiling mechanism and tested on a self-established drop test bench, which produced the impact load by a mass block dropped under gravity, and the impact speed was regulated by the drop height. According to the total force comparison, the unsteady extension of the quasi-steady model estimates the characteristics of the device better than the original. Moreover, the controllability of the magnetorheological energy absorber is fully verified at the conditions of zero field and saturated excitation, and the greater the impact speed is, the lower the controllable ratio will be for the magnetorheological energy

absorber because of the larger increase in the uncontrollable Coulomb damping force. Finally, the phenomenon of a rippled peak of the total force is highlighted, and it is explained with the flow modeling that the rigid flow layer is dynamically changing to regulate the peak force of the magnetorheological valving under the saturated excitation, and the rippled peak will disappear if the impact speed is high enough to make the rigid flow layer disappear before the maximum piston speed arrives.

Data availability statement

The original contributions presented in the study are included in the article/Supplementary Material, further inquiries can be directed to the corresponding author.

Author Contributions

HZ, CL, and NW contributed to conception of the study. NW organized the discussion and drafting. HZ and CL designed the experimental apparatus and took charge of the fabrication. ZZ carried out the modeling, experimental verification and wrote the first draft of the manuscript. HZ provided the project support for the study, revised the manuscript and made the corrections. All authors contributed to manuscript revision, read, and approved the submitted version.

Funding

This research was supported by the National Natural Science Foundation of China (no. 62073050).

Conflict of interest

The authors declare that the research was conducted in the absence of any commercial or financial relationships that could be construed as a potential conflict of interest.

The reviewer XD declared a shared affiliation with the authors to the handling editor at the time of review.

Publisher's note

References

Bai, X.-X., Wereley, N. M., Choi, Y.-T., and Wang, D.-H. (2012). "A bi-annular-gap magnetorheological energy absorber for shock and vibration mitigation," in Proc. SPIE 8341, Active and Passive Smart Structures and Integrated Systems 2012. 834123. doi:10.1117/12.917479

Bucchi, F., Forte, P., Frendo, F., Musolino, A., and Rizzo, R. (2014). A fail-safe magnetorheological clutch excited by permanent magnets for the disengagement of automotive auxiliaries. *J. Intelligent Material Syst. Struct.* 25, 2102–2114. doi:10.1177/1045389x13517313

Du, X., Liao, C., Gan, B., Zhang, Y., Xie, L., and Zhang, H. (2021). Analytical modeling and experimental verification for linearly gradient thickness disk springs. *Thin-Walled Struct.* 167. doi:10.1016/j.tws.2021.108153

Hu, G., Liao, M., and Li, W. (2016). Analysis of a compact annular-radial-orifice flow magnetorheological valve and evaluation of its performance. *J. Intelligent Material Syst. Struct.* 28, 1322–1333. doi:10.1177/1045389x16672561

Hu, H., Jiang, X., Wang, J., and Li, Y. (2012). Design, modeling, and controlling of a large-scale magnetorheological shock absorber under high impact load. *J. Intelligent Material Syst. Struct.* 23, 635–645. doi:10.1177/1045389x12436727

Li, G., and Yang, Z.-B. (2020). Modelling and analysis of a magnetorheological damper with nonmagnetized passages in piston and minor losses. *Shock Vib.* 2020, 1–12. doi:10.1155/2020/2052140

Li, H., Jönkkäri, I., Sarlin, E., and Chen, F. (2021). Experimental comparison of constitutive models for magnetorheological fluids under different conditions. *Braz J. Phys.* 51, 1735–1746. doi:10.1007/s13538-021-00989-2

Li, Z. C., and Wang, J. (2012). A gun recoil system employing a magnetorheological fluid damper. *Smart Mater. Struct.* 21. doi:10.1088/0964-1726/21/10/105003

Mao, M., Hu, W., Choi, Y.-T., Wereley, N. M., Browne, A. L., Ulicny, J., et al. (2013). Nonlinear modeling of magnetorheological energy absorbers under impact conditions. *Smart Mater. Struct.*, 22. doi:10.1088/0964-1726/22/11/115015

Ouyang, Q., Hu, H., Zhao, W., Wang, J., and Li, Z. (2020). Feasibility analysis of magnetorheological absorber in recoil systems: Fixed and field artillery. *Front. Mater.*, 7. doi:10.3389/fmats.2020.00254

Park, J.-Y., Kim, G.-W., Oh, J.-S., and Kim, Y.-C. (2021). Hybrid multi-plate magnetorheological clutch featuring two operating modes: Fluid coupling and mechanical friction. *J. Intelligent Material Syst. Struct.* 32, 1537–1549. doi:10.1177/1045389x20988086

Powers, B. E., Wereley, N. M., and Choi, Y.-T. (2016). Analysis of impact loads in a magnetorheological energy absorber using a Bingham plastic model with refined minor loss factors accounting for turbulent transition. *Meccanica* 51, 3043–3054. doi:10.1007/s11012-016-0552-6

Poznic, A., Miloradovic, D., and Juhas, A. (2017). A new magnetorheological brake`s combined materials design approach. *J. Mech. Sci. Technol.* 31, 1119–1125. doi:10.1007/s12206-017-0210-5

Rizzo, R., Musolino, A., Bucchi, F., Forte, P., and Frendo, F. (2015). A multi-gap magnetorheological clutch with permanent magnet. *Smart Mater. Struct.*, 24. doi:10.1088/0964-1726/24/7/075012

R, J. (1948). The magnetic fluid clutch. *Electr. Eng.* 12, 1167. doi:10.1109/T-AIEE.1948.5059821

Sheng, C., Zhu, H., and Li, L. (2022). Hybrid vibration control using magnetorheological dampers and elastomers for civil structural. *AIP Adv.* 12. doi:10.1063/5.0076450

Shou, M., Liao, C., Zhang, H., Li, Z., and Xie, L. (2018). Modeling and testing of magnetorheological energy absorbers considering inertia effect with non-averaged acceleration under impact conditions. *Smart Mat. Struct.* 27, 115028. doi:10.1088/1361-665x/aae6a0

Wang, H., and Bi, C. (2020). Study of a magnetorheological brake under compression-shear mode. *Smart Mater. Struct.*, 29. doi:10.1088/1361-665x/ab5162

Wang, M., Chen, Z., and Wereley, N. M. (2020). Adaptive magnetorheological energy absorber control method for drop-induced shock mitigation. *J. Intelligent Material Syst. Struct.* 32, 449–461. doi:10.1177/1045389x20957100

Wang, W., Hua, X., Wang, X., Wu, J., Sun, H., and Song, G. (2018). *Mechanical behavior of magnetorheological dampers after long-term operation in a cable vibration control system.* Urbana: Structural Control and Health Monitoring, 26. doi:10.1002/stc.2280

Wereley, N. M., and Pang, L. (1998). Nondimensional analysis of semi-active electrorheological and magnetorheological dampers using approximate parallel plate models. *Smart Mat. Struct.* 7, 732–743. doi:10.1088/0964-1726/7/5/015

frontiers | Frontiers in Materials

ORIGINAL RESEARCH
published: 22 July 2022
doi: 10.3389/fmats.2022.933119

Performances of Planetary Magnetorheological Transmission Devices

*Xuli Zhu[1], Shanshan Ma[1], Dong Dong[1], Kefeng Zong[1], Liang Li[1] and Guirong Teng[2]**

[1]School of Mechanical and Electronic Engineering, Shandong University of Science and Technology, Qingdao, China, [2]School of Energy and Mining Engineering, Shandong University of Science and Technology, Qingdao, China

Magnetorheological transmission devices (MRTDs) are a type of power transmission device using magnetorheological fluids (MRFs) as the transmission medium, which have the advantages of rapid response and continuously adjustable output performances. A new type of structure of planetary MRTDs is proposed to improve the performances of MRTDs in this study. A planetary MRTD was fabricated, and the performances of it were tested on the self-made testing system. The experimental results show that the continuously variable transmission of MRTDs under constant torque can be realized by adjusting the excitation current. The output speed or torque can be adjusted by adjusting the control current when the input speed is constant. The output torque increases with the increase in the input speed when the excitation current is constant. The performances of the MRTD were analyzed according to the properties of MRFs in complex flow and magnetic field. MRFs in complex flow and magnetic fields can produce more stable and higher responses to external magnetic fields than being simple sheared; thus, the planetary MRTDs have better performances and are useful structures for the application of MRFs in transmission.

Keywords: magnetorheological fluid, magnetorheological transmission device, planetary structure, speed control, torque control

OPEN ACCESS

Edited by:
Miao Yu,
Chongqing University, China

Reviewed by:
Xufeng Dong,
Dalian University of Technology, China
Ying-Qing Guo,
Nanjing Forestry University, China

****Correspondence:***
Guirong Teng
tgrzxl@sina.com

Specialty section:
This article was submitted to Smart Materials, a section of the journal Frontiers in Materials

Received: *30 April 2022*
Accepted: *20 June 2022*
Published: *22 July 2022*

Citation:
Zhu X, Ma S, Dong D, Zong K, Li L and Teng G (2022) Performances of Planetary Magnetorheological Transmission Devices. Front. Mater. 9:933119. doi: 10.3389/fmats.2022.933119

INTRODUCTION

The development of intelligent mechanical equipment has gradually increased the requirements for the transmission performance of transmission devices, especially in the controllability of torque and speed. The controllability of the apparent viscosity of smart fluids provides the possibility to realize performance-controllable mechanical transmission by controlling the external fields. As a kind of smart material, magnetorheological fluids (MRFs) are suspensions of micron-size magnetizable particles in a viscous matrix fluid enriched with additives. Under the action of an applied magnetic field, an MRF transforms from a viscous fluid to a solid-like state, and its physical properties (e.g., mechanical, electromagnetic, and thermal properties) change simultaneously, which is called the magnetorheological effect. The magnetorheological effect has the advantages of being continuously controllable, fast, and reversible (Ashtiani, et al., 2015; Kumar, et al., 2019) and makes MRFs show a strong potential for applications in the field of transmission control.

Magnetorheological transmission devices (MRTDs) are a new type of transmission device that use MRFs as the power transmission medium and utilizes the magnetorheological effect for transmission control. MRTDs can change the shearing state of MRFs between transmission interfaces by adjusting the external magnetic field and then control the output parameters. MRTDs are convenient for

controlling their real-time torque and speed during operation and have the advantages of fast response, high shock resistance, and stepless speed adjustment (Tian, et al., 2015; Wang, et al., 2018).

Güth and Maas, 2016 proposed an MRF brake based on the Taylor vortex for application in wind turbines, whose torque performance was better than that of other conventional brakes using dry friction. Wang et al. (2019) designed a high-torque squeezing magnetorheological brake and studied the squeeze strengthening effect of a silicone oil-based magnetorheological fluid with the addition of nanometer-sized Fe_3O_4. It was found that the braking torque showed a nearly linear increase with the increase in the squeezing stress. Sarkar and Hirani, 2013 proposed a method to apply pressure to the MRF to increase the output torque of the magnetorheological brake. A single-disc magnetorheological brake was developed, and it was found that the braking torque of the brake was higher when pressure was applied to the magnetorheological fluid than that of a brake operating only under shear. Bucchi et al. (2014) developed an auxiliary device based on MRFs for engaging and disengaging a combustion engine combined with a magneto-thermographic method. The magnetorheological clutch was allowed to operate as the main clutch. Song et al. (2021) designed a small magnetorheological brake based on a hybrid mode of shear and flow, which can provide higher torque using a relatively small amount of the magnetorheological fluid. Tian et al. (2022) studied the time response characteristics of MRTDs and found that changing the parameters of the excitation coil and the number of taps can effectively shorten the current response time. Qiu et al. (2022) used the electromagnetic force generated after the excitation coil being electrified to squeeze the magnetorheological fluid along the direction of the magnetic field and improve the shear yield stress of the magnetorheological fluid, thus greatly improving the transmission performance of the magnetorheological fluid. Moghani and Kermani, 2020 designed a lightweight magnetorheological brake using the hybrid magnetization of an electromagnetic coil and a permanent magnet, which can reduce the magnetic saturation in the magnetic circuit and reduce the volume of materials used in the magnetic circuit. The output torque performance of the composite magnetorheological clutch which was proposed by Dai et al. (2013) was enhanced over the simple disc-shearing clutches. Li et al. (2014) optimized the MRF working area inside the actuator to increase the working interface and improve the performance of the actuator. Wang (2014) analyzed the transmission characteristics under high transmission power and the temperature characteristics of MRF in the working process. It was concluded that using a water cooling system to cool the MRTD was effective and can improve the working reliability of the device. Chen (2014) developed a transmission device–combined MRF and shape memory alloy, which could compensate for the lack of MRF performance at high temperature through the driving effect of the shape memory alloy.

The development trends of MRTDs are high torque, high power, compact design, reliable operation, convenient control, wide adjustable range, etc. Now, MRTDs are gradually moving closer to practicality. Summarizing the mechanisms of MRTDs, it can be seen that the working modes of MRFs are basically simple shearing with a uniform magnetic field. These designs cannot overcome the problem of MRF shear thinning at high shear rates. The MRFs are prone to solid–liquid separation under strong centrifugal forces because transmission devices are all rotating at high speeds. For these reasons, a new structure of planetary MRTD is proposed in this study which can effectively overcome the problems of shear thinning and solid–liquid separation of MRFs. This new structure is expected to achieve controllable and stable high-power transmission.

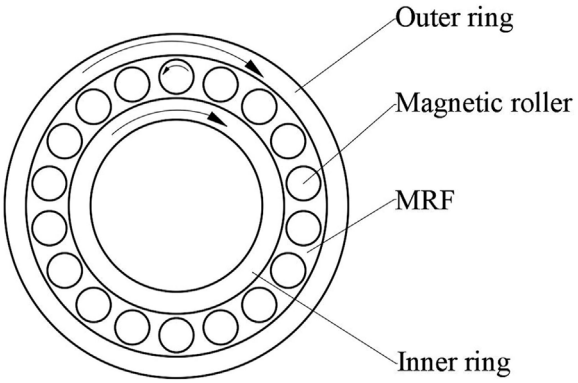

FIGURE 1 | Structural diagram of a planetary MRTD.

TRANSMISSION MECHANISM

Basic Mechanism

The basic conceptual mechanism of planetary MRTDs is shown in **Figure 1**. The inner and outer rings are used as the input and output components, respectively; several magnetic rollers are placed at the middle of the gap between the inner and outer rings, and there are clearances between the rollers and the rings, and the MRF fills the gap between rings. This transmission device is a two-degree-of-freedom planetary mechanism with the magnetic rollers taking planetary motion during transmission. The state of the MRF is controlled by the applied magnetic field to realize the adjustable power transmission between the inner and outer rings.

The mechanism analysis of the planetary MRTD is shown in **Figure 2**. The working status parameters of the planetary MRTD are that the inner and outer rings rotate with angle speeds of ω_1 and ω_2, respectively, as the magnetic rollers rotate with an angle speed of ω_0. The relative velocity of the surface a magnetic roller to surfaces of rings is shown by the blue arrows in the figure. Then, the working region of the MRF can be divided into four parts, where the MRF is squeezed in regions I and III and is stretched in regions II and IV. A slight shearing rate can be obtained on the surfaces of the rings and rollers by the transformation of the strain rate tensor, which can produce shear stress. The surfaces of regions I and II generate driving torque to the roller, and regions III and IV generate resistance torque. The torque acting on the roller should be balanced according to mechanical analysis. Based on the same principle,

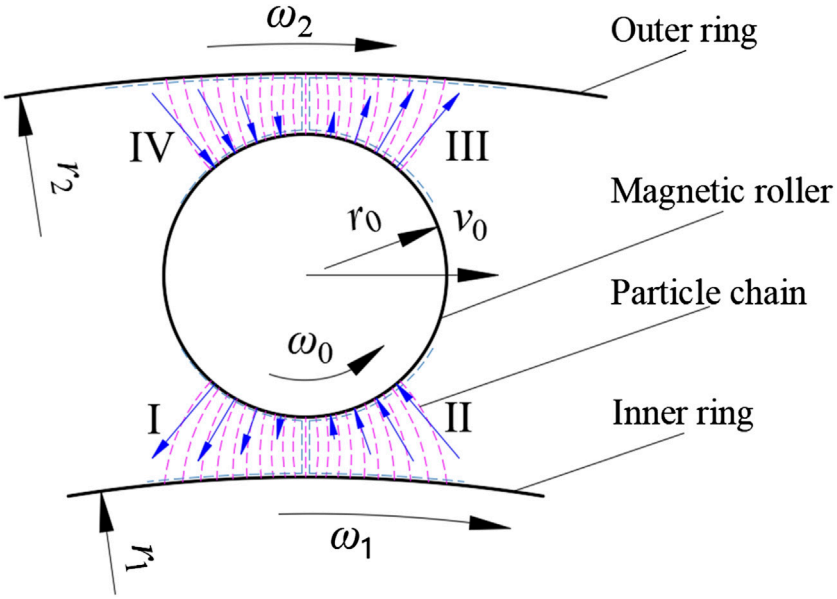

FIGURE 2 | Mechanism analysis of the planetary MRTD.

the shear stress on the inner ring surface can produce the resistance torque to the inner ring, and the shear stress on the outer ring surface can produce the driving torque to the outer ring. The shear stress of MRF is very large under the action of the magnetic field so that the transmission torque of the planetary MRTD is large. It can be seen from the aforementioned analysis that the planetary MRTD can realize large controllable torque transmission.

Considering the actual situation of a planetary MRTD, the roller takes planetary motion, and the aforementioned rotation should be superimposed with the clockwise movement of the roller as a whole. When there is a rotation speed difference between the inner and outer rings, the working state of the MRF is squeeze shear combination or stretch shear combination. The power is transmitted from the inner ring to the outer ring due to the transmission of MRF. The higher the apparent viscosity of the MRF, the greater the power is transmitted.

The planetary MRTD makes the power transfer regions characterized by high magnetic field strength and low strain rate, which can improve the adverse effect of MRF shear thinning at high shear rates. Therefore, the rotation of the magnetic roller can realize the MRF rheological effect of extrusion enhancement to enhance its transmission ability. Moreover, due to the cyclic stirring effect of the planetary motion of multiple magnetic rollers, solid–liquid separation problems of MRF will not occur. So the planetary MRTDs can be expected to effectively overcome the problems caused by MRF shear thinning and high centrifugal force and can achieve a reliable and stable controlled transmission.

Simulation Analysis

The MRF flow inside a planetary MRTD is complex flow under a complex magnetic field. The flow field and magnetic field are all coupled problems due to the mutual influence of the magnetic field and fluid flow. These complexities lead to great difficulty in analyzing the performances of a planetary MRTD. In order to simplify the simulation, the default MRF has a constant magnetic permeability during the flow, so the magnetic field simulation and the flow field simulation can be performed independently. The finite element analysis package COMSOL Multiphysics was used to simulate the fluid flow and the magnetic field. The geometric model was simplified according to the symmetry of the planetary MRTD. The sub region surrounded by two adjacent rollers and the rings is selected for flow field simulation, which can be called the representative unit of the planetary MRTD. Speed of the rings and the rollers were used as boundary conditions. **Figure 3A** shows the simulation result of the flow field with certain parameters of the viscosity of the MRF. The two half-rollers and the region of the flow field were used together as the sub region for magnetic field simulation. Different magnetic scalar potentials were applied on the inner and outer rings as boundary conditions. **Figure 3B** shows the simulation result of the magnetic field with certain parameters of permeability of the MRF and the rollers.

According to the simulation results of the flow field and magnetic field, it can be seen that the flow field and magnetic field of the MRF are all complex non-uniform fields induced by the interference of magnetic rollers. In the regions of magnetic rollers near the inner and outer rings, the magnetic field intensity is large, and the relative velocity is small. The velocity vector conforms to the analysis results in **Figure 2**. The magnetic field intensity near the apex of the magnetic roller near the inner ring is the largest. The regions of magnetic rollers near the inner and outer rings are the main power transmission areas. The characteristics of the flow field and magnetic field in these regions are conducive to avoiding the influence of shear

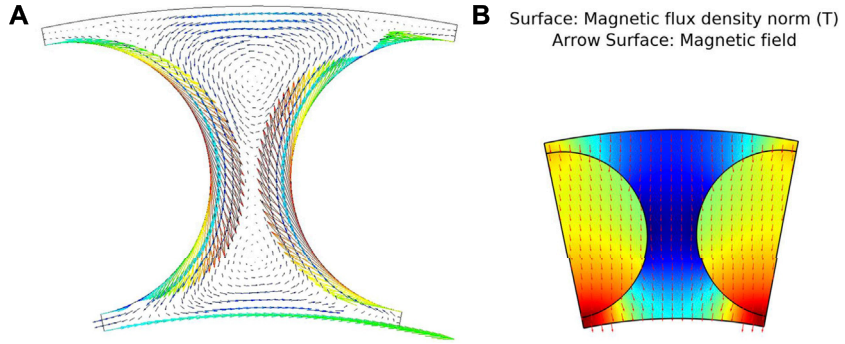

FIGURE 3 | Simulation of a representative unit of a planetary MRTD. **(A)** Flow field simulation diagram and **(B)** magnetic field simulation diagram.

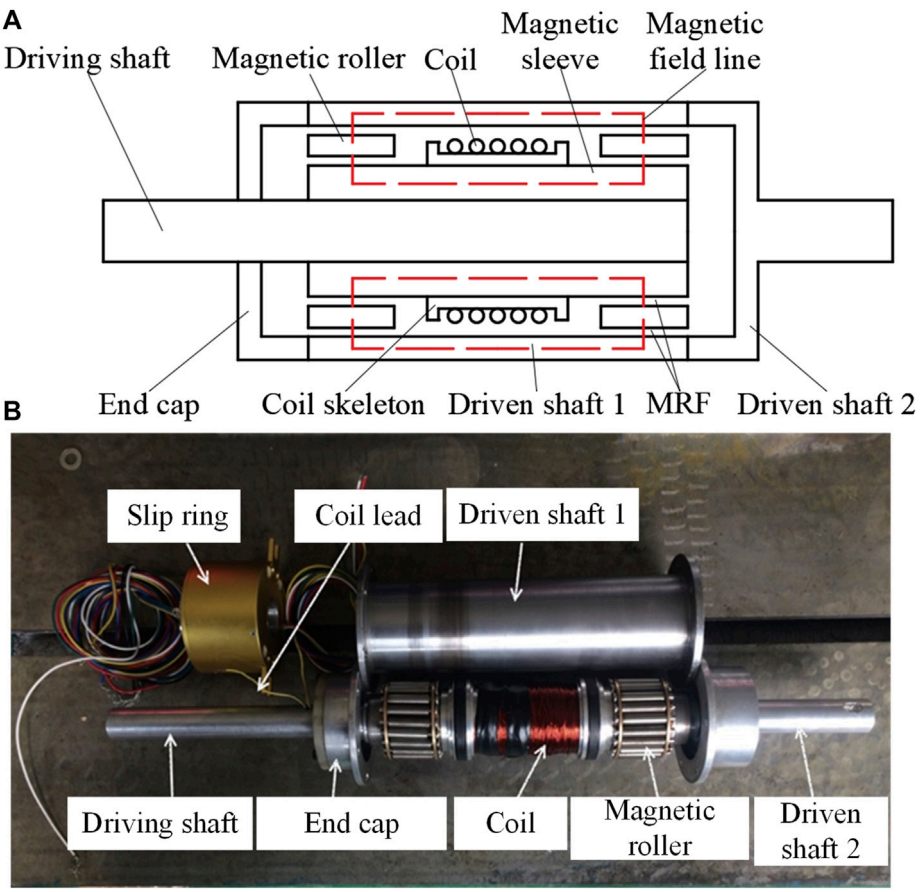

FIGURE 4 | Structure of a planetary MRTD. **(A)** Principle diagram of the planetary MRTD and **(B)** image of the planetary MRTD.

thinning of MRF and enhancing the transmission torque. In the area where the rollers are close to each other, the magnetic field intensity is small but the relative velocity is large, and there are local vortices. The characteristics of the flow field and magnetic field in the region where the rollers are close to each other are helpful to prevent solid–liquid separation and enhance the uniformity and stability of the MRF.

EXPERIMENTS

Experimental Prototype

The structure of the planetary MRTD is shown in **Figure 4**. The device mainly consists of the magnetic roller, end cap, driving shaft, driven shaft, excitation coils, magnetic sleeve, and slip ring. The driven shaft consists of driven shaft 1 and driven shaft 2. The

TABLE 1 | Main parameters of the planetary MRTD.

Design parameter	Value
Outer diameter of the inner ring	45 mm
Inner diameter of the outer ring	62 mm
Length of the magnetic roller	60 mm
Diameter of the magnetic roller	7.5 mm
Number of coil turns	1,114

excitation coil is assembled on the driving shaft equipped with a magnetic sleeve and connected to the power by a slip ring. The principle diagram of the planetary MRTD is shown in **Figure 4A**. The magnetic field lines form closed loops along the path driven shaft 1-MRF-magnetic roller-magnetic sleeve-magnetic roller-MRF-driven shaft 1. The components of the magnetic circuit are made of permeability magnetic materials, and the other components are made of non-magnetic materials. Magnetic circuit components include the magnetic sleeve, the magnetic roller, and driven shaft 1. Non-magnetic circuit components include driven shaft 2, the end cap, driving shaft, and coil skeleton. An MRF with a particle volume fraction of 25% was prepared and used to fill the gap between the inner and outer rings. The spherical carbonyl iron powder (MRF-R35, Jiangsu Tianyi Ultrafine Metal Powder Co., Ltd.) with an average diameter of 3.14 μm was used as magnetizable particles, and the dimethyl silicone oil with the viscosity of 20 centistoke was used as the matrix liquid. The main parameters of the planetary MRTD are shown in **Table 1**.

The planetary MRTD designed in this study can form a working magnetic field along the radial direction of the transmission device after the excitation coil is connected to the power. The magnetic field lines pass through the MRF and the magnetic rollers. The MRF is magnetized under the action of the magnetic field and forms particle structures to resist relative movement and

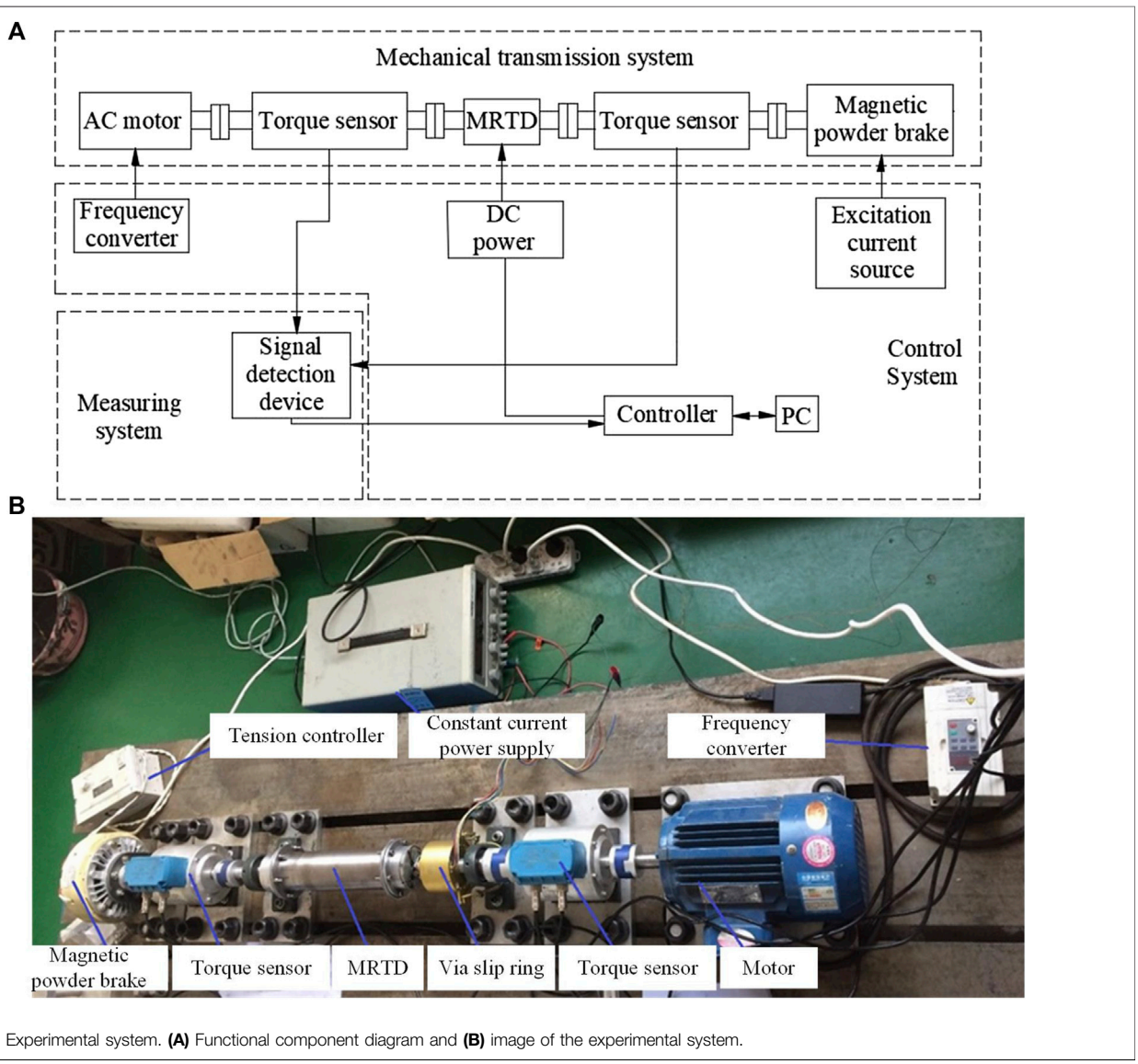

FIGURE 5 | Experimental system. **(A)** Functional component diagram and **(B)** image of the experimental system.

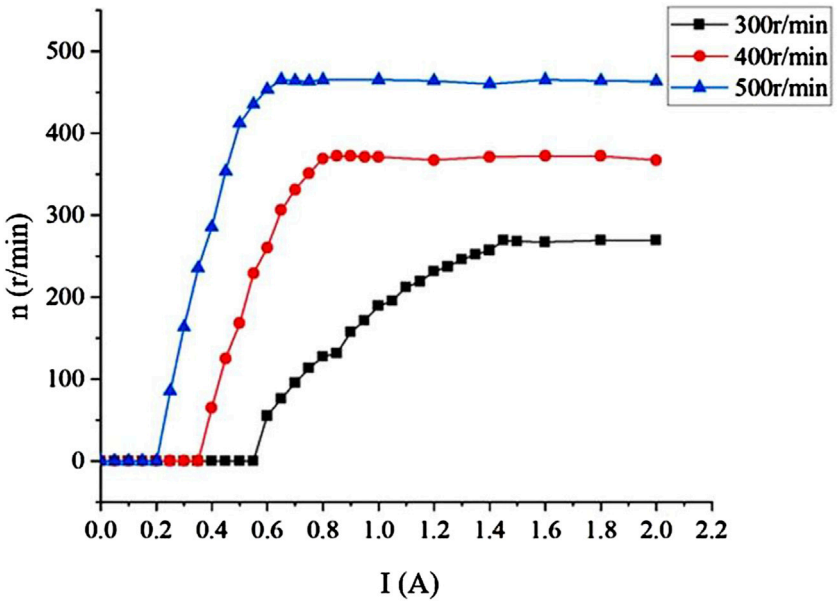

FIGURE 6 | Dependence of output speed on the excitation current.

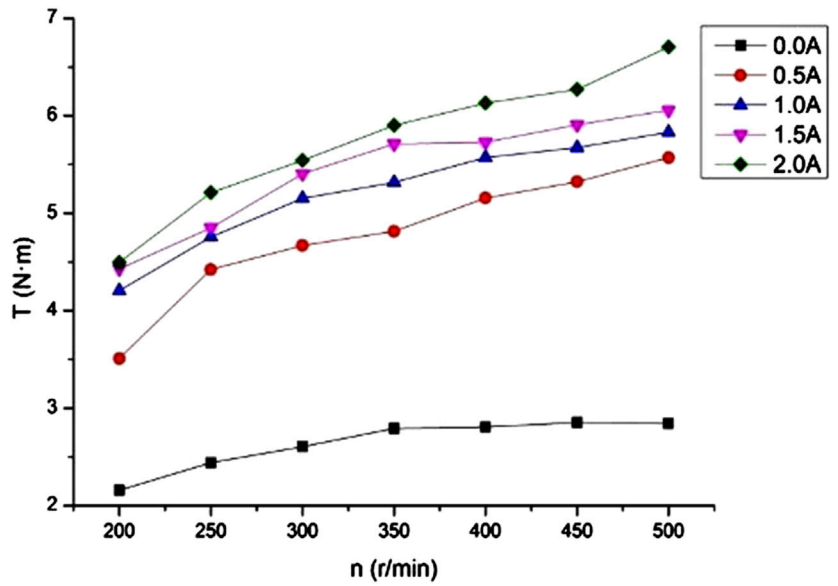

FIGURE 7 | Dependence of torque on the input speed.

deformation. The output speed and torque of planetary MRTDs can be controlled by adjusting the excitation current of the coil. The complex magnetic field and flow field formed by the magnetic roller improve the ability of the MRF to transmit torque.

Experimental Platform

The experimental platform is mainly composed of the mechanical transmission system, measuring system, and control system, as shown in **Figure 5**. The transmission system includes an AC motor, two torque sensors, and a magnetic powder brake. The control system includes a frequency converter to control the speed of the motor; a controllable 24 V conversion DC power was used as the excitation source for the coil, and the experimental data were input to the computer through an acquisition card. The measuring system connects the sensors and the controller to measure values of speed and torque and input the measuring data

to the computer. It was measured that the maximum of the excitation current for the coil of the planetary MRTD prototype was 2.7A.

Experiments

The planetary MRTD was tested at room temperature in our laboratory, and the temperature was 20–25°C. In order to reduce the influence of the device heating on the results during the experiments, the device was cooled naturally for half an hour after each experiment. In order to test the speed control performance of the planetary MRTD at constant output torque, the braking torque of the magnetic powder brake was set to 4 N · m and kept constant during the experiments. The input speeds of the planetary MRTD were set to 300, 400, and 500 r/min, respectively, by controlling the output speed of the motor of the testing system. The excitation current of the electromagnetic coil was adjusted from 0 to 2.3A with a step of 0.05A. The frequency of the data acquisition card was set to 10 Hz. The data were input into the computer and were converted to speed values.

To test the torque control performance of the planetary MRTD, the output shaft of the MRTD was fixed. The input speed of the planetary MRTD was adjusted from 200 r/min to 500 r/min with a step of 50 r/min. The excitation current of the electromagnetic coil was adjusted from 0 to 2A with a step of 0.5A. The frequency of the data acquisition card was set to 10 Hz. The data were input into the computer and were converted to torque values.

RESULTS AND DISCUSSION

Speed Control Performance

The results of the speed control performance of the planetary MRTD are shown in **Figure 6**. The output speed of the planetary MRTD can be adjusted continuously by adjusting the excitation current when the input speed is constant. When the excitation current is small, the output speed of the device is zero due to the low magnetic field strength inside the MRF transmission region; at that magnetic field strength, the torque generated by the planetary MRTD is smaller than the braking torque applied. When the input speed is 300, 400, and 500 r/min, the initial current required to start the output of planetary MRTD is 0.55, 0.35, and 0.2A, respectively. The output speed is linear with the excitation current in a certain current range. When the input speed is 300r/min, 400r/min, and 500r/min, the linear variation ranges of the output speed are 0.6–1.2A, 0.35–0.7A, and 0.2–0.5A, respectively. The higher the input speed, the lower is the current required for the planetary MRTD to reach the initial torque and the faster the output speed increases. The reason is that the deformation rate in the MRF transmission region is larger when the input speed is higher, and a certain increment of the current can produce a larger change of the output speed. When the excitation current reaches a certain large value, the output speed remains a constant value, and the slip ratio between the inner and outer rings remains basically constant. The particle volume fraction of the MRF and the maximum excitation current are all relatively low in the experiments so that the magnetic saturation of the MRF is not obvious, and the dependence of output speed on excitation current is basically linear.

Torque Control Performance

The torque control performance of the planetary MRTD is shown in **Figure 7**. The output torque of the planetary MRTD is greatly improved when there is a current passed through the coil compared to when no current is present. The output torque increases with the increase in the motor speed when the excitation current is constant. The dependence of the output torque on speed is basically linear, which means that the MRF shear thinning does not occur. When the speed changes from 200r/min to 500r/min, the increment of the output torque of the planetary MRTD increases from 2.5 N · m to 4.2 N · m as the excitation current changes from 0 to 2A. It is similar to the results of the speed control performance experiments.

CONCLUSION

The structure of the planetary MRTD was proposed. A prototype of the planetary MRTD was designed and fabricated. The transmission mechanism of the planetary MRTD was analyzed basically. The performances of speed and torque control of the planetary MRTD were tested using the self-made experimental platform. The results were analyzed, and the main conclusions are as follows:

1) The MRF transmission regions have the characteristics of low shear rate and high magnetic field, which can effectively overcome the MRF shear thinning and solid–liquid separation problems and enhance the MRF performance.
2) The continuously output speed control of the planetary MRTD can be obtained by adjusting the excitation current of the electromagnetic coil. The larger the excitation current, the higher rotation speed can be output.
3) The continuously output torque control of the planetary MRTD can be obtained by adjusting either the excitation current of the electromagnetic coil or the input speed of the device. The larger the excitation current or higher the input speed, the larger torque can be transmitted .

DATA AVAILABILITY STATEMENT

The original contributions presented in the study are included in the article/Supplementary Material; further inquiries can be directed to the corresponding author.

AUTHOR CONTRIBUTIONS

XZ and GT conceptualized the idea. XZ and SM performed the methodology. SM and LL ran the software. SM, DD, KZ, and LL performed the experiment. SM, DD, KZ, and LL wrote the original draft. All authors have read and agreed to the published version of the manuscript.

FUNDING

The research of this study is supported by the National Natural Science Foundation of China, grant number 51575323.

ACKNOWLEDGMENTS

The authors would like to thank the research grant support from the National Natural Science Foundation of China.

REFERENCES

Ashtiani, M., Hashemabadi, S. H., and Ghaffari, A. (2015). A Review on the Magnetorheological Fluid Preparation and Stabilization. *J. Magnetism Magnetic Mater.* 374, 716–730. doi:10.1016/j.jmmm.2014.09.020

Bucchi, F., Elahinia, M., Forte, P., and Frendo, F. (2014). A Passive Magneto-Thermo-Mechanical Coupling Actuated by SMA Springs and MR Fluid. *Int. J. Str. Stab. Dyn.* 14, 1440031. doi:10.1142/S0219455414400318

Chen, S. (2014). *Analysis and Application of Composite Transmission Theory of MR Fluid and Shape Memory Alloy under Thermal Effect*. Chongqing: Chongqing University. [dissertation/master's thesis].

Dai, S., Du, C., and Yu, G. (2013). Design, Testing and Analysis of a Novel Composite Magnetorheological Fluid Clutch. *J. Intelligent Material Syst. Struct.* 24, 1675–1682. doi:10.1177/1045389X13483026

Güth, D., and Maas, J. (2016). Long-term Stable Magnetorheological Fluid Brake for Application in Wind Turbines. *J. Intelligent Material Syst. Struct.* 27, 2125–2142. doi:10.1177/1045389X15624794

Kumar, J. S., Paul, P. S., Raghunathan, G., and Alex, D. G. (2019). A Review of Challenges and Solutions in the Preparation and Use of Magnetorheological Fluids. *Int. J. Mech. Mat. Eng.* 14, 1–18. doi:10.1186/s40712-019-0109-2

Li, G. F., Zhao, P., Liu, C., Gao, W., Shan, C. Y., and Zhang, J. Y. (2014). Development and Experiment of Layered Magneto-Rheological Torque Transmission Devices. *J. Jiangsu Univ. Sci. Ed.* 35, 20–24. doi:10.3969/j.issn.1671-7775.2014.01.004

Moghani, M., and Kermani, M. R. (2020). A Lightweight Magnetorheological Actuator Using Hybrid Magnetization. *IEEE/ASME Trans. Mechatron.* 25, 76–83. doi:10.1109/tmech.2019.2951340

Qiu, R., Xiong, Y., and Huang, J. (2022). Study on Transmission Performance of Multi-Disc Magnetorheological Fluid by Electromagnetic Extrusion. *Mech. Sci. Technol. Aerosp. Eng.*, 1–7. doi:10.13433/j.cnki.1003-8728.20200556

Sarkar, C., and Hirani, H. (2013). Theoretical and Experimental Studies on a Magnetorheological Brake Operating under Compression Plus Shear Mode. *Smart Mat. Struct.* 22, 115032. doi:10.1088/0964-1726/22/11/115032

Song, B.-K., Hong, S.-W., Kim, B.-G., and Choi, S.-B. (2021). A New Design of Small-Sized Magnetorheological Brakes Based on the Mixed Mode Operation for High Torque Efficiency. *Smart Mat. Struct.* 30, 117001. doi:10.1088/1361-665X/AC277E

Tian, Z.-Z., Chen, F., and Wang, D.-M. (2015). Influence of Interface Deformation on Transmittable Torque of Disk-type Magnetorheological Clutch. *J. Intelligent Material Syst. Struct.* 26, 414–424. doi:10.1177/1045389X14529027

Tian, Z. Z., Wu, X. F., Xie, F. W., and Guo, Z. Y. (2022). Time Response Characteristics of Magnetorheological Fluid Transmission Device. *Chin. Hydraul. & Pneumatics* 46, 190–195. doi:10.11832/j.issn.1000-4858.2022.05.023

Wang, D. M. (2014). *Research on High-Power Magnetorheological Transmission Technology and Temperature Effect*. Xuzhou (Jiangsu): China University of Mining and Technology. [dissertation/master's thesis].

Wang, N., Liu, X., and Zhang, X. (2019). Squeeze-Strengthening Effect of Silicone Oil-Based Magnetorheological Fluid with Nanometer Fe_3O_4 Addition in High-Torque Magnetorheological Brakes. *J. Nanosci. Nanotechnol.* 19, 2633–2639. doi:10.1166/jnn.2019.15895

Wang, S., Chen, F., Tian, Z., Dou, J., and Wu, X. (2018). Development of Water-Cooling Transmission Device for Magnetorheological Fluid. *Jmag* 23, 285–292. doi:10.4283/JMAG.2018.23.2.285

Conflict of Interest: The authors declare that the research was conducted in the absence of any commercial or financial relationships that could be construed as a potential conflict of interest.

Publisher's Note: All claims expressed in this article are solely those of the authors and do not necessarily represent those of their affiliated organizations, or those of the publisher, the editors, and the reviewers. Any product that may be evaluated in this article, or claim that may be made by its manufacturer, is not guaranteed or endorsed by the publisher.

frontiers | Frontiers in Materials

ORIGINAL RESEARCH
published: 22 July 2022
doi: 10.3389/fmats.2022.932079

Experimental Analysis on the Dependence of the Capacitance of Magnetorheological Fluids on Frequency

Xuli Zhu[1], *Shanshan Ma*[1], *Haidong Huang*[1], *Zhongling Liu*[1], *Huimin Sun*[2] *and Guirong Teng*[3]*

[1]School of Mechanical and Electronic Engineering, Shandong University of Science and Technology, Qingdao, China, [2]Qingdao Metro Group Co., Ltd, Qingdao, China, [3]School of Energy and Mining Engineering, Shandong University of Science and Technology, Qingdao, China

The capacitance characteristics of magnetorheological fluids (MRFs) were studied experimentally based on simulation analysis. The nonlinear relationship between the capacitance of MRFs and electric field frequency was measured by the self-made circuit device. The effects of magnetic induction intensity and particle volume fraction on the capacitance characteristics of MRFs were investigated. The results show that the nonlinear dependence of the capacitance of an MRF on frequency induced by the effect of tunnel current decreases with the increase in frequency. The capacitance of an MRF is directly related to the particle structures. The capacitance of the MRF with a chain particle structure is greater than that of the MRF with a random particle distribution. The smaller the clearance between the adjacent particles, the greater the capacitance of the MRF. The network particle structure and particle contact will reduce the capacitance of an MRF. The capacitance of an MRF increases with the increment of external magnetic field. The capacitance of an MRF with higher particle volume fraction is smaller than that of an MRF with lower particle volume fraction.

Keywords: magnetorheological fluids, capacitance, frequency, particle structures, magnetic field

OPEN ACCESS

Edited by:
Miao Yu,
Chongqing University, China

Reviewed by:
Qing Ouyang,
Jiaxing University, China
Xufeng Dong,
Dalian University of Technology, China

****Correspondence:***
Guirong Teng
tgrzxl@sina.com

Specialty section:
This article was submitted to Smart Materials, a section of the journal Frontiers in Materials

Received: *29 April 2022*
Accepted: *17 June 2022*
Published: *22 July 2022*

Citation:
Zhu X, Ma S, Huang H, Liu Z, Sun H and Teng G (2022) Experimental Analysis on the Dependence of the Capacitance of Magnetorheological Fluids on Frequency. Front. Mater. 9:932079. doi: 10.3389/fmats.2022.932079

INTRODUCTION

Magnetorheological fluids (MRFs) are a class of controllable smart materials characterized by fast, tunable, and reversible changes in their rheological properties, which are suspensions of micron-size magnetizable particles in a viscous carrier fluid enriched with additives (Rabinow, 1948; Ashour, 1996). Magnetorheological effects occur in magnetorheological fluids under the action of an applied magnetic field, which makes the soft magnetic particles magnetize to form a chain-like structure, called a particle chain (Chen, et al., 2013; He, et al., 2013; Mahesh, et al., 2021). The particles are ferromagnetic with good conductivity, and the particle chains can form conductive channels to make the MRFs conductive. The conductive mechanism of magnetorheological materials is relatively complicated. The proposed models are mostly based on the conductive channel theory and tunneling effect theory (Zhu, et al., 2010b; Wang, 2017). Conductive channel theory is usually used to describe the mechanism of composite polymers with fillers inside. The tunnel effect theory is used to explain the movement of the electrons inside the composite material based on quantum mechanics, that is, to analyze the conductivity of the material from the microscopic perspective.

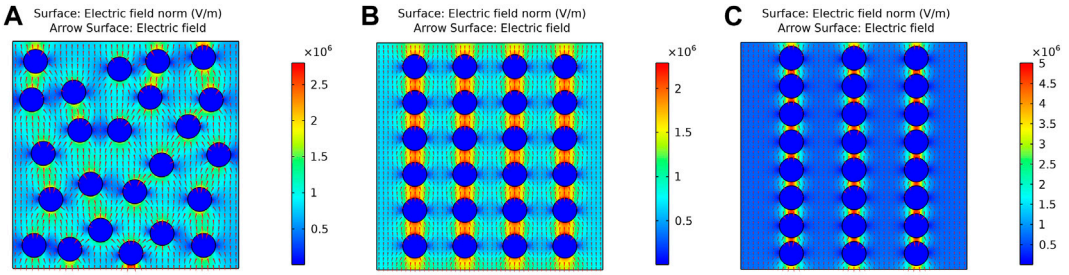

FIGURE 1 | Capacitance simulation results. **(A)** Random distribution; **(B)** Loose chain; **(C)** Tight chain.

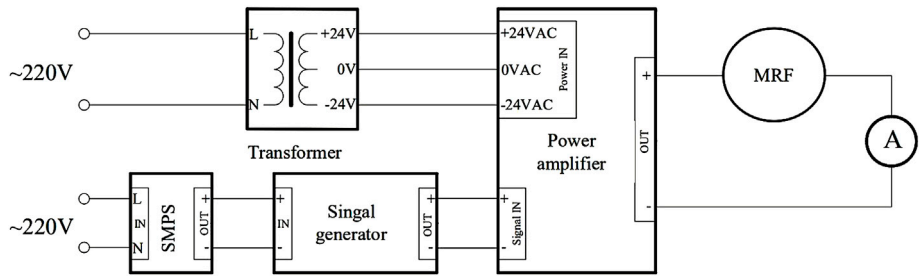

FIGURE 2 | Schematic of the circuit device.

MRFs, similar to conductive polymer composites, can be used widely with high practical value in various sensors, capacitors, and other fields (Wang, 2012; Kaluvan and Choi, 2014). The magneto-conductive properties of MRFs and their solid-state analogs and magnetorheological elastomers are currently receiving increasing attention. Yang et al. (2017) demonstrated that the appropriate amount of ferromagnetic particles is beneficial in improving the electrical conductivity of MRFs. Ruan et al. (2017) analyzed the effect of magnetic field, volume fraction of carbonyl iron powder particles, and applied oscillatory shear force on the conductivity of MRFs and modeled the resistance between particles to explain the resistance changes of MRFs. Wang et al. (2011) deduced the formula between magnetorheological capacitance and dielectric constant and experimentally verified the conclusion that the increase in MRF capacitances induced by the dielectric constant increases when the magnetic field increases. Bica (2009) studied the capacitance of a flat plate capacitor with magnetorheological elastomer as the dielectric as a function of magnetic field strength, and the results showed that the capacitance gradually increases and eventually remains constant when the magnetic field was applied. Huang et al. (2016) prepared MRFs with silver-coated carbonyl iron particles dispersed in silicone oil. The experimental results showed a significant improvement in the electrical properties of MRFs. It can be seen that the current research mainly focuses on the static conductivity properties of MRFs. The dynamic conductivity properties and the interfering factors should be studied further.

The capacitance characteristics of MRFs under an external magnetic field were investigated experimentally in this paper. Firstly, the capacitance of inter-particles was simulated and analyzed according to the dispersing state of particles inside of MRFs. A tunable AC experimental device was designed and assembled, which was used to measure the effects of the applied magnetic field and the particle volume fraction on the capacitive characteristics of MRFs. The conclusions are helpful to understand the state of particle structures in MRFs, to deepen the understanding of the relationship between particle structures and capacitance characteristics of MRFs, and to contribute to the development of MRF application devices in complex working modes.

SIMULATION ANALYSIS

Magnetizable particles are distributed randomly inside the matrix liquid without the appearance of an external magnetic field. Adjacent particles are close to each other and gradually form chain-like structures when an external magnetic field is applied (Donado, et al., 2017; Wang, et al., 2020). There would be a capacitance between two adjacent particles when every particle seems to be an equipotential body. The equivalent capacitance of an MRF comes from the actions of all micro-capacitance between particles. The capacitance of a particle chain is the sum of the capacitance between particles because the micro-capacitance is connected in parallel, and a larger capacitance can be obtained. The reciprocal of total capacitance of an MRF is equal to the sum

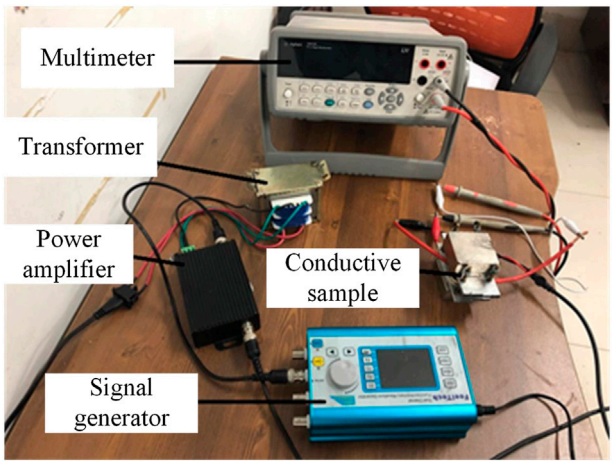

FIGURE 3 | Photo of the circuit device.

of the reciprocal of the capacitance of each particle chain, and the total capacitance will be smaller than the capacitance of a particle chain.

The capacitance characteristics of an MRF containing several particles were investigated using COMSOL Multiphysics according to the mechanism mentioned above. The 2D geometric model was created by the Model Wizard module of the package. Three models of random distribution, loose chain, and tight chain were created to correspond to the state of zero magnetic field, low magnetic field, and high magnetic field, respectively. The capacitance of the three models was simulated and calculated using the physical field of electrostatics of the AC/DC module. The area ratio of the circle in the three models was consistent, which represented the consistent particle volume fraction inside the MRF.

A simple ideal model was established to simulate the effect of particle structures on the capacitance of MRFs qualitatively. The spherical particle size was set to 3.14 μm according to a commercial carbonyl iron powder (MRF-R35, Jiangsu Tianyi Ultrafine Metal Powder Co., Ltd.). The magnetic conductivity of the particles and the matrix liquid were defined, respectively. The particle clearances in the loose chain and the tight chain are 1.54 and 0.5 μm respectively. A 20 V potential was applied to the upper boundary of the model, the lower boundary was defined as grounding, and a suspension potential boundary condition was defined for each particle. The simulation results of the distribution of electric fields are shown in **Figure 1**.

The capacitance values were obtained through the global calculation of capacitance in COMSOL Multiphysics, and the values were recorded. The capacitances of the three models were calculated by the package. They are 13.734 pF of the random distribution, 14.531 pF of the loose chain, and 18.567 pF of the tight chain, respectively. The simulation results show that the capacitance of an MRF under the action of a magnetic field is larger than that of a zero field condition, and the capacitance value increases with the increase of the magnetic field strength.

TABLE 1 | MRF sample numbers.

Numbering	Carbonyl Iron Powder (%)	Dimethicone (%)	Magnetic Field (mt)
A	1	99	150
B	5	95	150
C	10	90	150
D	1	99	0
G	1	99	100

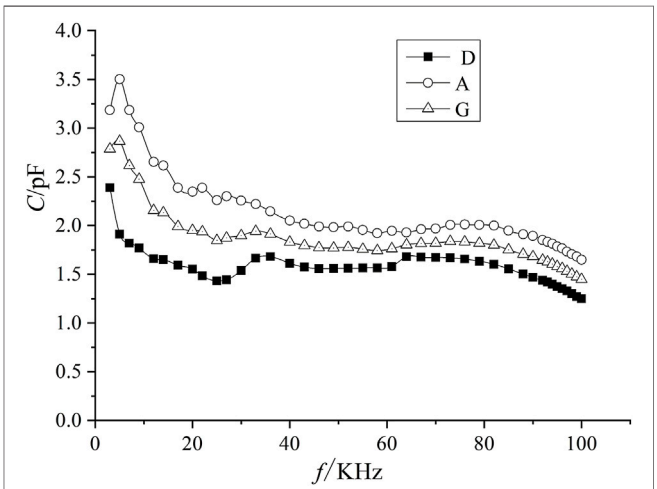

FIGURE 4 | The dependence of capacitance of MRFs on frequency under the action of different applied magnetic fields.

EXPERIMENT

The schematic of the self-made circuit device is shown in **Figure 2**. 220 V 50 Hz AC was transformed by a transformer (Zhengzhou Xinxing Electronics Co., Ltd.) to 24 V AC to provide power to the amplifier (FPA1016, FeelTech Co., Ltd.). The amplifier and a bench-type digit multimeter (Agilent Co., Ltd.) were connected in series in the circuit, along with the MRFs. The maximum frequency of the signal generator (FY2302, Zhengzhou Feiyi Technology Co.) is 100 kHz, the full power sinusoid bandwidth of the amplifier is also 100 kHz, and the accuracy of the multimeter is 1 μA. The photo of the circuit device is shown in **Figure 3**.

MRF samples with different particle volume fractions were prepared, as shown in **Table 1**. The carbonyl iron powder (MRF-R35, Jiangsu Tianyi Ultrafine Metal Powder Co., Ltd.) was used as magnetizable particles and the dimethyl silicone oil with a viscosity of 20 centistoke was used as the matrix liquid. The prepared MRFs sample is placed between two copper plates. The diameter of the polar plates and the distance between them are 20 and 4 mm, respectively. Permanent magnets were used as the external magnetic field. Different magnetic field strengths were obtained by adjusting the gap between the permanent magnets. The magnetic induction intensity between permanent magnets is measured by using a Tesla meter (HT20, Shanghai Hengtong

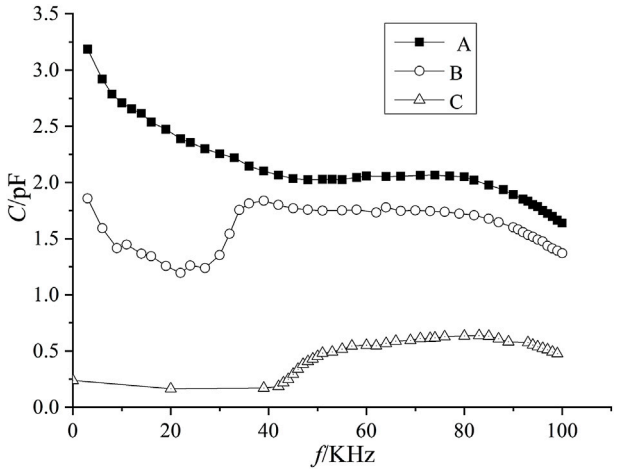

FIGURE 5 | Dependence of capacitance of MRFs with different particle volume fractions on frequency.

Magnetoelectric Technology Co., Ltd.), and the magnetic field direction is perpendicular to the plate surfaces.

During the experiments, the AC voltage in the circuit was set to 20 V, the frequency of the output sinusoidal wave was adjusted to change from 0 to 100 kHz, and the corresponding current values displayed by the digit multimeter in the circuit were observed and recorded. The above experiments were repeated by changing the magnitude of the applied magnetic induction strength and the particle volume fraction, respectively. The recorded data were used to analyze the dependence of MRF capacitance characteristics on frequency with the controlled parameters.

RESULTS AND DISCUSSION

The current values of MRFs at 0–100 kHz are measures by a desktop multimeter (34410A, Agilent Technology Co., Ltd.). The capacitive values of the MRFs were calculated by the following formula:

$$C = \frac{I}{2\pi f U}, \tag{1}$$

where I and U are RMS current and voltage respectively, and f is the frequency of the supply power. Based on the theoretical analysis of the conductivity mechanism of MRFs, the current consists of resistance current, tunnel current, and capacitive current. The resistance current can be omitted because of the very low conductivity of the matrix fluid. It is difficult to measure the tunnel current and the capacitive current, respectively. Thus, the measured current in the experiment is the sum of the capacitive current and the tunnel current. The variation curve of capacitance with frequency is plotted and analyzed.

Effect of External Magnetic Field

Three comparable experiments of the MRF samples with the same particle volume fraction were carried out under the condition of different magnetic induction intensity. The samples were A, D, and G. The calculated dependence of MRF capacitance on frequency is shown in **Figure 4**. It can be seen that the capacitances of the MRFs have a similar trend with frequency under different external magnetic fields. The trends are roughly downward and have a large slope when the frequency is less than 25 kHz. Samples D and G have a rising range from about 25 to 35 kHz, and the decreasing trend of sample A becomes slow. The capacitances of all the three samples are relatively stable in the range from 35 to 75 kHz, and then decreases slowly as the frequency increases . It can also be seen that capacitances of MRFs increase with the increase in magnetic induction intensity at the same frequency, which is consistent with the simulation results.

The magnetizable particles align themselves to form chain structures inside MRFs under the action of magnetic field. The clearance between two adjacent particles decreases to increase the capacitance of an MRF. Under the action of a strong magnetic field, the particle gap becomes smaller and then makes the capacitance larger. The current in the circuit consists of capacitive current and tunnel current. The capacitances in **Figure 4** are calculated from the total

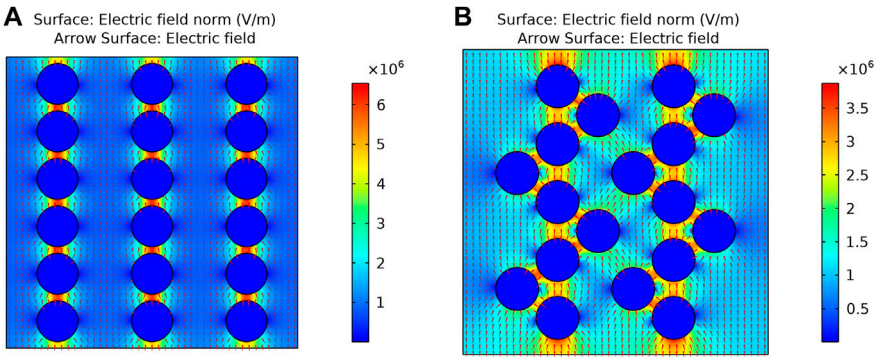

FIGURE 6 | Effect of particle aggregation on capacitance. **(A)** Single chain structure; **(B)** Column-like structure.

current. Tunnel current is the main reason for the variation of capacitance with frequency. Theoretically, the tunnel current is proportional to the square of the voltage and is independent of frequency. Thus, the effect of tunnel current on capacitance becomes weaker with the increase of frequency.

Effect of Particle Volume Fraction

Three groups of samples with different particle volume fractions, A, B, and C, were used to carry out the comparable experiments under a constant applied magnetic field. The results of the variation of capacitance versus frequency for three MRF samples are shown in **Figure 5**. It can be seen that the capacitance of MRFs with different particle volume ratios have different trends with frequency under the same magnetic induction intensity. The capacitance of the MRF with a particle volume fraction of 1% has an overall decreasing trend and is relatively smooth in the range from 35 to 75 kHz. The capacitance of the MRFs with the large particle volume fraction fluctuates greatly before about 40 kHz. The capacitance of the MRF with a particle volume fraction of 5% shows a stable and slow decline when the frequency is greater than 35 kHz, while that of the MRF with a particle volume fraction of 10% undergoes an increase, flattening and decreasing the processes when the frequency is larger than 40 kHz. It can also be seen that the capacitance of the MRF with a larger particle volume fraction is lower than that of the MRF with a smaller particle volume fraction at the same frequency.

When the particle volume fraction is relatively small, the particle structures are mostly independent single chains inside the MRFs. As the particle volume fraction increases, the particle structures become more and more complex to be column structure and network structure (Zhu, et al., 2010a), which leads to the capacitances of the MRFs being similar to the random particle distribution model in the zero-field state, and some adjacent particles will contact each other and destroy the capacitive structure. These reasons lead to the negative correlation between MRF capacitance and particle volume fraction. The reason why the capacitance is not constant is that the effect of tunnel current decreases with the increase of frequency.

To study the effect of particle aggregation on the capacitance of MRFs, the capacitances of MRFs with single chain structure and column-like structure were further simulated and analyzed, as shown in **Figure 6**. The capacitance is 21.437 pF when the particle structure is an independent single chain and 17.254 pF when the particle structure is column-like. The capacitance decreases significantly from structures of single chain to column-like. **Figure 6** shows that the more micro-capacitances formed between the particles in a column-like structure and these micro-capacitances connect in series. The more the micro-capacitances, the smaller the equivalent capacitance. Therefore, when the particle volume fraction is large, the particles form a column-like structure and induce the smaller capacitance of MRFs.

CONCLUSION

The capacitance characteristics of MRFs were experimentally analyzed in this paper. Considering the effect of external magnetic field and the particle volume fraction, the dependences of capacitance of MRFs on frequency were summarized. The work provides an accurate reference for the measurement of capacitance characteristics, and lays a foundation for further study on the evolution process of the particle structures inside MRFs under complex working modes. The main conclusions are:

(1) The capacitance of an MRF is related to the particle structures. The capacitance of the MRF with chain particle structure is greater than that of the MRF with random particle distribution.
(2) The dependence of capacitance of an MRF on frequency is not constant. The reason is that the effect of tunnel current decreases with the increase in frequency.
(3) The clearance between two adjacent particles decreases to increase the capacitance of an MRF when an external magnetic field is applied. The particle gap becomes smaller and then the capacitance increases when the magnetic field becomes stronger.
(4) The capacitance of MRF is negatively correlated with particle volume fraction. The network particle structure and particle contact will reduce the capacitance of MRF.

DATA AVAILABILITY STATEMENT

The original contributions presented in the study are included in the article/Supplementary Material; further inquiries can be directed to the corresponding author.

AUTHOR CONTRIBUTIONS

XZ and GT conceptualized the idea. XZ and SM performed the methodology. SM and HS ran the software. SM, HH, ZL, and HS performed the experiment. SM, HH, ZL, and HS wrote the original draft. All authors have read and agreed to the published version of the manuscript.

FUNDING

This research was supported by the National Natural Science Foundation of China, grant number 51575323.

ACKNOWLEDGMENTS

The authors would like to thank the National Natural Science Foundation of China for the research grant support.

REFERENCES

Ashour, O., Rogers, C. A., and Kordonsky, W. (1996). Magnetorheological Fluids: Materials, Characterization, and Devices. *J. Intelligent Material Syst. Struct.* 7, 123–130. doi:10.1177/1045389X9600700201

Bica, I. (2009). Influence of Magnetic Field upon the Electric Capacity of a Flat Capacitor Having Magnetorheological Elastomer as a Dielectric. *J. Industrial Eng. Chem.* 15, 605–609. doi:10.1016/j.jiec.2009.02.005

Chand, M., Shankar, A., Pratap Singh, A., Chandra Mathpal, M., Prasad Pant, R., and Deperyot, J. (2021). Mechanism of Chain Formation under Shearing Forces in Magneto-Rheological Fluids. *Mater. Today Proc.* 47, 1575–1579. doi:10.1016/J.MATPR.2021.03.675

Chen, X., Zhu, X., Xu, Z., Lin, Y., and He, G. (2013). The Research of the Conductive Mechanism and Properties of Magnetorheological Fluids. *Phys. B Condens. Matter* 418, 32–35. doi:10.1016/j.physb.2013.02.042

Donado, F., Sausedo-Solorio, J. M., and Moctezuma, R. E. (2017). Dynamical and Structural Properties of a Granular Model for a Magnetorheological Fluid. *Phys. Rev. E* 95, 022601. doi:10.1103/PhysRevE.95.022601

He, J., Gao, L. X., Long, Z., Liu, Y. Z., and Liu, X. M. (2013). Theoretic and Experimental Study of Chain-Formation Mechanism for MRF. *J. Funct. Mater.* 44, 522–526. doi:10.1016/j.jmmm.2010.11.046

Huang, Y., Jiang, Y., Yang, X., Sun, H., Piao, H., and Xu, R. (2016). Enhanced Conductivity of Magnetorheological Fluids Based on Silver Coated Carbonyl Particles. *J. Mater Sci. Mater Electron* 27, 255–259. doi:10.1007/s10854-015-3748-y

Kaluvan, S., and Choi, S.-B. (2014). Design of Current Sensor Using a Magnetorheological Fluid in Shear Mode. *Smart Mat. Struct.* 23, 127003. doi:10.1088/0964-1726/23/12/127003

Rabinow, J. (1948). The Magnetic Fluid Clutch. *Trans. Am. Inst. Electr. Eng.* 67, 1308–1315. doi:10.1109/t-aiee.1948.5059821

Ruan, X., Wang, Y., Xuan, S., and Gong, X. (2017). Magnetic Field Dependent Electric Conductivity of the Magnetorheological Fluids: the Influence of Oscillatory Shear. *Smart Mat. Struct.* 26, 035067. doi:10.1088/1361-665X/aa5fe5

Wang, N., Liu, X., Sun, S., Królczyk, G., Li, Z., and Li, W. (2020). Microscopic Characteristics of Magnetorheological Fluids Subjected to Magnetic Fields. *J. Magnetism Magnetic Mater.* 501, 166443. doi:10.1016/j.jmmm.2020.166443

Wang, S., He, G. T., Wang, P., Song, L., Ran, Y. C., and Zhang, D. S. (2011). The Research of Capacitance Characteristics of MRF. *J. Funct. Mater.* 42, 1386–1389.

Wang, S. (2012).The Research of MR's Electromagnetic Characteristics and its Sensor Technology. Chongqing: Chongqing normal university. [dissertation/master's thesis]. [Chongqing].

Wang, Y. (2017). Study on Mechanical-Electro-Magnetic Coupling Properties of Magnetorheological Elastomers [dissertation/master's thesis]. [Hefei (Anhui)]. China: University of Science and Technology of China.

Yang, X., Huang, Y., Hou, Y., Wu, H., Xu, R., and Chu, P. K. (2017). An Experimental Study of Magnetorheological Fluids on Electrical Conductivity Property. *J. Mater Sci. Mater Electron* 28, 8130–8135. doi:10.1007/s10854-017-6519-0

Zhu, X. L., Meng, Y. G., and Tian, Y. (2010a). Effects of Particle Volume Fraction and Magnetic Field Intensity on Particle Structure of Magnetorheological Elastomers. *J. Tsinghua Univ. Technol.* 50, 167552. doi:10.16511/j.cnki.qhdxxb.2010.02.006

Zhu, X., Meng, Y., and Tian, Y. (2010b). Nonlinear Pressure-dependent Conductivity of Magnetorheological Elastomers. *Smart Mat. Struct.* 19, 117001. doi:10.1088/0964-1726/19/11/117001

Conflict of Interest: HS was employed by Qingdao Metro Group Co., Ltd.

The remaining authors declare that the research was conducted in the absence of any commercial or financial relationships that could be construed as a potential conflict of interest.

frontiers | Frontiers in Materials

TYPE Original Research
PUBLISHED 25 July 2022
DOI 10.3389/fmats.2022.930124

OPEN ACCESS

EDITED BY
Tongfei Tian,
University of the Sunshine Coast, Australia

REVIEWED BY
Xufeng Dong,
Dalian University of Technology, China
Marcin Szczęch,
AGH University of Science and Technology, Poland

*CORRESPONDENCE
Decai Li,
lidecai@mail.tsinghua.edu.cn

SPECIALTY SECTION
This article was submitted to Smart Materials, a section of the journal Frontiers in Materials

RECEIVED 27 April 2022
ACCEPTED 05 July 2022
PUBLISHED 25 July 2022

CITATION
Yu W, Li D, Zang G, Wang D and Zhang Z (2022), Influence of magnetic fluid evaporation on pressure resistance of magnetic fluid seal.
Front. Mater. 9:930124.
doi: 10.3389/fmats.2022.930124

Influence of magnetic fluid evaporation on pressure resistance of magnetic fluid seal

Wenjuan Yu[1], Decai Li[1,2]*, Guobao Zang[1], Deyi Wang[1] and Zhili Zhang[1]

[1]School of Mechanical Electronic and Control Engineering, Beijing Jiaotong University, Beijing, China, [2]State Key Laboratory of Tribology, Tsinghua University, Beijing, China

Magnetic fluid seals have the advantages of zero leakage, long life, simple structure and high reliability, and have become one of the most widely used applications of magnetic fluids. In this paper, the effect of magnetic fluid evaporation on the pressure resistance of magnetic fluid seals is studied. In terms of theory, through theoretical calculation and simulation analysis, a calculation method for the pressure resistance of magnetic fluid seals is established. In terms of experiments, firstly, five groups of control groups were set up to conduct evaporation experiments under the same conditions, and magnetic fluids with different evaporation rates were obtained; Secondly, the performance of magnetic fluids with different evaporation rates was tested, and the flow curves, viscosity-temperature curves, and magnetic-viscosity curves of magnetic fluids were obtained respectively, and the effect of evaporation on the performance of magnetic fluids was analyzed; Finally, magnetic fluid sealing experiments with different evaporation rates were carried out. It is found that evaporation increases the pressure resistance of static seal to a certain extent, which is of great significance.

KEYWORDS

magnetic fluid, evaporation, seal, finite element, pressure resistant

Introduction

Magnetic fluid is a new type of nano-scale functional material, which is composed of magnetic particles, surfactant and base carrier liquid, which has both the magnetic properties of solid and the fluidity of liquid (Chi et al., 1993; Rosensweig, 2002; Li, 2003). Magnetic fluid seal is a new type of sealing method, which has the advantages of zero leakage, long life and high reliability (Chi et al., 1993; Chen et al., 2018; Yu et al., 2021). In the practical application of the magnetic fluid sealing device, the magnetic fluid exists in the gap between the pole teeth and the rotating shaft, forming several "O"-shaped sealing rings, which achieves the sealing effect (Chi, 2011; Li et al., 2021; Niu, 2021).

With the increasing application of magnetic fluid seals, the requirements for the pressure resistance performance of magnetic fluid seals are also getting higher and higher. In recent years, some scholars have carried out many studies on the factors affecting the pressure resistance of magnetic fluid seals. Zou et al. (2002) studied that centrifugal force

will lead to the decline of the rotary sealing ability of magnetic fluids. He et al. (2019a) believed that under the condition of large diameter and large gap, gravity will seriously affect the pressure resistance performance of magnetic fluid seals. The results show that magnetic fluid seal has a limit size that is directly proportional to the magnetic field gradient in the sealing gap and is inversely proportional to the ratio of magnetic fluid density to the magnetization. When the diameter of magnetic fluid "O" rings is much smaller than the limit size, gravity has almost no effect. When approaching or even exceeding the limit size, gravity will cause the pressure resistance of the magnetic fluid seal to drop. Cheng et al. (2021) studied the effect of rheology on the sealing starting torque, and used perfluoropolyether-based magnetic fluids and diester-based magnetic fluids to conduct dynamic sealing experiments, and found that magnetic fluids with higher viscosity showed correspondingly higher starting torque. Saurabh et al. (Parmar et al., 2021) studied the influence of magnetic fluid volume, pole-piece thickness, radial clearance and particle volume fraction of a fluid on the pressure resistance of the seal combined with the finite element method, and obtained the optimum volume of a fluid is 10 mm^3 for the optimum pole-piece thickness 3.5 mm and radial clearance 0.275 mm. Yuan et al. (Yuan et al., 2022) studied the magnetic fluid seal with large shaft diameter, and believed that the radial swing of the main shaft during the operation had a serious impact on the sealing performance. Therefore, an axial-radial series magnetic fluid sealing structure is designed to limit the swing displacement of the main shaft, thereby maintaining the overall pressure-resistant stability of the seal. Yang et al. (Yang and Li, 2016) designed a new type of stepped magnetic fluid seals in order to improve the pressure resistance of magnetic fluid large-gap seals. By comparing and analyzing the new seal and the traditional seal structure by experimental method, it is found that the divergent stepped magnetic fluid seal has better performance and is an effective method to improve the large gap magnetic fluid sealing ability. These studies have a certain effect on the pressure resistance of magnetic fluid seals, but there is little research on the effect of magnetic fluid evaporation on the seal pressure resistance. The relationship between the evaporation of the magnetic fluid in the sealing device and the sealing pressure value is not clear. Since the magnetic fluid is inside the sealing device, the evaporation rate of the magnetic fluid cannot be controlled. There are many difficulties in studying the effect of the evaporation of the magnetic fluid sealing.

In this paper, the magnetic fluid is evaporated separately to obtain samples with different evaporation rates, and then the rheological performance test and the sealing pressure test are carried out. Including the viscosity change of the magnetic fluid with different evaporation rates, the magnetic viscosity curve of the magnetic fluid, the flow performance of the magnetic fluid, etc. The analysis shows that the evaporation of the magnetic fluid makes the viscosity of the magnetic fluid increase and the fluidity worsens. For the rotary seal, the torque will increase, which is not conducive to the dynamic seal; but to a certain extent, the pressure resistance of the static seal will increase.

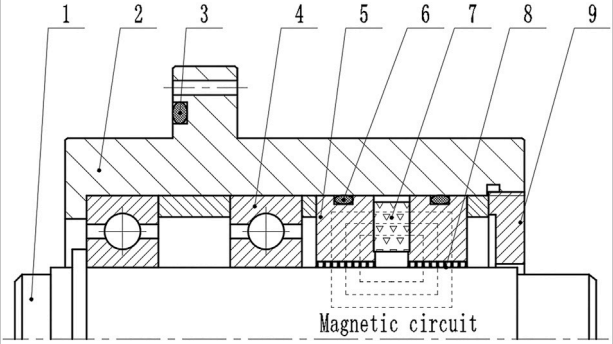

FIGURE 1
Main structure diagram of magnetic fluid seal. 1-rotation shaft, 2-shell, 3-sealing ring, 4-bearing, 5-pole shoe, 6-sealing ring, 7-permanent magnet, 8-magnetic fluid, 9-end cover.

Theoretical basis

Principle of magnetic fluid sealing

The main structure of the magnetic fluid seal is shown in the Figure 1. The magnetic fluid seal is mainly composed of a pole piece, a permanent magnet and a magnetic conductive shaft. There is a certain gap between the pole piece and the shaft, and the surface adjacent to the pole piece and the magnetic conducting shaft is provided with tooth slots to form several pole teeth. The permanent magnet provides a magnetic source, forms a magnetic circuit with the pole piece and the magnetic conducting shaft, and adsorbs the magnetic fluid at the pole teeth to form several liquid sealing rings. The sealing ring exists in the gap between the pole piece and the rotating shaft to achieve the purpose of sealing. Both static sealing and dynamic sealing can be achieved. Dynamic seals include rotary seals and reciprocating seals (He et al., 2019b; Chen, 2019; Matuszewski and Bela, 2021; Zhang et al., 2022).

Pressure calculation of magnetic fluid seal

Derivation of Bernoulli's equation

According to the equation of motion of magnetic fluids (Wang, 2019; Zhang et al., 2019)

$$\rho_f \frac{\partial \boldsymbol{V}}{\partial t} + \rho_f \boldsymbol{V} \quad \boldsymbol{V} = \rho_f \boldsymbol{g} - \quad p^* \quad \mu_0 \boldsymbol{M} \quad \boldsymbol{H} + \eta_H \quad ^2\boldsymbol{V} \quad \frac{1}{3}\eta_H \quad (\quad \boldsymbol{V}) \quad J\frac{1}{2t_s} \quad (\boldsymbol{\Omega} - \omega) \tag{1}$$

And

$$p^* = p + \mu_0 \int_0^H M\,\mathrm{d}H - \mu_0 \int_0^H \rho_\mathrm{f} \frac{\partial M}{\partial \rho_\mathrm{f}} \mathrm{d}H \tag{2}$$

In the formula: ρ_f is the density of the magnetic fluid; $\boldsymbol{V}$ is the velocity of the magnetic fluid; t_s is the relaxation time; $\boldsymbol{g}$ is the acceleration of gravity; μ_0 is the vacuum permeability; $\boldsymbol{M}$ is the magnetization of the magnetic fluid; $\boldsymbol{H}$ is the magnetic field strength; J is the moment of inertia around the axis of all solid-phase particles in the magnetic fluid per unit volume; $\boldsymbol{\omega}$ is the vortex velocity of the base carrier liquid of the magnetic fluid; $\boldsymbol{\Omega}$ is the rotational speed of the solid-phase particles; p is the normal stress, that is, the pressure of the magnetic fluid; η_H is the viscosity of the magnetic fluid in the magnetic field.

Suppose:

1) Magnetic fluid density is constant. Eq. 4 can be obtained from the continuous Equation 3 of fluid motion.

$$\frac{\mathrm{d}\rho_\mathrm{f}}{\mathrm{d}t} + \rho_\mathrm{f} \nabla \cdot \boldsymbol{V} = 0 \tag{3}$$

$$\nabla \cdot \boldsymbol{V} = 0 \tag{4}$$

2) The flow is a vortex flow. $\nabla \times \boldsymbol{V} = 0$ or $\boldsymbol{\omega} = 0$ is obtained according to the definition of ilrotary flow, and there is a potential function to get $\boldsymbol{V} = -\nabla \varphi_v$.
3) Magnetic fluid is intrinsic, and the change of external magnetic field does not cause the rotation of magnetic solid particles (Parmar et al., 2021). So we get $\boldsymbol{\Omega} = 0$. Under the assumption of intrinsic properties, it is generally considered that the magnetization of the magnetic fluid is parallel to the external magnetic field, that is,

$$\mu_0 \boldsymbol{M} \cdot \nabla \boldsymbol{H} = \mu_0 M \nabla H \tag{5}$$

And $M = M(H, T)$, T is temperature, combined with Leibniz formula, Eq. 5 becomes

$$(\nabla M)_H = \frac{\partial M}{\partial T} \nabla T \tag{6}$$

Change gravity to gradient form, h is the height of the analysis object to the reference point,

$$\rho_f \boldsymbol{g} = -\nabla\left(\rho_f g h\right) \tag{7}$$

According to the identity transformation, the simultaneous Eqs 1–7, the general form of the Bernoulli equation for magnetic fluids is obtained as,

$$\begin{aligned} &\nabla\left[-\rho_\mathrm{f} \frac{\partial \phi_v}{\partial t} + \frac{1}{2}\rho_\mathrm{f} V^2 + \rho_\mathrm{f} g h + p^* - \mu_0 \int_0^H M\mathrm{d}H \right] \\ &+ \mu_0 \int_0^H \frac{\partial M}{\partial T} \nabla T \mathrm{d}H \\ &= 0 \end{aligned} \tag{8}$$

When the magnetic fluid is in steady isothermal flow, Eq. 8 can be simplified as

$$p^* + \frac{1}{2}\rho_\mathrm{f} V^2 + \rho_\mathrm{f} g h - \mu_0 \int_0^H M\mathrm{d}H = \mathrm{const} \tag{9}$$

Determination of boundary conditions

By the general expression of boundary conditions (Li, 2010)

$$\boldsymbol{n}^0 \cdot (\tau_1 - \tau_2) = -\left[\left(p_1^* + p_{1n}\right) - \left(p_2^* + p_{2n}\right) \right] \boldsymbol{n}^0 \tag{10}$$

In the formula: the subscripts "1" and "2" represent the two sides of the interface, "1" represents the magnetic fluid side, "2" represents the sealed medium side; $\boldsymbol{n}^0$ is the unit normal vector; τ is the surface stress; $p_n = \frac{\mu_0}{2} M_n^2$, where M_n is the normal component of the saturation magnetization of the magnetic fluid;

The formula for calculating the surface tension p_c of the contact surface is

$$p_\mathrm{c} = \sigma\left(\frac{1}{R_1} + \frac{1}{R_2}\right) \tag{11}$$

In the formula: R_1 is the radius of curvature of the magnetic fluid at the contact interface; R_2 is the radius of curvature of the sealed medium at the contact interface; σ is the surface tension constant, the direction of the surface tension p_c is always opposite to the direction of the outer normal of the surface, and we get

$$\boldsymbol{n}^0 \cdot (\tau_1 - \tau_2) = -p_c \boldsymbol{n}^0 \tag{12}$$

Combining Eqs 10–12, we get

$$p_1^* + p_{1n} = p_2^* + p_{2n} + p_\mathrm{c} \tag{13}$$

Derive the formula for sealing pressure

Suppose:1) consider that the magnetic field lines coincide with the isomagnetic field lines; 2) ignore the gravity and surface tension of the magnetic fluid itself.

Applying Bernoulli's equation to the boundary surface, we have

$$p_1^* - \mu_0 \int_0^{H_1} M\mathrm{d}H = p_2^* - \mu_0 \int_0^{H_2} M\mathrm{d}H \tag{14}$$

Combined with the boundary condition (13), we get

$$p_1^* = p_1, p_2^* = p_2 \tag{15}$$

Substitute Eq. 15 into Eq. 14 to get

$$\Delta p = p_1 - p_2 = \mu_0 \int_{H_2}^{H_1} M\mathrm{d}H \tag{16}$$

Equation 16 is the formula for calculating the pressure difference between the two sides of the magnetic fluid at a single pole tooth. When the magnetic field strength in the sealing gap of the magnetic fluid is very high and the magnetic fluid is in the state of saturation magnetization, the Formula (16) can be simplified as

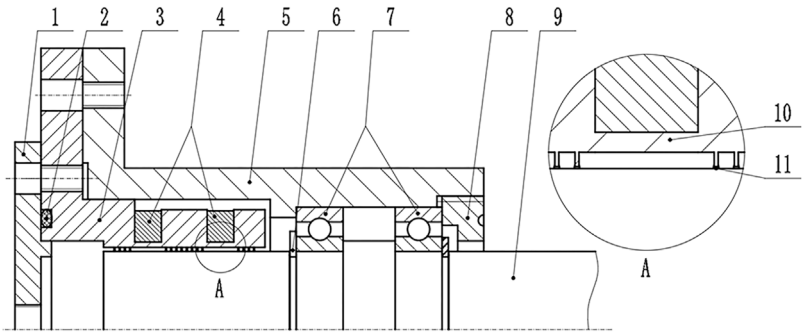

FIGURE 2
Magnetic fluid sealing device. 1-upper end cover, 2-sealing ring, 3-integrated pole shoe, 4-shell, 5-permanent magnet, 6-circlip, 7-bearing, 8-lower end cover, 9-rotation shaft,10-thin wall, 11-magnetic fluid.

$$\Delta p = \mu_0 M_s (H_1 - H_2) = \mu_0 M_s \Delta H \quad (17)$$

In the formula, M_s is the saturation magnetization of the magnetic fluid, and the total withstand pressure P of the magnetic fluid sealing structure should be the sum of the withstand pressures of all pole teeth.

Magnetic fluid sealing structure and simulation calculation

Magnetic fluid sealing structure

Figure 2 shows the main structural of the magnetic fluid sealing device used in the sealing experiment. Different from the traditional structure, this sealing structure has three pole pieces in total. The pole piece is cylindrical as a whole, with an inner diameter of 30.2 mm and an outer diameter of 50 mm. Each pole piece is connected by a thin wall with a thickness of 1 mm. The integrated pole shoe structure has the advantages of easy disassembly and assembly, low processing precision requirements, and the pole teeth are not easily damaged. The permanent magnet is installed at the thin wall, and the two permanent magnets are cylindrical magnets. The circular plane is the polar surface, the diameter of which is 6 mm and the thickness is 5 mm. The two polar surfaces of the magnet correspond to the side walls of the pole shoe. The polarity arrangement is N-S for S-N, or S-N for N-S. The permanent magnets are installed at the thin wall, and the cylindrical magnets used in the two permanent magnets have the polarity arrangement of N-S corresponding to S-N, or S-N corresponding to N-S. Bearings use deep groove ball bearing 61,906. The diameter of the rotating shaft is 30mm, the unilateral gap with the inner ring of the pole shoe is 0.1mm, and the material of the rotating shaft and the pole shoe is 2Cr13. The material of the shaft and pole piece is 2Cr13. In this experiment, only the four pole teeth of this sealing structure are used, and the position shown in Figure 2 is the four pole teeth at the left first-level pole piece. During the installation process, the pole pieces and shell are installed last. After the magnetic fluid is injected into the four pole teeth of the left pole piece, the pole piece is installed from left to right into the shell equipped with the rotating shaft, so that the magnetic fluid can be guaranteed to be all at the left pole piece.

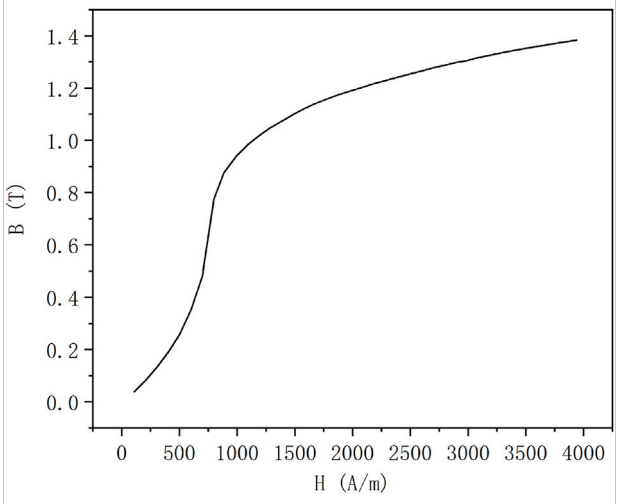

FIGURE 3
2Cr13 material B-H curve.

Simulation analysis of sealing structure

ANSYS software is used to simulate the static magnetic fluid seal. The magnetic field distribution at the sealing gap in the magnetic fluid sealing structure can be obtained, and then the theoretical withstand pressures value can be calculated.

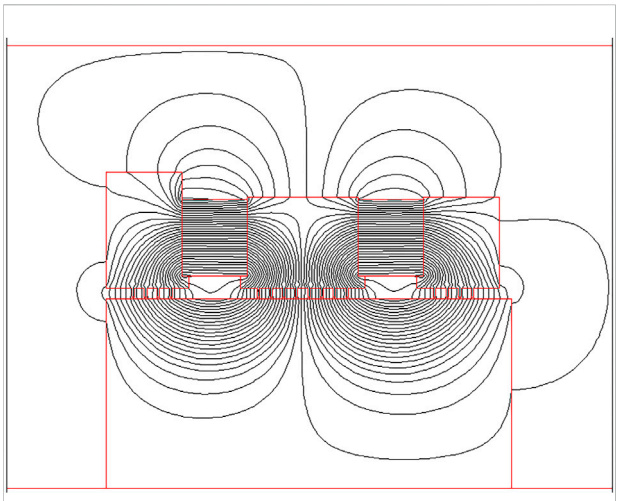

FIGURE 4
Magnetic line distribution.

Assumptions: 1) The permanent magnet is a ring-shaped magnet, and the magnetization is uniform; 2) The magnetic permeability of the magnetic fluid is the same as that of the air.

The material settings of each part: the permeability of the air domain is set to one; the permanent magnet is a NdFeB magnet with a grade of N38, its permeability is set to 1.138, and the coercive forces on both sides are set to 1.089×10^6A/m and -1.089×10^6A/m; the pole piece and the shaft are defined as 2Cr13 material, and the BH curve of the 2Cr13 material is shown in Figure 3.

Through the intelligent size control technology in ANSYS, use the SMARTSIZE command to divide the mesh and subdivide it to 0.1 for mesh division processing. Next, define the boundary condition, that is, the infinite magnetic field is parallel to the model boundary. Finally, the magnetic field is solved for the model, and the completion mark is iterative convergence. The distribution of magnetic field lines is shown in Figure 4, and it can be seen that most of the magnetic field lines pass through the pole teeth.

Select a path at the sealing gap, the radial distance from the rotating shaft is 0.01mm, and parallel to the rotating shaft. Since only the four pole teeth of the sealing device are used in the experiment in this paper, only the magnetic induction intensity value at the four pole teeth is obtained, The starting point 1 and the ending point 2 of the path are shown in Figure 5. The magnetic induction intensity distribution at the path is obtained as shown in Figure 6.

It can be seen from Figure 6 that the magnetic field intensity reaches the maximum value at the middle of the pole teeth, and the magnetic field intensity is the minimum at the middle part of the two pole teeth. Through calculation, the sum of the difference between the maximum magnetic induction intensity and the minimum magnetic induction intensity at the pole teeth is 1.95T, and then the theoretical withstand pressure value can be calculated.

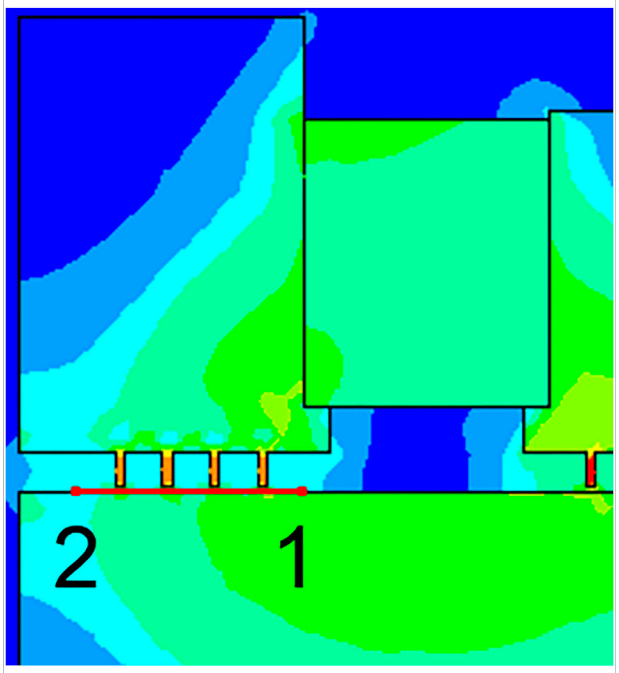

FIGURE 5
Path selection diagram.

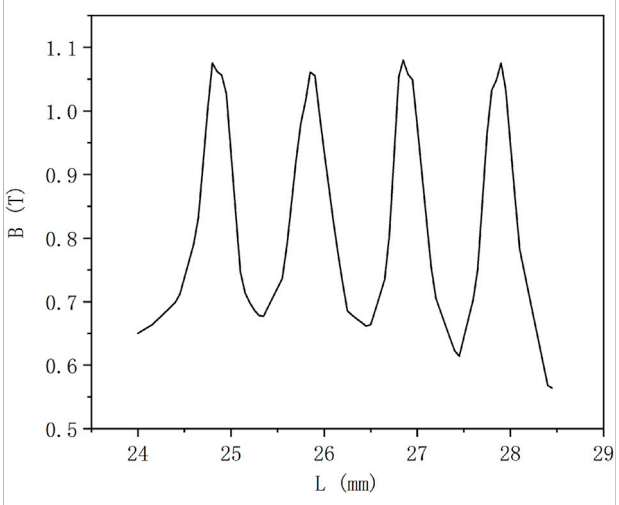

FIGURE 6
Magnetic induction strength distribution.

Experimental method

Due to the particularity of the magnetic fluid seal, the evaporation of the magnetic fluid cannot be directly judged from the outside of the sealing device. In order to quantitatively study the effect of different evaporation rates on the pressure

FIGURE 7
Kerosene-based magnetic fluid evaporation control group.

resistance of magnetic fluid seals, the experiment is divided into two parts. One is the magnetic fluid evaporation experiment, and the magnetic fluid samples with different evaporation rates are obtained; The second is the pressure test of magnetic fluid sealing, and the pressure test is carried out on magnetic fluid samples with different evaporation rates respectively.

Magnetic fluid evaporation experiment

This paper uses kerosene-based magnetic fluid to conduct evaporation experiments, where the size of the magnetic particles is 10 nm. (Yu et al., 2022). The kerosene-based magnetic fluid was injected into four identical flat-bottomed test tubes in equal amounts, and an evaporation experiment in the same environment was carried out in a high and low temperature test chamber as shown in Figure 7. Four kinds of kerosene-based magnetic fluids with different evaporation rates were obtained, which were 0, 3, 6, 9, and 11%, respectively. The calculation formula of the evaporation rate E in this paper is, $E = m/m_0$, where m is the mass of the magnetic fluid evaporated, and m_0 is the mass of the initial magnetic fluid.

Magnetic fluid sealing experiment

A magnetic fluid static sealing experimental platform is built, and the schematic diagram of the experimental device is shown in Figure 8. The air compressor is connected with the pressure reducing valve through the pressure transmission pipe, and the other side is connected with the throttle valve, which is used to control the gas flow rate, and then connected with the pressure inlet of the sealing device. A pressure sensor is connected to the pressure inlet of the sealing device, which is transmitted to a computer through a paperless recorder to record data. Among them, the paperless recorder is produced by Hangzhou Meikong Automation Technology Co., Ltd., and the model is MIK-R200T. The pressure sensor has a range of 1 MPa and an accuracy of 0.25%. By adjusting the pressure reducing valve and the throttle valve, the gas slowly enters the seal, the pressure in the seal will change, and the pressure change is recorded by the pressure sensor, and the actual pressure resistance value of the seal can be obtained.

The static sealing pressure test was carried out on kerosene-based magnetic fluids with different evaporation rates. It is known that when the magnetic fluid evaporates in the sealing device, the quality of the magnetic fluid in the sealing gap will decrease. In order to approximate the simulation, the filling mass of the samples with different evaporation rates b is $b = 0.3 \times (1 - a)$g. The filling mass and corresponding filling volume of magnetic fluid with different evaporation rates are shown in Table 1, and the corresponding sealing pressure value is obtained.

Results and discussion

Magnetic fluid performance characterization

The magnetization curve of the magnetic fluid was measured using a vibrating sample magnetometer. The rheological curves of the magnetic fluids were all measured with Anton Paar's MCR302 magnetorheological instrument. The temperature of the test was constant temperature of 20°C, and 0.1 ml of the magnetic fluid sample was taken and injected into the magnetorheology between the rotor and the stator of the magnetorheological instrument. In the gap, the shear motion inside the magnetic fluid is formed by the relative motion of the rotor and stator surfaces. Through the evaporation experiment, it is found that when the evaporation rate of the kerosene-based magnetic fluid reaches 11%, there is almost no fluidity, and the magnetic fluid cannot be uniformly injected into the sealing structure for the sealing pressure test, which is not for reference. Therefore, only four kinds of kerosene-based magnetic fluids with evaporation rate of 0, 3, 6 and 9% are respectively characterized.

Magnetic fluid magnetization curve

Figure 9 shows the magnetization curves of the evaporation rates of 0, 3, 6 and 9%. It can be seen that the saturation magnetization of the magnetic fluid increases with the increase of the evaporation rate. This is because a large amount of the base carrier liquid evaporates during the evaporation process, and the

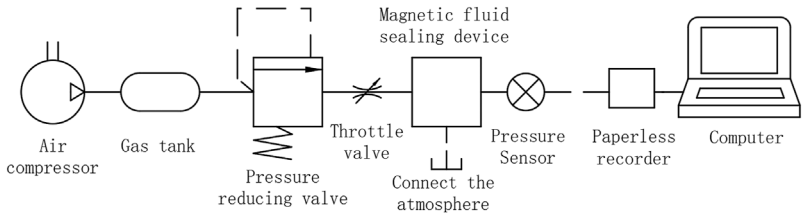

FIGURE 8
Static sealing experimental device schematic.

TABLE 1 Injection amount of kerosene-based magnetic fluid with different evaporation rates.

Evaporation rates	0%	3%	6%	9%
Injection quality/(g)	0.077	0.075	0.072	0.07
Injection volume/(ml)	0.05	0.048	0.044	0.038

TABLE 2 Different evaporation rate magnetic fluid density and saturation magnetization intensity.

Evaporation rates	0%	3%	6%	9%
Density/(g/cm^3)	1.539	1.556	1.641	1.864
Saturation magnetization (kA/m)	50.75	51.84	55.52	63.25

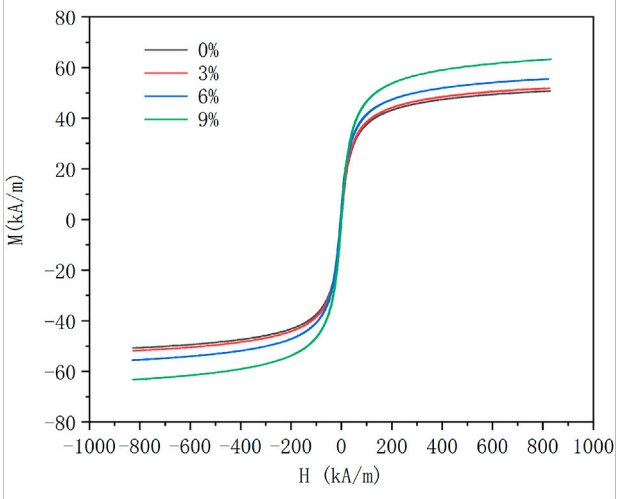

FIGURE 9
Magnetization curves of magnetic fluids with different evaporation rates.

volume fraction of the magnetic particles in the magnetic fluid increases, resulting in an increase in the magnetization. The density and saturation magnetization of magnetic fluids with different evaporation rates are shown in Table 2.

Magnetic viscous properties of magnetic fluids

As shown in Figures 10A,B, the magneto-viscosity curves with evaporation rates of 0 and 9% are respectively set with five shear rates (25s^{-1}, 50s^{-1}, 75s^{-1}, 100s^{-1}) control group. It can be seen from Figure 10A that the viscosity of the magnetic fluid with the evaporation rate of 0% increases with the increase of the magnetic field strength and finally tends to be flat, and has little relationship with the shear rate. It can be seen from Figure 10B that the viscosity of the kerosene-based magnetic fluid with an evaporation rate of 9% first increases with the increase of the magnetic field strength. When the magnetic field exceeds a certain value, the viscosity of the magnetic fluid decreases. This is most pronounced at lower shear rates.

Figure 11 shows the comparison of the magnetic viscosity curves of kerosene-based magnetic fluids with evaporation rates of 0, 6 and 9% when the shear rate is 100 s^{-1}. It is not difficult to see that the viscosity of the magnetic fluid with a larger evaporation rate is larger. In the absence of a magnetic field, the viscosity of the kerosene-based magnetic fluid with an evaporation rate of 0% is 118.91 mPa s, the viscosity of the kerosene-based magnetic fluid with an evaporation rate of 6% is 564.62 mPa s, and the viscosity of kerosene-based magnetic fluid with an evaporation rate of 9% is as high as 3387.4 mPa s. Evaporation has a great influence on the viscosity of the magnetic fluid, and also has an effect on the magnetic viscosity characteristics of the magnetic fluid.

In addition, taking the shear rate as the independent variable and the viscosity as the dependent variable, the change curves of the viscosity of the kerosene-based magnetic fluid with the shear rate of the evaporation rate of 0, 3, 6 and 9% were obtained. As shown in Figures 12A,B, the results are obtained under the condition that the magnetic field strength is 0 and 0.2 T, respectively. Under the condition of no magnetic field, it can

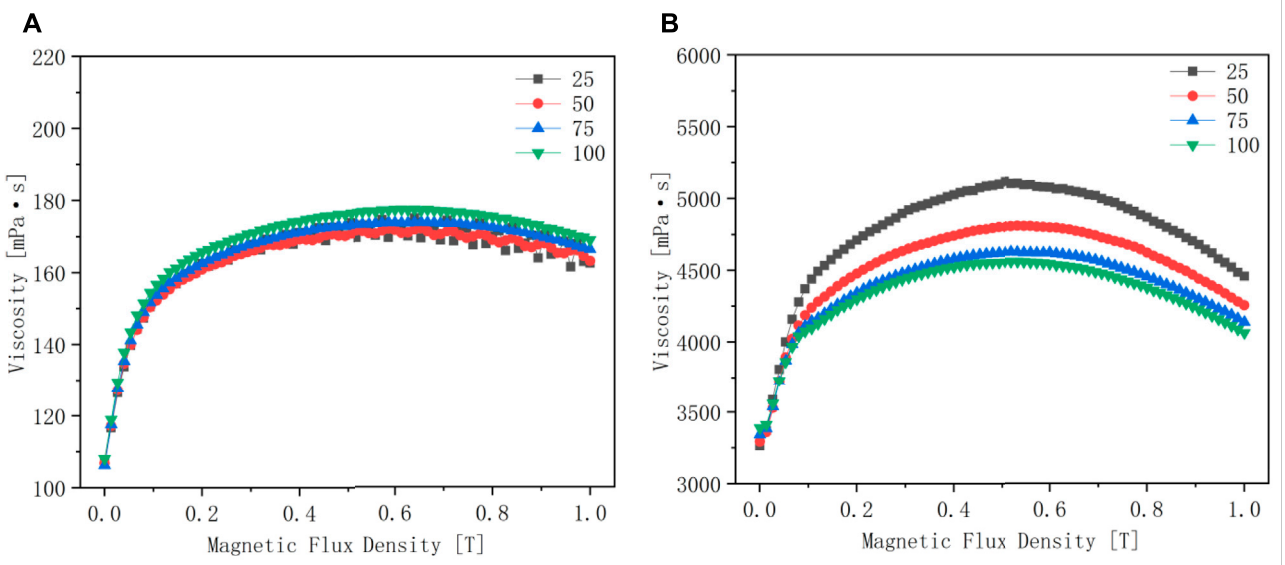

FIGURE 10
Magnetic viscosity curves of kerosene-based magnetic fluids with different evaporation rates. **(A)** is the magnetic viscosity curve when the evaporation rate is 0%. **(B)** is the magnetic viscosity curve when the evaporation rate is 9%.

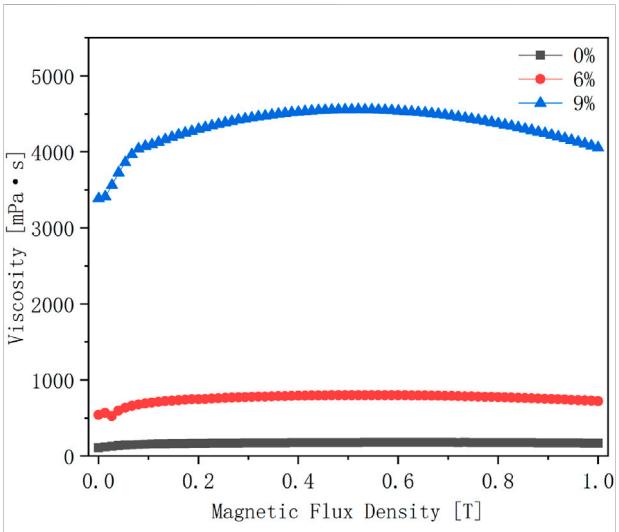

FIGURE 11
Magnetic-viscosity curves of kerosene-based magnetic fluids with different evaporation rates at a shear rate of 100 S^{-1}.

be seen that when the evaporation rate is less than 6%, with the increase of shear rate, the viscosity of the magnetic fluid remains basically constant, and the phenomenon of shear thinning is not obvious, but for a magnetic fluid with an evaporation rate of 9%, when the shear rate is close to 100 s^{-1}, it is clear that the viscosity decreases with increasing shear rate. It can be obtained that the greater the evaporation rate of the magnetic fluid, the more obvious the shear thinning phenomenon will be. When the magnetic field strength is 0.2 T, the viscosity of the magnetic fluid with the evaporation rate of 0% remains stable regardless of the shear rate. For the evaporated magnetic fluid, the viscosity decreases with the increase of the shear rate. The greater the evaporation rate, the more obvious the decrease in viscosity with the increase of the shear rate. It can be obtained that in the presence of a magnetic field, the evaporation of the magnetic fluid has a great influence on the viscosity.

Magnetic fluid flow properties

Figures 13A,B show the relationship between shear stress and shear rate of four different evaporation rates (0, 3, 6, and 9%) of kerosene-based magnetic fluids under the conditions of magnetic field strength of 0 and 0.2T, respectively. It can be seen that the trends of the four different evaporation rates of kerosene-based magnetic fluids are consistent with or without a magnetic field. When the shear rate is less than 100 s^{-1}, the shear stress does not change significantly with the shear rate. When the shear rate increases to a certain value, the shear stress increases with the increase of the shear rate, and this trend is most obvious in the kerosene-based magnetic fluid with the larger evaporation rate. As shown in Figure 13A, when the shear rate is 1000 s^{-1}, the shear stress of 0% evaporation rate is 100.2 Pa, the shear stress of 3% evaporation rate is 131.8 Pa, and the evaporation rate of 6% is 131.8 Pa. The shear stress reaches 412.4 Pa, and the shear stress with an evaporation rate of 9% is as high as 1820.5 Pa, which is 18 times that of the unevaporated magnetic fluid. This results in increased starting torque for magnetic fluid rotary seals.

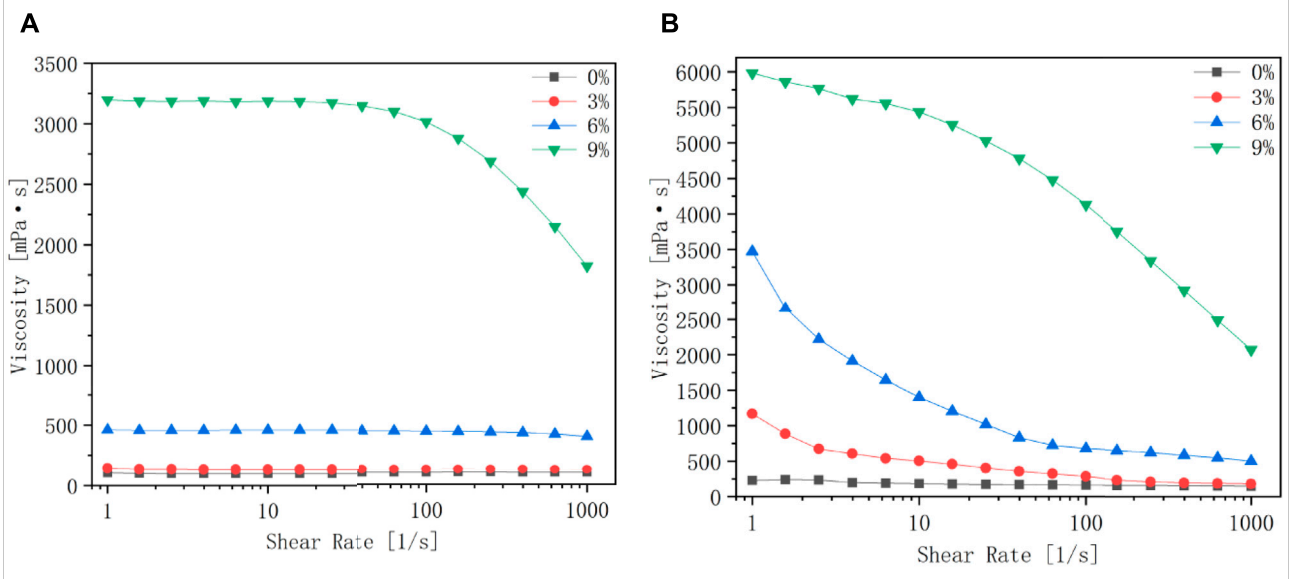

FIGURE 12
Variation of viscosity with shear rate for kerosene-based magnetic fluids with different evaporation rates under different magnetic field strengths. **(A)** is the magnetic field strength at 0T; **(B)** is the magnetic field strength at 0.2T.

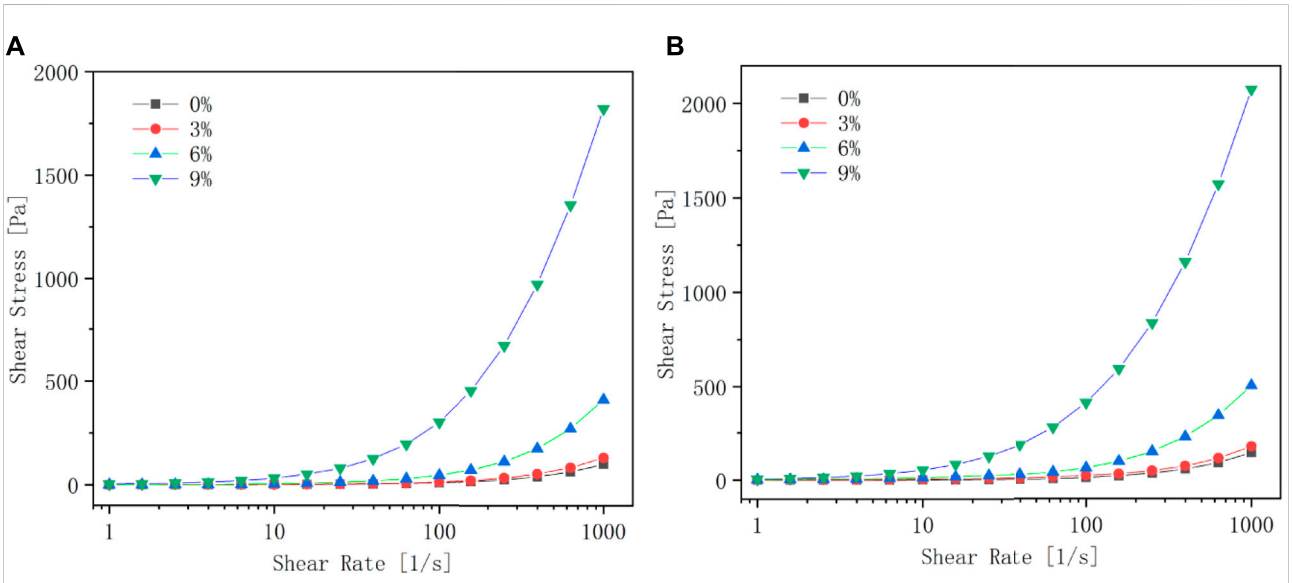

FIGURE 13
Flow curves of kerosene-based magnetic fluids with different evaporation rates under different magnetic field strengths. **(A)** is when the magnetic field strength is 0T; **(B)** is when the magnetic field strength is 0.2T.

Magnetic fluid seal pressure resistance

Through the calculation of the above pressure resistance formula, combined with the maximum magnetic induction intensity difference at the pole teeth obtained by simulation analysis, and the saturation magnetization value, the theoretical pressure resistance value of kerosene-based magnetic fluid with different evaporation rates can be obtained, and the actual pressure

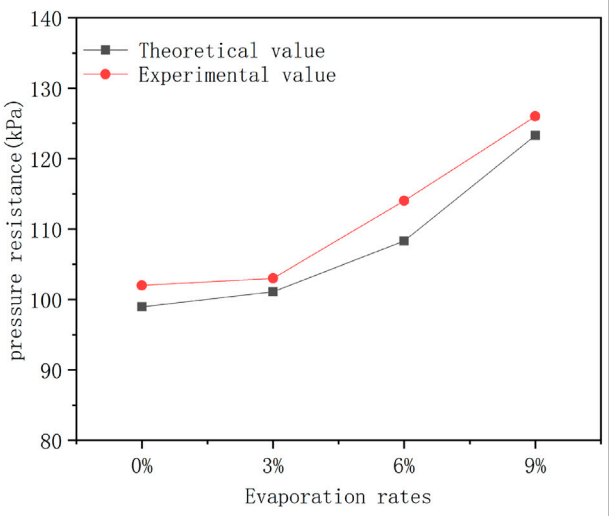

FIGURE 14
Different evaporation rate kerosene magnetic fluid withstand pressure.

resistance can be obtained through experiments. The comparison between the theoretical withstand pressure value and the actual withstand pressure value is shown in Figure 14.

It can be obtained that the actual withstand pressure value of all samples is larger than the theoretical withstand pressure value. This is because during the experiment, the magnetic fluid is blown to the next pole piece to form a new sealing ring, which increases a certain pressure resistance capacity, so the actual pressure resistance will be larger than the theoretical pressure resistance. In addition, it is not difficult to see that with the increase of the evaporation rate of the magnetic fluid, the pressure resistance value of the seal also increases.

According to the above analysis, although evaporation will reduce the magnetic fluid in the sealing gap, it will also increase the saturation magnetization of the magnetic fluid. According to the magnetic fluid sealing theory, it can be known that the sealing pressure value will increase accordingly, and the experiment also proves the correctness of the theory.

Conclusion

1) By characterizing the magnetization properties of magnetic fluids with different evaporation rates, it is obtained that the magnetic fluids with higher evaporation rates have higher saturation magnetization. To a certain extent, the pressure resistance value of the magnetic fluid seal is increased.
2) Characterize the rheological properties of magnetic fluids with different evaporation rates, including the flow curves and magnetic viscosity curves of kerosene-based magnetic fluids with different evaporation rates. The analysis shows that evaporation has a great influence on viscosity. The greater the evaporation rate, the greater the viscosity and the worse the fluidity. This will increase the starting torque of the magnetic fluid rotary seal.
3) Through the static sealing experiment of magnetic fluid with different evaporation rates, the experimental withstand pressure value is larger than the theoretical withstand pressure value, because in the withstand pressure experiment, the magnetic fluid is blown to the next stage pole piece, which increases the number of sealing rings, the withstand pressure increases accordingly. Although evaporation will reduce the magnetic fluid at the sealing gap, the experimental results show that the withstand pressure will increase, which proves the correctness of the theory and the feasibility of simulation.

Data availability statement

The original contributions presented in the study are included in the article/supplementary material, further inquiries can be directed to the corresponding authors.

Author contributions

DL was in charge of the whole trial; WY wrote the manuscript and did laboratory analyses; GZ, DW, and ZZ contributed to the revision of the manuscript.

Funding

Supported by National Natural Science Foundation of China (Grant Nos. 51735006, 51927810, U1837206), and Beijing Municipal Natural Science Foundation of China (Grant No. 3182013).

Conflict of interest

The authors declare that the research was conducted in the absence of any commercial or financial relationships that could be construed as a potential conflict of interest.

Publisher's note

References

Chen, J. W., Li, D. C., and Hao, D. (2018). Investigation on the influence of temperature on starting torque of magnetic fluid seal. *J. Magnetics* 23, 436–441. doi:10.4283/jmag.2018.23.3.436

Chen, Y. B. (2019). *Research on magnetic fluid sealing under high speed*. [Beijing]: University of Science and Technology Beijing. (in Chinese).

Cheng, Y. H., Li, D. C., and Li, Z. K. (2021). Influence of rheological properties on the starting torque of magnetic fluid seal. *IEEE Trans. Magn.* 57, 1–8. doi:10.1109/tmag.2019.2934716

Chi, C. Q. (2011). *Physics basis and application of ferrofluid*. Beijing: Beihang University Press. (in Chinese).

Chi, C. Q., Wang, Z. S., and Zhao, P. Z. (1993). *Ferrohydrodynamics*. Beijing: Beihang University Press. (inChinese).

He, X. Z., Miao, Y. B., Wang, L., and Li, D. C. (2019). A brief description of the progress of magnetic fluid sealing liquid technology. *J. Vac. Sci. Technol.* 39, 361–366. (in Chinese).

He, X. Z., Wang, L., Yu, J., and Li, D. C. (2019). Influence of gravity on the anti-pressure ability of magnetic fluid seal. *Int. J. Appl. Electromagn. Mech.* 60, 21–32. doi:10.3233/jae-180054

Li, D. C. (2003). *Theory and application of magnetic fluid*. Beijing: Science Press. (in Chinese).

Li, D. C. (2010). *Theory and application of magnetic fluid seal*. Beijing: Science Press. (in chinese).

Li, Z. X., Li, S. X., Wang, X., and Li, D. (2021). Numerical simulation and experimental study on magnetorheological fluid seals with flexible pole pieces. *IEEE Trans. Magn.* 57, 1–7. doi:10.1109/tmag.2021.3094868

Matuszewski, L., and Bela, P. (2021). New designs of magnetic fluid seals for reciprocating motion. *Pol. Marit. Res.* 28, 151–159. doi:10.2478/pomr-2021-0057

Niu, S. F. (2021). *Theoretical and experimental research on key issues of magnetic fluid seal for electro-optical pod*. [Beijing]: Beijing Jiaotong University. (in chinese).

Parmar, S., Upadhyay, R. V., and Parekh, K. (2021). Optimization of design parameters affecting the performance of a magnetic fluid rotary seal. *Arab. J. Sci. Eng.* 46, 2343–2348. doi:10.1007/s13369-020-05094-1

Rosensweig, R. E. (2002). *Ferrohydrodynamics*. NewYork: Dover Publications.

Wang, Z. Z. (2019). *Research on magnetic fluid sealing liquid medium*. [Beijing]: Beijing Jiaotong University. (in Chinese).

Yang, X. L., and Li, D. C. (2016). Experimental investigation of diverging stepped magnetic fluid seals with large sealing gap. *Int. J. Appl. Electromagn. Mech.* 50, 407–415. doi:10.3233/jae-150117

Yu, W. J., Li, D. C., Li, Y. W., Zhang, Z. L., and Dong, J. H. (2021). Design of small magnetic fluid seal for vacuum coating machine. *J. Beijing Jiaot. Univ.* 45, 124–129. (inChinese). doi:10.11860/j.issn.1673-0291.20210025

Yu, W., Li, D., and Niu, S. (2022). An experimental validation study on ferrofluid evaporation. *Chin. J. Mech. Eng.* 35, 50. doi:10.1186/s10033-022-00721-4

Yuan, F., Wang, S. Q., Li, D. C., Chen, D., Di, N. N., and Li, W. Y. (2022). Theoretical research on new structure and pressure resistance performance of magnetic fluid seals. *Chin. J. Mech. Eng.* 58, 213–220. (in Chinese).

Zhang, T., Li, D. C., and Li, Y. W. (2022). Structural design and optimization of combined seal of magnetic fluid seal and labyrinth seal. *Chin. J. Mech. Eng.*, 1–10.

Zhang, Y. J., Chen, Y. B., Li, D. C., Yang, Z., and Yang, Y. (2019). Experimental validation and numerical simulation of static pressure in multi-stage ferrofluid seals. *IEEE Trans. Magn.* 55, 1–8. doi:10.1109/tmag.2017.2744606

Zou, J. B., Li, X. H., Lu, Y. P., and Hua, J. H. (2002). Numerical analysis on the action of centrifuge force in magnetic fluid rotating shaft seals. *J. Magnetism Magnetic Mater.* 252, 321–323. doi:10.1016/s0304-8853(02)00672-8

frontiers | Frontiers in Materials

TYPE Original Research
PUBLISHED 05 August 2022
DOI 10.3389/fmats.2022.957446

OPEN ACCESS

EDITED BY
Yancheng Li,
Nanjing Tech University, China

REVIEWED BY
Wenling Zhang,
Nanjing University of Science and Technology, China
Xufeng Dong,
Dalian University of Technology, China

*CORRESPONDENCE
Decai Li,
lidecai@mail.tsinghua.edu.cn

SPECIALTY SECTION
This article was submitted to Smart Materials,
a section of the journal
Frontiers in Materials

RECEIVED 31 May 2022
ACCEPTED 27 June 2022
PUBLISHED 05 August 2022

CITATION
Chen N, Li D, Xue J, Yin Y and Li Y (2022), Magnetic fluid sealing status estimation based on acoustic emission monitoring. *Front. Mater.* 9:957446.
doi: 10.3389/fmats.2022.957446

Magnetic fluid sealing status estimation based on acoustic emission monitoring

Nuo Chen[1], Decai Li[1]*, Jinyu Xue[2], Yuan Yin[1] and Yanwen Li[1]

[1]State Key Laboratory of Tribology, Tsinghua University, Beijing, China, [2]School of Mechanical, Electronic and Control Engineering, Beijing Jiaotong University, Beijing, China

The aim of the study was to analyze acoustic emission (AE) signals generated in different magnetic fluid sealing processes to estimate the status of the seal. Based on a magnetic fluid rotary sealing experimental setup, the AE sensor is respectively attached to the shell at the corresponding position of the seal, and the external pressure is applied to the magnetic fluid seal by a gas supply system. As the pressure gradually increases, the magnetic fluid sealing rings under different pole teeth are gradually broken, and processes such as pressure transfer between the seal stages occur. These processes generate different AE signals, which are collected by the sensors. The results show that the root-mean-square values of AE signals generated at the moment of sealing failure are different from those generated before and after. At the same time, by analyzing the characteristic values of AE signals generated in the whole process, we can infer the time when the rupture begins under different pole pieces and further estimate the status of the magnetic fluid seal. For the first time, this research demonstrates the experimental and data analysis procedures of AE technology for magnetic fluid seals.

KEYWORDS

magnetic fluid, seal, acoustic emission, sealing failure, pressure transfer

1 Introduction

As a new type of functional material, magnetic fluid has unique properties with both magnetism and fluidity (Odenbach, 2003; Kadau et al., 2016). Therefore, it has been widely used in various fields like tilt measurement sensors (Medvegy et al., 2017) and rotary seals (Huang and Rui, 2011; Wang et al., 2017; Parmar et al., 2018; Li et al., 2021). Compared with traditional sealing, the biggest advantage of magnetic fluid seals is the zero-leakage characteristics, so it plays a very important and irreplaceable role in many fields.

To improve the pressure resistance and durability of the magnetic fluid seal, the sealing gap should be very small, which is generally about 0.1–0.3 mm. Once injected into the structure, it is difficult to estimate the working status of the magnetic fluid in the gap and then predict the failure. This hinders the further application of magnetic fluid seals. Therefore, it is imperative to find a non-destructive testing method to estimate the sealing status of the magnetic fluid seal.

For now, there are few related studies. In 1999, Odenbach S used magnetic small angle neutron scattering (MSANS) to detect the flow pattern of the concentrated magnetic fluids (Odenbach et al., 1999). In 2010, A García-Arribas described a microfluidic device for the determination of the concentration of magnetic micro and nanoparticles, under a continuous flow of the carrier fluid, by means of the Giant Magneto-Impedance effect (Garcia-Arribas et al., 2010). These methods can be used to estimate the status of the magnetic fluid but cannot be applied to the sealing fields. In 2014, Weiming Gao used X-rays and CT to detect the distribution of the magnetic fluid in the sealing gap, but the results were not good enough (Gao, 2014).

AE method is a non-destructive monitoring method that can provide real-time information about changes in the internal structure of materials. This method can not only detect the deformation and fracture of materials but also collect information regarding the second type of acoustic emission sources as well, such as friction and collision (Fan et al., 2020). Thus, it has been well used in the field of mechanical seals (Li et al., 2016; Yin et al., 2018; Yin et al., 2020). It is proved that as long as sliding occurred between two rings, it becomes the major contributor of AE signals (within particular frequency bands) from a tribo-pair. So the RMS of AE signals can represent the instant severity of friction.

Studies have been carried out to prove that such processes such as bubble leakage, magnetic fluid barriers rupture, airflow, and pressure transfer during the sealing failure (Pinkus, 1982; Szczech, 2018; Szczech, 2019; Zhou et al., 2021; Guan and Yang, 2022; Sun et al., 2022). We believe these processes will theoretically generate different AE signals compared to the fully-sealed periods, which can be collected and analyzed. So, we did this research, applied the AE technology to magnetic fluid seals for the first time, and achieved some good results accordingly.

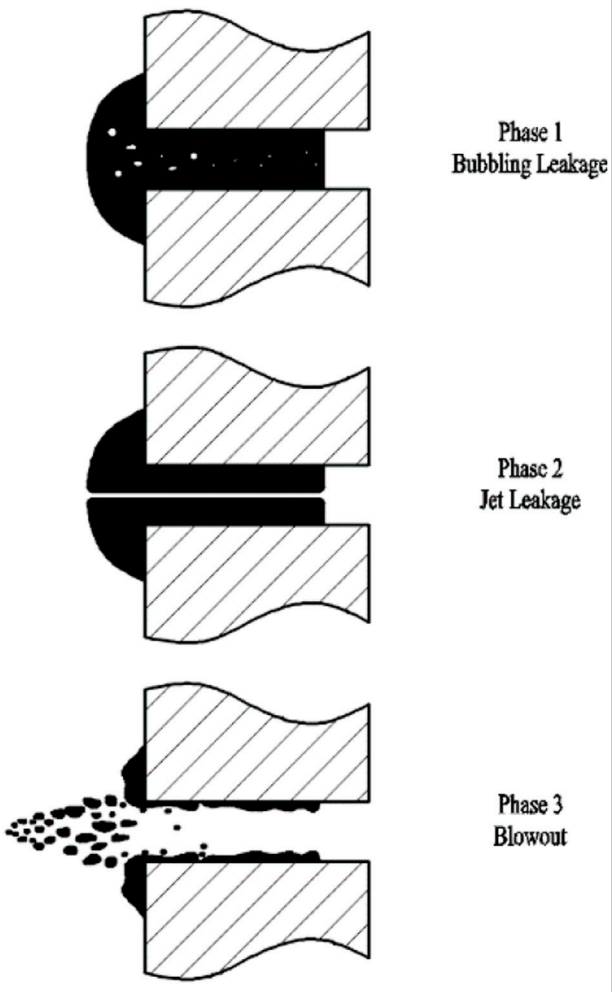

FIGURE 1
Phases in magnetic fluid sealing failure.

2 Magnetic fluid rotary sealing theory

The magnetic fluid in the seal is in the magnetization saturation in most cases. In addition, if the influence of the gravitational field and the surface tension forces are ignored, the critical pressure for one stage can be determined by:

$$\Delta p_{cr} = \int_{H_{min}}^{H_{max}} \mu_0 M dH \approx M_s (B_{max} - B_{min}). \quad (1)$$

Here, $H_{\min}$ and $H_{\max}$ are the minimum and maximum magnetic field strengths. μ_0 is the permeability of the vacuum. $\boldsymbol{M}$ is the magnetization of the magnetic fluid. M_s is the saturation magnetization of magnetic fluid. $\boldsymbol{N}$ is the number of pole teeth. $B_{\max}$ and $B_{\min}$ are the maximum magnetic flux density.

However, the critical pressure is limited when the seal has only one stage, so most of the seal applications use a multi-stage structure. The total sealing capability of the magnetic fluid seal can be approximately expressed as follows:

$$p_{cr} = \sum_{i=1}^{N} \Delta p_{cr_i}. \quad (2)$$

Furthermore, Marcin Szczech had performed a series of tests on a transparent model of a multistage magnetic fluid seal (Szczech, 2018). He thought a leak in the magnetic fluid would occur when applied pressure (ΔP) exceeded the critical pressure of the first stage and would cause the second stage to be pressurized. If the upstream pressure further increased, the fluid in the second stage (as well as in the first stage) would spring a leak, which would cause the next stage to be pressurized. These processes would continually happen until all stages were loaded. Oscar Pinkus figured out that three distinctive phases would occur during the failure of a magnetic fluid seal, which was as follows and shown in Figure 1 (Pinkus, 1982):

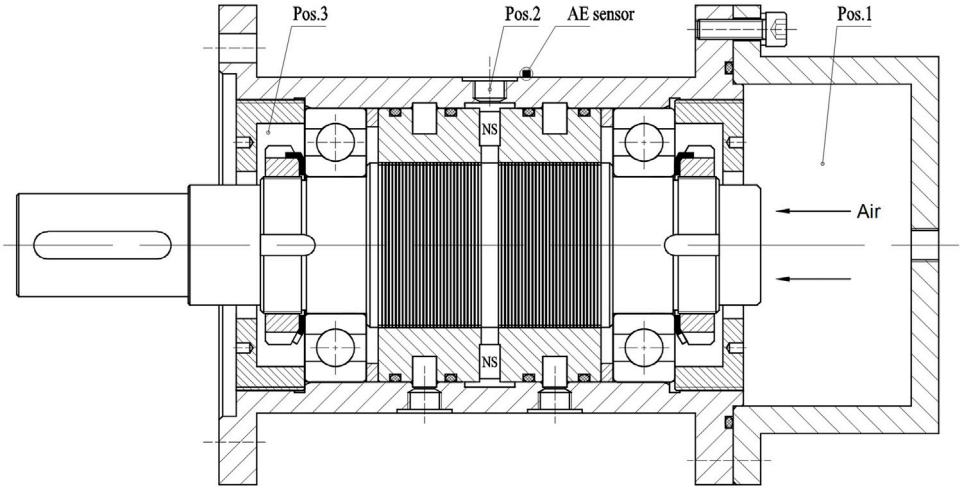

FIGURE 2
Structure of the multi-stage seal used in the research.

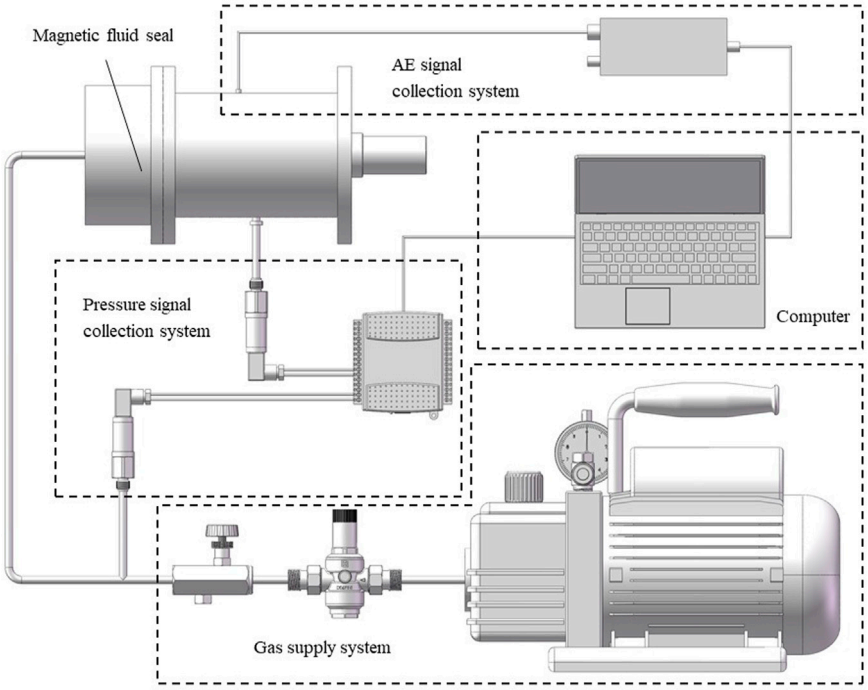

FIGURE 3
Schematic diagram of the experimental setup.

Phase 1: When the ΔP exceeded the critical pressure of the seal, bubbles of the sealed air began to percolate to the low-pressure side. If the ΔP was raised, the flowing rate of the bubbles would increase as well.

Phase 2: When ΔP was raised further, the bubbles merged into a thin jet-like passage through which steady leakage took place.

Phase 3: When ΔP was raised still further, particles of the magnetic fluid began to be hung out from the gap, until, at

sufficiently high ΔP, the whole fluid film was ejected, and the seal was destroyed.

3 Experimental setup and method

A multi-stage seal is used in this work. As shown in Figure 2, the magnetic fluid seal consists of a rotary shaft, two pole pieces, a permanent magnet, a shell, and some other parts. The material of the permanent magnet is Nd-Fe-B with an N35 grade. The shell was made of 304 stainless steel, of which permeability is approximately equal to vacuum permeability. The magnetic fluid was synthesized by our laboratory. The materials of the pole pieces and the rotary shaft are 2Cr13 stainless steel with high magnetic permeability. There are 30 pole teeth evenly distributed on the rotating shaft at the corresponding position of each pole piece, which means there are 60 pole teeth at all. The diameter of the shaft is 50 mm. The gap height is 0.1 mm. The distance from the gap to the outer surface of the shell is approximately 25 mm where we put our AE sensor.

As shown in Figure 3, the experimental setup had the following parts: gas (air) supply system, pressure signal collection system, AE signal collection system, the magnetic fluid seal, and the computer.

During the test, compressed air is delivered from a high-pressure air cylinder. A pressure-reducing valve is installed at the pressure inlet to create a stable high-pressure environment. Then, the airflow rate is regulated by a throttle valve. The sealing region is divided into 3 chambers by two pole pieces. The right chamber (Pos.1) is connected to the pressure inlet, and the left chamber (Pos.3) is connected to the atmosphere. Two sensors are equipped to measure the air pressure. The sensor labeled as P1 measures the air pressure in the right chamber (Pos.1). The P2 sensor measures the pressure between seal stages 1 and 2 (Pos.2). The diameter of the pressure measuring hole is 1.5 mm and simulations show that the hole has little influence on the magnetic field distribution. The measurement range is from 0 to 100 kPa, and the measurement accuracy is 0.5%. The pressure signal is sent to the acquisition card (National Instruments), which communicates with the computer using LabVIEW software.

A miniature sensor, PICO, produced by Physical Acoustics Corporation, was employed in the AE measuring system. The sensor was mounted to the shell at the corresponding position of the seal, allowing the clear monitoring of AE signals from the gap and concealing AE signals from other parts of the seal. The signals were acquired by AE win software provided by the same company. An AE wave was recorded every 1.3 ms for further processing. Each AE wave contained 1,024 sampling points at a sampling rate of 2000 kHz. In this experiment, the obtained acoustic emission signal was continuous. Therefore, we used the root mean square (RMS) to represent the energy of the AE signal. The calculation formula is expressed as follows:

$$RMS = \sqrt{\frac{1}{M}\sum_{i=1}^{M} U_i^2}. \quad (3)$$

During the research presented in this article, the rotational speed of the seal keeps zero. Tests under dynamic situations will be conducted in future work.

4 Results and discussion

In the earlier stages of the magnetic fluid seal, the air pressure kept increasing. After the failure occurred the air pressure began to decrease. The pressure curves obtained throughout the whole period are shown in Figure 4A, which includes the first-stage-sealed period, second-stage-sealed period, and full-failure period. The AE RMS curves are shown in Figure 4B. To smooth out short-term fluctuations, a moving average method was implemented for AE signals.

It can be seen from Figure 4A, that before time t1, the air pressure in the right chamber increased with time. The pressure difference between the two sides of the fluid ring-free surface under the first tooth also increased. When the pressure reached the critical value, the magnetic fluid barrier ruptured, which led to the flow of compressed air through the first tooth and brought some pressure to the second tooth. Then, some of the blew-out magnetic fluid moved back to the gap under the first tooth because of the magnetic force. The magnetic fluid barrier recovered in a short time. But soon it ruptured again. With the right chamber's air pressure keeping increase, the same processes like rupture and recovery under other teeth continuously happened. Until time t1, all the 30 barriers under the first pole piece ruptured and the compressed air flowed from the right chamber into the middle chamber, which led to a rapid increase in pressure in the middle chamber. It meant the seal turned to the second-stage-sealed period from the first-stage-sealed period. After the big rupture, the pressure difference between the two chambers decreased because the pressure in the middle chamber increased with the air inflow. Because of the self-recovering property of the magnetic fluid, the first pole piece regained the ability to hold some pressure. At time t2, another big rupture was observed. Meanwhile, the air pressure in the right chamber continuously increased. During the period from t2 to t3, all magnetic fluid barriers under the first pole piece ruptured and recovered several times, and the pressure increased slowly in the middle chamber. After time t3, the inlet pressure reached the critical value of the seal, all fluid barriers ruptured entirely. The leakage channels in the magnetic fluid barriers connectingthe low-pressure side and high-pressure side. At the same time, the pressures in different chambers decreased rapidly.

It can be seen from Figure 4B, that throughout the whole period of the magnetic fluid seal, the energy of the AE signals continually increased before the rupture occurred and then decreased. In our

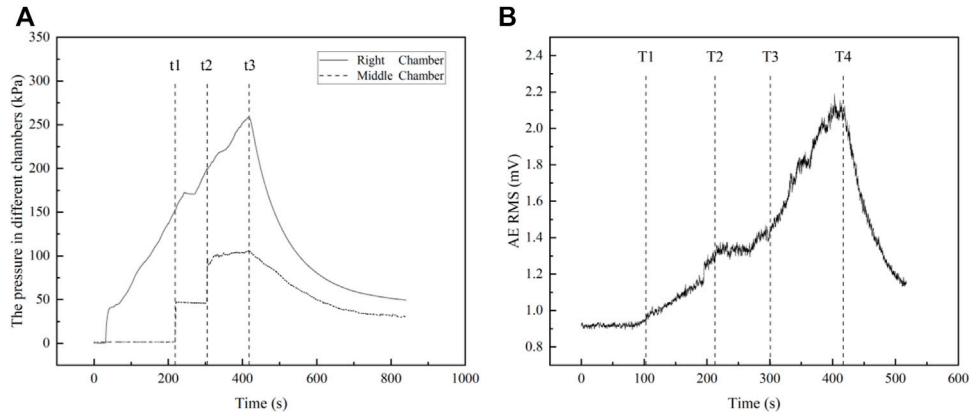

FIGURE 4
(A) Pressure curves; **(B)** AE RMS curves.

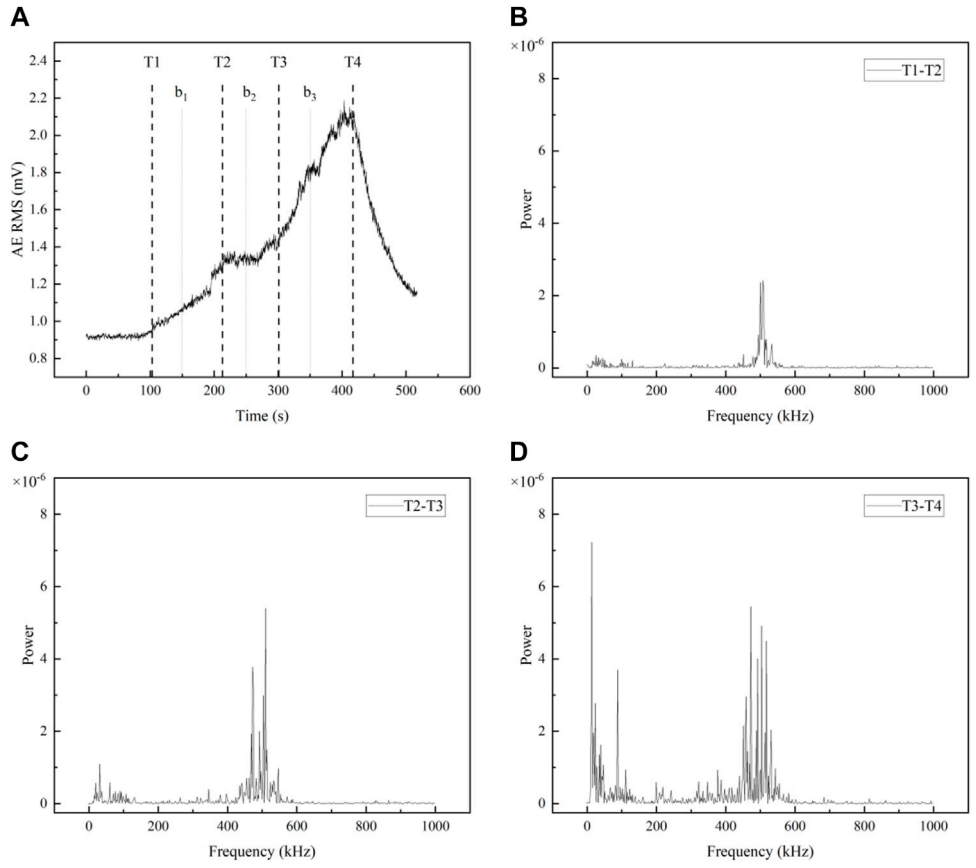

FIGURE 5
(A) AE RMS curves; **(B–D)** Frequency distributions of AE RMS in different periods.

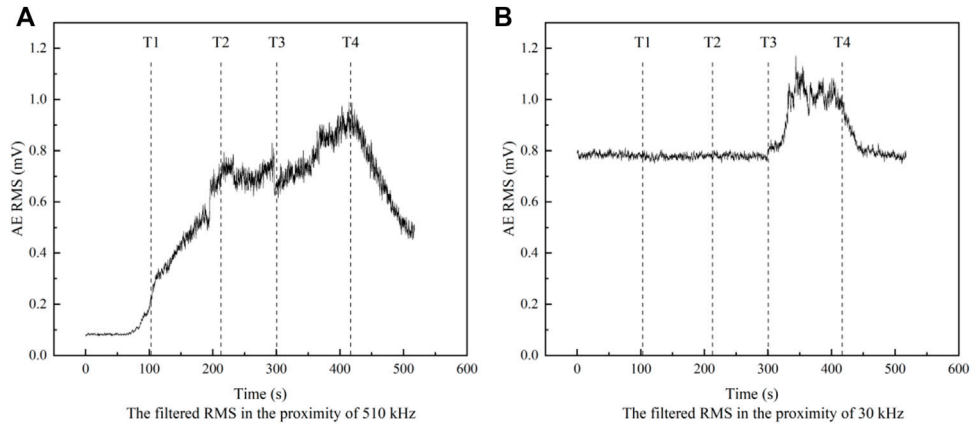

FIGURE 6
Filtered RMS in the proximity of **(A)** 510 and **(B)** 30 kHz.

case, AE signals came from three parts: the magnetic fluid seal, the gas supply system, and the environment. After we set down the outlet pressure of the air pump and the gas flow rate controlled by the throttle valve, the gas supply system remained in a stable state without any change during the whole process. At the same time, we chose to complete the experiment in a noiseless environment, and there were no sudden AE signals caused by human factors. Therefore, the reason for the change of the AE signals could only come from the process that occurred inside the magnetic fluid seal. When the air pressure gradually increased and exceeded the critical pressure, the magnetic fluid barrier under the pole piece would rupture and the air would flow, which would lead to the increase of the AE signals. For further research, we analyzed the frequency spectrums of a few AE waves from different periods, which were illustrated in Figure 5.

They imply that the AE power is concentrated on several fixed bands. The frequency distribution of the AE waves at different times had different modes. It can be seen from Figure 5B, that the AE power tended to concentrate in the proximity of 510 and 30 kHz. Then, the time series of RMS before filtering and after filtering (with a band-pass filter of $510 \pm 40\,kHz$ and a lowpass filter) could represent the dynamic fluctuations of AEs, as shown in Figure 6. Different features were observed in the sequential status of the whole sealing processes, as follows:

4.1 Fully-sealed period

Before time T1, the air pressure was not high enough to blow the magnetic fluid out from the pole tooth. The seal was kept full and no rupture occurred. The filtered RMS in the proximity of 510 kHz kept stable at a low value. The filtered RMS in the proximity of 30 kHz stayed at a relatively high value, which was obviously caused by the ambient noise.

4.2 First-stage-seal-failure period

During the period between time T1 and T2, because of the increasing air pressure, some of the magnetic fluid barriers ruptured and led to the flow of compressed air through the teeth, as described before. So, the RMS began to increase along with the increasing rupture level. The filtered RMS in the proximity of 510 kHz had the same trend. While the filtered RMS in the proximity of 30 kHz remained unchanged. Therefore, we believed the AE signals in the proximity of 510 kHz reflected the rupture under the first pole piece.

4.3 Second-stage-fully-sealed period

Before time T3, the first pole piece regained the ability to hold some pressure. The pressure difference between the middle and left chambers wasn't big enough to cause a failure so the seal in the second stage remained full. The filtered RMS kept stable in a relatively high value in the proximity of 510 kHz due to the ruptures under the first stage and remained unchanged in the proximity of 30 kHz.

4.4 Second-stage-failure period

At time T3, the first-stage seal failed again and a lot of air flew into the middle chamber, which caused the ruptures under the second stage. The filtered RMS in the proximity of both 510 and 30 kHz began to increase. Considering this, we believed the AE signals in the proximity of 30 kHz contained the information of the rupture under the second pole piece in addition to the ambient noise.

4.5 Full-failure period

After time T4, all fluid barriers ruptured entirely. The pressures in different chambers decreased and the filtered RMS in the proximity of both 510 and 30 kHz decreased as well.

Comparing the sealing status obtained by the analysis of the pressure and AE signals, the processes are barely the same and the latter is even more detailed. In our case, the increase of the filtered RMS in high frequency can indicate when the first-stage seal begins to fail, and the increase in the filtered RMS in low frequency can indicate when the second-stage seal begins to fail. Therefore, the way we estimate magnetic fluid sealing status based on acoustic emission monitoring works.

5 Conclusion

In this article, the method using acoustic emission monitoring to estimate the magnetic fluid sealing status has been studied by experiments. The conclusions and recommendations are as followed:

1). The power of AE signals is concentrated in several fixed frequency bands with different modes at an acoustic timescale. Therefore, we can obtain the different information carried by corresponding frequency bands by performing spectrum analysis on the RMS of AE signals. And the different information can reflect the different statuses of the magnetic fluid seal.

2). In this case, the increase of the filtered RMS in high frequency which is in the proximity of 510 kHz can indicate when the first-stage seal begins to fail. The increase of the filtered RMS in low-frequency proximity of 30 kHz can indicate when the second-stage seal begins to fail.

3). In further research, the effect of rotational speed, shaft diameter, temperature, the structure of the seal, and other factors on AE signals will be studied.

Data availability statement

The raw data supporting the conclusion of this article will be made available by the authors, without undue reservation.

Author contributions

NC, DL, and JX contributed to the conception and design of the research. NC designed the experiment. NC and JX performed the statistical analysis. NC wrote the first draft of the manuscript. DL, YY, and YL contributed to manuscript revision, read, and approved the submitted version.

Funding

The work was supported by the National Key R&D Program of China (grant no. 2020YFB2006900) and the National Natural Science Foundation of China (grant nos. 51927810, U1837206, and 51735006).

Conflict of interest

The authors declare that the research was conducted in the absence of any commercial or financial relationships that could be construed as a potential conflict of interest.

Publisher's note

All claims expressed in this article are solely those of the authors and do not necessarily represent those of their affiliated organizations, or those of the publisher, the editors, and the reviewers. Any product that may be evaluated in this article, or claim that may be made by its manufacturer, is not guaranteed or endorsed by the publisher.

References

Fan, W. J., Huang, W. F., Liu, Y., Yin, Y., Liu, X. F., Wang, Y. M., et al. (2020). State evolution of dry gas seal during repeated start-stop operation using acoustic emission method. *Tribol. Trans.* 63 (1), 173–181. doi:10.1080/10402004.2019.1674984

Gao, W. (2014). *Research on the seal design and properties of magnetic fluid in the space environment [M.S]*. Beijing: Beijing Jiaotong University.

Garcia-Arribas, A., Martinez, F., Fernandez, E., Ozaeta, I., Kurlyandskaya, G., Svalov, A., et al. (2010). GMI magnetic-particle concentration detection in continuous flow. *Procedia Eng.* 5, 1324–1327. doi:10.1016/j.proeng.2010.09.358

Guan, Y., and Yang, X. (2022). Experimental study on the pressure transfer mechanism of embedded magnetic fluid seals. *Tribol. Trans.* 2022, 1–10. doi:10.1080/10402004.2022.2066039

Huang, J. F., and Rui, Y. N. (2011). Design of magnetic fluid sealed structure for the high-speed non-woven loom needle spindle. *Appl. Mech. Mater* 43, 519–524. doi:10.4028/www.scientific.net/amm.43.519

Kadau, H., Schmitt, M., Wenzel, M., Wink, C., Maier, T., Ferrier-Barbut, I., et al. (2016). Observing the Rosensweig instability of a quantum ferrofluid. *Nature* 530 (7589), 194–197. doi:10.1038/nature16485

Li, X. H., Fu, P., Chen, K., Lin, Z. B., and Zhang, E. Q. (2016). The contact state monitoring for seal end faces based on acoustic emission detection. *Shock Vib.* 2016, 1–8. doi:10.1155/2016/8726781

Li, X. R., Li, Z. G., Zhu, B. S., Cheng, J., Li, W. X., and Yuan, J. Y. (2021). Optimal design of large gap magnetic fluid sealing device in a liquid environment. *J. Magn. Magn. Mater* 540, 168472. doi:10.1016/j.jmmm.2021.168472

Medvegy, T., Molnar, A., Molnar, G., and Gugolya, Z. (2017). Analysis of a ferrofluid core differential transformer tilt measurement sensor. *J. Magn. Magn. Mat.* 428, 189–193. doi:10.1016/j.jmmm.2016.12.026

Odenbach, S. (2003). Ferrofluids - Magnetically controlled suspensions. *Colloids Surfaces A Physicochem. Eng. Aspects* 217 (1-3), 171–178. doi:10.1016/s0927-7757(02)00573-3

Odenbach, S., Gilly, H., and Lindner, P. (1999). The use of magnetic small angle neutron scattering for the detection of flow profiles in magnetic fluids. *J. Magn. Magn. Mat.* 201, 353–356. doi:10.1016/s0304-8853(99)00032-3

Parmar, S., Ramani, V., Upadhyay, R. V., and Parekh, K. (2018). Design and development of large radial clearance static and dynamic magnetic fluid seal. *Vacuum* 156, 325–333. doi:10.1016/j.vacuum.2018.07.055

Pinkus, O. (1982). Model testing of magnetic-fluid seals. *A S L E Trans.* 25 (1), 79–87. doi:10.1080/05698198208983068

Sun, R., Li, D. C., and Jin, L. C. (2022). Experimental and theoretical investigation on magnetic fluid seal in capillary tube. *J. Magn. Magn. Mat.* 546, 168869. doi:10.1016/j.jmmm.2021.168869

Szczech, M. (2018). Experimental study on the pressure distribution mechanism among stages of the magnetic fluid seal. *IEEE Trans. Magn.* 54 (6), 1–7. doi:10.1109/tmag.2018.2816567

Szczech, M. (2019). The loss of continuity in a liquid ring formed by a magnetic fluid. *IEEE Trans. Magn.* 55 (9), 1–8. doi:10.1109/tmag.2019.2916322

Wang, Z. Z., Li, D. C., and Zhou, J. (2017). Non-uniform distribution of magnetic fluid in multistage magnetic fluid seals. *J. Magn.* 22 (2), 299–305. doi:10.4283/jmag.2017.22.2.299

Yin, Y., Huang, W. F., Liu, X. F., Liu, Y., Wang, Z. X., Fan, W. J., et al. (2018). Analysis of the dynamic friction of a gas face seal based on acoustic emissions. *Tribol. Lett.* 66 (3), 85. doi:10.1007/s11249-018-1037-7

Yin, Y., Liu, X. F., Huang, W. F., Liu, Y., and Hu, S. T. (2020). Gas face seal status estimation based on acoustic emission monitoring and support vector machine regression. *Adv. Mech. Eng.* 12 (5), 168781402092132. doi:10.1177/1687814020921323

Zhou, H. M., Chen, Y. B., Zhang, Y. J., and Li, D. C. (2021). Simulation and experimental study on pressure transfer mechanism in multitooth magnetic fluid seals. *Tribol. Trans.* 64 (1), 31–41. doi:10.1080/10402004.2020.1777361

frontiers | Frontiers in Materials

ORIGINAL RESEARCH
published: 05 August 2022
doi: 10.3389/fmats.2022.932662

Research on a Large Diameter Magnetic Fluid Seal With Thin-Wall Parts

Yunqi Guo[1], Decai Li[1,2], Guobao Zang[1], Zhiqiang Qi[1] and Zhili Zhang[1]*

[1]School of Mechanical, Electronic and Control Engineering, Beijing Jiaotong University, Beijing, China, [2]State Key Laboratory of Tribology, Department of Mechanical Engineering, School of Mechanical Engineering, Tsinghua University, Beijing, China

Magnetic fluid seal is a new type of sealing method, which has been applied in many fields. For some fields, such as aviation and aerospace, high sealing performance, large shaft diameter, and small design space are required, which brings difficulties to the sealing design. Therefore, it is necessary to study a large diameter magnetic fluid seal with thin-wall parts. In this article, the effects of seal clearance and shaft deflection on the magnetic field distribution of magnetic fluid seal are analyzed by the finite element method. At the same time, the force of seal shaft in the assembly process is also simulated. The influence of the amount of magnetic fluid on the pressure resistance is analyzed. The low-temperature starting torque and high-temperature pressure resistance of magnetic fluid seal are experimentally studied, and the optimal injection amount of magnetic fluid is obtained. The research content of this article can be used as a reference for the design of a large diameter magnetic fluid seal with thin-wall parts.

Keywords: magnetic fluid, magnetic fluid seal, large diameter, thin-wall parts, finite element simulation

OPEN ACCESS

Edited by:
Yang Yu,
Western Sydney University, Australia

Reviewed by:
Stefano Giordano,
Institut d'électronique, de microélectronique et de nanotechnologie (IEMN), France
Yoshinori Mitamura,
Hokkaido University, Japan

****Correspondence:***
Decai Li
lidecai@mail.tsinghua.edu.cn

Specialty section:
This article was submitted to Smart Materials, a section of the journal Frontiers in Materials

Received: *30 April 2022*
Accepted: *22 June 2022*
Published: *05 August 2022*

Citation:
Guo Y, Li D, Zang G, Qi Z and Zhang Z (2022) Research on a Large Diameter Magnetic Fluid Seal With Thin-Wall Parts. Front. Mater. 9:932662. doi: 10.3389/fmats.2022.932662

INTRODUCTION

Magnetic fluid (MF), also known as ferrofluid, is a new type of smart material. It comprises magnetic particles with a diameter of about 10 nm, surfactants and base carrier liquid (Li et al., 2002; Li, 2010). It is characterized by both magnetism and fluidity, which makes it irreplaceable in engineering application.

Rheology is one of the hot topics of research on magnetic fluids; for example, magnetic fluids have a magnetoviscous effect that other fluids do not have. Odenbach et al. systematically studied the rheological properties of magnetic fluid. Under the constant shear rate, the viscosity of the magnetic fluid increases with the increase of the magnetic field. They also proposed the influence of particle size on viscosity and found that the larger the particle size of magnetic particles in magnetic fluid under magnetic field, the higher the viscosity (Odenbach and Störk, 1998; Odenbach, 2000). Shah et al. showed that magnetic particles with large particle size increase the yield stress of magnetic fluids (Shah et al., 2012). Li et al. studied the thixotropic yielding behavior of magnetic fluids with different particle volume concentrations for a long enough time (Li et al., 2019).

Magnetic fluid seal is one of the most successful applications of magnetic fluid, and magnetic fluid seal has the advantages of zero leakage and long service life. The performance of magnetic fluid seals is closely related to the rheological properties of the magnetic fluid itself. The study of the frictional torque of the seal and the starting torque of the seal is one of the hot spots of magnetic fluid seal research in recent years. Li Decai et al. studied the low-temperature large-diameter magnetic fluid rotary seal and investigated the low-temperature starting torque of the magnetic fluid seal with an

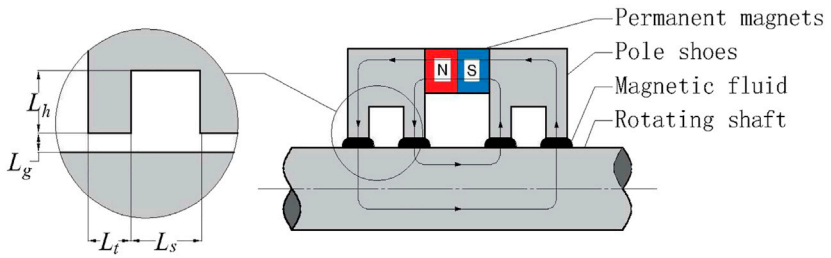

FIGURE 1 | Magnetic fluid seal structure.

operating temperature of −40°C. The factors affecting the starting torque of the seal were systematically studied (Li et al., 2001; Li et al., 2004). Chung kyun kim et al. investigated the frictional torque of magnetic fluid seal with different pole tooth shapes and parameters (Kim and Kim, 1997). He xinzhi et al. showed that the yield stress is one of the main factors affecting the pressure resistance and starting torque of magnetic fluid seal (He et al., 2015). Zhixin studied the variation of starting torque of the magnetic fluid seal with the resting time. It was found experimentally that the starting torque of the seal increased with the increase of the resting time and then tended to saturate (Li, 2002). They attributed the abovementioned phenomenon to the magnetic fluid film under the magnetic field in which the Cai et al. found that large magnetic particles and low temperature environment would change the microstructure of magnetic fluid and proposed a method to reduce the large size particles in the magnetic fluid (Cai and Xing, 2013). Chen et al. found that the magnetic fluid seal starting torque would increase sharply with the decrease of temperature through the experimental study (Chen et al., 2018). Cheng Yanhong et al. studied the factors affecting the starting torque of fluoroether oil-based magnetic fluid seals (Cheng et al., 2021). Thus, it can be seen that the starting torque of magnetic fluid seals is one of the key points of the seal research.

The magnetic fluid seal faces various design problems in the environment of limited space. For example, how to design the distribution of magnetic field strength, the influence of installation accuracy and deformation of thin-walled parts on the magnetic field, and the size of magnetic field force during the assembly should be studied on the design basis. In this article, the abovementioned problems are simulated by ANSYS Maxwell software. The simulation results show that the large-diameter thin-wall magnetic fluid sealing structure has guiding significance.

THEORY

Theory of Pressure Resistance of Magnetic Fluid Seal

Sealing is the most extensive and successful application of magnetic fluid in engineering. It has outstanding advantages of zero leakage, long service life, and high reliability, especially in vacuum containers, vacuum pumps, and other vacuum sealing effects. The basic structure of magnetic fluid seal is composed of rotating shaft, pole shoe, permanent magnets, and magnetic fluid, as shown in **Figure 1**.

Under the action of the magnetic field, the magnetic fluid forms liquid rings similar to "O" rings in the gap between the pole teeth and the shaft so as to play a sealing role.

The biggest difference between the magnetic fluid and other fluids is its response to the magnetic field, which is also reflected in the Bernoulli equation. The Bernoulli equation of general fluid is

$$P + \frac{1}{2}\rho V^2 + \rho g h = C. \quad [1]$$

Rosensweig derived the Bernoulli equation of magnetic fluid (Rosensweig, 1985; Li, 2010):

$$P + \frac{1}{2}\rho_f V^2 + \rho_f g h - \mu_0 \int_0^H M \mathrm{d}H = C. \quad [2]$$

Compared with the Bernoulli equation of general fluid, magnetic fluid has one more magnetic energy product term, so the flow characteristics of magnetic fluid are more complex than those of the general fluid, and it also has irreplaceable applications in engineering.

For the calculation of pressure resistance of magnetic fluid seal, it is assumed that the gravity and magnetic force of magnetic fluid are relatively small and can be ignored; The magnetic field line can be approximately replaced by an arc, and the equal magnetic field line coincides with the magnetic field line; the surface tension of the magnetic fluid is ignored. At this time, the pressure resistance of magnetic fluid single-stage seal is

$$\Delta P_{max} = \mu_0 \sum_{i=1}^{n} \int_{H\min}^{H\max} M \mathrm{d}H. \quad [3]$$

Torque of Magnetic Fluid Seal

Unlike traditional contact seals, such as packing seals and mechanical seals, magnetic fluid seals have no solid friction, so their friction torque is low and there is no wear. However, under the strong magnetic field or low temperature conditions, the rheological properties of magnetic fluid will change obviously, which affects the application of magnetic fluid seal. Therefore, it is necessary to study the torque of magnetic fluid seal. Magnetic fluids usually behave like H-B fluids under the action of a

magnetic field (Rosensweig, 1985; Yang et al., 2006; Hong et al., 2007; Li et al., 2019), so we assume that:

$$\tau = \tau_s + k\dot{\gamma}^n, \quad [4]$$

where τ is the shear stress, τ_s is the yield stress, $\dot{\gamma}$ is the shear rate, k is the consistency index, and n is the shear thinning exponent. k and n are the fitting parameters that can be obtained by experiments. The starting torque of the magnetic seal is

$$T = r_1 \cdot F = r_1 \cdot \tau \cdot S, \quad [5]$$

where F is the minimum value of the force that allows the shaft to rotate, r_1 is the radius of the rotating shaft, and S is the area of the contact surface between the shaft and the magnetic fluid. The surface area S is given by

$$S = 2\pi N r_1 \cdot l_t. \quad [6]$$

From **Eqs 4–6**

$$\begin{aligned} T &= r_1 \cdot \left(\tau_s + k\dot{\gamma}^n\right) \cdot 2\pi N r_1 \cdot l_t, \\ &= 2N\pi r_1^2 L_t \tau_s + 2\mathrm{N}\pi k r_1^2 L_t \left(\frac{r_1 \omega}{L_g}\right)^n, \\ &= 2N\pi r_1^2 L_t \tau_s + \frac{2\mathrm{N}\pi k \omega r_1^{(2+n)} L_t}{L_g^n}, \end{aligned} \quad [7]$$

where ω is the speed of the shaft, L_t is the width of the pole teeth, L_g is the width of the sealing gap, and N is the number of the pole teeth.

Force Calculation Method of Magnetic Fluid Seal Rotating Shaft

Electromagnetic calculation is a part of the design of magnetic fluid seal and one of the important bases for the normal operation of equipment. There are two classical electromagnetic force calculation methods, Maxwell stress method and the virtual displacement method. For the virtual displacement method, according to the principle of virtual work, the force on the object in the Q direction is (Yan et al., 2003; Mingli et al., 2007; Yang et al., 2009):

$$F = -\frac{\partial W_m}{\partial q}, \quad [8]$$

where W_m is the magnetic field energy of the system, $W_m = \int_v \int_0^B H^{\circ} \mathrm{d}B \mathrm{d}v$

For Maxwell's stress method, it usually starts from Maxwell's stress constant T.

$$f = \nabla \cdot \boldsymbol{T}. \quad [9]$$

T is a second-order tensor in which the elements are

$$\begin{aligned} T_{ij} &= H_i B_j - \delta_{ij} w_m, \\ \delta_{ij} &= \begin{cases} 1 & i = j \\ 0 & i \neq j \end{cases}, \end{aligned} \quad [10]$$

where δ_{ij} is the Kronecker's operator and w_m is the magnetic co-energy density.

Then, the combined force acting on the magnetic mass is

$$F = \int_v \nabla \cdot T \mathrm{d}v = \oint_s T \mathrm{d}S, \quad [11]$$

where S is any one of the closed surface surrounding the magnetic mass, S is usually set in the air around the magnetic mass, and for a two-dimensional problem, this area fraction is reduced to a closed curve, and the combined force F can be expressed as

$$\boldsymbol{F} = \oint_l \left[(B_n H_t)\boldsymbol{t} + \frac{1}{2}\left(\frac{1}{\mu_0} B_n^2 - \mu_0 H_t^2\right)\boldsymbol{n} \right] \mathrm{d}l, \quad [12]$$

where **t** and **n** are the tangential and normal unit vectors of the integration path, respectively.

MAGNETIC FIELD SIMULATION AND ANALYSIS

Modeling and Magnetic Field Analysis in the Ideal State

The key factor in the design of magnetic fluid seal is the magnetic field design, which is directly related to the pressure resistance of the seal. Ideally, the sealing clearance of the magnetic fluid seal is 0.1mm, which is guaranteed by the bearings installed on both sides of the pole shoe. For a large-diameter magnetic fluid seal, the installation accuracy of thin-walled shaft has a significant impact on the pressure resistance of magnetic fluid seal. At the same time, thin-walled parts are easy to deform during transportation, assembly, and loading. Therefore, it is very necessary to study the pressure resistance of thin-walled parts under deformation.

The design requirements of the seal are the radius of the shaft r_1 = 173 mm and the shaft width is 18 mm, and the seal pressure resistance is not less than 0.08 MPa in the temperature range of -55–70°C.

The magnetic field strength (H) and magnetic flux density (B) at the seal gap can be obtained quickly and accurately by simulation using ANSYS Maxwell. First, a simplified calculation of the magnetic fluid seal structure is performed. It is assumed that the magnetic permeability of the non-magnetic material parts such as bearings, bearing seats, and end caps is 1; the relative permeability of the magnetic fluid is much smaller than the relative permeability of the material of the rotating shaft and the pole shoe, so it is assumed that the magnetic fluid has a permeability of 1; and the magnetic field provided by multiple sets of cylindrical magnets is assumed to be uniformly distributed. Based on the abovementioned assumptions, the simulation model can be simplified to **Figure 2**, and the three-dimensional problem can be simplified to a two-dimensional problem. Since the magnetic permeability of parts such as bearings is assumed to be 1, which is always the same as that of the air domain, these parts can be ignored in this analysis.

The following is a description of the finite element simulation modeling: the material used for the pole shoe and the shaft is 2Cr13 with a relative permeability of 4,000; the permanent magnet is N35 with a relative permeability of 1.1, and a coercivity of 890 kA/m. The saturation magnetization strength

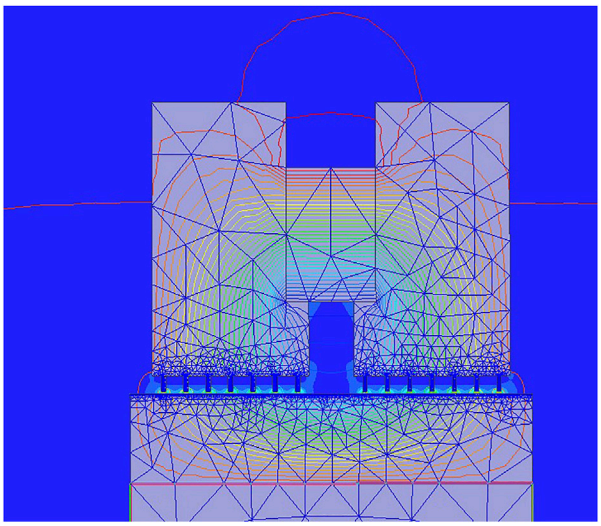

FIGURE 2 | Cloud diagram of magnetic field strength at 0.1 mm sealing gap.

of the magnetic liquid is 450Gs; each pole shoe has seven pole teeth, and a total of 14 pole teeth are designed with a width of 0.2 mm and a height of 0.7 mm, and the distance between the two adjacent pole teeth is 0.8 mm. Since the ratio of axial constancy to the radial length is 0.052 for the seal structure analyzed in this article, the seal structure is a large diameter thin-wall magnetic fluid seal. At the sealing gap, we set the maximum length of the element to 0.01 mm, we set the maximum number of passes to 10, the percentage error to 1, and the optimal pass rate to 30%, the maximum number of passes as 10, percent error as 1, and refinement per pass as 30%.

First, the magnetic field in the ideal state of magnetic fluid seal is analyzed, and the magnetic field strength of the model can be obtained through calculation. The cloud diagram of magnetic field intensity after analysis is shown in **Figure 2**, and the distribution of magnetic field intensity under the polar teeth is shown in **Figure 3**. Assuming that the magnetic fluid is in the best working position when receiving the pressure, the coordinates of the highest point and the lowest point are taken and the pressure resistance of the seal as 0.28 MPa is calculated according to the formula (Odenbach and Störk, 1998).

Analysis of Magnetic Field Forces During Assembly

In the assembly of magnetic fluid seal, the two pole shoes and permanent magnet are generally assembled before installation. During installation, due to the magnetic force, the pole shoe and the rotating shaft attract each other, resulting in eccentricity, which eventually leads to the hanging of the pole teeth and the shaft during installation, which will seriously lead to the deformation and damage of the pole teeth. Therefore, it is necessary to explore the magnetic force on the shaft sleeve during installation. The axial force of the shaft sleeve can be calculated by changing the *x*-axis coordinate of the shaft sleeve and using the energy gradient method or Maxwell stress tensor. It can be seen from the calculation results that the force received is quasi periodic, as shown in **Figure 4**, which is caused by the polar tooth structure. According to the calculation results, the maximum value is 1.436 kN.

In the practical application of magnetic fluid seals, most magnetic fluid seals require custom designs, except for standard parts from companies such as Ferrotec. In addition, most magnetic fluid seals are small-diameter seals, so manual assembly is sufficient to meet the assembly accuracy requirements. However, for large-diameter thin-walled magnetic fluid seals, the abovementioned study shows that the axial force during the assembly is up to 1.436 kN, which makes manual assembly impossible to ensure that the process is free from scratches and knocks. In order to solve the abovementioned problem situation, a large diameter fixture should be designed to fit the assembly. The principle is to ensure the coaxiality between the machine shoe and the rotating shaft in the assembly by the clearance fitting surface of the upper and lower fixture. The axial distance during assembly is adjusted by screws, and the installation of sealing parts is completed under the premise

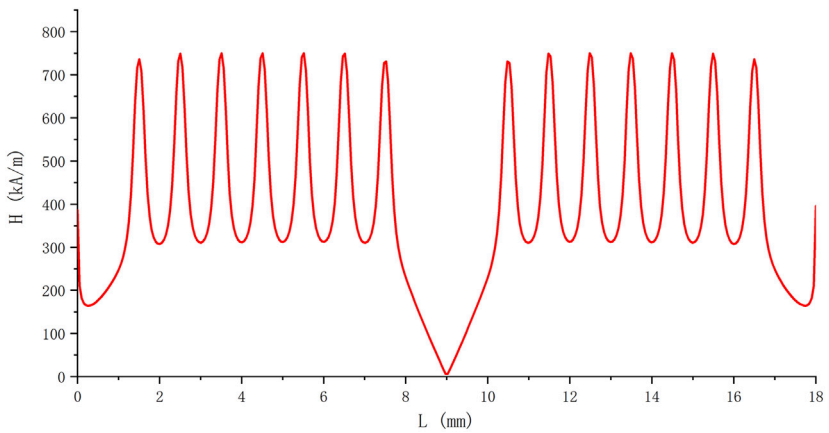

FIGURE 3 | Magnetic field intensity distribution in the sealing gap at 0.1 mm sealing gap.

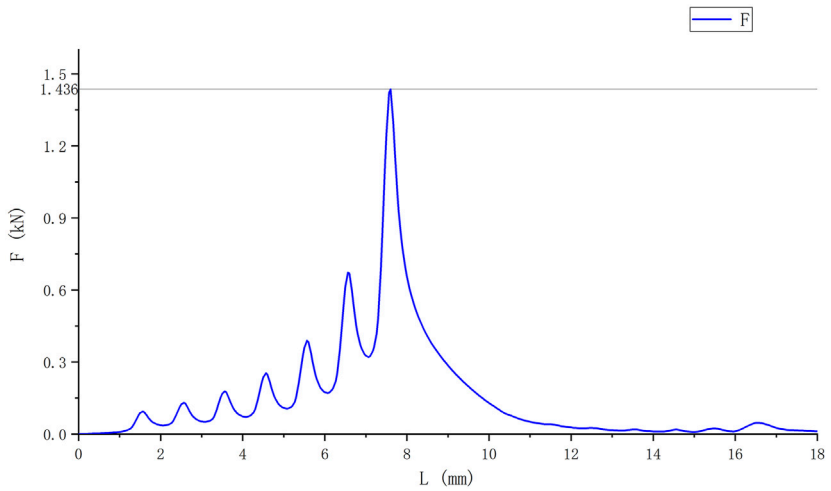

FIGURE 4 | Axial magnetic field force on the rotating shaft.

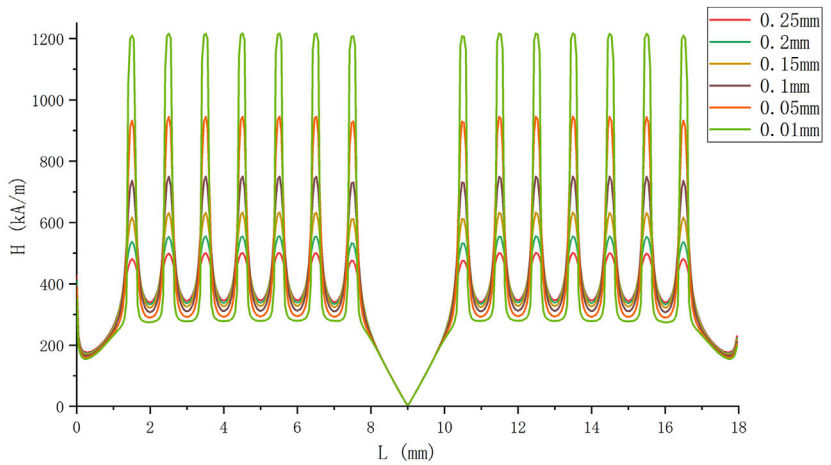

FIGURE 5 | Distribution of sealing magnetic field strength under different sealing gaps.

of ensuring the coaxiality, thus effectively avoiding scraping and collision caused by the magnetic field force.

Analysis of the Effect of Different Parameters on the Seal

The thin-wall parts are prone to deformation during machining, especially for large-diameter thin-walled shafts. Therefore, it is necessary to study the effect of different sealing clearances on the pressure resistance and thus use it as a basis for designing the tolerance of the pole shoes and the rotating shafts. This research can play a key role in the design of thin-wall seals.

As can be seen from **Figures 5**, **6**, the pressure resistance of the seal decreases significantly with the increase of the seal clearance. When the sealing gap is greater than 0.6 mm, the pressure resistance of the seal is 0.0241 MPa, which is less than 1/10 of that when the sealing gap is 0.1 mm. It can be considered that when the sealing gap is greater than 0.6, the magnetic fluid seal has no sealing ability and the seal fails. It is worth mentioning that when the thin-walled rotating shaft is deformed due to the force, the shape of the shaft will change, and the magnetic fluid seal gap under the pole teeth will be uneven. Here, the change of magnetic field strength caused by the shaft deformation is ignored, and the maximum value of sealing gap at each level is taken to calculate the pressure resistance. Similarly, this method can be used to calculate the pressure resistance, when the bearing runout is large or when the accuracy of the shape tolerance is low.

The sealing structure studied in this article has 14 pole teeth, and the actual requirement of sealing is 0.08 MPa, and the sealing medium is nitrogen or dry air. When the sealing gap is larger than 0.31 mm, the theoretical pressure resistance is 0.0791 Mpa, and the sealing performance cannot meet the design requirements at

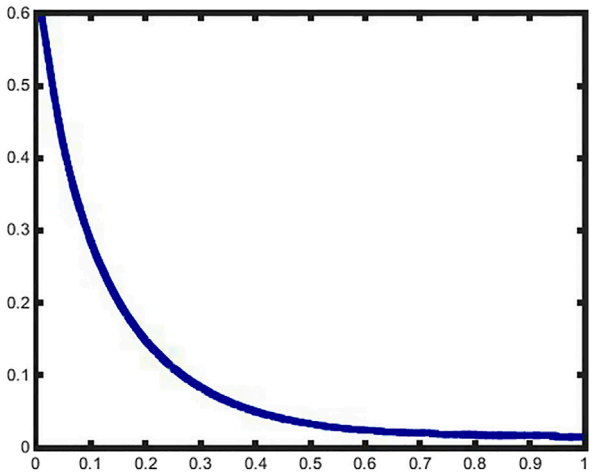

FIGURE 6 | Relationship between the sealing gap and sealing pressure resistance.

all. When the seal gap is 0.1 mm, the theoretical pressure resistance is 0.2854 Mpa, and this value is consistent with the design experience. If the magnetic field design requires that the pressure resistance should be 2.5 times larger than that of the application, which means that the pressure resistance is not less than 0.2 Mpa, it is known from the simulation results that the seal gap should not be larger than 0.15 mm. The simulation results are not only applicable to the design of the seal structure but also can be used to analyze the pressure resistance after the deformation of the thin-walled sleeve or to analyze the effect of the eccentricity of the sleeve, that is, for the cumulative tolerance offset of the design on the radius should not be greater than 0.05 mm.

If the shaft is subjected to radial forces, the shaft may also be deflected, so it is necessary to study the magnetic field intensity distribution when the pole shoe is not parallel to the shaft. By calculation, for this sealing mechanism, the shaft and the pole shoe will contact when the shaft is rotated by 0.66°, so this research studies the change of magnetic field intensity distribution, when the rotation shaft deflection angle is from 0° to 0.66°, and obtains the effect of deflection angle on the seal pressure resistance.

As can be seen from **Figure 7**, the magnetic field intensity under the right pole shoe increases significantly with the increase of deflection angle, and the magnetic field intensity under the left pole shoe decreases with the increase of deflection angle. In this article, the three-dimensional problem is simplified into a two-dimensional model, so the value of the minimum magnetic field strength under each pole tooth should be taken after calculating the sealing pressure resistance. Through calculation, the relationship between different rotation angles and sealing pressure resistance can be obtained in **Figure 8**. The results show that the pressure resistance of the seal decreases with the increase of the deflection angle of the rotating shaft. It should be noted that the maximum deflection angle is 0.66°, and the calculated sealing pressure resistance is 0.2045 Mpa. Compared with the deflection angle of 0, the sealing pressure resistance is 0.02853 Mpa, a decrease of 28.3%. However, this does not mean that the deflection of the shaft has less influence on the seal. Considering the bearing life and seal life, the design and assembly should still minimize the deflection angle of the rotating shaft.

Under normal assembly conditions, an overfilling of magnetic fluid should be injected to ensure a long life of the magnetic fluid seal. However, excess magnetic fluid will increase the sealing torque, a problem that is not significant in ambient temperature environments. However, if there is a need for low temperature sealing, such as in a −55°C environment, the start-up torque of the magnetic fluid seal will increase significantly, which may cause damage to the motor and other components. If there is a strict requirement for the rotational torque of the seal, it is necessary to study the relationship between the volume of the magnetic fluid and the pressure resistance. In the seal gap, the distribution interface of the magnetic fluid will coincide with isomagnetic lines. To facilitate the calculation, the isomagnetic lines is reduced to a circular arc, as shown in **Figure 9**.

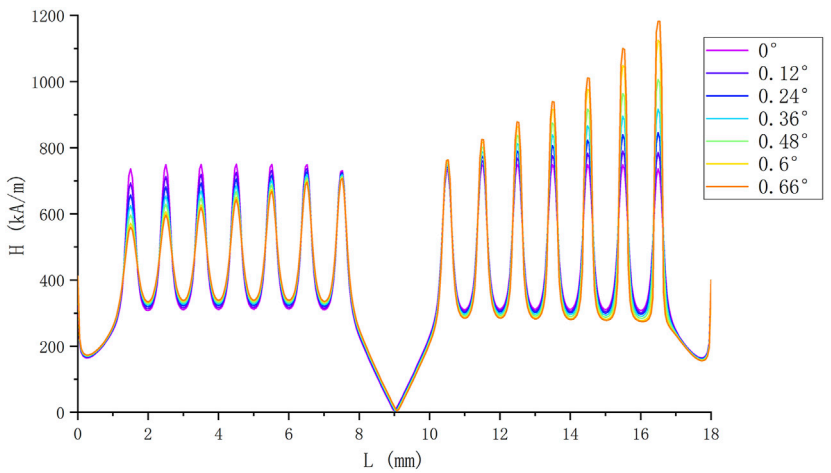

FIGURE 7 | Effect of different rotation angles of the shaft on the distribution of magnetic field strength.

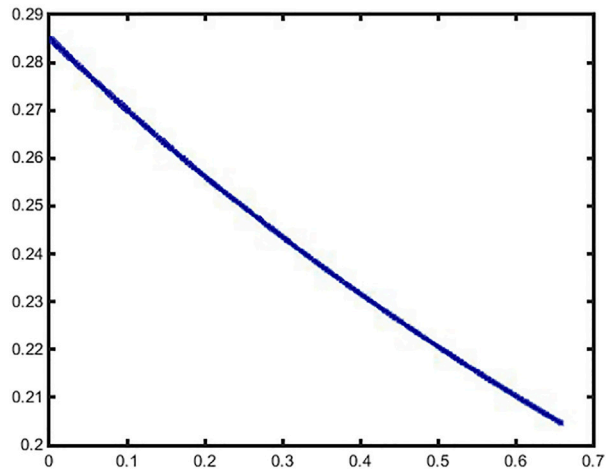

FIGURE 8 | Relationship between different rotation angles of the shaft and the pressure resistance.

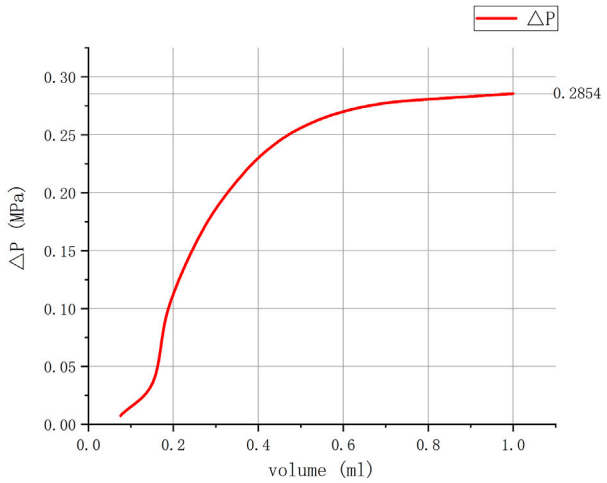

FIGURE 10 | Effect of different volumes of magnetic fluid on the pressure resistance of the seal.

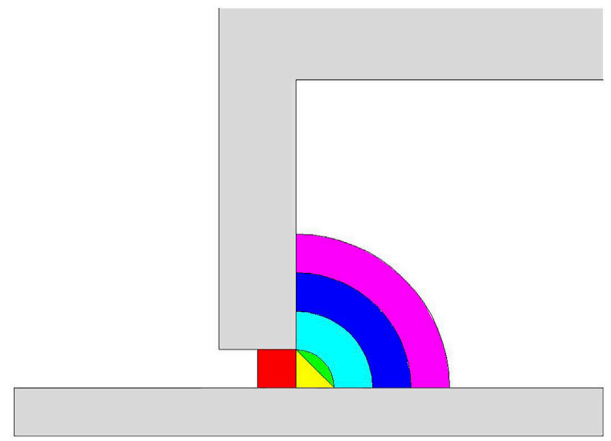

FIGURE 9 | Distribution of magnetic fluid under the polar teeth.

The abovementioned analysis results are calculated based on the finite element magnetic field strength analysis. According to the abovementioned curve, when the volume of magnetic fluid reaches 0.6 ml, the pressure resistance reaches 0.27 MPa, which is only a theoretical decrease of 3.5% compared to the pressure resistance of an excess of magnetic fluid, as shown in **Table 1** and **Figure 10**. Therefore, it can be assumed that the volume of magnetic fluid seal used in this study is at least 0.6 ml. It is worth discussing that in the general assembly process of magnetic fluid seal, it is usually necessary to inject an excess amount of magnetic fluid and only a small amount of magnetic fluid is adsorbed at the pole teeth. Also, due to different assembly processes, the magnetic fluid may be adsorbed directly on the permanent magnet, resulting in waste. Therefore, it is necessary to explore a new magnetic fluid seal structure and its assembly method.

EXPERIMENTAL ANALYSIS

Experimental conditions: after holding at −55°C for 2 hours, conduct low temperature sealing pressure and low temperature starting torque test. After heating to 70°C and holding for 2 hours, the high-temperature pressure resistance test is conducted.

Experimental equipment: high- and low-temperature environmental chamber.

Test method. Measure the length of the long rod connected to the rotating shaft with an arm length of L. Hang a bucket on one end of the long rod and add the weights slowly and sequentially to the bucket. The weight m is measured after the rotating axis is rotated. The starting torque is calculated according to the following formula:

$$\tau = m \cdot g \cdot L.$$

The graph below shows the relationship between the magnetic fluid volume and the low temperature start-up torque of the magnetic fluid seal at a low temperature of −55°C. The viscosity and yield stress increase as the temperature decreases. Also, the viscosity and yield stress of the magnetic fluid increase with

TABLE 1 | Relationship between the volume of magnetic fluid and pressure resistance.

V (ml)	0.076	0.152	0.190	0.272	0.362	0.443	0.522	0.600	0.678	0.755	Excess
△P (MPa)	0.007	0.037	0.102	0.169	0.215	0.243	0.260	0.270	0.276	0.279	0.285

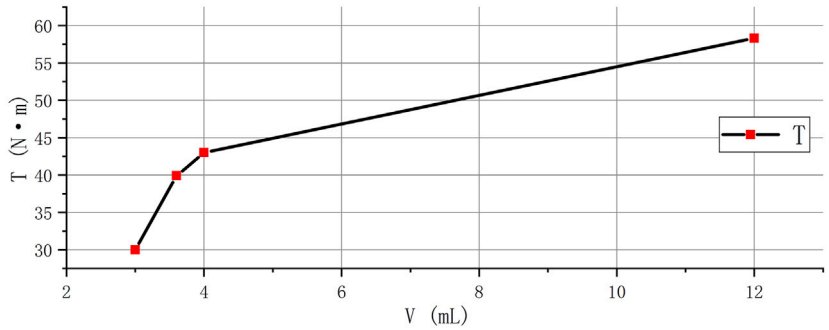

FIGURE 11 | Magnetic fluid volume versus starting torque in −55°C environment.

FIGURE 12 | Large diameter magnetic fluid seal with thin-walled parts.

increasing magnetic field strength due to the response of the magnetic fluid to the magnetic field. Therefore, for magnetic fluid in large diameter magnetic fluid seal, the magnetic force in the seal gap is very high. At a low temperature of −55°C, the viscosity and yield stress of the magnetic fluid increase significantly. This leads to a significant increase in the low temperature start-up torque of the magnetic fluid seal compared to that at the room temperature and high temperature. The relationship between the magnetic fluid injection volume and the low-temperature start-up torque of a large-diameter magnetic fluid seal was investigated. The experimental results are shown in **Figure 11**. With a magnetic fluid volume of 3 ml, the start-up torque of the seal can be as low as 30 Nm at a sealing pressure of 0.08 MPa. The pressure does not decrease after the seal is rotated. The results show that the low-temperature starting torque of the large-diameter magnetic fluid seal increases with the increase of the magnetic fluid volume. It should be noted that the lubrication performance of the magnetic fluid seal bearing is poor at low temperature, which also affects the starting torque and rotating torque. When the volume of the magnetic fluid is less than 3 ml, the magnetic fluid seal will leak above 70°C. Therefore, in the design, it is necessary to consider both the connection of reducing the low-temperature starting torque and the high-temperature seal failure. Large diameter magnetic fluid seal with thin-walled parts are shown in **Figure 12**.

Since there is no rheometer dedicated to measure the yield stress of magnetic liquids in −55°C, the calculation can be performed by equation (7). The starting torque of the seal is measured with a small rotational speed of the rotating shaft, $\omega \approx 0$,N = 14, r_1 = 173 mm, L_t = 0.2 mm, and T = 30 Nm. Thus, we obtained the yield stress of the magnetic liquid in a strong magnetic field after 2 hours of holding at −55°C. The yield stress t_s = 57 kPa.

CONCLUSION

Based on the principle of magnetic fluid seal, the influencing factors of magnetic field distribution of a large-diameter thin-walled magnetic fluid seal are studied by the finite element method, and the low-temperature starting torque of magnetic fluid seal is studied by the experiment.

1) The pressure resistance formula of magnetic fluid seal, the torque of magnetic fluid, and the force on the rotating shaft of magnetic fluid seal are analyzed.
2) Through the finite element analysis method, the magnetic field force of the rotating shaft of large-diameter magnetic fluid seal during the assembly is simulated and analyzed.
3) The influencing factors of magnetic field distribution in magnetic fluid seals were analyzed by the finite element method. The effects of seal gap and shaft deflection angle on the magnetic field distribution in the magnetic fluid seal gap were analyzed to help the tolerance design of the parts.
4) The effect of magnetic fluid volume on the pressure resistance of magnetic fluid seal is analyzed.
5) The effect of the volume of the magnetic fluid on the low-temperature starting torque and the pressure resistance of the magnetic fluid seal was analyzed by the experiment.

DATA AVAILABILITY STATEMENT

The raw data supporting the conclusion of this article will be made available by the authors, without undue reservation.

AUTHOR CONTRIBUTIONS

YG and DL conducted the theoretical study and finite element simulation study of magnetic fluid seal. YG, DL, GZ, ZQ, and ZZ have participated in the experimental study of the starting torque of the seal in the low-temperature environment.

FUNDING

This work was supported by the National Natural Science Foundation of China (Grant Nos. 51735006, 51927810, and U1837206) and Beijing Municipal Natural Science Foundation of China (Grant No. 3182013).

REFERENCES

Cai, Y. Q., and Xing, N. (2013). The Analysis on the Starting Friction Torque Increase of Magnetic Fluid Revolving Sealing. *Amm* 275-277, 429–432. doi:10.4028/www.scientific.net/amm.275-277.429

Chen, J., Li, D., and Hao, D. (2018). Investigation on the Influence of Temperature on Starting Torque of Magnetic Fluid Seal. *J. Magneics* 3 (23), 436–441. doi:10.4283/jmag.2018.23.3.436

Cheng, Y., Li, D., and Li, Z. (2021). Influence of Rheological Properties on the Starting Torque of Magnetic Fluid Seal. *IEEE Trans. Magn.* 57 (3), 1–8. doi:10.1109/tmag.2019.2934716

He, X., Li, D., and Hao, R. (2015). The Influence of Magnetic Fluid Yield Stress on the Performance of Magnetic Fluid Seal. *Acta Armamentarii* 36 (01), 175–181. doi:10.3969/j.issn.1000-1093.2015.01.025

Hong, R. Y., Ren, Z. Q., Han, Y. P., Li, H. Z., Zheng, Y., and Ding, J. (2007). Rheological Properties of Water-Based Fe_3O_4 Ferrofluids. *Chem. Eng. Sci.* 62 (Issue 21), 5912–5924. doi:10.1016/j.ces.2007.06.010

Kim, C. K., and Kim, H. G. (1997). A Study on the Friction Torque and Temperature Distribution of Magnetic Fluid Seals. *Trans. Korean Soc. Mech. Eng. A* 21 (1), 53–61. doi:10.22634/KSME-A.1997.21.1.53

Li, D., Hong, J., and Yang, Q. (2002). The Study on the Magnetic Fluid Sealing of Dry Roots Pump. *Vac. Sci. Technol.* 22 (04), 78–81. doi:10.13922/j.cnki.Cjovst.2002.04.019

Li, D. (2010). *Magnetic Fluid Sealing Theory and Application*. Beijing: Science Press.

Li, D., Xu, H., Liao, P., and Cui, H. (2004). Study on the Breakaway Torque of Magnetic Fluid Sealing at Low Temperature and Large Diameter. *J. Funct. Mater.* 35, 566. doi:10.3321/j.issn:1001-9731.2004.z1.150

Li, D, Xu, L, Wang, Q, and Chui, H (2001). "Study of low temperature and large diameter magnetic fluid rotatory sealing," in Proceedings of the 4th China Academic Conference on Functional Materials and Applications; 2001, 568, Xiamen, China, Ocotober 1, 2001.

Li, Z., Li, D., Chen, Y., Guo, Y., and Zhang, Z. (2019). Thixotropic Yielding Behaviors of Ferrofluids. *J. Magnetism Magnetic Mater.* 486, 165277. doi:10.1016/j.jmmm.2019.165277

Li, Z., Li, D., Cui, H., Zhang, Y., and Wang, H. (2019). Influence of the Carrier Fluid Viscosity on the Rotational and Oscillatory Rheological Properties of Ferrofluids. *J. Nanosci. Nanotechnol.*, 19, 5572–5581. doi:10.1166/jnn.2019.16525

Li, Z. (2002). Magnetic Fluid Seals for DWDM Filter Manufacturing. *J. Magnetism Magnetic Mater.* 252 (1-3), 327–329. 2002-01-01. doi:10.1016/s0304-8853(02)00681-9

Mingli, S., Decai, L., Xinzhi, H., and Ruican, H. (2007). Simulation and Design of Magnetic Fluid Sealing Devices. *Chin. J. Vac. Sci. Technol.* 27 (03), 269–272. 2007-05-15. doi:10.3969/j.issn.1672-7126.2007.03.021

Odenbach, S., and Störk, H. (1998). Shear Dependence of Field-Induced Contributions to the Viscosity of Magnetic Fluids at Low Shear Rates. *J. Magn. Magn. MATER* 183 (1-2), 188–194. doi:10.1016/s0304-8853(97)01051-2

Odenbach, S. (2000). Magnetoviscous Effects in Ferrofluids. *Appl. Rheol.* 10 (4), 178–184. doi:10.1515/arh-2000-0011

Rosensweig, R. E. (1985) *Rosensweig. Ferrohydrodynamics.* England: Cambridge University Press.

Shah, K., Upadhyay, R. V., and Aswal, V. K. (2012). Influence of Large Size Magnetic Particles on the Magneto-Viscous Properties of Ferrofluid. *Smart Mater Struct.* 21 (7), 75005. 2012-07-01. doi:10.1088/0964-1726/21/7/075005

Yan, X., Xie, D., Gao, Z., and Yu, C. (2003). Research on Integration Path Selection of Maxwell Stress Tensor Method Used in Electromagnetic Force FEM Analysis. *Trans. China Electrotech. Soc.* 18 (05), 32–36. doi:10.3321/j.issn:1000-6753.2003.05.007

Yang, W., Li, D., Cai, Y., Huang, Y., and Li, Q. (2009). Numerical Calculation of Magnetic Field and Magnetic Force Exerted on the Shaft with Eccentricity in Magnetic Fluid Seal. *Lubr. Eng.* 34 (12), 48–51. doi:10.3969/j.issn.0254-0150.2009.12.013

Yang, Y., Li, L., Chen, G., and Li, W. (2006). Magnetorheological Properties of Aqueous Ferrofluids. *J. Soc. Rheol. Jpn.* 34 (1), 25–31. doi:10.1678/rheology.34.25

Conflict of Interest: The authors declare that the research was conducted in the absence of any commercial or financial relationships that could be construed as a potential conflict of interest.

Publisher's Note: All claims expressed in this article are solely those of the authors and do not necessarily represent those of their affiliated organizations, or those of the publisher, the editors, and the reviewers. Any product that may be evaluated in this article, or claim that may be made by its manufacturer, is not guaranteed or endorsed by the publisher.

frontiers | Frontiers in Materials

ORIGINAL RESEARCH
published: 05 August 2022
doi: 10.3389/fmats.2022.932854

Full-Scale Simulation of the Fluid–Particle Interaction Under Magnetic Field Based on IIM–IBM–LBM Coupling Method

Wei Peng[1], *Yang Hu*[1]*, *Decai Li*[1,2] *and Qiang He*[2]

[1]School of Mechanical, Electronic and Control Engineering, Beijing Jiaotong University, Beijing, China, [2]State Key Laboratory of Tribology, Tsinghua University, Beijing, China

In this article, a full-scale computational model for fluid–particle interaction under a magnetic field is developed. In this model, the fluid field is solved by the lattice Boltzmann method, and the hydrodynamic force acting on the particle is computed by the immersed boundary method . The numerical solutions of the magnetic field in the fluid–solid domain are achieved by the immersed interface method with a finite difference scheme, in which the normal and tangential jump conditions of the magnetic field intensity are applied to modify the standard finite difference scheme. The magnetic stress tensor along the fluid–particle interface can be calculated accurately. Unlike the widely used point–dipole model, the magnetic force acting on the particle is determined by the stress integration method. Numerical simulation of several numerical tests are carried out to validate the proposed model. The numerical results demonstrate the validity of the present model. Moreover, the magnetoviscous effect is studied by simulating the motion of elliptical particles under the uniform magnetic field in shear flow.

Keywords: full-scale simulation, fluid-particle interactions, magnetic field, immersed interface method, immersed boundary method, lattice Boltzmann method

OPEN ACCESS

Edited by:
Xuan Shouhu,
University of Science and Technology of China, China

Reviewed by:
Huaxia Deng,
University of Science and Technology of China, China
Xufeng Dong,
Dalian University of Technology, China

***Correspondence:**
Yang Hu
yanghu@bjtu.edu.cn

Specialty section:
This article was submitted to Smart Materials, a section of the journal Frontiers in Materials

Received: *30 April 2022*
Accepted: *03 June 2022*
Published: *05 August 2022*

Citation:
Peng W, Hu Y, Li D and He Q (2022) Full-Scale Simulation of the Fluid–Particle Interaction Under Magnetic Field Based on IIM–IBM–LBM Coupling Method. Front. Mater. 9:932854. doi: 10.3389/fmats.2022.932854

INTRODUCTION

Fluid–particle two-phase flows under a magnetic field can be usually found in nature and engineering applications, ranging from mineral screening (Ku et al., 2015), microfluidic control systems (Cao et al., 2014), magnetorheological fluid (Climent et al., 2004), and other chemical and biological applications. For the modeling of such flows, the two most important issues are to calculate the interaction forces between the particles and fluid/magnetic fields accurately and efficiently.

Fluid–particle interaction is one of the research hotspots in the computational fluid community. The existing models for fluid–particle interaction can fall into two categories: the Eulerian–Eulerian models and the Eulerian–Lagrangian models (Chiesa et al., 2005; Patel et al., 2017). The Eulerian–Eulerian models can capture the collective behavior of particles. However, it needs complex constitutive equations, and it is difficult to predict the details of the flow. Alternatively, the Eulerian–Lagrangian models easily obtain the detailed flowing behavior around the particles. The Eulerian–Lagrangian models can also be classified into two types: the point source model and the full-scale model (Luo et al., 2007; Hu et al., 2018). For the point source model, the empirical drag force formula is utilized to compute the fluid-particle interaction force. However, the point model *i* lacks enough accuracy for cases with dense or large-sized particles. For full-scale simulation, the fluid

is governed by the Navier–Stokes equations, and the particle motion is solved by the Newtonian laws. The interaction force between the fluid and particle is determined by the no-slip condition. From this point of view, the full-scale model is most suitable for the study of flow mechanisms. Within the framework of full-scale models, the fixed mesh methods, which do not require time-consuming mesh generation, have received considerable attention in recent years. Unlike the body-fitted mesh methods, the governing equations of the fluid field are discretized on a fixed mesh, and the boundary is tracked by a set of Lagrangian points or captured by an implicit function. As a result, the computational efficiency is greatly improved. Kang et al. applied the distributed Lagrange multiplier/fictitious domain method to solve flows with suspended paramagnetic particles, in which the no-slip boundary condition on the particle boundary is implemented by Lagrange multipliers (Kang et al., 2008). Kang and Suh proposed the one-stage smoothed profile method for simulation of flows with suspended paramagnetic particles, in which the sigmoid function was used to construct body force by ensuring the rigidity of particles (Kang and Suh, 2011a). Kim and Park presented a level-set method for the analysis of magnetic particle dynamics on a fixed mesh (Kim and Park, 2010). Ke et al. introduced an IBM to simulate the behavior of magnetic particles in a fluid with an external magnetic field (Ke et al., 2017). These works show the effectiveness of fixed mesh methods in handling the fluid–particle interaction under a magnetic field.

In terms of calculation of magnetic force, the calculation models can also be divided into the point–dipole model and the force integration model. For example, Sand et al. developed a point–dipole model to simulate the magnetic particle suspension flow in which the single particle attraction force towards the magnetic pole was computed by a simple Kelvin force formula, and the interaction force between two nearby particles was computed by a magnetic dipole model (Sand et al., 2016). Like the point source model for fluid–particle interaction, the point–dipole model for particle–magnetic field interaction also suffers from inaccurate force estimation in nondilute flow or particle shape-dependent conditions. To this end, some work based on the force integration model has been done. In these models, the governing equation of the magnetic field in the multimedia zone was solved firstly. Then, the magnetic force acting on the particle can be obtained by integrating the force density. The magnetic force density can be calculated by the Helmholtz force density (Kang et al., 2008) or the virtual air gap scheme (Kang and Suh, 2011b). It should be pointed out that the fluid–particle interface is smeared out over several mesh cells in these above-the-force integration models. However, the magnetic stress force at the interface is treated as the continuous smoothed form, which will cause the loss of numerical accuracy.

In this paper, we develop a fully resolved simulation method for the fluid–particle interaction under a magnetic field. The LBM, which is a simple and efficient flow field solver, is adopted. The fluid–particle interaction is handled by the momentum-exchange-based IBM. More importantly, we give a Maxwell stress integration method to calculate the magnetic force based on the IIM with a finite difference scheme. According to the normal and tangential jump conditions of magnetic scalar potential along the medium interface, the discretized difference scheme is modified to ensure second-order accuracy. Then, the Maxwell stress tensor at the interface can be calculated accurately. The magnetic force acting on the particle can be obtained by integrating the magnetic stress force along the interface. Several numerical examples are simulated to validate the present IIM–IBM–LBM coupling model. The numerical results indicate that the present calculated stress force values agree well with the numerical results obtained by the body-fitted mesh. The circular particle sedimentation and motion of elliptical particles in shear flow under the magnetic field are also studied.

MATHEMATICAL MODEL AND NUMERICAL METHOD

In this study, LBM is used to simulate fluid flow, IBM is used to simulate the interaction between fluid and particles, and IIM is used to calculate magnetic field. In this section, we introduce the numerical implementation procedures of LBM, IBM, and IIM.

Lattice Boltzmann Model for Incompressible Fluid Flow

Using a standard uniform Cartesian grid with lattice space h, the single relaxation time LB evolution equation with external force term is as follows (Chen and Doolen, 1998):

$$f_\alpha(x + e_\alpha\Delta t, t + \Delta t) - f_\alpha(x,t) = -\frac{1}{\tau}\left[f_\alpha(x,t) - f_\alpha^{eq}(x,t)\right] + F_\alpha\Delta t\,, \tag{1}$$

where f_α is the density distribution function. The dimensionless relaxation time reads

$$\tau = \frac{\mu}{\Delta t c_s^2} + 0.5\,, \tag{2}$$

where μ is the coefficient of kinetic viscosity, f_α^{eq} is the equilibrium distribution function, and F_α is the external force term in discrete velocity space. Then, f_α^{eq} and F_α could be separately written as

$$f_\alpha^{eq} = \omega_\alpha\rho_f\left[1 + \frac{\boldsymbol{e}_\alpha\cdot\boldsymbol{u}}{c_s^2} + \frac{(\boldsymbol{e}_\alpha\cdot\boldsymbol{u})^2}{2c_s^2} - \frac{\boldsymbol{u}^2}{2c_s^2}\right], \tag{3a}$$

$$F_\alpha = \left(1 - \frac{1}{2\tau}\right)\omega_\alpha\left[\frac{\boldsymbol{e}_\alpha - \boldsymbol{u}}{c_s^2} + \frac{\boldsymbol{e}_\alpha\cdot\boldsymbol{u}}{c_s^4}\boldsymbol{e}_\alpha\right]\cdot\boldsymbol{f}\,, \tag{3b}$$

where $c_s = \frac{c}{\sqrt{3}} = \frac{h}{\Delta t\sqrt{3}}$ is the lattice sound speed and $\boldsymbol{f}$ is the body force. In the D2Q9 model, the discrete velocity $\boldsymbol{e}_\alpha$ and weight coefficients separately reads

$$\boldsymbol{e}_\alpha = \begin{cases} (0,0), & \alpha = 0 \\ c\left(cos\left[(\alpha-1)\frac{\pi}{2}\right], sin\left[(\alpha-1)\frac{\pi}{2}\right]\right), & \alpha = 1,2,3,4 \\ \sqrt{2}c\left(cos\left[(2\alpha-1)\frac{\pi}{4}\right], sin\left[(2\alpha-1)\frac{\pi}{4}\right]\right), & \alpha = 5,6,7,8 \end{cases}, \tag{4a}$$

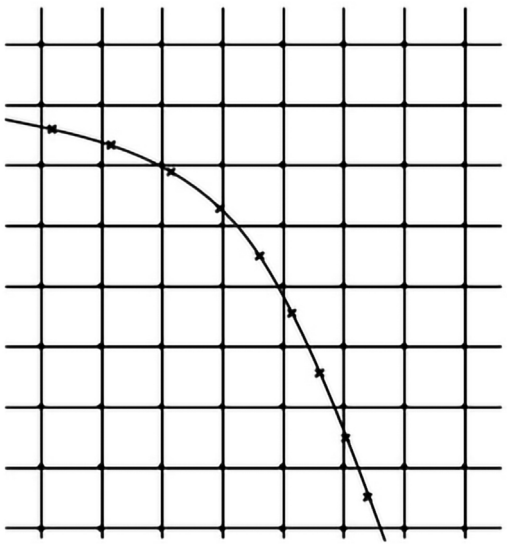

FIGURE 1 | Configuration of the grids used in the IBM. Euler points (circles) represent the flow field and Lagrange points (crosses) represent the fluid–solid interface.

$$\omega_0 = 4/9, \omega_1 = \omega_2 = \omega_3 = \omega_4 = 1/9, \omega_5 = \omega_6 = \omega_7 = \omega_8 = 1/36\,. \tag{4b}$$

The density and macrovelocity are written as

$$\rho_f = \sum_\alpha f_\alpha\,, \tag{5a}$$

$$\boldsymbol{u} = \left(\sum_\alpha \boldsymbol{e}_\alpha f_\alpha + \frac{1}{2}\boldsymbol{f}\Delta t\right)\Big/\rho\,. \tag{5b}$$

Immersed Boundary Method for the Fluid–Particle Interaction

The momentum exchange-based IBM proposed by Niu et al. (2006) is used to calculate the interaction force between fluid and solid particles. In **Figure 1**, the flow domain is covered with a uniform Cartesian grid, and the fluid–solid interface is divided into a series of Lagrange points $\boldsymbol{X}_l$ with the arc length ΔS_l. The relation between the body force $\boldsymbol{f}$ on the Eulerian nodes $\boldsymbol{x}_i = (x_i, y_i)$ and the force density $\boldsymbol{f}$ on the Lagrange points $\boldsymbol{X}_l = (X_l, Y_l)$ is expressed as

$$\boldsymbol{f}(\boldsymbol{x}_i, t) = \sum_i \boldsymbol{F}(\boldsymbol{X}_l, t) D(\boldsymbol{x}_i - \boldsymbol{X}_l)\Delta S_l\,, \tag{6}$$

where $D\ (\boldsymbol{x}_i - \boldsymbol{X}_l)$ is the two-dimensional discrete Dirac function. In this study, the expression of $D(\boldsymbol{x}_i - \boldsymbol{X}_l)$ proposed by Peskin (Peskin, 2002) is adopted:

$$D(\boldsymbol{x}_i - \boldsymbol{X}_l) = \frac{1}{h^2}\delta\left(\frac{x_i - X_l}{h}\right)\delta\left(\frac{y_i - Y_l}{h}\right), \tag{7}$$

where

$$\delta(r) = \begin{cases} \frac{1}{4}\left(1 + cos\left(\frac{\pi r}{2}\right)\right) & |r| \le 2 \\ 0 & |r| > 2 \end{cases}. \tag{8}$$

The calculation of the force density $\boldsymbol{F}(\boldsymbol{X}_l, t)$ is the key problem in IBM, and it is usually determined by the no-slip condition on the boundary of the rigid particle. For the present momentum exchange-based IBM, the no-slip condition is implemented by the bounce-back rule. Firstly, the density distribution function $f_\alpha(\boldsymbol{X}_l, t)$ at Lagrange points is obtained by an interpolation method, i.e.,

$$f_\alpha(\boldsymbol{X}_l, t) = \sum_{i,j} D(\boldsymbol{x}_i - \boldsymbol{X}_l) f_\alpha(\boldsymbol{x}_i, t) h^2\,. \tag{9}$$

Then, the new distribution function $f_\alpha^{new}(\boldsymbol{X}_l, t)$ could be solved according to the bounce-back rule:

$$f_\alpha^{new}(\boldsymbol{X}_l, t) = f_{-\alpha}(\boldsymbol{X}_l, t) - 2\omega_{-\alpha}\rho\frac{\boldsymbol{e}_{-\alpha}\cdot\mathbf{U}_B^d(\boldsymbol{X}_l, t)}{c_s^2}, \tag{10}$$

where $\mathbf{U}_B^d(\boldsymbol{X}_l, t)$ is the velocity at Lagrange point and $-\alpha$ is the opposite direction of α. Next, the force density $\boldsymbol{F}(\boldsymbol{X}_l, t)$ of the flow field acting on the boundary point is calculated as

$$\boldsymbol{F}(\boldsymbol{X}_l, t) = \sum_\alpha \boldsymbol{e}_\alpha\left[f_\alpha^{new}(\boldsymbol{X}_l, t) - f_\alpha(\boldsymbol{X}_l, t)\right]\frac{h}{\Delta t}. \tag{11}$$

Furthermore, we define

$$\begin{cases} \boldsymbol{F}_{pf}^{'} = -\sum_l \boldsymbol{F}(\boldsymbol{X}_l, t)\Delta S_l \\ \boldsymbol{T}_{pf}^{'} = -\sum_l \left(\boldsymbol{X}_l - \boldsymbol{X}_p\right) \times \boldsymbol{F}(\boldsymbol{X}_l, t)\Delta S_l \end{cases}. \tag{12}$$

The hydrodynamic force $\boldsymbol{F}_{pf}$ and moment $\boldsymbol{T}_{pf}$ acting on the solid particle can be obtained by removing the effect of internal mass

$$\begin{cases} \boldsymbol{F}_{pf} = \boldsymbol{F}_{pf}^{'} + \frac{\rho_f}{\rho_p} M_p \frac{d\boldsymbol{U}_p}{dt} \\ \boldsymbol{T}_{pf} = \boldsymbol{T}_{pf}^{'} + \frac{\rho_f}{\rho_p} I_p \frac{d\boldsymbol{\omega}_p}{dt} \end{cases}, \tag{13}$$

where $\boldsymbol{X}_p$ is the centroid of the solid particle, ρ_p is the particle density, M_p is the mass of particle, I_p is the moment of inertia, $\boldsymbol{U}_p$ is the translational velocity, and $\boldsymbol{\omega}_p$ is the rotational velocity, respectively.

Immersed Interface Method for Magnetic Field Calculation

The magnetic field in the multimedia zone can be solved by the Maxwell equations with the interface conditions. As shown in **Figure 2**, we consider two types of methods to impose the magnetic field: one is the given external uniform magnetic field, and the other is the permanent magnetic field. The Maxwell equations without current are expressed as follows:

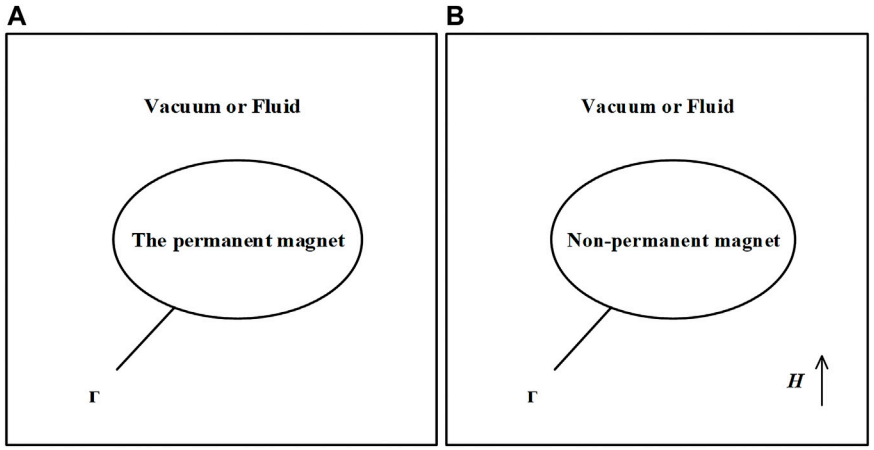

FIGURE 2 | Interface problems of permanent magnetic field **(A)** and uniform magnetic field **(B)**.

$$\begin{cases} \nabla \cdot \boldsymbol{B} = 0 \\ \nabla \times \boldsymbol{H} = 0 \end{cases}, \tag{14}$$

where $\boldsymbol{B}$ is magnetic induction and $\boldsymbol{H}$ is magnetic field intensity. To solve the two Maxwell's equations, the constitutive relationships between magnetic flux density and magnetic field (**Eq. 15**) are needed

$$\begin{cases} \boldsymbol{B} = \mu \boldsymbol{H} \\ \boldsymbol{B} = \boldsymbol{\mu_0}(\boldsymbol{H} + \boldsymbol{M}) \quad (\text{for permanent magnet}) \end{cases}, \tag{15}$$

where μ_0 is permeability of vacuum, μ is relative permeability, and $\boldsymbol{M}$ is the remanence of permanent magnet. At a current-free interface between two media, the following two continuity conditions are satisfied:

$$\begin{cases} B_{1\mathrm{n}} = B_{2n} \\ H_{1\tau} = H_{2\tau} \end{cases}, \tag{16}$$

where n and τ are the normal and tangential directions, respectively. At the interface between permanent magnet and other media, the normal component of $\boldsymbol{B}$ is still continuous across the interface. However, the tangential component of $\boldsymbol{H}$ has a jump discontinuity.

$$\begin{cases} B_{1\mathrm{n}} = B_{2n} \\ H_{1\tau} - H_{2\tau} = M_{2\tau} \end{cases}. \tag{17}$$

Due to the irrotationality condition of $\boldsymbol{H}$ field, the scalar magnetic potential V is introduced:

$$\boldsymbol{H} = -\nabla V. \tag{18}$$

The equations for solving the magnetic potential V can be obtained:

$$\begin{cases} \nabla \cdot \mu(-\nabla V) = 0 \\ -\nabla \cdot \mu_0(\nabla V - \boldsymbol{M}) = 0 \quad (\text{for permanent magnet}) \end{cases}. \tag{19}$$

The interface conditions for V could be obtained from **Formula 19** as follows:

$$\begin{cases} [[\mu \nabla V \cdot \boldsymbol{n}]] = 0 \\ [[\nabla V \cdot \boldsymbol{\tau}]] = 0 \end{cases} \quad (\text{nonpermanent magnet}), \tag{20}$$

$$\begin{cases} [[\nabla V \cdot \boldsymbol{n}]] = \boldsymbol{M} \cdot \boldsymbol{n} \\ [[\nabla V \cdot \boldsymbol{\tau}]] = \boldsymbol{M} \cdot \boldsymbol{\tau} \end{cases} \quad (\text{permanent magnet}). \tag{21}$$

In order to solve the magnetic field and compute magnetic force accurately, the IIM is used. The basic idea of IIM is to adopt the interface jump conditions to modify the finite difference scheme near the interface. As a result, second-order solutions can be achieved in the whole domain. A finite difference scheme for Poisson equation (**Eq. 19**) can be written as

$$\sum_k \gamma_k V_{i+i_k, j+j_k} = C_{ij}, \tag{22}$$

for use at the point (x_i, y_j). To sum over k involves points (not more than six points selected near the interface) neighboring point (x_i, y_j), so the value of each i_k, j_k is set to $(-1, 0, 1)$. The coefficients γ_k and indices i_k, j_k depend on (i, j). The correction term C_{ij} is nonzero only if the grid point is irregular. For more details, please refer to LeVeque et al. (1994).

The following formula is used to solve the magnetic field force.

$$\boldsymbol{F}_m = \oint \boldsymbol{n} \cdot \boldsymbol{\sigma}_m dS. \tag{23}$$

The Maxwell stress tensor is

$$\boldsymbol{\sigma}_m = -\frac{1}{2}\mu_0 H^2 \boldsymbol{I} + \boldsymbol{BH}, \tag{24}$$

where $\boldsymbol{I}$ is the identity operator**.** Moreover, the magnetic field force $\boldsymbol{F}_m$ is solved by the following formula (Blūms et al., 1997):

$$\begin{aligned} \boldsymbol{F}_m &= \oint \left(-\frac{1}{2}\mu_0 \boldsymbol{n} \cdot H^2 + (\boldsymbol{n} \cdot \boldsymbol{B})\boldsymbol{H} \right) dS, \\ &\approx \sum_l \left(-\frac{1}{2}\mu_0 \boldsymbol{n}(\boldsymbol{X}_l) \cdot H(\boldsymbol{X}_l)^2 + (\boldsymbol{n}(\boldsymbol{X}_l) \cdot \boldsymbol{B}(\boldsymbol{X}_l))\boldsymbol{H}(\boldsymbol{X}_l) \right) \Delta S_l, \end{aligned} \tag{25}$$

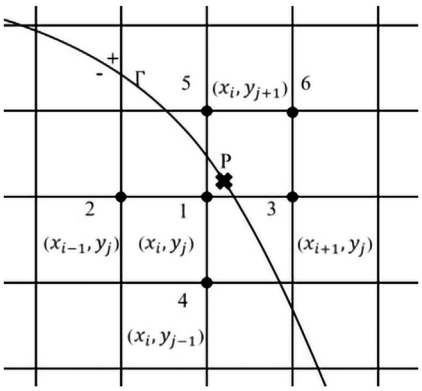

FIGURE 3 | Selection of six points in the modified six-point method. Select the Euler point 1 closest to the Lagrange point (P), and the sixth point is the Euler point closest to the Lagrange point (P) except points 1 to 5.

where $\boldsymbol{n}$ is the normal vector. So, the magnetic field intensity at the interface needs to be determined.

Here, we introduce a six-point interpolation method to calculate from the correct side of the interface. In **Figure 3**, for the point P on the interface, we find the nearest point (x_i, y_j) in the Cartesian grid. So, the stencil for six points is (x_{i-1}, y_j), (x_i, y_j), (x_{i+1}, y_j), (x_i, y_{j-1}), (x_i, y_{j+1}), (x_{i+i_0}, y_{j+j_0}), and they transform them into interface coordinates as follows. (ξ_1, η_1), (ξ_2, η_2), (ξ_3, η_3), (ξ_4, η_4), (ξ_5, η_5), (ξ_6, η_6).

Applying the Taylor expansion method for each point, we have

$$u(\xi_k, \eta_k) = u^{\pm} + \xi_k u_{\xi}^{\pm} + \eta_k u_{\eta}^{\pm} + \frac{1}{2}\xi_k^2 u_{\xi\xi}^{\pm} + \xi_k \eta_k u_{\xi\eta}^{\pm} + \frac{1}{2}\eta_k^2 u_{\eta\eta}^{\pm} + O(h^3). \tag{26}$$

Ignoring the high order term $O(h^3)$, we can obtain a six-variable linear equation for.

$u^{\pm}, u_{\xi}^{\pm}, u_{\eta}^{\pm}, u_{\xi\xi}^{\pm}, u_{\xi\eta}^{\pm}, u_{\eta\eta}^{\pm}$. Once $u^{\pm}, u_{\xi}^{\pm}, u_{\eta}^{\pm}$ are obtained, we can get $V^{\pm}, H_{\xi}^{\pm}, H_{\eta}^{\pm}$ at point P on the interface.

Particle Dynamics

In this study, the dynamics of particle adopts Newton's equation of motion, and the equations controlling particle translation and rotation are as follows:

$$\begin{cases} \left(1 - \frac{\rho_f}{\rho_p}\right) M_p \frac{d\boldsymbol{U}_p}{dt} = \boldsymbol{F}_{pf}' + \boldsymbol{F}_m + \boldsymbol{F}_g \\ \left(1 - \frac{\rho_f}{\rho_p}\right) I_p \frac{d\boldsymbol{\omega}_p}{dt} = \boldsymbol{T}_{pf}' + \boldsymbol{T}_m \end{cases}, \tag{27}$$

$$\begin{cases} \frac{d\boldsymbol{X}_p}{dt} = \boldsymbol{U}_p \\ \frac{d\boldsymbol{\theta}_p}{dt} = \boldsymbol{\omega}_p \end{cases}, \tag{28}$$

where $\boldsymbol{\theta}_p$ is the rotation angle, $\boldsymbol{F}_g$ is the gravity force, and $\boldsymbol{F}_{pf}'$ and $\boldsymbol{F}_m$ are the hydrodynamics force and magnetic force acting on the particle. To avoid the numerical instability due to the low-density ratio, the following time-stepping scheme for **Eq. 29** is utilized:

$$\begin{cases} \boldsymbol{U}_p(t_{n+1}) = \left[b\boldsymbol{U}_p(t_n) + c\boldsymbol{U}_p(t_{n-1}) + \frac{\Delta t\left(\boldsymbol{F}_{pf}' + \boldsymbol{F}_m + \boldsymbol{F}_g\right)}{M_p} \right] \Big/ a \\ \boldsymbol{\omega}_p(t_{n+1}) = \left[b\boldsymbol{\omega}_p(t_n) + c\boldsymbol{\omega}_p(t_{n-1}) + \frac{\Delta t\left(\boldsymbol{T}_{pf}' + \boldsymbol{T}_m\right)}{I_p} \right] \Big/ a \end{cases}, \tag{29}$$

where $a = 3(\rho_p/\rho_f - 1)$, $b = 2a - (\rho_p/\rho_f - 1)$, and $c = (\rho_p/\rho_f - 1) - a$ (Hu et al., 2015). We could easily obtain the center of mass $\boldsymbol{X}_p(t_{n+1})$, the rotation angle $\boldsymbol{\theta}_p(t_{n+1})$, the

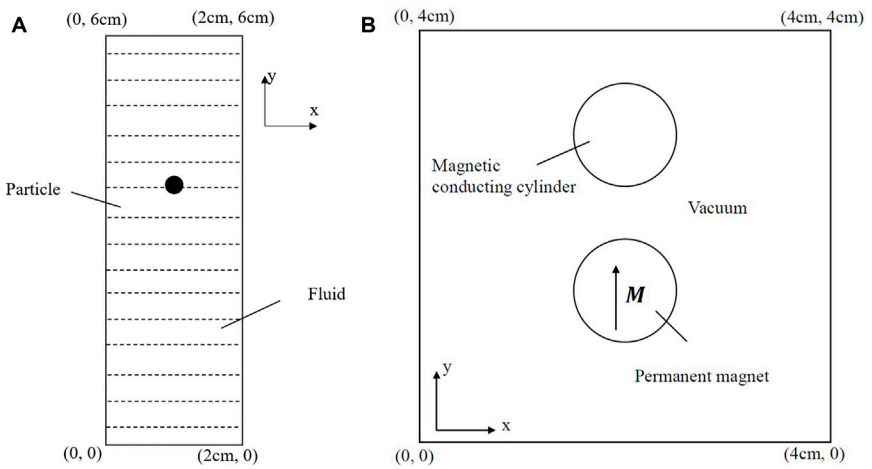

FIGURE 4 | Model of free settlement of a single particle **(A)**. Model of permanent magnet attracting magnetic conducting cylinder **(B)**.

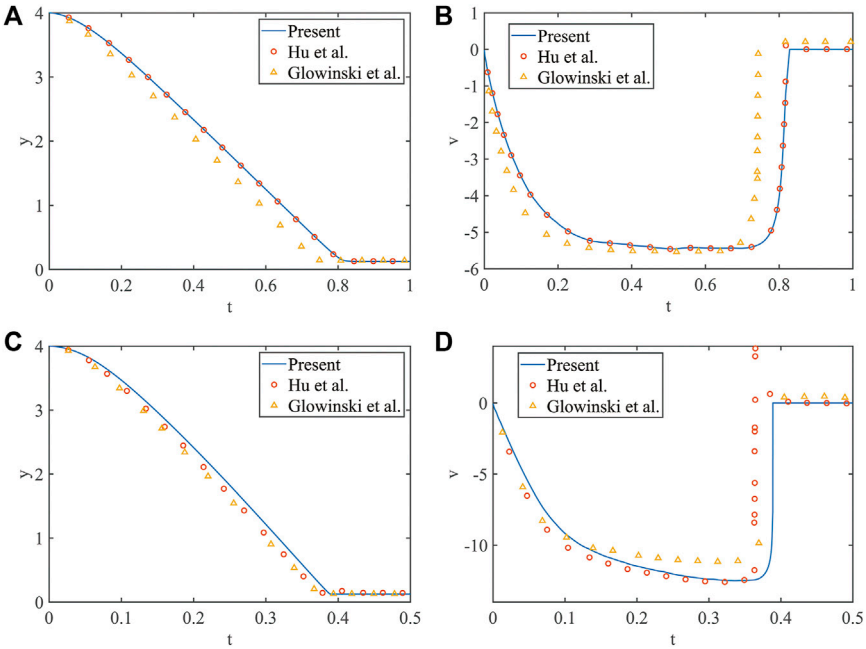

FIGURE 5 | The position of the center of the particle for $\rho_p = 1.25g/cm^2$, $\nu = 0.1cm^2/s$ **(A);** $\rho_p = 1.5g/cm^2$, $\nu = 0.01cm^2/s$ **(C)**, and the velocity of that for $\rho_p = 1.25g/cm^2$, $\nu = 0.1cm^2/s$ **(B)**; $\rho_p = 1.5g/cm^2$, $\nu = 0.01cm^2/s$ **(D)**.

translational velocity $\boldsymbol{U}_p(t_{n+1})$, and the rotational velocity $\boldsymbol{\omega}_p(t_{n+1})$ of particle at time $t_{n+1} = t_n + \Delta t$.

$$\begin{cases} \boldsymbol{X}_p(t_{n+1}) = \boldsymbol{X}_p(t_n) + \dfrac{1}{2}\left[\boldsymbol{U}_p(t_{n+1}) + \boldsymbol{U}_p(t_n)\right]\Delta t \\ \boldsymbol{\theta}_p(t_{n+1}) = \boldsymbol{\theta}_p(t_n) + \dfrac{1}{2}\left[\boldsymbol{\omega}_p(t_{n+1}) + \boldsymbol{\omega}_p(t_n)\right]\Delta t \end{cases}. \tag{30}$$

Then, the velocity $\mathbf{U}_B^d(\boldsymbol{X}_l)$ at the boundary point can be written as

$$\mathbf{U}_B^d(\boldsymbol{X}_l) = \boldsymbol{U}_p + \boldsymbol{\omega}_p \times \left(\boldsymbol{X}_l - \boldsymbol{X}_p\right). \tag{31}$$

NUMERICAL RESULTS AND DISCUSSION

In this section, the present IIM–IBM–LBM model is used to simulate several problems with fluid–particle–magnetic interaction.

Numerical Method Validation

Particle Dynamics Verification of IB–LBM

In order to examine the accuracy of the present IB–LBM, the free settlement of a single particle is simulated, which has been used by some scholars as a benchmark problem (Glowinski et al., 2001; Hu et al., 2015). In **Figure 4A**, we use a fluid domain with a width of 2 cm and a height of 6 cm, where the fluid density is $\rho_f = 1.0g/cm^2$. A circular particle with a diameter of 0.25 cm falls freely from the position of 1 cm and 4 cm under the effect of gravity. The particle density is set as $\rho_p = 1.25g/cm^2$ and $1.5g/cm^2$, and the corresponding kinematic viscosity is $\nu = 0.1cm^2/s$ and $0.01cm^2/s$, respectively.

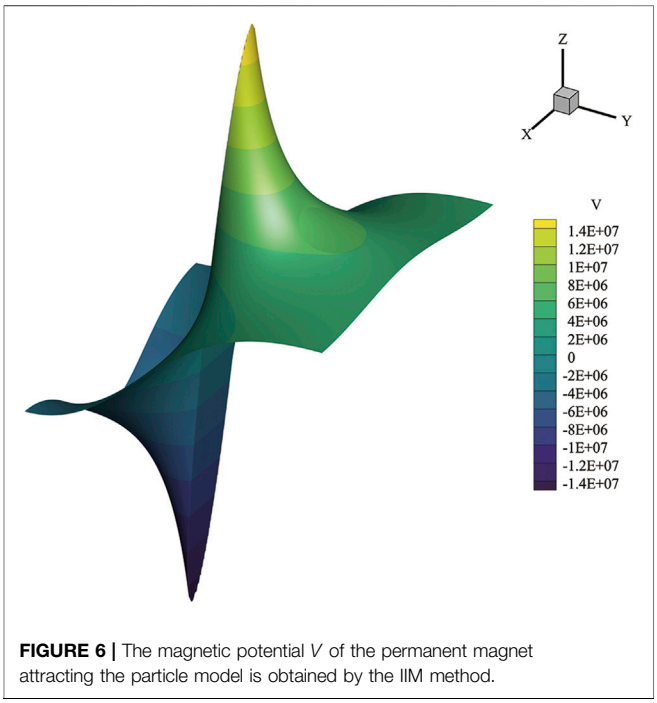

FIGURE 6 | The magnetic potential *V* of the permanent magnet attracting the particle model is obtained by the IIM method.

A 200 × 600 grid is used for the numerical simulation. **Figures 5A,B** show the variations in vertical position and velocity of the particle center with time when $\rho_p = 1.25g/cm^2$ and $\nu = 0.1cm^2/s$,

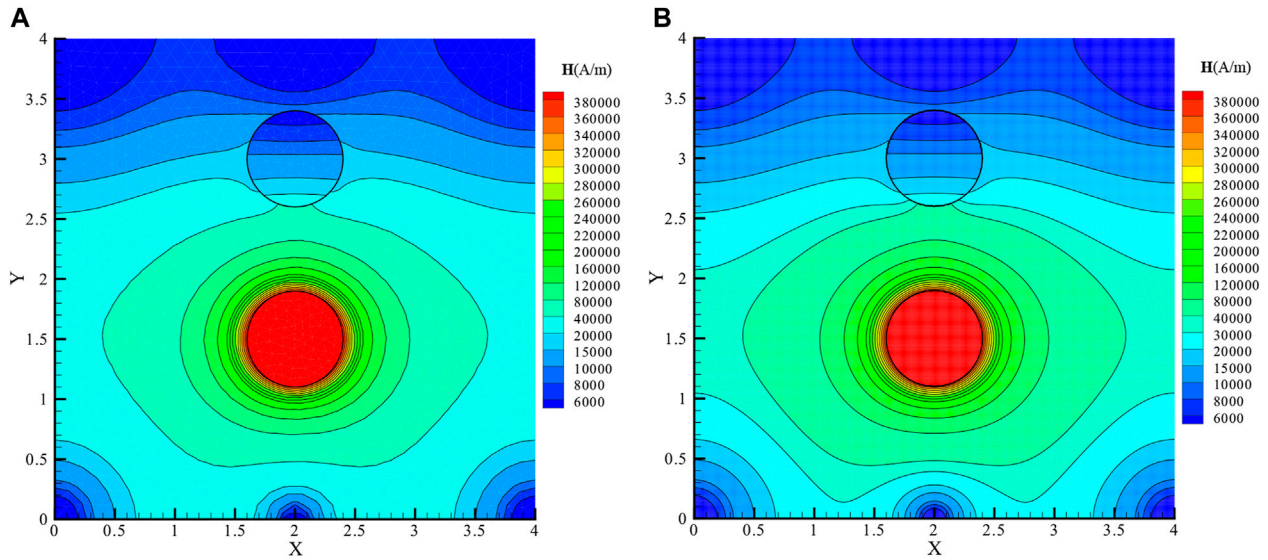

FIGURE 7 | The permanent magnet attracts the magnetic field of the magnetic conducting cylinder model, which is calculated by COMSOL **(A)** and IIM **(B)**.

respectively. Obviously, the particle quickly reaches the terminal velocity, and the velocity becomes small when the particle is close to the bottom wall at about $t = 0.8s$. The results are in good agreement with those of Hu et al. (Hu et al., 2015) and Glowinski et al. (Glowinski et al., 2001). Similarly, we simulate the case with $\rho_p = 1.5g/cm^2$ and $\nu = 0.01cm^2/s$. As shown in **Figures 5C,D**, the desired results are obtained.

Verification of Magnetic Field Calculation of IIM

To test the accuracy of IIM in terms of calculation of magnetic field, the problem of a permanent magnet attracting a magnetic conducting cylinder is studied. The results obtained are compared with those calculated by COMSOL in which the body-fitted mesh is used. As shown in **Figures 4A,B**, a circular permanent magnet with remanence $\boldsymbol{M} = (0, 75000\text{A/m})$ and a circular magnetic conducting object with $\mu_r = 2.0$ are centered at (2 cm, 1.5 cm) and (2 cm, 3 cm), respectively. Both circular solids are 0.8 cm in diameter. The computational domain is a square with a side length of 4 cm.

This numerical simulation is carried out in a 400×400 grid. **Figure 6** displays the distribution of magnetic potential V, and it can be seen clearly that the jump of the magnetic field is in the normal direction across the interface. **Figure 7** shows the magnetic field distribution. It could be observed that the closer the permanent magnet, the stronger the magnetic field intensity. Also, the contours of $|\mathbf{H}|$ across magnetic conducting cylinder interface have a jump. We can see that the present results agree well with those of COMSOL (**Figure 7**). The horizontal and vertical components of magnetic stress f_m along the interface are plotted in **Figure 8**, and the symmetrical distribution of them can be found. The numerical results of the total magnetic force acting on the magnetic conducting cylinder are shown in **Table 1**. As expected, compared with the results obtained by the diffusion interface method, IIM based on the non-body–fitted grid technology can obtain the calculation accuracy similar to that of COMSOL based on the body-fitted grid technology.

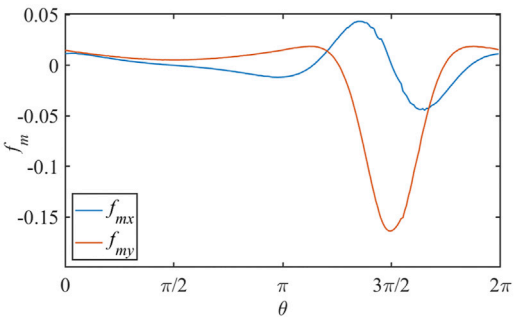

FIGURE 8 | Magnetic stress f_m along the interface of the circular conducting magnet.

Particle Sedimentation Under Permanent Magnetic Field

The diagram of particle sedimentation under a permanent magnetic field is shown in **Figure 9**. The computational domain for the magnetic field is 8 cm wide and 8 cm high. The computational domain for the flow field is 2 cm wide and 6 cm high. The circular particle with $\mu_{rp} = 2.0$ and diameter of 0.25 cm is located (4 cm, 6 cm), and the circular permanent magnet with diameter of 0.8 cm is located (4 cm, 1 cm). The remanence of the permanent magnet is $\boldsymbol{M} = (0, 75000\text{A/m})$. In this study, the relative permeability μ_{rf} of the flow field is set to 1.0.

TABLE 1 | The magnetic force on the magnetic conducting cylinder.

The position of permanent magnet center in the *y* direction (cm)	IIM		Comsol		Diffuse interface method	
	F_{mx} /N	F_{my} /N	F_{mx} /N	F_{my} /N	F_{mx} /N	F_{my} /N
1.5	0.0084	−3.0857	−0.0068	−3.1410	−0.9100	−5.0882
1.25	0.0027	−1.0788	−0.0022	−1.0982	−0.2429	−1.8545
1.0	0.00095	−0.4015	−0.00081	−0.4081	−0.0731	−0.7075
0.75	0.00034	−0.1488	−0.00030	−0.1508	−0.0231	−0.2662

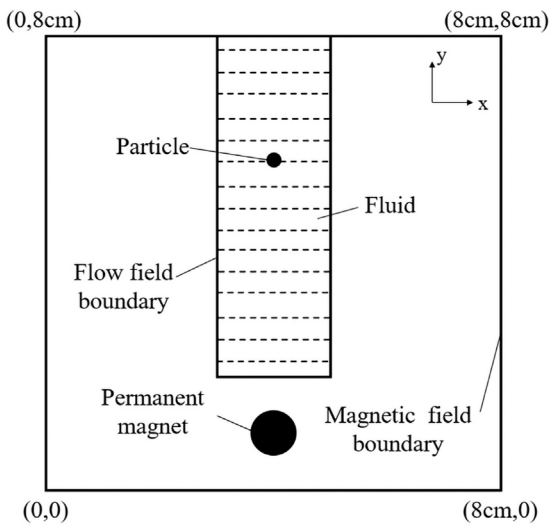

FIGURE 9 | Model of particle sedimentation under the action of permanent magnet.

A 800×800 grid is used for the present numerical simulation. The flow field simulation is carried out on a 200×600 grid. **Figure 10** shows the variations in vertical position and velocity of the particle center with time when $\rho_p = 1.25 g/cm^2$ and $\nu = 0.1 cm^2/s$, respectively. Due to the coexistence of magnetic force and gravity force, the particle settling velocity becomes larger compared with that without the effect of a permanent magnet. The closer the particle is to the permanent magnet, the greater the magnetic force and the faster the particle velocity. When $t = 0.5s$, the acceleration effect of magnetic force on particles is dominant. **Figure 11** displays the variety of magnetic stress at the particle interface at $t = 0.4s$, $0.5s$, $0.6s$. Similarly, we also study the case with $\rho_p = 1.5 g/cm^2$ and $\nu = 0.01 cm^2/s$ and reached similar conclusions (as shown in **Figure 12**).

Shear Viscosity of Suspension Containing Elliptical Particles Under the Magnetic Field

It should be pointed out that the point–dipole model is suitable for spherical-like particles. We also consider an ellipsoidal particle immersed in the two-dimensional shear flows, as shown in **Figure 13**. In order to verify the reliability of the numerical method, we calculate an example of an elliptic particle rotating in a simple shear flow when Reynolds number $Re = 1$ and the ratio of major axis to minor axis of ellipse $\alpha = 2$. The curve of angular velocity changing with angular rotation is obtained in **Figure 14** and compared with the exact solution calculated by Jeffery (Jeffery, 1922). The simulation results of this paper agree well with Jeffery's exact solution.

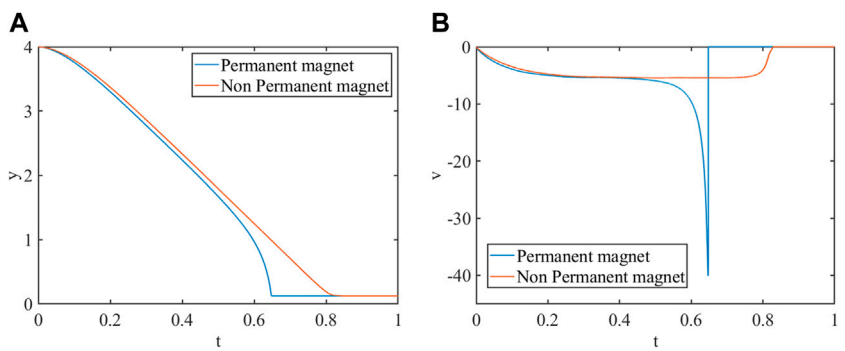

FIGURE 10 | Position **(A)** and velocity **(B)** of the center of the particle for $\rho_p = 1.25 g/cm^2$ and $\nu = 0.1 cm^2/s$.

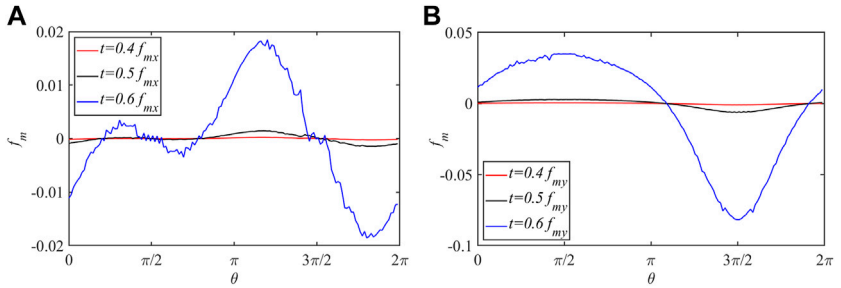

FIGURE 11 | The magnetic stress f_m in *x*-direction **(A)** and in *y*-direction **(B)** on the particle interface at t = 0.4*s*, 0.5*s*, 0.6*s*.

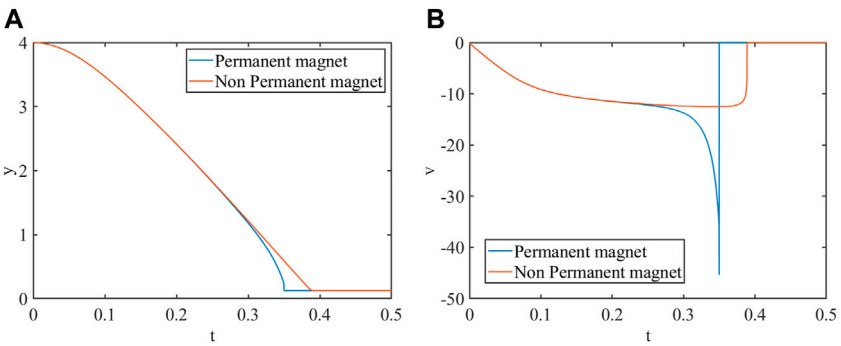

FIGURE 12 | Position **(A)** and velocity **(B)** of the center of the particle for $\rho_p = 1.5g/cm^2$ and $\nu = 0.01cm^2/s$.

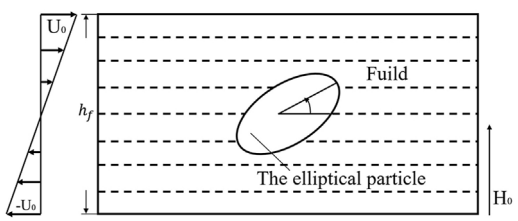

FIGURE 13 | An ellipsoidal particle in the two-dimensional shear flows under uniform magnetic field.

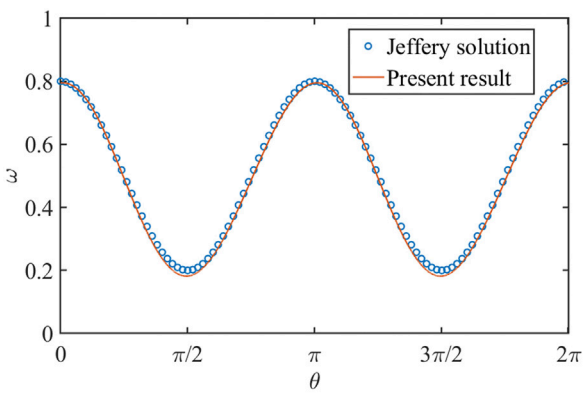

FIGURE 14 | Comparison of Jeffery solution (Jeffery, 1922) and the present simulation result.

The relation between angular velocity ω and angle θ of the elliptic particle in shear flow obtained by Jeffery (Jeffery, 1922) is as follows:

$$\omega = \frac{G}{m^2 + n^2}\left(m^2 \cos^2\theta + n^2 \sin^2\theta\right), \tag{32}$$

where the fluid shear rate $G = 2U_0/h_f$ and m, n are the length of long and short half axle.

Then, we study the shear viscosity of suspension containing elliptical particles under the magnetic field. The computational domain is 2 cm long and 1 cm wide, in which the velocities of the upper and lower planes are $U_0 = 0.1cm/s$ and $-U_0$, respectively. The elliptical particle with length–width ratio $AR = 2.0$ and relative permeability $\mu_{rp} = 2.0$ is located at the center of the computational domain. Under an external uniform magnetic field $\boldsymbol{H_b} = (0, H_0)$, the force acting on the paramagnetic ellipsoid particle is zero, but the torque is not zero.

The shear stress at the fluid node is calculated as

$$\sigma_{xy} = -\left(1 - \frac{1}{2\tau}\right)\sum_{\alpha=0}^{8}\left(f_\alpha - f_\alpha^{eq}\right)e_{\alpha x}e_{\alpha y}\,. \tag{33}$$

To study the simple rheological properties of a suspension containing elliptical particles under the external magnetic field, the effective viscosity of the suspension is calculated:

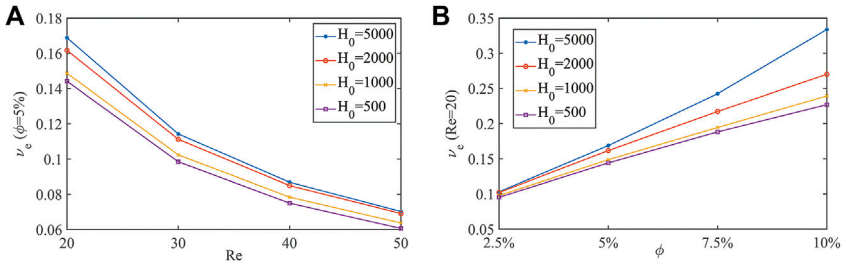

FIGURE 15 | Variation of effective kinematic viscosity ν_e of suspension with Reynolds number in different magnetic field strength H_0 when φ is 5% **(A)**. Variation of effective kinematic viscosity ν_e of suspension with volume fraction in different magnetic field strength H_0 when *Re* is 20 **(B)**.

$$\nu_e = \bar{\sigma}_{xy} h_0 / (\rho U_0), \tag{34}$$

where h_0 is the distance between two plates and U_0 is the speed of the top plate. $\bar{\sigma}_{xy}$ is the average shear force acting on the moving plane wall (Huang et al., 2012).

A grid of 200 × 100 is used for the calculation domain, and the left and right boundaries are subjected to the periodic boundary conditions. We set the initial deflection angle of the ellipse particle θ_e to *pi*/4. When the flow field becomes steady state, the effective shear viscosity ν_e of the suspension containing the elliptical particle under the magnetic field can be obtained. Through the present direct numerical simulation, the effective shear viscosities under different magnetic field strength $\boldsymbol{H}_0$, Reynolds number *Re*, and volume fraction φ of elliptical particles in suspension are compared, as shown in **Figure 15**. Obviously, the effective kinematic viscosity ν_e increases with an increase in Reynolds number *Re* and decreases with an increase in volume fraction φ. Moreover, the effective kinematic viscosity ν_e increases with the increase of magnetic field strength H_0.

CONCLUSION

The fluid–particle–magnetic interactions are modeled using the IIM–IBM–LBM coupling method. The fluid flow simulations are handled by the simple and efficient LBM. The particle motion and the hydrodynamics interaction between the particle and the flow field are computed by the momentum exchange-based IBM. Especially, we use the IIM to solve the magnetic field and calculate the magnetic force with the aid of the interface jump conditions. Unlike the point-source model or point dipole model, the hydrodynamics and magnetic forces acting on the particle are calculated using an integration method, in which the flow details and magnetic distribution around the particle are considered. Two numerical examples are simulated to verify the numerical accuracy of the present full-scale model. Moreover, particle sedimentation under a permanent magnetic field and shear viscosity of suspension containing elliptical particles under the magnetic field are also studied by the present model. The obtained results indicate that the present model has the potential to treat the complex fluid–particle–magnetic interactions.

DATA AVAILABILITY STATEMENT

The original contributions presented in the study are included in the article/supplementary material; further inquiries can be directed to the corresponding author.

AUTHOR CONTRIBUTIONS

All authors listed have made a substantial, direct, and intellectual contribution to the work and approved it for publication.

FUNDING

This work was supported by the National Natural Science Foundation of China (grant nos. 12172039, 12102228, and 11802159) and Fundamental Research Funds for the Central Universities (grant no. 2020RC201).

REFERENCES

Blūms, E., T̄Sebers, A. O., Cebers, A. O., and Maiorov, M. M. (1997). *Magnetic Fluids*. Berlin, Germany: Walter de Gruyter.

Cao, Q., Han, X., and Li, L. (2014). Configurations and Control of Magnetic Fields for Manipulating Magnetic Particles in Microfluidic Applications: Magnet Systems and Manipulation Mechanisms. *Lab. Chip* 14 (15), 2762–2777. doi:10.1039/c4lc00367e

Chen, S., and Doolen, G. D. (1998). Lattice Boltzmann Method for Fluid Flows. *Annu. Rev. Fluid Mech.* 30 (1), 329–364. doi:10.1146/annurev.fluid.30.1.329

Chiesa, M., Mathiesen, V., Melheim, J. A., and Halvorsen, B. (2005). Numerical Simulation of Particulate Flow by the Eulerian-Lagrangian and the Eulerian-Eulerian Approach with Application to a Fluidized Bed. *Comput. Chem. Eng.* 29 (2), 291–304. doi:10.1016/j.compchemeng.2004.09.002

Climent, E., Maxey, M. R., and Karniadakis, G. E. (2004). Dynamics of Self-Assembled Chaining in Magnetorheological Fluids. *Langmuir* 20 (2), 507–513. doi:10.1021/la035540z

Glowinski, R., Pan, T. W., Hesla, T. I., Joseph, D. D., and Périaux, J. (2001). A Fictitious Domain Approach to the Direct Numerical Simulation of Incompressible Viscous Flow Past Moving Rigid Bodies: Application to Particulate Flow. *J. Comput. Phys.* 169 (2), 363–426. doi:10.1006/jcph.2000.6542

Hu, Y., Li, D., Shu, S., and Niu, X. (2015). Modified Momentum Exchange Method for Fluid-Particle Interactions in the Lattice Boltzmann Method. *Phys. Rev. E Stat. Nonlin Soft Matter Phys.* 91 (3), 033301. doi:10.1103/PhysRevE.91.033301

Hu, Y., Li, D., Niu, X., and Shu, S. (2018). Fully Resolved Simulation of Particulate Flows with Heat Transfer by Smoothed Profile-Lattice Boltzmann Method. *Int. J. Heat Mass Transf.* 126, 1164–1167. doi:10.1016/j.ijheatmasstransfer.2018.05.137

Huang, H., Yang, X., Krafczyk, M., and Lu, X.-Y. (2012). Rotation of Spheroidal Particles in Couette Flows. *J. Fluid Mech.* 692, 369–394. doi:10.1017/jfm.2011.519

Jeffery, G. B. (1922). The Motion of Ellipsoidal Particles Immersed in a Viscous Fluid. *Proc. R. Soc. Lond. Ser. A Contain. Pap. Math. Phys. Character* 102 (715), 161–179. doi:10.1098/rspa.1922.0078

Kang, S., and Suh, Y. K. (2011). An Immersed-Boundary Finite-Volume Method for Direct Simulation of Flows with Suspended Paramagnetic Particles. *Int. J. Numer. Meth. Fluids* 67 (1), 58–73. doi:10.1002/fld.2336

Kang, S., and Suh, Y. K. (2011). Direct Simulation of Flows with Suspended Paramagnetic Particles Using One-Stage Smoothed Profile Method. *J. Fluids Struct.* 27 (2), 266–282. doi:10.1016/j.jfluidstructs.2010.11.002

Kang, T. G., Hulsen, M. A., den Toonder, J. M. J., Anderson, P. D., and Meijer, H. E. H. (2008). A Direct Simulation Method for Flows with Suspended Paramagnetic Particles. *J. Comput. Phys.* 227 (9), 4441–4458. doi:10.1016/j.jcp.2008.01.005

Ke, C.-H., Shu, S., Zhang, H., and Yuan, H.-Z. (2017). LBM-IBM-DEM Modelling of Magnetic Particles in a Fluid. *Powder Technol.* 314, 264–280. doi:10.1016/j.powtec.2016.08.008

Kim, Y. S., and Park, I. H. (2010). FE Analysis of Magnetic Particle Dynamics on Fixed Mesh with Level Set Function. *IEEE Trans. Magn.* 46 (8), 3225–3228. doi:10.1109/tmag.2010.2045747

Ku, J., Chen, H., He, K., and Yan, Q. (2015). Simulation and Observation of Magnetic Mineral Particles Aggregating into Chains in a Uniform Magnetic Field. *Miner. Eng.* 79, 10–16. doi:10.1016/j.mineng.2015.05.002

LeVeque, R. J., and Li, Z. (1994). The Immersed Interface Method for Elliptic Equations with Discontinuous Coefficients and Singular Sources. *SIAM J. Numer. Anal.* 31 (4), 1019–1044. doi:10.1137/0731054

Luo, K., Wang, Z., Fan, J., and Cen, K. (2007). Full-Scale Solutions to Particle-Laden Flows: Multidirect Forcing and Immersed Boundary Method. *Phys. Rev. E Stat. Nonlin Soft Matter Phys.* 76 (6), 066709. doi:10.1103/PhysRevE.76.066709

Niu, X. D., Shu, C., Chew, Y. T., and Peng, Y. (2006). A Momentum Exchange-Based Immersed Boundary-Lattice Boltzmann Method for Simulating Incompressible Viscous Flows. *Phys. Lett. A* 354 (3), 173–182. doi:10.1016/j.physleta.2006.01.060

Patel, R. G., Desjardins, O., Kong, B., Capecelatro, J., and Fox, R. O. (2017). Verification of Eulerian-Eulerian and Eulerian-Lagrangian Simulations for Turbulent Fluid-Particle Flows. *AIChE J.* 63 (12), 5396–5412. doi:10.1002/aic.15949

Peskin, C. S. (2002). The Immersed Boundary Method. *Acta Numer.* 11, 479–517. doi:10.1017/s0962492902000077

Sand, A., Stener, J. F., Toivakka, M. O., Carlson, J. E., and Pålsson, B. I. (2016). A Stokesian Dynamics Approach for Simulation of Magnetic Particle Suspensions. *Miner. Eng.* 90, 70–76. doi:10.1016/j.mineng.2015.10.015

Conflict of Interest: The authors declare that the research was conducted in the absence of any commercial or financial relationships that could be construed as a potential conflict of interest.

Publisher's Note: All claims expressed in this article are solely those of the authors and do not necessarily represent those of their affiliated organizations or those of the publisher, the editors, and the reviewers. Any product that may be evaluated in this article, or claim that may be made by its manufacturer, is not guaranteed or endorsed by the publisher.

frontiers | Frontiers in Materials

TYPE Original Research
PUBLISHED 08 August 2022
DOI 10.3389/fmats.2022.932697

OPEN ACCESS

EDITED BY
Yang Yu,
Western Sydney University, Australia

REVIEWED BY
Tadeusz Szumiata,
Kazimierz Pułaski University of Technology and Humanities in Radom, Poland
Guoyuan Zhang,
Xidian University, China

*CORRESPONDENCE
Decai Li,
lidecai@mail.tsinghua.edu.cn

SPECIALTY SECTION
This article was submitted to Smart Materials,
a section of the journal
Frontiers in Materials

RECEIVED 30 April 2022
ACCEPTED 07 July 2022
PUBLISHED 08 August 2022

CITATION
Liu S, Li D, He X and Zhang Z (2022), Structure design study of vacuum magnetic fluid seal.
Front. Mater. 9:932697.
doi: 10.3389/fmats.2022.932697

Structure design study of vacuum magnetic fluid seal

Sijia Liu[1], Decai Li[1,2]*, Xinzhi He[1] and Zhili Zhang[1]

[1]School of Mechanical, Electronic Control Engineering, Beijing Jiaotong University, Beijing, China, [2]State Key Laboratory of Tribology, Tsinghua University, Beijing, China

In response to the requirement of high vacuum and leakage rate of a small-diameter low-speed device of an enterprise, a double magnet multistage magnetic fluid sealing device is designed by analyzing the advantages and disadvantages of four different vacuum magnetic fluid sealing devices. The Ansys simulation software is used to analyze and calculate the magnetic field strength and distribution of this magnetic fluid sealing device, discuss the influence of the number of intermediate section pole teeth and the seal gap size on the pressure resistance of the magnetic fluid seal, and summarize the law. The proposed structure of the double magnet multistage magnetic fluid sealing device is optimized and determined by the influence law of structural parameters. Compared with traditional sealing forms, the advantages of the sealing device proposed in this article can be summarized as low processing difficulty, good reliability, and high pressure resistance. The reliability and rationality of this magnetic fluid sealing device are demonstrated by Ansys simulation results, which provide a reference for the structural design and analysis of small-diameter low-speed vacuum magnetic fluid sealing devices.

KEYWORDS

magnetic fluid seal, structure design, finite element analysis, pressure resistance, vacuum device

Introduction

With the rapid development of industrial equipment and machinery manufacturing, the sealing device to protect the working medium from leakage or pollution is increasingly important. The failure of the sealing device will cause the working medium to leak and pollute the surrounding environment, whereas external impurities will also invade the equipment to seriously affect the normal operation of the equipment, which will cause huge economic losses and production waste (Szydło et al., 1999). With the development of aerospace, military equipment, vacuum equipment, petroleum exploration, biomedical and other industries, and society's continued attention to resource conservation, environmental protection, etc. (Radionov, 2015), these industries have increasingly high requirements for the sealing performance of equipment, especially the leakage rate and reliability. Traditional sealing forms have been difficult to meet these demanding requirements; compared with mechanical seals, packing seals, centrifugal seals, and other traditional sealing methods, magnetic fluid seals have many advantages (Jain et al., 2017), and their scope of application is expanding.

Magnetic fluid, also known as ferrofluid, etc., is a new type of functional material (Li, 2003), mainly composed of a mixture of nanometer-diameter strong magnetic particles, carrier fluids, and surfactants. The magnetic fluid contains strong magnetic particles with very small diameters, mostly below 10 nm. The chaotic Brownian motion of these particles in the carrier fluid can counteract the settling effect of their own gravity and weaken the electromagnetic cohesion between the particles, making the magnetic fluid appear as a stable gel, which does not easily produce precipitation and cohesion. Magnetic fluid is similar to ordinary colloids in the absence of an applied magnetic field and exhibits magnetic properties in the presence of an applied magnetic field (Li, 2016), which can be controlled by a magnetic field and thus have many unique magnetic, rheological, optical, and acoustic properties (Yang and Huang, 2017). Because magnetic fluids have both the fluidity of liquids and the magnetism of solid magnetic materials, they have high academic value and wide application prospects. Magnetic fluid sealing is one of the most successful applications thus far (Berkovsky et al., 1993), mainly used in the field of vacuum sealing and low and medium pressure differential gas sealing (Wang, 2019). When sealing gases, magnetic fluid sealing technology can not only eliminate the frictional wear of traditional sealing structures but also achieve "zero" leakage (Li, 2003), and because of the low viscous friction of a magnetic fluid, its service life can reach more than 10 years.

In 2002, Gu Hong et al. (Gu et al., 2002) studied the effect of saturation magnetization strength of magnetic fluid and the amount of injected magnetic fluid on the sealing performance of the magnetic fluid. In 2014, He Xinzhi et al. (He et al., 2014) studied the effect of gravity on the sealing performance of magnetic fluid with large diameters and large seal gaps. In 2020, Chen Yibiao et al. (Chen et al., 2020) studied the variation law of temperature of magnetic fluid and its effect on sealing performance. The above-mentioned literature analyzes the influence of the properties of magnetic fluids themselves on sealing applications. In 2007, Sun Mingli et al. (Sun et al., 2007) applied Ansys software to simulate and analyze the magnetic field distribution of a three-tooth, four-slot magnetic fluid seal structure and optimize the pole tooth size. In 2008, He Xinzhi et al. (He et al., 2008) designed and studied a large-diameter magnetic fluid static sealing device. In 2016, Wang Hujun et al. (Wang et al., 2016a) compared and studied the pressure resistance performance of magnetic fluid seal gas and liquid. In 2020, Lv Taotao et al. (Lv et al., 2020) applied Maxwell analysis software for magnetic field analysis of large gap magnetic fluid seal structures. Most of the literature focuses on the study of large-diameter magnetic fluid seals, and there are fewer structural designs and discussions for small-diameter magnetic fluid seals.

Based on the above analysis, the authors take a small-diameter low-speed vacuum device of an enterprise as the research object and design and build a model of a double magnet multistage magnetic fluid sealing device. The authors analyze and calculate the magnetic field strength and distribution of this sealing device using Ansys simulation software and discuss the influence of the number of pole teeth in the intermediate section and the size of the seal gap on the pressure resistance. It can provide a reference basis for the structural design of a small-diameter low-speed vacuum magnetic fluid sealing device. It also lays the foundation for the subsequent physical processing of the vacuum device.

Design of vacuum magnetic fluid sealing device

Principle of magnetic fluid seal and pressure resistance formula

As a new type of seal, the magnetic fluid seal uses a polymagnetic structure to achieve a nonuniform magnetic field distribution to confine the magnetic fluid in the seal gap, forming a liquid "O" seal ring (Li et al., 2014) to achieve the sealing effect.

The Bernoulli equation (Li, 2010; Chi, 2011) for magnetic fluid can be simplified as

$$p^* + \frac{1}{2}\rho_f V^2 + \rho_f g h - \mu_0 \int_0^H M dH = C \tag{1}$$

where $p^* = p + \mu_0 \int_0^H M dH - \mu_0 \int_0^H \rho_f \frac{\partial M}{\partial \rho_f} dH$. p is the pressure on the magnetic fluid; ρ_f is the density of the magnetic fluid; V is the velocity of the magnetic fluid; g is the acceleration of gravity; h is the height of the magnetic fluid film; μ_0 is the vacuum permeability, $\mu_0 = 4\pi \times 10^{-7} N/A^2$; M is the magnetization strength of the magnetic fluid; and H is the magnetic field strength.

When the magnetic fluid sealing device is at medium or low speeds, its pressure resistance is approximately equal to that of the static seal, so the effect of centrifugal force can be disregarded (Wang et al., 2016b). According to Eq. 1 and its corresponding assumptions, the single-stage pressure resistance formula (He et al., 2014) for magnetic fluid seals can be introduced as

$$\Delta p_i = \mu_0 M_s (H_{i\max} - H_{i\min}) = \mu_0 M_s \Delta H_i \tag{2}$$

where M_s is the saturation magnetization strength of the magnetic fluid and ΔH_i is the difference between the maximum and minimum magnetic field strength at the i-th level of pole teeth.

For multistage magnetic fluid seals, the total pressure resistance formula (Li et al., 2002) is

$$\Delta P = \mu_0 M_s \sum_{i=1}^{N} \Delta H_i \tag{3}$$

where N is the total number of pole teeth in the magnetic fluid seal.

TABLE 1 Physical parameters of magnetic fluid used in this article.

Physical parameters	Density/$[g/cm^3]$	Saturation magnetization strength/$[kA/m]$	80°C evaporation/$[(g/cm^2)\cdot h]$
Ester-based magnetic fluid	1.27	31.6	5.1×10^{-6}

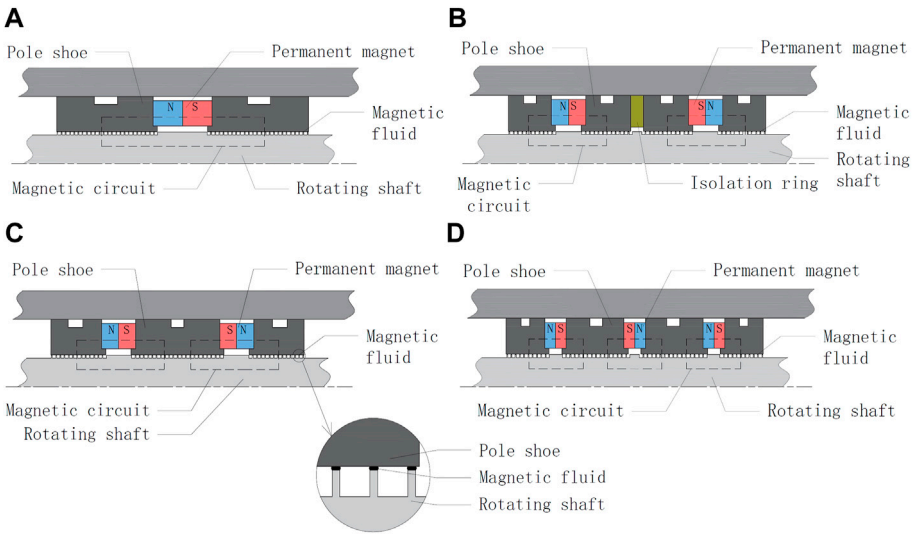

FIGURE 1
Structural design of vacuum magnetic fluid sealing device. **(A)** Single magnet multistage sealing structure. **(B)** Double magnets plus isolation ring multistage sealing structure. **(C)** Double magnets multistage sealing structure. **(D)** Three magnets multistage sealing structure.

Selection of magnetic fluids

The magnetic fluid can be better bound by the magnetic field in the seal gap thus ensuring the sealing effect, at a higher saturation magnetization strength. At the same time, to avoid the influence of gravity and temperature rise (Cheng, 2020), the magnetic fluid used for sealing should preferably have a higher saturation magnetization strength, a lower density, and a lower evaporation volume. In this article, a certain ester-based magnetic fluid prepared by the chemical coprecipitation method group is used; the specific parameters are shown in Table 1.

Overall structure design and selection

The vacuum side of the device contains gaseous sodium fluoride corrosive gas, the requirements for vacuum and leakage rate are very high, requires a magnetic fluid sealing device operating temperature of 50℃, a rated speed of 750 rpm, a spindle section shaft diameter of 15 mm. Theoretically known magnetic fluid formed "O" seal ring less than 150 mm is a small diameter (Li and Du, 2018), so the device is a small-diameter low-speed vacuum magnetic fluid sealing device.

According to the actual installation space requirements of the device, limiting the overall length of the magnetic fluid sealing device remains unchanged, based on previous design experience (Li, 2010), this article proposes four different vacuum magnetic fluid sealing device structures as shown in Figure 1.

The structure shown in Figure 1A is a single magnet multistage sealing structure with only one magnetic circuit, which is simple and easy to use. However, because of the pressure resistance requirement, there are many single-side pole teeth and large magnetic flux, which require the use of permanent magnets with large magnetic energy product, and their corresponding volume and weight will be larger, and the overall pressure resistance of the device will be reduced when the number of pole teeth is too many. The structure shown in Figure 1B is a multistage sealing structure with two magnets and an isolation ring, in which the two magnetic circuits exist independently and are separated by a nonconducting magnetic isolation ring. The outer diameter of the isolation ring is the same as the outer diameter of the pole shoes, but the precision of the sealing structure is high, and adding the isolation ring will

increase the overall weight. The structure shown in Figure 1C is a double magnet multistage sealing structure, which is a deformation of the structure shown in Figure 1B. Instead of separating two independent magnetic circuits with an isolation ring, two permanent magnets are connected in series in the direction of homogeneous repulsion, thereby increasing the length of the intermediate section of the pole shoe and the number of corresponding pole teeth, making it common for two permanent magnets, reducing the occurrence of magnetic leakage, generating a strong magnetic field, and significantly increasing the overall pressure resistance of the device. However, because the permanent magnets are opposite to each other, it is necessary to use permanent magnet materials with good demagnetization resistance. The structure shown in Figure 1D is a three-magnet multistage sealing structure, in which three permanent magnets are connected in series in the direction of two and two homogeneous repulsions to form three independent magnetic circuits; however, this sealing structure is difficult to process, the installation accuracy is difficult to ensure, and the increase in permanent magnets will increase the overall weight.

Based on the above analysis, after considering the processing accuracy, installation difficulty, weight, and pressure resistance requirements, the double magnet multistage sealing structure shown in Figure 1C is selected, including the magnetic conductive rotating shaft, two permanent magnets, two end pole shoes, and one intermediate pole shoe.

Design and selection of key components

The size of the pressure resistance of the magnetic fluid sealing device is affected by many factors, among which the size and material of the permanent magnet, the structure of the pole shoe, the shape and number of teeth of the pole teeth, and the size of the seal gap are its main influencing factors (Zou et al., 1994), which are also the focus of the sealing device design.

It is known that the pressure resistance of a magnetic fluid sealing device is related to the magnetic field distribution in the seal gap. The larger the parameters of remanent magnetism and coercivity of permanent magnet, the larger the magnetic field gradient in the seal gap and the larger the pressure resistance of the magnetic fluid sealing device. Among several common permanent magnet materials, Nd–Fe–B permanent magnet material has the best value in terms of remanence, coercivity, maximum magnetic energy product, etc. (Song and Chen, 1984); moreover, its hardness is high and the economy is good, so Nd–Fe–B is chosen as the permanent magnet material. The permanent magnet adopts an integral ring structure, which has little magnetic leakage and better magnetic stability. Through calculation, an inner diameter of 18 mm, an outer diameter of 30 mm, and a thickness of 8 mm were determined for a permanent magnet.

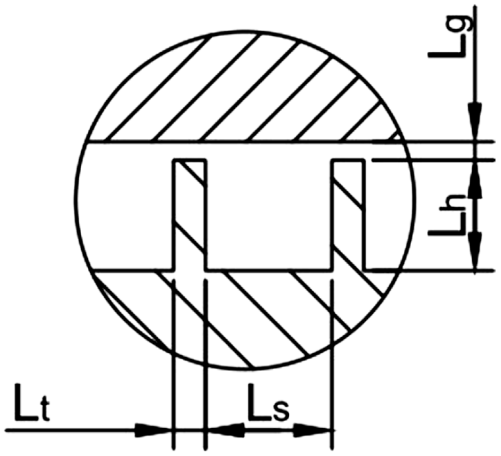

FIGURE 2
Pole tooth morphology.

The pole shoe is an important part of the magnetic fluid sealing device (Xu et al., 2019), and the material chosen is 2Cr13, a soft magnetic material with excellent magnetic properties and good machinability. A groove is machined on the outside of the pole shoe, and a seal is used to ensure a static seal between the pole shoe and the nonconducting magnetic housing. Moreover, to facilitate the installation and positioning of the permanent magnet, a tab is machined on the side of the pole shoe that contacts the permanent magnet.

Because of the small shaft diameter of the spindle section of the device, the inner diameter of the corresponding pole shoe is also small. To facilitate processing and installation, the pole teeth are designed on the magnetic guide shaft. The shape and size of the pole teeth are very important for the pressure resistance of the magnetic fluid seal. Compared with the three common tooth shapes: triangular teeth, rectangular teeth, and trapezoidal teeth (Cheng, 2016), rectangular teeth are easier to process, performance can be easily guaranteed, and the magnetic force lines are more concentrated under the rectangular teeth. Thus, rectangular teeth are chosen for the pole tooth shape; the tooth shape parameters of rectangular teeth (Cheng, 2016) are $L_t/L_g = 2$, $L_s/L_g = 8$, and $L_h/L_s = 0.875$. According to the domestic and international design experience and the actual operation of the equipment, this article takes $L_g = 0.1mm$, gets tooth width $L_t = 0.2mm$, slot width $L_s = 0.8mm$, and tooth height $L_h = 0.7mm$; the design is shown in Figure 2.

In this article, the number of intermediate section pole teeth and the seal gap size of the magnetic fluid sealing device are changed accordingly. The magnetic field distribution under different structures is simulated and analyzed using the finite element method.

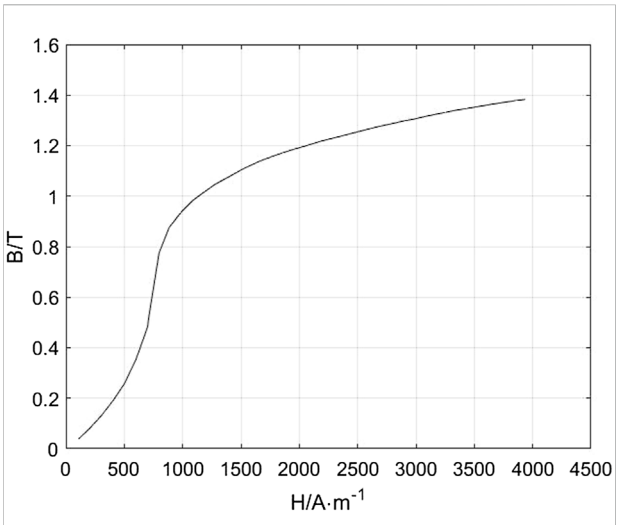

FIGURE 3
B–H curve of 2Cr13.

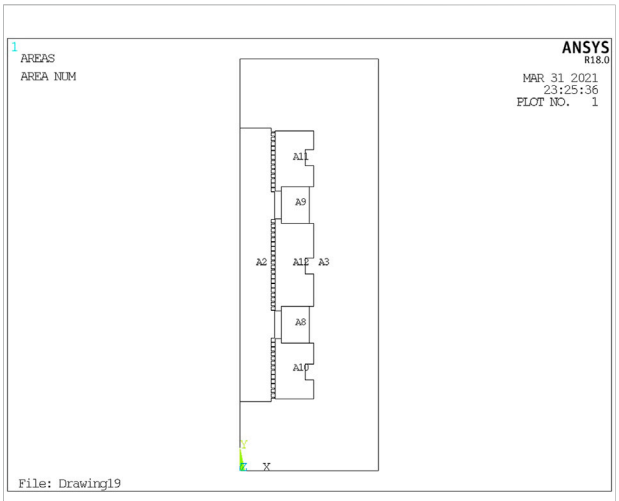

FIGURE 4
Import structure diagram.

Finite element analysis of magnetic field of magnetic fluid sealing device

Because the vacuum magnetic fluid seal is an axisymmetric structure, the magnetic field of the permanent magnet does not change with time. To simplify the calculation, this article uses Ansys simulation software to perform a 2D static analysis and makes the following assumptions (Li, 2010; Li et al., 2002).

1) The permanent magnet is assumed to be magnetized uniformly, and its uniformity is not affected by the magnetic field.
2) The distribution of seal gaps in this sealing device is assumed to be uniform.
3) The magnetic fluid is assumed to have approximately the same magnetic permeability as the vacuum.
4) All errors generated during machining and assembly are ignored.

Creating the physical environment

First, create the physical environment in Ansys simulation software, and define the material properties of the two permanent magnets, the three pole shoes, the rotating shaft, and the air as follows: the vacuum permeability of air $\mu_r = 1.0$ for material 1; the Nd–Fe–B permanent magnets $\mu_M = 1.05$; and coercive force $H_{c1} = 890000A/m$ and $H_{c2} = -890000A/m$ for materials 2 and 3, respectively; define the B–H curves of the pole shoe and the permeable spool material 2Cr13 as shown in Figure 3 for material 4.

Importing the model

As an example, the number of pole teeth in each end is 13, the number of pole teeth in the intermediate section is 19, and the seal gap is $L_g = 0.1mm$. The model of the magnetic fluid sealing device drawn in computer-aided design is imported into Ansys simulation software for analysis. In the established two-dimensional model, the y-axis is the rotation axis and the symmetry axis of the air domain, permanent magnet, and pole shoe. A3 represents the air domain, and since the magnetic fluid and vacuum permeability are assumed to be approximately the same, the magnetic fluid and air are assigned to material 1. A8 and A9 represent the permanent magnets, which are assigned to materials 2 and 3, respectively, two Nd–Fe–B permanent magnets with opposite coercivity directions. A10–12 and A2 represent the pole shoe and rotating shaft, respectively, and are assigned to material 4, which is called 2Cr13. The structure of the introduction device is shown in Figure 4.

Dividing the grid

Setting the smart grid division accuracy level to 5, triangle or quadrilateral grids are automatically generated on the plane by 2D free meshes. The grid accuracy can be controlled by the number of grids, edge lengths, and curvature in Ansys. It can be seen that the grid at the pole tooth is more dense, which is convenient for subsequent analysis of the magnetic field strength. After the mesh division, the boundary condition of parallel magnetic lines is selected to restrict the magnetic lines inside the boundary in order to prevent the magnetic leakage phenomenon. After dividing the grid and loading the boundary conditions, it is shown in Figure 5 shows the structure schematic.

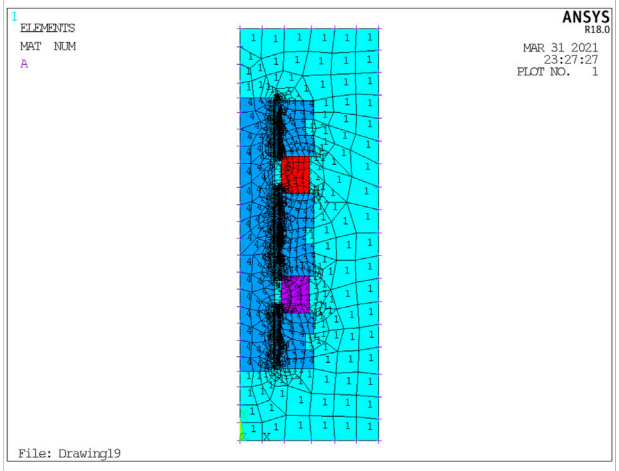

FIGURE 5
Delineate the grid and load the boundary conditions.

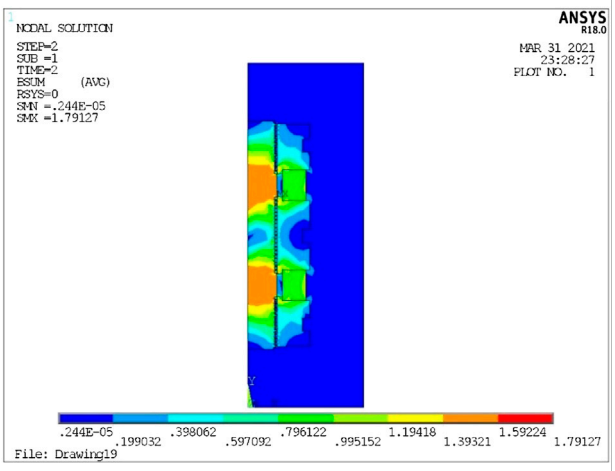

FIGURE 7
Node magnetic flux density cloud.

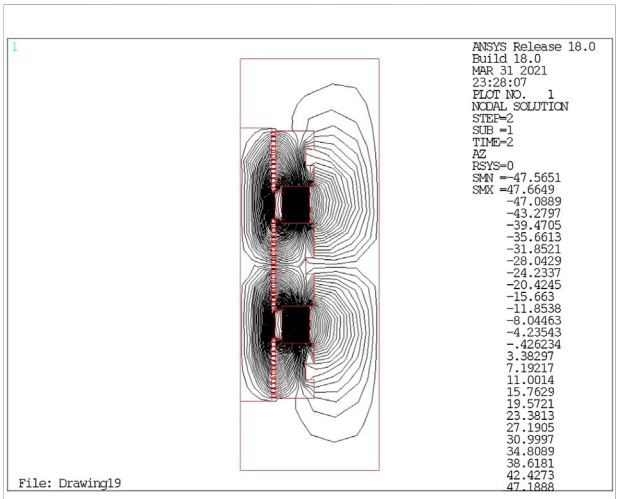

FIGURE 6
Magnetic line distribution map.

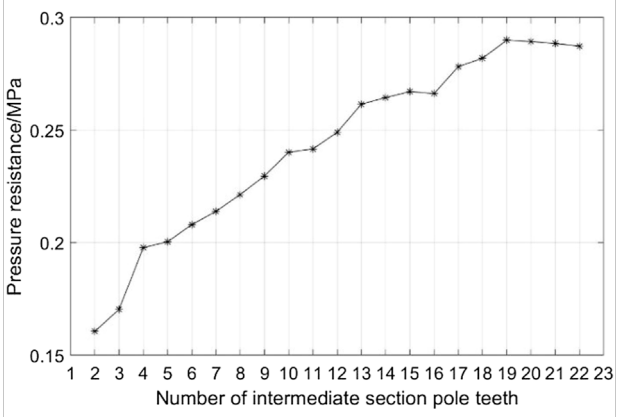

FIGURE 8
Relationship between the number of intermediate section pole teeth and pressure resistance.

Static solution

After the preprocessing is completed, the static analysis can be further solved. The simulation analysis results are converged, and the processing results can be viewed after the successful solution as shown in Figure 6 and Figure 7.

As shown in Figure 6, the magnetic lines of force are distributed. It can be seen that the magnetic lines of force start from the permanent magnet and return to the permanent magnet after passing through the pole shoe, magnetic fluid, and rotating shaft, forming two closed magnetic circuits. In the seal gap between the pole teeth and the pole shoe, the magnetic lines are the most dense, and only a small amount of magnetic lines are distributed in the air, which means the magnetic flux at the gap is the largest and the magnetic field distribution is more concentrated. At the same time, most of the magnetic lines of force pass through the pole teeth, which means that the pole teeth give full play to the role of accumulating magnetic lines of force and firmly adsorb the magnetic fluid at the seal gap, making the sealing device more reliable.

As shown in Figure 7, the nodal magnetic flux density clouds visually reflect the magnetic field strength of each part of the device. It can be seen that the magnetic flux density in the intermediate section of the pole teeth is higher than that on both sides because the pole teeth in the intermediate section are supplied by permanent magnets with opposite poles on the

TABLE 2 Relationship between seal gap size and magnetic field strength and pressure resistance.

Seal gap/mm	Sum of magnetic field strength difference $\sum_{i=1}^{N}\Delta H_i/[A\cdot m^{-1}]$	Pressure resistance/Mpa
0.1	7299386	0.2899
0.15	4550040	0.1807
0.2	3159390	0.1255
0.25	2854130	0.1133

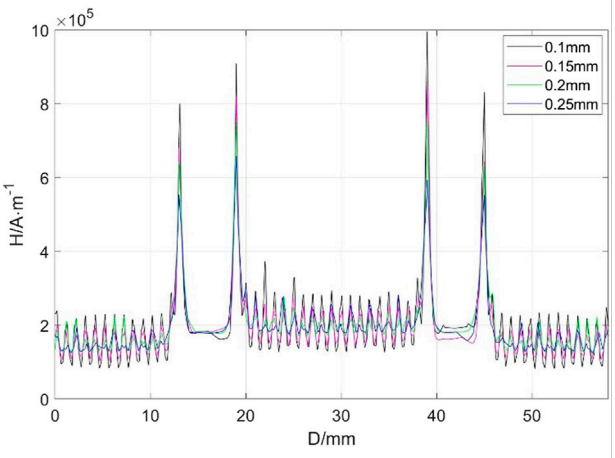

FIGURE 9
Magnetic field distribution under different seal gaps.

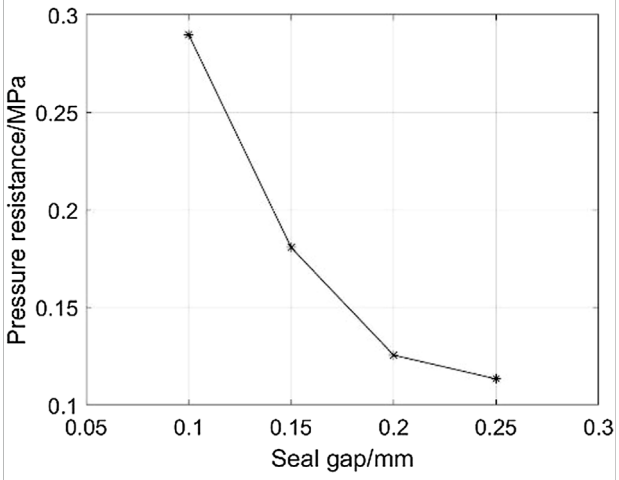

FIGURE 10
Relationship between seal gap size and pressure resistance.

left and right sides. The pole teeth on both sides are supplied by a single permanent magnet, and the magnetic flux density is relatively small. The magnetic flux density is the highest in parts where the pole teeth are close to the pole shoe, indicating that the magnetic field is the strongest at the pole teeth, so the structure of the magnetic fluid seal is reasonably designed. The pressure resistance of the seal is verified by specific numerical calculations below.

Simulation analysis of the device under different structural parameters

Influence of the number of intermediate section pole teeth on the pressure resistance

The number of pole teeth directly affects the magnetic field gradient and magnetic flux in the gap of the vacuum magnetic fluid sealing device (Fan, 2019), which directly affects the effect of sealing pressure resistance. Therefore, the reasonable design of the number of teeth is of great significance to improve the pressure resistance of the magnetic fluid seal.

In this article, we fix the size and material of two permanent magnets, and the number of pole teeth on both ends is 13; we also discuss the influence of the number of pole teeth in the intermediate section on the pressure resistance. The number of pole teeth in the intermediate section is from 2 to 22 for simulation calculation, and the total difference in magnetic field strength of multistage teeth is obtained. The pressure resistance is calculated by substituting the data into Eq. 3.

The relationship between the pressure resistance and the number of pole teeth in the intermediate section is shown in Figure 8. It is not difficult to find that when the number of intermediate section pole teeth increases from 2 to 15 and from 16 to 19; the pressure resistance of the sealing device increases with the increase in the number of teeth. When the number of intermediate section pole teeth is 16, the pressure capacity decreases slightly. It may be because of the calculation error caused by simulation grid division, which has little effect on the overall trend. When the number of

intermediate section pole teeth increases from 19 to 22, the pressure resistance of the sealing device decreases with the increase in the number of teeth. This is because the maximum magnetic energy product provided is certain when the size and number of permanent magnets are fixed. The magnetic fluid in the intermediate section reaches magnetic saturation, and the magnetic field line distributed to each pole tooth decreases. Then, the magnetic field strength difference under each pole tooth decreases, resulting in a decrease in the pressure resistance of the device.

Therefore, it is beneficial to set more number of pole teeth within the allowed axial length to improve the pressure resistance of the vacuum magnetic fluid sealing device but not too many, generally not more than 20 pole teeth.

Effect of seal gap size on pressure resistance

In the general magnetic fluid seal structure, the seal gap refers to the gap between the top of the pole tooth and the shaft or sleeve; for this vacuum magnetic fluid sealing device, the seal gap refers to the gap between the top of the pole tooth and the pole shoe. In general, the seal gap in the magnetic fluid seal structure of less than 0.25 mm means a small gap (Yang, 2014). Because of the small diameter of the shaft, the device is designed for small gaps. The number of pole teeth at both fixed ends is 13, and the number of pole teeth in the intermediate section is 19, which are taken as 0.1, 0.15, 0.2, and 0.25 mm for simulation calculation. The total difference of magnetic field strength of multistage pole teeth is obtained, which is substituted into Eq. 3 to calculate the pressure resistance, shown in Table 2.

In Ansys simulation software, a number of key points are taken from the bottom up along the positive direction of y-axis at the seal gap. These points are connected to form a path through the seal gap, and the distribution of magnetic lines is mapped to this path to obtain the magnetic field intensity values and their distribution at the corresponding points in the seal gap. The simulation results of the magnetic field under different seal gaps are shown in Figure 9. It can be seen that the magnetic field strength is highest at the tip of the pole tooth and lowest at the groove on both sides of the pole tooth for the seal gap from 0.1 to 0.25 mm. At the same time, the difference in magnetic field strength between the tip and the groove decreases as the seal gap increases. The tip effect exists at the shoulder of the shaft, where many magnetic lines of force are gathered and the magnetic field strength is the highest. Because of the large number of pole teeth of the device, the magnetic lines of force gathered at the shoulder of the shaft do not have much influence on the final result, which further reflects the rationality of the seal structure design.

The relationship between the pressure resistance and the seal gap size is shown in Figure 10. The pressure resistance at a seal gap of 0.15 mm decreases by approximately one-third compared with that at a seal gap of 0.1 mm and decreases even more at a seal gap of 0.2 and 0.25 mm. This reflects that for small gap magnetic fluid sealing devices, the pressure resistance of magnetic fluid seal decreases with the increase in the seal gap, under the condition that other parameters remain unchanged.

Conclusion

In this article, a double magnet multistage magnetic fluid sealing device meeting the requirements of industrial applications is designed by analyzing the advantages and disadvantages of four different structures of vacuum magnetic fluid sealing devices under the condition of a fixed overall length of the sealing device. The proposed structure of the double magnet multistage magnetic fluid sealing device is optimized and determined by the design of key parts, simulation of the finite element of the magnetic field, and the calculation of sealing pressure resistance under different structural parameters. The proposed optimized structure is that the number of polar teeth at both ends is 13, the number of polar teeth in the intermediate section is 19, and the sealing clearance is 0.1 mm.

Compared with the traditional single magnet magnetic fluid sealing device, the advantages of the proposed device can be summarized as follows:

1) The processing difficulty of the three pole shoes and the installation difficulty of the whole device are both reduced by designing the pole teeth on the magnetic guide rotating shaft.
2) The overall withstand voltage capability of the device is greatly improved using two permanent magnets with the same pole and opposite pole to form two magnetic circuits.

Ansys simulation results show that the proposed structural design of the device is reliable and reasonable, and the theoretically calculated withstand voltage value can reach 0.2899 Mpa, which meets the working requirements. This article lays a foundation for the subsequent physical processing of vacuum devices and also provides a reference for the structural design and analysis of small-diameter low-speed vacuum magnetic fluid sealing devices.

Data availability statement

The original contributions presented in the study are included in the article/supplementary materials; further inquiries can be directed to the corresponding author.

Author contributions

SL: Built the logic of the article, wrote the article, modeled the analysis, designed and produced the simulation, and summarized the data conclusions. DL: Inspected the article and evaluated the results. XH: Checked the article and guided the model simulation. ZZ: Analyzed the model building.

Funding

Supported by the National Natural Science Foundation of China (Grant Nos. 51735006, 51927810, and U1837206) and Beijing Municipal Natural Science Foundation of China (Grant No. 3182013).

Conflict of interest

The authors declare that the research was conducted in the absence of any commercial or financial relationships that could be construed as potential conflicts of interest.

Publisher's note

All claims expressed in this article are solely those of the authors and do not necessarily represent those of their affiliated organizations or those of the publisher, the editors, and the reviewers. Any product that may be evaluated in this article or claim that may be made by its manufacturer is not guaranteed or endorsed by the publisher.

References

Berkovsky, B. M., Medvedev, V. F., and Krakov, M. S. (1993). *Magnetic fluids engineering applications[M]*. New York: Oxford University Press.

Chen, Yibiao, Li, Decai, Zhang, Yanjuan, Li, Z., and Zhou, H. (2020). The influence of the temperature rise on the sealing performance of the rotating magnetic fluid seal. *IEEE Trans. Magn.* 56 (11), 1–10. doi:10.1109/tmag.2020.3023018

Cheng, H. (2016). *Research on magnetic fluid seal of reaction kettle device [D]*. Beijing: Beijing Jiaotong University.

Cheng, Y. (2020). *Theoretical and experimental study of heat transfer characteristics of magnetic fluids based on high-speed seals [D]*. Beijing: Beijing Jiaotong University.

Chi, C. (2011). *Physical fundamentals and applications of ferromagnetic fluids [M]*. Beijing: Beijing University of Aeronautics and Astronautics Press, 6–12.

Fan, C. (2019). *Numerical analysis and experimental verification of magnetic fluid seal for hydraulic cylinder of construction machinery[D]*. Liuzhou: Guangxi University of Science and Technology.

Gu, H., Song, P., and Zhu, L. (2002). Experimental study on the performance of magnetic fluid seal[J]. *Lubr. Seal.* (03), 32–34.

He, X., Li, D., and Sun, M. (2008). Experimental study of magnetic fluid static seal for large diameter flanges[J]. *J. Vac. Sci. Technol.* 28 (2), 179–181.

He, X., Li, D., and Wang, H. (2014). Influence of gravity on performance of magnetic fluid seal [J]. *J. Vac. Sci. Technol.* 34 (11), 1160–1163.

Jain, K., Pant, R. P., and Pathak, S. (2017). Magnetic fluid based high precision temperature sensor[J]. *IEEE sensors J.* 17 (9), 2670–2675. doi:10.1109/JSEN.2017.2675440

Li, D., and Du, H. (2018). Research progress on key issues of magnetic fluid rotary seal[J]. *J. Vac. Sci. Technol.* 38 (7), 564–574.

Li, D., Hong, J., and Yang, Q. (2002). Study on magnetic fluid seal of dry Roots vacuum pump[J]. *Vac. Sci. Technol.* (473), 78–81.

Li, D. (2016). *The magical magnetic liquid [M]*. Beijing: Science Press, 7–27.

Li, D. (2010). *Theory and application of magnetic fluid seals [M]*. Beijing: Science Press.

Li, D. (2003). *Theory and applications of magnetic fluids [M]*. Beijing: Science Press.

Li, D., Wang, Z., and Yao, J. (2014). New magnetic fluid seal[J]. *J. Beijing Jiaot. Univ.* 38 (4), 1–6.

Lv, T., Wang, L., and Chen, Y. (2020). Finite element simulation analysis and research on magnetic field strength of magnetic fluid sealing device[J]. *Mechanics* 47 (10), 41–47.

Radionov, A. V. (2015). Application of magnetic fluid seals for improving reliability of air coolers. *Chem. Pet. Eng.* 51 (7-8), 481–486. doi:10.1007/s10556-015-0073-5

Song, H., and Chen, P. (1984). *Permanent magnetic materials and their applications [M]*. Beijing: Mechanical Industry Press.

Sun, M., Li, D., and He, X. (2007). Numerical analysis and optimal design of magnetic field for magnetic fluid seal[J]. *J. Vac. Sci. Technol.* (3), 269–272.

Szydło, Z., Zachara, B., and Ochoński, W. (1999). "Ferro-magnetic fluids and their application in machine building (in Polish)," Krynica: in 1st Conference on automation of machines, devices and processes.

Wang, H., Li, D., and He, X. (2016). Experimental study on the effect of rotational speed of rotating shaft on the pressure resistance of magnetic fluid-liquid dynamic seal[J]. *J. Vac. Sci. Technol.* 36 (08), 945–949.

Wang, H., Li, D., and Shaobo, Z. (2016). Comparative study of the failure pressure between sealing liquids and gas with magnetic fluid [J]. *Food Mach.* 32 (11), 68101–68170.

Wang, Z. (2019). *Research on magnetic fluid sealing of liquid media [D]*. Beijing: Beijing Jiaotong University.

Xu, H., Bao, J., and Yin, Y. (2019). Design and simulation of roller sealing and lubrication based on magnetic nanofluid[J]. *Lubr. Seal.* 44 (6), 109–112.

Yang, J., and Huang, W. (2017). A brief review on the progress of magnetic liquid lubrication technology[J]. *Surf. Technol.* 46 (6), 61–68.

Yang, X. (2014). *Theoretical and experimental study of large gap stepped magnetic fluid rotary seal[D]*. Beijing: Beijing Jiaotong University.

Zou, J., Lu, H., and Qi, Y. (1994). Magnetic fluid seals and their development status[J]. *J. Tribol.* (03), 279–285.

frontiers | Frontiers in Materials

ORIGINAL RESEARCH
published: 19 August 2022
doi: 10.3389/fmats.2022.929795

Status Recognition of Magnetic Fluid Seal Based on High-Order Cumulant Image and VGG16

Aixin Dai[1], *Yancai Xiao*[1,2]*, *Decai Li*[1,3] *and Jinyu Xue*[1]

[1]School of Mechanical, Electronic and Control Engineering, Beijing Jiaotong University, Beijing, China, [2]Key Laboratory of Vehicle Advanced Manufacturing, Ministry of Education, Measuring and Control Technology (Beijing Jiaotong University), Beijing, China, [3]State Key Laboratory of Tribology, Tsinghua University, Beijing, China

A magnetic fluid seal is often used in complex working conditions with harsh environmental requirements. Timely and accurate identification of the seal status can help avoid the major economic losses and even casualties caused by the seal failure. However, research on the recognition of magnetic fluid seal status is still at the exploratory stage internationally. Aiming at the problem of inclusion of other components and Gaussian noise when using acoustic emission nondestructive testing technology to detect the magnetic fluid seal status, a new recognition method based on the combination of high-order cumulant image and VGG16 convolutional neural network is proposed to identify the magnetic fluid seal status in this paper. In this method, high-order cumulant images are used for the denoising and feature selecting of detected signals, and the VGG16 convolutional neural network is trained to automatically learn image features to classify and recognize high-order cumulant images representing different sealing states. Experiments show that the accuracy of image recognition using VGG16 is significantly higher than that of other methods. The VGG16 method can identify the magnetic fluid seal state accurately and effectively, with strong robustness and Gaussian noise suppression ability.

Keywords: magnetic fluid seal, high-order cumulant image, state recognition, convolution neural network (CNN), VGG16

OPEN ACCESS

Edited by:
Miao Yu,
Chongqing University, China

Reviewed by:
U. Ubaidillah,
Sebelas Maret University, Indonesia
Wei Huang,
Nanjing University of Aeronautics and Astronautics, China
Yibiao Chen,
Wenzhou University, China

***Correspondence:**
Yancai Xiao
ycxiao@bjtu.edu.cn

Specialty section:
This article was submitted to Smart Materials, a section of the journal Frontiers in Materials

Received: *27 April 2022*
Accepted: *06 June 2022*
Published: *19 August 2022*

Citation:
Dai A, Xiao Y, Li D and Xue J (2022) Status Recognition of Magnetic Fluid Seal Based on High-Order Cumulant Image and VGG16. Front. Mater. 9:929795. doi: 10.3389/fmats.2022.929795

1 INTRODUCTION

A magnetic fluid seal is a new sealing method that is often applied to important parts that have strict requirements on sealing performance (Hasegawa et al., 2016; Mitamura and Durst, 2017), such as movable parts of spacesuits, X-ray diffractometer, radar waveguide components, and the main pump shaft of a sodium cooled fast reactor, etc. The operating conditions of these components are complicated. Seal failure can not only cause significant economic losses but also serious environmental pollution and even casualties. It is therefore necessary to accurately identify the seal status when using magnetic fluid to seal components so that timely preventive measures can be taken to ensure the safe operation of seals.

To date, there is no mature identification method of magnetic fluid seal status, and relevant research is mainly focused on the exploration of magnetic fluid seal performance and failure mechanisms. For example, Chen et al. (Chen et al., 2020) used pressure sensors to measure magnetic fluid seal signals and simulated the seal status. Parmar et al. (Parmar et al., 2020) tested the performance of a two-stage magnetic fluid seal under variable speed and radial clearance. Gao, (2014) used X-ray and CT image brightness to detect the existence of magnetic liquid in sealing clearance.

Wang, (2018) achieved real-time monitoring of magnetic fluid leakage by using a pressure detection device. The above research provides a good beginning for monitoring the status of the magnetic fluid seal, but the detection technology has certain limitations and is destructive to the seal. In this paper, acoustic emission nondestructive testing technology is used to detect the seal status without destroying the original structure of the seal.

In recent years many recognition methods for acoustic signals have been developed, mainly including K-means clustering (Glowacz, 2019), fully integrated empirical mode decomposition (Delgado-Arredondo et al., 2017), support vector machine (Shi et al., 2018), and convolutional neural network (CNN) (Zhang D. et al., 2020), etc. In this research field, a recognition method based on CNN that automatically extracts signal features is one of the present research hotspots. Han et al. (Han et al., 2020) used CNN to effectively identify the two-dimensional time-domain waveform image features of signals. Chen et al. (2015) used CNN to identify frequency spectrum images of timing signals and achieved high accuracy. In addition, studies have shown that the convolutional neural network model of VGG16 has better performance in the practical application of abstract image recognition (Qassim et al., 2018; Theckedath and Sedamkar, 2020). Therefore, the recognition process can be more efficient by converting one-dimensional signals into images and inputting them into the VGG16 model. Among the many methods of transforming one-dimensional signals into two-dimensional images, high-order cumulant image processing has the characteristics of suppressing Gaussian colored noise and depicting signal phase information and has more advantages than traditional images such as time-spectrum graphs (Shao et al., 2008).

In this paper, a state recognition method based on a high-order cumulant image and VGG16 convolutional neural network is proposed, which provides a new approach to effectively identifying the magnetic fluid seal state. In this method, the acoustic signal of the magnetic fluid seal is collected by an acoustic emission experiment, and the magnetic fluid seal states can be detected without damage. The high-order cumulant image processing method for detecting acoustic signals is introduced theoretically, and the generated image samples are input into the VGG16 convolution neural network. Finally, by comparing the NIN, GooLeNet, and ResNet models, we found that the VGG16 model can effectively identify the magnetic fluid seal state and that the network performance is significantly better than other models.

2 RELATED THEORY

2.1 Higher Order Cumulant Image

High-order cumulant is a new signal processing technology, which has the advantages of suppressing Gaussian colored noise and extracting phase information (Shao et al., 2008; Wang et al., 2014). It is gradually being applied to signal filtering, signal detection, and target classification and recognition. High-order cumulant image is a grayscale image transformed from a sealed acoustic signal through high-order cumulant calculation and data mapping, which is used as the input sample data of VGG16 and other convolutional network models, and it can contain richer feature information while suppressing various noises. **Figure 1** shows a schematic diagram of the high-order cumulant image transformation process.

As shown in **Figure 1**, the key Cto generating high-order cumulant images lies in high-order cumulant calculation and data mapping processing. The calculation formula of high-order cumulant is as follows:

$$\boldsymbol{c_{kx}(\tau_1, \tau_2, \cdots, \tau_{k-1}) = cum\{x(t), x(t+\tau_1), \cdots, x(t+\tau_{k-1})\}} \quad (1)$$

Where $x(t)$ is the random signal, k is the order, $\tau_1, \tau_2, \cdots, \tau_{k-1}$ is the delay.

In a Gaussian stochastic process with zero mean, the third-order and higher-order cumulants are equal to zero, that is, the third-order and higher-order cumulants can suppress the influence of additive Gaussian noise in the signal theoretically. Therefore, the third-order cumulant with less computation is used in this paper, and the calculation formula is as follows:

$$\begin{aligned} \boldsymbol{c_{3x}(\tau_1, \tau_2)} &= \boldsymbol{cum\{x(t), x(t+\tau_1), x(t+\tau_2)\}} \\ &= \boldsymbol{E\{x(t)x(t+\tau_1)x(t+\tau_2)\}} \end{aligned} \quad (2)$$

Where τ_1 and τ_2 are the delay quantities. E is the expected value.

The one-dimensional acoustic signal is calculated by the third-order cumulant and the two-dimensional matrix is obtained. The delay τ_1 and τ_2 are the independent variables in the calculation process. The initial values of matrix elements are normalized and rounded after being multiplied by the gray value of the maximum level. The calculated result P is the gray value at the corresponding pixel position (m, n), and the calculation formula is as follows:

$$\boldsymbol{p(m,n) = round\left(\frac{x - x_{min}}{x_{max} - x_{min}} \times 255\right)} \quad (3)$$

Where, x represents the initial value of matrix elements, and round represents the rounding. After the above calculation, high-order cumulant images of acoustic signals can be obtained. Different images represent different magnetic fluid seal states, which can be identified as input of the VGG16 convolutional neural network.

2.2 VGG16 Convolutional Neural Network

2.2.1 Convolutional Neural Network

Convolutional Neural Networks (CNN), a feedforward Neural network, are widely used in image recognition, text recognition, and speech recognition. Typical CNN is mainly composed of an input layer, convolution layer, activation function, pooling layer, full connection layer, and output layer, among which, the convolution layer, pooling layer, and full connection layer are relatively key components. The convolutional layer is mainly used to extract the features of the input image, the pooling layer is mainly used to reduce the size of the feature image, and the full connection layer is mainly used to classify the feature vectors obtained.

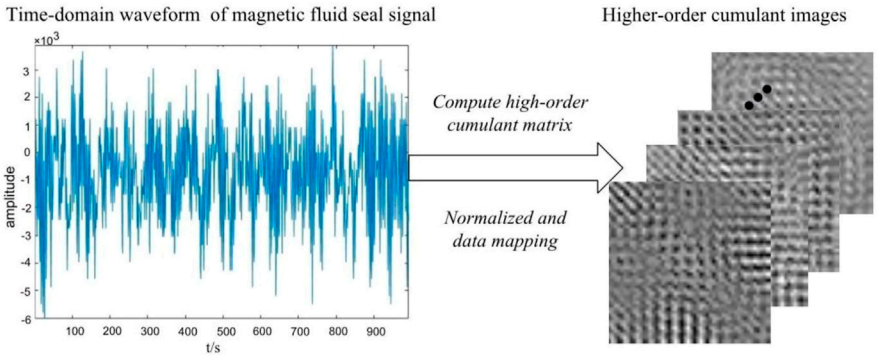

FIGURE 1 | Schematic diagram of high-order cumulant image transformation process in the magnetic fluid seal state.

Many excellent CNN models have evolved based on the classic network structure of CNN, such as VGGNet, NIN, GoogLeNet, and ResNet (Alzubaidi et al., 2021). VGGNet is mainly divided into VGG16 and VGG19 according to different network layers. All the convolution layers of VGGNet use the same small convolution kernel (3 × 3), such connection mode makes the number of network parameters smaller, and the use of a multi-layer activation function makes the learning ability of the network stronger. In the NIN model, multi-layer perceptron is used for filtering operation, and global average pooling is introduced to replace the last full connection layer, which effectively improves the parameter inflation problem and nonlinear mapping ability of the network model. The core of GoogLeNet is the Inception structure. Inception Module uses multiple parallel and small dense convolution and pooled connections. In addition, the auxiliary classifier adopted by GoogLeNet solves the problem of gradient disappearance. Resnet-50 was one of the first networks to adopt batch regularization by designing deeper network layers to improve network generation. These CNN models gradually reduce the error rate of image classification while improving the universality and robustness of the model. In particular, VGG16, with its simplicity and practicability, has been widely used in image classification. VGG16 model is used to identify the seal states with the high-order cumulant images of acoustic signals in this paper.

2.2.2 VGG16 Model

VGG16 is a CNN model capable of image recognition with high accuracy. Proposed by the Visual Geometry Group of Oxford University in 2014, VGG16 is an ideal choice for image recognition problems of high-order cumulants with abstract characteristics. The structure of the VGG16 model is very regular, and the main components are the repeatedly stacked convolutional layers and pooling layers, as well as the full connection layer and output layer at the bottom of the model (Simonyan and Zisserman, 2008). The convolution layer achieves the purpose of extracting image features by convolution operation in two ways: "local perception" and "parameter sharing". The convolution kernel size $F_{w,h}$ of the convolution operation is 3 × 3, the step size S is 1, and the effective filling size P is 1. Then the size of the feature image output after l convolution operation is $M^l_{w,h}$, and the calculation formula is as follows:

$$\boldsymbol{M^l_{w,h}} = \frac{\boldsymbol{M^{l-1}_{w,h}} - \boldsymbol{F_{w,h}} - 2\boldsymbol{P}}{\boldsymbol{S}} \tag{4}$$

It can be found from the above formula that although the convolution operation of this model increases the number of channels, it does not change the size of the image. Therefore, pooling is required after several convolutional operations. After pooling, the size of feature images is reduced to half of the original, which can greatly reduce the computing requirements. The pooling method of this model is maximum pooling. The size of the pooling box is 2 × 2 and the step size is 1. $a^l_{i,j}$ represents the pixel value at position (i, j) on the feature map of layer l, $'a^l_{i',j'}$ represents the new eigenvalue at the corresponding position, and $Max\_pool(\cdot)$ represents the maximum pooling function. The calculation formula of the new eigenvalue is as follows:

$$\boldsymbol{a^{l'}_{i',j'}} = \boldsymbol{Max\_pool}\left(\boldsymbol{a^l_{i,j}}\right) \tag{5}$$

The full connection layer and output layer at the bottom of the model are responsible for sample classification (Liu et al., 2018). **Figure 2** shows the schematic diagram of the VGG16 convolutional neural network. The input size of the 224 × 224×3 image enters the convolution layer, after two convolution operations and the ReLU function, the size becomes 224 × 224×64, and then a Max pooling layer is connected. In this way, after repeatedly stacking convolutional layers and pooling layers, three fully connected layers are connected, and the probability distribution of sample recognition is obtained by the softmax activation function.

3 EXPERIMENT RESEARCH

3.1 Signal Acquisition of Magnetic Fluid Seal

In this study, the signal acquisition experiment was carried out in the State Key Laboratory of Tribology, Tsinghua University. Taking the magnetic fluid seal as the research object, acoustic emission nondestructive testing technology was used to collect

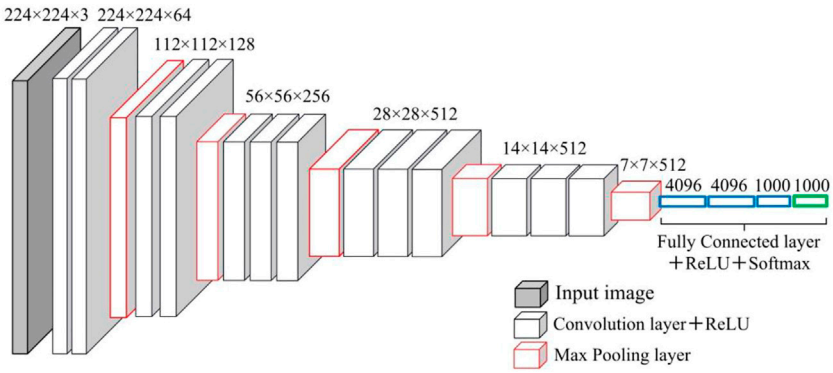

FIGURE 2 | Schematic diagram of VGG16 convolutional neural network.

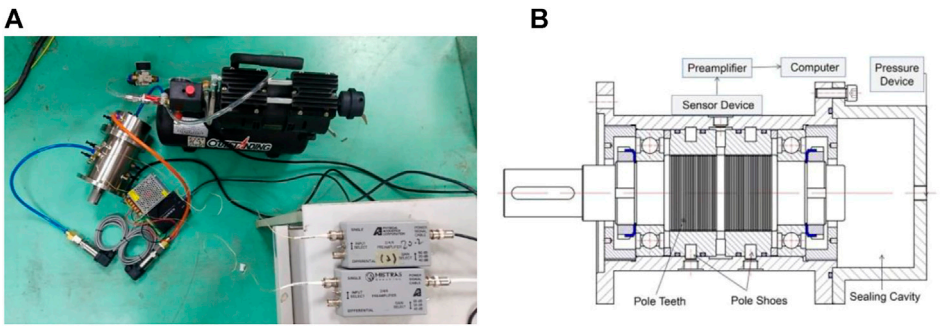

FIGURE 3 | Schematic diagram of magnetic fluid seal signal acquisition experiment. **(A)** Device of magnetic fluid seal signal acquisition experiment, **(B)** Principle of magnetic fluid seal signal acquisition experiment.

signals during the failure process of the magnetic fluid seal under static conditions. Magnetic fluid seal mainly uses the response characteristics of the magnetic fluid to the magnetic field. Under the action of the magnetic field, the magnetic fluid filled the magnetic loop, forming several liquid ring seals. These magnetic fluid ring seals will remain well sealed under the action of the magnetic field. However, when the external instability worsens, the liquid film of some annular sealing rings will appear multiple times of rupture and self-recovery, until each magnetic fluid annular sealing ring flows at the same time, and the sealing ring generates an air gap resulting in seal failure. Based on the failure principle of the magnetic liquid seal, combined with the application of acoustic emission in liquid film seal monitoring and two-phase flow pattern identification (Zhang Y. et al., 2020), this paper adopts acoustic emission nondestructive testing technology to monitor magnetic liquid seal status. **Figure 3** is the schematic diagram of the magnetic fluid seal signal acquisition experiment.

In this experiment, the magnetic fluid seal selected is a two-stage pole shoe seal structure, each stage of the pole shoe is distributed under 30 pole teeth, the distance between the pole teeth is 0.1mm, and the distance between the magnetic liquid film and the shell is about 25 mm. The acoustic signal acquisition equipment is THE PICO acoustic emission sensor of PAC. Two acoustic emission sensors are respectively glued to the ends of the two pole boots of the seal, and the coupling agent is applied on the contact surface to avoid acoustic signal loss between the sensor plane and the rotating shaft surface. The acoustic emission sensor transmits the collected acoustic signal through the preamplifier to the AE-WIN software provided by PAC. The software records a short acoustic emission wave with a specified sampling rate and number of sampling points at specific time intervals, and the data contained in each short acoustic wave are saved as a sample. In this experiment, the short-time wave recording period is T_w = 1.3 m s, the sampling rate is F_s = 2MHz, and the sampling number of each sample is N = 1,024. A total of 401,185 acoustic signal samples were collected in the whole seal failure experiment. The pressure signal was used as a reference for analysis, and 500 acoustic signal samples of no leakage, micro leakage, and complete leakage in the magnetic fluid seal state were selected.

3.2 High-Order Cumulant Image of the Magnetic Fluid Seal Signal

The collected one-dimensional acoustic signal samples are processed by high-order cumulant image processing on Matlab, and the third-order cumulants of the three kinds of acoustic signal samples are calculated respectively. The maximum

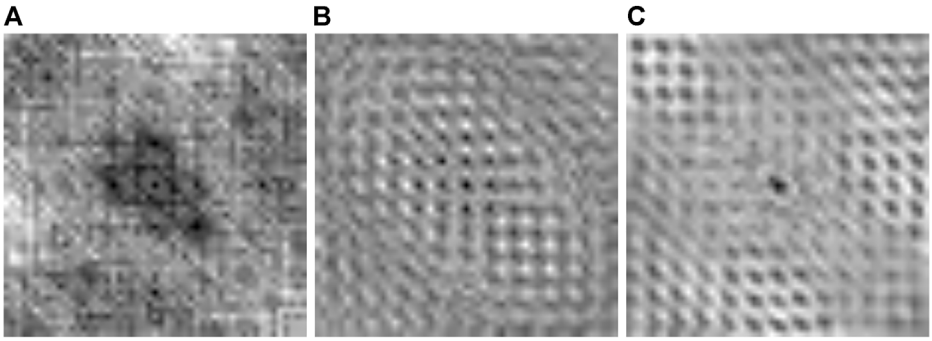

FIGURE 4 | High-order cumulant grayscale images in different magnetic fluid seal states. **(A)** No Leakage, **(B)** Micro Leakage, **(C)** Complete Leakage.

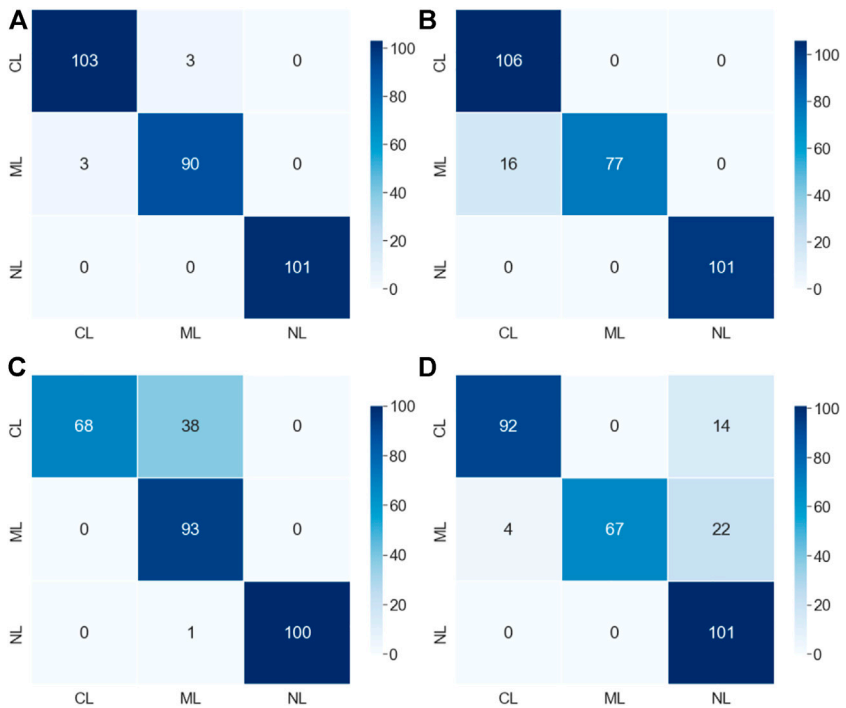

FIGURE 5 | Confusion matrix charts of the seal state identification results obtained by different CNN models. **(A)** VGG16, **(B)** NIN, **(C)** GooLeNet, **(D)** ResNet50.

delay is 25 ($-25 \leq \tau_1, \tau_2 \leq 25$), and the delay is dimensionless. After calculation, the third-order cumulant matrix was obtained, which was normalized and mapped to obtain 500 grayscale images of high-order cumulant representing the three sealing states of no leak, micro leak, and complete leak. **Figure 4** shows the grayscale images of high-order cumulants in different magnetic fluid seal states.

3.3 Recognition Based on VGG16 for Magnetic Fluid Seal

In this section, the model was built based on python and the deep learning framework Tensorflow2.6.0, and the software environment was Pycharm. To verify the superiority of the VGG16 convolutional neural network in the recognition of magnetic fluid seal, other convolutional network models, including NIN, GooLeNet, and ResNet50, are also used for comparative experiments.

The experimental samples were high-order cumulant grayscale images, including 500 samples in each of the three sealed states: no leakage (NL), micro leakage (ML), and complete leakage (CL). The three types of samples were randomly divided into training and testing in a ratio of 4:1, i.e., 400 training samples and 100 testing samples were included respectively. Among them, the validation set is divided into the training set of each category according to the ratio of 1: 9, which is used to evaluate the

TABLE 1 | Comparison table of the comprehensive evaluation of experimental results of different CNN models.

Model	State	Precision (%)	Recall (%)	F1-score (%)	Accuracy
VGG16	No Leakage	100	100	100	98.00% (294/300)
	Micro Leakage	97	97	97	
	Complete Leakage	97	97	97	
NIN	No Leakage	100	100	100	94.67% (284/300)
	Micro Leakage	100	83	91	
	Complete Leakage	87	100	93	
GooLeNet	No Leakage	100	99	100	87.00% (261/300)
	Micro Leakage	70	100	83	
	Complete Leakage	100	64	78	
ResNet50	No Leakage	100	99	100	86.67% (260/300)
	Micro Leakage	97	95	96	
	Complete Leakage	95	98	97	

accuracy of the current model after the completion of each epoch, while the testing set is used for the final model evaluation.

After the samples were divided, they were input into four convolutional neural network models (VGG16, NIN, GooLeNet, and ResNet50) for training and testing. The gray image is processed by multi-channel to adapt to the original image input format of the model. The cross-entropy loss function was adopted in the training process, the optimization algorithm was Adam (Adaptive Moment), the learning rate was set as 0.0001, and the confusion matrix was introduced to visualize the testing results. **Figure 5** is the comparison diagram of the confusion matrix of the testing recognition results of different CNN models.

In the confusion matrix, the row corresponds to the prediction class, the column corresponds to the real class, the diagonal unit corresponds to correct classification, and the non-diagonal unit corresponds to wrong classification. The number is displayed in each cell. It can be seen from the confusion matrix in **Figure 5** that the four convolutional neural network models, VGG16, NIN, GooLeNet, and ResNet50, all have good recognition effects on the grayscale image samples in this experiment. To verify the superiority of the VGG16 model in the recognition of magnetic fluid seal status, evaluation indexes such as *Accuracy*, which are commonly used in image recognition tasks, are introduced for comparison, and the calculation formula is as follows:

$$\boldsymbol{Accuracy} = \frac{\boldsymbol{TP} + \boldsymbol{TN}}{\boldsymbol{Total}} \tag{6}$$

Where, TP is True Positive, indicating the number of Positive predictions. TN is True Negatives, which is the amount of Negatives needed to predict correctly, and $Total$ is the total number of predicted samples. Accuracy can be used to evaluate the classification results of the model, but it is not always effective in some cases, such as the imbalance between positive and negative samples. Therefore, it is necessary to introduce Precision 、 Recall and F1 − Sc*o*re.

$$\boldsymbol{Precision} = \frac{\boldsymbol{TP}}{\boldsymbol{TP} + \boldsymbol{FP}} \tag{7}$$

$$\boldsymbol{Recall} = \frac{\boldsymbol{TP}}{\boldsymbol{TP} + \boldsymbol{FN}} \tag{8}$$

$$\boldsymbol{F1 - Score} = \frac{2\boldsymbol{TP}}{2\boldsymbol{TP} + \boldsymbol{FP} + \boldsymbol{FN}} \tag{9}$$

Where, FP is Flase Positive, indicating the number of Positive errors; FN is Flase Negatives to represent the number of Negatives for misprediction. *Precision* refers to the ratio of true samples and *Recall* refers to the ratio of true samples. $F1 - Score$ can be used to weigh the values of Precision and Recall. The larger $F1 - Score$ is, the more convincing the recognition effect of this model is. **Table 1** shows the comparison table of the comprehensive evaluation of experimental results of different CNN models.

It can be seen from the experimental results that the VGG16 model has a recognition rate of 98.67%, which is significantly higher than the NIN, GooLeNet, and ResNet50 convolutional network models. In addition, the comprehensive evaluation index of the VGG16 model for all kinds of samples is above 97%, indicating that the model is stable for the identification of samples with different magnetic fluid seal states.

CONCLUSION

In this paper, a method based on a high-order cumulant image and VGG16 convolution neural network is proposed to identify the magnetic fluid seal state. The main innovations of this study are as follows:

1) The signal acquisition experiment of magnetic fluid seal status adopts the acoustic emission technology, which minimizes the damage to the seals to the greatest extent and realizes the nondestructive testing of the magnetic fluid seal components.
2) High-order cumulant image processing is carried out on the acoustic signals collected in the experiment. One-dimensional acoustic signals are transformed into two-dimensional high-order cumulant images, which retain the original signal characteristics to the maximum extent and suppress Gaussian-colored noise.
3) The comparison experiment proves that the VGG16 model can effectively recognize the high-order cumulant image of the magnetic fluid seal state, providing a new method for the recognition of the magnetic fluid seal state.

In the next step, based on the characteristics of magnetic fluid seal status, the VGG16 convolutional neural network model will be improved to further enhance the recognition accuracy of seal status and the generalization of the model. In addition, the universality of the identification method of magnetic fluid seal status in this study can be explored and improved through repeated experiments on seals with different structures and working conditions.

DATA AVAILABILITY STATEMENT

The raw data supporting the conclusion of this article will be made available by the authors, without undue reservation.

AUTHOR CONTRIBUTIONS

AD contributed to paper writing. AD and YX contributed to the entire revision process. DL and JX performed the experiment.

FUNDING

The study was supported by the National Natural Science Foundation of China (grant number 51735006), the National Natural Science Foundation of China (grant number U1837206), the National Natural Science Foundation of China (grant number 51927810), and the Beijing Municipal Natural Science Foundation (grant number 3182013).

REFERENCES

Alzubaidi, L., Zhang, J., Humaidi, A. J., Al-Dujaili, A., Duan, Y., Al-Shamma, O., et al. (2021). Review of Deep Learning: Concepts, CNN Architectures, Challenges, Applications, Future Directions. *J. Big Data* 8 (1), 53. doi:10.1186/s40537-021-00444-8

Chen, Y., Li, D., Zhang, Y., Li, Z., and Zhou, H. (2020). The Influence of the Temperature Rise on the Sealing Performance of the Rotating Magnetic Fluid Seal. *IEEE Trans. Magn.* 56 (11), 1–10. doi:10.1109/TMAG.2020.3023018

Chen, Z., Li, C., and Sanchez, R. V. (2015). Gearbox Fault Identification and Classification with Convolutional Neural Networks. *Shock Vib.* 2015, 1–10. doi:10.1155/2015/390134

Delgado-Arredondo, P. A., Morinigo-Sotelo, D., Osornio-Rios, R. A., Avina-Cervantes, J. G., Rostro-Gonzalez, H., Romero-Troncoso, R. d. J., et al. (2017). Methodology for Fault Detection in Induction Motors Via Sound and Vibration Signals. *Mech. Syst. Signal Process.* 83, 568–589. doi:10.1016/j.ymssp.2016.06.032

Gao, W. (2014). *Research on the seal design and properties of magnetic fluid in the space environment*. [master's thesis]. [Beijing: Beijing Jiaotong University.

Glowacz, A. (2019). Acoustic Fault Analysis of Three Commutator Motors. *Mech. Syst. Signal Process.* 133, 106226. doi:10.1016/j.ymssp.2019.07.007

Han, T., Tian, Z., Yin, Z., and Tan, A. C. C. (2020). Bearing Fault Identification Based on Convolutional Neural Network by Different Input Modes. *J. Braz. Soc. Mech. Sci. Eng.* 42 (9), 474. doi:10.1007/s40430-020-02561-6

Hasegawa, N., Yoshioka, H., and Shinno, H. (2016). Noncontact Gravity Compensator with Magnetic Fluid Seals. *J. Adv. Mech. Des. Syst. Manuf.* 10 (5), JAMDSM0078. doi:10.1299/jamdsm.2016jamdsm0078

Liu, B., Zhang, X., Gao, Z., and Chen, L. (2018). "Weld Defect Images Classification With VGG16-Based Neural Network," in *Digital TV and wireless multimedia communication*. Editors G. Zhai, J. Zhou, and X. Yang (Springer Singapore), 215–223.

Mitamura, Y., and Durst, C. A. (2017). Miniature Magnetic Fluid Seal Working In Liquid Environments. *J. Magn. Magn. Mater.* 431, 285–288. doi:10.1016/j.jmmm.2016.09.032

Parmar, S., Ramani, V., Upadhyay, R. V., and Parekh, K. (2020). Two Stage Magnetic Fluid Vacuum Seal for Variable Radial Clearance. *Vacuum* 172, 109087. doi:10.1016/j.vacuum.2019.109087

Qassim, H., Verma, A., and Feinzimer, D. (2018). "Compressed Residual-VGG16 CNN Model for Big Data Places Image Recognition," in The Proceedings of 2018 IEEE 8th Annual Computing and Communication Workshop and Conference (CCWC) (Piscataway: IEEE), 169–175.

Shao, R., Huang, X., Liu, H., and Xu, Y. (2008). Fault Detection and Diagnosis of Gear System Based on Higher Order Cumulants. *J. Mech. Eng.* 6, 161. doi:10.3901/jme.2008.06.161

Shi, W., Fan, X., and Zhang, C. (2018). Armored Vehicle Classification Based on Spectral Dynamic Feature and Cuckoo Search-Support Vector Machine. *J. Comput. Appl.* 38 (S1), 44–47.

Simonyan, K., and Zisserman, A. (2008). Very Deep Convolutional Networks for Large-Scale Image Recognition [Preprint]. Available at: https://arxiv.org/abs/1409.1556 (Accessed March 15, 2022).

Theckedath, D., and Sedamkar, R. R. (2020). Detecting Affect States Using VGG16, ResNet50 and SE-ResNet50 Networks. *SN Comput. Sci.* 1 (2), 79. doi:10.1007/s42979-020-0114-9

Wang, Y., Fan, J., and Yao, Y. (2014). Online Monitoring of Multivariate Processes Using Higher-Order Cumulants Analysis. *Ind. Eng. Chem. Res.* 53 (11), 4328–4338. doi:10.1021/ie401834e

Wang, Z. (2018). *The study of sealing liquid with magnetic fluid*. [dissertation]. [Beijing]: Beijing Jiaotong University.

Zhang, D., Stewart, E., Entezami, M., Roberts, C., and Yu, D. (2020). Intelligent Acoustic-Based Fault Diagnosis of Roller Bearings Using A Deep Graph Convolutional Network. *Measurement* 156, 107585. doi:10.1016/j.measurement.2020.107585

Zhang, Y., Du, S., Gu, C., Xia, Q., Liu, P., and Xu, C. (2020). Acoustic Emission Detection Of Horizontal Gas-Liquid Two-Phase Flow Pipeline Leakage Based On Experimental Research. *China Offshore Oil Gas* 33 (1), 158–165. doi:10.11935/j.issn.1673-1506.2021.01.020

Conflict of Interest: The authors declare that the research was conducted in the absence of any commercial or financial relationships that could be construed as a potential conflict of interest.

Publisher's Note: All claims expressed in this article are solely those of the authors and do not necessarily represent those of their affiliated organizations, or those of the publisher, the editors and the reviewers. Any product that may be evaluated in this article, or claim that may be made by its manufacturer, is not guaranteed or endorsed by the publisher.

frontiers | Frontiers in Materials

TYPE Original Research
PUBLISHED 25 August 2022
DOI 10.3389/fmats.2022.959489

OPEN ACCESS

EDITED BY
Yancheng Li,
Nanjing Tech University, China

REVIEWED BY
Huixing Wang,
Nanjing University of Science and Technology, China
Shaoqi Li,
Nanjing Tech University, China
Ying Dan Liu,
Yanshan University, China

*CORRESPONDENCE
Nur Azmah Nordin,
nurazmah.nordin@utm.my
Ubaidillah,
ubaidillah_ft@staff.uns.ac.id

†These authors have contributed equally to this work

SPECIALTY SECTION
This article was submitted to Smart Materials, a section of the journal Frontiers in Materials

RECEIVED 01 June 2022
ACCEPTED 25 July 2022
PUBLISHED 25 August 2022

CITATION
Khaidir REM, Nordin NA, Mazlan SA, Abd Rahman H, Ubaidillah, Abdul Aziz SA and Nazmi N (2022), Stiffness enhancement of magnetorheological foam by structural modification using silica nanoparticles additive. *Front. Mater.* 9:959489. doi: 10.3389/fmats.2022.959489

Stiffness enhancement of magnetorheological foam by structural modification using silica nanoparticles additive

Rahayu Emilia Mohamed Khaidir[1†], Nur Azmah Nordin[1*†], Saiful Amri Mazlan[1†], Hamimah Abd Rahman[2†], Ubaidillah[3*†], Siti Aishah Abdul Aziz[4†] and Nurhazimah Nazmi[1†]

[1]Engineering Materials and Structures (eMast) ikohza, Malaysia–Japan International Institute of Technology (MJIIT), Universiti Teknologi Malaysia, Kuala Lumpur, Malaysia, [2]Faculty of Mechanical and Manufacturing, Universiti Tun Hussein Onn Malaysia, Parit Raja, Malaysia, [3]Mechanical Engineering Department, Universitas Sebelas Maret, Sukarta, Indonesia, [4]Faculty of Applied Sciences, Universiti Teknologi MARA (UiTM), Cawangan Pahang, Kampus Jengka, Pahang, Malaysia

Magnetorheological (MR) foam is a newly developed porous smart material that is able to change its properties continuously, actively, and reversibly in response to controllable external magnetic stimuli. Unfortunately, the stiffness or also known as storage modulus of MR foam is still rather low and insufficient, in the range of below 100 kPa only, due to weak interparticle interaction between CIPs and the foam matrix, which consequently restricts the potential of MR foam to be used in future sensor applications or in other semi-active devices. Therefore, the aim of this research is to enhance the structural and storage modulus of MR foam by adding silica nanoparticles as an additive. Consequently, MR foam samples with different compositions of silica nanoparticles in the range of 0–5 wt% were prepared *via* an *in situ* method. The rheological properties were tested under an oscillatory shear mode with the absence and presence of magnetic fields using a rheometer, with the input parameters of strains between 0.001% and 10% and range of magnetic flux density between 0 and 0.73 T for a magnetic field sweep test. The rheological findings show that with the addition of silica nanoparticles, particularly at 4 wt%, have enhanced the storage modulus of MR foam by 260%, which attributed to the highest stiffness from 45 to 162 kPa. Meanwhile, the change of storage modulus under the influence of magnetic fields (0 T–0.73 T) somehow showed small increment, about Δ1 kPa for each concentration of silica nanoparticles in MR foams, due to non-magnetic behavior of silica. The morphological characteristics of MR foams were described by an elemental analysis carried out by a using variable pressure scanning electron microscope (VPSEM) equipped with energy dispersive x-ray spectroscopy (EDX). The micrographs demonstrated large open-cell pores for MR foam, while MR foam with silica nanoparticles exhibited more closed-cell pores, associated with the enhancement of its storage modulus. It indicates that the silica nanoparticles have encouraged well dispersion of the particles in the foam matrix, which improved and strengthened the microstructure of MR foams through formation of silane coupling bonds of silica in the filler-matrix structure. Overall, incorporation of silica nanoparticles as an additive in the MR foam could provide advantage in

enhancing the structure and mechanical properties of MR foam, for various future smart devices.

KEYWORDS

magnetorheological foams, carbonyl iron particles, silica nanoparticles, storage modulus, porosity, silane coupling

1 Introduction

Nowadays, the progression of advance technologies such as soft robotics, soft grippers, soft actuators, and sensor devices have been developing, which leads to the innovation of advance materials that can be stimulated rapidly and sensitively under the influence of external stimuli. Since the last decade, magnetorheological (MR) foam has emerged as a newly developed smart soft solid material that can change its behavior continuously, actively, and reversibly under the influence of a magnetic field (Gong et al., 2013). It is attributed to the embedded magnetic particles in the foam as a matrix phase. In comparison with other MR solid material, such as MR elastomer (Umehara et al., 2018), MR foam has a unique porous and cellular structure that forms chemically by trapping gases in the liquid phase during the foaming process (Cain et al., 2013). Its porous structure has not only entitled the material to be low in density and physically lightweight (Davino et al., 2012) but also contributes to a great cushioning effect to absorb vibrations and shock impact (Linde et al., 1972). In fact, embedding magnetic particles in the structure of foam has emphasized the material to be evolved from a rigid system to a controllable one as MR foam has responded well to the tunable magnetic field stimuli (Schümann et al., 2015). In recent years, one of the challenging problems which arises in this domain application has been mentioned by Yin et al. (2017), who stated that soft robotic grippers are always lacking in variable stiffness and thus limits the function of the gripper to be adjustable into desired stiffness according to the operational object. Therefore, the indicated features of MR foam have been intriguing and growing appeals among researchers as its flexibility and controllable stiffness corresponding to the applied magnetic fields would result in its potential for future soft robotic gripper material. The improvement is also in line with the development of material's technology in which researchers attempt to provide an adjustable material for soft robotic grippers (Zaidi et al., 2021), since the improvement of finger-like operating mechanism is crucial to move and handle various objects conveniently during the operations (Meng et al., 2020).

In order to address more potential applications of MR foam, researchers have examined the rheological properties of the material in terms of capability to store more energy upon applied shear stress before fracture. In addition, the enhancement of the storage modulus of MR foam has become a significant concern in order to broader its stiffness range for various purposes (Muhazeli et al., 2020). Theoretically, the storage modulus, G′, is a term for the amount of energy stored in a viscoelastic material before distorting, which refers to the stiffness of the material (Boczkowska et al., 2012; Zhang et al., 2019). There are several methods introduced to enhance the properties of MR foam, including storage modulus for wider spectrum of technology advancement such as increasing CIP's content (Muhazeli et al., 2019), using particles coating (Scarpa and Smith, 2004), dual-matrix method (Ge et al., 2015), and incorporating additives into MR materials (Saiz-Arroyo et al., 2011). Previous studies have stated that by reinforcing higher composition of magnetic filler (CIPs) into the MR foam, the magnetic responsiveness of the MR foam could be enhanced as a result of the increased magnetic saturation of the material. In addition, under the influence of magnetic field excitations, MR foam has broaden its range of storage modulus from a low to higher level, making it suitable to be potential components in soft robotics sensor technology (Rizuan et al., 2021). Unfortunately, the reported storage modulus of MR foam thus far is insufficient, since the application of soft robotic material requires stiffness of more than 100 kPa (Zaidi et al., 2021). For example, in the previous study carried out by Gong et al. (2013), a flexible MR foam with 60 wt% of CIPs exhibited the storage modulus up to 72 kPa. Meanwhile, Rizuan et al., 2021 incorporated more CIPs of about 75 wt% in the MR foam, which enhanced the storage modulus up to 75 kPa, by about 3% increment only. These findings in return have restricted the potential of MR foam to be used in stated applications or in other semi-active devices. It is noted that the ability to store energy is a key aspect for the elastic materials to sustain greater applied stress elastically, especially under different magnetic field values and dynamic frequencies (Scarpa and Smith, 2004). Therefore, improvement in the storage modulus of the MR foam has become a significant concern in order to enhance the strength of the material upon deformation for the MR foam to become more advantageous and widen its potential for various purposes.

On the other hand, introducing additives into MR solid materials has become a more practical approach in providing significant enhancement toward the corresponding properties, with simpler procedure and a cost effective approach (Tamaddoni moghaddam and Naimi-Jamal, 2017; Zainudin et al., 2020). In fact, incorporating additives into MR elastomers (MRE) include, but not limited to, graphite (Li et al., 2009; Tian et al., 2011; Shabdin et al., 2019), cobalt ferrite (Aziz et al., 2019), carbon nanotubes (CNTs) (Kumar and Lee, 2019), and silica (Abd Rashid et al., 2021), and the additives have been proven to result in the enhancement toward specific properties of the material. These additives have their own roles and purposes to enhance some

properties of MRE such as conductivity, MR effect, and magnetic interaction depending on the amount and type of additives that were being incorporated (Ahmad Khairi et al., 2019). In 2009, Li et al. introduced 25 wt% of graphite into the mixture of 55 wt% CIPs and 20 wt% silicon rubber (MRE), and it was observed that the graphite has increased the conductivity of MRE as well as reduced its resistance by more than 85% (Li et al., 2009). Meanwhile, a study by Tian et al. who stated that the addition of 23.81% micron-sized graphite particles in the MRE has increased the storage modulus up to 1 MPa, particularly under the influence of 400 mT of the applied magnetic field as compared to the sample without additive (Tian et al., 2011). Nevertheless, Shabdin et al. added 20 g of graphite into the mixture of 12.5 g of CIPs, 22.5 g of silicon rubber, and 5 g of silicon oil, and the result showed that the MR effect of the MRE was increased by about 3% as compared to the non-additive sample (Shabdin et al., 2019). However, the composition of CIPs and addition of graphite as an additive need to be controlled as adding more would lead to brittleness of MRE, which would accelerate the deformation of the material (Zainudin et al., 2020). On the other hand, Aziz et al. introduced Ni–Mg–cobalt ferrite nanoparticles, with an average size of 35–80 nm into an MRE, and the result revealed that the MRE with Ni–Mg–cobalt ferrite nanoparticles exhibited 43% higher storage modulus as compared to the MRE without the additive (Aziz et al., 2019). However, cobalt ferrite nanoparticle have been stated to induce extreme toxicity to human and biological systems that may cause cell death and DNA damage. Thus, the used of cobalt ferrite–based additives have been restricted for wider applications. Meanwhile, CNT, which is known to possess high elastic and strong bond due to its multi-layer nature, has been used in MRE generally to enhance the storage modulus and lower the loss factor of the MRE (Eatemadi et al., 2014). Similarly, Kong et al. have proven that a significant increment in the storage modulus of MRE, particularly from 600 to 1200 kPa, has been achieved by the MRE with the rising percentage of the CNT from 1 to 6 wt% added into the composite, respectively (Kong et al., 2018). Unfortunately, CNTs involve a very complex synthesis process that is highly toxic to human body and environment (Eatemadi et al., 2014).

Nevertheless, silica nanoparticles are commonly used as an additive to enhance material's properties due to its non-toxic property, significantly low density, simpler fabrication process, great nucleating agent for crystallinity growth, and high thermal stability (Anuar et al., 2018; Khaidir et al., 2020). Abd Rashid et al., 2021 studied the addition of silica nanoparticles in the range of 0 per hundred rubber (phr) to 20 phr in the ethylene propylene diene monomer (EPDM)–based MRE, and the MRE showed good interfacial bonding between the filler and matrix phases; in addition, it led to the improvement of particle's dispersion. As a result, the initial storage modulus of the MRE was observed to be increased from 0.29 to 0.45 MPa with the addition of silica nanoparticles from 0 to 11 wt%, respectively, as the adhesiveness of silica has improved the interactions between the CIPs and the EPDM matrix (Abd Rashid et al., 2021). It is notable as well that the increment in the rheological properties of MRE was parallel with the enhancement of the tensile strength and elongation break of the MRE. Specifically, the enhancement in tensile strength of the MRE was stated by about 20%, from 52 to 62 shore A with the silica content added from 0 to 11 wt% (Abd Rashid et al., 2021).

On the other hand, the used of nanosized particles have also given advantages for it to be used in polymer composite to improve hardness, mechanical stiffness, and thermal stability (Anuar et al., 2018; Khaidir R. E. et al., 2019, Khaidir et al., 2019 R., 2020). This is because the nanoparticles have a relatively high surface area attributed to the nanoscale dimensions; hence, the nanoparticles can mix well with the polymer chains at the molecular level and improve mechanical and thermal properties (Saha et al., 2008). Furthermore, the nanosized particles can fill the voids between the micron-sized CIPs and thus offer higher MR effect as a result of enhance stiffness or storage modulus of the MR material (Bastola and Hossain, 2020). For example, Nikje and Tehrani, 2010 showed a great improvement in elastic modulus of rigid polyurethane (PU) foam from 3.7 MPa to 6.3 MPa after 1 wt% of n-(2-aminoethyl)-3-aminopropyltrimethoxy-silane (AEAP)-silica nanoparticles was added into the PU foam. Meanwhile, Saiz-Arroyo et al. stated that the silica nanoparticles has the ability to disperse well in the polymer matrices (Saiz-Arroyo et al., 2011). In fact, by adding silica content from 0 to 3 wt% in the low-density polyethylene (LDPE) foam, the elastic modulus of the composite foam could be enhanced by 51% (Saiz-Arroyo et al., 2011). These studies somehow show the ability of silica nanoparticles that act as additive to enhance the storage modulus of a polymer-based material. However, there has been no study related to the used of silica nanoparticles to enhance properties of the MR foam, particularly at low stiffness of the material. Therefore, a new fabrication sample of MR foams with the addition of silica nanoparticles as additive will be introduced with the range of silica nanoparticles from 1 to 5 wt%, in order to enhance the storage modulus as well as other rheological properties of the MR foam. It is expected that the addition of silica nanoparticles could result in the enhancement of the filler–matrix interactions in the MR foam which, simultaneously correspond to the improvement in the foam's properties physically, mechanically, and rheologically. Consequently, with enhanced stiffness of the MR foam with the addition of silica nanoparticles has the ability to store more energy; thus, it could grasp and move the object more securely as compared to the low stiffness of the MR foam.

2 Experimental method

2.1 Sample preparation

Figure 1 shows the synthesis process of flexible MR foam samples that were prepared by the *in situ* polymerization method. The two main components needed to produce the

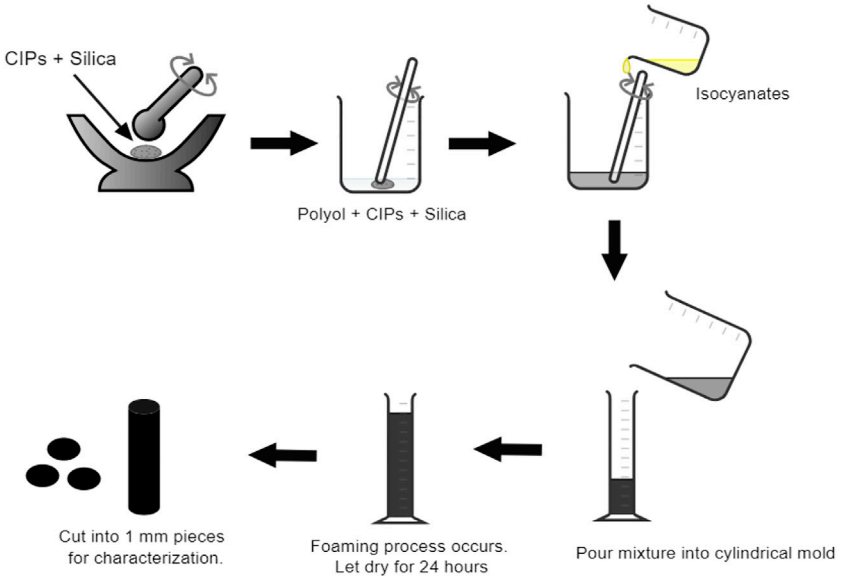

FIGURE 1
The synthesis process of MR foam with the addition of silica nanoparticles.

polyurethane foam are polyol and isocyanates that acted as a chemical reactant and agent, respectively. In particular, polyether polyols (PPG)–based triol with a molecular weight of 6000 g/mol and the density of 1.03 g/ml together with the 4,4′-methylene bis(phenyl isocyanate) benzene that has the density of 1.00 g/ml were purchased from Smooth-On. Inc., United States. Meanwhile, the reinforced magnetic particles were carbonyl iron particles (CIPs) that was purchased from CK Materials Lab Co. Ltd., Seoul, Korea. It was an OM-typed with an average size of 3–5 μm and exhibited the density of 4.5 g/cm^3. As for the additive silica nanoparticles (SiO_2), it was derived from rice husk *via* using the solid state method, having the average size of 700 nm and was collaboratively received from UTHM, Johor.

The MR foam was prepared by mixing the fixed concentration of CIPs, 75wt%, into the total weight of main components of foam, polyols, and isocyanates (20 g). Upon the *in situ* fabrication of MR foam, the CIPs was added into the 50wt% of polyols, which was about 10 g, and it was stirred at a speed of 550 rpm for about 30 s by using a Multimix High Speed Dispersed (HSD) mechanical stirrer in order to ensure well mixing of the mixture. Then another 50 wt% of isocyanates (10 g) was poured into the mixture of polyols and CIPs, and it was continuously stirred for another 20 s. Then the final mixture of the materials was immediately poured into a cylindrical open tube as a mold, and the foaming process of MR foam took place taking the shape of the mold. The mold was prepared with a dimension of 20 mm in diameter and 15 cm in thickness. Prior to the addition of silica nanoparticles to the MR foam, the additive varied from 0 to 5 wt% respective to the total of MR foam. Thus, the calculation for each material was carried out, as shown in Table 1.

In order to prepare MR foams with silica nanoparticles, the additive was firstly grounded with CIPs using a mortar and pestle to ensure the homogeneous mixing of the particles, as illustrated in Figure 1. Then the solid mixture of the particles was poured into the polyols (10 g) and was stirred for about 30 s, at a speed of 550 rpm. The isocyanates with the amount of 10 g was then added to the mixture, stirred for another 20 s, and the final mixture was immediately poured into the cylindrical mold as the foaming process would take place shortly. The foaming process would occur vigorously and the samples would solidify instantly. All samples were left for 24 h at room temperature of 25 °C to ensure that the samples were fully hardened before the samples were being cut for testing and characterization procedures.

2.2 Sample characterization and rheological testing

The rheological properties of MR foams were analyzed and evaluated by using a MCR302 modular compact rheometer (MCR) from Anton Paar, Germany. The rheometer was equipped with a controllable parallel plate (PP20/MRD/T1/P2) that has a patented Toolmaster™ technology with a diameter of 20 mm and a constant 1 mm gap setup measured by Trugap™ feature that recognizes the real measuring gap. In this current work, MR foams underwent an oscillatory shear mode test to investigate the effect of different concentrations of silica nanoparticles to the viscoelastic properties of the MR foam, especially in terms of storage modulus and the MR effect. The variation of the final properties of MR foams would be

TABLE 1 Materials composition in flexible MR foam with addition of silica nanoparticles.

No of Samples	Isocyanates (g)	Polyols (g)	CIPs (g)	Silica		Total weight (g)
				(wt%)	(g)	
A	10	10	15	0	0.00	35.00
B	10	10	15	1	0.35	35.35
C	10	10	15	2	0.70	35.70
D	10	10	15	3	1.05	36.05
E	10	10	15	4	1.40	36.40
F	10	10	15	5	1.75	36.75

further analyzed by varying input parameters of 0.001%–10% sweep strains, with different constant current input from 0 A to 4 A and constant 1 Hz frequency to evaluate the elasticity and deformation value of the MR foam through the determination of the linear viscoelastic (LVE) range. The current input of 0 A, 1 A, 2 A, 3 A, and 4 A are approximately equivalent to 0 T, 0.17 T, 0.35 T, 0.53 T, and 0.73 T, respectively. The magnetic flux density, B (T) were manipulated during current sweep test or also known as the magnetic field–dependent test to analyze the absolute MR effect of the MR foam with different composition of silica nanoparticles. Upon the rheological test, each sample was cut into 1-mm-thick and 20-mm-diameter sections. All samples were tested under room temperature and each of the samples was tested with 30 interval points for every measurement.

Nevertheless, the morphological characteristics of MR foams were observed through variable pressure scanning electron microscopy (VPSEM), by using the JSM-IT300LV model from JEOL Ltd, Tokyo, Japan. VPSEM provided a high resolution of 3.0 nm at 30 kV and unsurpassed low kV performance; thus, it has the ability to identify fine pore images of the MR foam. In this work, the MR foam samples were cut into 1-mm thickness with a diameter of 20 mm each and primarily coated with platinum using the sputter coating method before being analyzed under VPSEM. The SEM micrograph were characterized on the cross-sectional part to observe the pores and strut structures of the MR foam. Notably, the images were taken under ×50 to × 2000 magnifications, and all testing were carried out at room temperature of 25 °C. Equipped with the energy dispersive X-ray spectroscopy (EDX) in the VPSEM, the EDX would provide mapping information on the element compositions in MR foams.

3 Results and discussion

3.1 Storage modulus of MR foams

3.1.1 Strain dependent test

A strain sweep test was conducted under the oscillatory shear mode with a controlled range of shear strains from 0.001% to 10% and a fixed frequency of 1 Hz. In this research, the effect of silica as an additive toward the improvement of storage modulus of MR foams was mainly observed, and the change in the linear viscoelastic (LVE) region of MR foams were determined. The LVE region gives rigidity information of the MR material by indicating the range which the material could withstand, given shear strain before the structure begin to deform permanently (Kang et al., 2020). Moreover, it is crucial to determine the limit value of the LVE region in order to ensure that further testing including frequency sweep and magnetic field sweep can be performed within specified strain without destroying the sample. As for solid-based materials, it does not flow; thus, the stiffness or storage modulus, G′, would be considered to describe the elasticity of the material rather than its viscosity. Therefore, as shown in Figure 2, the storage modulus, G′, of MR foams with the addition of silica in different concentrations were plotted, corresponding to the applied shear strains and with respective to the off-state and on-state conditions.

In particular, Figure 2 presents the changed in the storage modulus of MR foams that have been embedded with silica nanoparticles as an additive, in the range of 0–5 wt% concentrations. The samples were tested under different applied magnetic flux density of 0 T (off-state) and 0.73 T (on-state). It can be seen that all samples showed constant storage modulus, G′, along with the increasing applied strains, especially from 0.001% to 0.1%. This shows that the elastic region of the overall samples was in the stated range, where the structure would be returned to its original position even after the removal of applied strains. Thus, the graphs show no change in the value of the storage modulus (linear). However, it was observed that the graphs started to show its downturn after the strains were increased more than 0.6%. This phenomenon corresponded to the deformation phase of MR foams caused by the applied strain beyond its elastic limit of the samples. In the deformation phase, the samples would continue being stretched but was unable to return to its original position, indicating the transition of the samples from elastic to plastic deformation. Hence, it explained the drop values of storage modulus, G′, as lesser energy can be stored by the samples upon further deformation of the samples.

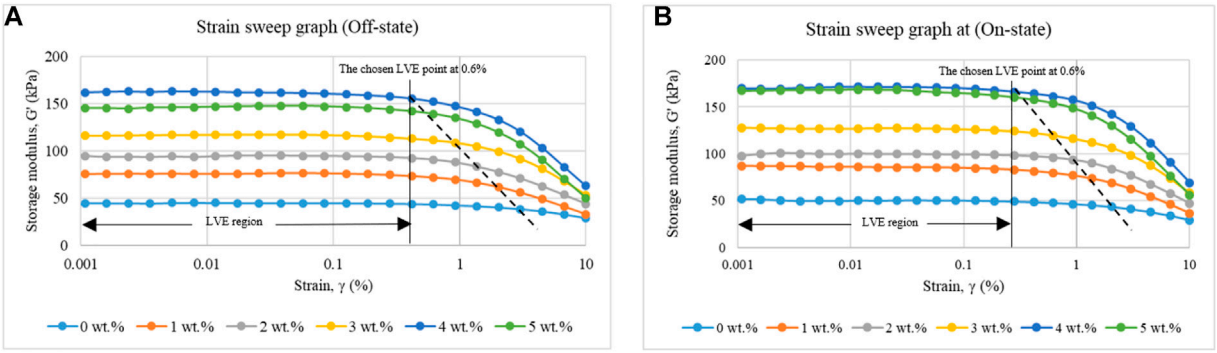

FIGURE 2
Change of storage modulus of MR foams with different concentrations of silica nanoparticles during **(A)** off-state (0 T) and **(B)** on-state (0.73 T) conditions.

Overall, the LVE region of MR foam samples would be determined by using the Agire-Olabide's method where the point deviates by at least 10% after the downturn slope (Yunus et al., 2019). The slanting lines (dash lines) were drawn on the graphs indicating the drop point of the LVE limit for each MR foam, especially with different concentration of silica nanoparticles from 1 to 5 wt%. Based on the graphs, it was observed that the LVE regions have started to reduce when silica nanoparticles were added to the MR foam samples. In fact, during the off-state condition, the pure MR foam exhibited the lowest storage modulus but a slightly longer LVE region, between 0.001% and 3.03% of applied strains. Then when silica nanoparticles were added to MR foams up to 5 wt%, the storage modulus increased regularly but a shorter range of LVE regions were noted correspondingly. For instance, the MR foam with 4 wt% of silica nanoparticles presented the highest storage modulus, but in return, the LVE region become shorter, in between 0.001% and 0.62% particularly at the off-state condition. In addition, all MR foams at the on-state condition exhibited further shorter LVE regions as compared to the ones at the off-state conditions, as shown in Figure 2B. The shorter LVE regions indicated that the samples have become stiffer with the addition of silica nanoparticles and even stiffer under the influence of a magnetic field (on-state condition). A similar trend has been reported by Abdul Rashid et al., who stated that MRE samples with the addition of silica nanoparticles as an additive possessed shorter LVE region as compared to the MRE without silica (Abd Rashid et al., 2021). These results implied that the LVE limit of MR foams are dependent on the concentration of silica nanoparticles in the matrix phase. In fact, it is a common phenomenon in a polymer composite as the addition of filler particles or additives in the polymer matrix would lead to the deterioration of the material's structure as the shorter elastic region would be acquired, known as the Payne effect (Mohd Nasir et al., 2021). Thus, it explained the shorter LVE region of

TABLE 2 | Initial storage modulus, G_0', value of MR foam with different composition of silica nanoparticle at the off-state and on-state conditions.

Magnetic flux density, B (T)	Composition of nanoparticle silica (wt%)					
	0	1	2	3	4	5
	Storage modulus, G_0', value (kPa)					
0.00	45	76	95	116	162	145
0.17	46	81	97	119	165	159
0.35	47	82	98	127	169	160
0.53	51	87	99	128	170	167
0.73	52	88	102	129	173	172

MR foams with higher concentrations of silica nanoparticles. Nevertheless, based on the finding of the LVE region for all MR foams, the selected constant strain value for other testing procedure is about 0.6% to ensure that all testing samples were in the LVE region; hence, the testing samples were still in the elastic region.

Generally, the viscoelastic materials that are subjected to shear stress would be undergo shear deformation. When the shear stress has exerted onto the material, some amount of energy would be stored and can be retrieved after each cycle. Meanwhile, the rest of the energy would be dissipated as heat and could not be retrieved. Hence, the stored energy in the material is referred as stiffness and also known as storage modulus, G′, the amount of energy could be stored by the material upon deformation. Based on the graphs in Figure 2A, it shows that the addition of silica nanoparticles has caused increment in the storage modulus of MR foams, particularly at the off-state condition from 1 to 4 wt%. The values were then increased slightly at the on-state condition when 0.73 T was applied to

all the samples, indicating the stiffer MR foams and more energy could be stored by the samples elastically. In fact, Table 2 summarizes the values of storage modulus of MR foams with different concentrations of silica nanoparticles, and at both conditions of off-state and on-states, respectively. It can be observed that at 0 wt% of silica nanoparticles, the storage modulus of MR foam was noted around 45 kPa, particularly at zero magnetic field. This value has been very slightly increased when the magnetic flux density was applied to the MR foam from 0.17 T to 0.73 T. The increment values were noted to be around 1–4 kPa only and this finding is in a good agreement with the study stated by Rizuan et al., 2021 in which the storage modulus, G' of MR foam increased slightly, around 1 kPa–5 kPa when the magnetic field was between 0.0 T and 0.73 T. In comparing with the off-state condition, the CIPs are distributed randomly in the polymer matrix of PU foam in the absence of the magnetic field causing the low initial storage modulus values (Li et al., 2020b). Meanwhile, with the presence of the magnetic field, the result showed the increment in the storage modulus of MR foam during the on-state condition which was attributed to the enhancement in the interparticle magnetic forces between the CIPs, as toward the applied magnetic field simultaneously. Nevertheless, by comparing MRE to MR foam, the slight increment in the storage modulus of MR foams is due to the porous structure of foam itself, where the CIPs were embedded in the struts of foam and were separated by the pores, causing the CIPs are quite farther between the pores. When the magnetic field was induced to the MR foam, CIPs would tend to attract to one another in the strut walls thus slightly increased the storage modulus of MR foams. Meanwhile in an MRE, the CIPs are distributed in a smaller area of the rubber matrix and no foaming process occurred in an MRE during curing thus, interparticle of CIPs are much closer resulted in stronger magnetic forces between the particles when the magnetic field was applied, thus explaining the greater storage modulus increment as compared to MR foams. The similar trend was observed for other MR foams that were incorporated with different concentrations of silica nanoparticles.

In contrast, when 1 wt% of silica nanoparticles were added to the MR foam, the corresponding storage modulus has been significantly increased from 45 to 76 kPa, at the off-state condition. Despite at zero magnetic field influence, the increment in the storage modulus of MR foams have continued to enhance to 95 kPa, 116 kPa and 162 kPa for silica nanoparticles of 2, 3 and 4 wt%, respectively. In MR foam, silica nano-particles would act as a cross-linker and not as a chain extender, in which silica nano-particles would strengthen the matrix-fillers interaction by cross-linking interactions. This would increase the interfacial bonding between the filler and polymer matrix that subsequently enhanced the modulus of MR foams. There has been a study conducted by Burgaz and Kendirlioglu (2019) regarding the interactions between the PU foam and silica nanoparticles. The study stated that the silica possessed the hydrophilic behavior in which it encourages the silanol functional groups of silica to have a bond *via* H-bonding interactions with ether oxygens of polyol, or also known as the silane coupling agent (Burgaz and Kendirlioglu, 2019). Since silica used was in nanosized particles, it has a larger surface area, which provides a better dispersion in the polymer matrix thus creating more silane coupling agents in the matrix phase (Nikje et al., 2009). The silane coupling agents that are presented in the MR foam would hinder the relaxation of mobility of particles in the polymer segment thus, making the particles difficult to move (Nikje et al., 2009). This has explained the stiffer progression of MR foams with the addition of silica nanoparticles as compared to the one without silica. Nevertheless, at the on-state conditions 0.17–0.73 T that were applied to the MR foam, the storage modulus somehow showed a slight increment, particularly in the range 1–5 kPa indicating the non-magnetic behavior of silica nanoparticles to respond to the applied magnetic fields. Therefore, the increment in the storage modulus of MR foams is due to the CIP's responsiveness toward the increasing values of magnetic field strength. As magnetic polarization of CIPs in MR foams become stronger with magnetic fields, the respective chain-like structures of MR foam enhanced thus explaining the increased value of storage modulus (Chuah et al., 2015).

Nevertheless, it was observed that when the concentration of silica nanoparticles was added up to 5 wt%, the storage modulus was noted lower than the 4 wt% of silica nanoparticles in the MR foam. In fact, the value of storage modulus has dropped from 162 kPa (4 wt%) to 145 kPa (5 wt%), particularly at the off-state condition. This finding might be due to the agglomeration of silica nanoparticles in the polymer matrix when silica was added excessively. Generally, silica is known as an inorganic material that act as a nucleating agent for the polymer-matrix materials that at every addition or increasing its composition, it increases the crystallinity of the polymer composite via the interparticle connection that build between the silica particles and matrix polymer by silane coupling agent (Saiz-Arroyo et al., 2011). Hence, when excessive silica nanoparticles were added, the crystallinity of the material increased which might lead to the formation of particle's aggregation in the foam matrix phase. This resulted in the imbalance distribution of silica nanoparticles that affected the dimensional stability of foam's cellular structure and finally caused reverse effect of stiffness enhancement in the MR foam. Therefore, the storage modulus of MR foam with 5 wt% silica nanoparticles has decreased indicating the excessiveness of the additive added more than 4 wt%. Somehow, at presence of magnetic fields (on-state condition), the storage modulus with 5 wt% silica nanoparticles still increased slightly attributed to the CIPs that responded to the applied magnetic field, as discussed in previous paragraph.

3.1.2 Magnetic field–dependent test

The magnetic field–dependent test of MR foams with different composition of silica nanoparticles was

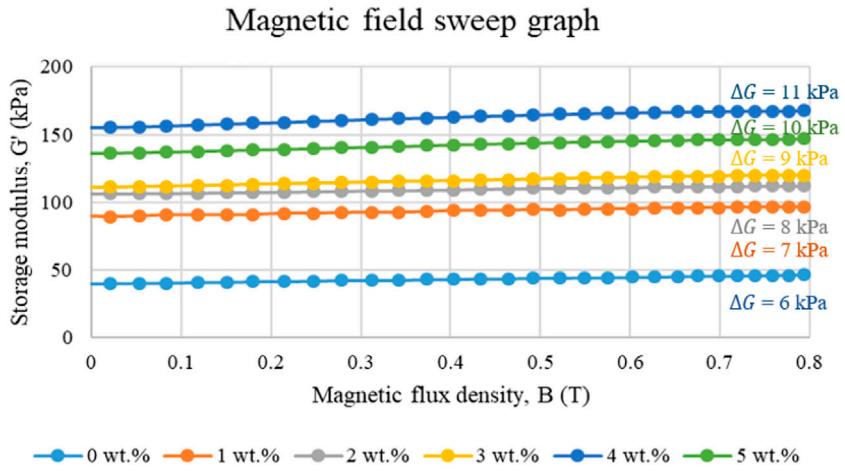

FIGURE 3
Change of storage modulus, G′, of MR foams with different composition of silica nanoparticles under the influence of different magnetic flux density, B.

conducted under the fixed strain of 0.6% and a constant frequency of 1 Hz. The chosen strain of 0.6% lies under the LVE region in which the amount of given strain is within the range of elastic limit. Correspondingly, the absolute MR effect were extracted and presented, as shown in Figure 3.

Figure 3 shows the relationship between the storage modulus, G′ of MR foams with different compositions of silica nanoparticles under the influence of different magnetic flux density, B. Overall, it could be observed that as the magnetic flux density increased, the storage modulus of MR foams increased, up to 0.8 T. The increment of the storage modulus of all MR foams are due to the responsiveness of the CIPs in the foam's structure toward the applied magnetic fields that subsequently caused changes in the stiffness of the material, reversibly and continuously, and it is also known as MR effect (Plachy et al., 2018; Li et al., 2021). The MR effect analysis is one of the important resultant parameters to measure the responsiveness of MR foams in terms of the changeable storage modulus under the influence of applied magnetic fields, and the output would be advantageous for the material to be applied in controllable actuator and soft robotic sensors (Kang et al., 2020). The change in the behaviors of MR foam under the influence of magnetic stimuli can be expressed by the absolute MR effect. The absolute MR effect, ΔG, can be calculated by using Eq. 1 below:

$$\Delta G = \left(G' - G_0'\right) \quad (1)$$

where ΔG is the difference between the maximum storage modulus, G', and initial modulus, G_0' at the maximum and zero applied magnetic field, respectively. The absolute MR effect of MR materials may vary depend on several factors such as frequency rates, magnetic field strength, composition of magnetic fillers, type of magnetic materials, and particle sizes. In this characterization, the magnetic flux densities varied in the range of 0 T–0.8 T.

In particular, the initial storage modulus of MR foam without the silica nanoparticles is about 40 kPa and the value was increased slightly to 46 kPa when the magnetic flux density was applied at 0.8 T. Hence, the difference or absolute MR effect of the MR foam was about 6 kPa. This finding is in consistent with a study done by Rizuan et al., 2021, who stated that the pure MR foam with 75 wt% of CIPs has the increment of 6 kPa in modulus when the magnetic field was from 0 to 0.8 T. Figure 4A shows the illustration of MR foam indicating the distribution of CIPs and silica nanoparticles over the composite area, particularly at the off-state condition. The large surface area of nanosized silica particles in the MR foam has created more silane coupling agents formed between the O-H functional group of silica with ether-oxygen of polyol *via* H-bonding interactions. These bonds have enhanced the interparticle interactions between the CIPs and silica nanoparticles to the matrix structure of MR foam. Thus, the silica nanoparticles should be observed over the CIPs surfaces and in the matrix phase of MR foam. However, there are gaps between the particles as no magnetic field was induced to the MR foam, and the stiffness of the material is completely dependent on the composite foam that embeds both CIPs and silica nanoparticles. At the on-state condition or when there was induction of the magnetic field, the storage modulus of the MR foam increased, indicating the magnetic interactions between the CIPs and its responsiveness toward the magnetic field stimuli. This phenomenon somehow caused shrink of the MR foam slightly due to reducing gap between the attraction of

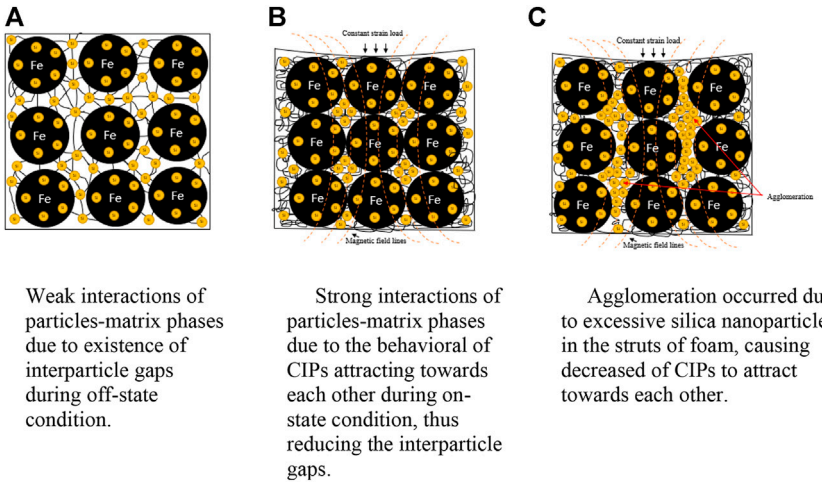

FIGURE 4
Schematic illustration of particles–matrix interactions in MR foam, at off- and on-state conditions. **(A)** Weak interactions of particles–matrix phases due to existence of interparticle gaps during the off-state condition. **(B)** Strong interactions of particles–matrix phases due to the behavioral of CIPs attracting toward each other during the on-state condition, thus reducing the interparticle gaps, **(C)** Agglomeration occurred due to excessive silica nanoparticles in the struts of foam, causing decrease of CIPs to attract toward each other.

the particles, especially among the CIPs (Wang et al., 2020). The phenomenon can be illustrated in Figure 4B showing stronger interaction between particles-matrix phases with applied magnetic fields. Indeed, as shown in Figure 3, the storage modulus of MR foam with 1 wt% of silica nanoparticles has increased by 7 kPa, from 89 kPa at the off-state condition to 96 kPa at the on-state condition. Similar small increasing trend of 8, 9 and 11 kPa in the absolute MR effect, ΔG were observed for other MR foams with silica nanoparticles of 2, 3 and 4 wt% respectively, and it showed the stiffer MR foams with the strength of magnetic fields. Even though the changes are found to be small for each MR foam, the increasing value of storage modulus somehow showed the structural transformation of MR foam with induction of the magnetic field (Alekhina et al., 2019). In fact, MR foam that under the influence of the magnetic field would cause the magnetic domain of the CIPs were aligned according to the direction of magnetic fields (Rizuan et al., 2020). Thus, the stiffness of MR foams increased in line with the increasing value of storage modulus, particularly with greater strength of magnetic fields as stronger magnetic interactions would be taken place between the CIPs (Li et al., 2020a).

However, in terms of silica nanoparticles that were added into MR foams in different concentrations, the value of storage modulus at zero magnetic field showed a significant increment. As observed in Figure 3, the initial storage modulus, G_0' of each MR foam increased with the increased of silica nanoparticles, particularly from 1 wt% to 4 wt% samples. These findings indicated the stiffer MR foams at the initial state or with absence of the magnetic field as more silica nanoparticles were embedded in the foam structure. Then as magnetic fields were induced to MR foams, for instance at 0.8 T, the increased in storage modulus from one MR foam sample to another were noted very slightly, about 1 kPa increment showing the non-magnetic behaviour possessed by the silica nanoparticles toward the applied magnetic field. In fact, these findings were in agreement with the work done by Abd Rashid et al. (2021) who stated that a small increment were observed for the initial storage modulus of MRE samples, between 0.03 and 0.06 MPa for different concentrations of silica nanoparticles, about 3 to 6wt%. Indeed, the small increment in the storage modulus of MR foams indicated the improvement of particles-matrix interaction when silica nanoparticles were added in the structure of MR foam. Hence, the changed in the storage modulus of MR foams increased simultaneously with the increasing composition of silica nanoparticles. This positive trend also has been discussed in previous section of strain sweep test as adding more silica nanoparticles resulted in the significant enhancement of storage modulus of MR foams, particularly at the initial state and not under the influence of applied magnetic fields.

On the other hand, the absolute MR effect, Δ*G* of MR foam with 5 wt% of silica nanoparticles showed a decrement from 11 to 10 kPa. The graph in Figure 3 also showed the position of storage modulus with 5 wt% of silica nanoparticles was quite lower compared to the MR foam with 4 wt% silica, at both off- and on-state conditions. A similar pattern was reported by Saiz-Arroyo et al. (Saiz-Arroyo et al., 2011) where the rigid polyurethane foam has showed a decreasing pattern of elastic modulus with 5 wt% of silica nanoparticle. It was reported that the aggregation of the silica nanoparticle could occur when it was

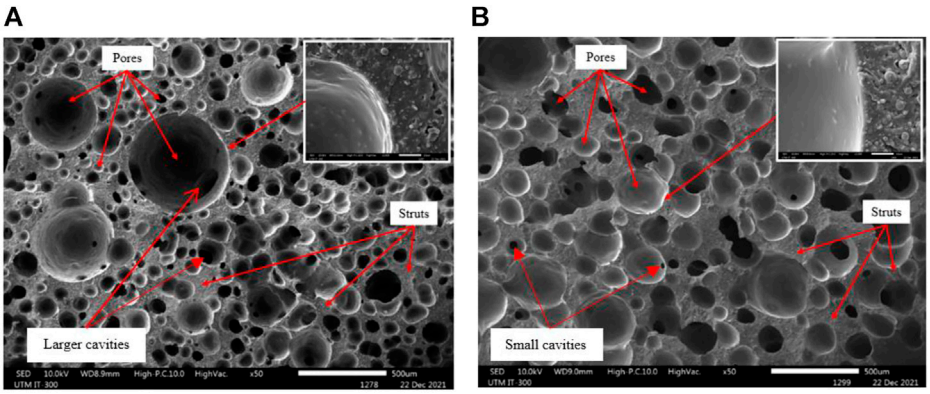

FIGURE 5
Micrograph of **(A)** MR foam and **(B)** MR foam with 4 wt% silica nanoparticles.

added excessively in the foam structure (Saiz-Arroyo et al., 2011). Similar phenomenon might occur to the MR foam when silica nanoparticles was added excessively with 5 wt%. As regards, when the magnetic field was induced to the MR foam, the CIPs were still attracted to one another, but the gap between the CIPs might become distanced hindered by the aggregation of silica nanoparticles that might be taken place in the strut structure of MR foam. Figure 4, particularly (C) illustrates the mechanism of fillers-matrix interactions in the MR foam, including the CIPs and silica particles showing the agglomeration of the silica in the struts of foam causing the decrement of attraction between the CIPs during the on-state condition.

3.2 Morphological characterizations of MR foams

Figure 5 shows the micrograph of MR foams with (A) the MR foam without silica additive and (B) the MR foam with 4 wt% of silica nanoparticles. Generally, the structure of MR foam includes cell pores that are enclosed by struts as shown in both Figures 5A,B. It was observed that the MR foam (Figure 5A exhibited more open cell pores correspond to the typical structure of flexible foam while MR foam with silica nanoparticles are observed to have more closed cell pores (Figure 5B) (Scarpa et al., 2004). The resultant structure of MR foam is mainly due to the particle's dispersion including the silica nanoparticles that play a significant role in controlling the cell size of the pores during the polymerization process. The process includes gas formation, cell nucleation growth and cells distribution that would lead to the stabilization of the foam structure (Tamaddoni Moghaddam et al., 2019).

In general, the magnetic particles are embedded in the struts and cell walls of MR foam during foaming process. The distribution of the particles is separated by the pores of the foam matrix, in which would affect the rheological properties of the MR foam. As shown in Figure 5A, significant numbers of non-uniform sized of open-cell pores with large cavities like tunnel have been observed. The formation of pores began with the bubbles of carbon dioxide, CO_2 that were formed via reaction of isocyanate groups with water, thus releasing CO_2 during the gas formation process. Then the bubbles started to grow from the expansion of the blowing gas and merged into coalescent pores structure during the 2nd stage, cell nucleation growth process. In this case, the nucleation growth of pores in MR foam occurred where gas bubbles from the neighboring phase diffused and created randomly large bubbles, resulted in more open-cell pores structure. This resultant open-cell pores structure of MR foam also similar and has been discussed by Rizuan et al., 2021 where the porosity and deep cavities MR foam with 75 wt% of CIPs were characterized. The presence of deeper cavities was influenced by the coalescent of more bubbles, subsequently forming connecting not only deeper but large cavities in the structure of MR foam. Hence, the distribution of the particles is more scattered and significant distance between CIPs were observed due to the existence of large pores. Referring to the result of strain dependent test that has been discussed in previous sub-section, MR foam basically exhibited low storage modulus, about 45 kPa correlated to the nature porosity of MR foam which would affect its ability to withstand higher applied load. The addition of silica nanoparticles is expected to alter the resultant structure of MR foam and simultaneously enhanced the storage modulus of MR foam, accordingly.

In fact, MR foam with 4 wt% of silica nanoparticles possessed improved storage modulus, around 162 kPa and the respective micrograph as shown in Figure 5B, the MR foam looks more closed-cell pores structure with smaller size cavities. At first, the gas bubbles (CO_2) were released through the reaction between isocyanate groups of PU foam that in contact with water. Then

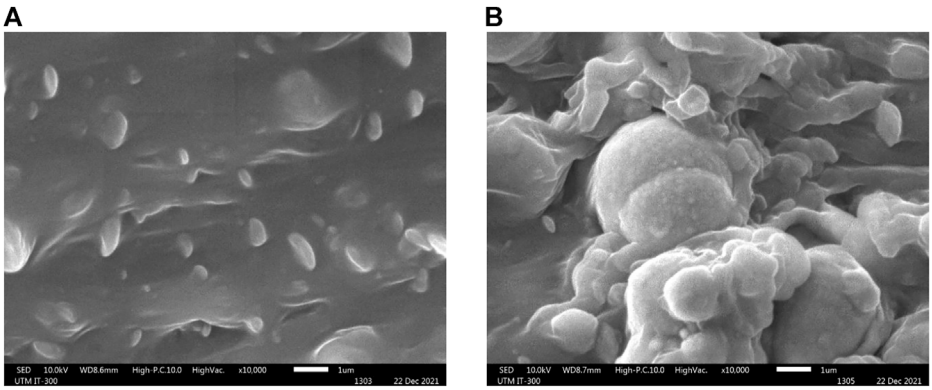

FIGURE 6
Micrograph of **(A)** non-agglomerated particles in MR foam with 4 wt% of silica nanoparticles and **(B)** agglomerated particles in MR foam with 5 wt% of silica nanoparticles.

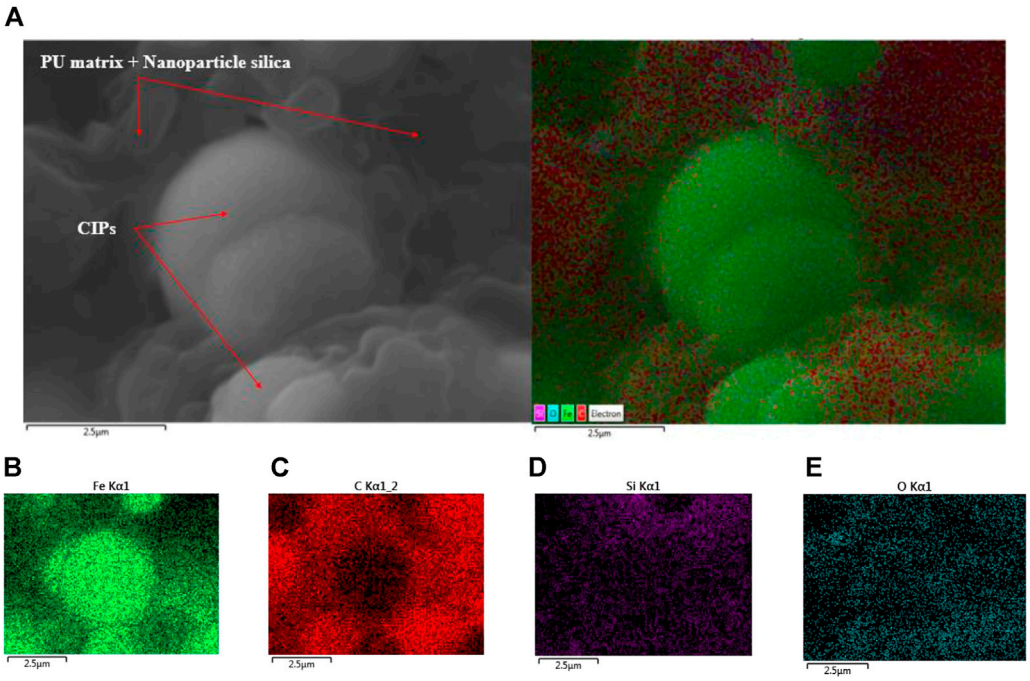

FIGURE 7
Mapping analysis of **(A)** MR foam with addition of silica nanoparticles and respective elements of **(B)** iron, Fe; **(C)** carbon, C; **(D)** silicon, Si; and **(E)** oxide, O.

on the second stage of cell nucleation growth process, silica nanoparticles in the MR foam began to act as nucleation sites for the silane coupling bond to form via H-bonding, that improved the bonding between particles and matrix phase (polyol). In addition, the advantage of nano-sized silica particles is its large surface area where nucleation growth of bubbles becomes more intense, and a greater number of silica nanoparticles could create more silane coupling bonds in the matrix phase. Thus, the mixture turned out to be more viscous and aided bubbles nucleation process resulted in closed-cell pores formation and less porous structure in the MR foam. The growth of bubbles then stopped upon foaming process end, creating porous structure of MR foam. Hence, the distribution of particles including CIPs and silica are more compact due to reduced gaps between smaller

pores and adjacent struts would become nearer. The morphological structure also become more compact and denser causing the MR foam became stiffer and as a result the storage modulus of the material has been enhanced. This phenomenon corresponds to the significant increment in the storage modulus of MR foam with more silica nanoparticles. In fact, when the magnetic field was induced to the MR foam, stronger magnetic forces between the CIPs are acquired due to closer gap between the particles in the struts of MR foam, resulting stiffer composite material. Nevertheless, the increment storage modulus of MR foam with magnetic fields are smaller indicating non-magnetic behavior owned by the silica nanoparticles which are unable to respond to the magnetic field stimuli.

However, the excessive silica nanoparticles in the MR foam, particularly with 5 wt% somehow resulted in negative impact toward the structural and properties of MR foam. Figure 6A showed the micrograph of non-agglomerated particles in the foam matrix when 4 wt% of silica nanoparticles were added to the MR foam. The CIPs and silica nanoparticles were well distributed and embedded in the structure of polymer foam matrix. However, the agglomeration of particles was observed in the MR foam with 5 wt% of silica nanoparticles as shown in Figure 6B. It is attributed to the excessive silica nanoparticles where the amount of polymer that is available to build up bonds with the silica is limited during the polymerization process (Davino et al., 2012), causing agglomeration of silica in the matrix phase. The aggregation of silica nanoparticles also would affect the dimensional stability of the cellular structure of MR foam, thus explaining a decrement in the storage modulus of the material, as has been highlighted in previous section.

Figure 7 depicts the EDX mapping analysis of MR foam with the addition of silica nanoparticles and the analysis showed presence of iron (Fe), carbon (C), silicon (Si) and oxygen (O) correspond to the CIPs (Fe), silica nanoparticles (SiO_2) and carbon for matrix phase. In addition, it was observed that the silica nanoparticles have been well distributed entire the composite area as presented in Figure 7D, including the silica on the surface of the CIPs and in matrix phase of MR foam. This finding also corresponded to the schematic illustrated in Figure 4A.

4 Conclusion

In this work, MR foams with fixed 75 wt% of CIPs have been fabricated with different composition of silica nanoparticles in the range of 0–5 wt%., with the increment of 1 wt% The samples were run to investigate the effects of silica nanoparticles toward the enhancement of the viscoelastic properties, particularly storage modulus and morphological of MR foams. It was identified that under the influence of applied strains, MR foam with 4 wt% of silica nanoparticles demonstrated significant increment in storage modulus, about 260% increase as compared to the MR foam without the addition of silica nanoparticles. In fact, under the influence of magnetic fields from 0 T to 0.73 T, the absolute MR effect of the MR foam was enhanced by about 11kPa, attributed to the responsiveness of the CIPs toward the induced magnetic stimuli showing stiffer MR foam at the on-state condition. Similar findings for other MR foams were observed as the corresponding storage modulus increased with the increased of silica nanoparticles, simultaneously with applied magnetic fields. The findings somehow showed the stiffer MR foams with more embedded particles in the matrix structure, including CIPs and silica nanoparticles (1–5 wt%), at the off-state condition. The enhancement is attributed to the presence of silica nanoparticles that has strengthened the filler-matrix bonding by the formation of silane coupling bond between silica to the PU matrix and CIPs. The stiffness of each MR foam was further increased at the on-state condition due to stronger magnetic interaction of the CIPs and toward the applied magnetic fields. However, the MR foam with 5 wt% of silica nanoparticles showed drop in storage modulus due to the agglomeration of particles in the cellular matrices. Meanwhile, the change in modulus, ΔG, from one to another MR foam with increment of 1 wt% of silica nanoparticles showed small increment as well, about 1 kPa particularly at the on-state condition showing the non-magnetic properties of silica additive toward the applied field. Furthermore, the micrograph images have shown the open-cell pores structure with large cavities in the structure of the MR foam while less porous and closed-cell pores structure were observed for MR foam with silica nanoparticles. The silica nanoparticles also were well distributed entire the MR foam indicating the homogeneity properties of the material.

Data availability statement

The original contributions presented in the study are included in the article/Supplementary Material; further inquiries can be directed to the corresponding authors.

Author contributions

All authors listed have made a substantial, direct, and intellectual contribution to the work and approved it for publication.

Funding

This research work is supported and funded by the Universiti Teknologi Malaysia (UTM) Zamalah (Vot No. 0060N) and the Japan International Cooperation Agency Fund (JICA Fund) (Vot No. 4B696). The authors also declared that this research was funded by Universitas Sebelas Maret through Hibah Kolaborasi

Internasional (HKI) 2022 (Contract No. 254/UN27.22/PT.01.03/2022).

Conflict of interest

The authors declare that the research was conducted in the absence of any commercial or financial relationships that could be construed as a potential conflict of interest.

Publisher's note

References

Abd Rashid, R. Z., Johari, N., Mazlan, S. A., Abdul Aziz, S. A., Nordin, N. A., Nazmi, N., et al. (2021). Effects of silica on mechanical and rheological properties of EPDM-based magnetorheological elastomers. *Smart Mat. Struct.* 30, 105033. doi:10.1088/1361-665X/ac1f64

Ahmad Khairi, M. H., Mazlan, S. A., Ubaidillah,Choi, S. B., Abdul Aziz, S. A., Mohamad, N., et al. (2019). Role of additives in enhancing the rheological properties of magnetorheological solids: A review. *Adv. Eng. Mat.* 21, 1–13. doi:10.1002/adem.201800696

Alekhina, Y. A., Omelyanchik, A. S., Peddis, D., Spiridonov, V. V., Rodionova, V. V., Perov, N. S., et al. (2019). Magnetorheological foams for multiferroic applications. *J. Magn. Magn. Mat.* 485, 413–418. doi:10.1016/j.jmmm.2019.04.001

Anuar, M. F., Fen, Y. W., Zaid, M. H. M., Matori, K. A., and Khaidir, R. E. M. (2018). Synthesis and structural properties of coconut husk as potential silica source. *Results Phys.* 11, 1–4. doi:10.1016/j.rinp.2018.08.018

Aziz, S. A. A., Mazlan, S. A., Ubaidillah, U., Shabdin, M. K., Yunus, N. A., Nordin, N. A., et al. (2019). Enhancement of viscoelastic and electrical properties of magnetorheological elastomers with nanosized Ni-Mg cobalt-ferrites as fillers. *Mater. (Basel)* 12, 1–18. doi:10.3390/ma1221353110.1016/j.compositesb.2020.108348

Bastola, A. K., and Hossain, M. (2020). A review on magneto-mechanical characterizations of magnetorheological elastomers. *Compos. Part B Eng.* 200, 108348. doi:10.1016/j.compositesb.2020.108348

Boczkowska, A., Awietjan, S. F., Pietrzko, S., and Kurzydłowski, K. J. (2012). Composites : Part B mechanical properties of magnetorheological elastomers under shear deformation. *Compos. Part B Eng.* 43, 636–640. doi:10.1016/j.compositesb.2011.08.026

Burgaz, E., and Kendirlioglu, C. (2019). Thermomechanical behavior and thermal stability of polyurethane rigid nanocomposite foams containing binary nanoparticle mixtures. *Polym. Test.* 77, 105930. doi:10.1016/j.polymertesting.2019.105930

Cain, A. A., Nolen, C. R., Li, Y. C., Davis, R., and Grunlan, J. C. (2013). Phosphorous-filled nanobrick wall multilayer thin film eliminates polyurethane melt dripping and reduces heat release associated with fire. *Polym. Degrad. Stab.* 98, 2645–2652. doi:10.1016/j.polymdegradstab.2013.09.028

Chuah, W. H., Zhang, W. L., Choi, H. J., and Seo, Y. (2015). Magnetorheology of core-shell structured carbonyl iron/polystyrene foam microparticles suspension with enhanced stability. *Macromolecules* 48, 7311–7319. doi:10.1021/acs.macromol.5b01430

Davino, D., Mei, P., Sorrentino, L., and Visone, C. (2012). Polymeric composite foams with properties controlled by the magnetic field. *IEEE Trans. Magn.* 48, 3043–3046. doi:10.1109/TMAG.2012.2198634

Eatemadi, A., Daraee, H., Karimkhanloo, H., Kouhi, M., Zarghami, N., Akbarzadeh, A., et al. (2014). Carbon nanotubes: Properties, synthesis, purification, and medical applications. *Nanoscale Res. Lett.* 9, 1–13. doi:10.1186/1556-276X-9-393

Ge, L., Xuan, S., Liao, G., Yin, T., and Gong, X. (2015). Stretchable polyurethane sponge reinforced magnetorheological material with enhanced mechanical properties. *Smart Mat. Struct.* 24, 037001. doi:10.1088/0964-1726/24/3/037001

Gong, Q., Wu, J., Gong, X., Fan, Y., and Xia, H. (2013). Smart polyurethane foam with magnetic field controlled modulus and anisotropic compression property. *RSC Adv.* 3, 3241–3248. doi:10.1039/c2ra22824f

Kang, S. S., Choi, K., Nam, J. Do, and Choi, H. J. (2020). Magnetorheological elastomers: Fabrication, characteristics, and applications. *Mater. (Basel)* 13, 1–24. doi:10.3390/ma13204597

Khaidir, R. E. M., Fen, Y. W., Zaid, M. H. M., Matori, K. A., Omar, N. A. S., Anuar, M. F., et al. (2019b). Exploring Eu^{3+} -doped ZnO-SiO_2 glass derived by recycling renewable source of waste rice husk for white-LEDs application. *Results Phys.* 15, 102596. doi:10.1016/j.rinp.2019.102596

Khaidir, R. E. M., Fen, Y. W., Zaid, M. H. M., Matori, K. A., Omar, N. A. S., Anuar, M. F., et al. (2020). Addition of ZnO nanoparticles on waste rice husk as potential host material for red-emitting phosphor. *Mat. Sci. Semicond. process.* 106, 104774. doi:10.1016/j.mssp.2019.104774

Khaidir, R. E. M., Fen, Y. W., Zaid, M. H. M., Matori, K. A., Omar, N. A. S., Anuar, M. F., et al. (2019a). Optical band gap and photoluminescence studies of Eu^{3+} -doped zinc silicate derived from waste rice husks. *Optik* 182, 486–495. doi:10.1016/j.ijleo.2019.01.061

Kong, L., Li, F., Wang, F., Miao, Y., Huang, X., Zhu, H., et al. (2018). High-performing multi-walled carbon nanotubes/silica nanocomposites for elastomer application. *Compos. Sci. Technol.* 162, 23–32. doi:10.1016/j.compscitech.2018.04.008

Kumar, V., and Lee, D. J. (2019). Mechanical properties and magnetic effect of new magneto-rheological elastomers filled with multi-wall carbon nanotubes and iron particles. *J. Magn. Magn. Mat.* 482, 329–335. doi:10.1016/j.jmmm.2019.03.075

Li, S., Li, Y., and Li, J. (2021). Thixotropy of magnetorheological gel composites: Experimental testing and modelling. *Compos. Sci. Technol.* 214, 108996. doi:10.1016/j.compscitech.2021.108996

Li, S., Liang, Y., Li, Y., Li, J., and Zhou, Y. (2020a). Investigation of dynamic properties of isotropic and anisotropic magnetorheological elastomers with a hybrid magnet shear test rig. *Smart Mat. Struct.* 29, 114001–114023. doi:10.1088/1361-665x/ab9e09

Li, S., Tian, T., Wang, H., Li, Y., Li, J., Zhou, Y., et al. (2020b). Development of a four-parameter phenomenological model for the nonlinear viscoelastic behaviour of magnetorheological gels. *Mat. Des.* 194, 108935. doi:10.1016/j.matdes.2020.108935

Li, W., Kostidis, K., Zhang, X., and Zhou, Y. (2009). "Development of a force sensor working with MR elastomers," in *IEEE/ASME int. Conf. Adv. Intell. Mechatronics, AIM*, 233–238. doi:10.1109/AIM.2009.5230010

Linde, R. K., Seaman, L., and Schmidt, D. N. (1972). Shock response of porous copper, iron, tungsten, and polyurethane. *J. Appl. Phys.* 43, 3367–3375. doi:10.1063/1.1661721

Meng, J., Gerez, L., Chapman, J., and Liarokapis, M. (2020). "A tendon-driven, preloaded, pneumatically actuated, soft robotic gripper with a telescopic palm," in *2020 3rd IEEE int. Conf. Soft robot. RoboSoft*, 476–481. 2020. doi:10.1109/RoboSoft48309.2020.9115986

Mohd Nasir, N. A., Nazmi, N., Mohamad, N., Ubaidillah, U., Nordin, N. A., Mazlan, S. A., et al. (2021). Rheological performance of magnetorheological grease with embedded graphite additives. *Mater. (Basel)* 14, 1–15. doi:10.3390/ma14175091

Muhazeli, N. S., Nordin, N. A., Mazlan, S. A., Rizuan, N., Choi, S., Abd Fatah, A. Y., et al. (2019). Characterization of morphological and rheological properties of rigid magnetorheological foams via *in situ* fabrication method. *J. Mat. Sci.* 54, 13821–13833. doi:10.1007/s10853-019-03842-9

Muhazeli, N. S., Nordin, N. A., Ubaidillah, U., Mazlan, S. A., Aziz, S. A. A., Nazmi, N., et al. (2020). Magnetic and tunable sound absorption properties of an *in-situ* prepared magnetorheological foam. *Mater. (Basel)* 13, 1–16. doi:10.3390/ma13245637

Nikje, M. M. A., Garmarudi, A. B., Haghshenas, M., and Mazaheri, Z. (2009). Improving the performance of heat insulation polyurethane foams by silica nanoparticles. *Nanotechnol. Constr.* 3, 149–154. doi:10.1007/978-3-642-00980-8_19

Nikje, M. M. A., and Tehrani, Z. M. (2010). Thermal and mechanical properties of polyurethane rigid foam/modified nanosilica composite. *Polym. Eng. Sci.* 50, 468–473. doi:10.1002/pen.21559

Plachy, T., Kratina, O., and Sedlacik, M. (2018). Porous magnetic materials based on EPDM rubber fi lled with carbonyl iron particles. *Compos. Struct.* 192, 126–130. doi:10.1016/j.compstruct.2018.02.095

Rizuan, N., Mazlan, S. A., Ubaidillah, U., Sedlacik, M., Aziz, S. A. A., Nazmi, N., et al. (2021). Sensitivities of rheological properties of magnetoactive foam for soft sensor technology. *Sensors* 21, 1–19. doi:10.3390/s21051660

Rizuan, N., Mazlan, S. A., UbaidillahAbdul Aziz, S. A., Nazmi, N., and Yunus, N. A. (2020). Enhancement of sensitivity of magnetostrictive foam in low magnetic fields for sensor applications. *Polymer* 211, 123083. doi:10.1016/j.polymer.2020.123083

Saha, M. C., Kabir, M. E., and Jeelani, S. (2008). Enhancement in thermal and mechanical properties of polyurethane foam infused with nanoparticles. *Mater. Sci. Eng. A* 479, 213–222. doi:10.1016/j.msea.2007.06.060

Saiz-Arroyo, C., Escudero, J., Rodríguez-Pérez, M. A., and De Saja, J. A. (2011). Improving the structure and physical properties of LDPE foams using silica nanoparticles as an additive. *Cell. Polym.* 30, 63–78. doi:10.1177/026248931103000202

Scarpa, F., Bullough, W. A., and Lumley, P. (2004). Trends in acoustic properties of iron particle seeded auxetic polyurethane foam. *Proc. Institution Mech. Eng. Part C J. Mech. Eng. Sci.* 218, 241–244. doi:10.1243/095440604322887099

Scarpa, F., and Smith, F. C. (2004). Passive and MR fluid-coated auxetic PU foam - mechanical, acoustic, and electromagnetic properties. *J. Intell. Mat. Syst. Struct.* 15, 973–979. doi:10.1177/1045389X04046610

Schümann, M., Seelig, N., and Odenbach, S. (2015). The effect of external magnetic fields on the pore structure of polyurethane foams loaded with magnetic microparticles. *Smart Mat. Struct.* 24, 105028. doi:10.1088/0964-1726/24/10/105028

Shabdin, M. K., Rahman, M. A. A., Mazlan, S. A., UbaidillahHapipi, N. M., Adiputra, D., et al. (2019). Material characterizations of gr-based magnetorheological elastomer for possible sensor applications: Rheological and resistivity properties. *Mater. (Basel)* 12, 1–15. doi:10.3390/ma12030391

Tamaddoni moghaddam, S., and Naimi-Jamal, M. R. (2017). *Effect of novel magnetic nanoparticles on morphology properties of polyurethane foam*, 4828. doi:10.3390/ecsoc-21-04828

Tamaddoni Moghaddam, S., Naimi-Jamal, M. R., Rohlwing, A., Hussein, F. B., and Abu-Zahra, N. (2019). High removal capacity of arsenic from drinking water using modified magnetic polyurethane foam nanocomposites. *J. Polym. Environ.* 27, 1497–1504. doi:10.1007/s10924-019-01446-7

Tian, T. F., Li, W. H., Alici, G., Du, H., and Deng, Y. M. (2011). Microstructure and magnetorheology of graphite-based MR elastomers. *Rheol. Acta* 50, 825–836. doi:10.1007/s00397-011-0567-9

Umehara, Y., Yamanaga, Y., Akama, S., and Kato, S. (2018). *Railway actuator made of magnetic elastomers and driven by a magnetic Field*, 1–7. doi:10.3390/polym10121351

Wang, N., Liu, X., Sun, S., Królczyk, G., Li, Z., and Li, W. (2020). Microscopic characteristics of magnetorheological fl uids subjected to magnetic fields. *J. Magn. Magn. Mat.* 501, 166443. doi:10.1016/j.jmmm.2020.166443

Yin, H., Zhang, X., Li, J., Cao, J., Zhao, Y. M., and Cheng, B. L. (2017). Effects of selenium on Fusarium growth and associated fermentation products and the relationship with chondrocyte viability. *Biomed. Environ. Sci.* 30, 134–138. doi:10.3967/bes2017.017

Yunus, N. A., Mazlan, S. A., UbaidillahAbdul Aziz, S. A., Shilan, S. T., Abdul Wahab, N. A., and Abdul Wahab, N. (2019). Thermal stability and rheological properties of epoxidized natural rubber-based magnetorheological elastomer. *Int. J. Mol. Sci.* 20, 1–19. doi:10.3390/ijms20030746

Zaidi, S., Maselli, M., Laschi, C., and Cianchetti, M. (2021). Actuation technologies for soft robot grippers and manipulators: A review. *Curr. Robot. Rep.* 2, 355–369. doi:10.1007/s43154-021-00054-5

Zainudin, A. A., Yunus, N. A., Mazlan, S. A., Shabdin, M. K., Aziz Abdul, S. A., Nordin, N. A., et al. (2020). Rheological and resistance properties of magnetorheological elastomer with cobalt for sensor application. *Appl. Sci. (Basel).* 10, 1–12. doi:10.3390/app10051638

Zhang, G., Wang, H., Wang, J., Zheng, J., and Ouyang, Q. (2019). The impact of CIP content on the field-dependent dynamic viscoelastic properties of MR gels. *Colloids Surfaces A Physicochem. Eng. Aspects* 580, 123596. doi:10.1016/j.colsurfa.2019.123596

frontiers | Frontiers in Materials

TYPE Original Research
PUBLISHED 12 September 2022
DOI 10.3389/fmats.2022.984761

OPEN ACCESS

EDITED BY
Yancheng Li,
Nanjing Tech University, China

REVIEWED BY
Qing Ouyang,
Jiaxing University, China
Xiaomin Dong,
Chongqing University, China

*CORRESPONDENCE
Decai Li,
lidecai@mail.tsinghua.edu.cn

SPECIALTY SECTION
This article was submitted to Smart Materials, a section of the journal Frontiers in Materials

RECEIVED 02 July 2022
ACCEPTED 23 August 2022
PUBLISHED 12 September 2022

CITATION
Li Z and Li D (2022), A comparative study of magnetic seals by ferrofluids, magnetorheological fluids and magnetic powders.
Front. Mater. 9:984761.
doi: 10.3389/fmats.2022.984761

A comparative study of magnetic seals by ferrofluids, magnetorheological fluids and magnetic powders

Zhenghao Li and Decai Li*

State Key Laboratory of Tribology, Tsinghua University, Beijing, China

Magnetic seals as a class of non-contact sealing technology have been a research focus. In these seals, magnetic materials, usually ferrofluids or magnetorheological fluids are attracted in sealing gaps as sealing medium. Recently, a novel sealing method using nano-micron sized magnetic powders has been raised up as well. However, the working performance of these magnetic seals has not been studied thoroughly and comparatively yet. Here, we provide a comparative study of magnetic seals by ferrofluid, magnetorheological fluid and magnetic powder theoretically and experimentally. The formulas of pressure capability are derived based on their different properties. A modified empirical formula of magnetic powder seals is proposed, taking the frictional effect into consideration. The magnetic field distribution is calculated by the finite element method. Finally, a test bench for static magnetic seals is established. The pressure capability and leakage rate of three materials are measured by sealing experiments. The differences in mechanism of pressure transfer and the ability of self-recovery are discussed. This research summarizes the characteristics of different magnetic seals, and provides a guidance for sealing medium selection and structure design.

KEYWORDS

ferrofluid, magnetorheological fluid, magnetic powder, seal, pressure capability, leakage rate

1 Introduction

Magnetic seals are a class of non-contact sealing technology using magnetic materials as sealing medium. In these seals, a magnetic circuit is established by a magnetic source and magnetically conductive parts to generate a magnetic field gradient in sealing gaps, and the magnetic medium is attracted there firmly by the magnetic force. Compared to traditional sealing technology, magnetic seals possess unique advantages such as low leakage rate, simple structures and long lifetime (Parmar et al., 2020; Zhou et al., 2020; Liu et al., 2022). Ferrofluids (FFs) and magnetorheological fluids (MRFs) are commonly used as sealing medium, while a novel sealing method using nano-micron magnetic powders (MPs) has been presented recently as well (Li and Li, 2022a).

FFs are colloidal liquid composed of magnetic nanoparticles coated with certain surfactants and dispersed stably in a carrier fluid (Zang et al., 2022). Because of their special characteristics such as superparamagnetism and biocompatibility, FFs have been applied in hyperthermia, information storage, optical sensors and so on (Das et al., 2019; Huang et al., 2021). Specifically, FF seals are used in high demand conditions for its zero leakage, high reliability and low resistance torque. Fan et al. (2021) designed an FF seal for an aerospace air cylinder and solved the problem of leakage and service life. However, the performance of FF seals is restricted by their limited pressure capability per stage and intolerance of high temperature (Matuszewski, 2019). MRFs are composed of soft ferromagnetic or paramagnetic particles (about 1–10 μm) dispersed in a carrier fluid. Their rheological properties are magnetically controllable, and may change from Newtonian to Bingham behavior under an external magnetic field (Choi and Han, 2012). Therefore, they are widely used in automobiles, polishing machines, etc. (Wang and Meng, 2001) Liang et al. (2018) presented a dynamic sealing technique for external gear pumps by MRF seals in the clearance between the gear and housing. The volumetric loss of gear pumps was reduced without greater friction or higher manufacturing precision. But the stability and the friction torque of MRF seals have always been a concern in applications (Kubík et al., 2019). MPs have been recently adopted in magnetic seals. Generally, nano or micron-sized Fe_3O_4 particles coated with proper surfactants or lubricants are prepared by the chemical coprecipitation method or the high energy ball-milling method. Due to the absence of carrier fluid, MP seals have wider temperature tolerance and better stability against sedimentation. Li and Li. (2022b) derived the simplified formula of pressure capability of MP seals based on the principle of virtual work, and proposed a method of designing the pole tooth structure. But the leakage rate of MP seals is rather high compared to FF seals, and the prediction of the pressure capability still needs to be modified (Li and Li, 2022c).

In conclusion, previous researches have investigated the properties of FFs, MRFs, and MPs, and applied them in a wide range of sealing conditions. However, the working performance of seals by these materials has not been studied thoroughly and comparatively.A lack of guidance to select the proper magnetic medium according to different sealing requirements still exists.

In this research, a comparative study of FF, MRF, and MP seals is provided theoretically and experimentally. The formulas of pressure capability are derived based on their different properties. Taking the frictional effect into consideration, a modified empirical formula of MP seals is proposed. Then the distribution of magnetic field intensity is calculated by the finite element method. Further, a sealing prototype is designed and manufactured, and a test bench is established for magnetic seals. The pressure capability and leakage rate of all magnetic seals with various widths of pole teeth are measured by sealing experiments. The differences in mechanism of pressure transfer and the ability of self-recovery are discussed. This research summarizes the characteristics of different magnetic seals, and gives a guidance for sealing medium selection and structure design.

2 Materials

The FF and the MP used in this research are prepared in our lab. The FF is prepared by the chemical coprecipitation method and uses motor oil as the carrier fluid. The volume fraction of Fe_3O_4 is around 7%. The MP is prepared by the high energy ball-milling method. Fe_3O_4 nanoparticles with an average size of 100 nm are ball-milled with low density polyethylene for 6 h. The mass ratio of Fe_3O_4 nanoparticles to low density polyethylene is 6:1. The MRF is Model A172 purchased from *Bohai New Material Corp.*, with 72 wt% of carbonyl iron inside and synthetic hydrocarbon as the carrier fluid. The magnetic particles in the FF and the MP are characterized by a transmission electron microscope (TEM). As is shown in Figure 1, the average particle sizes of the FF and the MP are approximately 10 nm and 200–300 nm, respectively. The Fe_3O_4 particles in the FF maintains great dispersibility, while the particles of the MP agglomerate after dissolution and desiccation. The magnetic properties of three materials (*M-H* curves) are measured by a vibrating sample magnetometer, as is shown in Figure 2. All these materials approach magnetic saturation under the magnetic field of 15,000 Oe, where the magnetization intensity of the FF, MP and MRF is 25.03, 64.81 and 144.79 emu/g, respectively. The MRF has the strongest magnetization intensity, and the FF has the weakest.

3 Theoretical basis

The main pressure capability of magnetic seals comes from the gradient of the magnetic field intensity in sealing gaps. For incompressible Newtonian steady-state flow and an irrotational flow field, the FF follows the Bernoulli equation (Rosensweig, 2013).

$$p + \frac{1}{2}\rho_f v^2 + \rho_f gh - \mu_0 \int_0^H MdH = C \tag{1}$$

Where p is the pressure, ρ_f is the density, v is the velocity, h is the height of FFs, μ_0 is vacuum permeability, M is the magnetization intensity, H is the magnetic field intensity and C is a constant. It is assumed that in static FF seals, the gravity and surface tension of FFs are neglectable, so

$$p_1 - \mu_0 \int_0^{H_1} MdH = p_2 - \mu_0 \int_0^{H_2} MdH \tag{2}$$

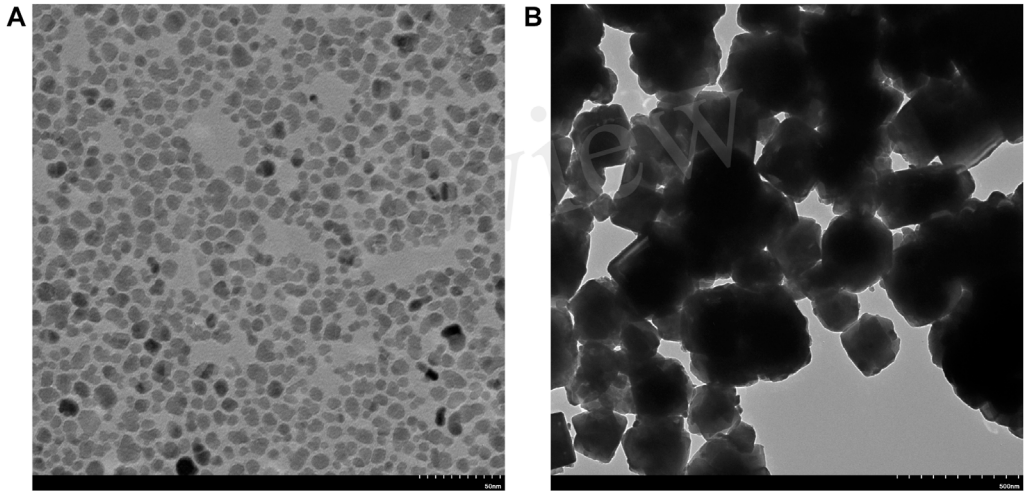

FIGURE 1
TEM images of **(A)** the FF and **(B)** the MP.

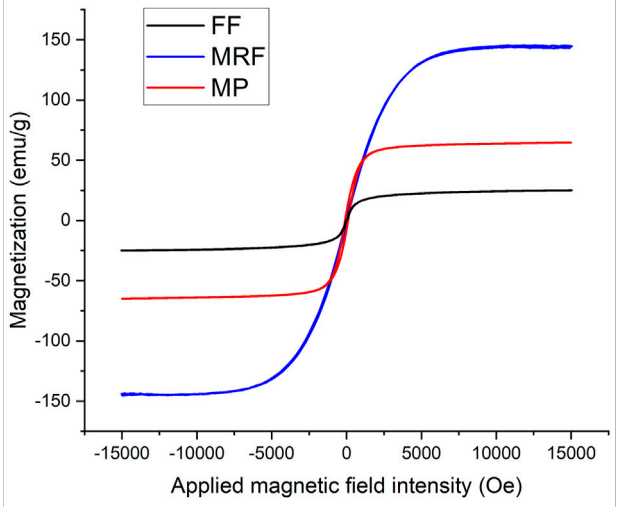

FIGURE 2
M-H curves of the FF, MRF, and MP at room temperature.

$$\Delta p_{\max} = \mu_0 \int_{H_{\min}}^{H_{\max}} MdH \approx \mu_0 M_s (H_{\max} - H_{\min}) \tag{3}$$

where H_{max} and H_{min} are the maximum and minimum magnetic field intensity in the sealing gap, respectively, and M_s is the saturation magnetization of the FF. Eq. 3 indicates two methods of increasing pressure capability, by improving the magnetic properties of FFs or the magnetic field.

In MRF seals, chain-like structures are formed along the magnetic field direction, and the yield stress increases significantly. Therefore, an extra portion of pressure capability comes from the elasto-plastic property of MRFs (Zhang et al., 2018)

$$\Delta p = \mu_0 \int_{H_1}^{H_2} MdH + 2\tau_0 \frac{b}{\delta} \tag{4}$$

where τ_0 is the yield stress of MRFs, δ is the height of the sealing gap and b is the width of the pole tooth. The equations above are based on the Bernoulli equation, which neglects the viscosity of the fluid. In fact, the viscosity of FFs is relatively low. For example, four types of commercial FFs from *Ferrotec Corp.* have viscosity from 0.6 to 1.2 Pa·s at 25°C (Szczech, 2018). Therefore, the friction in static FF seals is usually neglected. On the other hand, the influence by the viscosity of MRFs under a magnetic field is represented by the yield stress.

For MP seals, the Bernoulli equation no more applies to the powdery state of the sealing medium, but the MPs in sealing gaps can be assumed to follow the principle of virtual work. For a virtual displacement of MPs, the virtual work by the pressure equals the overall change of the magnetic energy approximately. Therefore, the pressure capability is derived as (Li and Li, 2022b)

$$\Delta p_{\max} = \frac{1}{2}\left((\lambda_H \mu_H H^2)_{\max} - (\lambda_H \mu_H H^2)_{\min} \right)_{r=\bar{r}} \tag{5}$$

where $\lambda_H = \int_0^B H \cdot dB / (\frac{1}{2} BH)$, μ_H is the permeability at the magnetic field intensity H and $\bar{r}$ is the radius of the central sealing gap. However, the pressure capability is likely to be overestimated by Eq. 5 due to the uniformity and loose packing problems during the loading process. Moreover, this equation neglects the friction between MPs and the structural parts, which results in evident errors especially when the friction coefficient is large. The friction is mainly determined by the rheological properties of the MPs as well as the normal force between MPs and pole teeth.

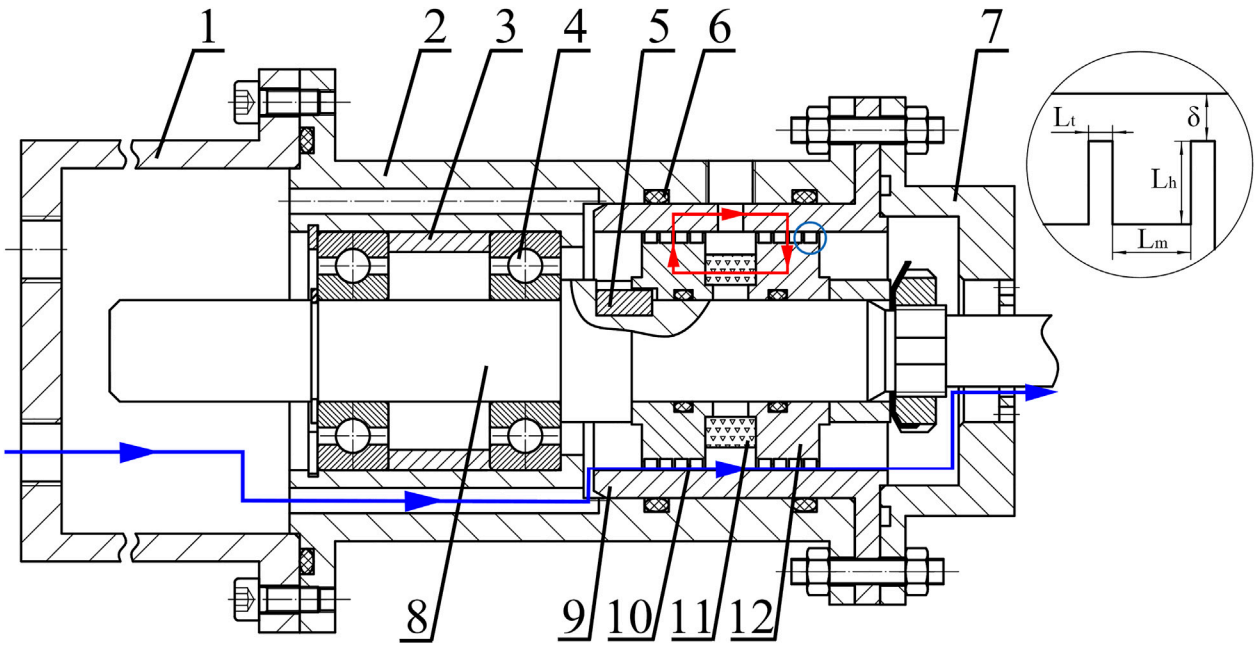

FIGURE 3
Schematic of the sealing prototype (1-gas chamber, 2-shell, 3-sleeve, 4-bearing, 5-key, 6-rubber ring, 7-cover, 8-shaft, 9-inner sleeve, 10-pole tooth, 11-permanent magnet, 12-pole piece).

Therefore, a modified empirical formula is proposed as a combination of the magnetic part and the friction part

$$\Delta p = \alpha \cdot \Delta\left(\lambda_H \mu_H H^2\right) + \beta \cdot \bar{M}\left(H_{r_2} + H_{r_1}\right) b\bar{r} \tag{6}$$

where α is an empirical coefficient related to the magnetic force and energy and β is an empirical coefficient related to the friction between MPs and the sealing structure. These two coefficients may be obtained by fitting sufficient amount of experimental data. $\bar{M}$ is the average magnetization intensity of MPs in the sealing gap, Hr_2 and Hr_1 are the magnetic field intensity of the outer and inner diameter of MP rings, respectively. Hr_2+Hr_1 represents the average magnetic field intensity in the sealing gap, which together with $\bar{M}$ is a main determinant of the magnetic force on MPs. Meanwhile, b and $\bar{r}$ are related to the contact area of MPs and the sealing structure. Compared to the former formula, Eq. 6 shows a better consistency with the sealing experiments below.

4 Methods

4.1 Structure design

Figure 3 shows the schematic diagram of the sealing prototype. The red circuit indicates the magnetic circuit, which is composed of a permanent magnet, two pole pieces with pole teeth on them, an inner sleeve and the magnetic medium. A certain type of magnetic medium is attracted in the sealing gaps between the inner sleeve and pole teeth. It is difficult for magnetic medium of poor fluidity to fill in the gaps uniformly, such as MPs. For the convenience of loading the magnetic medium, pole teeth are designed on the external surface of the pole pieces. In Figure 3, the sealing area is enlarged on the right, and key structural parameters are marked. In total, five pairs of pole pieces are manufactured and used. Four of them have one pole tooth per pole piece, with the height of pole tooth L_h = 2 mm and the width L_t = 0.5, 1.0, 1.5, 2.0 mm, respectively. One pair have five pole teeth per pole piece, with L_h = 2 mm, L_t = 0.5 mm and the interval between adjacent pole teeth L_m = 2.5 mm. The sealing gap is δ = 0.3 mm.

The blue line in Figure 3 indicates the flow path of the sealed gas through the magnetic seal. The gas in the gas chamber is compressed slowly, and flows via two holes in the shell. For magnetic seals with a leakage rate, the gas passes through the magnetic medium and enters the atmosphere. Other paths are sealed by rubber rings. Through-holes are made on the gas chamber, the shell and the inner sleeve, so that the pressure on the first and second sealing stages can be monitored simultaneously to study the mechanism of pressure transfer among stages.

4.2 Numerical simulation

The structure of magnetic seals is a magnetostatic system with no electric currents. The solving of magnetic parameters is

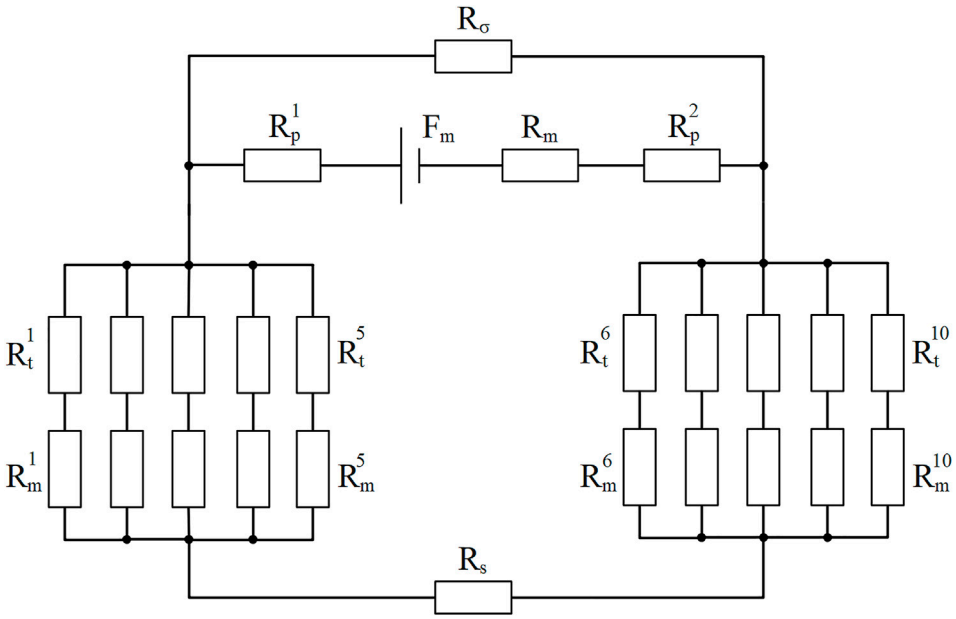

FIGURE 4
Equivalent magnetic circuit of the sealing structure. (F_m is the magnetomotive force of the magnet, and R_m, R_p, R_t, R_m, R_s, R_σ are the magnetic resistance of the magnet, pole piece, pole tooth, magnetic sealing media, shaft and magnetic flux leakage path, respectively.)

on the basis of Magnetic Flux Conservation and Ampere's Law. With reference to electric circuits, the equivalent magnetic circuit of the sealing structure from Figure 3 is plotted in Figure 4. R_σ represents the total magnetic resistance of the leakage path of the magnetic flux through the air, the shaft and the shell, etc. This schematic diagram illustrates the transfer of the magnetic circuit and the loss of magnetic energy, and provides a visual guidance to the magnetic and structural design. With the definition of the demagnetizing curve of the magnet and magnetizing curves of other parts, magnetic parameters of the whole field can be calculated.

The finite element method is usually used in the simulation of magnetic field distribution. To simplify the modeling and calculating process, an axisymmetric model is applied, and only the magnetic source and magnetically conductive parts are modelled. These materials are defined by their magnetic properties (*B-H* curves), while others are considered to have a permeability equal to vacuum. A rectangular air domain of 80 mm width and 110 mm height is established. The axisymmetric boundary condition is applied on the symmetric axis, and the magnetic insulation boundary condition is applied on the air boundaries. The initial magnetic scalar potential is zero. The minimum meshing number in sealing gaps is 10. The tolerance set while solving the model is 0.001. After meshing and calculation, the distributions of magnetic field lines and magnetic field intensity in sealing gaps are plotted.

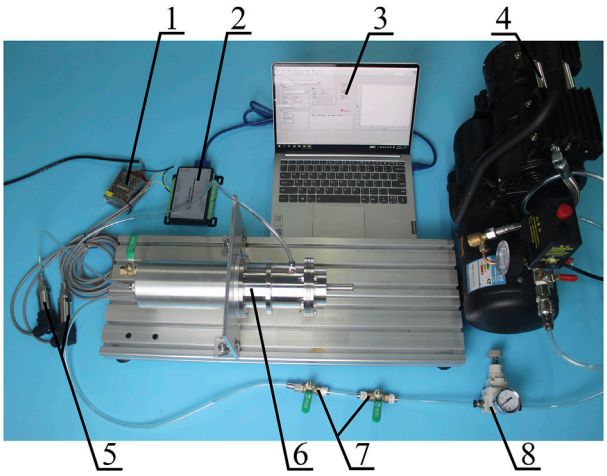

FIGURE 5
Test bench for magnetic seals (1-power supply, 2-data acquisition card, 3-computer, 4-air compressor, 5-pressure sensor, 6-sealing prototype, 7-ball valve, 8-regulator valve).

4.3 Experimental setups

To study the sealing performance of different magnetic seals, a sealing test bench is established in Figure 5. Key components include a sealing prototype, an air compressor, pressure sensors,

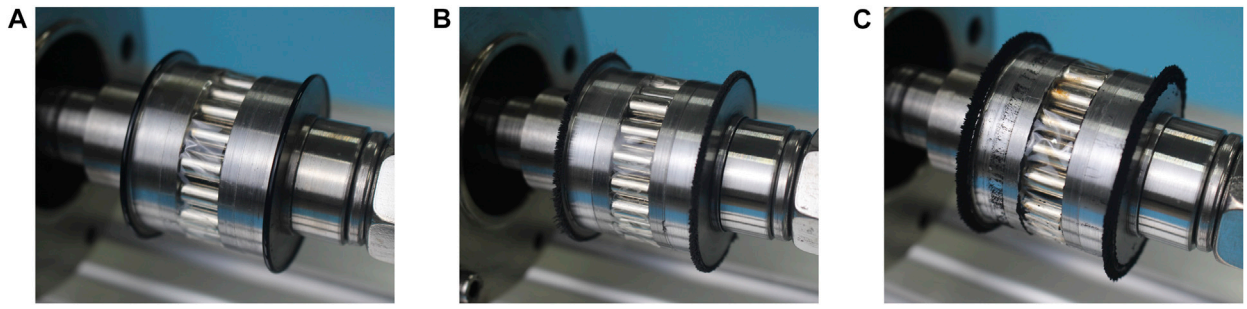

FIGURE 6
Pole teeth loaded with magnetic sealing medium **(A)** FFs, **(B)** MRFs and **(C)** MPs.

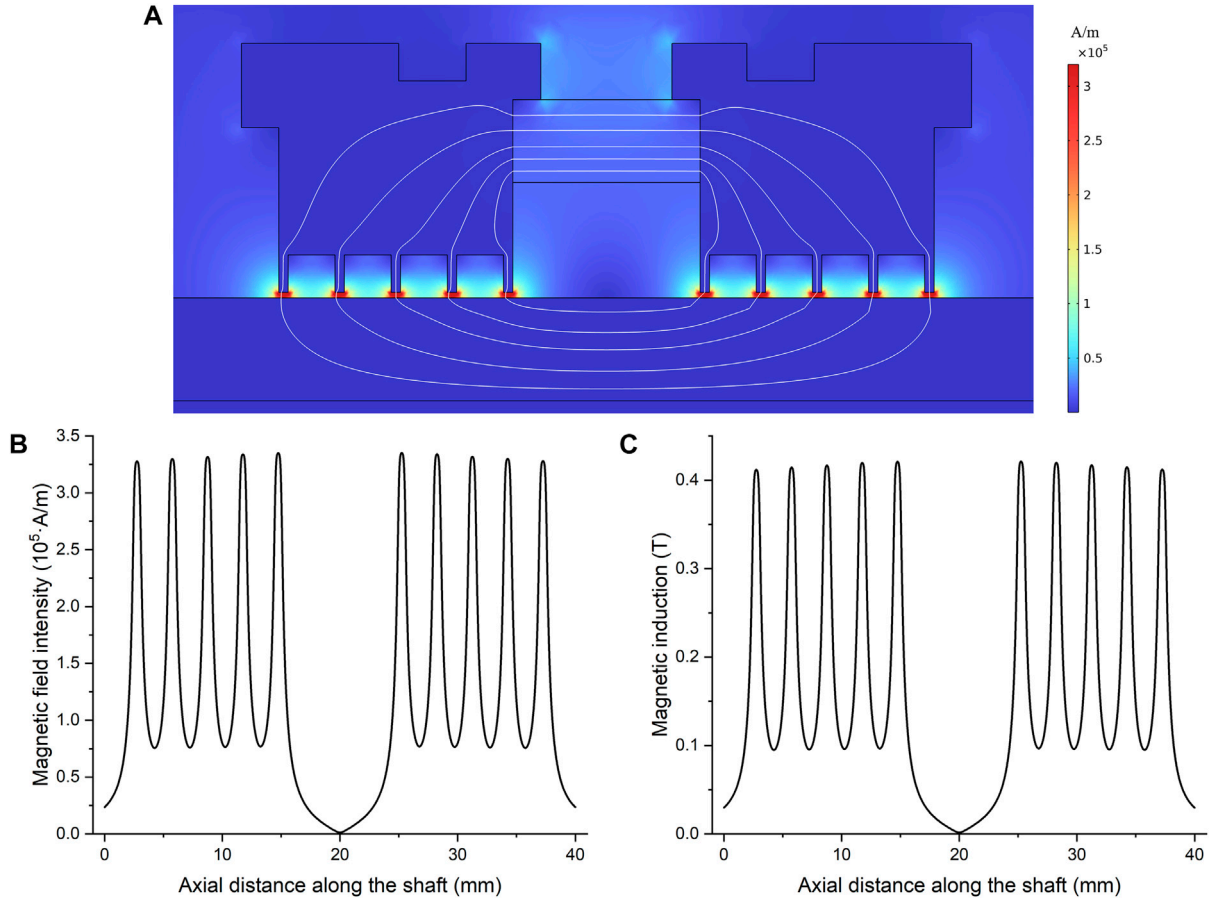

FIGURE 7
(A) Distribution of magnetic field intensity and magnetic induction lines, **(B)** magnetic field intensity and **(C)** magnetic induction in sealing gaps along the axial direction.

valves, a computer, etc. During one experiment, a pair of pole pieces are first assembled on the shaft. The magnetic medium is injected or smeared on each pole tooth circularly, as is shown in Figure 6. Then the shaft is pushed in the shell and fixed. After the assembly of the sealing prototype and connection of electric and gas circuits, the gas is compressed by a compressor. The pressure

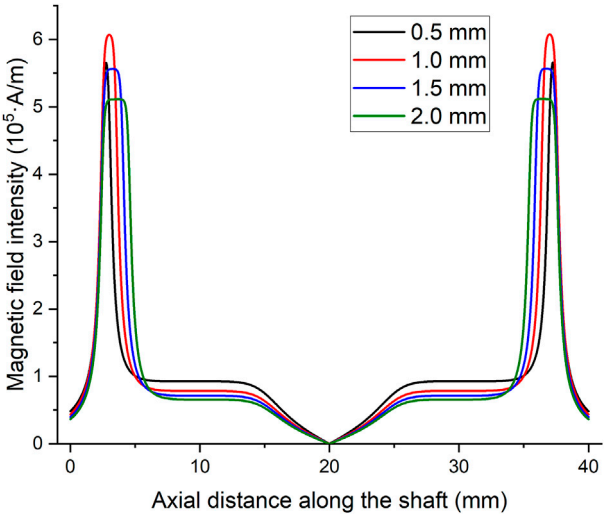

FIGURE 8
Magnetic field intensity in sealing gaps along the axial direction for single pole teeth of different widths.

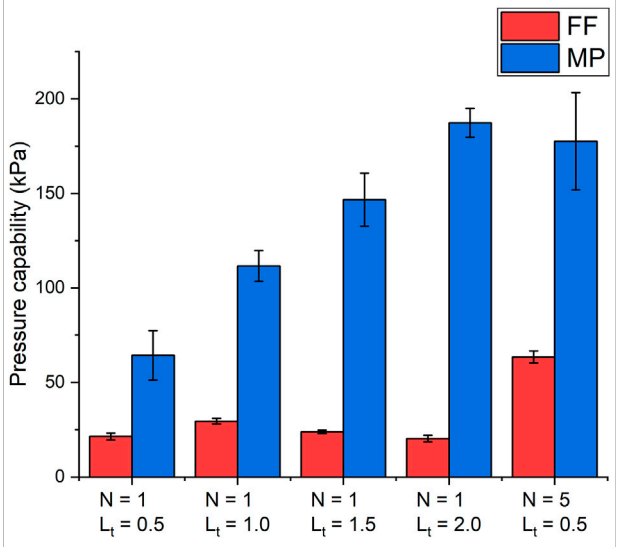

FIGURE 9
Pressure capability of FF and MP seals of different pole pieces.

as well as the flow rate is adjusted by a regulator valve and two ball valves before the gas chamber. The pressure on both stages of the magnetic seal is monitored and collected by pressure sensors. To test the pressure capability, the pressure in the gas chamber is elevated slowly until a sudden pressure drop occurs. For the leakage rate, the air in the gas chamber is first pressed to a certain value (20 kPa for example), and then the ball valves are turned off. The pressure drop in the next five minutes is used to indicate the leakage rate quantitatively. For each sealing condition, the experiments are repeated three times.

5 Results and discussion

5.1 Numerical simulation

Magnetic field distributions of different pole pieces are simulated separately. Each solution reaches convergence within limited steps. The results of pole pieces with five pole teeth are illustrated in Figure 7. With pole teeth acting as a concentration of magnetic lines, a large gradient of the magnetic field intensity exists under each pole tooth. The maximum magnetic field intensity in the sealing gaps is about 3.5×10^5 A/m, and the minimum is 7.6×10^4 A/m. However, the magnetic field under different pole teeth is not exactly the same. Sealing stages far from the permanent magnet have a slightly weaker magnetic field than those near the magnet. The possible reason is the magnetic resistance of pole pieces and the shaft in a longer magnetic circuit. In comparison, the distributions of the magnetic field intensity in sealing gaps for single pole teeth of different widths are plotted in Figure 8. The maximum magnetic field intensity varies from 5.1×10^5 to 6.1×10^5 A/m. The simulation results show that the maximum magnetic field intensity of the single pole tooth is larger than that of five pole teeth. The magnetic energy provided by the permanent magnet is divided among several stages. In other words, with the magnetic source fixed, increasing the number of pole teeth will lower the pressure capability of a single sealing stage.

5.2 Pressure capability

For FF and MP seals, a sudden pressure drop occurs at the moment of sealing failure, and the maximum pressure is regarded as the pressure capability. Pressure capability of different pole pieces is plotted in Figure 9. N is the number of pole teeth per pole piece and L_t is the width of pole teeth. The error bars represent the standard errors of three repeated experiments of the same sealing condition. In general, MP seals possess much larger pressure capability than FF seals. The main reason is the difference in the magnetization intensity. The saturation magnetization of MPs mainly depends on the mass ratio of Fe_3O_4 to lubricants, and it can reach to more than 60 emu/g with good dispersibility. On the contrary, to avoid sedimentation while working, the volume fraction of Fe_3O_4 in FFs is usually lower than 10% in practice (Parmar et al., 2018). As a result, according to Eq. 3., the pressure capability is restricted by FFs' magnetization intensity.

Table 1 shows comparison between simulation and experimental results of different sealing structure. Because the FFs in the sealing gaps do not reach complete magnetic

TABLE 1 Comparison between simulation and experimental results of different FF sealing structures.

Number of pole teeth per pole piece	Width of pole teeth (mm)	Experimental result (kPa)	Simulation result (kPa)	Relative error (%)
1	0.5	21.42 ± 1.81	32.72	34.5
1	1.0	29.55 ± 1.51	36.61	19.3
1	1.5	23.93 ± 0.91	33.56	28.7
1	2.0	20.35 ± 1.75	30.09	32.4
5	0.5	63.50 ± 3.17	77.30	17.9

TABLE 2 Comparison between simulation based on previous formula and experimental results of different MP sealing structures.

Number of pole teeth per pole piece	Width of pole teeth (mm)	Experimental result (kPa)	Simulation result based on previous formula (kPa)	Relative error (%)
1	0.5	64.30 ± 13.06	290.93	77.9
1	1.0	111.61 ± 8.12	352.19	68.3
1	1.5	146.70 ± 13.98	305.31	52.0
1	2.0	187.26 ± 7.62	257.54	27.3

saturation, the integral form in Eq. 3 is adopted. For FF seals with different widths of the single pole tooth, the largest pressure capability 29.55 kPa appears at L_t = 1.0 mm, which is consistent with the trend of the maximum magnetic field intensity. Generally, a narrow pole tooth concentrates the magnetic flux better, so the magnetic field intensity is higher. However, an excessively narrow pole tooth leads to the magnetic saturation of the steel, and the magnetic field intensity decreases consequently. By using pole pieces of five pole teeth, the pressure capability almost doubles. The increasing range is moderate, partly because of the separation of the magnetic source. On the other hand, more sealing stages require more FFs and installation volume. Possible reasons for the differences between simulation and experimental results include the loss or redistribution of FFs during the assembling of sealing parts, the dimension error by manufacturing, the pressure elevating process and so on.

For MP seals with the single pole tooth, the simulation prediction based on the previous formula Eq. 5 is compared with experimental results in Table 2. Obviously, a large deviation exists between simulation and experimental results with the present setup, and the difference decreases as the pole teeth become wider. On the one hand, Eq. 5 overestimates the pressure capability of MP seals, probably because the MPs are not packed densely or distributed uniformly in the circular direction in sealing gaps. On the other hand, pressure capability increases with the width of pole teeth, which is clearly different from FF seals. This indicates a greater influence on the pressure capability by the friction between MPs and structural parts than the magnetic field intensity. The increase by the frictional effect surpasses the decrease of the magnetic field intensity with wider pole teeth. This phenomenon cannot be fully explained by Eq. 5 from the previous study, probably because the frictional effect is intensified with narrow sealing gaps or certain types of MPs of strong friction and interparticle forces. Therefore, Eq. 6 has an additional term to describe the frictional effect. The frictional term includes the rheological and magnetic properties of MPs, the average magnetic field intensity in radial direction and the contact area. The magnetic term and the frictional term are combined by corresponding empirical coefficients, which can be obtained by fitting sufficient amount of experimental data. Based on the experimental data above, the empirical coefficients are solved as $\alpha = 2.0 \times 10^{-2}$ and $\beta = 5.5 \times 10^{-2}$ N/(A·m)^2. However, the empirical formula and coefficients require further verification by a number of experiments. For example, pole teeth with multiple widths and heights should be manufactured and tested.

Furthermore, the pressure capability of five pole teeth is higher than that of single pole teeth with L_t = 0.5 mm, but lower than single pole teeth with L_t = 2.0 mm. The main reason is the difficulty in the MP loading process. Due to the poor fluidity of MPs than FFs, they can hardly be distributed on pole teeth uniformly circularly. The problem is even more serious for multiple pole teeth, because the interval between pole teeth is narrow. If there is one loading deficiency on a pole tooth, the whole sealing stage loses its pressure capability. So in fact, only limited sealing stages work to resist the pressure difference. The standard errors of experimental results also show an uncertainty of the MP loading process.

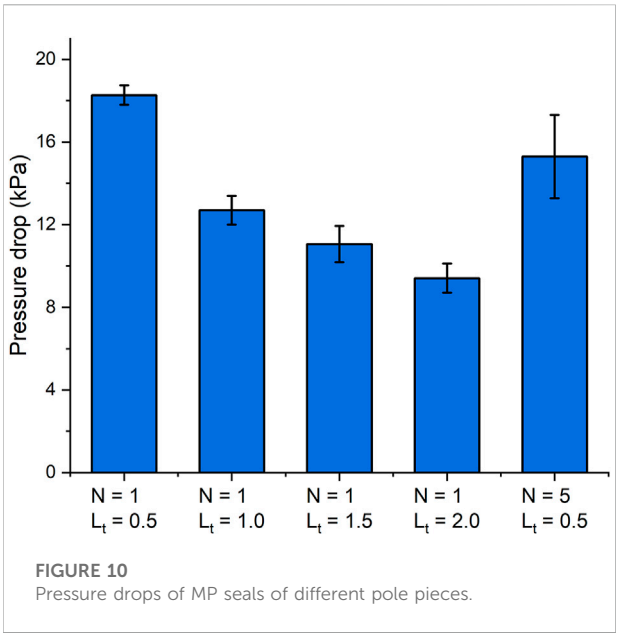

FIGURE 10
Pressure drops of MP seals of different pole pieces.

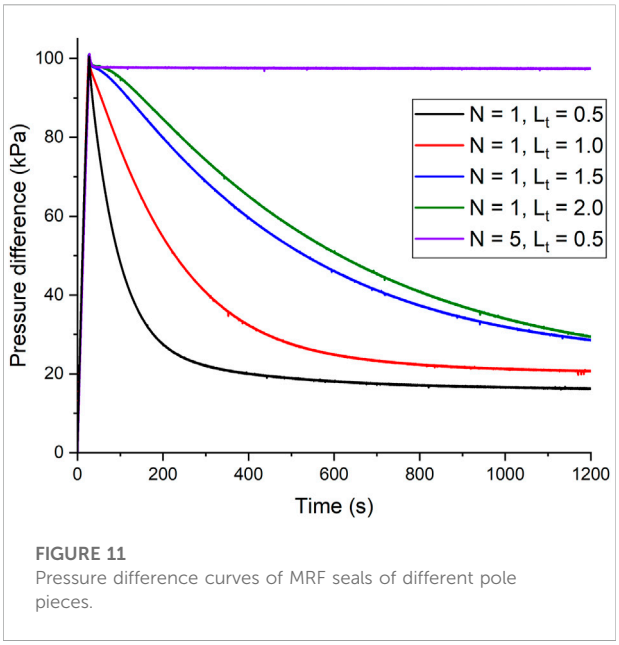

FIGURE 11
Pressure difference curves of MRF seals of different pole pieces.

An evident phenomenon of an MRF sealing failure is not observed in experiments. Unlike FFs or MPs, which have a sudden pressure drop and bursting out, MRFs cannot be pushed out of sealing gaps, and the pressure does not decrease suddenly, even when the pressure is far higher than the theoretical value. Instead, small bubbles are observed as the pressure elevates, and some carrier fluid runs away. In other words, a specific value of pressure capability does not exist, and the pressure difference only affects the leakage rate of MRF seals. As a result, the experimental results of MRF seals are not compared with Eq. 4.

5.3 Leakage rate

A significant characteristic of FF seals is their almost zero leakage, which is verified by the experiments. But for MP seals, the leakage rates can be rather large, and are affected by structural parameters. In this research, the pressure is first elevated to 20 kPa, then the inlet air is cut off. The pressure drop in the next five minutes is measured to represent the leakage rate quantitatively, as is shown in Figure 10. The leakage rate decreases with the increase of the width of the pole tooth. The form of MPs in sealing gaps is similar to porous media. While the packing structure remains unchanged, a wider pole tooth leads to a thicker powder ring, and the resistance of the leaking air increases. As a result, the leakage rate is lowered. As for multiple pole teeth, the leakage rate is even higher than wider single pole teeth. It confirms the inference above, that some sealing stages do not perform normally due to the loading difficulty.

At an initial pressure of 20 kPa, MRF seals are nearly leakage-free like FFs. However, as the pressure rises, air leaking happens gradually. Figure 11 indicates the pressure changing curves of MRF seals at an initial pressure of 100 kPa. For pole pieces with five pole teeth, sealing still operates well and almost no leakage occurs. But for pole pieces with the single pole tooth, the leakage is evident and the leakage rate is higher when the pressure difference is larger. Besides, a wider pole tooth decreases the leakage rate to a great extent. It is reported by former literature that MRFs tend to form chain-like structures under a strong magnetic field, and MRFs preform solid-like characteristics as a result. When the pressure is low, the chains are pushed modestly, and magnetic particles and the carrier fluid remain great dispersibility, so the leakage rate is low. But when the pressure is high, an excessive deformation or even breakage of chains is likely to happen. The carrier fluid is deformed at the same time, because the magnetic particles are dispersed inside. As a result, small pores as leakage paths appear and expand in MRFs, instead of being pushed out of sealing gaps like FFs.

5.4 Mechanism of pressure transfer and self-recovery

To study the mechanism of pressure transfer, pole pieces with single pole teeth at L_t = 1.0 mm are taken as an example, and the pressure of the inlet air remains constant. The pressure in the first and second sealing stages is monitored by two pressure sensors, respectively. As is shown in Figure 3, the first stage indicates the pressure in the gas chamber before the left pole piece, which is monitored by a pressure sensor connected to the gas chamber. The second stage indicates the pressure between the left and the right pole piece, which

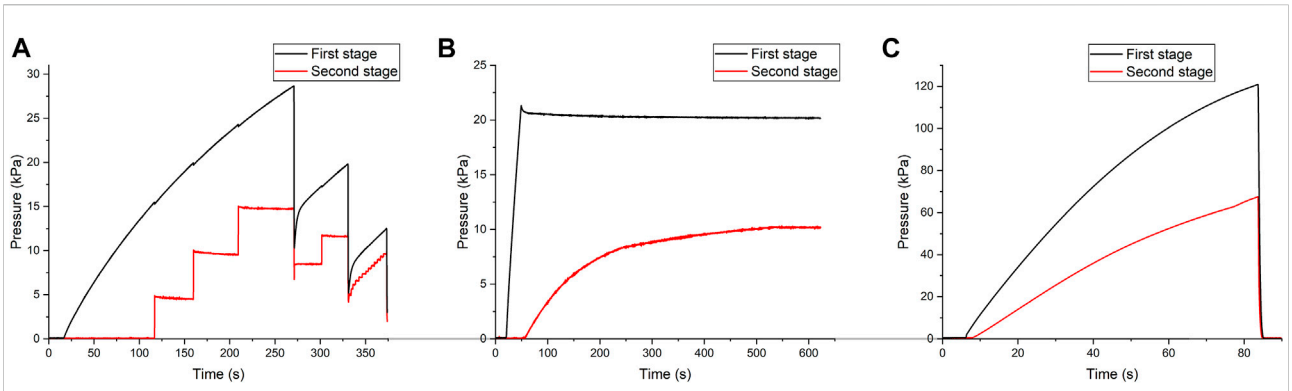

FIGURE 12
Pressure curves of two sealing stages of **(A)** FF, **(B)** MRF and **(C)** MP seals.

is monitored by the other pressure sensor connected to the shell. In other words, the pressure difference between the first and the second stage is resisted by the left pole piece, and that between the second stage and the atmosphere is resisted by the right pole piece. A simultaneous monitoring on both stages reveals the mechanism of pressure transfer.

In Figure 12A, FF seals have several obvious phases of pressure transfer. First, the first stage resists all pressure difference, and the second stage remains zero. Then several sudden increases of pressure in the second stage occur, probably because the first stage is broken through. After that, the first stage is self-recovered, until the pressure is high enough to break both sealing stages. However, after the first sealing failure, the pressure in the gas chamber is down to about 10 kPa, and the FF seal can still resist limited pressure. The pressure capability is lower, because some FFs are burst out. After the second sealing failure, the first sealing stage can hardly resist a pressure difference due to an excessive loss of FFs.

In Figure 12B, the inlet air of MRF seals is cut off after 50 s. When the pressure is rather low, only the first stage resists a pressure difference, and the second stage remains zero. But then the pressure of the second stage starts to elevate. The speed is fast but then slows down. A possible reason is that, when the pressure increases, small pores emerge as leaking paths. As the pressure of the second stage increases, former deformation of the magnetic particle chains partly recovers under the influence of the magnetic force, and the pores are self-closed, so the pressure becomes stable. The self-recovery behavior is also observed in Figure 11, where the leakage rate decreases with the descending pressure, and the pressure keeps stable in the end.

As for MP seals, the pressure distribution is average basically. The pressure of the second stage increases with the first stage from beginning, because the porous structure of MPs has an unavoidable leakage rate. Meanwhile, after the sealing failure, MPs are pushed out and cannot redistribute due to their poor fluidity. MP seals do not possess the ability of self-recovery.

6 Conclusion

This research provides a comparative study of magnetic seals by FFs, MRFs, and MPs. The formulas of pressure capability based on their different properties are derived. A sealing prototype is designed and manufactured. The magnetic field distribution is calculated by the finite element method. Finally, a test bench for magnetic seals is established, and the pressure capability, leakage rates as well as the mechanism of pressure transfer and self-recovery ability are studied. For rotating seals, this procedure is still fundamental and referable, but the influence of the centrifugal force and elevating temperature should be considered. The friction causes the rising of temperature, especially at a high speed or long working time. Consequently, the magnetization intensity of magnetic materials decreases. The characteristics of the three magnetic seals are summarized as follows:

(1) FF seals have almost zero leakage and high lifetime, which makes them the only feasible solution for specific sealing environment. Loading and supplementation of FFs are easy because of their well fluidity. However, their pressure capability is the lowest (about 10–20 kPa per stage), and the pressure transfer among stages needs time. To enhance the pressure capability, FFs of high saturation magnetization and narrow pole teeth are preferred. FF seals are suitable for sealing conditions of zero leakage, low pressure difference (typically one atmospheric pressure) and modest temperature. Potential applications include the sealing of silicon crystal growing furnaces, robot joints and so on.
(2) MRF seals do not have an evident phenomenon of sealing failure. Instead, their leakage rate rises with the elevation of pressure. After the pressure drops, the pores inside MRFs disappear, which indicates the ability of self-recovery. However, under a high pressure difference, the

dispersibility of MRFs is broken, and the leakage rate is rather large. To lower the leakage rate, wide pole teeth are suggested. MRF seals are suitable for sealing conditions of high pressure (several atmospheric pressure or higher) or sudden strong impacts, and tolerance of limited gas leaking. Potential applications include magnetorheological dampers and clutches, where the same fluid is used for damping and sealing.

(3) MP seals possess much higher pressure capability than FF seals (about 50–100 kPa per stage), but the price is a high leakage rate. The pressure capability is affected by both magnetic forces and the frictional effect. Meanwhile, wider pole teeth decrease the leakage rate significantly, but multiple pole teeth are not preferred. MP seals are suitable for sealing conditions of high pressure, extreme temperature, short sealing time and tolerance of gas leaking. Potential applications include the sealing of thrust vectoring nozzles, or combination with mechanical seals. In particular, they are suitable for occasions requiring sealing and heat dissipation at the same time.

Data availability statement

The original contributions presented in the study are included in the article/supplementary material, further inquiries can be directed to the corresponding author.

Author contributions

ZL: numerical simulation, sealing experiments and manuscript. DL: material preparation, theory and supervision.

Funding

This work was supported by the National Natural Science Foundation of China (grant numbers U1837206, 51735006 and 51927810).

Conflict of interest

The authors declare that the research was conducted in the absence of any commercial or financial relationships that could be construed as a potential conflict of interest.

Publisher's note

All claims expressed in this article are solely those of the authors and do not necessarily represent those of their affiliated organizations, or those of the publisher, the editors and the reviewers. Any product that may be evaluated in this article, or claim that may be made by its manufacturer, is not guaranteed or endorsed by the publisher.

References

Choi, S., and Han, Y. (2012). *Magnetorheological fluid technology: Applications in vehicle systems*. Boca Raton, Florida, United States: CRC Press.

Das, P., Colombo, M., and Prosperi, D. (2019). Recent advances in magnetic fluid hyperthermia for cancer therapy. *Colloids Surfaces B Biointerfaces.* 174, 42–55. doi:10.1016/j.colsurfb.2018.10.051

Fan, C., Chongfeng, Z., and Xiaolong, Y. (2021). Numerical analysis and experimental verification of magnetic fluid sealing for air cylinder in Aerospace Engineering. *Int. J. Appl. Electrom.* 66 (4), 581–597. doi:10.3233/JAE-201572

Huang, T., Song, F., Wang, R., and Huang, X. (2021). Numerical simulation study of tracking the displacement fronts and enhancing oil recovery based on ferrofluid flooding. *Front. Earth Sci. (Lausanne).* 9. doi:10.3389/feart.2021.759862

Kubík, M., Pavlí Ek, D., Machá Ek, O., Strecker, Z., and Roupec, J. (2019). A magnetorheological fluid shaft seal with low friction torque. *Smart Mat. Struct.* 28 (4), 047002. doi:10.1088/1361-665X/ab0834

Li, Z., and Li, D. (2022a). A novel sealing method using nano-micro magnetic powders and its leakage rate analysis. *IEEE Trans. Magn.* 58 (8), 1–5. doi:10.1109/TMAG.2021.3115336

Li, Z., and Li, D. (2022c). Leakage rate control of magnetic powder seals by lubricant coatings on magnetic nanoparticles and flow field simulation. *IEEE Trans. Magn.* 58 (8), 1–5. doi:10.1109/TMAG.2022.3144476

Li, Z., and Li, D. (2022b). Pressure capability analysis of magnetic powder seals and pole tooth design by multiparameter optimization. *Powder Technol.* 403, 117410. doi:10.1016/j.powtec.2022.117410

Liang, Y., Alvarado, J. R., Iagnemma, K. D., and Hosoi, A. E. (2018). Dynamic sealing using magnetorheological fluids. *Phys. Rev. Appl.* 10 (6), 064049. doi:10.1103/PhysRevApplied.10.064049

Liu, J., Li, D., and Zhang, Z. (2022). Experimental study and simulation on the seal pressure of a ferrofluid seal using radial-charged magnets. *Front. Mat.* 9. doi:10.3389/fmats.2022.879699

Matuszewski, L. (2019). New designs of centrifugal magnetic fluid seals for rotating shafts in marine technology. *Pol. Marit. Res.* 26 (2), 33–46. doi:10.2478/pomr-2019-0023

Parmar, S., Ramani, V., Upadhyay, R. V., and Parekh, K. (2018). Design and development of large radial clearance static and dynamic magnetic fluid seal. *Vacuum* 156, 325–333. doi:10.1016/j.vacuum.2018.07.055

Parmar, S., Ramani, V., Upadhyay, R. V., and Parekh, K. (2020). Two stage magnetic fluid vacuum seal for variable radial clearance. *Vacuum* 172, 109087. doi:10.1016/j.vacuum.2019.109087

Rosensweig, R. E. (2013). *Ferrohydrodynamics*. Chelmsford, Massachusetts, United States: Courier Corporation.

Szczech, M. (2018). Experimental study on the pressure distribution mechanism among stages of the magnetic fluid seal. *IEEE Trans. Magn.* 54 (6), 1–7. doi:10.1109/TMAG.2018.2816567

Wang, J., and Meng, G. (2001). Magnetorheological fluid devices: Principles, characteristics and applications in mechanical engineering. *Proc. Institution Mech. Eng. Part L J. Mater. Des. Appl.* 215 (3), 165–174. doi:10.1243/1464420011545012

Zang, G., Zhang, Z., Yu, W., Wang, D., and Li, D. (2022). Effects of different fatty acids as surfactants on the rheological properties of kerosene-based magnetic fluids. *Front. Mat.* 9, 334–342. doi:10.3389/fmats.2022.930633

Zhang, Y., Li, D., Chen, Y., and Li, Z. (2018). A comparative study of ferrofluid seal and magnetorheological fluid seal. *IEEE Trans. Magn.* 54 (12), 1–7. doi:10.1109/TMAG.2018.2868298

Zhou, H., Zhao, W., Zhang, H., Wang, Y., Wu, X., and Sun, Z. (2020). Magnetorheological seal: A review. *Int. J. Appl. Electrom.* 62 (4), 763–786. doi:10.3233/JAE-190082

frontiers | Frontiers in Materials

TYPE Original Research
PUBLISHED 28 September 2022
DOI 10.3389/fmats.2022.933076

OPEN ACCESS

EDITED BY
Weihua Li,
University of Wollongong, Australia

REVIEWED BY
Ying-Qing Guo,
Nanjing Forestry University, China
Lei Deng,
University of Wollongong, Australia

*CORRESPONDENCE
Qing Ouyang,
yangqing@zjxu.edu.cn

SPECIALTY SECTION
This article was submitted to Smart Materials,
a section of the journal
Frontiers in Materials

RECEIVED 30 April 2022
ACCEPTED 08 August 2022
PUBLISHED 28 September 2022

CITATION
He W, Ouyang Q, Hu H, Ye X and Lin L (2022), Semi-active control of crankshaft skyhook based on magnetorheological torsional damper. *Front. Mater.* 9:933076.
doi: 10.3389/fmats.2022.933076

Semi-active control of crankshaft skyhook based on magnetorheological torsional damper

Wei He[1,2], Qing Ouyang[2,3,4]*, Hongsheng Hu[2], Xudan Ye[3] and Lizhong Lin[5]

[1]School of Mechanical Engineering and Automation, Zhejiang Sci-Tech University, Hangzhou, China, [2]College of Information Science and Engineering, Jiaxing University, Jiaxing, China, [3]School of Mechanical Engineering, Nanjing University of Science and Technology, Nanjing, China, [4]Taizhou Jiuju Technology Co. Ltd., Taizhou, China, [5]Ningbo Sedsun Vibration Damper Co. Ltd., Ningbo, China

The purpose of this study was to solve the problem that the damping of rubber or silicone oil torsional dampers used in crankshafts is not adjustable and cannot effectively control torsional vibration at different resonant frequencies. Based on the controlled rheological properties of magnetorheological (MR) smart materials, this study designed a new type of variable damping MR torsional damper (MRTD) and proposed a semi-active control method to effectively control the torsional vibration of the crankshaft under multiple harmonic resonances. First, a mechanical model of the MRTD and a lumped parametric mass model of the crankshaft system were developed, and the resonance frequency harmonic range of the crankshaft system operation was determined by the torsional vibration characteristics analysis. Then a semi-active skyhook control method for the MRTD was proposed, and a joint control simulation analysis was performed using Amesim and Matlab software. The torsional vibration control effects of the crankshaft system with no damper, MRTD with different damping coefficients, and MRTD with skyhook control under acceleration and uniform speed conditions were comprehensively investigated. The simulation results indicated that the skyhook damping control significantly reduced the torsional vibration amplitude under both acceleration and uniform speed conditions, verifying the effectiveness of the skyhook-based control strategy for MRTD.

KEYWORDS

magnetorheological fluid, torsional damper, crankshaft system, semi-active control, skyhook damping control

1 Introduction

The crankshaft system is subjected to periodic inertia moment, which causes torsional vibration of the crankshaft (Xiong 2019). Severe torsional vibration will lead to fatigue damage of the crankshaft (Sun et al., 2016), wear of meshing gears (Shen et al., 2018), harmful noise (Zhong et al., 2020), and loss of transmission energy (Zhang 2013).

Therefore, effective torsional vibration suppression measures should be adopted to control the torsional vibration of the crankshaft in a suitable range to ensure the reliability of the system.

Currently, passive vibration dampers, such as silicone oil viscous dampers (Li and Zhang 2020; Venczel et al., 2021a; Venczel et al., 2021b) and rubber dampers (Penkov 2008; Ning et al., 2013; Willenborg and Kroger 2017), are usually adopted to protect the engine camshaft and crankshaft from the possible damage caused by torsional vibrations and help to avoid the barred speed ranges. The vibration energy is converted into heat, which then dissipates from the damper's surface into the ambient air. In addition, some studies have put forward compound or hybrid vibration reduction methods on the basis of the abovementioned facts. Yu (2003) designed a torsional-bending composite rubber damper, and Haşmet. (2021) used a hybrid damping method to optimize the design of the damper for damping, which illustrates that a hybrid damping method is more effective than a single damping method.

However, after the design of the passive torsional damper is completed, the dynamic parameters, including damping and stiffness, will be fixed (Ngoc et al., 2018). It means that the deviation of processing and installation technology, the temperature-dependent performance decay, and other factors, may cause problems such as poor performance matching between the designed torsional dampers and crankshaft system and narrow tuning range (Sinyayski 2019). The damper based on magnetorheological fluid (MRF) intelligent material has the excellent characteristics of adjustable damping, wide dynamic range, fast response, and low power consumption (Deng et al., 2022) and is widely used in various intelligent vibration suppression applications (Ahamed et al., 2016; Lin and Jheng 2017; Krauze et al., 2018; Zhou et al., 2021), including crankshaft torsional vibration damper. As for the magnetorheological torsional damper (MRTD), many scholars have performed relevant research and exploration works. Wang et al. (2018) studied the torsional vibration control method of engine/helicopter, which effectively suppressed torsional vibration. Philipp et al. (2017) carried on the simulation optimization design to the torsional vibration damper. Ye and Williams (2005) studied the torsional vibration control of MRF brake and proposed a new torsional vibration control method. In addition, Dong et al. (2020) designed a variable damping and variable stiffness torsional damper, which effectively suppressed the torsional vibration of the vehicle transmission system. But less research work has been conducted on the engine torsional vibration of crankshaft systems, and several of the research works have focused on the design of structural components for torsional dampers (Christopher 1992; Shook 2008; Abouobaia et al., 2015); there are few studies on control strategies. Thus, how to design a reasonable and effective control strategy to realize adaptive vibration control of the crankshaft system is of great significance.

In this study, the principle and structural mechanics of a variable damping torsional damper are analyzed, and a torsional vibration model of the crankshaft system is developed for engine crankshaft torsional vibration. In addition, Amesim and Matlab are used for co-simulation, and the torsional vibration of the crankshaft under various working conditions is discussed. The vibration of the crankshaft with and without dampers installed at the free end of the crankshaft and the influence of the damping coefficient on the torsional vibration of the crankshaft are studied. Finally, the skyhook damping semi-active control method is proposed, and simulation results show that it has a preferable damping effect and also provides a theoretical basis for the design of future crankshaft system control methods.

2 Design principle of MRTD with variable damping

2.1 Dynamic parameter analysis of torsional damper

The MRTD studied in this research study adopts a vibration-absorbing mode of operation. Based on the theoretical analysis of the engine crankshaft system torsional vibration model, the crankshaft system is equivalently transformed into a single-degree-of-freedom undamped system with a torsional damper attached to the shaft end to form a double torsional pendulum system (Hoang 2013), and the natural frequency and system energy of the system before and after simplification remain unchanged. The equivalent model diagram of the double torsional pendulum system is shown in Figure 1. The response characteristics of each dynamic parameter to the crankshaft torsional vibration system are analyzed, and the setting principle of those parameters in the device design is discussed so as to achieve the minimum torsional vibration response amplitude of the crankshaft system.

An MRTD is installed at the free end of the crankshaft to achieve the desired damping state by controlling the current and varying the damping coefficient. The mechanical equations of the model are shown in Eq. 1.

$$\begin{cases} J_d\ddot{\theta}_d + K_d\left(\theta_d - \theta_g\right) + C_d\left(\dot{\theta}_d - \dot{\theta}_g\right) = 0 \\ J_g\ddot{\theta}_g + K_g\theta_g + K_d\left(\theta_g - \theta_d\right) + C_d\left(\dot{\theta}_g - \dot{\theta}_d\right) = Me^{iwt}. \end{cases} \tag{1}$$

Eq. 1 is the external disturbance moment; w is the external disturbance force frequency, and $\boldsymbol{M}$ is the external disturbance torque. The solution to this equation is shown in Eq. 2.

$$\boldsymbol{\theta} = \left[\theta_d\theta_g\right]^T e^{iwt}, \tag{2}$$

$$\boldsymbol{\theta}_d = \frac{\nabla_d}{\nabla}\ \boldsymbol{\theta}_g = \frac{\nabla_g}{\nabla}, \tag{3}$$

where

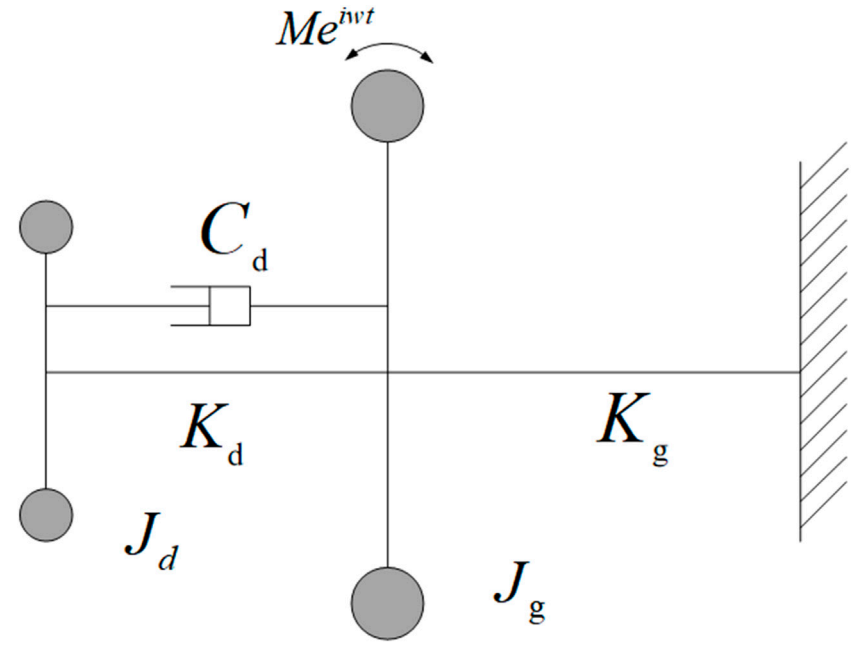

FIGURE 1
Equivalent model diagram of the double torsion pendulum system.

$$\nabla = \begin{vmatrix} K_d - J_d + iwC_d & -K_d - iwC_d \\ -K_d - iwC_d & K_d + K_g - J_g w^2 + iwC_d \end{vmatrix}, \quad (4)$$

$$\nabla_d = \begin{vmatrix} 0 & -K_d - iwC_d \\ M & K_d + K_g - J_g w^2 + iwC_d \end{vmatrix}, \quad (5)$$

$$\nabla_g = \begin{vmatrix} K_d - J_d w^2 + iwC_d & 0 \\ -K_d - iwC_d & M \end{vmatrix}. \quad (6)$$

In the above equations, θ_τ, J_τ, K_τ, and C_τ are the torsional angle, rotational inertia, torsional stiffness, and the torsional damper damping coefficient, respectively, where the subscript τ is the g and d, it refers to the engine equivalent crankshaft system and the torsional damper, respectively.

The amplification factor of torsional vibration R is the ratio of the static variable of the crankshaft system to the amplitude of the shafting main vibration system; the expression is shown in Eq. 7.

$$R = \frac{A_g}{A_{st}} = \sqrt{\frac{\left(\lambda^2 - \zeta^2\right)^2 + (2\zeta\gamma)^2}{\left[\mu\zeta^2\lambda^2 - \left(\zeta^2 - 1\right)\left(\zeta^2 - \lambda^2\right)\right]^2 + 4n\gamma^2}}, \quad (7)$$

where A_{st} is the shaft system main vibration system amplitude, A_g is the shaft system static shape variable, $\zeta = \frac{w}{p}$ is the frequency ratio, $\mu = \frac{J_d}{J_g}$ is the inertia ratio, $n = 1 - (\mu + 1)\zeta^2$, $\gamma = \frac{C_d}{2J_d p}$ is the damping ratio, $\lambda = \frac{w_d}{p}$ is the fixed ratio, $p = \sqrt{\frac{K_g}{J_g}}$ is the crankshaft system self-oscillation frequency, and w_d is the damping damper frequency.

As can be seen from Eq. 7, for the amplification factor of torsional vibration, the damping effect of the crankshaft system with the crankshaft torsional damper installed is mainly determined by inertia ratio, setting ratio, and damping ratio. The greater the dynamic amplification factor, the more violent the vibration. The effect of these three factors on torsional vibration can be seen in Figure 2.

The damping ratio, inertia ratio, and setting ratio of the torsional damper have an obvious effect on the dynamic amplification factor of the crankshaft system. Since the inertia ratio and setting ratio are determined during device design, the damping ratio needs to be changed to attenuate the vibration. Therefore, it is required to design an effective control method to output the optimal damping in real-time.

2.2 MRTD structure and mechanical model

In the MRTD structure design, the crankshaft MRTD designed in this study is a disc-type structure of the damper. The structure includes the shell, end cover, and inertia block, as shown in Figure 3, where the yellow part is the magnetic induction line. The free end of the crankshaft is connected to the outer casing of the MR damper, and the outer casing and inertia block are filled with MRF. The outer shell is fixed at the free end of the crankshaft, and when working, torsional vibration

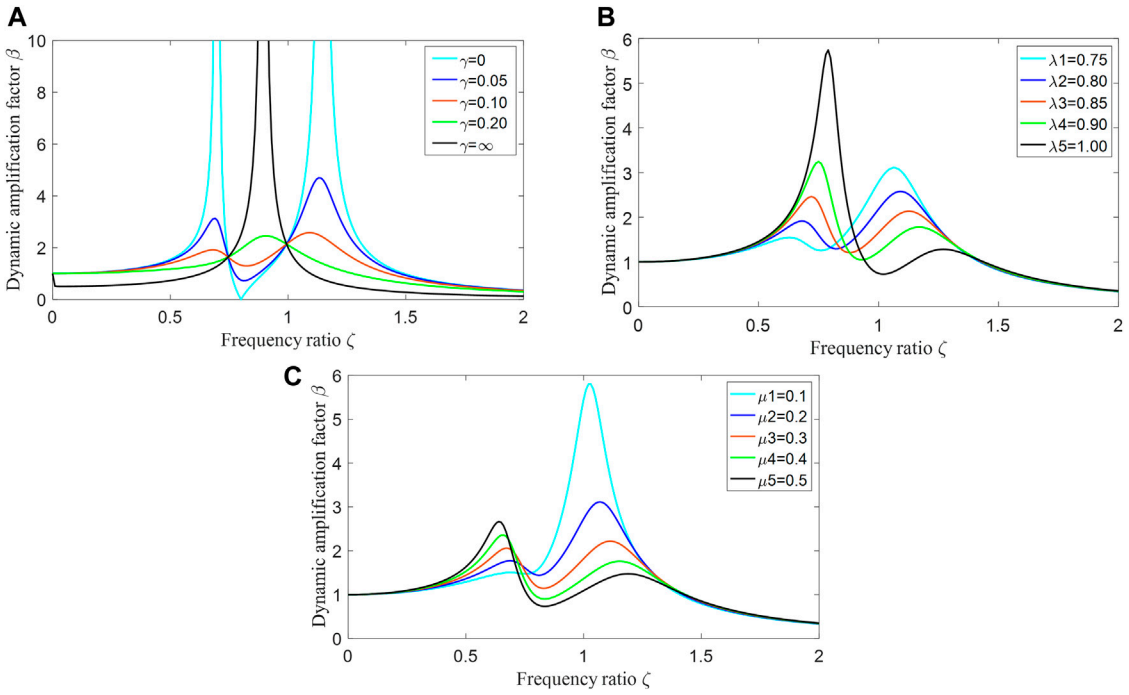

FIGURE 2
Parametric analysis of torsional dampers; **(A)** Damping ratio; **(B)** Fixed ratio; **(C)** Inertia ratio.

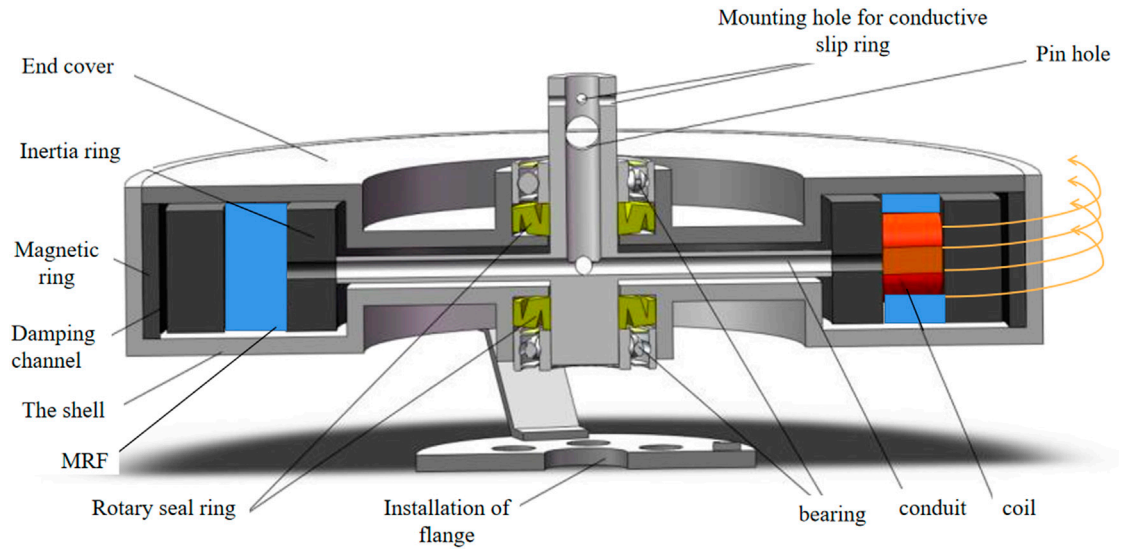

FIGURE 3
MRTD model diagram.

occurs with the shafting. Owing to the inertia block and the outer shell not being directly connected, it keeps uniform rotation under the influence of its own inertia. At this time, the outer shell moves relative to the inertia block, and the energy of torsional vibration is consumed by adjusting the appropriate damping due to the filling of magnetorheological fluid. When the current is

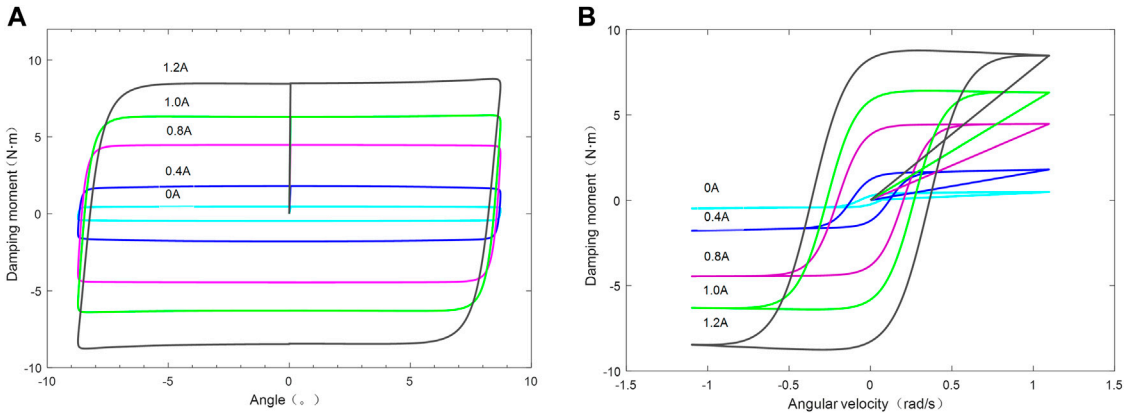

FIGURE 4
Mechanical characteristics of MRTD; **(A)** Angular rotation; **(B)** Angular velocity.

changed, the magnetic field in the MR damper changes, and thus the damping of the MRF change to achieve the effect of vibration control. The basic parameters of MRTD are damping: 0.00427 kg.m^2 and stiffness: 8000 Nm⁄rad.

When applying MRF to semi-active control, a suitable parametric model is required due to its strong non-linear and hysteretic characteristics. The hyperbolic tangent model used in this study has the advantages of simple structure, easy identification of model parameters, and easy solution of the inverse model. The damping force expression is as in Eq. 8.

$$F = c\dot{x} + kx + \alpha tanh\left(\beta\dot{x} + \delta sign\left(x\right)\right) + f_0, \tag{8}$$

where c is the damping coefficient; k is the stiffness coefficient; α is the proportional coefficient related to the hysteretic characteristics; β is the proportional coefficient related to the slope of the hysteretic curve; δ is the half-width of the hysteretic curve; and f_0 is the bias force.

In this study, relevant data are used to identify and fit the parameters of the model, and the nonlinear relationship between current and parameters is obtained (Dong et al., 2020). As shown in Figure 4, after obtaining the complete mechanical equation, the output of the relationship between the current and the damping force is used to pave the way for the damping control of the MRTD later, and the mathematical model is established to lay the foundation for the design of the control algorithm later.

3 Analysis of torsional vibration characteristics of the crankshaft system

3.1 Crankshaft system dynamics modelling

To model the corresponding dynamics of torsional vibrations in the crankshaft system, an MRTD is installed at the free end of the crankshaft, as shown in Figure 5. When the engine crankshaft is working, the damping of MRTD is adjusted by changing the current so as to change the natural frequency of the crankshaft system and achieve the effect of frequency shift to weaken the resonance of the crankshaft when it is working.

For the analysis of the dynamics of the crankshaft system, this study establishes a concentrated mass model of the crankshaft system. This model has the advantages of simplified component calculation and small deviation of model calculation results, so it is widely used. The model is shown in Figure 6. According to the principle of energy conservation, the crankshaft system is simplified to an equivalent system consisting of an inelastic inertia disc and a massless elastic shaft.

Simplification of elastic, inertial, and damping variables according to the equivalent model of torsional vibration of the crankshaft system, the following kinetic equation can be obtained:

$$\begin{cases} J_1\ddot{\theta}_1 + C_1\left(\dot{\theta}_1 - \dot{\theta}_2\right) + K_1\left(\theta_1 - \theta_2\right) = T \\ J_2\ddot{\theta}_2 + C_2\left(\dot{\theta}_2 - \dot{\theta}_3\right) + K_2\left(\theta_2 - \theta_3\right) = C_1\left(\dot{\theta}_1 - \dot{\theta}_2\right) + K_1\left(\theta_1 - \theta_2\right) = 0 \\ J_3\ddot{\theta}_3 + C_3\left(\dot{\theta}_3 - \dot{\theta}_4\right) + K_3\left(\theta_3 - \theta_4\right) = C_2\left(\dot{\theta}_2 - \dot{\theta}_3\right) + K_2\left(\theta_2 - \theta_3\right) = 0 \\ J_4\ddot{\theta}_4 + C_4\left(\dot{\theta}_4 - \dot{\theta}_5\right) + K_4\left(\theta_4 - \theta_5\right) = C_3\left(\dot{\theta}_3 - \dot{\theta}_4\right) + K_3\left(\theta_3 - \theta_4\right) = 0 \\ J_5\ddot{\theta}_5 + C_5\left(\dot{\theta}_5 - \dot{\theta}_6\right) + K_5\left(\theta_5 - \theta_6\right) = C_4\left(\dot{\theta}_4 - \dot{\theta}_5\right) + K_4\left(\theta_4 - \theta_5\right) = 0 \\ J_6\ddot{\theta}_6 + C_5\left(\dot{\theta}_5 - \dot{\theta}_6\right) + K_5\left(\theta_5 - \theta_6\right) = 0 \end{cases} \tag{9}$$

In the equation established from the model, J_i (i = 1–6) represents the rotational inertia of each segment of the crankshaft; K_i (i = 1–5) is the torsional stiffness between each mass point; C_i (i = 1–5) is the damping between each inertia, respectively; and θ_i (i = 1–6) is the torsional angle of each inertia.

The above differential equation is represented by the matrix as

$$[J]\left\{\ddot{\theta}\right\} + [C]\left\{\dot{\theta}\right\} + [K]\{\theta\} = T. \tag{10}$$

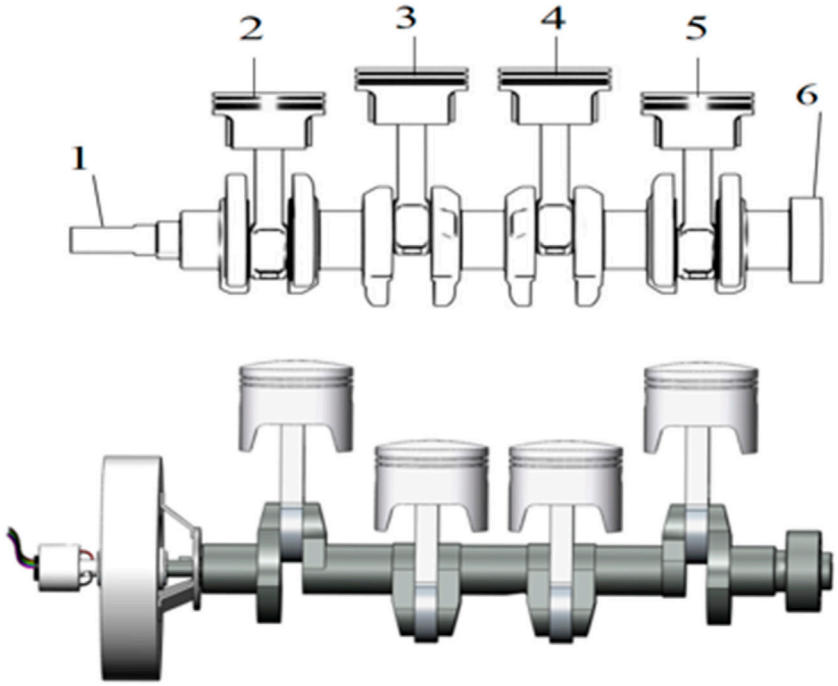

FIGURE 5
Schematic diagram of the crankshaft system (top). Schematic diagram of the crankshaft system with MR damper installed (bottom). 1. Free end of crankshaft 2. First cylinder piston 3. Second cylinder piston 4. Third cylinder piston 5. Fourth cylinder piston 6. Flywheel.

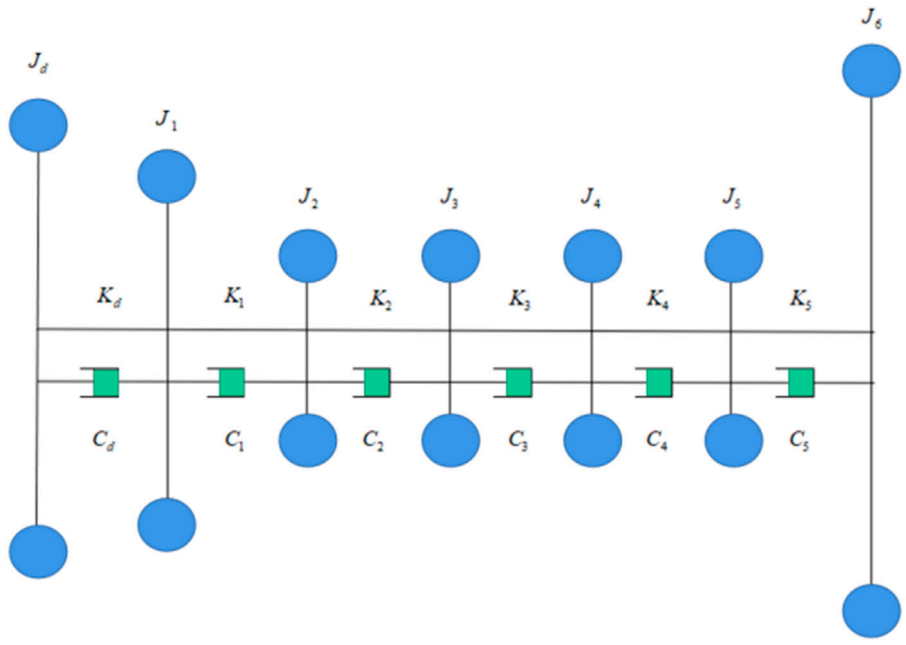

FIGURE 6
Equivalent model of crankshaft system torsional vibrations.

10.3389/fmats.2022.933076

TABLE 1 Main parameters of the crankshaft system.

Rotational inertia ($kg.m^2$)		Torsional stiffness ($10^5 Nm/rad$)	
J_1	0.00231	K_1	0.34
J_2	0.00545	K_2	1.35
J_3	0.00556	K_3	1.35
J_4	0.00556	K_4	1.35
J_5	0.00562	K_5	2.84
J_6	0.0754		

In Eq. 10, $[\boldsymbol{J}]$ is the system rotational inertia matrix; $[\boldsymbol{C}]$ is the system damping matrix; $[\boldsymbol{K}]$ is the system stiffness matrix; T is the system excitation moment; and $\{\boldsymbol{\theta}\}$ is the angular displacement vector of the crankshaft.

3.2 Torsional vibration analysis of crankshaft systems

In order to better study the torsional vibration characteristics, the free vibration and forced vibration of crankshaft systems are analyzed. In this study, a simplified calculation is performed according to the parameters of a certain four-cylinder engine. The required inertia and stiffness parameters of the crankshaft system are shown in Table 1. The general free mode is only related to the rotational inertia and torsional stiffness, so the damping parameters are not used in solving the free vibration.

According to Eqs 1 and 2 and the values of each parameter in Table 1, the inherent frequencies of the free vibration of the crankshaft system can be calculated, and the modal diagram of the inherent frequencies can be obtained by using MATLAB simulation, The first five inherent frequencies are shown in Table 2.

The calculated modal diagram for the first five inherent frequencies of the crankshaft system is shown in Figure 7.

As can be seen from the vibration pattern diagram, in the first three orders of the inherent frequency, 2, 3, 4, 5, these mass points' vibration pattern amplitude change more. Therefore, when the excitation frequency of the system and the inherent frequency are the same, the vibration caused by crankshaft resonance can cause damage to components, which will affect the service life of the crankshaft.

By establishing the differential equations for a simplified parametric model of the crankshaft system fitted with an MRTD, the inherent frequency of the crankshaft system fitted with the MRTD is calculated using the previous calculation method, and the harmonic order of its resonance is solved. The first four orders of the solved inherent frequencies are as follows.

$$\boldsymbol{w_1 = 0 rad/s \;\; w_2 = 1137.7 rad/s \;\; w_3 = 2188.2 rad/s \;\; w_4 = 4342.5 rad/s}$$

TABLE 2 Intrinsic frequency values of the crankshaft system.

Number of steps	1	2	3	4	5
Inherent frequency (rad/s)	0	1927.8	4032.7	5959.7	8382.4

According to the natural vibration frequency of the engine crankshaft, the resonance speed of the crankshaft can be obtained. That is, the external disturbance torque causing resonance is determined jointly with the working speed of the engine. The calculation for determining the harmonic times v is as follows:

$$\boldsymbol{vw = v\frac{2\pi n}{60} = \frac{2\pi N_v}{60}}, \tag{11}$$

$$\boldsymbol{vn = N_v}, \tag{12}$$

where n is the crankshaft speed, and N_v is the operating frequency of the interfering torque.

Taking the engine's operating speed range of the minimum speed as n_{min}, the maximum speed as n_{max}, and the crankshaft system of the inherent frequency as N_1; then, trigger the crankshaft resonance of the harmonic range is

$$\begin{cases} \boldsymbol{v_{max} = \frac{N_1}{n_{min}}} \\ \boldsymbol{v_{min} = \frac{N_1}{n_{max}}}. \end{cases} \tag{13}$$

When the number of resonant harmonic moments increases, the vibration amplitude decreases. Therefore, for the higher harmonic times (12 times or more) of the shaft resonance, the resonance amplitude caused is relatively small, and the harm caused to the crankshaft is not significant, so it is not considered for the time being.

This research work studies a four-cylinder engine, and its working range is 2000–5000 rpm. Through the torsional vibration analysis of the engine crankshaft system, it is found that the harmonic moment of the second natural frequency is the main harmonic order that causes the

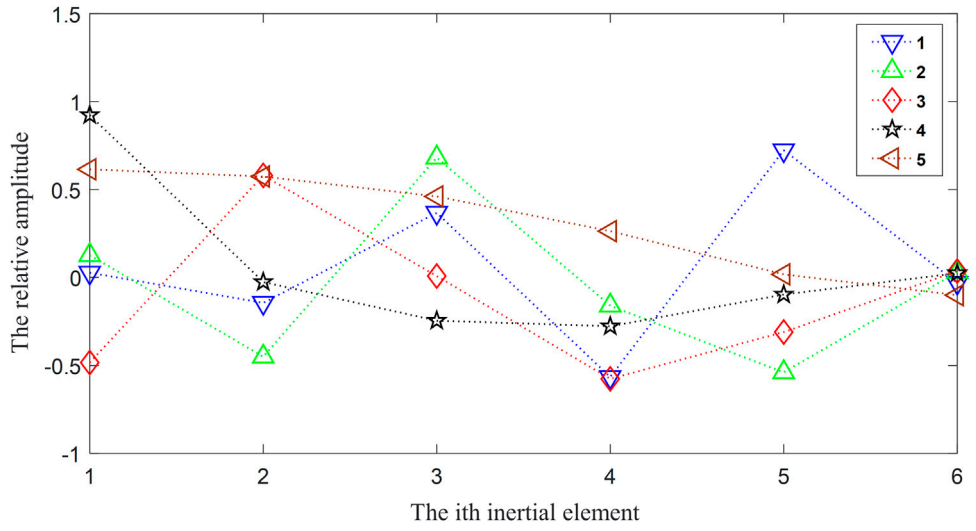

FIGURE 7
Modal diagram.

resonance. From Eq. 13, we can calculate the harmonic range of resonance is 2–12 harmonics. From this, we can calculate the critical speed of resonance; when the engine speed is the same as the critical speed, resonance will occur. So, the resonance should be different damping forces for different harmonics outputs to effectively reduce the crankshaft resonance.

4 Skyhook semi-active control design simulation

4.1 Skyhook semi-active control

The skyhook damping control strategy has an important place in the control strategy of semi-active suspensions and is the most commonly used control strategy in MR semi-active control. It is a classical method of semi-active suspension control proposed by Karnopp et al. in 1974. It has the characteristics of simple principle, easy implementation, and good robustness and is often used to compare with new control methods. The method is to install a damper between the reeded mass block and the virtual sky, taking the vertical vibration velocity of the reeded mass block as the object of study, and the damper generates a damping force opposite to the velocity of the reeded mass block. The model is based on a passive suspension for design, as shown in Figure 8.Here, c_{sky} is the skyhook damping factor, the size of which can be determined according to the suspension parameters, and the ideal skyhook damping force is

$$\boldsymbol{F_{sky}} = -\boldsymbol{c_{sky}}\dot{\boldsymbol{z}}_2. \tag{14}$$

The kinetic model is

$$\begin{cases} \boldsymbol{m_2}\ddot{\boldsymbol{z}}_2 = -\boldsymbol{k_2}(\boldsymbol{z_2} - \boldsymbol{z_1}) - \boldsymbol{c_e}(\dot{\boldsymbol{z}}_2 - \dot{\boldsymbol{z}}_1) - \boldsymbol{c_{sky}}\dot{\boldsymbol{Z}}_2 \\ \boldsymbol{m_1}\ddot{\boldsymbol{z}}_1 = -\boldsymbol{k_1}(\boldsymbol{z_1} - \boldsymbol{z_0}) - \boldsymbol{k_2}(\dot{\boldsymbol{z}}_2 - \dot{\boldsymbol{z}}_1) - \boldsymbol{c_1}(\dot{\boldsymbol{Z}}_2 - \dot{\boldsymbol{Z}}_1) \end{cases}, \tag{15}$$

where m_1 is the spring load mass; m_2 is the damper mass; k_1 is the spring load stiffness; k_2 is the damper stiffness; z_0 is the suspension displacement; z_1 is the spring load displacement; z_2 is the damper displacement; c_1 is the spring load damping factor; and $\dot{z}_1$ and $\dot{z}_2$ are the spring load and damper velocity, respectively.

The force F_{sky} in the skyhook damping control strategy is virtual, and it is impossible to realize in reality. When using MR dampers to replace the skyhook active control active actuator, the skyhook control strategy current switching principle should be satisfied: when the product of the crankshaft free end velocity fluctuation and acceleration is greater than zero, at this time, the crankshaft moves in the positive direction, the ideal skyhook damper gives the crankshaft a force in the opposite direction to impede the vibration of the free end, the output force of the MR damper should be equal to the ideal skyhook damper or input a larger current to obtain. When the product of velocity fluctuation and acceleration at the free end of the crankshaft is less than zero, then the MR damper should output the minimum damping force, which is also the minimum current control. Based on the abovestated discussion, from simplicity and practicality, taking into account the strong nonlinearity of the MR damper and the difficult characteristics of current inversion, the skyhook damping control can be expressed as:

$$\begin{cases} \boldsymbol{c} = \boldsymbol{c}_{max} & if\boldsymbol{e}\dot{\boldsymbol{e}} \geq \boldsymbol{0} \\ \boldsymbol{c} = \boldsymbol{c}_{min} & if\boldsymbol{e}\dot{\boldsymbol{e}} < \boldsymbol{0} \end{cases}, \tag{16}$$

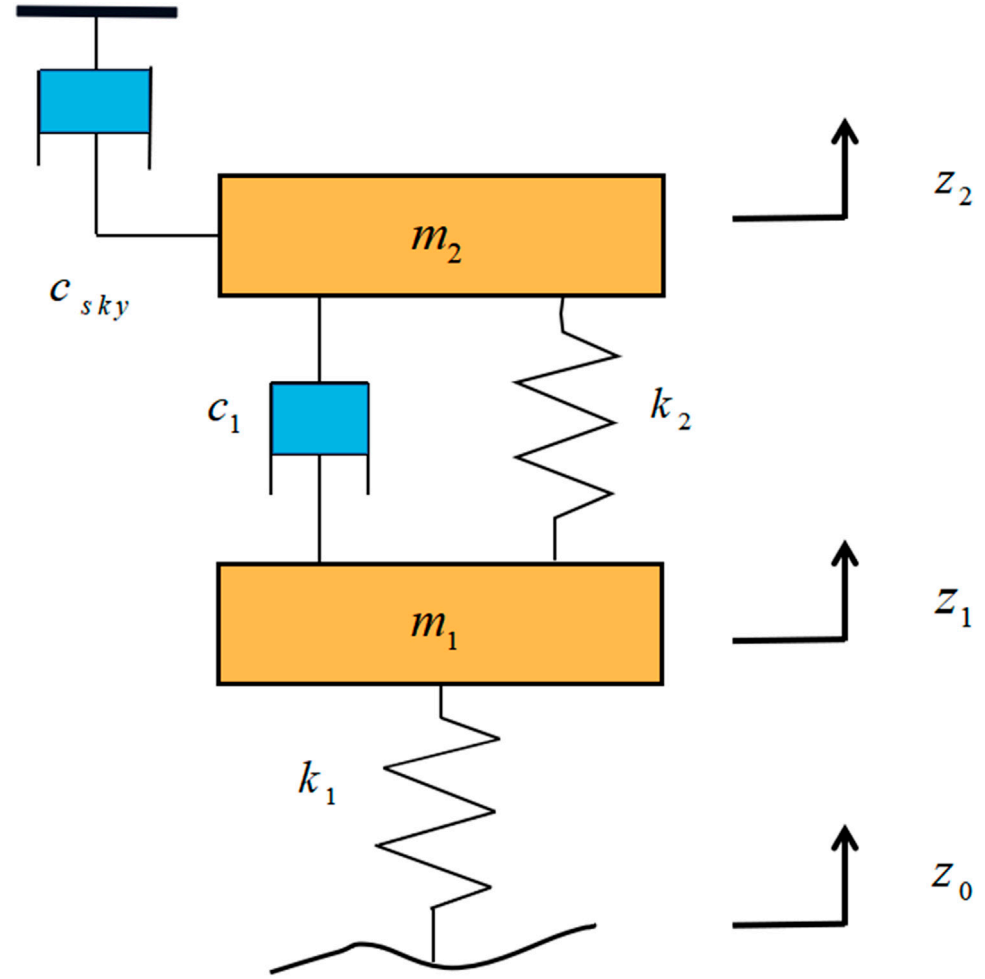

FIGURE 8
Diagram of the skyhook damping control model.

where c is the damping, c_{max} is the maximum damping factor, c_{min} is the minimum damping factor, e is the angular velocity fluctuation, and $\dot{e}$ is the angular acceleration.

Our actual control is to give the magnitude of the input current to the MR dampers; here, we simply give the current as 0 or I_{max} is 2 A. Essentially, skyhook damping control is a Bang–Bang control, where the magnetic field strength is proportional to the magnitude of the current; that is, when the current is 0, the Coulomb damping force is at its minimum, while when the current is I_{max}, the MR yield stress is also at its maximum, and, thus, the Coulomb damping force is at its maximum. This control algorithm is simple to calculate, easy to control, and easy to understand.

The control process for crankshaft torsional vibration is through the acquisition of real-time vibration signals from the free end of the crankshaft after the controller's data analysis and calculation to output a reasonable corresponding current. Then, the MRTD after the current is connected to output the corresponding damping force to achieve effective vibration damping. Thus, with the MRTD employing skyhook damping control, the block diagram of the control system is shown in Figure 9.

4.2 Simulation analysis of constant damping damper

The kinetic model is built from the established parametric equations using Amesim software to obtain the free end vibration curve more directly. The excitation signal of the model outputs the pressure torque according to the ignition sequence of the four-cylinder engine 1-3-2-4. The angular velocity and acceleration of the crankshaft free end during torsional vibration are then simulated and analyzed as the MRTD damping is controlled.

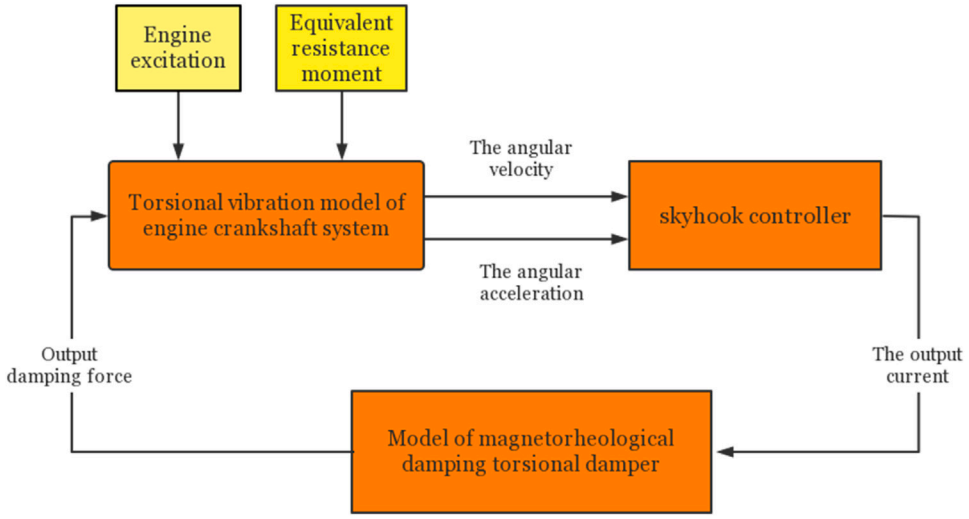

FIGURE 9
Block diagram of crankshaft torsional vibration control.

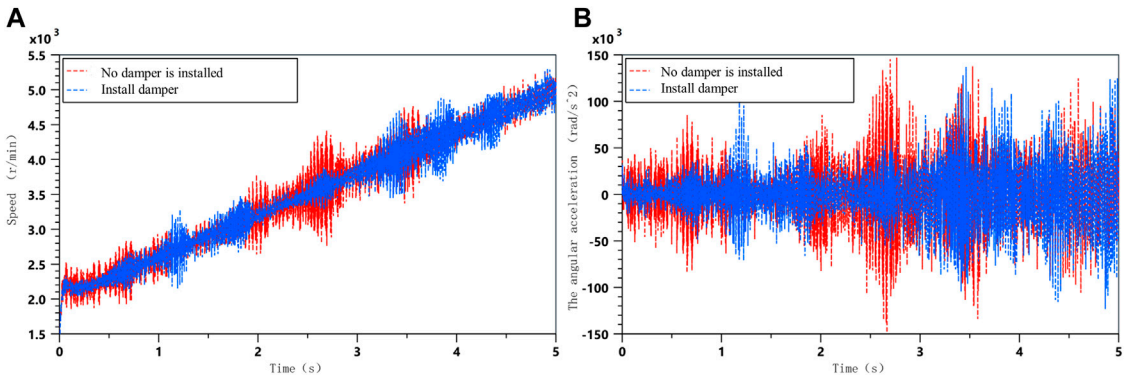

FIGURE 10
Comparison of vibration with and without torsional dampers; **(A)** Crankshaft angular velocity; **(B)** Crankshaft angular acceleration.

A comparison of the angular velocity and angular acceleration of the free end of the crankshaft system with the MRTD installed and without the torsional damper under accelerating conditions is shown in Figure 10, which shows that the torsional vibration of the crankshaft is effectively suppressed by the installation of the MR damper.

With an MRTD installed on the engine crankshaft, the damping coefficient can be adjusted by controlling the current to control the vibration of the crankshaft at different harmonic levels. When the damping coefficient of the MRTD is 0 and the damping coefficient is 4, the vibration signals of the free end of the crankshaft at acceleration and constant speed can be obtained, as shown in Figures 11 and 12. The dynamics of the model can be seen clearly in the angular acceleration and angular velocity of the free end of the crankshaft system at different damping factors. At the same time, in acceleration mode, Fourier transform is applied to vibration signals of free end speed and angular acceleration of crankshaft under different damping coefficients to obtain a frequency domain analysis diagram.

The time domain analysis diagram shows that when the damping factor is 4, some of the resonance of the crankshaft during acceleration is weakened, which verifies the effective damping performance of the damper. However, according to the frequency domain diagram, it can also be found that

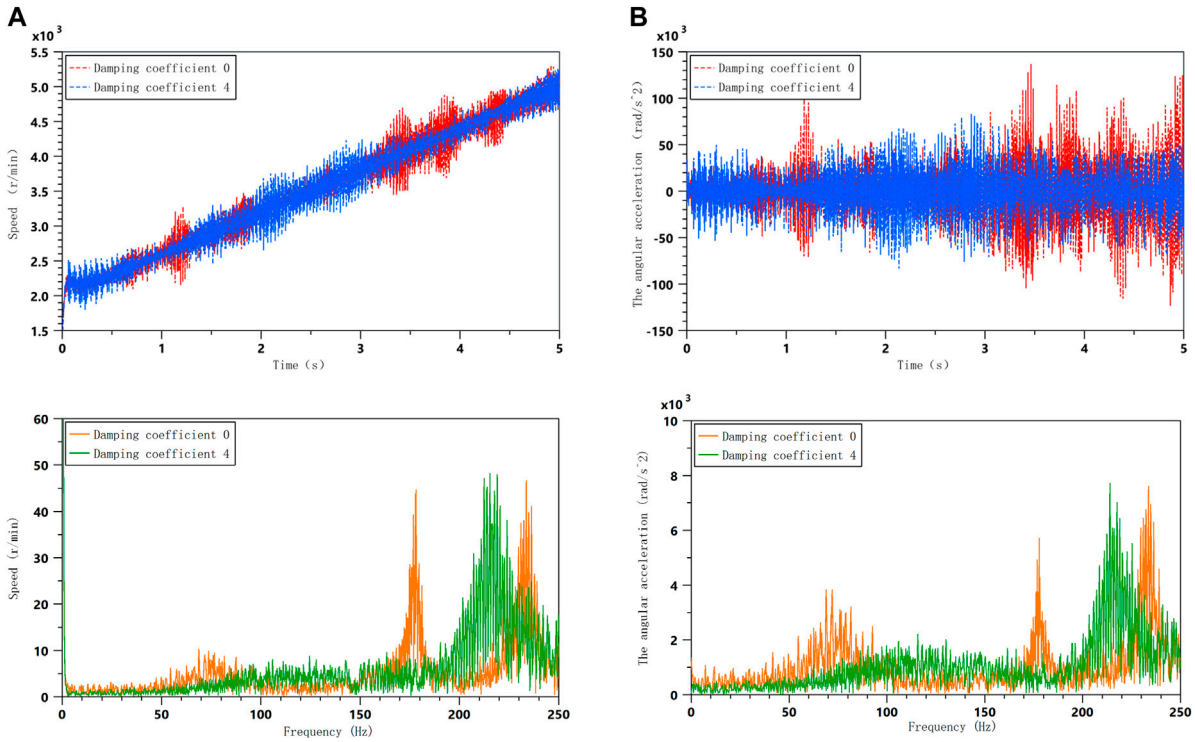

FIGURE 11
Comparison of vibration with different damping factors during acceleration; **(A)** Crankshaft angular velocity; **(B)** Crankshaft angular acceleration.

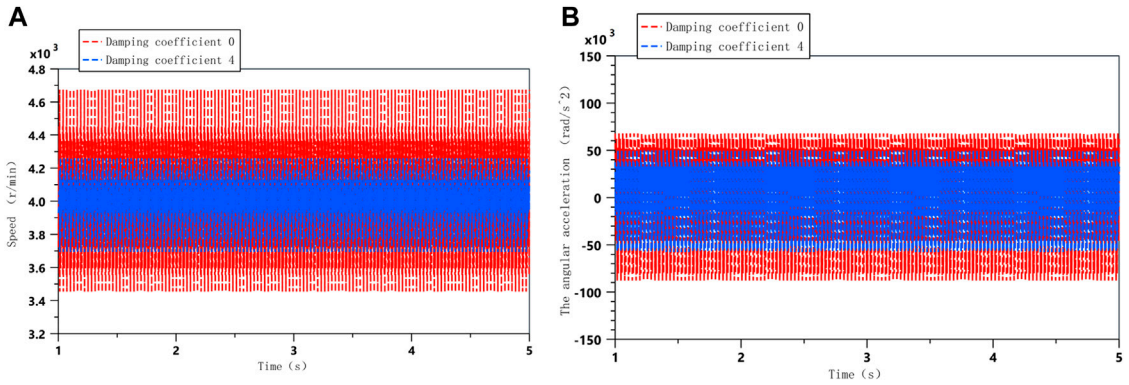

FIGURE 12
Comparison of vibrations with different damping factors at constant speed; **(A)** Crankshaft angular velocity; **(B)** Crankshaft angular acceleration.

during acceleration, the resonance is shifted, and the overall vibration is not effectively suppressed. This is due to the fact that the damping is not optimal at this point in time; so, in order to effectively suppress the resonance of the crankshaft system during acceleration, the optimal damping needs to be calculated for the main resonance frequencies.

4.3 Skyhook damping control simulation

A joint simulation using Matlab and Amesim was also used to verify the crankshaft system torsional vibration response under the skyhook damping control strategy at acceleration conditions. This is shown in Figure 13.

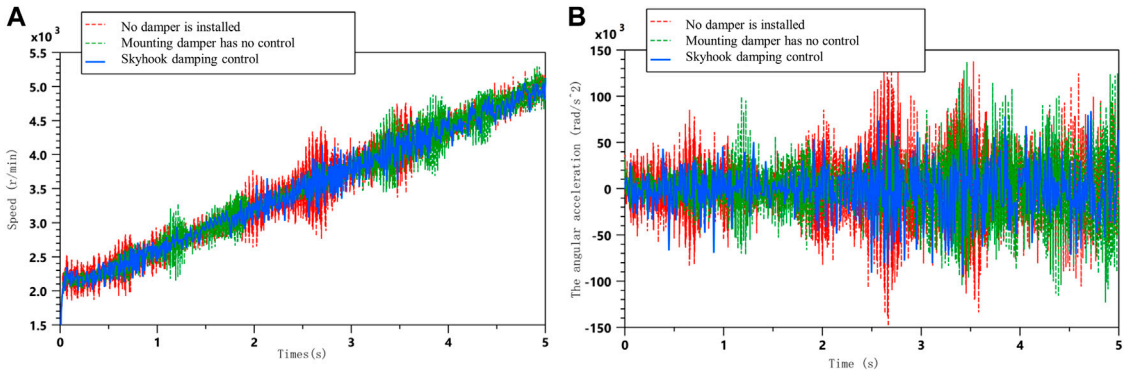

FIGURE 13
Comparison of simulation results for acceleration conditions; **(A)** Comparison of free end speeds of crankshaft systems under acceleration conditions; **(B)** Comparison of angular acceleration at the free end of the crankshaft system under acceleration conditions.

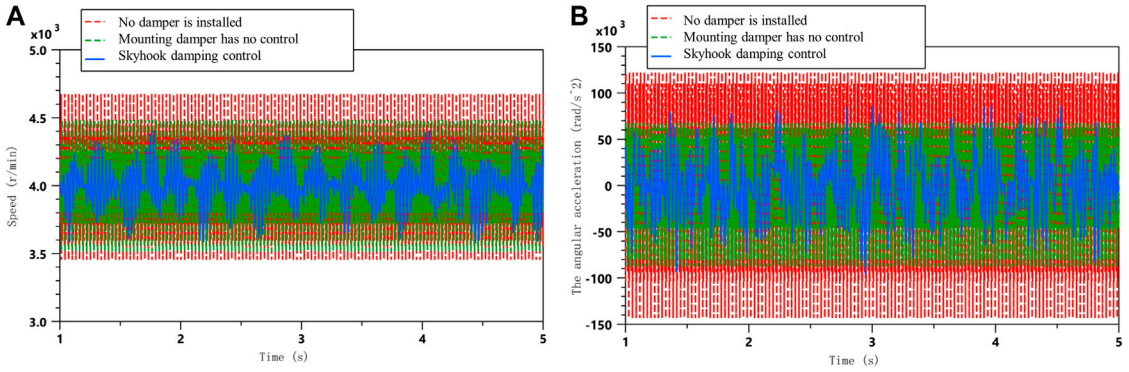

FIGURE 14
Comparison of simulation results for uniform speed conditions; **(A)** Comparison of free end speeds of crankshaft systems at constant speed; **(B)** Comparison of angular acceleration at the free end of the crankshaft system under uniform speed conditions.

The free end torsional vibration of the crankshaft system under steady running conditions is also compared using skyhook damping control, as shown in Figure 14.

As can be seen from the simulation analysis graph, the skyhook damping control is significantly more effective than the passive control, effectively suppressing the angular velocity and angular acceleration amplitude of the crankshaft free end vibration near the resonance frequency under acceleration conditions. The skyhook damping control also reduces the torsional vibration response to a certain extent during the smooth running phase.

Based on the abovementioned simulation results, the peak and RMS (root mean square) values of the angular velocity fluctuation at the free end of the crankshaft and the angular acceleration $\dot{e}$ were calculated for various scenarios, as shown in Tables 3 and 4. The figures in brackets are the rate of reduction in vibration response compared to the case without the torsional damper fitted.

As can be seen from the tables mentioned earlier, the skyhook damping control is able to significantly reduce the RMS value of the angular velocity fluctuations at the free end of the crankshaft and the angular acceleration fluctuations by 43.8 and 26.3%, respectively, as well as reducing the peak value by 28 and 44%, respectively, when compared to the passive control during acceleration conditions.

The tables show that the skyhook damping control is also superior to the passive control method under uniform speed conditions, with a reduction of 39.7 and 45.6% in the RMS value of the angular velocity and angular acceleration fluctuations, respectively, and a peak value of 40.9 and 43.3% for their fluctuations, respectively. The results of the abovementioned

TABLE 3 Peak and RMS values of torsional vibration response for acceleration condition.

Torsion control methods	RMS value of $e\,(r/min)$	RMS value of $\ddot{e}.10^3\,(rad/s^2)$	Peak of $e\,(r/min)$	Peak of $\ddot{e}.10^3\,(rad/s^2)$
No damper fitted	237.8	45.6	755	150
Installation of dampers	152.2 (35.9%)	37.3 (18.2%)	583 (22.7%)	137 (8.6%)
Skyhook damping control	133.6 (43.8%)	33.6 (26.3%)	543 (28%)	83.9 (44%)

TABLE 4 Peak and RMS values of torsional vibration response for uniform speed conditions.

Torsion control methods	RMS value of $e\,(r/min)$)	RMS value of $\dot{e}.10^3\,(rad/s^2)$	Peak of $e\,(r/min)$	Peak of $\ddot{e}.10^3\,(rad/s^2)$
No damper fitted	410.9	79.8	674	143
Installation of dampers	290 (29.4%)	49.4 (38.1%)	514 (23.7%)	67 (53.1%)
Skyhook damping control	247.6 (39.7%)	43.4 (45.6%)	398 (40.9%)	81 (43.3%)

analysis also validate the effectiveness of the semi-active control of skyhook torsion.

5 Conclusion

The MRTD of the variable-damping crankshaft system has been studied in this article. In order to improve the smoothness and stability of the crankshaft system, the application of the dynamics model and the skyhook damping control method were investigated through analytical calculations and numerical simulations. The following conclusions were obtained.

(1) The damping ratio, inertia ratio, and setting ratio of the MRTD have a relatively obvious influence on the dynamic amplification coefficient of the crankshaft system. After the structural parameters of the device have been determined, the damping ratio can be controlled to achieve effective torsional damping of the crankshaft system.
(2) Through the simulation analysis of the constant damping torsional damper, when the damping coefficient increases, the torsional amplitude of the crankshaft system decreases in a certain range under the conditions of acceleration and constant velocity. At the same time, the resonance frequency of the system is changed to achieve the effect of frequency shift. It can be seen that the torsional vibration of the crankshaft can be inhibited obviously by changing the damping coefficient of the torsional damper.
(3) The design of a skyhook damping control method to control the MRTD through the simulation of comparative analysis shows that the control method in the acceleration conditions crankshaft speed fluctuations e and angular acceleration fluctuations in the RMS and peak reductions of 43.8 and 26.3 and 28% and 44%, respectively. The RMS and peak reductions of crankshaft speed fluctuation e and angular acceleration fluctuation at constant speed are 39.7 and 45.6 and 40.9 and 43.3%, respectively, which shows that the skyhook damping control has a better damping effect than the constant damping.

The research is mainly based on theoretical analysis and simulations, but future experiments are needed to validate the results and further incorporate new intelligent control algorithms.

Data availability statement

The original contributions presented in the study are included in the article/Supplementary Material; further inquiries can be directed to the corresponding author.

Author contributions

Reviewing, guidance, and support: QO and HH; Modeling, simulation, and original draft preparation: WH; Data analysis and simulation results analysis: WH, XY, and LL.

Funding

This work was supported by the Zhejiang Provincial Natural Science Foundation of China (Grant Nos. LGG20E050022 and LGG19E050017) and in part by the National Natural Science Foundation of China (NSFC) grant funded by the Chinese Government (Grant No. 51805209) and the Jiaxing Municipal Science and Technology Project (Grant No. 2020AY10036).

Conflict of interest

Author LL was employed by Ningbo Sedsun Vibration Damper Co., Ltd. OQ works at Jiaxing University and has done postdoctoral research at Nanjing University of Science and Technology and Taizhou Jiuju Technology Co., Ltd.

The remaining authors declare that the research was conducted in the absence of any commercial or financial relationships that could be construed as a potential conflict of interest.

Publisher's note

All claims expressed in this article are solely those of the authors and do not necessarily represent those of their affiliated organizations, or those of the publisher, the editors, and the reviewers. Any product that may be evaluated in this article, or claim that may be made by its manufacturer, is not guaranteed or endorsed by the publisher.

References

Abouobaia, E., Bhat, R., and Sedaghati, R. (2015). Development of a new torsional vibration damper incorporating conventional centrifugal pendulum absorber and MR damper. *J. Intelligent Material Syst. Struct.* 27 (7), 980–992. doi:10.1177/1045389X15590275

Ahamed, R., Ferdaus, M. M., and Li, Y. C. (2016). Advancement in energy harvesting magneto-rheological fluid damper: A review. *Korea-Aust. Rheol. J.* 28 (4), 355–379. doi:10.1007/s13367-016-0035-2

Christopher, S. K. (1992). Prediction and control of heavyduty powertrain torsional vibration. *J. Commer. Veh.* 1992, 805–814.

Deng, L., Sun, S., Christie, M., Ning, D., Jin, S., Du, H., et al. (2022). Investigation of a seat suspension installed with compact variable stiffness and damping rotary magnetorheological dampers. *Mech. Syst. Signal Process.* 171, 108802. doi:10.1016/j.ymssp.2022.108802

Dong, X. M., Li, W. F., Yu, J., Pan, C., Xi, J., Zhou, Y., et al. (2020). Magneto-rheological variable stiffness and damping torsional vibration control of powertrain system. *Front. Mat.* 7, 121. doi:10.3389/fmats.2020.00121

Haşmet, Ç., and Tinkir, M. (2021). Optimization of torsional vibration damper of cranktrain system using a hybrid damping approach. *Eng. Sci. Technol. Int. J.* 24 (4), 959–973. doi:10.1016/j.jestch.2021.02.008

Hoang, N., Zhang, N., Li, W. H., and Du, H. (2013). Development of a torsional dynamic absorber using a magnetorheological elastomer for vibration reduction of a powertrain test rig. *J. Intelligent Material Syst. Struct.* 24 (16), 2036–2044. doi:10.1177/1045389x13489361

Krauze, P., Kasprzyk, J., Kozyra, A., and Rzepecki, J. (2018). Experimental analysis of vibration control algorithms applied for an off-road vehicle with magnetorheological dampers. *J. Low Freq. Noise Vib. Act. Control* 37 (3), 619–639. doi:10.1177/1461348418756018

Li, M. M., Zhang, J. Y., Wu, C., Zhu, R., Chen, W., Duan, C., et al. (2020). Effects of silicone oil on stiffness and damping of rubber-silicone oil combined damper for reducing shaft vibration. *IEEE ACCESS* 8, 218554–218564. doi:10.1109/access.2020.3041359

Lin, C. Y., and Jheng, H. W. (2017). Active vibration suppression of a motor-driven piezoelectric smart structure using adaptive fuzzy sliding mode control and repetitive control. *Appl. Sci. (Basel).* 7 (3), 240. doi:10.3390/app7030240

Ngoc, M. V., Shin, S. C., and Kim, G. W. (2018). Comparative study on non-traditional torsional vibration isolators for automotive clutch dampers. *Noise Control Eng. J.* 66 (6), 541–550. doi:10.3397/1/376645

Ning, S. K., Jia, L., and Ma, B. J. (2013). Optimization model of metal rubber buffer on artillery. *Front. Manuf. Des. Sci.* III, 271237–271241. doi:10.4028/www.scientific.net/amm.271-272.237

Penkov, B. (2008). A method for modeling the shock of a rubber buffer with a rigid body. *Transport* 23 (2), 119–123. doi:10.3846/1648-4142.2008.23.119-123

Philipp, M., Fidlin, A., Kruger, A., and GroB, H. (2017). Simulation based optimization of torsional vibration dampers in automotive powertrains. *Mech. Mach. Theory* 115, 244–266. doi:10.1016/j.mechmachtheory.2017.05.010

Shen, Z. X., Qiao, B. J., and Chen, X. F. (2018). "The influence of external spur gear surface wear on the mesh stiffness," in 2018 Prognostics and System Health Management Conference (PHM-Chongqing), Chongqing, China, 26-28 October 2018 (IEEE), 1232–1238.

Shook, D. A. (2008). Semi-active control of torsion ally-responsive structures. *Eng. Struct.* 31, 57–68. doi:10.1016/j.engstruct.2008.06.016

Sinyayski, V. V. (2019). "Results of simulation and experimental research of automobile gas diesel engine," in Systems of Signals Generating and Processing in The Field of On Board Communications, Moscow, Russia, 20-21 March 2019 (IEEE).

Sun, J., Shu, L., Song, X., Liu, G., Xu, F., Miao, E., et al. (2016). Multi-objective optimization design of engine crankshaft bearing. *Industrial Lubr. Tribol.* 68 (1), 86–91. doi:10.1108/ilt-03-2015-0040

Venczel, M., Bognar, G., and Veress, A. (2021b). Temperature-dependent viscosity model for silicone oil and its application in viscous dampers. *Processes* 9 (2), 331. doi:10.3390/pr9020331

Venczel, M., Steidl, M., and Veres, A. (2021a). Design modifications and thermal analysis of visco-dampers for extending silicone oil durability. *Acta Polytech. Hung.* 18 (8), 27–46. doi:10.12700/aph.18.8.2021.8.2

Wang, Y., Zheng, Q. G., Zhang, H., and Miao, L. Z. (2018). Adaptive control and predictive control for torsi-onal vibration suppression in helicopter/engine system. *IEEE ACCESS* 6, 23896–23906. doi:10.1109/access.2018.2829723

Willenborg, D., and Kroger, M. (2017). Isolation and damping properties of rubber-buffers. *Const. Models Rubber* X, 477–482. doi:10.1201/9781315223278-74

Xiong, J. Q. (2019). Research on subjective rating attenuation analysis of automobile NVH characteristics. *Procedia Comput. Sci.* 154, 383–388. doi:10.1016/j.procs.2019.06.055

Ye, S., and Williams, K. A. (2005). Torsional vibration control with an MR fluid brake. *Proc. Spie* 5760, 283–292. doi:10.1117/12.600174

Yu, S. (2003). Development of dual mode engine crank damper. SAE Paper 2003-01-1675.

Zhang, L. R. (2013). Brief analysis of torsional vibration of vehicle engine. *Adv. Mat. Res.* 1-4, 302–306. doi:10.4028/www.scientific.net/amr.694-697.302

Zhong, Y. X., Yang, D. L., and Hui, H. (2020). "Driveline torsional vibration analysis and research of a light van," in 5Th International Conference on Information Science, Computer Technology and Transportation (ISCTT 2020), Shenyang, China, 13-15 November 2020 (IEEE), 554–557.

Zhou, P., Liu, M., Kong, W., Xu, Y., and Li, H. (2021). Modeling and evaluation of magnetorheological dampers with fluid leakage for cable vibration control. *J. Bridge Eng.* 26 (2), 1666. doi:10.1061/(asce)be.1943-5592.0001666

frontiers | Frontiers in Materials

TYPE Original Research
PUBLISHED 12 October 2022
DOI 10.3389/fmats.2022.1011550

OPEN ACCESS

EDITED BY
Xun Yu,
New York Institute of Technology,
United States

REVIEWED BY
Ying-Qing Guo,
Nanjing Forestry University, China
Donghong Ning,
Ocean University of China, China

*CORRESPONDENCE
Decai Li,
lidecai@mail.tsinghua.edu.cn

SPECIALTY SECTION
This article was submitted to Smart Materials,
a section of the journal
Frontiers in Materials

RECEIVED 04 August 2022
ACCEPTED 05 September 2022
PUBLISHED 12 October 2022

CITATION
Li Y, Li D and Li Y (2022), Performance tests and design of a series of magnetic fluid shock absorbers with varying stiffness based on optimal stiffness formula.
Front. Mater. 9:1011550.
doi: 10.3389/fmats.2022.1011550

Performance tests and design of a series of magnetic fluid shock absorbers with varying stiffness based on optimal stiffness formula

Yanwen Li[1], Decai Li[1]* and Yingsong Li[2]

[1]State Key Laboratory of Tribology, Department of Mechanical Engineering, Tsinghua University, Beijing, China, [2]China Productivity Center for Machinery Co., Ltd., Beijing, China

With the rapid development of aerospace technology, the vibration problem of the spacecraft flexible structure urgently needs to be solved. Magnetic fluids are a type of multi-functional smart materials, which can be employed in shock absorbers to eliminate these vibrations. Referring to the calculation methods of stiffness coefficients of other passive dampers, the stiffness coefficient formula of magnetic fluid shock absorbers (MFSAs) was derived and refined. Meanwhile, a series of varying stiffness magnetic fluid shock absorbers (VS-MFSAs) were proposed and fabricated based on the second-order buoyancy principle. The range of stiffness coefficients covered by these VS-MFSAs contains the optimal stiffness coefficient estimated by formulas. The repulsive force measurement and vibration attenuation experiments were conducted on these VS-MFSAs. In the case of small amplitude, the relationship between the repulsive force and the offset distance was linear, which means the stiffness was linear. The simulation and experiment curves of the stiffness were in good agreement. The results of vibration attenuation experiments demonstrated that the rod length and the magnetic fluid mass influence the damping efficiency of VS-MFSAs. In addition, these results verified that the VS-MFSA with the optimal stiffness coefficient performed best. Therefore, the stiffness coefficient formula can guide the design of MFSAs.

KEYWORDS

magnetic fluid, shock absorber, optimal stiffness coefficient, vibration, spacecraft

Introduction

The vibration problem of the spacecraft's flexible solar panel is one of the most critical issues for the normal operation of spacecrafts (Jiang and Li, 2010). The solar panels are susceptible to residual oscillation and driving disturbance (Jiang and Li, 2011), because of their characteristics of small damping and low frequency, which results in vibration. These micro-vibrations are difficult to reduce in the space

environment so that vibration suppression of spacecraft's flexible structures has received a lot of attention in the past two decades (Hu et al., 2020).

One promising solution for this problem is to utilize shock absorbers with smart materials. Magnetic fluids (MFs) are a kind of smart materials, which are composed of nanoparticles, carrier liquids and surfactants (Rosensweig, 1987). Due to their chemical composition, MFs have a lot of good characteristics, such as rapid magnetic response, complex rheology, amazing levitation and so on (Rosensweig, 1966). According to these interesting properties, magnetic fluid shock absorber (MFSA) has many advantages, for instance, controllable damping, compact structure, high sensitivity, less energy consuming and long life, etc. (Li and Li, 2022a) These good features make MFSAs suitable for vibration suppression with low frequency and small amplitude. Magnetorheological fluids (MRFs) which were first prepared by Rabinow (Rabinow, 1948) in 1948 are easily confused with MFs. Unlike nano-scale magnetic particles in MFs, the particles in MRFs are micro-scale, so that these particles are more prone to aggregation and deposition (Li et al., 2022). As a result, the stability of MFs is much better than that of MRFs. Meanwhile MRFs possess stronger shear viscosity and yield stress than MFs. Based on these interesting characteristics of MRFs, they are usually used for vibration suppression of medium or high frequencies (Xu et al., 2021; Yang et al., 2021).

The first successful application of the MF viscous damper was presented by NASA in 1967, which was employed to suppress the oscillations of the Radio Astronomy Explorer Satellite in aerospace (Coulombre et al., 1967). Afterwards, MF dampers attracted more and more attention and scholars from various countries devoted great efforts to the development of MF dampers (Li et al., 2022). Ten years later, on the basis of levitation characteristics of MFs, Moskowitz et al. (Moskowitz et al., 1978) proposed a viscous fluid inertia damper working well in reducing the rotational vibrations of stepping motor shafts. In 2002, Bashtovoi et al. (Bashtovoi et al., 2002) created a novel MF dynamic absorber, which was regarded as a major breaktrough for dampening the spacecraft vibration. In order to improve its sensitivity, this MF dynamic absorber wasn't filled with MFs, which played an important role in subsequent development of MF inertia dampers. In the same period, on account of the controllable flow of MFs, researchers replaced ordinary liquids in tuned liquid dampers with MFs to raise their damping efficiency, which were called tuned MF dampers (Ohno et al., 2008; Ohno and Sawada, 2010; Ohno et al., 2011). Due to the aggravation of energy problems, energy harvesting has received increasing attention. Vibration energy harvesters have become a hotspot for studies on MF dampers in the past decade (Bibo et al., 2012; Choi et al., 2015). They are combination of energy harversters and MF dampers and can realize self-energizing, which boosts the development of equipment miniaturization (Seol et al., 2017). In the previous extensive literature, the damping coefficient of MF dampers has always been concerned (Li and Li, 2022b). However, there are far fewer studies involving stiffness coefficient.

Fortunately, there are sufficient studies on the stiffness coefficients of other dampers. The research approaches about stiffness coefficients in these studies can be transferred to MF dampers. Sun et al. (Sun et al., 2015) presented a novel compact shock absober with variable stiffness, which was suitable for vehicle suspension. Its stiffness was controlled by current applied to the shock absorber. Wang et al. (Wang et al., 2021) proposed a new tuned inerter negative stiffness damper for protecting primary structures under earthquake excitaions. Its negative stiffness combined with inertance were employed to enhance the energy dissipation ratio. Javanbakht et al. (Javanbakht et al., 2018) developed an analytical model to refine damper design by considering the negative and positive stiffness. The important parameters of negative stiffness dampers and positive stiffness dampers were predicted by the refined design formula. These design tools made dampers more sutiable to mitigate vibrations of stay cables. Weber et al. (Weber et al., 2010) created a novel adaptive tuned mass damper, of which damping and stiffness can be adjusted. This damper contained a magnetorheological damper that was used to control friction-viscous damping and stiffness of the whole damper. Combined with a controllable magnetorheological damper, this presented damper performed well over a wide frequency range.

In the paper, the optimal stiffness coefficient formula was derived in detail and a series of MF dampers with varying stiffness were presented. In section 2, the whole derivation process of the optimal stiffness coefficient was elaborated. Then, the design method of a new varying stiffness MF shock absorber (VS-MFSA) was proposed in section 3. Section 4 illustrated the experimental process and corresponding apparatus. The simulation and experiment results of repulsive force, as well as the vibration attenuation experiment results were given and discussed in section 5. Finally, the main conclusions were outlined in section 6.

Theoretical analysis

Oscillation model

The cantilevered elastic plate represented the simplified flexible solar panel of spacecrafts and generated maximum vibration at the end. Therefore, VS-MFSAs were generally placed at the end of plate, as shown in Figure 1A. Ulteriorly, the corresponding physical model was extracted from the experimental system model in Figure 1A, which was called two-degree-of-freedom oscillation model, as shown in Figure 1B.

Based on the vibration theory, the motion equations of the oscillation system in Figure 1B are:

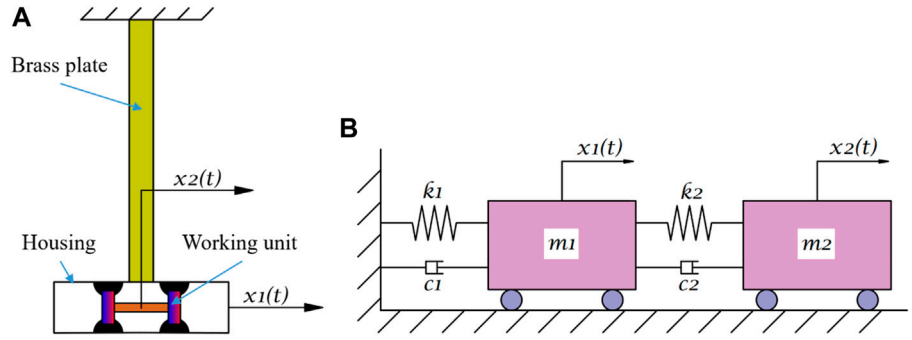

FIGURE 1
Simplified model. **(A)** Model of the experimental system. **(B)** Model of the oscillation system.

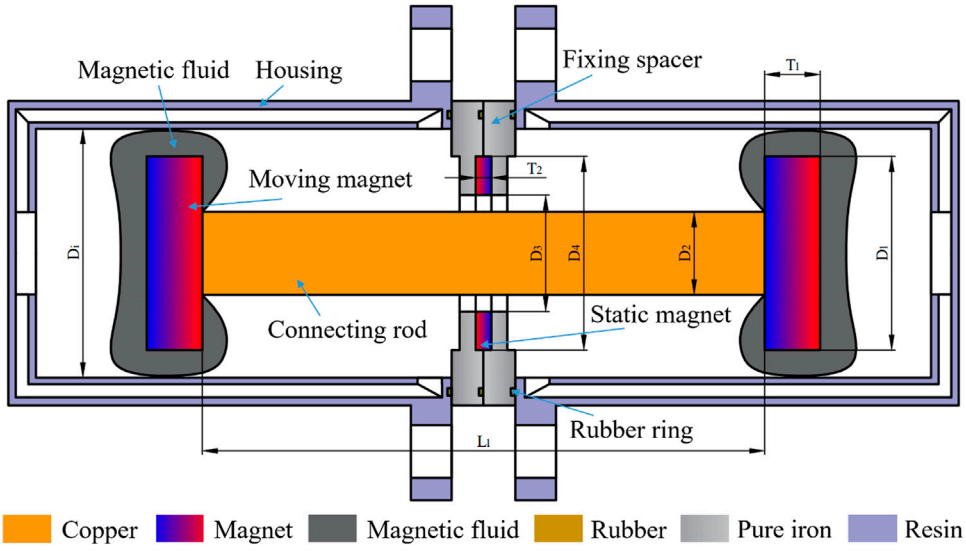

FIGURE 2
Section view of the varying stiffness magnetic fluid shock absorber.

$$m_1\ddot{x}_1 + C_1\dot{x}_1 + C_2(\dot{x}_1 - \dot{x}_2) + K_1x_1 + K_2(x_1 - x_2) = F, m_2\ddot{x}_2 - C_2(\dot{x}_1 - \dot{x}_2) - K_2(x_1 - x_2) = 0, \quad (1)$$

Where x_1 and x_2 are the displacement of the brass plate and the working unit respectively, m_1 is the equivalent mass of the brass plate and housing, m_2 is the equivalent mass of the working unit, K_1 is the equivalent stiffness coefficient of the brass plate, K_2 is the equivalent stiffness coefficient of the VS-MFSA, C_1 is the equivalent damping coefficient of the brass plate, C_2 is the equivalent damping coefficient of the VS-MFSA and F is the sinusoidal excitation force. In this paper, the main parameter we focused on was the equivalent stiffness coefficient of the VS-MFSA, of which the symbol was. K_2

According to the continuous beam theory, the equivalent stiffness coefficient of the brass plate can be expressed as,

$$K_1 = \frac{3EI}{l_c^3}, \quad (2)$$

Where $E = 9.7 \times 10^{10}Pa$ is the elastic modulus of the brass, $I = (ab^3/12)$ is the cross-section inertia of the brass plate, $l_c = 1.1m$, $a = 0.05m$ and $b = 0.005m$ are the length, width and thickness of the brass plate, respectively. From equation Eq. 2, $K_1 = 113.87N/m$ is obtained.

On the basis of the calculation method of the cantilever beam with a lumped mass at one end, the first-order natural frequency of the brass plate is,

TABLE 1 Main structural dimensions of the varying stiffness magnetic fluid shock absorber.

Parameters	Symbols	Values
Diameter of the moving magnet	D1	30 mm
Thickness of the moving magnet	T1	5 mm
Diameter of the connecting rod	D2	10 mm
Initial length of the connecting rod	L1	88 mm
Inner diameter of the static magnet	D3	30 mm
Outer diameter of the static magnet	D4	20 mm
Thickness of the static magnet	T2	2 mm
Inner diameter of the housing	Di	36 mm

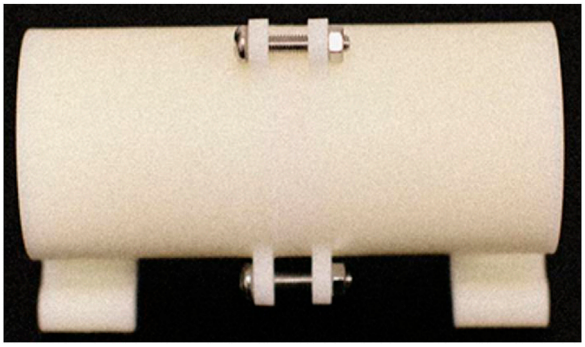

FIGURE 3
Appearance view of the varying stiffness magnetic fluid shock absorber.

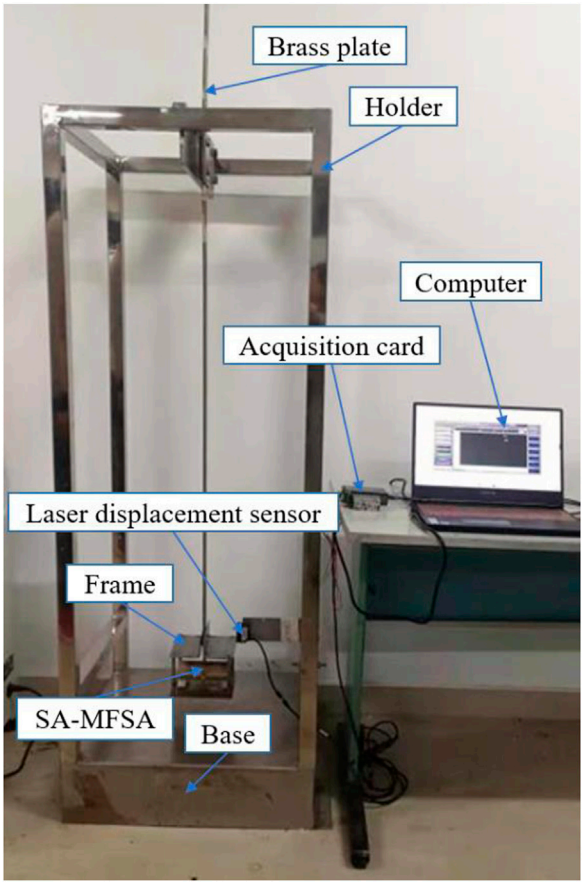

FIGURE 4
Photograph of experimental apparatus of vibration system.

$$f = \frac{1}{2\pi}\sqrt{\frac{K_1}{m_1}},$$
$$m_1 = m_0 + \frac{33}{140}m_c, \tag{3}$$

Where $m_0 = 1.55kg$ and $m_c = 2.25kg$ are the lumped mass and the own mass of the brass plate, respectively, which acquires that $m_1 = 2.08kg$. Due to obtained K_1 and m_1, it is obvious that $f = 1.18Hz$.

In order to facilitate the calculation, the sinusoidal excitation force and displacements are expressed in the form of complex variables function respectively.

$$F = \bar{F}e^{jwt},$$
$$x_1 = \overline{X_1}e^{jwt}, \tag{4}$$
$$x_2 = \overline{X_2}e^{jwt}.$$

By solving Equation Eq. 1 and applying $\overline{X_1}/\bar{F}$, $\overline{X_2}/\bar{F}$ as description form, that is,

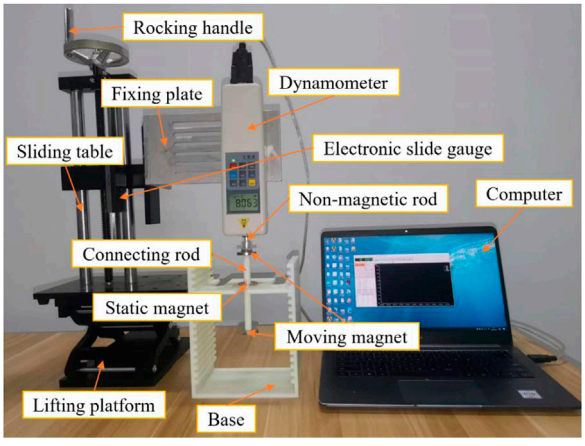

FIGURE 5
Photograph of experimental apparatus to measure repulsive force.

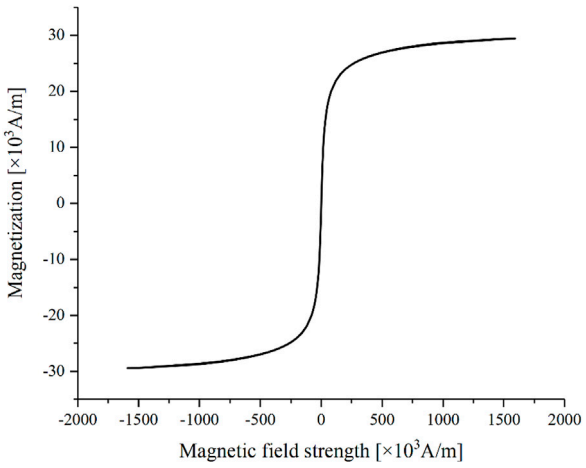

FIGURE 6
Magnetization curve of the magnetic fluid used in experiments.

$$\frac{\overline{X_1}}{\overline{F}}(w) = \frac{-m_2w^2 + K_2 + jC_2w}{\Delta_1},$$
$$\frac{\overline{X_2}}{\overline{F}}(w) = \frac{K_2 + jC_2w}{\Delta_1},$$
$$\Delta_1 = \left[m_1m_2w^4 - (m_1K_2 + m_2K_1 + m_2K_2 + C_1C_2)w^2 + K_1K_2\right] + j\left\{(C_2K_1 + C_1K_2)w - [m_1C_2 + m_2(C_1 + C_2)]w^3\right\}. \tag{5}$$

By adopting euler formula, the amplitude in the form of complex variables is subsitituted with the real amplitude and phase.

$$\psi_1 = \frac{X_1}{X_{st}}(w) = \frac{\sqrt{(\lambda^2 - \gamma^2)^2 + 4\lambda^2\varsigma^2\gamma^2}}{\sqrt{\Delta_2}},$$
$$\psi_2 = \frac{X_2}{X_{st}}(w) = \frac{\sqrt{\lambda^4 + 4\lambda^2\varsigma^2\gamma^2}}{\sqrt{\Delta_2}}, \tag{6}$$
$$\Delta_2 = 4\lambda^2\varsigma^2\gamma^2\left\{4\zeta^2\gamma^2 + \left[1 - (1+\mu)\gamma^2\right]^2\right\} + 8\lambda\zeta\gamma^6\mu\varsigma + \left\{\gamma^4 - \left[1 + (1+\mu)\lambda^2\right]\gamma^2 + \lambda^2\right\}^2 + 4\zeta^2\gamma^2(\lambda^2 - \gamma^2)^2,$$

Where $X_{st} = (\bar{F}/K_1)$(m) is the static deformation of the main system, $\varsigma = C_2/(2\sqrt{m_2K_2})$ is the damping ratio of the VS-MFSA, $\zeta = C_1/(2\sqrt{m_1K_1})$ is the damping ratio of the main system, $\mu = m_2/m_1$ is the mass ratio, $\lambda = w_n/\Omega_n$ is the natural angular frequency ratio, $\gamma = w/\Omega_n$ is the forced vibration frequency ratio, $w_n = \sqrt{K_2/m_2}$ (rad/s) is the natural angular frequency of the VS-MFSA, $\Omega_n = \sqrt{K_1/m_1}$ (rad/s) is the natural angular frequency of the main system.

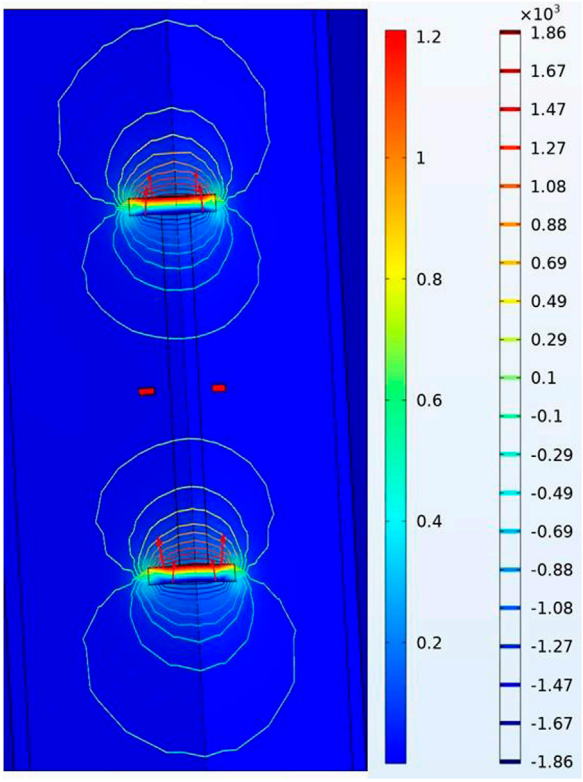

FIGURE 7
Simulated magnetic flux density of the working unit. [unit T].

By using Equation Eq. 6 which determains the amplitude ratio of the whole oscillation system, one of the most important parameters of VS-MFSAs, namely K_2, can be optimized design.

Optimal stiffness coefficient

In the case of ignoring the damping of the main system, which means that $C_1 = 0$, the optimal value of the natural angular frequency ratio λ'_{opt} can be represented by equation Eq. 7 and the optimal stiffness coefficient of the VS-MFSA K'_{2_opt} can be calculated by equation Eq. 8.

$$\lambda'_{opt} = \frac{1}{1+\mu}, \tag{7}$$
$$K_{2\_opt}' = m_2\frac{K_1}{m_1}\lambda_{opt}'^{\,2} = m_2\frac{K_1}{m_1}\left(\frac{1}{1+\mu}\right)^2. \tag{8}$$

When considering the damping of the main system, which means that $C_1 \neq 0$, Japanese scholars (池田健, 1977) revised the optimal stiffness coefficient formula under specific conditions through numerical calculation. The specific conditions were that the mass ratio μ is in the range of $0.1 \sim 0.3$ while the damping ratio ζ is in the range of $0 \sim 0.125$. The result of

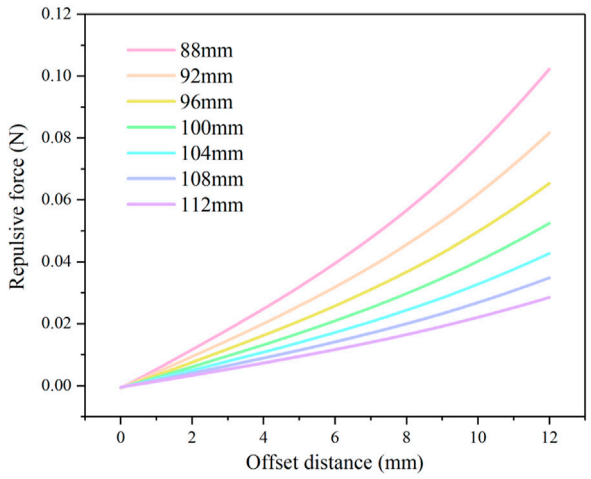

FIGURE 8
Simulated repulsive forces for different offset distances with various rod lengths.

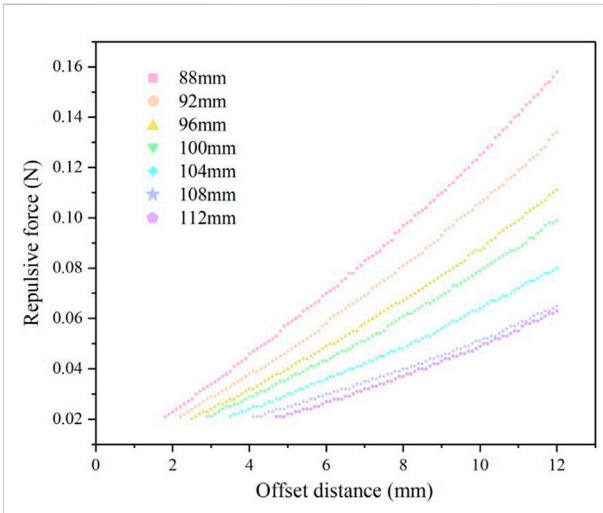

FIGURE 9
Measured repulsive forces for different offset distances with various rod lengths.

numerical calculation was that the optimal natural angular frequency ratio λ_{opt} is refined as equation Eq. 9, so that the optimal stiffness coefficient of the VS-MFSA K_{opt} can be expressed as equation Eq. 10.

$$\lambda_{opt} = \frac{1}{1+\mu} - (0.241 + 1.74\mu - 2.6\mu^2)\zeta - (1 - 1.9\mu + \mu^2)\zeta^2, \tag{9}$$

$$K_{2_{opt}} = m_2\frac{K_1}{m_1}\lambda_{opt}^2 = m_2\frac{K_1}{m_1}\left[\frac{1}{1+\mu} - (0.241 + 1.74\mu - 2.6\mu^2)\right.$$
$$\left.\zeta - (1 - 1.9\mu + \mu^2)\zeta^2\right]^2. \tag{10}$$

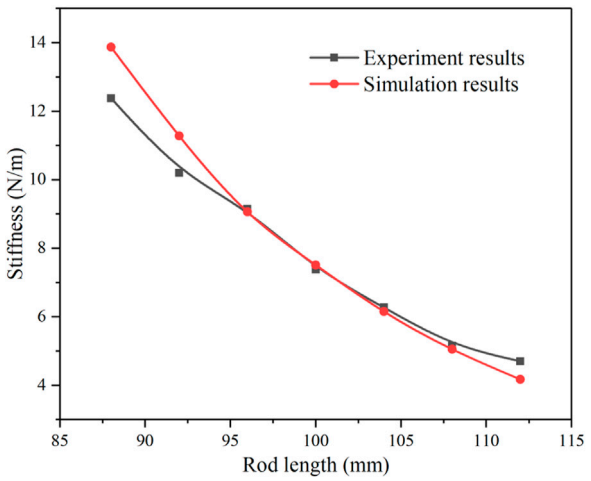

FIGURE 10
Compared simulation and experiment results of stiffness.

By putting into specific value, the optimal stiffness coefficient of the VS-MFSA was got, that is $K_{2_{opt}} = 5.25N/m$.

Structure design

Figure 2 depicts the section view of the VS-MFSA, including the major components and main dimensions. Meanwhile, Table 1 lists the main structural parameters, corresponding symbols and values. The VS-MFSA was designed on the basis of the second-order buoyancy principle of MFs. The connecting rod linked two moving magnets at both ends and the moving magnets adsorbed the MF, which formed the working unit. The MF was injected on each moving magnet respectively and wasn't filling the housing, as the gray part shown in Figure 2. Considering the inertial force, the initial connecting rod was made of copper. In order to adjust the stiffness of VS-MFSAs, the length of connecting rod was altered. To mitigate the influence of mass change, resin was chosen as the material of added connecting rod. As vibrations were excited, the working unit leaved from the initial equilibrium position and then was subjected to the repulsive force generated by the static magnet. The static magnet was fastened with two fixing spacers and aligned with the moving magnets to avoid non-axial repulsive force. Moreover, the moving magnets were suspended in the MF because of the second-order buoyancy principle of MFs. The rubber rings were mounted on the fixing spacers to ensure the MF sealed. The housing adopted the split strucutre and was fabricated with holes using to balance the pressure in the cavity. When the working unit reciprocating in the housing, the movement caused the MF flow, which dissipated the oscillation energy. The whole appearance of the VS-MFSA is shown in Figure 3.

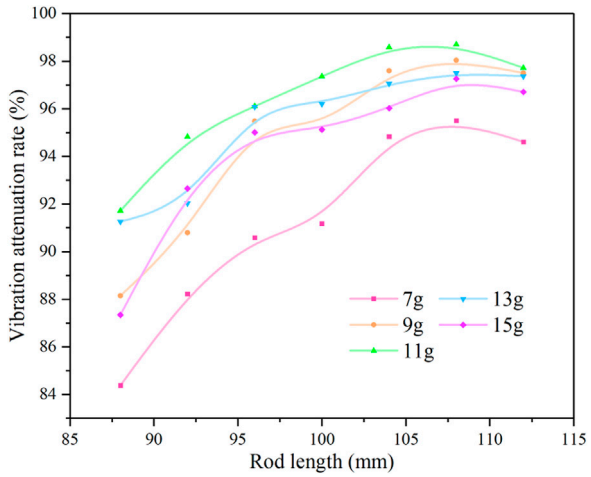

FIGURE 11
Vibration attenuation rate versus rod length with different magnetic fluid mass.

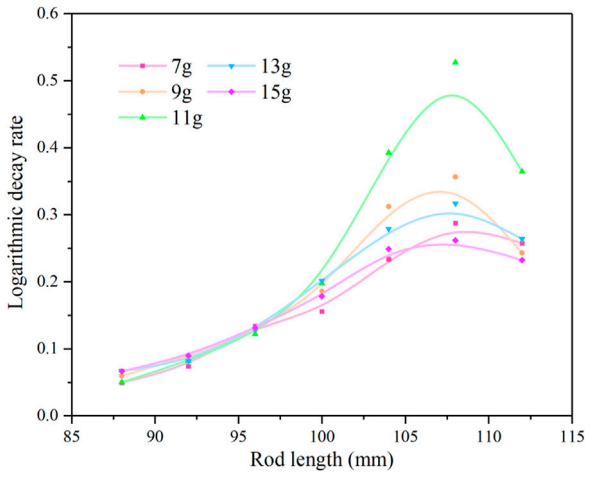

FIGURE 12
Logarithmic decay rate versus rod length with different magnetic fluid mass.

Experiments

It can be seen from Figure 4 that the vibration system was composed of a vibration table and a data acquisition system. The vibration table involved a base and a holder to immobilize one end of the brass plate. The other end of the brass plate was fitted with a frame using to install the VS-MFSA. The non-magnetic support stretched out from the holder for fixing the laser displacement sensor. The size of the cantilever elastic brass plate was 1100 mm*50 mm*5 mm, as well as the small amplitude and low frequency vibrations were generated by the plate. The frequency of the free oscillations of the cantilever elastic brass plate was equal to 1.18 Hz and the amplitude was set to 6 mm in the subsequent vibration reduction experiments. As for the data acquisition system, it included a acquisition card, a computer and an laser displacement sensor. The acquisition card USB-DAQ-7606i collected electrical signals and transmitted them to the computer with sampling frequency of 50 Hz. In order to meet the requirement of experiments, the laser displacement sensor HL-G108-A-C5 was chosen, of which the resolution was 2.5 mm.

The experiment apparatus shown in Figure 5 was employed to measure the repulsive force between the static magnet and moving magnets. The dynamometer was connected with the sliding table through the fixing plate. The eletronic slide gauge was concatenated with the sliding table to obtain the position of the dynamometer. The accuracies of the dynamometer and the eletronic slide gauge were 0.001 N and 0.01 mm, respectively. The static magnet was fixed on the base made of resin, as well as the moving magnet was attached to the non-magnetic rod, which ensured the results weren't affected by extra magnetic field. Besides, the non-magnetic rod, moving magnets and the static magnet were coaxial. First, we made the connecting rod center coincide with the static magnet center by adjusting the lifting platform and the sliding table, then set the dynamometer to zero. Second, rotating the rocking handle let moving magnets leave the equilibrium position and controlled the movement step length at 0.2 mm. In the end, the offset distances and corresponding repulsive forces were transmitted to the computer for subsequent analysis.

The MF used in experiments was prepared by our laboratory, of which the density, viscosity and saturation magnetization were 1.23g/cm3, 0.26Pa s and 450Gs, respectively. Figure 6 gave the magnetization curve of the MF.

Results and discussion

Stiffness coefficient

The length range of the connecting rod was 88 mm–112 mm and the increment between adjacent rods was 4 mm. The static magnet and the working unit with adjustable connecting rod, of which dimensions were same as Table 1, were put into COMSOL for simulation. Since moving magnets were subjected to repulsive force, the magnetic flux direction of moving magnets was set opposite to that of static magnet. Under the transient mode, the magnetic scalar potential was set to ensure the simulation convergence and a model was built as Figure 7 for parametric scanning to obtain the simulation results.

As a result, the relationship between the repulsive force and the offset distance was obtained and shown in Figure 8.

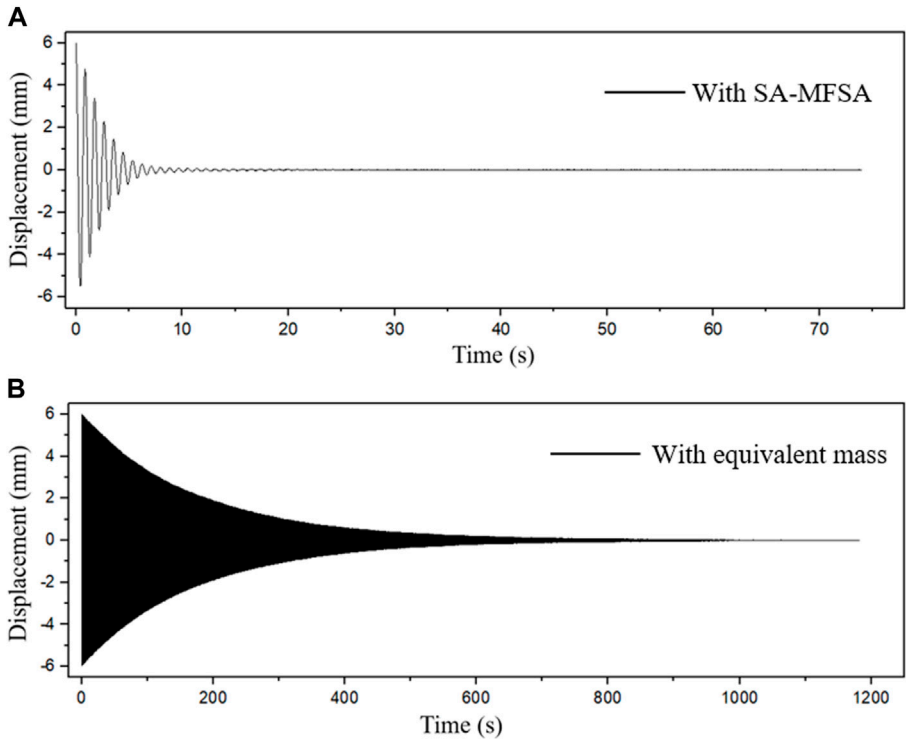

FIGURE 13
Displacement responses for initial excitation. **(A)** Response curve with VS-MFSA. **(B)** Response curve with equivalent mass.

TABLE 2 Comparison of the optimal magnetic fluid shock absorbers.

Year	Damper	Magnetic fluid mass	b*/a*
2022	Magnetic fluid shock absorber	22 g	1/70
2022	Magnetic fluid shock absorber	6 g	1/13
2022	Magnetic fluid shock absorber	25.5 g	1/7
2017	Magnetic fluid shock absorber		1/3
2016	Ferrofluid shock absorber		1/3
2013	Ferrofluid damper		1/3
2012	Magnetic fluid damper	27 g	1/3

a* the vibration decay time of the system with the equivalent mass.
b* the vibration decay time of the system with the optimal magnetic fluid shock absorber.

The experimental curves described the relationship between the repulsive force and the offset distance in Figure 9, which were measured by experimental apparatus in Figure 5. The offset distance was adjusted from 0 to 12 mm and the interval was 0.1 mm. Since the minimum reading of the dynamometer was 0.02N, all experimental curves started from the repulsive force equal to 0.02 N. The maximum amplitude of vibration reduction experiments was only 6mm, so actual offset distance would not exceed 6 mm. This ensured the distance between moving magnets and the static magnet was long enough. In this case, the repulsive force can be seen as linear with the offset distance, which means that the stiffness can be simplified to linear, as shown in Figure 8 and Figure 9. Therefore, the equation of stiffness coefficient can be approximated as:

$$F_m \approx K_2 x, \tag{11}$$

Where F_m is the repulsive force and x is the offset distance.

The simulation and experiment results of the stiffness coefficient with different rod lengths were calculated separately by equation Eq. 11. When rod length was equal to 108mm, the simulation and experiment resluts of the stiffness coefficient were 5.05N/m and 5.15N/m, respectively. Both results were close to the analytical solution 5.25N/m. At the same time, it can be seen from Figure 10 that the simualtion and experiment results were in good aggrement, especially when the rod lengths were taken from 96 to 108 mm. This illustrated that it was feasible to design VS-MFSA structure according to the optimal stiffness coefficient. The specific operation steps were: 1) First, through the theoretical model, the optimal stiffness coefficient was estimated. 2) Second, the VS-MFSA structure was designed based on simulation, which meant that adjusting the rod length made the optimal stiffness coefficient included within the rod length range. 3) Finally, the corresponding VS-MFSAs were fabricated and the correctness was verified by experimental apparatus in Figure 5.

Vibration reduction

The results of the vibration attenuation experiments were described in terms of the attenuation time and the attenuation amplitude, respectively. From the perspective of attenuation time, vibration attenuation rate η was introduced to quantify the damping efficiency of VS-MFSAs, of which the definition is as follow.t

$$\eta = 1 - \frac{T_n}{T_0}, \tag{12}$$

Where T_0 is the time taken by the equivalent mass when the amplitude decays to 2% of the initial amplitude, T_n is the time taken by the VS-MFSA when the amplitude decays to 2% of the initial amplitude.

It can be seen from Figure 8 and Figure 9 that by altering the connecting rod length the stiffness coefficient of VS-MFSAs was also changed. Besides, the stiffness coefficient of VS-MFSAs with different connecting rod length can be calculated by Eq. 11. Therefore, the relationship between damping efficiency and stiffness coefficient can be expressed by the following curves of damping efficiency versus rod length. Figure 11 depicts the relationship between vibration attenuation rate and rod length under different amount of MF. It is obvious that vibration attenuation rate increased with rod length becoming longer. In addition, it reached maximum value as rod length taken 108 mm and would slightly decrease when rod length exceeded 108 mm. Regarding the amount of MF, the following two points were mainly considered. First, in order to ensure the stable suspension of the working unit, MF mass should be greater than minimum critical value. Second, if using too much MF, the moving magnet couldn't fully adsorb MF and the extra MF might be bad for the performance of VS-MFSAs. Therefore, we chose 7–15 g MF on each moving magnet for experiments. It is observed that when MF ranged from 7 to 11 g, vibration attenuation rate continuously enhanced, which meant energy consumption became faster with more MF. However, when MF exceeded 11 g, vibration attenuation rate began to decrease. This was because too much MF hindered the working unit movement, which was detrimental to the damping performance.

According to the attenuation amplitude, logarithmic decay rate, another dimensionless number was used to quantify the damping efficiency of VS-MFSAs, of which the calculation equation is as below.

$$\delta = \frac{1}{i} ln\left(\frac{A_0}{A_i}\right), \tag{13}$$

Where A_0 is the initial amplitude, A_i is the amplitude of ith oscillation and i is equal to 5.

Figure 12 represents the dependence of logarithmic decay rate on rod length with different MF mass. Just like vibration attenuation rate, logarithmic decay rate also increased with rod lengthened. In the rod length range of 100–108 mm, logarithmic decay rate grew rapidly, but it dropped slowly as rod length longer than 108 mm. The peak of logarithmic decay rate also occurred at rod length equal to 108 mm. As for the effect of MF mass on logarithmic decay rate was basically the same as that on vibration attenuation rate. In general, both vibration attenuation rate curve and logarithmic decay rate curve proved that the VS-MFSA presented the best damping performance with rod length taken 108 mm.

From the above experiment curves, it can be concluded that the connecting rod length and the MF mass significantly influenced the performance of VS-MFSAs. As a result, the VS-MFSA possessed the best damping performance with rod length taken 108 mm and MF equal to 11 g. In other words, when the rod length was adjusted to make the VS-MFSA got the optimal stiffness coefficient, the corresponding VS-MFSA performed best. Therefore, the refined optimal stiffness formula can guide the design of MFSAs. The vibration decay time of this optimal VS-MFSA was 9.27s and its vibration attenuation rate was up to 98.7%. Figure 13 shows displacement responses for initial excitation with the optimal VS-MFSA or equivalent mass, respectively. It is clearly that the vibration decay time in Figure 12A was only a seventieth compared with the decay time in Figure 12B.

Through the ratio b*/a*, our proposed VS-MFSA was contrasted with the previous similar MFSAs. It can be seen from Table 2 that the damping performance of our proposed VS-MFSA was significantly better than that of MFSAs mentioned in other references. This strongly suggested that stiffness coefficient had great influence on the performance of MFSAs so that the damping efficiency of the VS-MFSA with optimal stiffness was remarkably improved.

Conclusion

The vibration problem of spacecraft flexible structure is the key issue obstructing advance in aerospace technology. The MFSA is one of the potential candidates for suppressing such vibration. In order to improve the damping performance of MFSAs, a new VS-MFSA was designed based on the stiffness coefficient formula. The specific conclusions were as follow.

1) According to the theoretical analysis of stiffness coefficients of other passive dampers, the stiffness coefficient formula which was suitable for MFSAs was got. Besides, the optimal stiffness coefficient was estimated to be equal to 5.25 N/m. Then, this value can guide the design of MFSAs.
2) A novel VS-MFSA was proposed, which possessed the varying stiffness by changing the connecting rod length. On the basis of 3D-printing, a series of VS-MFSAs were fabricated and their stiffness coefficient included the optimal value.
3) The repulsive force measurement was both simulated and verified by experiments. The simulation and experiment curves were in good agreement. Moreover, the relationship between the repulsive force and offset distance was linear in the small displacement section. It indicated that the rod length corresponding to the optimal stiffness coefficient can be decided by simulation first for subsequence experiments.
4) The vibration attenuation experiments were carried out and the damping performance of VS-MFSAs was evaluated by the vibration attenuation rate and logarithmic decay rate. As a result, the rod length had a significant influence on the damping efficiency of VS-MFSAs, which meant the stiffness coefficient played an important role in damping performance of VS-MFSAs. It was obvious that VS-MFSA with the optimal stiffness coefficient had the best damping performance.

In summary, the optimal stiffness coefficient can well guide the design of MFSAs. It is hope that the refined stiffness coefficient formula proposed by us can be applied in other liquid dampers in the future.

Data availability statement

The original contributions presented in the study are included in the article/supplementary material, further inquiries can be directed to the corresponding author.

Author contributions

YaL: Conceptualization, Methodology, Validation, Formal analysis, Investigation, Data Cleansing, Writing, Review, Editing. DL: Funding Acquisition. YiL: Investigation, Writing.

Funding

This work was supported by the National Natural Science Foundation of China (Grant No. 51735006, 51927810 and U1837206) and Beijing Municipal Natural Science Foundation (Grant No. 3182013).

Conflict of interest

Author Yingsong Li is employed by China Productivity Center for Machinery Co., Ltd.

The remaining authors declare that the research was conducted in the absence of any commercial or financial relationships that could be construed as a potential conflict of interest.

Publisher's note

All claims expressed in this article are solely those of the authors and do not necessarily represent those of their affiliated organizations, or those of the publisher, the editors and the reviewers. Any product that may be evaluated in this article, or claim that may be made by its manufacturer, is not guaranteed or endorsed by the publisher.

References

Bashtovoi, V. G., Kabachnikov, D. N., Kolobov, A. V., Samoylov, V., and Vikoulenkov, A. (2002). Research of the dynamics of a magnetic fluid dynamic absorber. *J. Magnetism Magnetic Mater.* 252, 312–314. doi:10.1016/s0304-8853(02)00599-1

Bibo, A., Masana, R., King, A., Li, G., and Daqaq, M. (2012). Electromagnetic ferrofluid-based energy harvester. *Phys. Lett. A* 376 (32), 2163–2166. doi:10.1016/j.physleta.2012.05.033

Coulombre, R. E., Schnee, L., and d'Auril, H., *Feasibility study and model development for a ferrofluid viscous damper*. Final report, contract No. NASS-9431, goddard space flight centre, Greenbelt, Maryland. Available at: https://ntrs.nasa. gov/citations/19680021013,1967.

Choi, Y., Ju, S., Chae, S. H., Jun, S., and Ji, C. H. (2015). Low-frequency vibration energy harvester using a spherical permanent magnet with controlled mass distribution. *Smart Mat. Struct.* 24 (6), 065029. doi:10.1088/0964-1726/24/6/065029

Hu, Y., Geng, Y., and Wu, B. (2020). Flexible spacecraft vibration suppression by distributed actuators. *J. Guid. Control, Dyn.* 43 (11), 2141–2147. doi:10.2514/1.g005190

Javanbakht, M., Cheng, S., and Ghrib, F. (2018). Refined damper design formula for a cable equipped with a positive or negative stiffness damper. *Struct. Control Health Monit.* 25 (10), e2236. doi:10.1002/stc.2236

Jiang, J., and Li, D. (2010). Optimal placement and decentralized robust vibration control for spacecraft smart solar panel structures. *Smart Mat. Struct.* 19 (8), 085020. doi:10.1088/0964-1726/19/8/085020

Jiang, J. P., and Li, D. X. (2011). Robust Hꝏ vibration control for smart solar array structure. *J. Vib. Control* 17 (4), 505–515. doi:10.1177/1077546310370688

Li, Y., Han, P., Li, D., Chen, S., and Wang, Y. (2022). Typical dampers and energy harvesters based on characteristics of ferrofluids. *Friction*, 1–22. doi:10.1007/s40544-022-0616-7

Li, Y., and Li, D. (2022). Hexagonal Structure Enhancing Damping Efficiency Inspired by Tree Frogs. Available at: https://chemrxiv.org/engage/chemrxiv/article-details/62833f2f7087675cfb554c87.

Li, Y., and Li, D. (2022). The dynamics analysis of a magnetic fluid shock absorber with different inner surface materials. *J. Magnetism Magnetic Mater.* 542. doi:10.1016/j.jmmm.2021.168473168473

Moskowitz, R., Stahl, P., and Reed, W. R. Inertia damper using ferrofluid, United States patent US 19784123675 (1978).

Ohno, K., and Sawada, T. (2010). An effect of vertical sloshing on a fluid pressure and a surface displacement in a tuned magnetic fluid damper. *Int. J. Appl. Electromagn. Mech.* 33 (3-4), 1411–1416. doi:10.3233/jae-2010-1268

Ohno, K., Shimoda, M., and Sawada, T. (2008). Optimal design of a tuned liquid damper using a magnetic fluid with one electromagnet. *J. Phys. Condens. Matter* 20 (20), 204146. doi:10.1088/0953-8984/20/20/204146

Ohno, K., Suzuki, H., and Sawada, T. (2011). Analysis of liquid sloshing of a tuned magnetic fluid damper for single and co-axial cylindrical containers. *J. Magnetism Magnetic Mater.* 323 (10), 1389–1393. doi:10.1016/j.jmmm.2010.11.052

Rabinow, J. (1948). The magnetic fluid clutch. *Transactions of the American Institute of Electrical Engineers* 67, 1308–1315. doi:10.1109/T-AIEE.1948.5059821

Rosensweig, R. E. (1966). Buoyancy and stable levitation of a magnetic body immersed in a magnetizable fluid. *Nature* 210 (5036), 613–614. doi:10.1038/210613a0

Rosensweig, R. E. (1987). Magnetic fluids. *Annu. Rev. Fluid Mech.* 19 (1), 437–461. doi:10.1146/annurev.fl.19.010187.002253

Seol, M., Jeon, S., Han, J., and Choi, Y. K. (2017). Ferrofluid-based triboelectric-electromagnetic hybrid generator for sensitive and sustainable vibration energy harvesting. *Nano Energy* 31, 233–238. doi:10.1016/j.nanoen.2016.11.038

Sun, S., Deng, H., Du, H., Li, W., Yang, J., Liu, G., Alici, G., and Yan, T. (2015). A compact variable stiffness and damping shock absorber for vehicle suspension. *Ieee. ASME. Trans. Mechatron.* 20 (5), 2621–2629. doi:10.1109/tmech.2015.2406319

Wang, H., Gao, H., Li, J., Wang, Z., Ni, Y., and Liang, R. (2021). Optimum design and performance evaluation of the tuned inerter-negative-stiffness damper for seismic protection of single-degree-of-freedom structures. *Int. J. Mech. Sci.* 212, 106805. doi:10.1016/j.ijmecsci.2021.106805

Weber, F., Boston, C., and Maślanka, M. (2010). An adaptive tuned mass damper based on the emulation of positive and negative stiffness with an MR damper. *Smart Mat. Struct.* 20 (1), 015012. doi:10.1088/0964-1726/20/1/015012

Xu, Z. D., Yang, Y., and Wu, R. (2021). Experimentally-verified micromechanical model of MR gels based on planar current loop model. *J. Eng. Mech.* 147 (8), 04021044. doi:10.1061/(asce)em.1943-7889.0001952

Yang, Y., Xu, Z. D., Guo, Y. Q., Sun, C., and Zhang, J. (2021). Performance tests and microstructure-based sigmoid model for a three-coil magnetorheological damper. *Struct. Control Health Monit.* 28 (11), e2819. doi:10.1002/stc.2819

池田健, 五. 百. 井. 俊. 宏. 減衰を有する振動系の動吸振器につい. 日本機械学會論文集 (1977) 43(369): 1707–1715.

frontiers | Frontiers in Materials

TYPE Original Research
PUBLISHED 03 November 2022
DOI 10.3389/fmats.2022.1034127

OPEN ACCESS

EDITED BY
Xinglong Gong,
University of Science and Technology of China, China

REVIEWED BY
Xian-Xu Bai,
Hefei University of Technology, China
Jian Yang,
Anhui University, China
Ying-Qing Guo,
Nanjing Forestry University, China

*CORRESPONDENCE
Mingfu Wen,
mfwen@stu.edu.cn
Xiaodong Niu,
xdniu@stu.edu.cn

SPECIALTY SECTION
This article was submitted to Smart Materials,
a section of the journal
Frontiers in Materials

RECEIVED 01 September 2022
ACCEPTED 21 October 2022
PUBLISHED 03 November 2022

CITATION
Wen M, Du Y, Liu R, Li Z, Rao L, Xiao H, Ouyang Y and Niu X (2022), Characterization of magnetorheological fluids based on capillary magneto-rheometer.
Front. Mater. 9:1034127.
doi: 10.3389/fmats.2022.1034127

Characterization of magnetorheological fluids based on capillary magneto-rheometer

Mingfu Wen*, Yueqian Du, Runduo Liu, Zeqin Li, Longshi Rao, Hongwei Xiao, Yi Ouyang and Xiaodong Niu*

Department of Mechanical Engineering, College of Engineering, Shantou University, Shantou, China

Magnetorheological fluids (MRFs) are a class of smart magnetic controlled materials whose rheological properties can be controlled by a magnetic field. These materials have advantages of short response time, high dynamic range and low energy consumption. Due to their excellent properties, MRFs have a widely application potential in the field of impact mitigation. As the shear rate dependent viscosity of MRFs is astonishing for the shear thinning effect, thus it is crucial to study the rheological properties cross a wide range of shear rates for guiding the design and application of MRFs based adaptive impact absorbers. Commercial rotational rheometers are usually used to test the rheological properties of MRFs, but their range of measuring shear rates are limited. Commercial capillary rheometers are designed to measure the rheological behavior over a wide range of shear rates, but they're usually lack of ability to measure with magnetic field. In order to study the rheological properties of MRFs under higher shear rate and applied magnetic field, a lab-made speed-controlled capillary magneto-rheometer is developed in the presnt work; The expressions for equivalent shear rate and apparent viscosity of MRFs under the dimensional constraint of the set-up are derived. In addition, the theoretical expression of shear rate of MRFs is modified by Rabinowitsch correction. Then, the rheological properties of three particle volume fractions (10%, 15%, and 20%)of MRFs with different magnetic field strengths (6 mT, 13 mT, 20 mT, and 25 mT)are tested and analyzed, and the rheological characteristic curves of MRFs with shear rate range of $10^1 s^{-1}$–$10^5 s^{-1}$ are obtained with the normalized characterization using Mason number. According to the experimental results, the MRFs show an obvious shear thinning phenomenon as shear rate increases, and in the Mason number based normalized characterization, the curves of different particle volume fractions are collapse to a master curve.

KEYWORDS

magnetorheological fluids, capillary magneto-rheometer, high shear rate, viscosity, mason number

1 Introduction

Magnetorheological fluids (MRFs) are a class of smart materials composed of micro soft ferromagnetic or paramagnetic particles dispersed in a carrier fluid, whose rheological properties can be controlled when stimulated with magnetic field (Rabinow., 1948; Kolekar et al., 2014; Kamble et al., 2015). When there is no external magnetic field, it exhibits like a Newtonian fluid with low viscosity. However, under the application of an external magnetic field, it exhibits like a Non-Newtonian fluid, and phase changes from a free-flowing liquid to a semi-solid or even a solid in a milliseconds level time, showing strong controllable rheological characteristics. This phenomenon is characterized by low energy consumption, easy control, reversible and rapid response (Carlson et al., 1996). Based on the above advantages, MRFs have attracted the research attention of many scholars in the field of impact mitigation applications over a large range of shear rate. Therefore, the study on the rheological characteristics of MRFs has a great guiding significance in device design and engineering application (Yang et al., 2002).

Rotational rheometers (Becnel et al., 2014) and capillary rheometers (Allebrandi et al., 2019) are usually used to measure the rheological properties of polymers. The rotational rheometers are the most widely used type of rheometer, which are used to measure the rheological properties of fluids at low shear rates. The capillary rheometers are used to measure the shear viscosity at high shear rates. It is divided into speed-controlled and pressure-controlled. The maximum shear rate of commercial rotational rheometers is usually below $10^5/s$, and some capillary rheometers can reach $10^7/s$. However, these lack the ability to apply a magnetic field. So, it is necessary to develop high shear rate rheometers with an applied magnetic field to study the rheological properties of magnetic liquids. Fernando (Goncalves et al., 2005) utilized a capillary rheometer to investigate the impact of residence time in the field on the degree of establishment of MRFs formation, when the shear rate range was 0.14×10^1–$2.5 \times 10^5/s$. Allebrandi (Allebrandi et al., 2019) designed an ultra-high shear rate rheometer with a magnetic field to measure the rheological properties of magnetic liquids at shear rates between 10^4–$1.16 \times 10^6/s$. Tammaro (Tammaro et al., 2021) designed of a microcapillary rheometer that allows to perform experiments rapidly and in a broad range of shear rates (i.e., from 10^{-1}–$10^3/s$), using small amounts of material (i.e., just few milligrams). In the study of rheological properties of polymers, in order to correlate the characterization of rheological features in the experiment under both low and high shear rates, Mason number (Klingenberg et al., 2007; Ruiz-López et al., 2017) is often used to produce the master curve representing the law of the experimental data with a dimensionless way, so as to achieve more accurately depicting the rheological properties of MRFs.

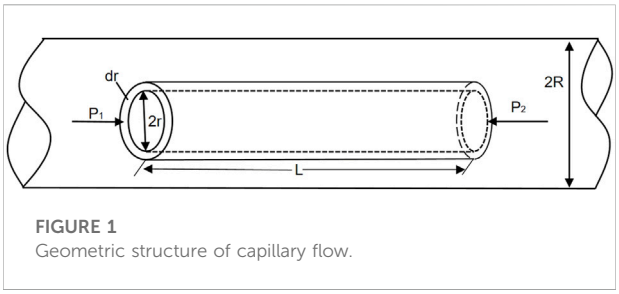

FIGURE 1
Geometric structure of capillary flow.

In this paper, a lab-made speed-controlled capillary magneto-rheometer was developed for rheological characterization of MRFs. It was utilized for testing the rheological properties of MRF prepared with different volume fractions and stimulated with different magnetic fields over a shear rates range from $10^1 s^{-1}$ to $10^5 s^{-1}$. Normalized rheological characteristics based on Mason number are conducted, and the corresponding characteristic curves were obtained and analyzed.

2 Principle and structure

2.1 Principle and structure of capillary rheology

A capillary magneto-rheometer proposed for characterizing the rheological properties of MRFs over a large range of shear rates and a lab-made prototype was built and employed in the experiments. The structure of the capillary channel can be simplified as shown in Figure 1.

The following five assumptions are made before deducing the equation of capillary rheological properties:

(1) Unidirectional shear;
(2) Laminar flow (no bubbles are produced during the flow);
(3) Wall adherence;
(4) Isothermal flow;
(5) Incompressible flow.

As shown in Figure 1, the Navier-Stokes equation (N-S equation) for the viscous fluid in the laminar flow inside a horizontal straight circular pipe with uniform pipe diameter is:

$$(\nabla \cdot \boldsymbol{v})\boldsymbol{v} + \frac{\partial \boldsymbol{v}}{\partial \boldsymbol{t}} = \boldsymbol{f} - \frac{\mathbf{1}}{\boldsymbol{\rho}}\nabla \boldsymbol{P} + \frac{\boldsymbol{\eta}}{\boldsymbol{\rho}}\nabla^2 \boldsymbol{v}, \quad (1)$$

where f is volume force on a fluid, P is pressure, v is velocity.

For a horizontal circular tube, the force of gravity on the fluid can be ignored and only the axial velocity is considered. By assuming that the continuity equation is satisfied, the pressure difference between two ends is constant and the fluid moves steadily, then the N-S equation can be simplified as:

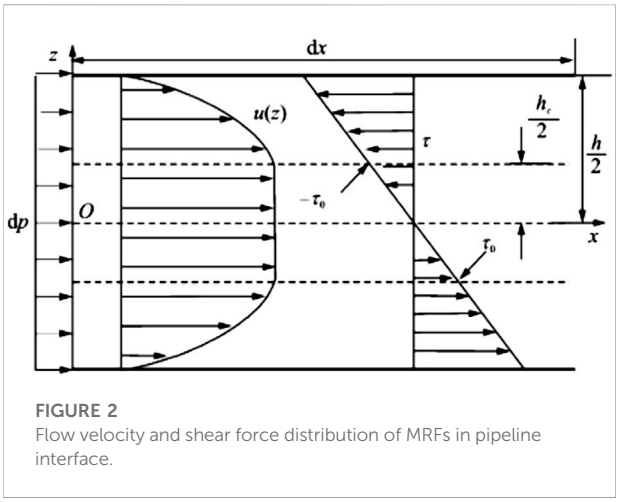

FIGURE 2
Flow velocity and shear force distribution of MRFs in pipeline interface.

$$\eta\nabla^2 \boldsymbol{v} - \nabla \boldsymbol{P} = \boldsymbol{0}. \tag{2}$$

According to the selected column coordinate system, z is the axial coordinate, r is the radial coordinate, then:

$$\begin{cases} \dfrac{\partial \boldsymbol{P}}{\partial \boldsymbol{r}} = \boldsymbol{0} \\ \dfrac{\partial^2 \boldsymbol{v}}{\partial \boldsymbol{r}^2} + \dfrac{\boldsymbol{1}}{\boldsymbol{r}} \dfrac{\partial \boldsymbol{v}}{\partial \boldsymbol{r}} = \dfrac{\boldsymbol{1}}{\boldsymbol{\eta}} \dfrac{\partial \boldsymbol{P}}{\partial \boldsymbol{z}} \end{cases}. \tag{3}$$

Figure 2 shows the distribution of pressure, velocity and shear force in the longitudinal cross profile of the pipeline. According to the boundary conditions and initial conditions, the integral of the above equation gives the following velocity profile:

$$\boldsymbol{v} = \frac{\Delta \boldsymbol{P}}{\boldsymbol{4\eta^* L}} \left(\boldsymbol{r_0^2} - \boldsymbol{r^2}\right). \tag{4}$$

Where η is viscosity, L is the length of capillary tube, r is radius of capillary tube.

With Eq 4, the quantitative relationships among volume flow Q, aspect ratio of pipe, outlet and inlet pressure difference, viscosity and shear rate can be described by Poiseuille's law:

$$\boldsymbol{Q} = \frac{\pi \boldsymbol{r_0^4}}{\boldsymbol{8\eta^* L}} \Delta \boldsymbol{P}. \tag{5}$$

According to the principle of pipe geometry and fluid mechanics, the shear rate at the wall is then calculated as:

$$\boldsymbol{\gamma} = \frac{\boldsymbol{dv}}{\boldsymbol{dr}} = \frac{\boldsymbol{4Q}}{\boldsymbol{\pi r_0^3}}, \tag{6}$$

and the shear force at the corresponding wall is given by:

$$\boldsymbol{\tau} = \frac{\Delta \boldsymbol{P^* \pi r_0^2}}{\boldsymbol{2\pi r_0^* L}} = \frac{\boldsymbol{r_0^* \Delta P}}{\boldsymbol{2L}} = \frac{\boldsymbol{\Delta P}}{\boldsymbol{4\dfrac{L}{D}}}. \tag{7}$$

Where D is the diameter of capillary tube.

Finally, according to the shear force and shear rate, the apparent viscosity can be described as:

$$\boldsymbol{\eta} = \frac{\boldsymbol{r_0^* \Delta P}}{\boldsymbol{2\gamma^* L}}. \tag{8}$$

Considering the actual geometry of the capillary tube and working conditions of magneto-rheometer, it is necessary to modify the calculation models to get the more accurate shear rate. Therefore, Rabinowitsch should be applied for the flow model, and reliable viscosity data can be obtained when these corrections are applied.

The Rabinowitsch correction:

$$\boldsymbol{\gamma_{true}} = \boldsymbol{\gamma_{app}} \left(\frac{\boldsymbol{3n+1}}{\boldsymbol{4n}}\right) = \frac{\boldsymbol{4Q}}{\boldsymbol{\pi r_0^3}} \left(\frac{\boldsymbol{3n+1}}{\boldsymbol{4n}}\right), \tag{9}$$

where γ_{true} is the corrected shear rate, γ_{app} is the calculated shear rate from the measured flow rate, n is the rheological index. The rheological index n is a parameter related to the material properties and the strength of the applied magnetic field. The rheological index varies with different magnetic field strengths and composition of MRFs.

In order to validate the Rabinowitsch correction for the shear rates in capillary tube, a finite element simulation of capillary flow based on COMSOL Multiphysics was conducted. The comparison of the shear rates estimated in different methods are shown in Table 1. In the simulations, the shear rates in first column were calculated from the given inlet flow rate using Eq 6, the shear rates in second column were calculated from the given inlet flow rate using the Rabinowitsch correction Eq 9, and the shear rates in third column were calculated from the outlet flow rate using Eq 6. According to the comparison results, it can be obtained that the accuracy of shear rates estimated after Rabinowitsch correction have been improved significantly.

2.2 Principle of viscosity calculation

In this paper, the theoretical magnetic response viscosity of MRFs with different magnetic field stimulations are calculated based on the theoretical equation.

The viscosity of particle suspension can be obtained by Einstein equation (Vand, 1945):

$$\boldsymbol{\eta_0} = \boldsymbol{\eta_b}\left(\boldsymbol{1} + \boldsymbol{2.5\phi}\right), \tag{10}$$

where η_b is the base fluid viscosity, and ϕ is the particle volume fraction. Here the Rosensweig's improved equation (Chi et al., 1993) is employed for larger particle volume concentration:

$$\boldsymbol{\eta_0} = \frac{\boldsymbol{\eta_b}}{\boldsymbol{1 + b\phi + c\phi^2}}, \tag{11}$$

where b and c are the coefficients identified under test. According to the fitting calculation, $b = -5.04$ and $c = 7.09$ is adopted for the lab-prepared MRFs in this paper.

TABLE 1 Comparison of the shear rates estimated in different methods.

Shear rates estimated from given inlet flow (1/s)	Shear rate estimated from the modified formula (1/s)	Shear rates estimated from outlet flow (1/s)
32.0	46.2	46.8
217	313	316
4,350	6,280	6,400
10,100	14,600	14,800
90,000	130,000	132,000

In the presence of an applied magnetic field, the increment of the magnetic response viscosity of MRFs relative to the zero-field viscosity can be calculated by the following equation; (Chen, 2007; Zuo, 2018):

$$\eta_{mag} - \eta_0 = \eta_0\left(\frac{3}{2}\phi\frac{0.5\alpha L(\alpha)}{1+0.5\alpha L(\alpha)}sin^2\beta\right), \tag{12}$$

according to the Langevin function:

$$M = M_p L(\alpha),\ \alpha = \frac{\pi d_p^3 \mu_0 H M_p}{6k_0 T},\ L(\alpha) = coth\,\alpha - \frac{1}{\alpha}, \tag{13}$$

the expression of magnetic response viscosity is simplified as follows:

$$\eta_{mag} = \eta_0 + \eta_0\left(\frac{3}{2}\frac{1}{\frac{1}{\phi}+\frac{12\kappa_0 T}{\pi d_p^3 \mu_0 H M}}\right), \tag{14}$$

where M_p is the Magnetization of solid particles, ϕ is the particle volume fraction, κ_0 is the Boltzmann's constant, $\kappa_0 = 1.38 \times 10^{-23} J/K$, T is the Absolute temperature, d_p is average diameter of aggregate molecules, μ_0 is the Vacuum permeability, H is external magnetic field strength, M is magnetization of MRFs, β is the Angle between the magnetic liquid vortex vector and the direction of the applied magnetic field.

3 Experimental

3.1 Experimental set-up

In order to describe the rheological properties of MRFs under high shear rate, a speed-controlled capillary rheometer was developed in this paper. The capillary rheometer is available to measure the apparent viscosity of materials in a wide range of shear rates by adjusting the capillary diameter and pressure/velocity in testing and studying the rheological properties of MRFs. The capillary tube can be divided into three parts: entrance development channel, damping channel and exit channel. In order to generate a completely laminar flow and reduce the influence of the inlet on pressure measurement, an injection inlet of the MRFs was utilized at the entrance channel

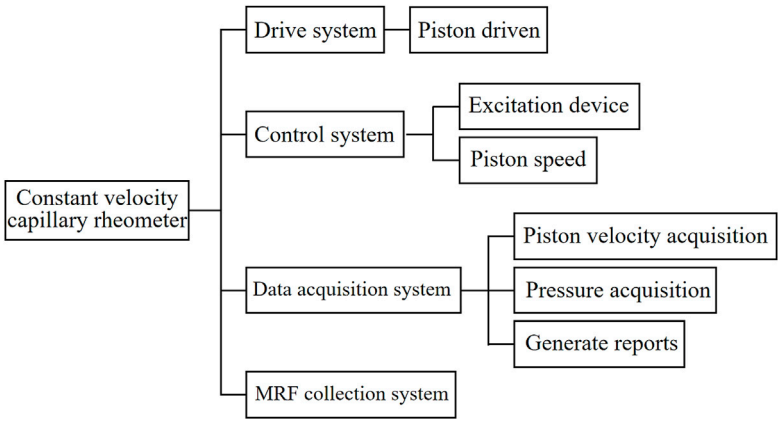

FIGURE 3
Principle structure block diagram of lab-made speed-controlled capillary rheometer.

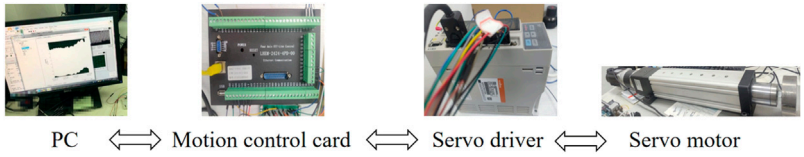

FIGURE 4
Composition of control system.

FIGURE 5
Composition of data acquisition.

and the measuring position is located in the damping channel of the rheometer. Generally, a magnetic field is applied in this section of the pipeline and a pressure sensor is installed; The outlet channel is used to drain the MRFs and recover it. The flow medium to be measured is injected into the capillary tube at different speeds under different magnetic field excitations to form a certain range of shear rate ($10^1 s^{-1}$–$10^5 s^{-1}$), the pressure difference and the flow rate at both ends of the capillary tube are measured to calculate the rheological characteristic curves of the flow medium to be measured.

The lab-made speed-controlled capillary magneto-rheometer mainly consists of four systems: Drive system, control system, data acquisition system and MRFs collection system. The construction scheme of the experimental set-up is shown in Figure 3:

The composition of the control system is shown in Figure 4, including PC, motion control card, servo driver and servo cylinder. Both control and data acquisition systems are achieved by programming with Labview. The PC side is connected with network cable, programmed with LabView, and handled the motion control card by calling the dynamic link library DLL function; The LHEM-2424-4PD-00 motion control card is adopted, which is equipped with network cable interface, USB interface and RS485 serial port. It has 24 IO input ports and 16 IO output ports, and it is able to carry out 4-axis operation control at the same time; ASD620B series Servo driver was adopted which can be used for speed control, position control and torque control; The model of servo motor with the ability of self-locking is 80ST-M02430A-N, whose maximum speed and minimum speed are 5,000 r/min and 1r/min,

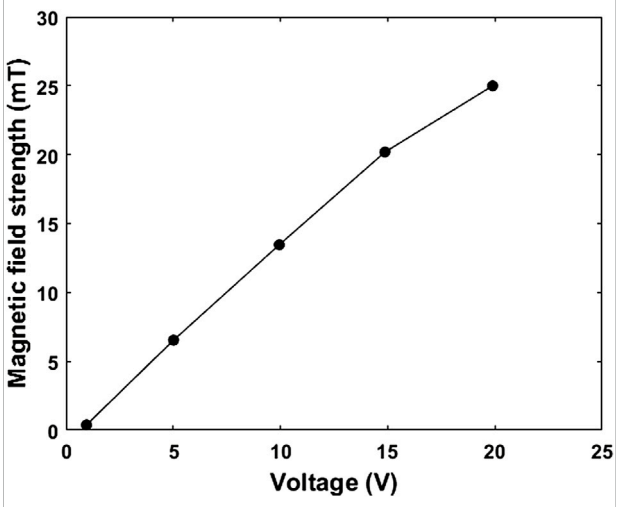

FIGURE 6
The magnetic field strength of Helmholtz coil varies with the output voltage of power supply.

respectively. The power supply is controlled by the servo driver, and the motor rotation angle is recorded by the encoder. The motor shaft is connected to an electric cylinder, which converts rotational motion into linear motion and pushes the needle piston into injection.

The composition of the data acquisition system is shown in Figure 5, which includes pressure sensors on both sides of the pipeline, flowmeters, and NI data acquisition cards. The

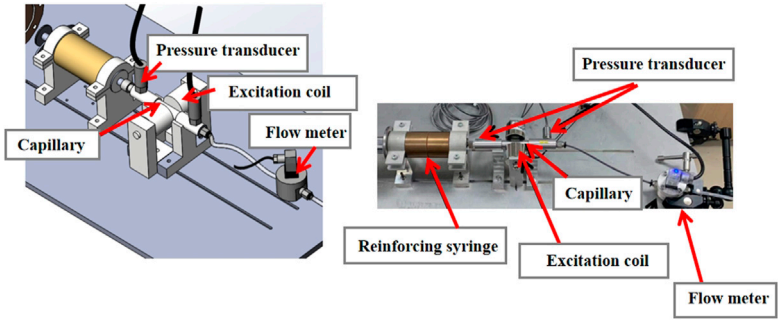

FIGURE 7
Structure diagram of lab-made speed-controlled capillary rheometer.

data acquisition card collects the voltage and pulse signal of the sensors, reads the signal in the Labview control panel and outputs with data table.Two pipe pressure sensors and a ring pressure sensor are used in this experimental system. Two pipeline pressure sensors are Aier AE-S series micro high-frequency dynamic pressure transmitters, with a range of 0–3.5 and 0–40 MPa, with an accuracy of ±0.25% of full scale. The annular pressure sensor is installed at the end of the push rod of the electric cylinder to measure the thrust of the push rod. The pressure measurement range is 30 KN and the measurement accuracy is ± 0.05%. The flowmeter is a small flow elliptical gear flowmeter, whose measurement range is 0.5–150 ml/min with a measurement accuracy of 0.2%. A Helmholtz coil is used to provide a stable magnetic field for the experiments. The Helmholtz coil has a cylindrical region with a height range of 0.8R and a radius range of 0.3R.

Using a programmed DC power supply with a maximum output voltage of 24 V, the magnetic field strength at the center of the Helmholtz coil is measured with a gaussmeter, and the variation curve of the magnetic field strength with the output voltage of the power supply is shown in Figure 6:

The four voltages selected for the experiment are 5, 10, 15, and 20 V, and the corresponding magnetic field strengths are 6, 13, 20, and 25 mT, respectively. The Helmholtz coils are arranged on both sides of the capillary tube, and a uniform magnetic field perpendicular to the pipe axis is applied to the capillary tube. The structure diagram and physical diagram of the lab-made capillary rheometer set-up finally built are shown in Figure 7 and Figure 8:

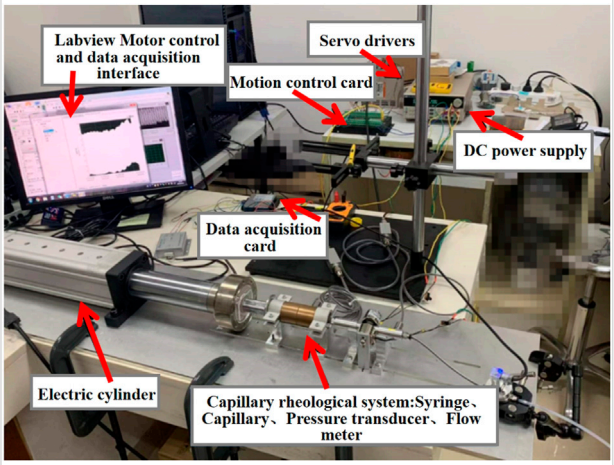

FIGURE 8
Physical picture of the test set-up.

3.2 Experiment

3.2.1 Experiment calibration

The given viscosity of a pure silicone oil and its measured viscosity using commercial rotary viscometer (SNB-2 Digital viscometer) are taken to compare for calibrating the lab-made capillary rheometer. Considering the given viscosity as standard, the corresponding mearsuring errors of the commercial rotary viscometer and the lab-made capillary rheometer were evaluated as shown in Table 2.

According to the comparison shown in Table 2, it can be obtained that the relative error measured by the commercial viscometer is 9.4% while the relative error measured by the lab-made capillary magneto-rheometer is 4.2%. Thus, the experimental data in the following subsections of this paper are all measured with the lab-made magneto-rheometer. The rheological properties of pure silicone oils were tested using the lab-made capillary rheometer at different shear rates, and the measured curves between shear stress and shear rate were obtained as shown in Figure 9. It can be seen that the relationship between shear stress and shear rate is linear, which satisfies the constant viscosity of pure silicone oil as a Newtonian fluid.

TABLE 2 Comparison of the viscosities obtained in different methods.

Given product parameters	The commercial rotary viscometer (SNB-2 digital viscometer)	Lab-made capillary experimental setup
0.971 (pa^*s)	0.88 (pa^*s)	0.93 (pa^*s)
—	9.4%	4.2%

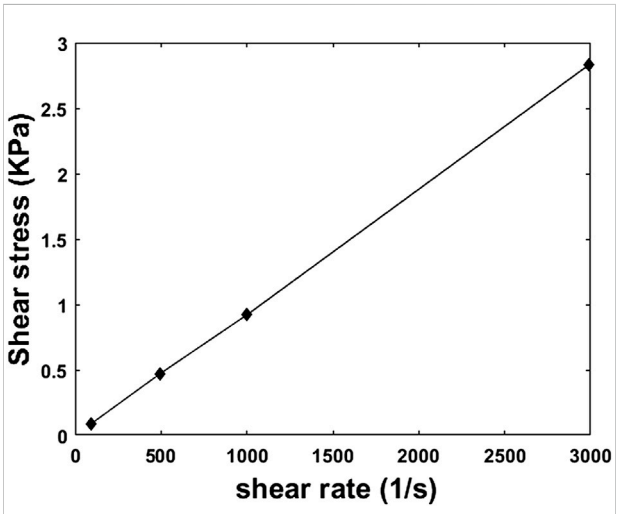

FIGURE 9
Relationship between shear stress and shear rate of silicone oil measured by the custom capillary rheometer.

TABLE 3 Mass fraction and zero field viscosity values of MRF with different volume fractions.

Volume fraction (%)	10	15	20
Mass fraction (%)	0.4747	0.5894	0.6703
Zero field viscosity (pa^*s)	1.69	2.43	3.54

3.2.2 Experimental study

In order to study the magnetorheological properties of MRFs over a large range of shear rate under magnetic field stimulation, a lab-made capillary magneto-rheometer is developed. The influence of different particle volume fraction and different magnetic fields on the rheological properties of MRFs over a large range of shear rate are experimentally studied. Among them, the selected MRF particle size is 2–3μm; The range of shear rate is 10^1s^{-1}–10^5s^{-1}, and the corresponding shear rates adopted in experiments are $4.62 \times 10^1s^{-1}$、$3.13 \times 10^2s^{-1}$、 $6.28 \times 10^3s^{-1}$, $1.46 \times 10^4s^{-1}$ and $1.30 \times 10^5s^{-1}$; Three MRFs with volume fractions of 10%, 15% and 20% are selected for testing, as shown in Table 3; Four magnetic fields with intensities 6, 13, 20 and 25 mT are selected for testing.

In the experiments, the calculated mass fraction values and measured zero field viscosity of MRFs with different volume fractions are also shown in Table 3.

In the experiments, the lab-made speed-controlled rheometer is employed to measure the pressure drop and flow rate at both ends of the capillary, and MRFs are prepared with different particle volume fractions. The shear force and viscosity are calculated by the pressure drop, flow rate and geometric dimension using the method described in Eq 7 and Eq 8. The effects of particle volume fraction and magnetic field excitation on the rheological characteristics of MRFs are experimentally studied.

When the tube flow rate is limited, the capillary with a smaller diameter should be chosen in order to achieve the shear rate 10^4s^{-1}–10^5s^{-1} according to the shear rate calculation Eq 9. The outer diameter shown in Table 4 is selected for adaptation in these experiments. The quartz glass capillary with small inner diameter is nested in the metal tube.

3.2.3 Experimental results and analysis

In the experiments, the pipeline pressure signals are collected and converted to obtain the pressure drop at steady state. The curves of shear stress and viscosity considering various influences (shear rate, volume fraction, magnetic field strength) were obtained experimentally. According to the geometry of capillary tube and fluid mechanics, the shear rate at the wall is determined with Eq 6.

In Figure 10, it is found that the internal pressure of the pipeline is too large for crystal tube when the shear rate exceeds 10^5s^{-1}. Therefore, in this work, we only discuss the situation of shear rates up to 10^5s^{-1}.

3.2.3.1 Rheological properties of MRFs in a wide range of shear rates

In order to describe the overall rheological characteristics of MRFs under the magnetic field stimulation over a large range of shear rate, an MR Fluids samlpe with volume fraction of 20% was prepared and tested under magnetic field of 25 mT and the rheological characteristic curve was obtained, as shown in Figure 10.

TABLE 4 The inner diameter and aspect ratio of the capillary used in the experiments.

Capillary section shape	Inner diameter (*mm*)	Length to diameter ratio-*L*/*D*
Circular	0.2	20
		30
		40
	0.4	20
		30
		40
	0.6	20
		30
		40

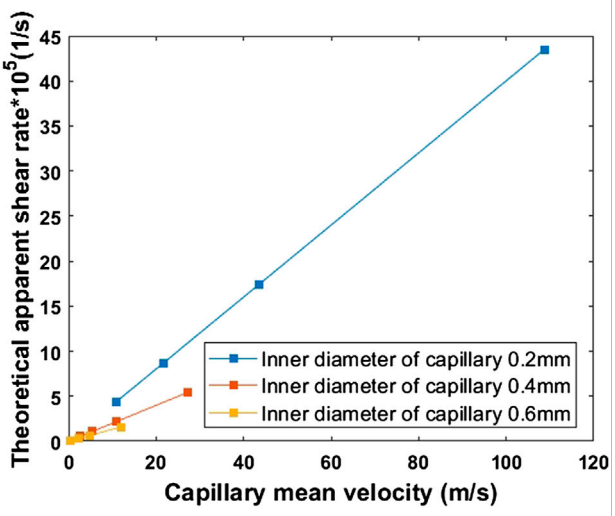

FIGURE 10
Relationship between mean velocity and theoretical apparent shear rate of capillary tubes with different inner diameters.

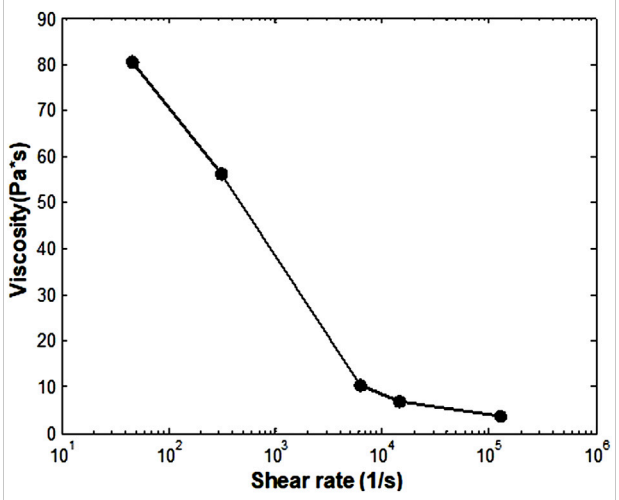

FIGURE 11
Apparent viscosity as a function of shear rate.

It can be seen from Figure 11 the apparent viscosity curve shows an obvious shear thinning phenomenon over $10^1 s^{-1}$–$10^5 s^{-1}$. When the shear rate is larger than $10^4 s^{-1}$, the phenomenon of shear thinning of the apparent viscosity is reduced, and the apparent viscosity is close to zero field viscosity (Table 3).

3.2.3.2 Influencing factors of apparent viscosity

The effects of the apparent viscosity in the non-Newtonian flow are usually described by the dimensionless Mason number (Sherman et al., 2015), which represents the relationship between fluid force F_τ and the couple force F_d of a single particle, that is, the relationship between the shear stress F_τ of MRFs and the microscopic magnetic force F_d:

$$Mn = \frac{F_\tau}{F_d} = \frac{9\eta_c\phi^2}{2\mu_0\mu_c}\frac{\gamma}{M^2}. \quad (15)$$

where η_c is the viscosity of carrier fluid, ϕ is the particle volume fraction of suspension, μ_0 is the vacuum permeability, μ_c is the permeability to the carrier fluids, and M is the overall magnetization. The Mason number demonstrate the connection between viscosity, shear rate, and magnetic field intensity, and this "data collapse" (Becnel et al., 2015) processing can explain how multiple factors interact to affect viscosity in a linear range. Compared with other conventional rheological characterization based on shear rate, the main advantage of normalized rheological characterization based on the Mason number is that a wide range of reliable rheological characteristic curves can be obtained through limited experiments, and the characteristic curves under different amplitudes can be folded and shrunk to one rheological master curve.

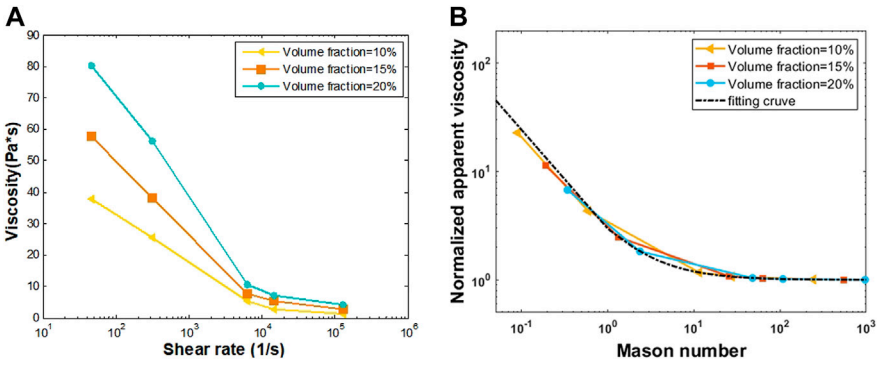

FIGURE 12
(A) The apparent viscosity *versus* apparent shear rate curves with different volume fraction under a magnetic field strength of 25 mT; **(B)** Apparent viscosity *versus* Mason number curves.

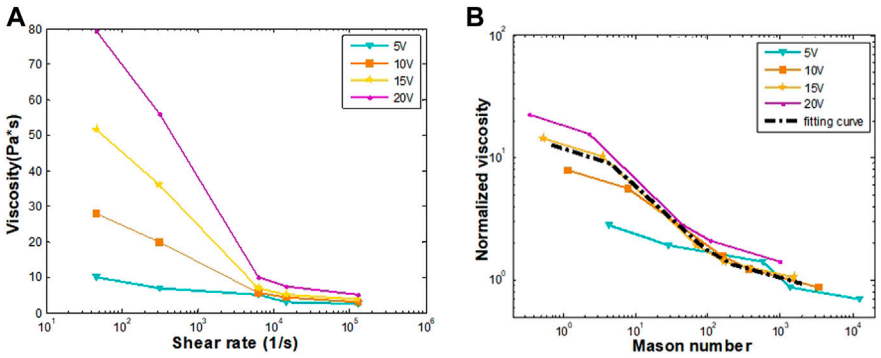

FIGURE 13
(A) The apparent viscosity *versus* apparent shear rate curves with different magnetic field intensities for 20% volume fraction MRFs; **(B)** Apparent viscosity *versus* Mason number curve.

When Mason number is used to normalize rheological curves, the following equation from can be used to fit the data (Becnel et al., 2015).

$$\eta_{app}/\eta_{\infty} = 1 + KMn^{-1}, \tag{16}$$

where η_{app} is the apparent viscosity, η_{∞} is the viscosity at high shear rates in the absence of an applied magnetic field, K is a fit parameter that can be expressed in terms of two physically relevant nondimensional ratios and is sometimes referred to in the literature as a "critical Mason number".

(1) Volume fraction

To investigate the effect of the volume fraction of MRFs on its rheological properties with a shear rate range over $10^1 s^{-1}$–$10^5 s^{-1}$, the rheological characteristic curves of MRFs with three different volume fractions under magnetic field stimulation of 25 mT are experimentally studied. The particle volume fractions of MRFs are 10%, 15% and 20%, respectively. The resulting curves are shown in Figure 12A.

It can be seen from Figure 12A, the phenomenon of shear thinning of magnetorheological fluid with different volume fractions appeared obviously. In specific, the shear thinning phenomenon is more obvious with the increase of particle volume fraction and this phenomenon is reduced when the shear rate higher than 4,000 s^{-1}. Under the same shear rate and magnetic field strength excitations, the larger the volume fraction, the higher the apparent viscosity.

The normalized apparent viscosity of MRFs with different volume fractions were calculated using Eq 16 and the Mason number of MRFs with different volume fractions were calculated using Eq 15. As shown in Figure 12B, the normalized rheological

characteristic curve is obtained. It can be seen that under the same magnetic field, the rheological characteristics of MRFs with different volume fractions keep the same trend and they're all approaching the formula fitting curve ($\eta_{app}/\eta_{\infty} = 1 + kMn^{-1}$).

(2) Magnetic field intensity

In order to study the effect of the magnetic field intensity of MRFs on its rheological properties with a shear rate range of $10^1 s^{-1}$–$10^5 s^{-1}$. The rheological characteristic curves under four different magnetic field intensities stimulation of MRFs with volume fraction of 20% are experimentally studied. The applied magnetic field intensities of MRFs are 6, 13, 20, and 25 mT, and the corresponding voltage excitations are 5, 10, 15, and 20, respectively. The resulting curves is shown in Figure 13A.

It can be seen from Figure 13A that when the samples are prepared with the same particle volume fraction and measured under the same shear rate, the greater the magnetic field strength, the higher the apparent viscosity; Under the condition of the same particle volume fraction, with the increase of shear rate, the apparent viscosity is lower, and the shear thinning phenomenon is more obvious with the increase of coil voltage. It is consistent with the conclusion of related field research.

In Figures 13A,B normalized characterization based on Mason number is conducted. The results show that the apparent viscosity curves obtained under different magnetic field intensities shrink to a master rheological curve. This feature allows us to reduce the number of tests in experiments, and it can be detected if one of the tests has abnormal error.

4 Conclusion

In order to study the rheological properties of MRFs within a wide shear rate range, a speed-controlled capillary magneto-rheometer is developed. The rheological properties of MRF over the shear rate range of $10^1 s^{-1}$–$10^5 s^{-1}$ are measured by the lab-made magneto-rheometer and the obtained rheological characteristic curves are normalized using Mason number. According to the experimental results, the shear thinning effect is observed over the whole shear rate range of $10^1 s^{-1}$–$10^5 s^{-1}$. The effects of particle volume fraction and magnetic field excitation on the rheological characteristics of MRFs are experimentally studied. In the Mason number based normalized characterizations, the master curves are obtained for different particle volume fractions and magnetic field strengths. According to the resulting curves of normalized apparent viscosity *versus* Mason number with different volume fractions, the obtained curves keep the same trend and they are all approaching the formula fitting curve ($\eta_{app}/\eta_{\infty} = 1 + 1.961/Mn$). In the normalized characterization with different magnetic field excitation, the obtained curves show that the apparent viscosity of MRFs is increased with the increase of applied magnetic field strength and preserve a common trend.

Data availability statement

The original contributions presented in the study are included in the article/Supplementary Material, further inquiries can be directed to the corresponding authors.

Author contributions

MW and XN contributed to conception of the study. MW, YD, and ZL organized the discussion and drafting. MW, ZL, and HX designed the experimental apparatus and took charge of the fabrication. RL, YD, LR, and YO conducted the modeling and experimental verification. YD wrote the first draft of the manuscript. MW and XN revised the manuscript and made the corrections. All authors contributed to manuscript revision, read, and approved the submitted version.

Funding

This research was supported by the STU Scientific Research Foundation (NTF20010, NTF19045) and the National Natural Science Foundation of China (NO. 12172203).

Conflict of interest

The authors declare that the research was conducted in the absence of any commercial or financial relationships that could be construed as a potential conflict of interest.

Publisher's note

References

Allebrandi, S. M., Van Ostayen, R. A. J., and Lampaert, S. G. E. (2019). Capillary rheometer for magnetic fluids. *J. Micromech. Microeng.* 30 (1), 015002. doi:10.1088/1361-6439/ab3f4c

Becnel, A. C., Hu, W., and Wereley, N. M. (2014). Mason number analysis of a magnetorheological fluid-based rotary energy absorber. *IEEE Trans. Magn.* 50 (11), 1–4. doi:10.1109/tmag.2014.2327634

Becnel, A. C., Sherman, S., Hu, W., and Wereley, N. M. (2015). Nondimensional scaling of magnetorheological rotary shear mode devices using the Mason number. *J. Magnetism Magnetic Mater.* 380, 90–97. doi:10.1016/j.jmmm.2014.10.049

Carlson, J. D., Catanzarite, D. M., and St. Clair, K. A. (1996). Commercial magneto-rheological fluid devices. *Int. J. Mod. Phys. B* 10, 2857–2865. doi:10.1142/s0217979296001306

Chi, C. Q., and Wang, Z. S. (1993). *Ferrofluid dynamics*. Beijing: Beijing University of Aeronautics and Astronautics Press (in Chinese).

Chen, M. (2018). *Numerical and experimental study of fluid-structure interference and enhanced heat transfer in MHD*. Shantou, China: Shantou University.

Chen, W. (2007). *Study on magnetorheological fluid for damping control of linear motor*. Guangzhou, China: Guangdong University of Technology. (in Chinese).

Daniele, T., Gaetano, D., Salvatore, C., Ernesto, D., Nino, G., and Maffettone, P. L. (2021). A microcapillary rheometer for microliter sized polymer characterization. *Polym. Test.* 102, 107332. doi:10.1016/J.POLYMERTESTING.2021.107332

Goncalves, F. D., and Ahmadian, M. (2005). A study on MR fluids subjected to high shear rates and high velocities. *Proc. Spie* 5760, 46–56. doi:10.1117/12.598530

Hu, W., and Wereley, N. M. (2011). Behavior of mr fluids at high shear rate. *Int. J. Mod. Phys. B* 25 (07), 979–985. doi:10.1142/S0217979211058535

Jha, S., and P, V. R. (2015). Design of parallel plate magnetorheometer for evaluating properties of magnetorheological polishing fluid. *Mater. Today Proc.* 2, 3251–3259. doi:10.1016/j.matpr.2015.07.134

Kamble, V. G., Kolekar, S., and Madivalar, C. (2015). Preparation of magnetorheological fluids using different carriers and detailed study on their properties. *Am. J. Nanotechnol.* 6 (1), 7. doi:10.3844/ajnsp.2015.7.15

Kang, L., Luo, Y., and Liu, Y. (2017). Testing device for rheological properties of magnetorheological fluid at high shear rate. *J. Fail. Anal. Preven.* 17 (3), 563–570. doi:10.1007/s11668-017-0277-4

Klingenberg, D. J., Ulicny, J. C., and Golden, M. A. (2007). Mason numbers for magnetorheology. *J. Rheology* 51 (5), 883–893. doi:10.1122/1.2764089

Kolekar, S. (2014). Preparation of magnetorheological fluid and study on its rheological properties. *Int. J. Nanosci.* 13 (02), 1450009. doi:10.1142/s0219581x14500094

Pieper, S., and Schmid, H. J. (2016). Guard ring induced distortion of the steady velocity profile in a parallel plate rheometer. *Appl. Rheol.* 26 (6), 18–24. doi:10.3933/applrheol-26-64533

Powell, L. A., Hu, W., and Wereley, N. M. (2013). Magnetorheological fluid composites synthesized for helicopter landing gear applications. *J. Intelligent Material Syst. Struct.* 24, 1043–1048. doi:10.1177/1045389X13476153

Rabinow, J. (1948). The magnetic fluid clutch. *Trans. Am. Inst. Electr. Eng.* 67, 1308–1315. doi:10.1109/T-AIEE.1948.5059821

Ruiz-López, J. A., Hidalgo-Alvarez, R., and De. Vicente, J. (2017). Towards a universal master curve in magnetorheology. *Smart Mat. Struct.* 26 (5), 054001. doi:10.1088/1361-665x/aa6648

Sherman, S. G., Becnel, A. C., and Wereley, N. M. (2015). Relating Mason number to Bingham number in magnetorheological fluids. *J. Magnetism Magnetic Mater.* 380, 98–104. doi:10.1016/j.jmmm.2014.11.010

Tammaro, D., D'Avino, G., Costanzo, S., Di Maio, E., Grizzuti, N., and Maffettone, P. L. (2021). A microcapillary rheometer for microliter sized polymer characterization. *Polymer Testing* 102, 107332.

Vand, V. (1945). Theory of viscosity of suspensions rigid spheres. *Nature* 155, 364–365. doi:10.1038/155364b0

Yang, G., Spencer, B. F., Jr, Carlson, J. D., and Sain, M. K. (2002). Large-scale MR fluid dampers: Modeling and dynamic performance considerations. *Eng. Struct.* 24 (3), 309–323. doi:10.1016/s0141-0296(01)00097-9

Zuo, Z. P. (2018). *Preparation of magnetic fluid oil filmbearing oil and experimental study onits lubricating properties*. Taiyuan, China: Taiyuan University of Science and Technology (in Chinese).

Frontiers in Materials

Investigates the discovery and design of materials for future application

A multidisciplinary journal that explores the breadth of materials science, engineering and mechanics - from carbon-based materials to smart materials.

Discover the latest Research Topics

See more →

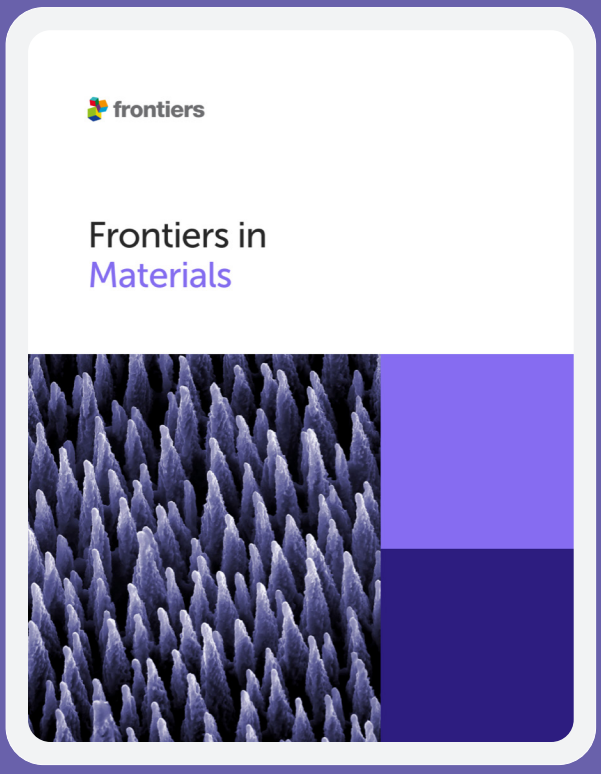

Frontiers

Avenue du Tribunal-Fédéral 34
1005 Lausanne, Switzerland
frontiersin.org

Contact us

+41 (0)21 510 17 00
frontiersin.org/about/contact